

Investigating the mechanism of action of the chemical probe QC6352



THE UNIVERSITY OF
SYDNEY

Jayden Sterling

A thesis submitted to fulfil requirements for the degree of
Doctor of Philosophy (Medicine)

Faculty of Medicine and Health

School of Medical Sciences

February 2024

The research reported in this thesis was supported by the award of a Research Training Program scholarship to the PhD Candidate.

For Felicia

Abstract

Glioblastoma, despite being the most aggressive form of brain cancer, has seen no significant advancement in patient survival rates since the introduction of the Stupp protocol in 2005. The stagnation in therapeutic progress highlights the complex challenges inherent to glioblastoma treatment, namely, a highly heterogeneous tumour population, an immunosuppressive microenvironment, and the restrictive blood-brain barrier. These challenges are compounded by a critical lack of robust data in preclinical studies, leading to suboptimal drug candidates that ultimately fail in clinical trials.

In a comprehensive systematic review of 662 primary-research articles, we assessed the adherence to expert-recommended practices in the use of chemical probes. Our findings revealed that only 4% of the analysed publications complied with the established guidelines. Improper use of chemical probes results in biased conclusions about the importance of certain proteins in disease models, embedding inaccurate information as the foundation for further drug development studies. Furthermore, the chemical probe QC6352, a known KDM4 inhibitor, was identified through the phenotypic screening of a library of epigenetic inhibitors to have potent antiproliferative efficacy in glioblastoma cells. While validating the antiproliferative efficacy of QC6352 in glioblastoma, discrepancies began to arise regarding the importance of KDM4 in QC6352's mechanism of action. Specifically, the orthogonal KDM4 inhibitor ML324 and KDM4-targeting siRNA molecules did not impact glioblastoma cell viability. By integrating diverse state-of-the-art investigations at the genomic, transcriptomic, and proteomic levels, a phenotype reflecting an activated MAPK pathway was identified and considered to result from the inhibition of PP5 by QC6352. To address the scarcity of orthogonal KDM4 inhibitors and find a potential replacement for QC6352, we developed a library of hydrazine-based analogues and evaluated these in KDM4A inhibition assays using AlphaScreen technology. A total of 83 compounds containing the promising hydrazine moiety were tested culminating in the most active compound, the p-isopropyl hydrazine **72**. After additional medicinal chemistry optimisations, such compounds may prove useful in future mechanistic studies focussing on the role of KDM4 in cancer.

This PhD thesis highlights the critical need in following best practice guidelines for preclinical mechanistic studies to establish robust findings and eliminate biased and potentially incorrect conclusions. If there is any realistic hope of obtaining improved glioblastoma therapies, it is crucial that the foundational research surrounding the novel target is derived from robust and well-controlled experiments.

Statement of originality

I hereby certify that, to the best of my knowledge, the content presented in this thesis is my own work. This document has not previously been presented for any academic qualification or for any other reason.

I certify that the intellectual contributions of this thesis are solely my own work and that and I have duly recognised any help or resources that have been utilised in its preparation.

Jayden Sterling

February 2024

Authorship contribution statement

This thesis contains previously published material by the author, Jayden Sterling.

Chapter 1: This contains sections from a published manuscript written during the author's PhD candidature wherein the author was a principal contributor to the writing and editing of the text. The manuscript was published in *International Journal of Cancer* (Sterling et al., 2020)¹. All other sections of the chapter were created entirely by the PhD candidate unless otherwise mentioned.

Chapter 2: The PhD candidate wrote the chapter and prepared the table. Dr. Lipin Loo assisted with writing sections 2.13.1 - 2.13.3. Dr. Sean Humphrey assisted with writing section 2.14.3.

Chapter 3: Publication in *Nature Communications* (Sterling et al., 2023)². PhD candidate performed all systematic analyses of publications, listed in the Supplementary Material and wrote the manuscript together with the lead author.

Chapter 4: The PhD candidate performed the experiments, wrote the chapter, and prepared the figures unless otherwise specified. FUCCI-transduced A172 cells were generated by Dr. Monira Hoque.

Chapter 5: The TKOv3 library was transduced into RKI1 cells and sequenced by Dr. Lipin Loo. All cell culturing of the transduced cells and subsequent analysis was performed by the PhD candidate. Dr. Antoine De Weck supervised the initial stages of the bioinformatic analysis. MS-CETSA was performed by Dr. Sean Humphrey and Dr. Dylan Harney. Analysis using the TPP package, and all subsequent analyses, were performed by the PhD candidate. RNA-sequencing was conducted by Dr. George Joun and analysed by the PhD candidate. All other sections were created entirely by the PhD candidate.

Chapter 6: Manuscript submitted to the journal *RSC Medicinal Chemistry* (Saxton et al., 2024). All Alphascreen biochemical analyses were performed by the PhD candidate. The author assisted in editing the manuscript and providing guidance on the areas of the text relating to biochemical testing and KDM4 biology.

Chapter 7: The PhD candidate wrote the chapter and prepared the figures.

Prof. Lenka Munoz supervised the PhD candidature, contributing to the experimental design and thesis revisions. Dr. Amanda Collins (in affiliation with the Sydney University Learning Hub) provided further guidance on thesis revisions. Dr. Alex Shaw (in affiliation with the Sydney University Informatics Hub) was consulted for all statistical analysis performed by the PhD candidate in this thesis. ChatGPT 4.0 was used to suggest improvements regarding sentence structure and readability after de-identifying sensitive information.

Permission

As primary supervisor for the candidature upon which this thesis is based, I can confirm that the authorship attribution statements above are correct.

As corresponding author for manuscripts used in this thesis, I give permission for their inclusion and confirm that appropriate acknowledgement of authorial contributions has been stated.

Lenka Munoz

February 2024

Table of Contents

| | |
|--|-----------|
| Abstract..... | iii |
| Statement of originality..... | iv |
| Authorship contribution statement..... | v |
| Permission..... | vi |
| Acknowledgements..... | x |
| List of abbreviations | xii |
| List of figures..... | xvii |
| List of tables..... | xix |
| Chapter 1. Introduction | 1 |
| 1.1. Glioblastoma..... | 2 |
| 1.1.1. Adult diffuse gliomas | 2 |
| 1.1.2. Current standard-of-care..... | 3 |
| 1.1.3. Challenges in glioblastoma therapy..... | 4 |
| 1.2. Glioblastoma heterogeneity | 5 |
| 1.2.1. Intra- and inter-tumour heterogeneity..... | 5 |
| 1.2.2. Cell plasticity..... | 7 |
| 1.2.3. Epigenetics and the histone code..... | 9 |
| 1.2.4. Lysine-specific histone demethylases..... | 10 |
| 1.2.5. KDMs in cancer..... | 12 |
| 1.3. The drug discovery process | 18 |
| 1.3.1. Target-based approach to drug discovery | 18 |
| 1.3.2. Phenotypic approach to drug discovery | 19 |
| 1.4. Thesis aims | 21 |
| Chapter 2. Materials and methods..... | 24 |
| 2.1. Cell line models | 25 |
| 2.2. CellTitre-Blue viability assay | 26 |
| 2.3. Clonogenic outgrowth assay | 26 |
| 2.4. Spheroid growth assay | 26 |
| 2.5. Reverse Transcription-Quantitative Polymerised Chain Reaction (RT-qPCR) | 27 |
| 2.6. Fluorescence Ubiquitin Cell Cycle Indicator (FUCCI) cell cycle analysis | 27 |
| 2.7. β -galactosidase staining | 27 |
| 2.8. Western blotting..... | 28 |
| 2.8.1. Sample preparation..... | 28 |
| 2.8.2. Immunoblotting | 28 |

| | |
|---|-----------|
| 2.9. Incucyte Annexin V apoptosis assay..... | 29 |
| 2.10. Immunofluorescence imaging | 29 |
| 2.11. Small interfering RNA (siRNA) transfection | 29 |
| 2.12. Incucyte proliferation confluency analysis..... | 30 |
| 2.13. CRISPR-Cas9 fitness and chemogenetic screens | 30 |
| 2.13.1. Lentivirus production | 30 |
| 2.13.2. Pooled genome-wide CRISPR screens in RKI1 cells | 30 |
| 2.13.3. sgRNA sequencing | 31 |
| 2.13.4. Chronos analysis..... | 31 |
| 2.13.5. Limma analysis..... | 32 |
| 2.14. Cellular Thermal Shift Assay (CETSA) | 32 |
| 2.14.1. Lysed-cell CETSA sample preparation | 32 |
| 2.14.2. Intact-cell CETSA sample preparation..... | 32 |
| 2.14.3. Mass spectrometry cellular thermal shift assay (MS-CETSA)..... | 33 |
| 2.14.4. TPP analysis | 34 |
| 2.15. RNA-sequencing..... | 34 |
| 2.16. AlphaScreen assay | 34 |
| 2.17. Statistical tests of comparison | 35 |
| 2.18. Reagents and chemicals..... | 36 |
| Chapter 3. Systematic literature review reveals suboptimal use of chemical probes in cell-based biomedical research..... | 41 |
| Preface | 42 |
| Chapter 4. Pharmacological evaluation of QC6352 in glioblastoma cells..... | 43 |
| 4.1. Introduction | 44 |
| 4.2. Results | 46 |
| 4.2.1. Efficacy of KDM4 inhibitors in glioblastoma stem cells | 46 |
| 4.2.2. QC6352 influences cellular processes related to growth and survival..... | 52 |
| 4.2.3. KDM4 expression and localisation in glioblastoma stem cells..... | 61 |
| 4.2.4. Target modulation by KDM4 inhibitors in glioblastoma stem cells..... | 65 |
| 4.2.5. Impact of KDM4 knockdown on proliferation and H3K9 tri-methylation | 69 |
| 4.2.6. Impact of KDM4A overexpression on glioblastoma cells..... | 72 |
| 4.3. Discussion..... | 77 |
| Chapter 5. Investigating the mechanism of action of QC6352..... | 81 |
| 5.1. Introduction | 82 |
| 5.1.1. CRISPR-Cas9 loss-of-function screens..... | 82 |
| 5.1.2. Mass-spectrometry based cellular thermal shift assay | 85 |

| | |
|---|------------|
| 5.1.3. RNA-sequencing and L1000 Query analysis | 86 |
| 5.2. Results | 87 |
| 5.2.1. Genome-wide CRISPR-Cas9 screen data quality validation | 87 |
| 5.2.2. Genome-wide CRISPR-Cas9 fitness screen in RKI1 glioblastoma cells | 90 |
| 5.2.3. Identification of resistance and sensitising genes for QC6352 efficacy | 96 |
| 5.2.4. Identification of proteins stabilised by QC6352 using Cellular Thermal Shift Assay | 99 |
| 5.2.5. QC6352 and ML324 target identification using intact-cell MS-CETSA | 101 |
| 5.2.6. QC6352 and ML324 target identification using lysed-cell MS-CETSA | 105 |
| 5.2.7. Validation of the MS-CETSA results | 110 |
| 5.2.8. RNA sequencing of QC6352-treated glioblastoma cells | 112 |
| 5.2.9. Pathway analysis of QC6352-treated glioblastoma cells | 114 |
| 5.2.10. Analysis of QC6352 gene signature with the Connectivity Map L1000 Query analysis | 116 |
| 5.3. Discussion | 120 |
| 5.3.1. Novel fitness genes affecting glioblastoma cell viability | 120 |
| 5.3.2. QC6352 target identification | 122 |
| 5.3.3. Protein phosphatase 5 as a potential target of QC6352 | 123 |
| Chapter 6. Exploration of hydrazines as metal chelators for KDM4 inhibition | 125 |
| Preface | 126 |
| Chapter 7. Final conclusions | 127 |
| 7.1. A robustness crisis in the use of chemical probes | 128 |
| 7.2. QC6352: another compound with relevant off-targets | 131 |
| 7.3. Concluding remarks and future directions | 134 |
| Chapter 8. References | 136 |

Acknowledgements

This thesis has been a wild rollercoaster, and I would like to thank each and every person I met on this crazy ride. The experiences and memories you've shared with me are priceless, and I will cherish them always. The kindness and support of each person mentioned have been indispensable to this thesis and I am profoundly grateful to have crossed paths with such remarkable individuals during my studies.

To my girlfriend, Felicia Simon, your unwavering support has been my cornerstone. I couldn't have lasted even a single month without you. During the most challenging moments of my degree, you have always been the light guiding me through it all. Better still, you have helped me grow into a better person and I'm so lucky for every moment I spend with you. I apologise for all the cancer biology information you've accrued from listening to my constant ramblings and theorising. Just know I appreciated every second you spent listening, I love you.

I would also like to express my deepest gratitude to my supervisor, Prof. Lenka Munoz. Your exceptional guidance and unwavering support surpassed all my expectations, equipping me with essential skills and knowledge. I am proud of the scientist you have helped me become and I could never have asked for a better role model.

This thesis could not have been made without the love and support of my entire lab group. To my fellow PhD student and close friend, Brianna Chen, I will always treasure the many memories shared together in the lab. You were always amazing to work with and added a constant source of liveliness and morale to everyone in the lab.

To all post-docs I had the pleasure of working with throughout my candidature; Dr. Ramzi Abbassi, Dr. Athena Phoa, Dr. Sharleen Menzies, Dr. Ariadna Recasens, and Dr. George Joun, thank you for your expert assistance and advice in the many experiments undertaken throughout the last 4 years. To the honours students who have graduated from our lab; Alexander Cerroti, Alexander Antonelli, Daniel Du Preez, Jacinda Holtsmark, Emma Kempe, and Karen Tran, you all brought a breath of fresh air with your unique personalities. It was an honour working with you all.

I want to especially thank Jacinda Holtsmark for her unwavering optimism and support over the past year. I really appreciate your help not just inside the lab but outside as well. You've got an infectious bright personality that has given me a deeper appreciation for the simple things in life. Whatever career you decide to follow in life, I have no doubt you will be a stunning success.

To the Simon family, I would be doing this acknowledgements section a disservice if I did not mention how eternally grateful I am for everything you have all done for me. You have all been so welcoming to me from the moment I entered your home. You are all so incredibly selfless and generous, constantly giving without ever asking for repayment and your character is something I will always aim to follow throughout my life. I am very lucky to have met you all in my life and you all have a very special place in my heart.

A special thank you to My Lovely Lottie, you are a very good man and I love the way you make me laugh. When you have a chat with me you make me happy again and we will be best buddies forever.

To my family thank you for all your support and encouragement. It is because of you that I pursued my interests in science and your love has gotten me where I am today. Thank you for being such a strong pillar of support whenever I needed you, I will never forget it.

I would also like to thank Dr. Lipin Loo and the Neely lab for assisting me in all matters relating to my CRISPR-Cas9 and lentiviral overexpression experiments. For years, I have dreamed of genetically engineering cells using CRISPR-Cas9 technology and your extensive knowledge on the subject and assistance guiding me through the process has only deepened my passion for the subject.

I'd like to express my deepest gratitude to Dr. Jennifer Baker, Angus Saxton, and Michael Hamilton from the University of Newcastle who were a big help synthesising the compound library tested in the KDM4A Alphascreen assay. I applaud your masterful work throughout my whole PhD, your work ethic and personability was something I strived for in my own work.

Thank you to Dr. Sean Humphrey and Dr. Dylan Harney for your hard work assisting with the mass spectrometry in my thesis, I'm very grateful for your expertise, you were both a pleasure to work with and I look forward to crossing paths in the future.

To Dr. Amanda Collins from the University of Sydney Learning Hub and Dr. Alex Shaw from the University of Sydney Informatics Hub, I really appreciated your time in our consultation sessions, your professionalism and personability is something I aim to emulate in my future endeavours.

Lastly, I'd like to thank the University of Sydney for providing financial assistance during my candidature through the Research Training Program (RTP) Stipend Scholarship.

List of abbreviations

| | |
|--------|---|
| 2-OG | 2-oxoglutarate |
| ABM | Astrocyte basal medium |
| AC | Astrocyte-like |
| ACTB1 | Actin beta 1 |
| ACTL6A | Actin-like 6A |
| ADMET | Absorption, distribution, metabolism, excretion, and toxicity |
| AML | Acute myeloid leukaemia |
| ANOVA | Analysis of variance |
| ARID | AT-rich interaction domain |
| ARMT1 | Aminoacyl tRNA synthetase complex-interacting multifunctional protein 1 |
| ASK1 | Apoptosis signal-regulating kinase 1 |
| ATM | Ataxia telangiectasia mutated |
| ATP | Adenosine triphosphate |
| ATR | Ataxia telangiectasia and Rad3 related |
| BAX | BCL2 associated X, apoptosis regulator |
| BCA | Bicinchoninic acid colorimetric assay |
| BET | Bromodomain and extra-terminal motif |
| BSA | Bovine serum albumin |
| BUB1 | BUB mitotic checkpoint serine/threonine kinase 1 |
| CARD8 | Caspase recruitment domain family member 8 |
| Cas9 | CRISPR-associated protein 9 |
| CBX5 | Chromobox 5 |
| CCLE | Cancer cell line encyclopedia |
| CCN | Cyclin |
| CD | Cluster of differentiation |
| CDK | Cyclin-dependent kinase |
| CDKN | Cyclin-dependent kinase inhibitor |
| CDT | Chromatin licensing and DNA replication factor |
| CENPO | Centromere protein |
| CEP | Centrosomal protein |
| CETSA | Cellular thermal shift assay |
| CHI3L1 | Chitinase 3 like 1 |
| CMap | Connectivity Map |
| CMV | Cytomegalovirus |
| CNS | Central nervous system |
| COLEC | Collectin sub-family member |
| CRISPR | Clustered regularly interspaced short palindromic repeats |
| CXCL | C-X-C motif chemokine ligand |
| CXXC | CXXC finger protein |
| DAPI | 4',6-diamidino-2-phenylindole |
| DCK | Deoxycytidine kinase |
| DEC2 | Differentially expressed in chondrocytes 2 |
| DEG | Differentially expressed gene |
| DHODH | Dihydroorotate dehydrogenase |

| | |
|---------|--|
| DMEM | Dulbecco's Modified Eagle Medium |
| DMSO | Dimethyl sulfoxide |
| DNA | Deoxyribonucleic acid |
| DNMT | DNA methyltransferase |
| DOT1L | DOT1-like |
| DR | Dopamine receptor |
| DUSP | Dual specificity phosphatase |
| DYRK | Dual specificity tyrosine-(Y)-phosphorylation regulated kinase |
| E2F1 | E2F transcription factor 1 |
| EC50 | Effective concentration 50 |
| ECACC | European Collection of Authenticated Cell Cultures |
| EDTA | Ethylenediaminetetraacetic acid |
| EEF1A | Eukaryotic translation elongation factor 1A |
| EGF | Epidermal growth factor |
| EGFR | Epidermal growth factor receptor |
| EIF2A | Eukaryotic translation initiation factor 2A |
| EIF2AK | Eukaryotic translation initiation factor 2-alpha kinase |
| ERK | Extracellular signal-regulated kinase |
| EZH | Enhancer of zeste homolog |
| FAK | Focal adhesion kinase |
| FBL | Fibrillarlin |
| FBS | Foetal bovine serum |
| FDR | False discovery rate |
| FGF | Fibroblast growth factor |
| FOS | Fos proto-oncogene, AP-1 transcription factor subunit |
| FOXO | Forkhead box |
| FPKM | Fragments per kilobase of transcript per million mapped reads |
| FUCCI | Fluorescent ubiquitination-based cell cycle indicator |
| FXR | Farnesoid x receptor |
| GAPDH | Glyceraldehyde-3-phosphate dehydrogenase |
| GEPIA | Gene expression profiling interactive analysis |
| GEM | Geminin |
| GFAP | Glial fibrillary acidic protein |
| GFP | Green fluorescent protein |
| GMO | Genetically modified organism |
| GR50 | Growth rate inhibition 50 |
| GSC | Glioblastoma stem cell |
| H3K9 | Histone H3 lysine 9 |
| H3K9me1 | Histone H3 lysine 9 monomethylated |
| H3K9me2 | Histone H3 lysine 9 dimethylated |
| H3K9me3 | Histone H3 lysine 9 trimethylated |
| HAT | Histone acetyltransferase |
| HDAC | Histone deacetylase |
| HEGF | Human epidermal growth factor |
| HEPES | 4-(2-Hydroxyethyl)-1-piperazineethanesulfonic acid |
| HIF | Hypoxia-inducible factor |

| | |
|----------|---|
| HRP | Horseradish peroxidase |
| HSP | Heat shock protein |
| IC50 | Inhibitory concentration 50 |
| IDH | Isocitrate dehydrogenase |
| IL | Interleukin |
| IPA | Ingenuity pathway analysis |
| ISG15 | Interferon-stimulated gene 15 |
| JAK | Janus kinase |
| JARID1A | Jumonji, AT rich interactive domain |
| JHDM1 | JmjC histone demethylase |
| JMJD1A | Jumonji domain containing |
| JNK | c-Jun N-terminal kinase |
| KAT | Lysine acetyltransferase |
| KDM | Lysine demethylase |
| KMT | Lysine methyltransferase |
| LARS2 | Leucyl-tRNA synthetase |
| LDS | Lithium dodecyl sulphate |
| LINCS | Library of integrated network-based cellular signatures |
| LRR | Leucine-rich repeat |
| MAPK | Mitogen-activated protein kinase |
| MAPKAPK2 | MAPK-activated protein kinase |
| MBP | Myelin basic protein |
| MCL | Myeloid cell leukemia apoptosis regulator |
| MCM5 | Minichromosome maintenance complex component |
| MDM2 | Mouse double minute 2 homolog |
| MEK | Mitogen-activated protein kinase kinase |
| MELK | Maternal embryonic leucine zipper kinase |
| MES | Mesenchymal-like |
| METTL2A | Methyltransferase like |
| MFAP4 | Microfibril associated protein |
| MGMT | O-6-methylguanine-DNA methyltransferase |
| MLL | Mixed lineage leukemia |
| MMP1 | Matrix metalloproteinase |
| MOI | Multiplicity of infection |
| MOPS | 3-(N-Morpholino)propanesulfonic acid |
| MS-CETSA | Mass spectrometry - cellular thermal shift assay |
| MT2A | Metallothionein 2A |
| MTIC | 5-(3-Methyltriazin-1-yl)imidazole-4-carboxamide |
| MTOR | Mechanistic target of rapamycin |
| NEK2 | NIMA-related kinase 2 |
| NES | Nestin |
| NF1 | Neurofibromin 1 |
| NFAT | Nuclear factor of activated T-cells |
| NHA | Normal human astrocytes |
| NOTCH | Neurogenic locus notch homolog protein |
| NPC | Neural-progenitor-like |

| | |
|---------|--|
| NPM1 | Nucleophosmin |
| NR2F1 | Nuclear receptor subfamily 2, group F, member 1 |
| OLIG2 | Oligodendrocyte transcription factor |
| OPC | Oligodendrocyte progenitor-like |
| OR7C2 | Olfactory receptor, family 7, subfamily C, member 2 |
| ORC1 | Origin recognition complex subunit 1 |
| ORF | Open reading frame |
| OSGEP | O-sialoglycoprotein endopeptidase |
| PAC3IN3 | Protein kinase C and casein kinase substrate in neurons |
| PARP | Poly (ADP-ribose) polymerase |
| PAX2 | Paired box 2 |
| PB1 | Polymerase basic protein 1 |
| PBS | Phosphate-buffered saline |
| PBST | Phosphate-buffered saline with tween 20 |
| PCA | Principal component analysis |
| PCR | Polymerase chain reaction |
| PDGFR | Platelet-derived growth factor receptor |
| PDK | Pyruvate dehydrogenase kinase |
| PERK | PKR-like endoplasmic reticulum kinase |
| PHD | Plant homeodomain |
| PHF2 | PHD finger protein 2 |
| PI3K | Phosphoinositide 3-kinase |
| PI4P5K | Phosphatidylinositol 4-phosphate 5-kinase |
| PKM2 | Pyruvate kinase M2 |
| PLC | Phospholipase C |
| PLD3 | Phospholipase D3 |
| PLK1 | Polo-like kinase 1 |
| PMAIP1 | Phorbol-12-myristate-13-acetate-induced protein |
| PML | Promyelocytic leukemia |
| PNUTS | Phosphatase 1 nuclear targeting subunit |
| PP5 | Protein phosphatase 5 |
| PPP1R10 | Protein phosphatase 1, regulatory subunit 10 |
| PRMT5 | Protein arginine methyltransferase 5 |
| PRPS1 | Phosphoribosyl pyrophosphate synthetase 1 |
| PRPSAP1 | Phosphoribosyl pyrophosphate synthetase-associated protein 1 |
| PTEN | Phosphatase and tensin homolog |
| PTM | Post-translational modification |
| QIMR | Queensland Institute of Medical Research |
| RACK7 | Receptor for activated C kinase 7 |
| RAR | Retinoic acid receptor |
| RASGRP1 | Ras guanyl releasing protein 1 |
| RBBP2 | Retinoblastoma-binding protein 2 |
| RBMX | RNA binding motif protein, X-linked |
| RBMXL1 | RNA binding motif protein, X-linked like |
| RIPK1 | Receptor-interacting serine/threonine-protein kinase 1 |
| RNAi | RNA interference |

| | |
|--------|---|
| ROCK1 | Rho-associated, coiled-coil containing protein kinase 1 |
| SDS | Sodium dodecyl sulphate |
| SEM | Standard error of the mean |
| SET | SET nuclear proto-oncogene |
| SIRT1 | Sirtuin 1 |
| SNAI2 | Snail family transcriptional repressor 2 |
| SOX | SRY-box transcription factor |
| SP1 | Specificity protein 1 |
| STAT | Signal transducer and activator of transcription |
| SWIRM | SWI/SNF and MuDR domain-containing protein |
| TAS | Transcriptional activity score |
| TBST | Tris-buffered saline and tween 20 |
| TGF | Transforming growth factor |
| TLN1 | Talin |
| TLX | T-cell leukemia homeobox |
| TMT | Tandem mass tags |
| TNF | Tumour necrosis factor |
| TPP-TR | Thermal proteome profiling - temperature range |
| TP53 | Tumour protein P53 |
| TPR | Tetratricopeptide repeat |
| TRAIL | TNF-related apoptosis-inducing ligand |
| TRP | Tetratricopeptide |
| TUBB2A | Tubulin beta 2A |
| UDP | Uridine diphosphate |
| UGT1A5 | UDP glucuronosyltransferase family 1 member A5 |
| UT | Untreated |
| UTX | Ubiquitously transcribed tetratricopeptide repeat, X chromosome (also known as KDM6A) |
| UTY | Ubiquitously transcribed tetratricopeptide repeat, Y chromosome (also known as KDM6C) |
| WDR77 | WD repeat domain 77 |
| WHO | World Health Organization |
| YPEL3 | Yippee like 3 |
| YY2 | YY2 transcription factor |

List of figures

| | |
|---|----|
| Figure 1.1. Classification of gliomas | 3 |
| Figure 1.2. Characteristic gene signatures of the glioblastoma subtypes..... | 6 |
| Figure 1.3. Comparison between healthy cell differentiation and glioblastoma heterogeneity | 8 |
| Figure 1.4. Drug discovery stages using a target-based approach and a phenotypic approach | 18 |
| Figure 1.5. Phenotypic screen of epigenetic probes in glioblastoma stem cell lines | 22 |
| Figure 4.1. Biochemical potency of KDM4 inhibitors | 46 |
| Figure 4.2. Efficacy and potency of QC6352 in glioblastoma stem cell lines | 48 |
| Figure 4.3. Efficacy of QC6352 in FPW1 and RKI1 cells followed by drug holidays..... | 49 |
| Figure 4.4. Antiproliferative efficacy of QC6352 in glioblastoma spheroids | 50 |
| Figure 4.5. Efficacy of orthogonal KDM4 inhibitors in glioblastoma stem cells | 51 |
| Figure 4.6. Efficacy of KDM4 inhibitors in normal human astrocytes..... | 51 |
| Figure 4.7. Cell cycle gene expression in QC6352-treated FPW1 cells | 52 |
| Figure 4.8. Cell cycle analysis in A172-FUCCI cells | 54 |
| Figure 4.9. Senescence-associated gene expression in QC6352-treated FPW1 cells | 55 |
| Figure 4.10. Senescence-associated protein expression in QC6352-treated FPW1 and RKI1 cells..... | 56 |
| Figure 4.11. Apoptosis-associated gene expression in QC6352-treated FPW1 cells..... | 57 |
| Figure 4.12. Apoptosis-associated protein expression in QC6352-treated in FPW1 and RKI1 cells ... | 58 |
| Figure 4.13. Differentiation-associated gene expression in QC6352-treated FPW1 cells..... | 59 |
| Figure 4.14. Differentiation status in QC6352-treated FPW1 cells | 60 |
| Figure 4.15. Expression of stemness markers in QC6352-treated FPW1 and RKI1 cells | 60 |
| Figure 4.16. Gene expression of histone-modifying enzymes in glioblastoma stem cell lines | 63 |
| Figure 4.17. KDM4 localisation in FPW1 and RKI1 cells | 64 |
| Figure 4.18. Heterogeneous H3K9 and H3K36 trimethylation in FPW1 cells..... | 67 |
| Figure 4.19. H3K9 and H3K36 trimethylation status in QC6352-treated FPW1 and RKI1 cells | 68 |
| Figure 4.20. H3K9 and H3K36 trimethylation status in ML324- and B3-treated RKI1 cells | 68 |
| Figure 4.21. siRNA validation of KDM4A-D knockdown | 70 |
| Figure 4.22. Phenotypic response to siKDM4A-D knockdown | 71 |
| Figure 4.23. Phenotypic response and QC6352 efficacy of KDM4A overexpression at MOI1 | 73 |
| Figure 4.24. Phenotypic response and QC6352 efficacy of KDM4A overexpression at MOI25 | 74 |
| Figure 4.25. H3K9 and H3K36 trimethylation in A172-KDM4A overexpressing cells..... | 75 |
| Figure 4.26. Gene expression of KDM and KMT families in A172-KDM4A overexpressing cells | 76 |
| Figure 4.27. Summary of findings from Chapter 4..... | 80 |
| Figure 5.1. Schematic of CETSA methods | 85 |
| Figure 5.2. Workflow of CRISPR-Cas9 fitness and chemogenomic screens | 88 |
| Figure 5.3. Principal component analysis of the CRISPR-Cas9 screen..... | 89 |

| | |
|--|-----|
| Figure 5.4. RKI1 fitness genes identified by Chronos analysis | 90 |
| Figure 5.5. KDM4 dependency genes in the CCLE..... | 92 |
| Figure 5.6. RKI1 fitness genes identified by Limma analysis | 93 |
| Figure 5.7. Ingenuity Pathway Analysis of fitness genes..... | 95 |
| Figure 5.8. Comparison of Chronos scores between treatment groups..... | 96 |
| Figure 5.9. QC6352 sensitising and resistance genes identified by Chronos analysis..... | 98 |
| Figure 5.10. Limma analysis of gene knockouts modulating QC6352 efficacy | 99 |
| Figure 5.11. KDM4A stabilisation by QC6352 and ML324..... | 100 |
| Figure 5.12. Akt stabilisation by MK2206..... | 101 |
| Figure 5.13. Proteome-wide screen of QC6352 binding partners using intact-cell MS-CETSA | 102 |
| Figure 5.14. Proteome-wide screen of ML324 binding partners using intact-cell MS-CETSA | 103 |
| Figure 5.15. Melt curves of significant binding partners using intact-cell MS-CETSA..... | 104 |
| Figure 5.16. Proteome-wide screen of QC6352 binding partners using lysed-cell MS-CETSA..... | 106 |
| Figure 5.17. Proteome-wide screen of ML324 binding partners using lysed-cell MS-CETSA | 107 |
| Figure 5.18. Proteome-wide screen of MK2206 binding partners using lysed-cell MS-CETSA | 108 |
| Figure 5.19. Melt curves of significant binding partners identified with lysed-cell MS-CETSA | 109 |
| Figure 5.20. Variability and sensitivity comparison between MS-CETSA data | 111 |
| Figure 5.21. Differential gene expression in QC6352-treated FPW1 cells..... | 113 |
| Figure 5.22. Ingenuity Pathway Analysis of DGEs in QC6352-treated FPW1 cells | 115 |
| Figure 5.23. Compounds with gene signatures positively correlating with QC6352-treated cells | 117 |
| Figure 5.24. Compounds with gene signatures negatively correlating with QC6352-treated cells | 119 |
| Figure 5.25. Identification of protein phosphatase 5 (PP5) as a potential target of QC6352..... | 124 |
| Figure 7.1. Proper and improper chemical probe use in the drug discovery process..... | 130 |
| Figure 7.2. Summary of findings from Chapters 4 and 5..... | 132 |

List of tables

| | |
|--|----|
| Table 1.1. Canonical histone lysine methylation sites and their regulated cellular processes | 10 |
| Table 1.2. Summary of KDM roles in cancer..... | 15 |
| Table 2.1. List of reagents and resources used in this thesis..... | 36 |
| Table 5.1. CRISPR-Cas9 screen glossary | 84 |

Chapter 1

Introduction

1.1. Glioblastoma

1.1.1. Adult diffuse gliomas

The central nervous system (CNS) is comprised of glia, vascular and neural cells. The glial cell types include astrocytes, oligodendrocytes, and microglia which function to nourish, support, and protect the neural cells³. These glial cells can become dysregulated and transform into a malignant brain tumour, known as a glioma⁴. Gliomas constitute approximately 80% of cancers originating in the CNS and can be further divided into four grades based on the tumour growth potential and aggressiveness⁵. Traditionally, glioma grades were based on only the histological appearance of the cells. However, molecular markers are now also considered in the grading of CNS tumours, as published in the fifth edition of the World Health Organization (WHO) “*Classification of Tumours of the CNS*” in 2021⁶ (**Figure 1.1a**).

Out of all the CNS malignant tumours, the adult diffuse gliomas are the most commonly occurring, comprised of astrocytoma, oligodendroglioma, and glioblastoma⁷. Similar to the classification of glioma grades, classification of tumour types has focused on the phenotypic and molecular characteristics rather than the cell origin. For instance, to differentiate glioblastoma from other adult diffuse gliomas, the mutational status of the isocitrate dehydrogenase (IDH) gene is used as a molecular marker⁸ (**Figure 1.1b**).

IDH is an enzyme of the metabolic Krebs cycle and often incurs a gain-of-function mutation further converting α -ketoglutarate into D-2-Hydroxyglutarate⁹. In the short term, a mutated *IDH* gene reprograms the cell metabolism, boosting the survivability and proliferation of the initiating tumour cells, while in the long term this leads to DNA and histone methylations inhibiting gene expression¹⁰. Because of this, a tumour carrying a mutated IDH gene is generally less aggressive and therefore considered a lower grade compared to IDH-wildtype high-grade tumours¹⁰.

Glioblastoma, defined as a grade 4 *IDH*-wildtype diffuse astrocytic tumour⁶, is the most common and most aggressive adult diffuse glioma. Approximately 50% of cancers in the CNS are glioblastomas¹¹. Patients with glioblastoma have a median survival rate of 12 months with less than 10% of patients surviving more than 5 years post-diagnosis¹². The cause of the disease is unknown with only 5% of patients having a family history of the disease and the remaining 95% occur sporadically¹³. The poor survival rate is due to a lack of effective therapies for treating patients. Consequently, there is a significant need for novel and efficacious drugs to treat glioblastoma.

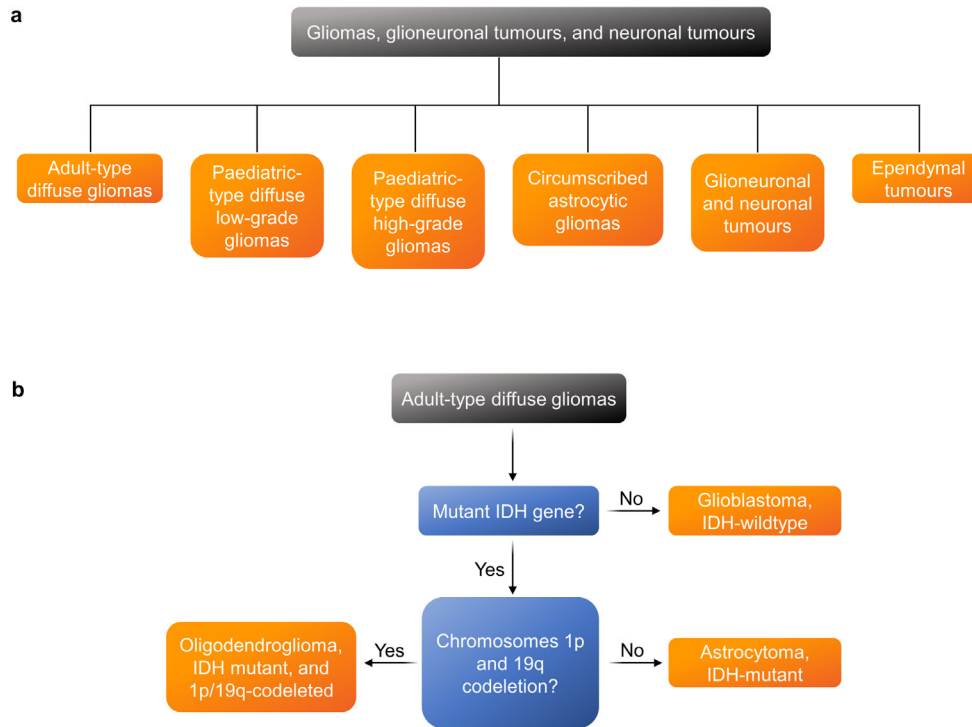


Figure 1.1. Classification of gliomas. a) Tumour types classified as a glioma. **b)** Characteristics defining the adult-type diffuse glioma subtypes. All classifications are according to the WHO “*Classification of Tumours of the CNS*” published in 2021⁶.

1.1.2. Current standard-of-care

The current standard-of-care for glioblastoma was developed in 2005 by Stupp et al.¹⁴ and has remained unchanged for 19 years. It consists of major surgical resection followed by concomitant radiotherapy and chemotherapy using the DNA alkylating agent, temozolomide. Temozolomide is a pro-drug which is quickly metabolised to the active form 5-(3-methyl)-1-triazene-1-yl-imidazole-4-carboximide (MTIC)¹⁵. MTIC primarily methylates the guanine base group in DNA, leading to a mismatch in base pairing during DNA replication where thymine, rather than cytosine, is generated in the complementary strand¹⁶. The DNA mismatch repair system cleaves the DNA-generating discontinuities which are also known as ‘nicks’¹⁷. If too many nicks are introduced in quick succession, or if the repair systems fail, the cell enters senescence or apoptosis¹⁸. DNA alkylating agents inherently lack selectivity since healthy cells also require DNA replication to survive¹⁹. However, cancer cells often exhibit dysregulated DNA repair pathways, which can make them more susceptible to the cytotoxic effects of DNA damage induced by alkylating agents²⁰. Conversely, healthy cells typically have more robust repair mechanisms, which can mitigate some of the damage.

Nevertheless, the efficacy of temozolomide treatment is limited by the cells' defence mechanisms against DNA alkylating agents¹⁶. One of the most important DNA repair enzymes which protects cellular DNA is O6-methylguanine-DNA methyltransferase (MGMT)²¹. MGMT eliminates the methyl group attached to the guanine nucleoside by permanently transferring the methyl group to the active site of the MGMT. The importance of MGMT is highlighted by its expression level often directly correlating with temozolomide resistance in glioblastoma patients²¹. However, silencing of the *MGMT* gene does not significantly increase treatment efficacy²², suggesting a more complex and redundant role of the DNA repair systems that is yet to be fully elucidated.

1.1.3. Challenges in glioblastoma therapy

The standard cytotoxic chemotherapy remains the only approved pharmacological modality to treat patients with glioblastoma²³. In order to develop novel drugs with improved therapeutic outcomes, it is important to understand all the challenges that need to be overcome to effectively eliminate the glioblastoma tumour. First, the drug must cross the blood-brain barrier. There are currently no definitive set of rules detailing which molecules can pass through the BBB and which cannot. However, current literature has established guidelines that are relevant for a majority of CNS permeable molecules. Generally, molecules move through the BBB using passive diffusion through endothelial cells with specialised tight junctions and a lipid bilayer²⁴. To diffuse across the blood-brain barrier, lipid-soluble compounds must be below 400 - 600 Da in size and uncharged²⁴, hence this criteria excludes 98% of small molecules from crossing into the CNS²⁵. Notably, some drugs may have partial BBB permeability, assessed by comparing free brain-to-free plasma concentrations. Reaching an efficacious concentration in the CNS therefore requires treatment at exceedingly high concentrations, which increases systemic exposure and heightens the risk of unintended side effects which limits the therapeutic potential of the drug²⁶.

Second, the CNS microenvironment is highly immunosuppressive which, alongside the blood-brain barrier, significantly limits immune surveillance²⁷. This characteristic reduces inflammation-induced neural damage and autoimmune reactions but also hinders the immune system's ability to target tumour cells. In peripheral tissues, the immune system plays a key role in the detection and elimination of immunogenic neoplastic cells²⁸. The immune system often acts synergistically with anti-cancer therapies to completely eradicate residual tumour cells, preventing recurrence in patients²⁹. However, since the CNS microenvironment is immunosuppressive, glioblastoma treatments traditionally eliminate the tumour cells without

the assistance of the immune system. A notable exception to this are the immunotherapeutics entering clinical trials which aim to evoke a controlled immune response to the brain tumour. For instance, a Phase 1 clinical trial (NCT05168423) used patient-derived T-cells genetically engineered to produce chimeric antigen receptors targeting EGFR and IL13Ra2 antigens that are frequently overexpressed in glioblastoma cells³⁰. Immunotherapy has been successful in acute lymphoblastic leukemia, chronic lymphocytic leukemia, and B cell lymphomas by targeting the overexpressed CD19 antigen^{31,32}. However, in glioblastoma, there has been limited success thus far attributed mainly to the fact that not all glioblastoma cells require EGFR or IL13Ra2 and some targeted cells can even transition to a state where these antigen targets are not expressed³⁰.

Finally, the few drugs that can reach the glioblastoma tumour are met with highly diverse and adaptable cancer cell populations which are either inherently resistant to drugs or adapt to cytotoxic stress in order to survive³¹. Thus, improving clinical outcomes for patients diagnosed with glioblastoma faces significant challenges, including the blood-brain barrier and the immunosuppressive CNS microenvironment. Furthermore, glioblastoma heterogeneity presents a significant therapeutic challenge requiring novel therapies to effectively eliminate a highly adaptive and heterogeneous tumour population³².

1.2. Glioblastoma heterogeneity

1.2.1. Intra- and inter-tumour heterogeneity

Heterogeneity refers to the genetic, molecular, or phenotypic diversity within a cell population³³. A heterogeneous cell population contains numerous subpopulations of cells with unique genotypes whereas a homogeneous cell population consists of cells that predominantly follow the same genotype³⁴. Glioblastoma is characterised by significant variability not only across different patients, known as inter-tumour heterogeneity, but also within a single tumour known as intra-tumour heterogeneity³⁵.

Using almost 200 gene expression profiles from glioblastoma tumours, Verhaak et al. in 2010 identified four transcriptomic subtypes of glioblastoma: classical, mesenchymal, pro-neural, and neural³⁶. However, a more recent study by Wang et al. could only confirm the classical, mesenchymal, and pro-neural subtypes and theorised that the neural subtype was likely to be contamination from normal neural tissue in the diffuse tumour samples³⁷. These subtypes are classified based on distinct genetics, and transcriptional profiles known as gene signatures (**Figure 1.2**).

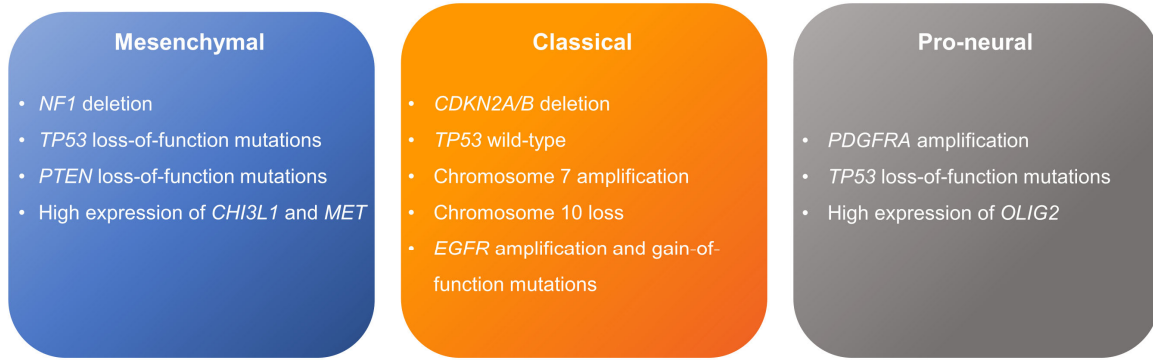


Figure 1.2. Characteristic gene signatures of the glioblastoma subtypes^{36,37}.

The mesenchymal glioblastoma subtype presents decreased *neurofibromin 1 (NF1)* gene expression, as well as *tumour protein p53 (TP53)* and *phosphatase and tensin homolog (PTEN)* loss-of-function mutations, and high expression of *chitinase 3 like 1 (CHI3L1)* and *MET*³². Moreover, the classical subtype harbours *cyclin-dependent kinases inhibitor 2A/B (CDKN2A/B)* gene deletions, no mutations to the *TP53* gene, chromosome 7 amplification, chromosome 10 loss, and amplification and mutation of *epidermal growth factor receptor (EGFR)*³². Lastly, the pro-neural subtype contains *platelet-derived growth factor receptor (PDGFRA)* gene amplification, *TP53* loss-of-function mutations, and high expression of *oligodendrocyte transcription factor 2 (OLIG2)*³². Identification and classification of these subtypes allows greater characterisation of patient outcome as the pro-neural subtype is associated with better overall survival³⁷. Personalised therapies that are based on the tumour subtype may enhance the success of novel treatments in the future, once they become viable and have passed clinical trials.

Although the three transcriptional subtypes outlining the distinct inter-tumoural heterogeneity have proven useful in understanding the disease, the subtypes were identified by averaging the gene expression levels of many glioblastoma tumours³⁷. In reality, however, each cell displays unique gene mutations, gene expression patterns and differential status which contribute to the failure of targeted therapies in these patients. For instance, some cells within the subpopulation carry the ligand-independent, constitutively active *EGFRvIII* mutant³⁸. In addition to promoting proliferation, survival, and angiogenesis, the *EGFRvIII* mutant decreases the efficacy of EGFR inhibitors and substantially contributes to the failure of these targeted therapies in clinical trials³⁹.

Non-genomic intra-tumour heterogeneity, including DNA methylation, miRNAs, and histone modifications also contribute to intra-tumour heterogeneity⁴⁰. In an attempt to

characterise the intra-tumoural heterogeneity in glioblastoma cells, Nefel et al. used single-cell analysis to identify four malignant transcriptional states: oligodendrocyte progenitor-like (OPC), neural-progenitor-like (NPC), astrocyte-like (AC), and mesenchymal-like (MES)⁴¹. When comparing between patients, most tumours contained all four transcriptional states with varying percentages for each state.

Finally, glioblastoma stem cells (GSCs), characterised by a high expression of stem cell markers, genetic instability, self-renewal capacity, and tumour-initiating potential are responsible for the initiation and heterogeneity of glioblastomas⁴². Moreover, GSCs also play a major role in tumour recurrence. The GSC population consists of a spectrum of cells expressing markers of differentiation as well as markers for stemness⁴². This diversity in differential status plays a critical role in the glioblastoma's adaptability - also known as cell plasticity - to changes in the tumour microenvironment, including cytotoxic stress induced by therapy³¹.

1.2.2. Cell plasticity

Plasticity is defined as the ability to convert from one cell state to another in a non-hierarchical manner and is therefore the primary driver of heterogeneity in glioblastoma³¹. In healthy tissues, the developmental pathway typically begins with totipotent stem cells, which possess the unique capacity to give rise to all cell types that form an organism⁴³. These stem cells undergo a series of tightly regulated differentiation processes, progressively losing their pluripotency as they transition towards more specialised, lineage-specific progeny. The differentiation of normal, non-cancerous cells is typically terminal and monodirectional⁴⁴. This means that these cells have a limited capacity for further change and cannot revert to a more primitive or undifferentiated state³¹ (**Figure 1.3a**). In healthy physiology, this restricted plasticity is crucial for maintaining tissue integrity and function. Each cell type performs specific roles, and the inability to revert to a stem-like state or change lineage ensures that tissues retain their specialised functions⁴⁵.

In contrast, glioblastoma stem cells do not terminally differentiate, often exhibiting a remarkable level of plasticity⁴⁶. Consequently, individual glioblastoma cells are able to self-renew and proliferate indefinitely, regardless of whether the cells have exhibited stem-like markers or not⁴⁷. Tumour populations with high plasticity tend to adopt a highly chaotic structure. In this structure, the tumour cells spread across all possible 'states' allowed by the microenvironment, driven by random variations in gene expression⁴⁸. As mentioned

previously, these states largely following the four malignant transcriptional states in glioblastoma⁴¹ (**Figure 1.3b**). The tumour microenvironment is constantly in a state of flux, with changes such as hypoxia, nutrient deprivation, and cytokine signalling acting as attractors to select cell states³¹. The subpopulation of cells that are intrinsically capable of surviving the change will survive and reestablish a new equilibrium of possible states in the new microenvironment⁴⁹.

Initially, cell plasticity was thought to be a consequence of Darwinian evolution following a ‘survival of the fittest’ mentality^{50,51}. Since cancer cells characteristically contain genomic instability, DNA mutations are regularly incurred and so changes in the microenvironment were thought to select for certain cell genotypes⁵¹. However, recent findings have shown glioblastoma, as well as other cancers, have substantial dysregulation of chromatin regulators which play a much more active role in driving cell plasticity compared to the accrument of DNA mutations⁵². Chromatin regulators change the state of histone proteins to regulate gene expression in an inducible and reversible manner and this is classified as epigenetics. Epigenetics is therefore a major driver of glioblastoma plasticity which establishes and maintains heterogeneity in a tumour population.

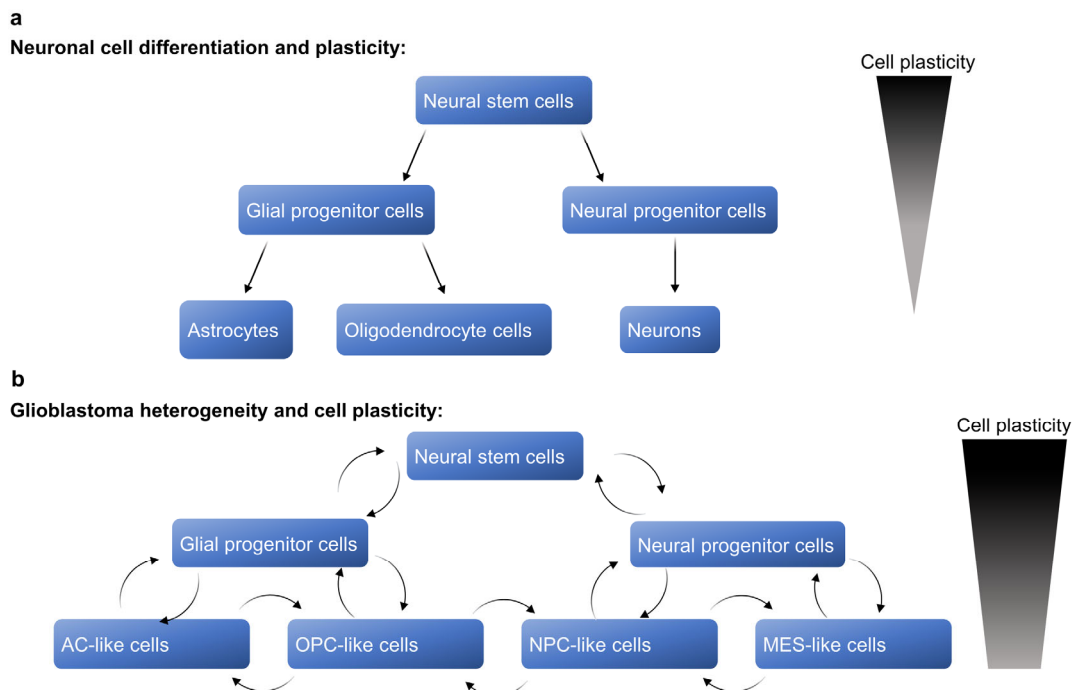


Figure 1.3. Comparison between healthy cell differentiation and glioblastoma heterogeneity. a) Neuronal stem cell lineage in healthy brain tissue. **b)** Differentiation and de-differentiation of glioblastoma cells while retaining their cell plasticity³¹.

1.2.3. Epigenetics and the histone code

In eukaryotic cells, DNA is wrapped around a central histone octamer (two each of histones H2A, H2B, H3 and H4) as a basic structural component known as nucleosome. When referring to the collective structure of the entire DNA wrapped around multiple histone octamers this is known as chromatin. Epigenetics refers to the regulation of gene expression without directly altering the DNA sequences but instead by manipulating the accessibility of the chromatin for transcription factors necessary for gene transcription⁵³. Epigenetic regulation involves inducible and reversible modifications to DNA methylation, histone post-translational modifications, and miRNA activity to influence the availability of transcriptional sites of DNA when complexed with histones. DNA methylation, miRNA activity, and some post-translational histone modifications inhibit gene expression while other histone modifications activate gene expression⁵⁴.

The histone code states that gene expression is largely regulated by modifications to the histone tail⁵⁵. Various post-translational modifications (PTMs) can be incurred to the tails of histone proteins which greatly affect the packaging of the chromatin structure. The process is regulated by enzymes that catalyse the formation of PTMs (writers), proteins that recognise PTMs (readers), and enzymes that remove PTMs (erasers)⁵⁶. PTMs on the histone tails include phosphorylation, sumoylation, and ubiquitination, however, the two most studied PTMs in cancer epigenetics are histone acetylation and methylation¹.

Histone acetylation by acetyltransferases (HATs) adds an acetyl group to the lysine residues on the histone tail, reducing their positive charge. This decreased positive charge lessens the attraction between the histone tails and the negatively charged DNA backbone, resulting in a loosened chromatin structure⁵⁷. This allows recruitment of ‘reader’ proteins containing a structural domain capable of recognising the modified histone tail, namely, bromodomains and tandem plant homeodomains⁵⁸. These proteins bind to acetylated histone sites and recruit transcription elongation factors for RNA transcription. Histone deacetylases (HDACs) regulate this process by removing the acetyl group to moderate gene expression in a constant push-and-pull state of equilibrium⁵⁷.

Histone methylation is the addition of methyl groups to the arginine and lysine residues on histone tails. Unlike histone acetylation, residues can be methylated up to three times and methylation can induce both gene activation and/or repression depending on the site of action⁵⁹ (**Table 1.1**). The canonical lysine methylation sites are found on histone H3 lysine residues K4, K9, K27, K36, K56, K79 and on histone H4 lysine residues K20⁶⁰. This substantial

combination of methylation states and sites of action results in a highly complicated regulatory system encompassing a vast array of biological processes. For instance, H3K4 methylation activates genes for differentiation and is involved in deciding the cell fate by regulating lineage-specific gene expression⁶¹. In contrast, H3K9 methylation is associated with gene silencing and inducing cellular senescence⁶². H3K27 methylation is also associated with gene repression and is essential for cell lineage specification in differentiating embryonic stem cells⁶³. H3K36 methylation is associated with gene activation by recruiting chromatin remodelling proteins to open the chromatin structure and also enhances DNA repair by the canonical nonhomologous end-joining repair process⁶⁴. H3K56 methylation marks a repressive chromatin state but is essential for genomic stability⁶⁵, whereas H3K79 methylation is gene-activating and highly associated with replication initiation sites for cell proliferation⁶⁶. Finally, H4K20 is associated with a euchromatic state when mono-methylated, and a heterochromatic state when di- or tri-methylated. H4K20me1 is maintained throughout the cell cycle while H4K20me3 maintains genomic integrity⁶⁷.

In summary, epigenetic regulation modulates gene expression without altering the DNA sequence, primarily through mechanisms regulating chromatin accessibility⁵³. These modifications can either enhance or inhibit gene expression, significantly impacting cellular processes. Histone acetylation generally loosens chromatin structure to promote gene expression⁵⁷, while histone methylation can either activate or repress genes, depending on the specific sites and contexts⁵⁹. These histone PTMs represent a sophisticated regulatory network controlling gene expression in response to intracellular and microenvironmental cues.

Table 1.1. Canonical histone lysine methylation sites and their regulated cellular processes.

| Histone lysine residue | Methylation outcome | Regulated cellular processes |
|------------------------|---------------------|-------------------------------|
| H3K4 | Gene-activation | Differentiation and cell fate |
| H3K9 | Gene-repression | Senescence |
| H3K27 | Gene-repression | Cell lineage specification |
| H3K36 | Gene-activation | DNA damage repair |
| H3K56 | Gene-repression | Genomic stability |
| H3K79 | Gene-activation | Cell proliferation |
| H4K20 | Gene-repression | Cell cycle progression |

1.2.4. Lysine-specific histone demethylases

Lysine histone methyltransferases (KMTs) and demethylases (KDMs) are the respective writers and erasers which act at histone methylation sites. There are currently 24 known KMTs divided into eight families⁶⁸ (KMT1-8). Two domains provide lysine

methyltransferase activity: the SET domain and the seven-beta-strand (7 β S) domain⁶⁰. Humans encode 55 proteins containing the SET domain while there are approximately 150 proteins containing the 7 β S domain⁶⁹. However, about half of the SET domain-containing proteins are inactive and the 7 β S domain is capable of methylating more than just histone residues, with its range of substrates including amino acid side chains, N-terminal α -amines, DNA, and RNA⁶⁹. This leaves 23 SET-containing proteins and one 7 β S-containing protein (DOT1L) methyltransferases acting on histone lysine residues. DOT1L is the only enzyme to methylate H3K79, while multiple KMT subtypes methylate H3K4, H3K9, and H3K36.

The 24 KDMs in the human genome are also divided into eight subfamilies (KDM1-8)⁶⁸. KDM1 uniquely contains a flavin adenine dinucleotide-dependent amine oxidase domain, which erases monomethylation and dimethylation marks⁷⁰. The amino oxidase domain acts by a hydride transfer on the ϵ -amine of lysine to form an unstable imine that spontaneously hydrolyses into formaldehyde⁷¹. Because this imine product formation requires a lone pair of electrons in the nitrogen of the methyl lysine, KDM1 enzymes cannot demethylate trimethyl groups as the quaternary amines do not have a lone pair of electrons⁷².

KDM2-8 subfamilies contain a catalytic Jumonji C (JmjC) domain and remove monomethylation, dimethylation and trimethylation marks on lysines⁷³. The demethylating activity of the JmjC domains requires Fe²⁺, 2-oxoglutarate (2-OG) and oxygen to hydroxylate the methyl to hydroxymethyl, which is then released as formaldehyde⁷³. In addition to the JmjC catalytic domains, all KDM subfamilies contain additional N-terminal interaction elements referred to as JmjN, which provide structural integrity without participating in active site formation⁷⁴.

Additionally, many KDMs contain F-box, Leucine-rich repeat (LRR), and tetratricopeptide (TRP) domains that are important for protein-protein interactions^{75,76} as well as a wide variety of DNA and histone binding domains such as Swi3p, Rsc8p and Moira domain (SWIRM), AT-rich interacting domain (ARID), plant homeodomain (PHD), zinc fingers and Tudor domain⁷⁷. For example, KDM2 and KDM7 both have one PHD domain^{78,79}, whereas KDM5s contain two or three PHD domains, which are necessary for the binding to H3K4⁸⁰. The N-terminal PHD domain binds to H3K4me1 and the C-terminal PHD domain binds to H3K4me3/me2⁸¹. The PHD domain of KDM7, in contrast, is reported as nonessential for its catalytic activity⁷⁹. Within the KDM family, only KDM4A-C contain a conserved double Tudor domain with slight variations, which create different lysine binding preferences between these three KDM4 isoforms⁸². KDM4D and KDM4E are shortened versions of the KDM4 enzymes.

As such, they do not contain Tudor domains and likely use the variation within the JmjC domain for lysine recognition⁸³. This suggests that the JmjC catalytic domain is also important for the KDMs' binding preferences.

In summary, KMTs and KDMs are critical machinery for the dynamic modulation of histone methylation, acting as the essential "writers" and "erasers" that determine the epigenetic landscape⁷⁶. Both enzyme families possess structural domains crucial for targeting specific lysine residues on histones, with notable overlap in the lysine sites they modify^{82,84}. While KMTs also play a significant role in epigenetic regulation within cancer biology, the scope of this thesis primarily focuses on the dysregulation of KDMs. This focus stems from their critical role in cancer development and the potential they hold for targeted therapeutic interventions⁸⁵.

1.2.5. KDMs in cancer

KDMs serve as key machinery regulating the epigenetics of cancer, with different family members serving roles in both tumorigenesis and tumour suppression^{86,87}. Various KDMs have been implicated in maintaining the stemness and plasticity of tumour cells, thereby contributing to tumour heterogeneity and enhancing survival against drug treatments⁸⁶. Conversely, other KDMs suppress cell proliferation and promote differentiation, acting as tumour suppressors⁸⁷. The complex activity of each KDM is a consequence of their specific lysine residue targets and their varying expression levels across different cancer types.

KDM1A is highly expressed in various cancers and, through its demethylase activity, mostly regulates the balance between self-renewal and differentiation of stem cells. In acute myeloid leukaemia cells, KDM1A maintains clonogenicity and inhibits differentiation through H3K4 demethylation⁸⁸. Similarly, differentiation of neural stem cells requires low KDM1A levels and an increase in H3K4 methylation. This results in the repression of the target genes of TLX⁸⁹, an important nuclear receptor that regulates cell cycle progression by upregulating p21 and downregulating cyclin D1⁹⁰. KDM1A inhibition results in proteasome-mediated degradation of HIF1 α , which in turn is sufficient to induce senescence in glioblastoma cells⁹¹. The overexpression and carcinogenic activities of KDM1A have been also reported in prostate⁹², liver⁹³, breast⁹⁴, colorectal⁹⁵, and lung cancers⁹⁶. In contrast, KDM1B has not been found to be altered in many cancers. One study has reported that knockdown of KDM1B reduces breast cancer cell colony formation by increasing H3K4 methylation⁹⁷. In glioblastoma, hypoxia-induced miR-215 is vital for adaptation of glioma-initiating cells to the hypoxic environment via suppression of KDM1B expression and associated modulation of glucose metabolism and angiogenesis⁹⁸.

KDM2A promotes progression of lung cancer by epigenetically enhancing ERK1/2 and JNK1/2 signalling⁹⁹. KDM2A-dependent H3K36 demethylation at the promoter of the dual-specificity protein phosphatase 3 (DUSP3) represses its expression, thus increasing ERK1/2 and JNK1/2 activities⁹⁹. This in turn promotes tumour growth and invasion to the lymph nodes. In mouse embryonic fibroblasts, KDM2B knockdown induces senescence whereas KDM2B re-introduction restores proliferation by decreasing the tumour suppressor p15Ink4b through H3K36me2 demethylation¹⁰⁰. KDM2B is essential for leukaemia stem cell self-renewal¹⁰¹ and proliferation of glioblastoma stem cells¹⁰². Knockdown of KDM2B in glioblastoma cells decreases the abundance of H3K36me2, reduces actively proliferating cells and causes DNA damage accumulation, implicating KDM2B in the maintenance of glioblastoma stem cells¹⁰².

KDM3A has been implicated as a potential therapeutic target in breast cancer where KDM3A is overexpressed and necessary for oestrogen receptor function¹⁰³. KDM3A also induces pro-invasive genes by erasing repressive H3K9me3 marks and promotes chemoresistance by demethylating nonhistone protein p53¹⁰⁴. KDM3B promotes the recurrence of aggressive prostate cancer cells after androgen deprivation therapy through its H3K9me2 demethylase activity at the specific promoters of genes needed for metabolism and proliferation¹⁰⁵. KDM3C appears to be critical for the growth of leukaemia stem cells where its overexpression upregulates several glycolytic enzymes. Notably, this metabolic function of KDM3C is independent of its demethylase activity as there are no changes in H3K9me2 levels of upregulated glycolytic genes¹⁰⁶.

Several studies demonstrate functional redundancy of KDM4 enzymes¹⁰⁷. While single knockout mice for KDM4A/B/C and double knockout mice for KDM4A/B and KDM4B/C are viable, KDM4A/C double- and KDM4A/B/C triple-knockout mice are embryonically lethal¹⁰⁸. Further analysis has shown that KDM4A and KDM4C redundantly regulate histone via demethylation of H3K9me3 and H3K36me3 at highly similar transcriptional start sites¹⁰⁸. Demethylation of H3K9me3 is required for transcriptional activation of the proliferative JAK-STAT pathway in leukaemia cells, but only the KDM4A/B/C triple knockout attenuates progression of acute myeloid leukaemia in mice¹⁰⁹. KDM4D and H3K9me3 demethylation promotes colorectal tumour formation in mice through increasing levels of β -catenin, c-Myc and cyclin D1, which has been reversed with single KDM4D knockdown¹¹⁰. No studies to date have focused on the role of KDM4E in cancer and KDM4E has been considered a pseudogene¹¹¹.

In breast cancer, KDM5A-mediated H3K4me3 demethylation downregulates expression of genes encoding tumour suppressor proteins p16 and p27¹¹². KDM5A also promotes proliferation of small cell lung cancer cells by repressing NOTCH1 and NOTCH2 tumour suppressors' target genes¹¹³. In further support of the oncogenic roles for KDM5A, potent and selective KDM5 inhibitors stops proliferation of myeloma cells¹¹⁴. KDM5B/C under-expression in primary melanoma and breast cancer cells is consistent with a possible tumour suppressive function^{115,116}. Lower levels of KDM5C in renal cancer cells promote a transcriptionally active H3K4me3, triggering genomic instability and poor prognosis in patients¹¹⁷. In prostate cancer, KDM5D represses invasive genes MMP1, MMP2, MMP3, MMP7 and SNAI2 through the demethylation of H3K4me3 at their promoter regions. In support of this, KDM5D expression is low in metastatic prostate tumours compared to primary tumours¹¹⁸.

In multiple myeloma, loss of KDM6A promotes proliferation and confers sensitivity to EZH2 inhibition¹¹⁹. Similarly, KDM6A is frequently inactivated in urothelial bladder carcinoma cells, which are sensitive to EZH2 inhibition. In vivo, EZH2 inhibition causes regression of KDM6A-null bladder tumours¹²⁰. The tumour suppressive function of KDM6A and its link to EZH2 are also critical to lung cancer progression. KDM6A deletion in vivo promotes lung cancer progression mainly through an increase in EZH2 and H3K27me3 levels. KDM6A-knockout lung cancer cells are sensitive to EZH2 inhibition, leading to significantly decreased proliferation and increased apoptosis¹²¹. KDM6B has tumour suppressive roles and has been found to be downregulated in neuroblastoma stem-like cells. An overexpression of KDM6B inhibits proliferation and induces differentiation genes, suggesting that the demethylase activity of KDM6B is responsible for neuroblastoma differentiation¹²².

Very few studies have focused on the function of KDM7 proteins, but some of these publications have implicated KDM7 enzymes as drivers of tumorigenesis¹²³. Knockdown of KDM7A, and consequently decreased H3K27me2 levels in hormone-sensitive prostate cancer cells, downregulate androgen receptor signalling and cell proliferation¹²⁴. KDM7A maintains viability of glioblastoma stem cells by ensuring low H3K9 and H3K27 methylation¹²⁵. Patients with laryngeal and hypopharyngeal squamous cell carcinoma showing high KDM7B expression and low H3K9me2/H3K27me2 levels have an increased chance of relapse¹²⁶. A study using neural progenitor cells found that KDM7C demethylates H3K9me2 at promoter regions of YY2 and E2F4 genes, which are responsible for progenitor self-renewal and cell cycle progression¹²⁷. In contrast, KDM7C has been found to be downregulated in colon and

stomach cancers, where it acts as a tumour suppressor in association with p53. KDM7C demethylates H3K9me2 at p53 target gene CDKN1A and MDM2 promoters, thereby activating transcription of p53 target genes and cell death¹²⁸.

The biochemical function of KDM8 remains elusive. Early studies identified KDM8 as a H3K36me2 demethylase, regulating cyclin A1 expression¹²⁹, but this assignment has not been validated subsequently^{130,131}. High-resolution crystal structures of the KDM8 catalytic domain in complex with the co-factor 2-OG suggest that KDM8 was not a lysine demethylase and biochemical assays show no demethylase activity on any H3 or H4 residue^{131,132}. Other studies suggest that KDM8 may function as a dioxygenase¹³⁰, as well as an aminopeptidase mediating proteolytic cleavage of monomethylated histone tails to modulate chromatin conformation^{133,134}. Finally, KDM8 has been reported to function as a JmjC arginyl-hydroxylase, the first such catalytic activity identified for a human enzyme¹³⁵. Taken together, these findings suggest that KDM8 may have some H3K36me2 demethylase activity in mammalian cells, but it is probably not a major demethylase at this site compared to the other H3K36 demethylases KDM2 or KDM4.

In summary, KDMs are instrumental in modulating gene expression by removing methyl marks from histones, thereby influencing cellular outcomes related to proliferation, differentiation, and apoptosis in a cancer-specific context⁸⁶ (**Table 1.2**). Consequently, targeting dysregulated KDMs in cancer has been proposed as a possible strategy to disable the adaptability of glioblastoma cells and improve the efficacy of future therapies⁸⁷.

Table 1.2. Summary of KDM roles in cancer.

| | Synonyms | Targets | Links to cancer |
|--------------|---|----------------------------|---|
| KDM1A | LSD1 AOF2 KIAA0601 | H3K4me2/me1 H3K9me2/me1 | Acute myeloid leukaemia - maintains clonogenicity and inhibits differentiation ¹³⁶ Glioblastoma - inhibition degrades HIF1 α and induces senescence ¹³⁷ Over-expressed in prostate ⁹² , liver ¹³⁸ , breast ⁹⁴ , colorectal ¹³⁹ and lung tumours ¹⁴⁰ |
| KDM1B | LSD2 AOF1 C6orf193 | H3K4me2/me1 | Breast cancer - knockdown reduces colony formation ⁹⁷ Glioblastoma - suppression maintains glioma-initiating cells in hypoxic environment ⁹⁸ |
| KDM2A | CXXC8 FBL7 FBXL11 JHDM1A KIAA1004 | H3K36me2 | Lung cancer - represses DUSP3 phosphatase, thereby activating ERK and JNK signalling, tumour growth and metastasis ¹⁴¹ |

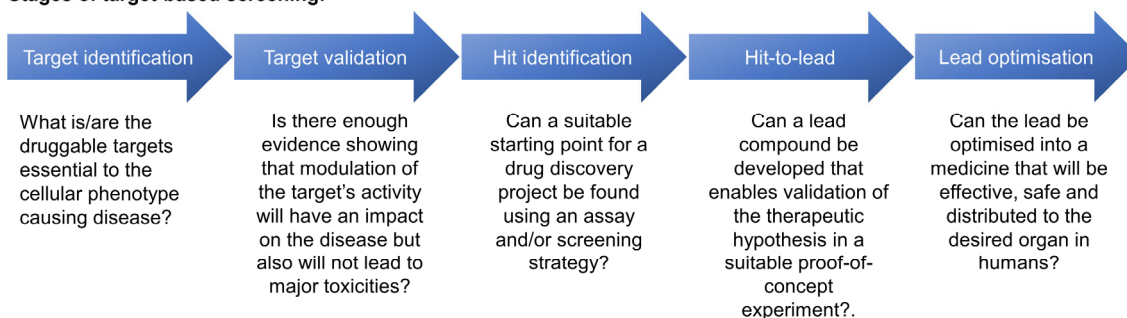
| | | | |
|--------------|---|--|--|
| KDM2B | CXXC2 FBL10 FBLX10 JHDM1B PCCX2 | H3K4me3 H3K36me2 | Glioblastoma - essential for proliferation of stem cells ¹⁴² Leukaemia - essential for self-renewal of stem cells ¹⁴³ |
| KDM3A | JMJD1A JHDM2A | H3K9me2/me1 | Colorectal cancer - activates Wnt target genes, thereby enhancing self-renewal of stem cell ¹⁴⁴ Prostate cancer - regulates proliferation, survival and drug resistance ¹⁴⁵ Breast cancer - activates invasion, drug resistance and stemness ¹⁰⁴ Lung cancer - drives tolerance to taxane-platin therapy ¹⁴⁶ |
| KDM3B | JMJD1B JHDM2B | H3K9me2/me1 | Colorectal cancer - activates Wnt target genes, thereby enhancing self-renewal of stem cell ¹⁴⁴ Prostate cancer - activates genes needed for metabolism and proliferation ¹⁰⁵ |
| KDM3C | JMJD1C JHDM2C | H3K9me2/me1 | Leukaemia - critical for the growth of stem cells, independent of demethylase activity ¹⁰⁶ |
| KDM4A | JMJD2A JHDM3A | H3K9me3/me2 H3K36me3/me2 H3K23me3 | Leukaemia - redundantly promotes proliferation ¹⁴⁷ Breast cancer - knockout decreases tumour growth ¹⁴⁸ |
| KDM4B | JMJD2B JHDM3B | H3K9me3/me2, H3K36me3/me2 H3K23me3 | Leukaemia - redundantly promotes proliferation ¹⁴⁷ Gastric cancer - knockdown reduces IL-8, CXCL5 gene expression ¹⁴⁹ |
| KDM4C | JMJD2C JHDM3C | H3K9me3/me2 H3K36me3/me2 | Leukaemia - redundantly promotes proliferation ¹⁴⁷ Glioblastoma - activates Wnt target genes ¹⁵⁰ Prostate cancer - knockdown reduces phosphorylation of proliferative kinases and increases expression of PTEN ¹⁵¹ |
| KDM4D | JMJD2D | H3K9me3/me2 | Colorectal cancer - promotes tumour formation in mice ¹¹⁰ |
| KDM4E | JMJD2E | H3K9me3/me2 | No function in cancer identified to date. |
| KDM5A | JARID1A RBBP2 | H3K4me3/me2 | Breast cancer - decreases expression of tumour suppressors p16 and p27 ¹⁵² Lung cancer - promotes proliferation by repressing NOTCH1/2 tumour suppressor target genes ¹¹³ Lung cancer - promotes tolerance to EGFR inhibitors ^{153,154} Glioblastoma – controls resistance to standard-of-care temozolomide ¹⁵⁵ |
| KDM5B | JARID1B | H3K4me3/me2 | Leukaemia - downregulates <i>Hox/Meis</i> genes required for acute myeloid leukaemia pathogenesis ¹⁵⁶ Melanoma - tumour suppressive role ¹⁵⁷ Melanoma - maintains slow-cycling stem cell population resistant to therapy ^{158,159} |

| | | | |
|--------------|----------------------------|---|---|
| | | | Myeloma - inhibition attenuates proliferation ¹¹⁴ |
| KDM5C | JARID1C | H3K4me3/me2 | Breast cancer - inhibits migration, invasion and angiogenesis ¹⁶⁰ Renal cancer - tumour suppressive function, downregulation triggers genomic instability ¹⁶¹ |
| KDM5D | JARID1D | H3K4me3/2 | Prostate cancer - represses invasive genes <i>MMP1</i> , <i>MMP2</i> , <i>MMP3</i> , <i>MMP7</i> and <i>SNAI2</i> ¹⁶² Renal cancer - reduces cell viability ¹⁶³ |
| KDM6A | UTX | H3K27me3/2 | Breast cancer - knockdown inhibits proliferation, colony formation and migration ¹⁶⁴ Pancreatic cancer - knockout decreases expression of the tumour suppressor genes ¹⁶⁵ Myeloma - depletion promotes tumorigenicity and confers sensitivity to EZH2 inhibition ¹¹⁹ Lung cancer - deletion promotes tumour progression through an increase in EZH2/H3K27me3 ¹²¹ Acute lymphoblastic leukaemia - bona fide tumour suppressor ¹⁶⁶ Pancreatic cancer - depletion induces metastasis in females ¹⁶⁷ Acute myeloid leukaemia - suppresses myeloid leukemogenesis through noncatalytic functions ¹⁶⁸ Glioblastoma - essential for stem cell transition to a drug-tolerant state ¹⁶⁹ |
| KDM6B | JMJD3 | H3K27me3/me2 | Neuroblastoma - inhibits proliferation and increases differentiation of stem-like cells ¹⁷⁰ |
| KDM6C | UTY | | Acute myeloid leukaemia - suppresses myeloid leukemogenesis through noncatalytic function, similar to KDM6A ¹⁶⁸ |
| KDM7A | JHDM1D KDM7 KIAA1718 | H3K9me2/me1 H3K27me2/me1 H4K20me1 | Prostate cancer - knockdown attenuates proliferation of hormone-sensitive cancer cells ¹⁷¹ Glioblastoma - maintains viability of stem cells ¹⁷² |
| KDM7B | PHF8 | H3K9me2/me1 H3K27me2/me1 H4K20me1 | Laryngeal and hypopharyngeal squamous cell carcinoma - high expression correlates with increased chance of relapse and decreased survival rate ¹⁷³ |
| KDM7C | PHF2 | H3K9me2 | Neural progenitor cells - essential for progenitor self-renewal and cell cycle progression in neural progenitor cells ¹⁷⁴ Colon cancer - activates transcription of p53 target genes and p53-mediated cell death ¹⁷⁵ |
| KDM8 | JMJD5 | H3K36me2 | Inhibits cell proliferation in various tumours ¹⁷⁶⁻¹⁷⁸ |

1.3. The drug discovery process

The main steps of drug discovery are target identification, target validation, hit-to-lead optimisation, pre-clinical lead development and clinical trials¹⁷⁹. Target identification aims to identify a protein which can be targeted for a desirable outcome. In cancer drug discovery, the aim is to find a protein which can be targeted to selectively eliminate the entire cancer cell population while remaining safe for patients¹⁸⁰. Drug targets can be identified using a target-based or phenotypic approach¹⁸¹ (**Figure 1.4**).

Stages of target-based screening:



Stages of phenotypic screening:

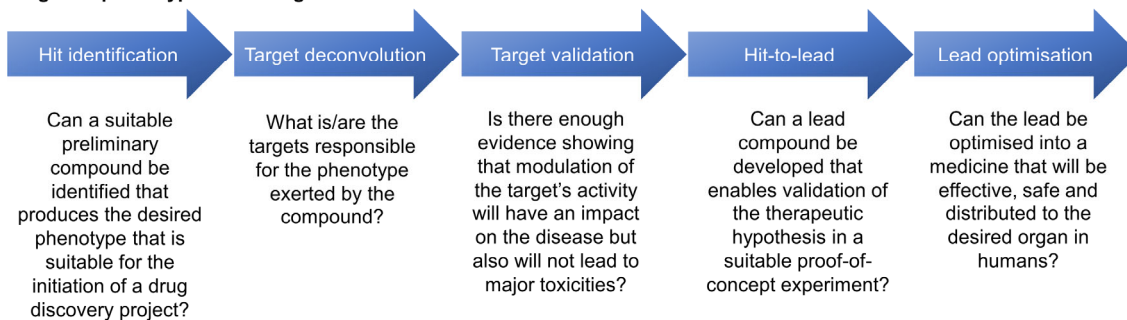


Figure 1.4. Drug discovery stages using a target-based approach and a phenotypic approach¹⁸¹.

1.3.1. Target-based approach to drug discovery

For target-based screens, delineating the molecular mechanism of a disease can identify a target protein with known structure, function, and pathological significance¹⁸². For example, aberrant signalling pathways or abnormal protein function identified in animal disease or clinical tissues can identify a suitable target based on the mechanisms of the disease¹⁸³. An increasingly common approach for target identification is data mining¹⁷⁹, which uses the bioinformatics to analyse chemogenomic or proteomic data sets¹⁸⁴. This analysis is primarily conducted by extracting co-occurring molecules or by identifying gene-gene or protein-protein relationships.

In addition to these target identification approaches, genome-wide screens using CRISPR-Cas9 and RNA interference (RNAi) platforms have emerged as powerful alternatives for uncovering new targets¹⁸⁵. These techniques allow researchers to systematically knock out genes across the genome and observe the phenotypic effects induced by knock-out of individual genes. This unbiased approach can reveal unexpected genes and pathways that play critical roles in disease processes, which might not have been identified through conventional hypothesis-driven research¹⁸⁶. CRISPR-Cas9 screens, with its ability to precisely and efficiently edit the genome, has revolutionised target discovery by enabling the direct link of gene function to disease phenotype¹⁸⁷. Similarly, shRNA screens provide a means to knock down gene expression on a large scale, offering insights into the importance of specific genes and their protein products in maintaining disease states¹⁸⁸.

Once a target is identified, it must be validated to confirm its crucial role in the disease. Following target validation, molecules targeting the protein of interest are developed during the hit-to-lead optimisation stage, where the primary focus is on improving potency and selectivity of the compounds¹⁷⁹. Throughout both the hit-to-lead and lead optimisation stages, it is important to continuously optimise various properties of the compounds. Initially, the focus is on *in vitro* parameters such as solubility, permeability, and metabolic stability. As the project progresses, the focus shifts to optimising more stringent parameters in *in vivo* studies, namely pharmacokinetics, absorption, distribution, metabolism, excretion, and toxicity (ADMET)¹⁸⁹. This ensures that compounds not only interact effectively with their target but also possess favourable drug-like properties, such as appropriate absorption rates, metabolic stability, and minimal toxicity, making them viable candidates for clinical development¹⁹⁰.

The advantage of a target-based approach to drug discovery is that it adopts a more focused approach to identifying targets based on known or genome-wide screening findings¹⁹¹. The strategy is therefore much more efficient and cost-effective since experiments are focused on a protein of interest. However, an in-depth understanding of the causes and mechanisms of the disease is required as prior knowledge in order to identify a correct target. Limited knowledge of some disease models is a major limitation to target-based drug discovery.

1.3.2. Phenotypic approach to drug discovery

In phenotypic drug discovery, the process follows a different order of events in which phenotypic screens of compound libraries are conducted as the first step (**Figure 1.4**). The aim is to induce a desirable phenotype without prior knowledge of the target. Compound libraries

are essential for drug discovery in general. For instance, diversity-oriented libraries encompass a wide range of chemical structures, molecular scaffolds and functional groups that enhance the likelihood of identifying biologically active compounds targeting diverse proteins/genes¹⁹².

Conversely, target-focused libraries are developed based on existing knowledge about specific targets or families of targets¹⁹³. These libraries include compounds that are either structurally similar to known ligands or designed to interact with particular biological target types, like kinases, G protein-coupled receptors, or ion channels¹⁹³. While often utilised in target-based screens, target-focused libraries can also be beneficial in phenotypic screens, particularly when certain pathways or target classes are suspected of playing a role in disease¹⁹⁴.

Natural product libraries draw from compounds isolated from natural sources, such as plants, fungi, and bacteria, leveraging the evolved chemical diversity of nature¹⁹⁵. Given their evolved interaction with biological molecules, natural products provide an extensive source of bioactive compounds with unique, complex structures that are often challenging to synthesise *in vitro*.¹⁹⁶⁻¹⁹⁸

Finally, drug repurposing libraries contain compounds already approved for clinical use or those that have undergone certain stages of clinical testing¹⁹⁹. With known pharmacokinetic and safety profiles, these libraries offer a strategic advantage in phenotypic-based screens for identifying new applications for existing drugs, potentially fast-tracking the clinical application process for new disease indications. However, the assertion that repurposed drugs allow for a faster pre-clinical process is contentious. According to Begley et al.²⁰⁰, while prior knowledge of side effects and toxicity can inform new indications, the clinical and regulatory pathways for repurposed drugs are often more complex than anticipated. Clinical equipoise, the ethical basis for conducting clinical trials, requires that the repurposed drug's efficacy and safety be rigorously compared to the standard of care²⁰¹. Additionally, financial and intellectual property considerations can impede the progress of drug repurposing initiatives²⁰⁰. The potential commercial opportunities must be clearly understood and aligned with regulatory requirements to ensure that the repurposed drug can successfully navigate the clinical trial landscape. Without addressing these aspects, drug repurposing programs may struggle to attract the necessary investment and support, limiting their ability to deliver on their promise of cost- and time-efficiency.

Following the identification of hits and/or drugs with desirable phenotypic effects, the next crucial step involves deconvoluting the mechanism of action of these hits/drugs to pinpoint

the exact target(s) responsible for the efficacy²⁰². Target validation must still be followed to ensure that the correct target is being attributed to the therapeutic outcome. After that, lead optimisation can commence based on the original compound hit from the phenotypic screening¹⁹⁰.

Phenotypic-based screens have the advantage of immediately identifying a biologically active compound for the specific disease model²⁰³. Furthermore, there is a greater chance of discovering novel mechanisms and/or targets as it does not build on preconceived or biased knowledge of the disease model²⁰⁴. However, deconvoluting the compound's mechanism of action can be challenging, often requiring complex and lengthy investigations.

Chemical probes are essential tools in the drug discovery process, serving multiple critical functions in identifying lead molecules, uncovering druggable targets, and validating those targets as relevant for therapeutic intervention²⁰⁵. These probes are chemical compounds which fulfill potency and selectivity criteria: they must adhere to an *in vitro* potency of less than 100 nM for inhibition of enzymatic activity, contain selectivity for the targeted protein at least 30-fold against sequence-related proteins of the same family, and demonstrate on-target cellular activity at concentrations ideally below 1 μM^2 .

Despite the stringent biochemical selectivity criteria, it is always possible that any given chemical probe has unknown off-target activity²⁰⁶. Therefore, it is essential to use a structurally orthogonal chemical probe, when available, which contains the potency towards a target to enable cross-validation studies²⁰⁷. Chemical probes are instrumental in the functional exploration of proteins in their biological context. Furthermore, chemical probes can be used in phenotypic screens. Phenotypic changes induced by a chemical probe can indicate the involvement of specific proteins or pathways in diseases²⁰⁸.

1.4. Thesis aims

Our laboratory has previously conducted a phenotypic screen to measure the viability of glioblastoma cells upon treatment with the Structural Genomics Consortium's library of chemical probes targeting epigenetic enzymes (**Figure 1.5**). From this screen, the KDM4 inhibitor QC6352 was identified as the most efficacious in reducing cell viability. QC6352 is a KDM4 inhibitor, with the greatest selectivity *in vitro* for KDM4C ($\text{IC}_{50} = 35 \text{ nM}$) followed by KDM4B ($\text{IC}_{50} = 56 \text{ nM}$) and KDM4A and KDM4D (both $\text{IC}_{50} = 104 \text{ nM}$)²⁰⁹. Compared against other JmjC domain-containing KDM family members, QC6352 is selective, showing no activity at up to 10 μM for all other KDMs except for KDM5B ($\text{IC}_{50} = 750 \text{ nM}$)²¹⁰. The potent

anti-proliferative efficacy of QC6352 at 200 nM in glioblastoma stem cells forms the basis of this PhD thesis.

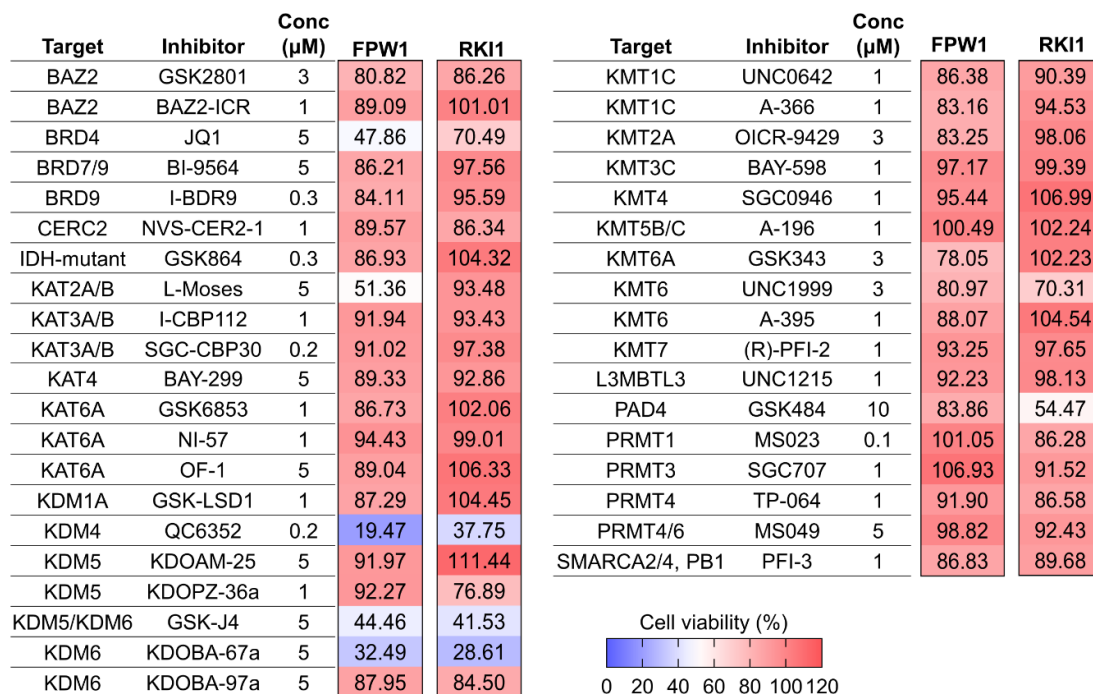


Figure 1.5. Phenotypic screen of epigenetic probes in glioblastoma stem cell lines. RKI1 and FPW1 glioblastoma stem cells were treated with epigenetic probes for 5 days and cell viability assays ($n = 3$) were performed (Ramzi Abbassi, PhD thesis, 2021).

Glioblastoma remains an incurable disease with no improvement in patients' survival since the introduction of the Stupp protocol in 2005¹¹. The failure of over 1,250 interventional glioblastoma trials has revealed unique challenges associated with glioblastoma therapy, which include tumour heterogeneity, an immunosuppressive tumour microenvironment, and the presence of the blood-brain barriers⁴⁹. A further challenge is the lack of data robustness in preclinical studies, which can mislead investigators to focus on drug candidates destined to fail in clinical trials. The overarching aim of this PhD candidature was, therefore, to advance glioblastoma drug discovery research.

Chemical probes and their correct use are essential for accurate mechanistic and target validation in preclinical research²⁰⁷. Numerous reviews and online resources list recommendations for use of chemical probes, yet adherence to these recommendations is poor²⁰⁶. Furthermore, while the suboptimal use of chemical probes has been widely discussed, the extent of this problem remains unknown. We aimed to quantify the extent of this issue by performing a systematic review of 662 primary-research articles and assessed the use of chemical probes in preclinical research (**Chapter 3**). Our work, published in *Nature*

Communications 2023, revealed that only 4% of analysed publications used chemical probes in line with recommendations. This indicates that the best practice with chemical probes is yet to be implemented in research, including glioblastoma drug discovery.

Phenotypic screens offer a promising path to identify a lead molecule and/or preclinical candidate able to target heterogeneous tumours such as glioblastoma²¹¹. In previous research, a phenotypic screen using the Structural Genomics Consortium's library of epigenetic inhibitors identified the KDM4 inhibitor QC6352 with potent antiproliferative efficacy in two glioblastoma stem cell lines. This PhD candidature aimed to establish the therapeutic potential of QC6352 (**Chapter 4**). These findings, while demonstrating potent anti-cancer efficacy of QC6352 in 2D and 3D glioblastoma models, revealed that the efficacy of QC6352 is likely not linked to KDM4 inhibition. Given this unexpected discovery, the subsequent experiments aimed to delineate QC6352's mechanism of action and identify target(s) responsible for QC6352's remarkable efficacy in glioblastoma (**Chapter 5**). Finally, given the lack of orthogonal KDM4-targeting chemical probes, we aimed, in collaboration with Dr Jennifer Baker at the University of Newcastle, to develop potent and selective KDM4 inhibitors structurally distinct from QC6352. Over 200 analogues synthesised at the University of Newcastle were tested for KDM4 inhibition as a part of this PhD candidature. The synthesis, characterisation, and structure-activity relationship of the first-generation hydrazine-based inhibitors (**Chapter 6**) have been finalised and submitted to the *RSC Medicinal Chemistry* journal.

Chapter 2

Materials and methods

2.1. Cell line models

RKI1, FPW1, and HW1 glioblastoma stem cell (GSC) lines were derived from glioblastoma specimens at QIMR Berghofer Medical Research Institute, Brisbane, Australia. Characterisation of these cell lines includes RNA sequencing, mutational profiling, subtype assignment, and proteomic data which are available online at: <https://www.qimrberghofer.edu.au/ourresearch/commercialisation/q-cell/>. The GBM6 GSC line was derived from patient samples. All GSC lines were cultured in KnockOut Dulbecco's Modified Eagle's Medium (DMEM)/F-12 basal medium supplemented with StemPro Neural Stem Cell Serum Free Medium, 2 mM GlutaMAX-ICTS, 20 ng/mL EGF, 10 ng/mL FGF- β and 1% Antibiotic-Antimycotic solution. Flasks were coated with Matrigel Matrix diluted 1:100 with cold Phosphate-Buffered Saline (PBS) at least 1 hour prior to use. Cells were maintained under standard conditions of 37°C, 5% CO₂ and passaged every 3 - 5 days by washing with sterile PBS and detaching with StemPro Accutase Cell Dissociation Reagent.

The A172 glioblastoma cell line was cultured in DMEM supplemented with 10% (v/v) Foetal Bovine Serum (FBS) and 1% (v/v) Antibiotic-Antimycotic solution, under standard conditions of 37°C, 5% CO₂. A172 cells were passaged every 3 - 5 days and were detached with TrypLE Express Enzyme.

To generate A172 cells expressing the Fluorescent Ubiquitination-based Cell Cycle Indicator (FUCCI) components, A172 cells were transduced as outlined by Monira Hoque et al.²¹². For glioblastoma cells over-expressing KDM4A, A172 cells underwent transduction with a pLenti-C-mGFP-P2A-Puro lentiviral vector containing the KDM4A gene tagged with mGFP at the C-terminal and a puromycin resistance gene. The transduction process was facilitated by 8 μ g/mL polybrene at a multiplicity of infection (MOI) ranging from 1 - 25 as described in figures. After 24 hours following transduction, cells were subjected to 2 μ g/mL puromycin selection and incubated for 72 hours before the media was replaced with fresh DMEM. The surviving cells were labelled A172-KDM4A cells.

Normal human astrocytes (NHAs) were cultured in astrocyte basal medium (ABM) supplemented with the SingleQuots supplement pack containing FBS, L-glutamine, GA-1000, ascorbic acid, HEGF, and insulin. NHAs were maintained in standard conditions of 37°C, 5% CO₂ until 80% confluency, at which point they were detached with a 0.025% trypsin/EDTA solution and neutralised with the Trypsin Neutralising Solution.

Access and use of patient-derived glioblastoma cell lines were approved by the Human Ethics Committee of The University of Sydney (HREC2013/131) and the Human Ethics Committee of the Royal Brisbane & Women's Hospital (RBWH2004/161). KDM4A lentiviral overexpression was approved for access and use by the Institutional Biosafety Committee of The University of Sydney (22N009). All cell cultures were tested for mycoplasma infection monthly, and the cumulative length of culturing did not exceed 20 passages for established cell lines, 15 passages for GSC lines, and 5 passages for NHAs.

2.2. CellTitre-Blue viability assay

Cells were seeded in 96-well plates (2×10^3 cells/well) and were treated with tested compounds for 5 days. CellTitre-Blue was added (1:10 dilution) to each well and incubated at 37 °C for 90 minutes. Fluorescence was measured with a Tecan M200 PRO+ microplate reader at excitation/emission 530/590 nm. Data were normalised to untreated cells (set as 1). Growth-rate corrected GR₅₀, GR_{max}, hGR, and GR_{AOC} metrics were calculated from viability data using the GRcalculator online tool. Proliferation rates for each cell line were calculated by comparing initial viability against final viability for each replicate. Graphs were recreated from the GRcalculator online tool using Prism v10.0 (GraphPad).

2.3. Clonogenic outgrowth assay

RKI1, FPW1, GBM6 and HW1 cells were seeded in 6-well plates (2×10^3 cells/well) and treated with QC6352, IOX1, B3 or ML324 for 10 days with or without a further 10-day recovery in drug-free media as described. The colonies were incubated with a fix/stain solution of 1% toluidine blue overnight at 4°C. Colonies were counted using the ImageJ ColonyArea software and normalised to untreated controls (set as 100%).

2.4. Spheroid growth assay

FPW1 and RKI1 cells were seeded in round bottom 96-well plates (2×10^3 cells/well) and left to form spheroids for 48 hours. The spheroids were then treated with QC6352 (50 and 100 nM). Spheroids were grown for two weeks, imaged at Day 7 and Day 14 using the phase contrast setting on a Zeiss Axio Scope.A1 microscope using ZEN 2 - blue edition software. The relative spheroid growth was analysed by measuring the spheroid circumference compared to the untreated spheroid using Fiji.

2.5. Reverse Transcription-Quantitative Polymerised Chain Reaction (RT-qPCR)

RT-qPCR was carried out according to standard protocols. FPW1 and A172 cells were seeded in a 10 cm petri dish (5×10^5 cells/dish) and treated with QC6352 as described. RNeasy mini kit was used to isolate RNA from cell lysates as per manufacturer's instructions. cDNA was generated using Applied Biosystems High-Capacity cDNA Reverse Transcription kit as per manufacturer's instructions. RT-qPCR was performed using Quantitect-validated primers listed in Table 2.1 with KAPA SYBR FAST Universal $2\times$ qPCR Master Mix (Kapa Biosystems). RT-PCR was run on LightCycler 480 (Roche). The cycling condition were as follows: 10 min at 95 °C followed by 45 cycles, each consisting of 10 s at 95 °C and 30 s at 60 °C. Threshold cycles (CT) were calculated using the LightCycler® 480 software. The *ACTB1*, *GAPDH*, *EEF1A* and *18S rRNA* primers were used as loading controls with *GAPDH* chosen as the representative quantification. Values were expressed as fold change over corresponding values for the control by the $2^{-\Delta\Delta CT}$ method.

2.6. Fluorescence Ubiquitin Cell Cycle Indicator (FUCCI) cell cycle analysis

A172-FUCCI cells were seeded in a 96-well plate (1×10^3 cells/well), treated with QC6352 at concentrations ranging from 50 - 500 nM, and placed into the IncuCyte ZOOM Live-cell analysis system for 120 hours. Four images per well were taken at regular 2-hour intervals using the $10\times$ objective in green (acquisition time 200 ms) and red channels (acquisition time 600 ms). The confluency of the cells (phase contrast) and number of cells in G₀-G₁ phases (red), G₁/S transition (yellow or overlap) and S-G₂-M phases (green) were quantified using IncuCyte Basic Analysis software. The percentage of cells in each phase was calculated based on the number of cells identified as red, yellow, or green for each timepoint.

2.7. β -galactosidase staining

FPW1, RKI1 cells were plated in 6-well plates (2×10^3 cells/well) and treated with 50 - 100 nM QC6352 for 10 days. Cells were then fixed and stained for β -galactosidase using the Senescence β -galactosidase Staining Kit, following manufacturer's instructions. The following day, images were taken at $40\times$ objective using the Zeiss Axio inverted microscope using ZEN 2 - blue edition software and scored using ImageJ. For scoring, cells were counted in randomly

chosen fields from each sample and β -galactosidase positive cells were calculated from the number of blue cells over the total number of cells counted.

2.8. Western blotting

2.8.1. Sample preparation

Cells were seeded in 10 cm petri dishes (5×10^5 cells/dish) and treated with QC6352 as stated in figures. For whole-cell lysis, cells were lysed with $1\times$ RIPA buffer supplemented with 1 mM sodium orthovanadate, 1 mM phenylmethylsulfonyl fluoride and $1\times$ phosphatase inhibitor. To ensure complete cell lysis, the lysates were sonicated 3 times for 10 seconds each. To remove cell debris, the lysates were centrifuged at 16,000 g for 20 minutes and the supernatant was collected. Histones were extracted from harvested cells using the Histone extraction kit as per manufacturer's instructions. Subcellular protein fractions were collected as per manufacturer's instructions using either the Subcellular Fractionation Kit or NE-PER Nuclear Cytoplasmic Kit as stated in figures.

2.8.2. Immunoblotting

Protein concentrations were determined using the Pierce BCA assay kit, following manufacturer's instructions. Samples were prepared with $1\times$ LDS loading buffer and $1\times$ sample reducing agent, then heated at 95 °C for 5 min. For electrophoresis, 1 μ g of histone extracts or 40 μ g of protein were loaded into Bis-Tris gels and was run using $1\times$ MOPS running buffer at 200 V for 30 minutes. Proteins were subsequently transferred onto nitrocellulose membranes using the iBlot 2 Dry Blotting System for at 15 V for 7 minutes. Membranes were blocked with 5% skim milk in Tris-Buffered Saline with 0.05% Tween 20 (TBST) for 1 hour at room temperature. For primary antibody incubation, membranes were incubated overnight at 4°C in 5% Bovine Serum Albumin (BSA) in TBST, using a 1:1000 dilution of the primary antibody. Following this, membranes were washed three times in TBST for 10 minutes each wash. The secondary antibody, diluted 1:5000 in 5% skim milk in TBST, was applied for 1 hour at room temperature. Afterward, membranes were washed three times in TBST for 10 minutes each wash. Detection was performed with Immobilon Western HRP Substrate Luminol-Peroxidase kit and the ChemiDoc MP Imaging System. Densitometry quantification was analysed using ImageLab software.

2.9. Incucyte Annexin V apoptosis assay

FPW1 and RKI1 cells were seeded in 96-well plates (1×10^3 cells/well) and treated with 50 - 500 μ M QC6352 for 10 days. After treatment, cells were placed into the IncuCyte ZOOM Live-cell analysis system and Annexin V Red Reagent was added at a 1:200 dilution to detect exposed phosphatidylserine as a marker of apoptosis. For each well, 16 images were taken one hour after adding the Annexin V reagent using phase contrast and red fluorescence (acquisition time 500 ms). Incucyte Basic Analysis Software was used to minimise background fluorescence and quantify confluency and fluorescence.

2.10. Immunofluorescence imaging

FPW1 and RKI1 cells were seeded in 24-well imaging plates (4×10^3 cells/well) and treated with 100 or 500 nM QC6352 for 7 and 10 days. Cells were fixed with 4% formaldehyde for 15 minutes at room temperature and washed 3 times with PBS. For blocking, a buffer containing PBS, 5% normal goat serum, 0.3% Triton X-100, and 1% BSA was used to incubate the cells for one hour at room temperature. Overnight incubation with the primary antibody was performed at 4 °C using a dilution of 1:200 in the blocking buffer. Cells were washed 3 times in PBS containing 0.3% Triton (PBST) and incubated in Alexa594-conjugated anti-rabbit IgG secondary antibody in blocking buffer for one hour in the dark. Cell nuclei were counterstained using Prolong Gold Mounting Media with 4',6-diamidino-2-phenylindole (DAPI). For each well, 16 images were taken using a 40 \times objective on a Zeiss Axio Scope.A1 microscope with ZEN 2 - blue edition software. The fluorescence of cells in each image was quantified using Fiji.

2.11. Small interfering RNA (siRNA) transfection

Cells were seeded in 6-well plates (5×10^5 cells/well) and incubated overnight. To inhibit KDM4A-D, siRNA transfections were performed using Lipofectamine RNAiMAX in combination with Opti-MEM Reduced Serum Medium. Solution A containing siRNA diluted in Opti-MEM was incubated for 5 minutes at room temperature. Concurrently, solution B containing Lipofectamine RNAiMax diluted in Opti-MEM was also incubated for 5 minutes at room temperature. Subsequently, solution A and solution B were mixed together to create the transfection solution and incubated for a further 5 minutes. The transfection solution was then diluted with complete DMEM media to create the final transfection media. Cells were washed with PBS and media was replaced with transfection media. Cells were incubated with

transfection media for 5 hours, after which the media was replaced with fresh DMEM media. The final concentration of each siRNA was 5 nM and the depletion of the targeted protein (compared to a scramble siRNA negative control) was confirmed by RT-qPCR.

2.12. Incucyte proliferation confluency analysis

A172 cells were seeded in 6-well plates (50×10^3 cells/well) and treated as described in figures. For each well, 25 images were taken in phase contrast every hour using the Incucyte ZOOM 10 \times objective lens. Incucyte ZOOM Basic Analysis software (Sartorius) was used to quantify the confluency of cells over time.

2.13. CRISPR-Cas9 fitness and chemogenetic screens

2.13.1. Lentivirus production

To generate lentivirus, TKOv3 plasmid library was co-transfected with packaging plasmids pCAG-VSVG and psPAX2. A T175 flask of 80% confluent HEK293T cells was transfected in OptiMEM using 19.5 μ g of the TKOv3 plasmid library, 6.5 μ g pCAG-VSVG, 19.5 μ g psPAX2, 87.5 μ l of P3000 Reagent, and 87.5 μ l of Lipofectamine 3000. Cells were incubated overnight and then media was changed to DMEM with 5% FBS. After 48 hours, viral supernatants were collected and centrifuged at 2000 rpm for 10 minutes to remove cell debris. The supernatant was filtered through a 0.45 μ m ultra-low protein binding filter and concentrated in a spin concentrator. Aliquots were stored at -80 $^{\circ}$ C.

2.13.2. Pooled genome-wide CRISPR screens in RKI1 cells

RKI1 cells were seeded in 24-well plates (1×10^4 cells/well) to determine functional titres of the TKOv3 library. Titrated virus was combined with 8 μ g/ml polybrene and added to each well. 24 hours after infection, the media was replaced with media containing puromycin (2 μ g/ml) and was incubated for 48 hours. The concentration of titrated virus was measured by determining the multiplicity of infection (MOI). To do this, the survival of infected cells was compared against non-infected control cells 72 hours after infection.

RKI1 cells were seeded in T175 flasks (7×10^7 cells) and infected with the TKOv3 lentiviral library at MOI of 0.3; approximately a 300-fold sgRNA coverage in the cell population. 24 hours after infection, media was changed to media containing puromycin (2 μ g/mL). 96 hours after infection, puromycin-selected cells were combined, and 70×10^6 cells were stored at -80 $^{\circ}$ C. The remaining cells (70×10^6) were seeded onto fresh, Matrigel-coated

T175 flasks as replicates in drug-free media and cultured until reaching 80% confluency. Once grown, cells were collected in 70×10^6 cell aliquots and stored at -80°C .

15 days post-selection (3rd overall cell harvesting time point), cells were seeded onto Matrigel-coated T175 flasks at 20% confluency and treated with QC6352 at EC₂₀ or EC₉₀ concentrations (25 and 70 nM) for 5 days. Cells were cultured until reaching 80% confluency, before collecting approximately 70×10^6 cell aliquots stored at -80°C . 26 days post-selection, cells were treated again at the same concentrations for another 5 days. 70×10^6 cell aliquots were continued to be collected until a total of 8 cell aliquots were taken.

2.13.3. sgRNA sequencing

Genomic DNA was extracted from harvested cells using the Bioline ISOLATE II Genomic DNA Kit according to manufacturer's instructions. Sequencing libraries were prepared by amplifying gRNA inserts via a 2-step PCR using primers that include Illumina adaptors with i5 and i7 indices. Resulting libraries were subsequently sequenced on an Illumina NovaSeq6000 to achieve a coverage of 300-fold per gRNA.

2.13.4. Chronos analysis

Read counts generated from sgRNA sequencing were loaded into a Python 3 coding environment (Project Jupyter) along with a list of positive and negative control genes. Positive controls were taken as the list of common essential genes in the Dependency Map (DepMap) public 23Q2 dataset, while negative controls were taken as unexpressed RKI1 genes based on publicly available Qcell gene expression data²¹³. The Chronos package was utilised to first identify false positive clonal outgrowths in the dataset and second train a model using a machine-learning algorithm to identify and quantify changes in RKI1 fitness genes within untreated, EC₂₀- and EC₉₀-treated RKI1 cells. A standard of 801 total epochs was used with a burn in period of 50 epochs for model training. The resultant table contained Chronos scores with negative scores representing decreased fitness and positive scores representing increased fitness. Chronos scores were normalised within each treatment group so that the median Chronos score from the list of positive controls was -1 and the median Chronos score from the list of negative controls was 0. The mean probability of gene dependency was calculated using the 23Q2 DepMap gene dependency probability dataset for all genes.

2.13.5. Limma analysis

Read counts generated from sgRNA sequencing were loaded into a R coding environment. The limma package was used to establish linear models of each sgRNA read count including interactions between treatment and time. Empirical Bayes statistics was computed for the linear model fit and the p-values were adjusted using the Benjamini-Hochburg method. The log fold change for each sgRNA targeting the same gene were averaged together using the weighting of guide efficacy calculated using the Chronos package. Adjusted p-values were also combined for each orthogonally-targeting sgRNA using Lancaster's method.

2.14. Cellular Thermal Shift Assay (CETSA)

2.14.1. Lysed-cell CETSA sample preparation

FPW1 or A172-KDM4A cells (24×10^6 cells) were seeded in T175 flasks at 80% confluency and incubated overnight at 37°C to attach before harvesting. Harvested cells were washed, resuspended in PBS, aliquoted based on the number of treatment conditions, and lysed by conducting 3 freeze-thaw cycles using liquid nitrogen and a 37°C waterbath. Each lysate was treated with QC6352, ML324, MK2206, or an equivalent volume of DMSO (1:10 dilution) as described in figures. Aliquots were heated at designated temperatures ranging from 40 - 60°C for 3 minutes using a ThermoCycler and immediately cooled on ice for 3 minutes. Finally, denatured proteins were pelleted by centrifuging at 100,000 g for 20 minutes at 4°C and the supernatant containing non-denatured proteins were taken for further analysis by Western blotting or mass spectrometry.

2.14.2. Intact-cell CETSA sample preparation

FPW1 cells (24×10^6 cells) were seeded in T175 flasks at 80% confluency and incubated overnight at 37°C to attach. Cells were treated with 20 μ M QC6352, ML324, or an equivalent volume of the vehicle DMSO for 5 hours at 37°C before harvesting. Harvested cells were washed, resuspended in PBS, and divided into 8 aliquots for each treatment condition. Aliquots were then heated at designated temperatures ranging from 40 - 60°C for 3 minutes using a ThermoCycler and immediately cooled on ice for 3 minutes. Cells were then lysed by conducting 3 freeze-thaw cycles using liquid nitrogen and a 37°C waterbath. Finally, denatured proteins were pelleted by centrifuging at 100,000 g for 20 minutes at 4°C and the supernatant

containing non-denatured proteins were taken for further analysis by Western blotting or mass spectrometry.

2.14.3. Mass spectrometry cellular thermal shift assay (MS-CETSA)

To each sample, a digest buffer consisting of 2% sodium deoxycholate, tris (100 mM, pH 8.5), Tris(2-carboxyethyl)phosphine hydrochloride (10 mM), and 2-chloroacetamide (40 mM) was mixed in equal parts (1:1 sample to digest buffer) and samples were incubated at 45 °C for 5 minutes with shaking (1,500 rpm) to reduce and alkylate disulfide bonds. Following reduction and alkylation, samples were digested by the addition of the proteases trypsin and lysyl endopeptidase (1:50 protein to enzyme) overnight at 37 °C.

Two stacked disks of styrenedivinylbenzene- reverse phase sulfonate (SDB-RPS) material was punched out using a blunt-tipped needle and packed into the bottom of 200 µL pipette tips, forming StageTips. Digested peptides were mixed 1:1 with 99% ethyl acetate/1% Trifluoroacetic acid (TFA), vortexed thoroughly, and loaded directly onto the StageTips, using a custom 3D-printed device enabling centrifugal loading. After all liquid had passed through, StageTips were washed once with 100 µL wash buffer 1 (99% isopropanol/1% TFA), followed by 100 µL of wash buffer 2 (5% acetonitrile/0.1% TFA). Peptides were subsequently eluted in 30 µL of elution buffer (5% ammonium hydroxide/30% acetonitrile) directly into clean PCR strip tubes. Eluted peptides were dried to completion in a rotary vacuum centrifuge.

Peptides were resuspended in 5 µL of MS loading buffer (0.3% TFA/2% acetonitrile) with mixing (2,000 rpm, 5 minutes) and loaded onto a 50 cm fused silica column with a 75 µm inner diameter and a pulled-tip emitter. Columns were packed in-house with 1.9 µm C18 ReproSil Pur-AQ 200Å particles (Dr. Maisch, GmbH). Reversed-phase chromatography was performed on a Dionex Ultimate 3000 HPLC, using a binary buffer system comprising 0.1% formic acid (buffer A) and 80% acetonitrile/0.1% formic acid (buffer B). Column temperature was maintained at 60°C using a column oven (Sonation, GmbH). Peptides were separated using a linear gradient of buffer B from 5% to 30% over 60 minutes at a flow rate of 400 nL/min and electrosprayed directly into an Orbitrap Exploris 480 mass spectrometer by the application of 2.4kV using a liquid junction connection installed immediately upstream of the column. The Exploris 480 was operated in data-independent acquisition (DIA) mode, acquiring MS1 scans from 350-1400 m/z followed by 47 data-independent MS2 scans (350-1022 m/z) with HCD fragmentation (target 3×10^6 ions, maximum injection time 22 ms, isolation window 14 m/z,

1 m/z window overlap, normalized collision energy 25%), with fragments detected in the Orbitrap with a resolution of 15,000.

MS data were analysed using MaxQuant (version 2.1.3.0) using default settings with minor changes: Oxidised Methionine (M), Acetylation (Protein N-term) were selected as variable modifications, and Carbamidomethyl (C) as fixed modification. Data were searched using Discovery DIA, against the UniProt Reference Proteome database, May 2021 (MaxQuant) releases.

2.14.4. TPP analysis

Protein abundance values analysed by MaxQuant were loaded into the R coding environment along with the TPP package. Melt curves for all detected proteins were fitted using the ‘analyzeTPPTR’ function. To use an appropriately sized (>100) dataset for normalisation, the ‘fcRequirements’ parameter was set to (4, 5, 8), the ‘thresholdLower’ parameter was set to (0.5, 0.2, 0.0) and the ‘thresholdHigher’ parameter was set to (0.8, 0.5, 0.2). All other parameters remained at the default settings.

2.15. RNA-sequencing

Library preparation for RNA sequencing was conducted using the Illumina Stranded mRNA Prep kit (Illumina; CA, USA), following the manufacturer's instructions. Briefly, FPW1 cells (5×10^5 cells) were seeded in T75 flasks and treated with 100 nM QC6352 for 24, 72, or 120 hours. 500 ng of extracted mRNA per sample was purified and fragmented, converted to cDNA, before end prep was performed. Once prepared, adaptors and indices were attached to ligate fragments, before PCR enrichment was conducted to enrich adaptor ligated fragments.

2.16. AlphaScreen assay

An assay buffer consisting of HEPES (50 mM), BSA (0.02% w/v), and Tween 20 (0.01% v/v) was prepared in ultrapure water (Milli-Q), pH adjusted to 7.5, and filtered through a sterilised 0.2 μm filter. The detection solution consisting of streptavidin donor beads (20 $\mu\text{g}/\text{mL}$), Protein A acceptor beads (20 $\mu\text{g}/\text{mL}$), and anti-H3K9me2 mouse IgG (30 ng/mL) were prepared in assay buffer and preincubated at room temperature in the dark for at least 1 hour. The substrate solution consisted of ammonium iron(II) sulfate hexahydrate (2 μM), disodium 2-oxoglutarate dihydrate (20 μM), L-ascorbic acid (200 μM), and biotinylated H3K9me3 (20 nM). The recombinant KDM4A plasmid enzyme was obtained as described by Ramzi Abbassi, PhD thesis, 2021. Briefly, the plasmid was amplified by PCR and transformed in E. coli cells.

The enzyme was extracted and purified through a combination of nickel-affinity, size-exclusion, and anion-exchange chromatography.

The enzyme solution consisting of KDM4A (3 nM) was prepared in assay buffer. The stop solution consisting of EDTA (30 mM) and NaCl (800 mM) were prepared in assay buffer. Compound stock solutions were prepared at 20 mM in anhydrous DMSO and diluted in assay buffer to generate dilution series ranging in concentration from 0.01 - 20 μ M.

The assay reaction was performed in 384-well ProxiPlates at a total volume of 10 μ L. Tested analogues were preincubated with KDM4A at 2 \times final concentration for 15 minutes at room temperature prior to adding the substrate solution to 1 \times final concentration to initiate the demethylation reaction for 20 minutes at room temperature. An uninhibited enzyme control was tested by diluting KDM4A to 2 \times final concentration and adding substrate solution to 1 \times final concentration for 20 minutes at room temperature. Background fluorescence was assessed by testing substrate solution diluted in assay buffer without KDM4A to 1 \times final concentration. The demethylation reaction was quenched by adding 5 μ L of the stop solution and 5 μ L of the detection solution was added to detect H3K9me2 abundance through AlphaScreen signalling.

AlphaScreen signals measuring the abundance of H3K9me2-biotin were detected using a Tecan INFINITE M1000 Pro plate reader with an excitation wavelength of 680 nm, a detection range of 520 - 620 nm, and an excitation time of 100 ms. Results were analysed by comparing inhibited KDM4A enzyme activity as a percentage of uninhibited KDM4A enzyme activity.

2.17. Statistical tests of comparison

The data and statistical analysis comply with the recommendations on experimental design and analysis by the Sydney Informatics Hub, a Core Research Facility of the University of Sydney. All statistical analyses were conducted on experiments repeated at least three times. All results are expressed as mean \pm SEM, unless otherwise indicated. One-sample t-tests were performed to compare data sets normalised to an untreated control group. Adjustments for multiple testing were made using the Bonferroni correction method, where each p-value was multiplied by the number of statistical tests conducted while keeping the alpha level unchanged. Significance in RT-qPCR data was tested using a paired t-test prior to normalisation to the untreated control and adjusted for multiple testing using the Bonferroni method. For live cell imaging analysis obtained using the Incucyte ZOOM, a two-way ANOVA followed by Bonferroni's multiple comparisons correction was employed. Details of other statistical

analyses are provided in their respective methodology sections. In all cases, an adjusted p-value < 0.05 was considered statistically significant.

2.18. Reagents and chemicals

Table 2.1. List of reagents and resources used in this thesis.

| Reagent or Resource | Source | Identifier |
|--|--|-----------------------------------|
| Glioblastoma Cell Lines | | |
| A172 | ECACC | Cat# 88062428 |
| FPW1 | QIMR Berghofer | QIMR-B002 |
| GBM6 | - | - |
| HW1 | QIMR Berghofer | QIMR-B003 |
| NHA | Lonza Bioscience | Cat# CC-2565 |
| RKI1 | QIMR Berghofer | QIMR-B008 |
| Cell Culture Products | | |
| Antibiotic-Antimycotic 100X | Life Technologies | Cat# 15240112 |
| DMEM, high glucose, GlutaMAX Supplement | Gibco | Cat# 10566016 |
| Dulbecco's phosphate-buffered saline | MerckMillipore | Cat# D8537 |
| Foetal bovine serum | Bovogen Biologicals | Cat# SFBS-f |
| KnockOut™ DMEM/F-12 | Gibco | Cat# 12660012 |
| Lipofectamine RNAiMax | Life Technologies | Cat# 13778150 |
| Matrigel basement membrane matrix | Corning Life Sciences | Cat# 356234 |
| Opti-MEM reduced serum medium | Life Technologies | Cat# 31985070 |
| StemPro accutase cell dissociation reagent | Life Technologies | Cat# A11105 |
| StemPro neural stem cell serum free medium | Gibco | Cat# A10509 |
| TrypLE express enzyme | ThermoFisher Scientific | Cat# 12604 |
| Antibodies | | |
| Akt | Cell Signaling Technology | Cat# 9272 |
| β-actin | Abcam | Cat# ab8227 |
| βIII-tubulin | Abcam | Cat# ab18207 |
| EDTA | Fisher Scientific | Cat# BP120 |
| GAPDH | Cell Signaling Technology | Cat# 97166 |
| GFAP | Cell Signaling Technology | Cat# 12389S |
| H3K36me3 | Abcam | Cat# ab9050 |
| H3K9me3 | Abcam | Cat# ab8898 |
| H3K9me2 | Abcam | Cat# ab1220 |
| Histone 3.3 | Abcam | Cat# ab176840 |
| HSP90 | R&D Systems | Cat# MAB3286 |
| KDM4A | Novus Biologicals Cell Signaling Technology | Cat# AF6434 Cat# 5328S |
| KDM4B | Bethyl laboratories Cell Signaling Technology | Cat# A301-478A Cat# 8639S |
| KDM4C | Novus Biologicals Santa Cruz Biotechnology | Cat# NBP1-49600 Cat# sc-515767 |
| KDM4D | Novus Biologicals Abcam | Cat# NBP1-03357 Cat# ab93694 |

| | | |
|---|---------------------------------|--------------------------------|
| KDM4E | MerckMillipore | Cat# ABE1081 |
| Lamin A/C | Cell Signaling Technology | Cat# 2032 |
| Mouse IgG, Alexa Fluor488 | Life Technologies | Cat# A10680 |
| Mouse IgG, HRP-linked | Cell Signaling Technology | Cat# 7076 |
| Sodium Chloride >99.5% | VWR Analar Normapur | Cat# 27810.364 |
| Rabbit IgG, AlexaFluor594 | Life Technologies | Cat# A11012 |
| Rabbit IgG, HRP-linked | Cell Signaling Technology | Cat# 7074 |
| SOX9 | Santa Cruz Technology | Cat# sc-166505 |
| Total H3 | Cell Signaling Technology | Cat# 4499 |
| Chemicals, Peptides, and Lentiviral particles | | |
| 1% Toluidine blue solution | Point Of Care Diagnostics | Cat# TB1%/1L |
| Ammonium Iron (III) Sulphate | Sigma-Aldrich | Cat# 221260 |
| α -ketoglutaric acid (2-OG) | Sigma-Aldrich | Cat# 75892 |
| Bolt Bis-Tris mini protein gels | Thermo Fisher Scientific | Cat# NW04122BOX, NW00122BOX |
| Bolt LDS Sample Buffer | Thermo Fisher Scientific | Cat# B0008 |
| Bolt MOPS SDS running buffer | Thermo Fisher Scientific | Cat# B000102 |
| Bolt sample reducing agent | Thermo Fisher Scientific | Cat# B0009 |
| Bovine serum albumin | Sigma-Aldrich | Cat# A7030 |
| Formaldehyde solution 4%, buffered, pH 6.9 | MerckMillipore | Cat# 1004965000 |
| H3K9Me2-biotin peptide | AnaSpec | Cat# AS-64359 |
| H3K9Me3-biotin peptide | AnaSpec | Cat# AS-64360 |
| HEPES free acid >99.5% | Gibco Life Technologies | Cat# 11344-041 |
| Incucyte Annexin V red dye for apoptosis | Sartorius | Cat# 4641 |
| IOX1 | Sigma-Aldrich | Cat# SML0067 |
| KDM4A human tagged ORF clone lentiviral particle | OriGene | Cat# RC200574L4V |
| L-ascorbic acid | Sigma-Aldrich | Cat# A5960 |
| Lentiviral control particles | OriGene | Cat# PS100093V |
| MK2206 | SelleckChem | Cat# S1078 |
| ML324 | Cayman Chemical | Cat# 17472 |
| NCGC00244536 | Cayman Chemical, SelleckChem | Cat# 18478, E0132 |
| Non-fat dry milk | Cell Signaling | Cat # 9999 |
| Normal goat serum | Thermo Fisher Scientific | Cat# 31872 |
| Phenylmethylsulfonyl fluoride | Sigma-Aldrich | Cat# 78830 |
| Phosphatase inhibitor | Roche | Cat# PPC1010 |
| Polybrene | MerckMillipore | Cat# TR-1003 |
| Prolong gold antifade mountant with DAPI | Thermo Fisher Scientific | Cat# P36935 |
| Puromycin | ThermoFisher Scientific | Cat# A1113803 |
| QC6352 | MedChemExpress | Cat# HY-104048 |
| RIPA lysis buffer | Sigma-Aldrich | Cat# 20-188 |
| siKDM4A | ThermoFisher Scientific | Assay ID: s18635, 21755 |
| siKDM4B | ThermoFisher Scientific | Assay ID: s22867, 148508 |
| siKDM4C | ThermoFisher Scientific | Assay ID: s225929, 108666 |
| siKDM4D | ThermoFisher Scientific | Assay ID: s31266, 109040 |
| Sodium orthovanadate | Sigma-Aldrich | Cat# S6508 |
| Streptavidin-HRP | GeneTex | Cat# GTX30949 |
| TKOv3 lentiviral library | Addgene | Cat# 90294 |
| Triton X-100 | MerckMillipore | Cat# X100 |

| | | |
|---|---------------------------|--------------------------|
| Tween-20 | Fisher Scientific | Cat# BPE-337-500 |
| Commercial Assays | | |
| AlphaScreen General IgG Detection Kit | PerkinElmer | Cat# 6760617 |
| Applied Biosystems High-Capacity cDNA Reverse Transcription kit | Thermo Fisher Scientific | Cat# 4368814 |
| CellTiter-Blue reagent | Promega | Cat# G808B |
| Histone Extraction Kit | Abcam | Cat# ab113476 |
| Immobilin Western HRP Substrate Luminol Peroxidase | MerckMillipore | Cat# WBKLS0500 |
| KAPA SYBR FAST Universal 2X qPCR MasterMix | Kapa Biosystems | Cat# KK4602 |
| NE-PER Nuclear and Cytoplasmic Extraction Reagents | ThermoFisher Scientific | Cat# 78833 |
| Pierce BCA protein assay kit | ThermoFisher Scientific | Cat# 23225 |
| RNeasy Mini Kit | Qiagen | Cat# 74104 |
| Senescence β -Galactosidase Staining Kit | Cell Signaling Technology | Cat# 9860 |
| Subcellular Fractionation Kit for Cultured Cells | ThermoFisher Scientific | Cat# 78840 |
| Validated QuantiTect Primers | | |
| Hs ACTB1 1 SG | Qiagen | GeneGlobe ID: QT00095431 |
| Hs BAX 1 SG | Qiagen | GeneGlobe ID: QT00031192 |
| Hs BUB1 1 SG | Qiagen | GeneGlobe ID: QT00082929 |
| Hs CCNA2 1 SG | Qiagen | GeneGlobe ID: QT00014798 |
| Hs CDKN1A 1 SG | Qiagen | GeneGlobe ID: QT00062090 |
| Hs CDKN1B 1 SG | Qiagen | GeneGlobe ID: QT00043302 |
| Hs DEC2 1 SG | Qiagen | GeneGlobe ID: QT00032697 |
| Hs EEF1A 1 SG | Qiagen | GeneGlobe ID: QT00999894 |
| Hs FOXO3 1 SG | Qiagen | GeneGlobe ID: QT00031941 |
| Hs GAPDH 1 SG | Qiagen | GeneGlobe ID: QT00079247 |
| Hs GFAP 1 SG | Qiagen | GeneGlobe ID: QT00081151 |
| Hs KDM1A 1 SG | Qiagen | GeneGlobe ID: QT00099442 |
| Hs KDM1B 1 SG | Qiagen | GeneGlobe ID: QT01153572 |
| Hs KDM2A 1 SG | Qiagen | GeneGlobe ID: QT00020888 |
| Hs KDM2B 1 SG | Qiagen | GeneGlobe ID: QT00087640 |
| Hs KDM3A 1 SG | Qiagen | GeneGlobe ID: QT00088879 |
| Hs KDM3B 1 SG | Qiagen | GeneGlobe ID: QT00085617 |
| Hs KDM3C 1 SG | Qiagen | GeneGlobe ID: QT00066976 |
| Hs KDM4A 1 SG | Qiagen | GeneGlobe ID: QT00028399 |
| Hs KDM4B 1 SG | Qiagen | GeneGlobe ID: QT00060949 |
| Hs KDM4C 1 SG | Qiagen | GeneGlobe ID: QT00027440 |
| Hs KDM4D 2 SG | Qiagen | GeneGlobe ID: QT01680609 |
| Hs KDM4E 3 SG | Qiagen | GeneGlobe ID: QT01862308 |
| Hs KDM5A 1 SG | Qiagen | GeneGlobe ID: QT00013265 |
| Hs KDM5B 1 SG | Qiagen | GeneGlobe ID: QT00060648 |
| Hs KDM5C 1 SG | Qiagen | GeneGlobe ID: QT00041503 |
| Hs KDM5D 1 SG | Qiagen | GeneGlobe ID: QT00014070 |
| Hs KDM6A 1 SG | Qiagen | GeneGlobe ID: QT00094654 |
| Hs KDM6B 1 SG | Qiagen | GeneGlobe ID: QT00098742 |
| Hs KDM7A 1 SG | Qiagen | GeneGlobe ID: QT00038654 |
| Hs KDM7B 1 SG | Qiagen | GeneGlobe ID: QT00023485 |
| Hs KDM7C 1 SG | Qiagen | GeneGlobe ID: QT00044555 |

| | | |
|-----------------------------|--------------------------------|---|
| Hs KDM8 1 SG | Qiagen | GeneGlobe ID: QT00026999 |
| Hs KMT1A 1 SG | Qiagen | GeneGlobe ID: QT00091042 |
| Hs KMT1B 1 SG | Qiagen | GeneGlobe ID: QT00094311 |
| Hs KMT1C 1 SG | Qiagen | GeneGlobe ID: QT00088627 |
| Hs KMT1D 1 SG | Qiagen | GeneGlobe ID: QT00084602 |
| Hs KMT1E 1 SG | Qiagen | GeneGlobe ID: QT00086142 |
| Hs KMT1F 1 SG | Qiagen | GeneGlobe ID: QT00067494 |
| Hs KMT2A 1 SG | Qiagen | GeneGlobe ID: QT00033194 |
| Hs KMT2B 1 SG | Qiagen | GeneGlobe ID: QT00033194 |
| Hs KMT2C 1 SG | Qiagen | GeneGlobe ID: QT00029316 |
| Hs KMT2D 1 SG | Qiagen | GeneGlobe ID: QT01762096 |
| Hs KMT2E 1 SG | Qiagen | GeneGlobe ID: QT00053900 |
| Hs KMT2F 1 SG | Qiagen | GeneGlobe ID: QT00042427 |
| Hs KMT2G 1 SG | Qiagen | GeneGlobe ID: QT01016799 |
| Hs KMT2H 1 SG | Qiagen | GeneGlobe ID: QT00083335 |
| Hs KMT3A 1 SG | Qiagen | GeneGlobe ID: QT00087416 |
| Hs KMT3B 1 SG | Qiagen | GeneGlobe ID: QT00035476 |
| Hs KMT3C 1 SG | Qiagen | GeneGlobe ID: QT00011886 |
| Hs KMT3D 1 SG | Qiagen | GeneGlobe ID: QT00080031 |
| Hs KMT3E 1 SG | Qiagen | GeneGlobe ID: QT00089950 |
| Hs KMT3F 1 SG | Qiagen | GeneGlobe ID: QT00008162 |
| Hs KMT3G 1 SG | Qiagen | GeneGlobe ID: QT00018998 |
| Hs KMT4 1 SG | Qiagen | GeneGlobe ID: QT00074032 |
| Hs KMT5A 1 SG | Qiagen | GeneGlobe ID: QT00058247 |
| Hs KMT5B 1 SG | Qiagen | GeneGlobe ID: QT00082229 |
| Hs KMT5C 1 SG | Qiagen | GeneGlobe ID: QT00052759 |
| Hs KMT6A 1 SG | Qiagen | GeneGlobe ID: QT00054614 |
| Hs KMT6B 1 SG | Qiagen | GeneGlobe ID: QT00030275 |
| Hs KMT7 1 SG | Qiagen | GeneGlobe ID: QT00079282 |
| Hs KMT8A 1 SG | Qiagen | GeneGlobe ID: QT00055300 |
| Hs KMT8B 1 SG | Qiagen | GeneGlobe ID: QT01023631 |
| Hs KMT8C 1 SG | Qiagen | GeneGlobe ID: QT01173774 |
| Hs KMT8D 2 SG | Qiagen | GeneGlobe ID: QT01665062 |
| Hs KMT8E 1 SG | Qiagen | GeneGlobe ID: QT00211169 |
| Hs KMT8F 1 SG | Qiagen | GeneGlobe ID: QT00016975 |
| Hs MBP 1 SG | Qiagen | GeneGlobe ID: QT00073528 |
| Hs MCM5 1 SG | Qiagen | GeneGlobe ID: QT00084000 |
| Hs NEK2 1 SG | Qiagen | GeneGlobe ID: QT00025221 |
| Hs NES 1 SG | Qiagen | GeneGlobe ID: QT00235781 |
| Hs NR2F1 1 SG | Qiagen | GeneGlobe ID: QT00089355 |
| Hs OLIG2 1 SG | Qiagen | GeneGlobe ID: QT00209685 |
| Hs ORC1 1 SG | Qiagen | GeneGlobe ID: QT00005341 |
| Hs PMAIP1 1 SG | Qiagen | GeneGlobe ID: QT01006138 |
| Hs PML 1 SG | Qiagen | GeneGlobe ID: QT00090447 |
| Hs RRN18S 1 SG | Qiagen | GeneGlobe ID: QT00199367 |
| Hs SOX2 1 SG | Qiagen | GeneGlobe ID: QT00237601 |
| Hs SOX9 1 SG | Qiagen | GeneGlobe ID: QT00001498 |
| Hs TUBB2A 1 SG | Qiagen | GeneGlobe ID: QT00081088 |
| Hs TUBB3 1 SG | Qiagen | GeneGlobe ID: QT00083713 |
| Hs YPEL3 1 SG | Qiagen | GeneGlobe ID: QT00078589 |
| Key Software and Algorithms | | |
| Chronos package | Dempster et al. ²¹⁴ | https://github.com/broadinstitute/chronos |

| | | |
|-------------------------|---|---|
| Fiji (ImageJ) v1.53 | ImageJ | https://imagej.net/Fiji/Downloads |
| GRcalculator | Harvard Medical School and University of Cincinnati | http://www.grcalculator.org/grcalculator/ |
| ImageJ v1.53 | ImageJ | https://imagej.nih.gov/ij/download.html |
| ImageLab v6.1 | Bio-Rad | http://www.bio-rad.com/en-au/product/image-lab-software?ID=KRE6P5E8Z |
| Incucyte Basic Analysis | Sartorius | - |
| IPA | Qiagen | https://analysis.ingenuity.com/pa/installer/select |
| Limma package | Ritchie et al. ²¹⁵ | https://bioconductor.org/packages/limma |
| Prism v10.0 | GraphPad | https://www.graphpad.com/scientific-software/prism/ |
| TPP package | Savitski et al. ²¹⁶ | https://bioconductor.org/packages/TPP |

Chapter 3

Systematic literature
review reveals suboptimal
use of chemical probes in
cell-based biomedical
research

Preface

Each step in the drug discovery process must be followed using rigorous scientific methods to ensure these compounds have a viable chance of success²¹⁷. Rushing through this process without foundational research leads to drug candidates failing due to poor efficacy. Such outcomes often stem from inadequate early-stage evaluations, underscoring the critical need for thorough and unbiased target validation studies²¹⁸.

Chemical probes play a crucial role in this early validation work. These highly potent, selective, and efficacious compounds are essential tools for investigating the modulation of specific proteins within live cells²¹⁹. However, their effectiveness relies on correct application, a principle which experts in the field say is often overlooked in practice²⁰⁶. Given that no compound can ever have complete specificity towards a single target, the misuse or misunderstanding of chemical probes can lead to improper target validation²⁰⁷.

In addressing this issue, we performed a systematic review of 662 primary research articles, examining the adherence to guidelines for chemical probe use in preclinical studies. Our findings, published in *Nature Communications* in 2023², assessed studies based on three questions: Was the chemical probe used at or below the recommended concentration? If an inactive control was available, was it used? If an orthogonal control was available, was it used?

This paper is the first to provide quantifiable evidence that less than half of the publications using these chemical probes are employing an inactive or orthogonal control and only 4% of eligible publications satisfied all three criteria. The results have garnered attention, with mentions in prestigious journals such as *Science*²²⁰, *Nature Reviews Drug Discovery*²²¹, and *Nature Chemical Biology*²²², highlighting the importance of our findings and strategies for improvement moving forward.

Systematic literature review reveals suboptimal use of chemical probes in cell-based biomedical research

Received: 10 September 2022

Accepted: 23 May 2023

Published online: 03 June 2023

 Check for updatesJayden Sterling¹, Jennifer R. Baker², Adam McCluskey² & Lenka Munoz¹ ✉

Chemical probes have reached a prominent role in biomedical research, but their impact is governed by experimental design. To gain insight into the use of chemical probes, we conducted a systematic review of 662 publications, understood here as primary research articles, employing eight different chemical probes in cell-based research. We summarised (i) concentration(s) at which chemical probes were used in cell-based assays, (ii) inclusion of structurally matched target-inactive control compounds and (iii) orthogonal chemical probes. Here, we show that only 4% of analysed eligible publications used chemical probes within the recommended concentration range and included inactive compounds as well as orthogonal chemical probes. These findings indicate that the best practice with chemical probes is yet to be implemented in biomedical research. To achieve this, we propose ‘the rule of two’: At least two chemical probes (either orthogonal target-engaging probes, and/or a pair of a chemical probe and matched target-inactive compound) to be employed at recommended concentrations in every study.

Chemical probes are well-characterised small molecules with potency and selectivity for a protein of interest^{1,2}. The term ‘chemical probe’ distinguishes compounds used in basic and preclinical research from ‘drugs’ used in the clinic, from the terms ‘inhibitor’, ‘ligand’, ‘agonist’ or ‘antagonist’ which are molecules targeting a given protein but are insufficiently characterised, and also from the term ‘probes’ which is often referring to laboratory reagents for biophysical and imaging studies³. Chemical probes are tools to understand the function of a targeted protein at the mechanistic level and have also reached a prominent role in target validation research. The development of first-in-class drugs often begins with the identification of a new target from -omics screens. In the target validation stage, various strategies are employed to evaluate whether the identified target has a key role in the disease process and whether its pharmacological modulation could lead to a therapeutic efficacy. In this stage, chemical probes are complementary to molecular probes such as CRISPR and RNA interference, because they offer unique advantages. Unlike molecular probes which induce target’s knock-down or knock-out over a longer timeframe, chemical probes rapidly inhibit the activity of a protein of interest.

Furthermore, when coupled with molecular probes, chemical probes can distinguish between effects due to the target’s presence in the cell, and effects due to the inhibition of catalytic or protein-protein interaction activity⁴.

The necessity of chemical probes for mechanistic and target validation research^{1–10} has led to a steadily growing number of high-quality chemical probes¹⁰. Every chemical probe must satisfy the minimal fundamental criteria, known as fitness factors: namely potency, selectivity, and cellular activity^{1,9}. While these properties may vary based on the nature of the targeted protein; in principle, chemical probes adhere to the in vitro potency of less than 100 nM, selectivity for the targeted protein being at least 30-fold against sequence-related proteins of the same family, and on-target cellular activity at concentrations ideally below 1 μM ^{1,2,9,11}. Similarly, the guidelines for the use of chemical probes in cell-based experiments may vary due to the different nature of the hypotheses being investigated. Nevertheless, the foremost recommendation is to use chemical probes at concentrations closest to the validated on-target effect^{1,9}. Even the most selective chemical probe will become non-selective if used at a high concentration. Second, it is

¹Faculty of Medicine and Health, Charles Perkins Centre, The University of Sydney, Camperdown, NSW 2006, Australia. ²Discipline of Chemistry, School of Environmental and Life Sciences, The University of Newcastle, Callaghan, NSW 2308, Australia. ✉ e-mail: lenka.munoz@sydney.edu.au

strongly encouraged that the chemical probe be accompanied by a target-inactive, but structurally similar analogue to serve as a negative control. Third, each protein should be targeted by another well-characterized orthogonal chemical probe having a different chemical structure. Thus, for any given protein, the ideal cell-based experiment would employ at least two orthogonal chemical probes at reasonable concentrations and be accompanied, when available, by structurally related but target-inactive derivatives^{8,9,11,12}.

There are many factors to consider when selecting and using a chemical probe to address a hypothesis, which can be challenging, especially for non-experts. To facilitate the correct use of chemical probes in biomedical research, open-access resources have been established by the chemical biology community¹¹. The Chemical Probes Portal (www.chemicalprobes.org)⁹, a user-friendly platform for non-chemists, at the time of writing includes 547 chemical probes that cover over 400 protein targets¹³. A total of 321 chemical probes have three or more stars and are therefore specifically recommended by the Portal to confidently study 281 protein targets. Furthermore, the Portal also lists an additional 248 compounds labelled as 'Historical Compounds'. These compounds should not be used to study the function of specific proteins as they are either seriously flawed or are outdated and superseded. This important resource is complemented by the Chemical Probes website of the Structural Genomics Consortium (<https://www.thesgc.org/chemical-probes>) and the Donated Chemical Probes website (www.sgc-ffm.uni-frankfurt.de)¹⁴, where a consortium of pharmaceutical companies offer access to their previously undisclosed chemical probes. While these portals are based on peer-review and recommendations by chemical biology experts, the Probe Miner (<https://probeminer.icr.ac.uk/>), a database of over 1.8 million small molecules, comprehensively analyses peer-reviewed literature and provides a relative ranking of the chemical probe based on objective statistical assessment of the large scale data¹⁵. Thus, the assessment of a chemical probe provided by the Probe Miner is a valuable complement to the experts' review basis of the above mentioned portals. Finally, the Probes & Drugs database (www.probes-drugs.org)¹⁶ contains over 4600 probes, of which over 1100 probes are approved by the Probes & Drugs community. In summary, these online resources provide information about chemical probes and some also list recommendations such as maximal in-cell concentration, availability of matched target-inactive control molecule, and orthogonal chemical probes. Adherence to these recommendations is crucial to generate robust findings.

The problem of inaccurate data has been publicly noted more than a decade ago. While reasons are diverse^{17,18}, the suboptimal use of chemical probes has emerged as one of the culprits in the robustness crisis³. However, while the suboptimal use of chemical probes has been widely discussed, the extent of this problem remains unknown. Therefore, we analysed how selected chemical probes targeting epigenetic and kinase targets - histone methyltransferases EZH2 and G9a/

GLP, histone demethylase KDM6, histone acetyltransferase CBBP/p300 and kinases Aurora, mTOR and CDK7 - have been applied in primary research articles (referred to as publications herein). In our analysis, we considered three questions: i) Has the chemical probe been used in cellular assays within the recommended concentration range? ii) If a matched target-inactive control molecule is available, has it been employed in cellular assays? iii) If orthogonal inhibitors targeting the protein of interest exist, have they been employed in cellular assays? Here, we show that while the frequency of chemical probes in research is encouragingly high, a worryingly low fraction of the analysed publications used chemical probes correctly.

Results

Study selection

Eight chemical probes (Table 1) were selected because they target proteins representing research fields of different sizes. PubMed search (Dec 2022) using the 'Advanced Search' function to include all synonyms of the chemical probes' primary targets retrieved 5908 (EZH2); 21,977 (G9a/GLP); 1656 (KDM6A); 20,733 (CREBBP); 54,733 (Aurora); 45,728 (mTOR) and 768 (CDK7) articles. While we provide a brief overview of all chemical probes for a given target, in the selection of chemical probes for the systematic review analysis, preferences were given to (i) 'older' probes disclosed at least five years ago; (ii) probes with matched target-inactive control compounds and/or (iii) commercially available chemical probes. Another factor was to select chemical probes with a manageable number of records. For example, PubMed search (Dec 2022) for the keyword 'rapamycin' (a chemical probe targeting mTOR kinases) retrieved over 51,000 records; it is not feasible to manually review such literature corpora. All selected chemical probes received three- or four-star recommendations in the Chemical Probes Portal and thus are endorsed by the Scientific Expert Review Panel to study the function of their primary targets (Table 1). The Global Score in the Probe Miner places UNC0638, GSK-J4, AMG900, AZD1152, AZD2014 in the top 10%, whereas A-485 is placed in the top 12%; making these chemical probes one of the best tools to interrogate their primary targets. The Global Scores for UNC1999 and THZ1 are low, 0.15 and 0.29, respectively (Table 1).

We screened 1131 articles and identified 662 primary research articles (i.e., publications) eligible for the systematic review analysis (Fig. 1)¹⁹. All eligible publications contained at least one figure panel presenting results obtained with a given chemical probe used in a cell-based assay, irrespective of the topics and research fields. To address the compliance with the recommended experimental design for chemical probes^{9,11}, full-text contents across these 662 publications were analysed for chemical probes' concentration in cell-based assays, use of negative control compounds and orthogonal inhibitors (Fig. 1). Analysed publications were considered complying or partially complying if they employed a given chemical probe within the recommended in-cell concentration range, used matched target-inactive

Table 1 | Overview of chemical probes selected for the study

| Probe | Primary target | Year of disclosure | Inactive control | Orthogonal chemical probes | Chemical Probes Portal score (Aug 2022) | Probe Miner global score & rank (Aug 2022) |
|---------|----------------|--------------------|------------------|----------------------------|---|--|
| UNC1999 | EZH2 | 2013 | UNC2400 | Supplementary Fig. 1 | 3 stars | 0.15 195/211 (top 93%) |
| UNC0638 | G9a/ GLP | 2011 | UNC0737 | Supplementary Fig. 3a | 3 stars | 0.54 19/329 (top 6%) |
| GSK-J4 | KDM6 | 2012 | GSK-J5 | Not available | 3 stars | 0.53 1/52 (top 2%) ^a |
| A-485 | CREBBP/p300 | 2017 | A-486 | Supplementary Fig. 6 | 3 stars | 0.39 35/302 (top 12%) |
| AMG900 | Aurora kinases | 2010 | Not available | Supplementary Fig. 8a | 4 stars | 0.58 20/2906 (top 1%) |
| AZD1152 | Aurora kinases | 2007 | Not available | Supplementary Fig. 8a | 4 stars | 0.75 1/1888 (top 1%) |
| AZD2014 | mTOR | 2013 | Not available | Supplementary Fig. 8b | 4 stars | 0.49 281/4230 (top 7%) |
| THZ1 | CDK7 CDK12/13 | 2014 | THZ-R1 | Supplementary Fig. 12 | 3 stars | 0.29 171/374 (top 46%) |

^aThe score and ranking refer to compound URY (<https://probeminer.icr.ac.uk/#/O15054>), which is the active hydrolysed GSK-J4 analogue structurally identical to GSK-J1.

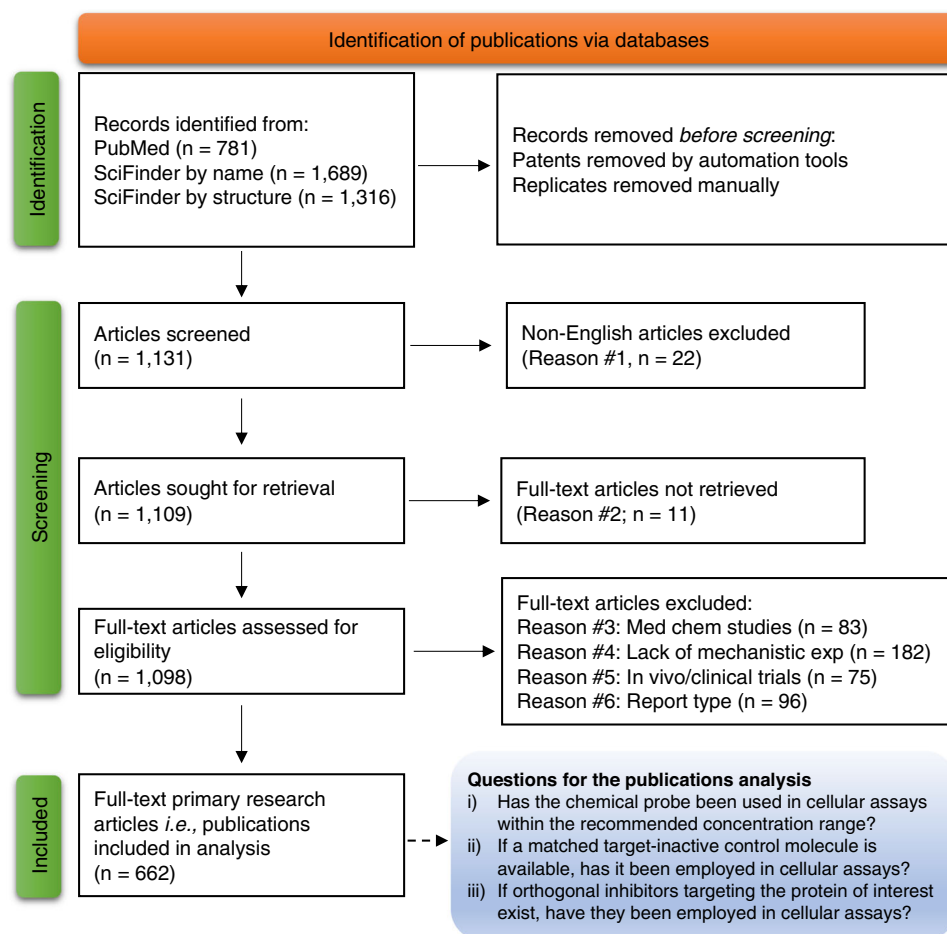


Fig. 1 | Preferred items for systematic reviews and meta-analysis (PRISMA) flow diagram. From 1131 records related to 8 chemical probes, we excluded articles (1) not written in English, (2) whose full text were not available via University of Sydney access; (3) describing the discovery of a given chemical probe and/or medicinal chemistry studies; (4) in which the chemical probe was used to generate chemical probe-resistant clones and/or articles lacking mechanistic experiments; (5)

containing only in vivo data and/or clinical trial results; and 6) reviews, commentaries, editorials, letters to the editors, conference proceedings, pre-prints. We analysed 662 eligible publications for the concentration of chemical probes in cell-based assays, the inclusion of negative control compounds and the inclusion of orthogonal chemical probes. PRISMA flow diagrams for each individual chemical probe are provided in the Supplementary Information file.

control compound (where available), and at least one orthogonal inhibitor (where available) (Fig. 2). Details of publications analyses are provided in the Supplementary Tables 1–16 and presented for each chemical probe in subsections below.

EZH2 chemical probe UNC1999

Methylation of lysine residues in histone tails by histone methyltransferases (KMTs) is a prevalent epigenetic modification. Enhancer of Zeste Homologue 2 (EZH2, also known as KMT6A) is the main catalytic subunit of the Polycomb Repressive Complex 2 responsible for mono-, di- and trimethylation of histone 3 (H3) at lysine (K) 27 (H3K27). EZH2 catalysed H3K27 methylation silences the transcription of nearby genes. EZH2 is often replaced by its closely related homologue EZH1 (also known as KMT6B) in differentiated and quiescent cells. EZH1 and EZH2 share 63% overall homology and 94% of their catalytic SET domain; hence EZH2 targeting chemical probes also target EZH1 with some potency^{20,21}.

An early tool compound targeting EZH2 was EPZ005687²², which while a potent EZH2 inhibitor, lacked the minimal fundamental criteria of a chemical probe. The first published EZH2 inhibitor now endorsed as a chemical probe is EI1 (Supplementary Fig. 1)²³. Optimisation of the EPZ005687's pharmacophore yielded chemical probes GSK343²⁴, EPZ-6438²⁵ (and the structurally-related EPZ011989²⁶) as well as UNC1999²⁷. UNC1999 is particularly noteworthy as it is one of the only two

available EZH2 targeting chemical probes to also have a dedicated inactive matched partner²⁷. UNC2400 has an *N*-methylated benzamide core to distinguish itself from its active counterpart UNC1999. This *N*-methylation makes UNC2400 over 1000-fold less potent than UNC1999, rendering it as a negative control in cell-based experiments. The indazole-based JQEZ5 was designed as an open-source chemical probe²⁸ and is another chemical probe to also have a structurally matched inactive analogue: JQEZ23 contains a methyl-substituted pyridine in place of JQEZ5's pyridino-moiety (Supplementary Fig. 1). CPI-169 and CPI-360²⁹ contain a 2-methyl indole core and differ only with the alkylation substitution of the indole amine. The third chemical probe in this family CPI-1205³⁰ also features the 2-methyl indole common to both CPI-169 and CPI-360 (Supplementary Fig. 1).

We conducted a systematic review of 49 eligible publications (Supplementary Fig. 2) presenting at least one figure panel using UNC1999 in a cell-based assay (Supplementary Table 2). As the recommended maximal in-cell concentration for UNC1999 varies between the Chemical Probes Portal and the Structural Genomics Consortium sites (400 nM and 3 μ M, respectively), we analysed compliance with both concentrations. We found 5 publications (10%) employing UNC1999 below the 400 nM concentration across most experiments. When considering the 3 μ M recommendation, in total 18 publications (37%) fully complied; and 14 publications (29%) were considered as partially complying because they reported UNC1999 at

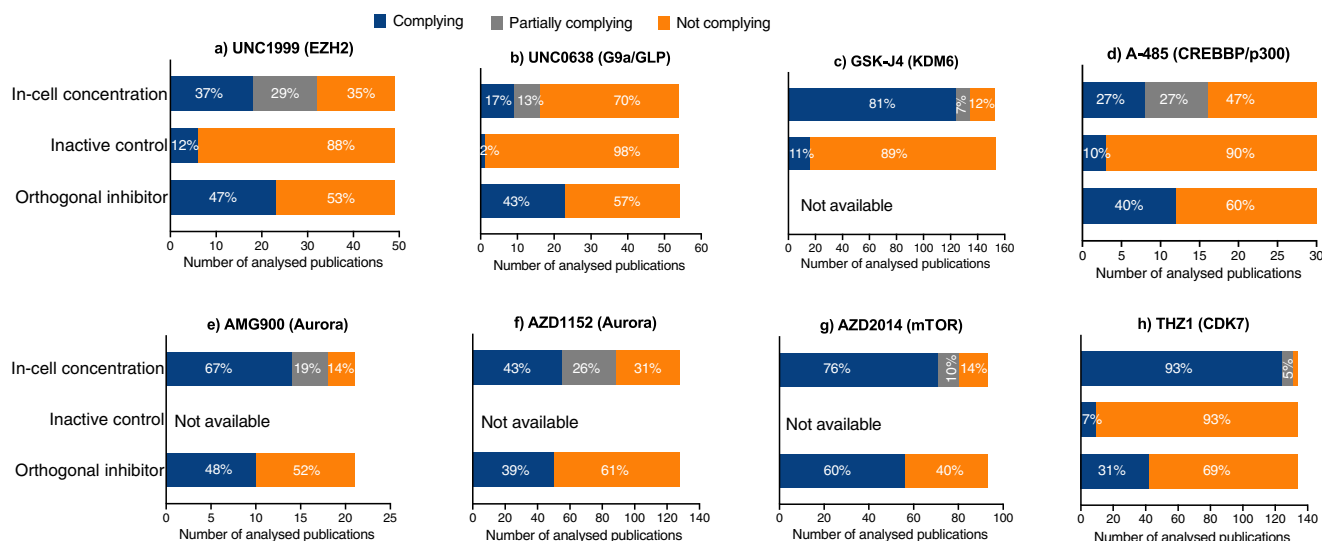


Fig. 2 | Percentages of publications complying (blue), partially complying (grey) and not complying (orange) with guidelines for a given chemical probe. The complying and partially complying publications employed a given chemical probe within the recommended in-cell concentration range: (a) UNC1999: up to 3 μ M; (b) UNC0638: up to 250 nM; (c) GSK-J4: up to 5 & 10 μ M; (d) A-485: up to 1 μ M;

(e) AMG900: up to 100 nM; (f) AZD1152: up to 100 nM; (g) AZD2014: up to 2 μ M; (h) THZ1: up to 1 μ M), used matched target-inactive control compound (where available) and at least one orthogonal inhibitor (where available). [Note: The in-cell concentration percentages for UNC1999 and A-485 total to 101% due to rounding up individual percentages.] Source data are provided as a Source Data file.

concentrations below and above 3 μ M. Of the analysed 49 publications, 6 publications (12%) included the inactive analogue UNC2400, and 23 publications (47%) performed experiments with orthogonal EZH2 inhibitors (Fig. 2a), some of which were endorsed chemical probes (e.g., GSK-343; Supplementary Table 2).

G9a/GLP chemical probe UNC0638

G9a (also known as EHMT2 or KMT1C) and the closely related G9a-like protein (GLP, also known as EHMT1 or KMT1D) are methyltransferases responsible for mono- and di-methylation of H3K9, with H3K9me1/me2 marks silencing gene transcription. Compound BIX01294 is one of the first G9a/GLP inhibitors; however, because of its lack of selectivity and high cellular toxicity³¹, there is a tight window between achieving cellular G9a/GLP target engagement while avoiding off-target toxicity. Follow-up chemistry based on the BIX01294 scaffold yielded G9a/GLP chemical probe UNC0638 (Supplementary Fig. 3a)³². The *N*-methyl analogue of UNC0638, compound UNC0737, is >300-fold less potent than UNC0638 and serves as a valuable inactive control³². Optimisation of UNC0638's short half-life led to the development of the first G9a/GLP in vivo chemical probe UNC0642³³. Another chemical probe targeting G9a/GLP is A-366³⁴, which has a scaffold different from UNC0638 and UNC0642; hence A-366 provides a valuable orthogonal tool (Supplementary Fig. 3a).

To gain an insight into the G9a/GLP research, we reviewed 54 eligible publications (Supplementary Fig. 4) with at least one figure panel presenting the results of cell-based experiments performed with UNC0638 (Supplementary Table 4). We identified 9 publications (17%) that treated cells with UNC0638 within the recommended concentration range (up to 250 nM)³² and 7 partially complying publications (13%) which employed UNC0638 at a higher concentration in some experiments. Of all analysed publications, only one publications (2%) included UNC0737 as a control compound and 23 (43%) publications used another G9a/GLP inhibitor alongside UNC0638 (Fig. 2b).

KDM6 chemical probe GSK-J4

Histone lysine demethylase A (KDM6A, also known as UTX) and KDM6B (also known as JMJD3) remove H3K27 methylation marks, thereby activating gene transcription³⁵. The liganded crystal structure of KDM6B enabled the development of GSK-J1, the first small-molecule

inhibitor of a histone lysine demethylase³⁶. While the GSK-J1's acid moiety is critical for binding to KDM6B, it adversely affects cellular permeability. As such, the non-cell permeable GSK-J1 (listed as a Historic Compound; <https://www.chemicalprobes.org/gsk-j1>) should not be used in cell-based assays that depend on inhibition of KDM6A/B. Masking the polarity of the acid group with an ethyl ester moiety yielded chemical probe GSK-J4 (Supplementary Fig. 3b) with enhanced cellular uptake and ability to inhibit KDM6A/B in cells following release of the free acid in the cytoplasm³⁶. Finally, recognizing the importance of the GSK-J4's pyridyl-pyrimidine bidentate interaction with the catalytic metal led to the development of inactive control compound GSK-J5 (Supplementary Fig. 3b). No other KDM6 inhibitors are listed on the Chemical Probes Portal; thus GSK-J4 and its matched target-inactive GSK-J5 remain unique tools to interrogate KDM6A/B function in cells.

For GSK-J4 study, 153 publications met the eligibility criteria (Supplementary Fig. 5, Supplementary Table 6). GSK-J4 must be hydrolysed in the cytoplasm and hence its recommended in-cell concentration on the Chemical Probes Portal is up to 5 μ M. 72 publications (47%) did not exceed this concentration in cell-based assays. The number of publications employing GSK-J4 within the 5 μ M – 10 μ M range (probably linked to GSK-J4's cellular IC₅₀ of 9 μ M in macrophages³⁶, a value listed on the Structural Genomics Consortium's Chemical Probes website) was 52 (41%). Hence, 124 publications (81%) fully complied with the recommendations of the Chemical Probes Portal or Structural Genomics Consortium's Chemical Probes website. We found 10 publications (7%) that used GSK-J4 below and above 10 μ M. However, only 16 publications (11%) employed GSK-J5 to validate cellular effects of GSK-J4 as a consequence of KDM6 inhibition (Fig. 2c).

CREBBP/p300 chemical probe A-485

Lysine acetylation by histone acetyltransferases is another prevalent post-translational modification on histone tails and leads to the activation of gene transcription. Cyclic-AMP response element binding protein (CREB) binding protein (CREBBP, also known as CBP or KAT3A) and its paralogue E1A binding protein p300 (also known as p300 or KAT3B), functioning as histone acetyltransferases and transcriptional co-factors, are indispensable for a multitude of cellular processes.

Given their high structural similarity and functional redundancy, they are often called CREBBP/p300 (or CBP/p300) and a significant focus has been placed on the development of CREBBP/p300 inhibitors^{36,37}.

Several inhibitors targeting either the catalytic acetyltransferase domain or the reader bromodomain of CREBBP/p300 have been endorsed as chemical probes (Supplementary Fig. 6). The chemical probe A-485 selectively targets CREBBP/p300 and its matched inactive analogue A-486 is 1000-fold less potent³⁸. The more recently developed CPI-1612 engages CREBBP/p300 in cells at 50 nM, making it one of the most potent epigenetic chemical probes³⁹. The remaining chemical probes target CREBBP/p300 bromodomains with varying selectivity over bromodomains of other proteins. For example, CPI-637 shows >700-fold selectivity for CREBBP/p300 over the BRD4 bromodomain 1, however it inhibits the bromodomain of BRD9⁴⁰. The structurally related GNE-781 and GNE-049 are both suitable to interrogate the function of CREBBP/p300 without the complication of BRD inhibition⁴¹. Chemical probe PF-CBP1, its matched bromodomain-inactive dimethyl derivative ISOX-INACT⁴², as well as structurally related SGC-CBP30⁴³ bind the CREBBP bromodomain with some degree of selectivity over BRD4. Similarly, I-CBP112⁴⁴ displays selectivity for bromodomains of CREBBP and p300 over the bromodomains of BRD4 (Supplementary Fig. 6).

In this cohort, 30 eligible publications (Supplementary Fig. 7) were reviewed for the concentration of A-485 and whether the inactive control A-486 and orthogonal inhibitors were employed (Supplementary Table 8). The recommended highest in-cell concentration for A-485 is 800 nM and we identified 8 publications (27%) that employed A-485 up to 1 μ M. Another 8 publications (27%) partially complied as the concentration of A-485 was higher in some experiments. Of the 30 publications, 3 publications (10%) used the inactive control A-486 and 12 publications (40%) employed orthogonal inhibitors (Fig. 2d), some of which are endorsed chemical probes (e.g., CPI-637; Supplementary Table 8).

Aurora chemical probes AMG900 and AZD1152

The three mammalian Aurora kinases (AURKA, AURKB, AURKC) are serine/threonine kinases with major roles in mitosis and meiosis⁴⁵. While a large number of Aurora kinase inhibitors have been developed, only four inhibitors are endorsed as chemical probes in the Chemical Probes Portal (Supplementary Fig. 8a). MK-5108 inhibits AURKA with picomolar in vitro and nanomolar in-cell potency⁴⁶. AZD1152 (barasertib) is a phosphate pro-drug that is rapidly cleaved to the active alcohol AZD1152-HQPA, which potently and selectively inhibits AURKB⁴⁷. While AZD1152 is suitable for in vivo studies, for cell-based experiments AZD1152-HQPA is a preferable chemical probe, since cleavage of the phosphate group in AZD1152 might not occur in cells. AMG900 inhibits all three Aurora kinases isoforms with nanomolar potency, and also has nanomolar affinity for several other kinases⁴⁸. Hence, it is recommended to use AMG900 together with orthogonal chemical probes, such as XMD-12 which is among the most kinase selective pan-Aurora inhibitors reported. Compared to AMG900, XMD-12 also targets all three AURK isoforms, but shows a better kinase-wide selectivity below 100 nM⁴⁹.

We identified 21 publications (Supplementary Fig. 9) that employed AMG900 in at least one figure panel (Supplementary Table 10). Of these publications, 14 (67%) did not exceed the recommended 100 nM in-cell concentration, 4 (19%) employed AMG900 below 100 nM in some experiments and 10 (48%) confirmed AMG900 results with additional Aurora inhibitors, such as orthogonal chemical probes AZD1152 and MK-5108 (Fig. 2e). Our search for the more popular chemical probe AZD1152 identified 128 publications (Supplementary Fig. 10) presenting data obtained from cells treated with AZD1152 (Supplementary Table 12). Of these, 55 publications (43%) did not exceed the recommended 100 nM in-cell concentration. An additional 33 publications (26%) partially complied with the 100 nM

recommendations, and 50 publications (39%) included in their experiments orthogonal Aurora inhibitors (Fig. 2f).

mTOR targeting probe AZD2014

Mammalian target of rapamycin (mTOR) is a serine/threonine protein kinase. mTOR is part of two structurally and functionally distinct mTOR complexes 1 and 2 (mTORC1/2) which regulate cellular growth and metabolism either through direct phosphorylation of kinases (e.g.; ribosomal protein S6 kinase, Akt kinase) or indirectly through downstream signalling effectors (e.g.; eIF4E binding protein, MYC, HIF1 α , SREBP1). Due to its involvement in numerous signalling pathways, mTOR is a master regulator of cell growth and metabolism^{50,51}.

Bearing the name of the target is the chemical probe rapamycin (also known as sirolimus, Supplementary Fig. 8b), a potent inhibitor of, primarily, mTORC1⁵². Poor solubility and pharmacokinetics led to the development of two water-soluble synthetic derivatives everolimus and temsirolimus. A phosphine oxide pro-drug version of rapamycin, ridaforolimus, was also developed (Supplementary Fig. 8b). These analogues of rapamycin, entitled rapalogs, are more suitable for in vivo studies but given their structural similarities, they cannot be considered as orthogonal chemical probes to rapamycin. One of the most well-characterised mTOR chemical probes is the pyridopyrimidine-based compound AZD2014⁵³. Based on an earlier mTOR inhibitor AZD8055⁵⁴, AZD2014 mimics the selectivity and potency of this earlier inhibitor, but with improved solubility and metabolic stability⁵⁵. The pyrazolopyrimidine eCF309 was discovered as part of a campaign to develop inhibitors of both mTORC1 and 2⁵⁶.

In the AZD2014 search, we identified 93 publications fulfilling the eligibility criteria (Supplementary Fig. 11), which were reviewed for the AZD2014's concentration and use of orthogonal mTOR inhibitors (Supplementary Table 14). We identified 71 complying and 9 partially complying publications (76 and 10%, respectively) that followed the recommended maximal in-cell concentration of 2 μ M. Of 93 eligible publications, 56 (60%) used orthogonal mTOR inhibitors, predominantly rapamycin and/or rapalogs (Fig. 2g).

CDK7 chemical probe THZ1

Cyclin-dependent kinase 7 (CDK7) is a master regulator of cell-cycle progression and gene transcription⁵⁷. CDK7, together with cyclin H and MAT1, comprise the CDK-activating kinase (CAK) complex that phosphorylates CDK1/2/4, leading to their full activation and cell cycle progression. Moreover, the CAK is a component of the multi-protein complex that is essential for RNA polymerase II (Pol II)-mediated transcription. However, whether CDK7 is required for Pol II phosphorylation has been challenged by a study demonstrating a non-essential role for CDK7 in Pol II phosphorylation and global gene expression⁵⁸. Given the multiple oncogenic and some controversial roles for CDK7, development of CDK7 inhibitors has gained momentum in the past decade⁵⁷.

The chemical probe THZ1 (Supplementary Fig. 12) inhibits CDK7 by covalently binding to a cysteine residue (C312) that lies outside the canonical ATP-binding site of the kinase and leads to decreased phosphorylation of CDK7 substrates. The non-covalent analogue, THZ1-R, lacking the acrylamide functionality responsible for the covalent bond with C312, is used as an inactive control compound for THZ1⁵⁹. Of note, THZ1 inhibits also CDK12/13 via the same covalent mechanism of action, and thus THZ1 is not ideally selective (hence the low Global Score in the Probe Miner, Table 1). To separate CDK7 and CDK12/13 inhibition, the chemical probe THZ531 was developed (Supplementary Fig. 12). THZ531 is a derivative of THZ1 with the same phenylaminopyrimidine core scaffold, which inhibits CDK12/13 approximately 20 times more potently than CDK7⁶⁰. Importantly, two target-inactive control compounds accompany THZ531. In the analogue THZ531R the electrophilic acrylamide is replaced with a propyl amide incapable of a covalent bond, and THZ532 is the enantiomer of

THZ531 (Supplementary Fig. 12). Both analogues are 50- to 100-fold less active on CDK12 and CDK13⁶⁰. A CDK7-selective covalent inhibitor YKL-5-124 was later developed by combining the pyrrolidinopyrazole core from a previously unexplored CDK-targeting scaffold with the covalent warhead from THZ1. Removal of the acrylamide functionality, and replacement with an ethyl chain, gave the inactive counterpart, YKL-5-167 (Supplementary Fig. 12)⁵⁸.

In the THZ1 cohort, 134 eligible publications (Supplementary Fig. 13) were included in the analysis (Supplementary Table 16). THZ1 is recommended for cell-based experiment at the maximal concentration of 1 μ M and we found 124 (93%) compliant and 7 (5%) partially compliant publications. However, only 9 (7%) publications validated data with the inactive control compound THZ1R. Given that THZ1 targets CDK7 and CDK12/13 with comparable potency, analysed publications focused on the role of CDK7 and/or CDK12/13. As such, orthogonal inhibitors were targeting either CDK7 or CDK12/13; in some publications pan-CDK inhibitors were employed. All publications using any CDK inhibitor were deemed as compliant and in total 42 publications (31%) included an additional CDK inhibitor (Fig. 2h).

Limitations

Before discussing the results of our analysis, it is important to recognise its limitations. Although we performed three independent searches for each chemical probe, there may be more publications based on cell-based experiments using a given chemical probe, which were not included. This unintentional oversight could have an impact on the percentages of compliance. It is plausible that we have missed studies correctly using the given chemical probe, which would increase compliance percentage. Furthermore, despite carefully reviewing each publication, there is a possibility that a small fraction of what appears to be non-compliant publications may in fact be a correctly designed study. The experimental design uniquely depends on the hypothesis being tested and some publications might have intentionally and for a valid reason used, for example, a higher concentration of a given chemical probe. To mitigate this limitation as much as possible, publications in which the chemical probes were used within a range of concentrations, some of which exceeded the in-cell recommendations, were regarded as partially complying if at least one figure presented data with a chemical probe below the recommended maximal concentration. This, however, could have resulted in suboptimal experimental designs counted as compliant, and thus unrealistically increasing the compliance percentage. Given that the eligible publications were across all research fields, many beyond our expertise, we did not feel confident to assess whether the chemical probe's concentration in each study was justifiable. We also recognize that 662 publications do not represent all literature corpora and our conclusions are only estimates of the status quo.

Discussion

Good news and bad news have emerged from our analysis. The good news is that high quality chemical probes, developed in response to the robustness crisis, have been increasingly employed in basic and pre-clinical research. In the past decades, a high percentage of novel drug targets could not be validated and this was partially compounded by using compounds that were inadequately characterised, had been later shown to be non-selective, flawed or containing pan-assay interference (PAINS) elements^{61,62}. Initiatives such as the NIH Molecular Libraries Program and Structural Genomics Consortium, as well as the dedication of the chemical biology community yielded a significant compendium of high-quality chemical probes. This resulted in one noticeable improvement: we found only few recent studies^{63–66} using Historical compounds such as PF-03814735 which inhibits 123 targets and GSK-J1 which is not cell-permeable; or molecules classifying as PAINS (e.g.; C646)⁶⁷. Another good news is that within the cohort of 662 analysed publications, only 22% have reported using chemical probes above the recommended in-cell concentration (Table 2). Of note, however, the non-compliance with the in-cell concentration varied greatly, ranging from 2 to 70% (Table 2). Moreover, when assessing the compliance with in-cell concentrations, we have given numerous studies ‘the benefit of the doubt’ and considered them partially compliant when at least one experiment was performed within the recommended range.

The bad news is that on average 58% of relevant publications ($n = 509$) used only one chemical probe and did not validate findings with orthogonal inhibitors. Of further concern is the quality of orthogonal inhibitors in the remaining (42%) compliant publications. We noticed that many studies relied on structurally related chemical probes, less selective molecules and/or pan-inhibitors at high(er) concentrations. Probably the most unexpected finding was the lack of matched inactive control compounds in 92% of relevant publications ($n = 420$, Table 2). Finally, within the cohort of 267 eligible publications related to UNC1999, UNCO638, A-485 and THZ1, chemical probes which are accompanied with matched target-inactive control compounds and orthogonal inhibitors, only a worryingly low 4% of publications (11/267) complied with all three recommendations: i.e., the chemical probe was below the recommended in-cell concentration in most figures and orthogonal as well as inactive control compounds were included in the study.

The consequence of the suboptimal (i.e., chemical probes at high concentration) or missing (i.e., lack of inactive and orthogonal compounds) experimental design would be best described as unfinished projects. It is predicted that the median number of protein targets per chemical molecule is up to 329 and thus even the highest quality chemical probes are not expected to be selective at the proteome scale⁶⁸. Rather, the selectivity of every chemical probe depends on the concentration used in experiments. Therefore, to minimise

Table 2 | Summary of non-compliance with guidelines for the use of selected chemical probes

| Target | Chemical probe | Inactive control compound | Number of publications (Jan 2023) | | | |
|----------|----------------|---------------------------|-----------------------------------|---|--------------------------------|-------------------------------------|
| | | | Analysed | Using higher than recommended in-cell concentration (%) | Not using inactive control (%) | Not using orthogonal inhibitors (%) |
| EZH2 | UNC1999 | UNC2400 | 49 | 17 (35%) | 43 (88%) | 26 (53%) |
| G9a/GLP | UNCO638 | UNCO737 | 54 | 38 (70%) | 53 (98%) | 31 (57%) |
| KDM6 | GSK-J4 | GSK-J5 | 153 | 19 (12%) | 137 (89%) | n/a |
| CBP/p300 | A-485 | A-486 | 30 | 14 (47%) | 27 (90%) | 18 (60%) |
| pan-AURK | AMG900 | n/a | 21 | 3 (14%) | n/a | 11 (52%) |
| AURKA | AZD1152 | n/a | 128 | 40 (31%) | n/a | 78 (61%) |
| mTOR | AZD2014 | n/a | 93 | 13 (14%) | n/a | 37 (40%) |
| CDK7 | THZ1 | THZ1-R | 134 | 3 (2%) | 125 (93%) | 92 (69%) |
| | | TOTAL | | 147/662 22% | 385/420 92% | 293/509 58% |

Source data are provided as a Source Data file.

engagement of off-targets it is critical to apply chemical probes at the lowest feasible concentration and demonstrate target modulation in cells at this concentration. Further, chemical probes are largely used to link the primary target of the probe to a phenotype, thus a phenotype observed under a narrow set of conditions (i.e., after a treatment with one chemical probe) must be validated with orthogonal chemical probes and structurally matched target-inactive compounds. The ideal inactive compound does not target the protein of interest but retains the activity against the off-targets. However, the majority of control compounds chemically deviate from the chemical probe by a single heavy atom and even this minimal change to the structure can diminish activity against 80% of the probe's targets⁶⁹. Therefore, although the inactive compounds should be used in parallel with the chemical probes, inclusion of two orthogonal chemical probes is particularly important for the robustness of findings. Employing orthogonal and inactive compounds only marginally increases the size of the experiment (e.g., a few more plates/wells to be treated, one or two additional lanes on immunoblots), however the associated results significantly increase data reliability. These low effort-high impact control experiments will finish the project by confirming that the phenotype obtained with a given chemical probe is indeed due to the targeting of the protein of interest, rather than a technical issue with the assay and/or off-targets of the probe.

The unfinished projects indirectly but significantly impact future research. Researchers generally do not precisely repeat the experiments reported by others. From a practical standpoint, in cancer research for example, the heterogeneity of cultured cells makes it often impossible to repeat one's experiments under the same conditions. Instead, researchers enquire whether the conclusions made by others, such as targeting a given protein kills cancer cells, is pertinent to their disease models. However, hypotheses that are guided by unfinished projects might generate unexpected results. Furthermore, scientists often reach out to publications for experimental design and unknowingly follow a suboptimal approach to answer their hypothesis. As a possible impact, we analysed 14,896 citations that 662 publications included in our analysis received by January 2023 (Table 3). We found that 2583 citations (17% of all citations) are linked to publications using chemical probes at higher than recommended in-cell concentrations; 7744 citations (83% of all relevant citations) are linked to publications not employing inactive control compounds and 7089 citations (59% of all relevant citations) are referring to publications using only one chemical probe. Given this high number of citations linked to unfinished projects, it appears that suboptimal application of chemical probes is an ongoing issue.

Future directions

The quality and quantity of chemical probes continue to rise, and we are on the way to achieving full human proteome coverage thanks to

initiatives such as Target 2035 (<https://www.target2035.net/>), which aims to create, by year 2035, chemogenomic libraries: chemical and/or biological probes for the entire human proteome⁷⁰. However, while the chemical probes are becoming increasingly accessible, their correct use needs to be promoted much more widely and effectively. The chemical probes resources (Table 4) are user-friendly and recommendations for cell-based experiments using chemical probes can be found in reviews^{6–9,11,12}. Free expert-delivered webinars (Table 4) are another easy way to understand chemical probes and learn how to apply them correctly. It is, however, important that scientists relying on research with chemical probes are informed about these resources. Therefore, those skilled with chemical probes could routinely include in their research talks and conference presentations a slide outlining the importance of best practice as well as listing resources to chemical probes and guidelines. The Chemical Probes Portal has developed a useful and informative pack of slides for this purpose (Table 4). Those less skilled in chemical probes should be encouraged to seek advice from experts in the field.

More than one molecular probe (e.g.; siRNA) and demonstrating phenotype in at least two cancer cell lines has become a standard requirement in many cancer journals. We would like to propose 'the rule of two' for chemical probes as well: at least two chemical probes (either orthogonal target-engaging chemical probes, or a pair of a chemical probe and matched target-inactive compound) to be employed at reasonable concentration in every study. If inactive and orthogonal probes are available for the targeted protein, both must be included in the experiments. During manuscript review process, a close attention should be given to this rule, and it is also critical that every manuscript provides evidence of target engagement and/or modulation of downstream pathways by a chemical probe within the recommended concentration range. These experiments should be performed in a hypothesis-relevant cell-based models and the concentration of the chemical probe that relates to the target engagement/modulation should be then applied through the whole study. Of note, while our publication focuses on chemical probes, it is necessary that correctly performed experiments with chemical probes are further validated with molecular probes.

Finally, we provide a simplified flowchart for researchers as a guide to select and use chemical probes correctly, as well as five checklist items that should be addressed when reviewing manuscripts (Fig. 3). Good practice can be achieved by frequent conversations and collaborations between probe developers and users. Good practice could be supported by a dedicated chemical biology reviewer or editor in all journals publishing manuscripts using chemical probes. By practicing good practice, we will use research funds more effectively and hopefully deliver trustworthy scientific breakthroughs at a faster pace.

Table 3 | Summary of citations for publications identified as non-compliant with recommendations

| Probe | Publications | Number of citations (Jan 2023) | | | |
|---------|--------------|--------------------------------|---|--|--|
| | | For all | For publications with higher than recommended in-cell concentration (%) | For publications not using inactive compound (%) | For publications not using orthogonal inhibitors (%) |
| UNC1999 | 49 | 909 | 220 (24%) | 650 (72%) | 327 (36%) |
| UNCO638 | 54 | 1273 | 811 (64%) | 1175 (92%) | 784 (62%) |
| GSK-J4 | 153 | 2890 | 216 (7%) | 2268 (78%) | n/a |
| A-485 | 30 | 503 | 295 (59%) | 403 (80%) | 158 (31%) |
| AMG900 | 21 | 271 | 5 (2%) | n/a | 231 (85%) |
| AZD1152 | 128 | 3189 | 682 (21%) | n/a | 2254 (71%) |
| AZD2014 | 93 | 2076 | 278 (13%) | n/a | 763 (37%) |
| THZ-1 | 134 | 3785 | 76 (2%) | 3248 (86%) | 2572 (68%) |
| TOTAL | 662 | 14,896 | 2583 / 14,896 (17%) | 7744 / 9360 (83%) | 7089 / 12006 (59%) |

Source data are provided as a Source Data file.

Table 4 | Links to selected resources, webinars and slides on chemical probes

| Resource type | URL |
|---|---|
| <i>Expert-curated portals</i> | |
| Chemical Probes Portal | www.chemicalprobes.org |
| Structural Genomics Consortium | https://www.thesgc.org/chemical-probes |
| Nathanael Gray Laboratory | https://graylab.stanford.edu/probe-resources/ |
| <i>Data-driven computational portals</i> | |
| Probe Miner | https://probeminer.icr.ac.uk/#/ |
| Probes & Drugs Portal | https://www.probes-drugs.org/home/ |
| Small Molecule Suite | https://lsp.connect.hms.harvard.edu/smallmoleculesuite/ |
| <i>Expert-delivered webinars</i> | |
| Chemical probes as essential tools for biological discovery | https://www.youtube.com/watch?v=ZthORK6mSLI |
| Best practices for validating chemical probes | https://www.youtube.com/watch?v=rBGU8CKskTE |
| Best practices for validating chemical probes: Case Study 1 – MALT1 protease inhibitors | https://www.youtube.com/watch?v=LuEqOLTzJlY&list=PLSvEKj6f3OHFeOeel4VZyHaLSPhVVFmec&index=7 |
| Target validation using chemical probes | https://www.youtube.com/watch?v=NEeaeU6-po |
| Chemical probes in disease modelling approaches | https://www.youtube.com/watch?v=h45NUCRqZM4 |
| Target 2035: Resource landscape for chemical probes | https://www.youtube.com/watch?v=vCAsE9LAJ8 |
| <i>Presentation slides for inclusion in talks</i> | |
| Link to the slides pack developed by the Chemical Probes Portal's team | https://www.chemicalprobes.org/information-centre#presentations |

Methods

Through the whole study, we adhered to the Preferred Items for Systematic Reviews and Meta-Analysis (PRISMA 2020) guidelines¹⁹.

Protocol and registration

We could not preregister the study as it did not include any health-related outcome. Details on the conception of this study and the protocol followed is described herein in this publication. All data and notes associated with it are provided in the Supplementary Information, Supplementary Data and Source Data files.

Database search

Searches were performed in 2022, with last searches to identify most recent articles completed between 16–20 January 2023. We used the PubMed database (<https://pubmed.ncbi.nlm.nih.gov>) of the United States National Library of Medicine at the National Institutes of Health and the SciFinderⁿ portal (<https://scifinder.cas.org/>) of the Chemical Abstract Service. All searches were performed with no language or time restrictions. The bibliographic records retrieved from a “text search” in SciFinderⁿ are sourced from CAPLUS and MEDLINE databases, whereas records retrieved in SciFinderⁿ substance search originate from CAS REGISTRY²¹. The chemical probe names (*i.e.*, UNC1999, UNC0638, GSK-J4, A-485, AMG900, AZD1152, Barasertib, AZD2014, THZ1) were used as the query in the PubMed and SciFinderⁿ keyword searches. The SciFinderⁿ structure-based search was completed with the structure of each chemical probe drawn into the structure query box. The outputs of these searches are provided in the Source Data file. The three searches for each chemical probe were combined, patents removed by an automation tool and duplicates/triplicates were removed manually, yielding a list of unique articles for each chemical probe. These searches were completed by JS and JRB.

Study selection

In the first steps of screening, we excluded articles not written in English (Supplementary Note 1 - Reason #1) and articles whose full text were not available via University of Sydney library access (Reason #2). In the next step, we retrieved available full-text and English written articles. We excluded articles describing the discovery of a given chemical probe and/or medicinal chemistry articles using the probe as

the lead compound (Reason #3); articles in which the chemical probe was used to generate chemical probe-resistant clones and/or articles lacking mechanistic experiments (Reason #4); articles containing only *in vivo* (animal/human tissue) data and/or clinical trials (Reason #5) and reviews, commentaries, editorials, letters to the editors, conference proceedings, pre-prints and similar (Reason #6). The screening process was completed independently by JS and JRB, full-text articles were checked for eligibility criteria (Supplementary Note 1) by JS and LM. Individual PRISMA flow charts for each chemical probe and reasons for exclusion are provided in the Supplementary Information.

Eligibility criteria

We included all primary research articles (referred to as ‘publications’) that contained at least one figure panel presenting results obtained with a given chemical probe in a cell-based assay, irrespective of the topics and research fields (Supplementary Note 1).

Data items and data collection

For each eligible publication (listed in Supplementary Tables 2, 4, 6, 8, 10, 12, 14, 16), JS extracted the following data: (i) concentration of a given chemical probe used in cell-based assays; (ii) inclusion of structurally matched target-inactive control compound (if available) and (iii) list of orthogonal inhibitors/chemical probes. These three items were defined based on previous recommendations^{9,11}. In the analysis of the chemical probes' concentrations, we assessed cell-based assays addressing a mechanistic investigation, target engagement, delineation of a signalling pathway and/or identification of a phenotype following treatment with a given chemical probe. The concentrations employed in cell viability and clonogenic assays were not considered as a range of concentrations above the recommended maximum is needed to construct dose-response curves for calculations of cellular IC₅₀/EC₅₀ values. Similarly, Cellular Thermal Shift Assay (CETSA, a direct assay to assess target engagement in cells)²² or toxicity assessments require higher concentrations of compounds and these concentration values were omitted in our analysis. When addressing the use of inactive control compounds (where available), we analysed (yes/no) whether the control compound was included: either shown in at least one figure panel or mentioned but data not shown. When addressing the use of orthogonal inhibitors, we listed all

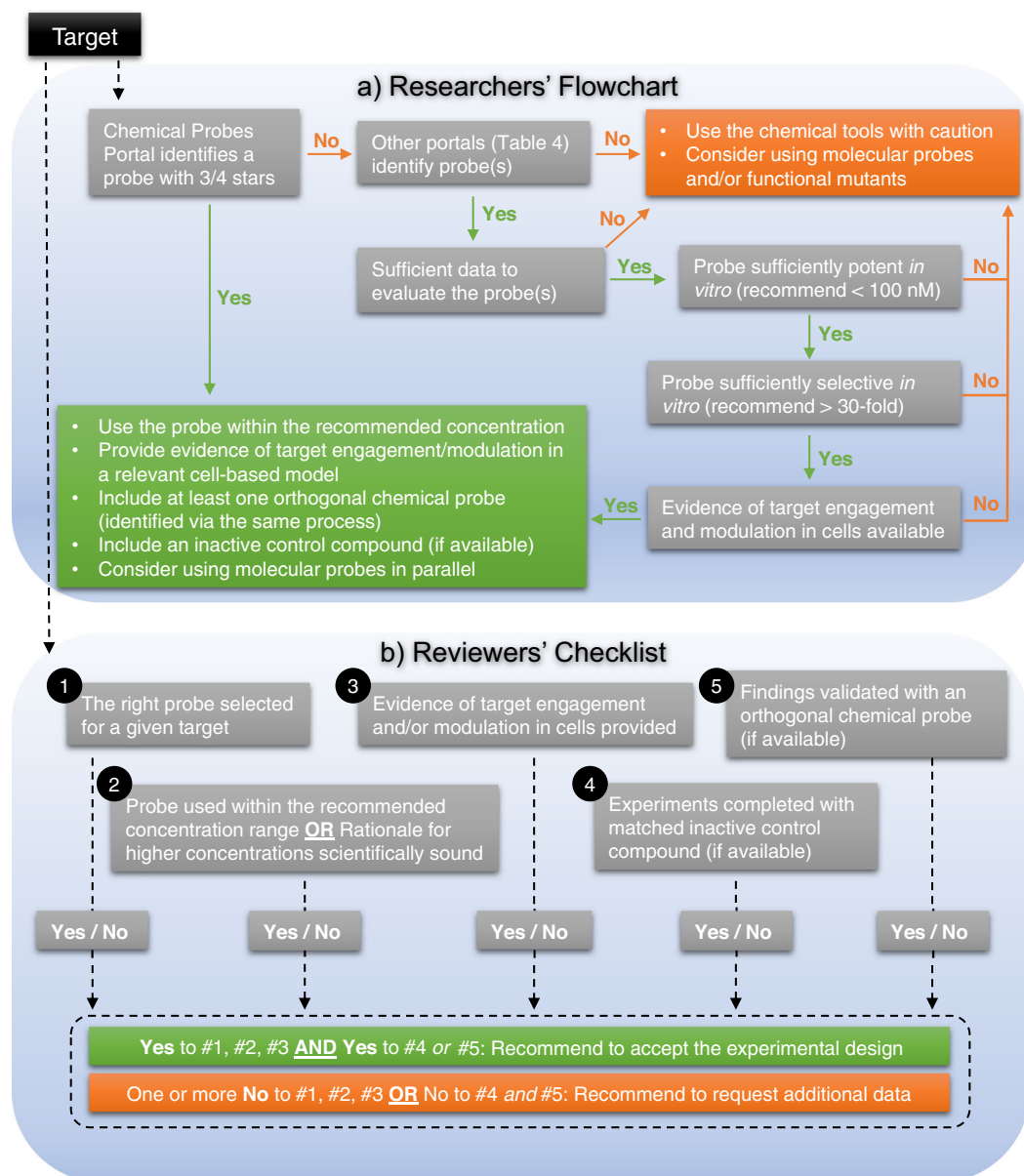


Fig. 3 | Schematic summarising key steps for researchers and reviewers to correctly use chemical probes in cell-based research. **a** For researchers, we recommend to start with the Chemical Probes Portal. If no probes are available on the Portal, other resources (listed in Table 4) can be used to identify a suitable probe. It is important to assess fitness factors of each probe and if the minimums are not met, we advise to use the chemical probe with caution and/or use molecular

probes instead. **b** For reviewers, we recommend to accept the experimental design only if the right chemical probe (assessed by using the Flowchart) has been used within the recommended concentration range and evidence of target engagement/modulation is demonstrated in a relevant cell-based assay (Yes to checklist items #1–3). To comply with ‘the rule of two’, at least one Yes is necessary to items #4 and #5.

chemical compounds that target the protein of interest and have been included in at least one figure panel. The number of citations were sourced from ScFinder[®]. There was a small number of publications not found in ScFinder[®] and for these publications citation numbers were sourced from the PubMed database.

Synthesis of results and analysis

As the recommendations for chemical probes' maximum in-cell concentration, we used values listed on the Chemical Probes Portal (www.chemicalprobes.org) and/or on the Structural Genomics Consortium's Chemical Probes (<https://www.thesgc.org/chemical-probes>) websites. If the entire publication reported a given chemical probe below the recommended in-cell concentration, the publication was considered complying. We found numerous publications in which the chemical probe was applied at various concentrations, some of which were

exceeding the recommended in-cell concentration. In this cohort, publications were considered partially complying if at least one experiment was performed with a concentration of a given chemical probe below the recommended maximum in-cell concentration. Finally, publications which used a given chemical probe at concentrations above the recommended values were considered non-complying. When addressing the use of matched inactive control compounds (where available), publications assessed with Yes were considered complying, and publications assessed with “No” considered non-complying. When assessing the use of orthogonal inhibitors, we considered every publication using at least one orthogonal inhibitor (regardless of their fitness factors and/or concentration) complying. We did not limit the compliance assessment to the application of endorsed orthogonal chemical probes. Publications not using any orthogonal chemical compounds were deemed non-

complying. All details are tabulated in the Supplementary Tables 2, 4, 6, 8, 10, 12, 14, 16; with compliant items highlighted in blue font. The percentages of compliance for each chemical probe were calculated as the sum of complying/partially-complying/non-complying publications over the number of included publications, the summary is presented in Fig. 2 prepared with GraphPad Prism 9 software. For the pooled analysis of data (Table 2), the percentages were calculated as a sum of all non-complying publications over the total number of all relevant eligible publications. Similarly, citations percentages (Table 3) were calculated as a sum of citations for all non-complying publications over the sum of all relevant citations (Supplementary Notes 2–9).

Reporting summary

Further information on research design is available in the Nature Portfolio Reporting Summary linked to this article.

Data availability

All data generated in this study are provided in this manuscript, Source Data and Supplementary Information files. Completed PRISMA checklists are available as Supplementary Data 1. Results of searches containing all considered records are available as Supplementary Data 2. Source data are provided with this paper.

References

1. Workman, P. & Collins, I. Probing the Probes: Fitness factors for small molecule tools. *Chem. Biol.* **17**, 561–577 (2010).
2. Frye, S. V. The art of the chemical probe. *Nat. Chem. Biol.* **6**, 159–161 (2010).
3. A conversation on using chemical probes to study protein function in cells and organisms. *Nat. Commun.* **13**, 3757 (2022).
4. Emmerich, C. H. et al. Improving target assessment in biomedical research: the GOT-IT recommendations. *Nat. Rev. Drug Discov.* **20**, 64–81 (2021).
5. Frye, S. V. et al. Tackling reproducibility in academic preclinical drug discovery. *Nat. Rev. Drug Discov.* **14**, 733–734 (2015).
6. Bunnage, M. E., Gilbert, A. M., Jones, L. H. & Hett, E. C. Know your target, know your molecule. *Nat. Chem. Biol.* **11**, 368–372 (2015).
7. Bunnage, M. E., Chekler, E. L. P. & Jones, L. H. Target validation using chemical probes. *Nat. Chem. Biol.* **9**, 195–199 (2013).
8. Munoz, L. Non-kinase targets of protein kinase inhibitors. *Nat. Rev. Drug Discov.* **16**, 424–440 (2017).
9. Arrowsmith, C. H. et al. The promise and peril of chemical probes. *Nat. Chem. Biol.* **11**, 536–541 (2015).
10. Licciardello, M. P. & Workman, P. The era of high-quality chemical probes. *RSC Medicinal Chem.* **13**, 1446–1459 (2022).
11. Antolin, A. A., Workman, P. & Al-Lazikani, B. Public resources for chemical probes: the journey so far and the road ahead. *Future Medicinal Chem.* **13**, 731–747 (2019).
12. Blagg, J. & Workman, P. Choose and use your chemical probe wisely to explore cancer biology. *Cancer Cell* **32**, 9–25 (2017).
13. Antolin, A. A. et al. The Chemical Probes Portal: an expert review-based public resource to empower chemical probe assessment, selection and use. *Nucleic Acids Res.* **51**, D1492–D1502 (2023).
14. Müller, S. et al. Donated chemical probes for open science. *Life* **7**, e34311 (2018).
15. Antolin, A. A. et al. Objective, quantitative, data-driven assessment of chemical probes. *Cell Chem. Biol.* **25**, 194–205 (2018).
16. Skuta, C. et al. Probes & Drugs portal: an interactive, open data resource for chemical biology. *Nat. Methods* **14**, 759–760 (2017).
17. Kaelin, W. G. Jr Common pitfalls in preclinical cancer target validation. *Nat. Rev. Cancer* **17**, 425–440 (2017).
18. Errington, T. M., Denis, A., Perfito, N., Iorns, E. & Nosek, B. A. Challenges for assessing replicability in preclinical cancer biology. *eLife* **10**, e67995 (2021).
19. Page, M. J. et al. The PRISMA 2020 statement: an updated guideline for reporting systematic reviews. *BMJ* **372**, n71 (2021).
20. Bhat, K. P., Ümit Kaniskan, H., Jin, J. & Gozani, O. Epigenetics and beyond: targeting writers of protein lysine methylation to treat disease. *Nat. Rev. Drug Discov.* **20**, 265–286 (2021).
21. Richart, L. & Margueron, R. Drugging histone methyltransferases in cancer. *Curr. Opin. Chem. Biol.* **56**, 51–62 (2020).
22. Knutson, S. K. et al. A selective inhibitor of EZH2 blocks H3K27 methylation and kills mutant lymphoma cells. *Nat. Chem. Biol.* **8**, 890–896 (2012).
23. Qi, W. et al. Selective inhibition of Ezh2 by a small molecule inhibitor blocks tumor cells proliferation. *Proc. Natl Acad. Sci. USA* **109**, 21360–21365 (2012).
24. Verma, S. K. et al. Identification of potent, selective, cell-active inhibitors of the histone methyltransferase EZH2. *ACS Med. Chem. Lett.* **3**, 1091–1096 (2012).
25. Knutson, S. K. et al. Selective inhibition of EZH2 by EPZ-6438 leads to potent antitumor activity in EZH2-mutant non-Hodgkin lymphoma. *Mol. Cancer Ther.* **13**, 842–854 (2014).
26. Campbell, J. E. et al. EPZ011989, a potent, orally-available EZH2 inhibitor with robust in vivo activity. *ACS Med. Chem. Lett.* **6**, 491–495 (2015).
27. Konze, K. D. et al. An orally bioavailable chemical probe of the lysine methyltransferases EZH2 and EZH1. *ACS Chem. Biol.* **8**, 1324–1334 (2013).
28. Zhang, H. et al. Oncogenic deregulation of EZH2 as an opportunity for targeted therapy in lung cancer. *Cancer Discov.* **6**, 1006–1021 (2016).
29. Bradley William, D. et al. EZH2 inhibitor efficacy in Non-Hodgkin's lymphoma does not require suppression of H3K27 monomethylation. *Chem. Biol.* **21**, 1463–1475 (2014).
30. Vaswani, R. G. et al. Identification of (R)-N-((4-Methoxy-6-methyl-2-oxo-1,2-dihydropyridin-3-yl)methyl)-2-methyl-1-(1-(1-(2,2,2-trifluoroethyl)piperidin-4-yl)ethyl)-1H-indole-3-carboxamide (CPI-1205), a Potent and Selective Inhibitor of Histone Methyltransferase EZH2, Suitable for Phase I Clinical Trials for B-Cell Lymphomas. *J. Med. Chem.* **59**, 9928–9941 (2016).
31. Kubicek, S. et al. Reversal of H3K9me2 by a small-molecule inhibitor for the G9a histone methyltransferase. *Mol. Cell* **25**, 473–481 (2007).
32. Vedadi, M. et al. A chemical probe selectively inhibits G9a and GLP methyltransferase activity in cells. *Nat. Chem. Biol.* **7**, 566–574 (2011).
33. Liu, F. et al. Discovery of an in vivo chemical probe of the lysine methyltransferases G9a and GLP. *J. Med. Chem.* **56**, 8931–8942 (2013).
34. Sweis, R. F. et al. Discovery and development of potent and selective inhibitors of histone methyltransferase g9a. *ACS Med. Chem. Lett.* **5**, 205–209 (2014).
35. Sterling, J., Menezes, S. V., Abbassi, R. H. & Munoz, L. Histone lysine demethylases and their functions in cancer. *Int J. Cancer* **148**, 2375–2388 (2021).
36. Kruidenier, L. et al. A selective jumonji H3K27 demethylase inhibitor modulates the proinflammatory macrophage response. *Nature* **488**, 404–408 (2012).
37. He, Z.-X. et al. Current development of CBP/p300 inhibitors in the last decade. *Eur. J. Med. Chem.* **209**, 112861 (2021).
38. Lasko, L. M. et al. Discovery of a selective catalytic p300/CBP inhibitor that targets lineage-specific tumours. *Nature* **550**, 128–132 (2017).
39. Wilson, J. E. et al. Discovery of CPI-1612: A potent, selective, and orally bioavailable EP300/CBP histone acetyltransferase inhibitor. *ACS Med. Chem. Lett.* **11**, 1324–1329 (2020).

40. Taylor, A. M. et al. Fragment-based discovery of a selective and cell-active benzodiazepinone CBP/EP300 bromodomain inhibitor (CPI-637). *ACS Med. Chem. Lett.* **7**, 531–536 (2016).
41. Romero, F. A. et al. GNE-781, a highly advanced potent and selective bromodomain inhibitor of cyclic adenosine monophosphate response element binding protein, binding protein (CBP). *J. Med. Chem.* **60**, 9162–9183 (2017).
42. Chekler Eugene, L. P. et al. Transcriptional profiling of a selective CREB binding protein bromodomain inhibitor highlights therapeutic opportunities. *Chem. Biol.* **22**, 1588–1596 (2015).
43. Hay, D. A. et al. Discovery and optimization of small-molecule ligands for the CBP/p300 bromodomains. *J. Am. Chem. Soc.* **136**, 9308–9319 (2014).
44. Picaud, S. et al. Generation of a selective small molecule inhibitor of the CBP/p300 bromodomain for leukemia therapy. *Cancer Res.* **75**, 5106 (2015).
45. Quartuccio, S. & Schindler, K. Functions of Aurora kinase C in meiosis and cancer. *Front Cell Dev. Biol.* **3**, 50 (2015).
46. Shimomura, T. et al. MK-5108, a highly selective Aurora-A kinase inhibitor, shows antitumor activity alone and in combination with docetaxel. *Mol. Cancer Ther.* **9**, 157 (2010).
47. Mortlock, A. A. et al. Discovery, synthesis, and in vivo activity of a new class of pyrazoloquinazolines as selective inhibitors of aurora B kinase. *J. Med. Chem.* **50**, 2213–2224 (2007).
48. Payton, M. et al. Preclinical evaluation of AMG 900, a novel potent and highly selective pan-Aurora kinase inhibitor with activity in taxane-resistant tumor cell lines. *Cancer Res.* **70**, 9846 (2010).
49. Kwiatkowski, N. et al. Selective Aurora kinase inhibitors identified using a taxol-induced checkpoint sensitivity screen. *ACS Chem. Biol.* **7**, 185–196 (2012).
50. Liu, G. Y. & Sabatini, D. M. mTOR at the nexus of nutrition, growth, ageing and disease. *Nat. Rev. Mol. Cell Biol.* **21**, 183–203 (2020).
51. Mossmann, D., Park, S. & Hall, M. N. mTOR signalling and cellular metabolism are mutual determinants in cancer. *Nat. Rev. Cancer* **18**, 744–757 (2018).
52. Brown, E. J. et al. A mammalian protein targeted by G1-arresting rapamycin-receptor complex. *Nature* **369**, 756–758 (1994).
53. Guichard, S. M. et al. AZD2014, an inhibitor of mTORC1 and mTORC2, is highly effective in ER+ breast cancer when administered using intermittent or continuous Schedules. *Mol. Cancer Ther.* **14**, 2508–2518 (2015).
54. Chresta, C. M. et al. AZD8055 is a potent, selective, and orally bioavailable ATP-competitive mammalian target of rapamycin kinase inhibitor with in vitro and in vivo antitumor activity. *Cancer Res.* **70**, 288–298 (2010).
55. Pike, K. G. et al. Optimization of potent and selective dual mTORC1 and mTORC2 inhibitors: the discovery of AZD8055 and AZD2014. *Bioorg. Med. Chem. Lett.* **23**, 1212–1216 (2013).
56. Fraser, C., Carragher, N. O. & Unciti-Broceta, A. eCF309: a potent, selective and cell-permeable mTOR inhibitor. *MedChemComm* **7**, 471–477 (2016).
57. Li, Z.-M., Liu, G., Gao, Y. & Zhao, M.-G. Targeting CDK7 in oncology: the avenue forward. *Pharm. Ther.* **240**, 108229 (2022).
58. Olson, C. M. et al. Development of a selective CDK7 covalent inhibitor reveals predominant cell-cycle phenotype. *Cell Chem. Biol.* **26**, 792–803.e710 (2019).
59. Kwiatkowski, N. et al. Targeting transcription regulation in cancer with a covalent CDK7 inhibitor. *Nature* **511**, 616–620 (2014).
60. Zhang, T. et al. Covalent targeting of remote cysteine residues to develop CDK12 and CDK13 inhibitors. *Nat. Chem. Biol.* **12**, 876–884 (2016).
61. Baell, J. & Walters, M. A. Chemistry: Chemical con artists foil drug discovery. *Nature* **513**, 481–483 (2014).
62. Baell, J. B. Feeling Nature’s PAINS: Natural products, natural product drugs, and Pan Assay Interference Compounds (PAINS). *J. Nat. Prod.* **79**, 616–628 (2016).
63. Tanaka, K. et al. Targeting Aurora B kinase prevents and overcomes resistance to EGFR inhibitors in lung cancer by enhancing BIM- and PUMA-mediated apoptosis. *Cancer Cell* **39**, 1245–1261 (2021).
64. Zhang, W. et al. Therapeutically targeting head and neck squamous cell carcinoma through synergistic inhibition of LSD1 and JMJD3 by TCP and GSK-J1. *Br. J. Cancer* **122**, 528–538 (2020).
65. Diesch, J. et al. Inhibition of CBP synergizes with the RNA-dependent mechanisms of Azacitidine by limiting protein synthesis. *Nat. Commun.* **12**, 6060 (2021).
66. Vogel, F. C. E. et al. Targeting the H3K4 Demethylase KDM5B Reprograms the Metabolome and Phenotype of Melanoma Cells. *J. Invest. Dermatol.* **139**, 2506–2516 (2019).
67. Shrimp, J. H. et al. Characterizing the covalent targets of a small molecule inhibitor of the lysine acetyltransferase P300. *ACS Med. Chem. Lett.* **7**, 151–155 (2016).
68. Zhou, H., Gao, M. & Skolnick, J. Comprehensive prediction of drug-protein interactions and side effects for the human proteome. *Sci. Rep.* **5**, 11090 (2015).
69. Lee, J. & Schapira, M. The promise and peril of chemical probe negative controls. *ACS Chem. Biol.* **16**, 579–585 (2021).
70. Müller, S. et al. Target 2035 - update on the quest for a probe for every protein. *RSC Med. Chem.* **13**, 13–21 (2022).
71. Gabrielson, S. SciFinder. *J. Med. Libr. Assoc.* **106**, 588–590 (2018).
72. Molina, D. M. et al. Monitoring drug target engagement in cells and tissues using the cellular thermal shift assay. *Science* **341**, 84–87 (2013).

Acknowledgements

The authors thank Paul Workman for discussions, support and insightful comments during the preparation of this manuscript. We thank Albert Antolin for help with the Probe Miner database.

Author contributions

J.S. performed literature searches, detailed analysis of all eligible publications and prepared Supplementary Tables 1–16 and individual PRISMA flowcharts (Supplementary Figs. 2, 4, 5, 7, 9, 10, 11, 13). J.R.B. performed literature searches, prepared Supplementary Figs. 1, 3, 6, 8, 12 and drafted chemistry sections on all chemical probes, with input from A.M. L.M. conceptualised the study, supervised the analysis of publications, performed data curation, prepared Tables 1–4 and Figs. 1–3. L.M. wrote the manuscript and all authors contributed with editing.

Competing interests

The authors declare no competing interests.

Additional information

Supplementary information The online version contains supplementary material available at <https://doi.org/10.1038/s41467-023-38952-1>.

Correspondence and requests for materials should be addressed to Lenka Munoz.

Peer review information *Nature Communications* thanks Bridget Wagner and the other, anonymous, reviewer(s) for their contribution to the peer review of this work. A peer review file is available.

Reprints and permissions information is available at <http://www.nature.com/reprints>

Publisher’s note Springer Nature remains neutral with regard to jurisdictional claims in published maps and institutional affiliations.

Open Access This article is licensed under a Creative Commons Attribution 4.0 International License, which permits use, sharing, adaptation, distribution and reproduction in any medium or format, as long as you give appropriate credit to the original author(s) and the source, provide a link to the Creative Commons license, and indicate if changes were made. The images or other third party material in this article are included in the article's Creative Commons license, unless indicated otherwise in a credit line to the material. If material is not included in the article's Creative Commons license and your intended use is not permitted by statutory regulation or exceeds the permitted use, you will need to obtain permission directly from the copyright holder. To view a copy of this license, visit <http://creativecommons.org/licenses/by/4.0/>.

© The Author(s) 2023

Systematic literature review reveals suboptimal use of chemical probes in cell-based biomedical research

Jayden Sterling¹, Jennifer R Baker², Adam McCluskey², Lenka Munoz^{1*}

¹ Faculty of Medicine and Health, Charles Perkins Centre, The University of Sydney, NSW 2006, Australia

² Discipline of Chemistry, School of Environmental and Life Sciences, The University of Newcastle, Callaghan, NSW 2308, Australia

*Corresponding author: lenka.munoz@sydney.edu.au

Content

| | |
|---|----------------|
| Supplementary Note 1. Reasons for exclusions of articles and eligibility criteria. | Page 2 |
| Supplementary Note 2. Citations for UNC1999 publications. | Page 9 |
| Supplementary Note 3. Citations for UNC0638 publications. | Page 17 |
| Supplementary Note 4. Citations for GSK-J4 publications. | Page 27 |
| Supplementary Note 5. Citations for A-485 publications. | Page 32 |
| Supplementary Note 6. Citations for AMG900 publications. | Page 38 |
| Supplementary Note 7. Citations for AZD1152 publications. | Page 53 |
| Supplementary Note 8. Citations for AZD2014 publications. | Page 63 |
| Supplementary Note 9. Citations for THZ1 publications. | Page 75 |
| | |
| Supplementary Figure 1. Overview of EZH2 chemical probes. | Page 3 |
| Supplementary Figure 2. PRISMA flow diagram: UNC1999 | Page 4 |
| Supplementary Figure 3. Overview of G9a/GLP and KDM6 chemical probes. | Page 10 |
| Supplementary Figure 4. PRISMA flow diagram: UNC0638. | Page 11 |
| Supplementary Figure 5. PRISMA flow diagram: GSK-J4. | Page 18 |
| Supplementary Figure 6. Overview of CREBBP/p300 chemical probes. | Page 28 |
| Supplementary Figure 7. PRISMA flow diagram: A-485. | Page 29 |
| Supplementary Figure 8. Overview of Aurora and mTOR chemical probes. | Page 33 |
| Supplementary Figure 9. PRISMA flow diagram: AMG900. | Page 34 |
| Supplementary Figure 10. PRISMA flow diagram: AZD1152. | Page 39 |
| Supplementary Figure 11. PRISMA flow diagram: AZD2014. | Page 54 |
| Supplementary Figure 12. Overview of CDK7 and CDK12/13 chemical probes. | Page 64 |
| Supplementary Figure 13. PRISMA flow diagram: THZ1. | Page 65 |
| | |
| Supplementary Table 1. List of excluded articles using UNC1999. | Page 5 |
| Supplementary Table 2. Overview of eligible publications using UNC1999. | Page 7 |
| Supplementary Table 3. List of excluded articles using UNC0638. | Page 12 |
| Supplementary Table 4. Overview of eligible publications using UNC0638. | Page 14 |
| Supplementary Table 5. List of excluded articles using GSK-J4. | Page 19 |
| Supplementary Table 6. Overview of eligible publications using GSK-J4. | Page 21 |
| Supplementary Table 7. List of excluded articles using A-485. | Page 30 |
| Supplementary Table 8. Overview of eligible publications using A-485. | Page 31 |
| Supplementary Table 9. List of excluded articles using AMG900. | Page 35 |
| Supplementary Table 10. Overview of eligible publications using AMG900. | Page 37 |
| Supplementary Table 11. List of excluded articles using AZD1152. | Page 40 |
| Supplementary Table 12. Overview of eligible publications using AZD1152. | Page 46 |
| Supplementary Table 13. List of excluded articles using AZD2014. | Page 55 |
| Supplementary Table 14. Overview of eligible publications using AZD2014. | Page 59 |
| Supplementary Table 15. List of excluded articles using THZ1. | Page 66 |
| Supplementary Table 16. Overview of eligible publications using THZ1. | Page 68 |

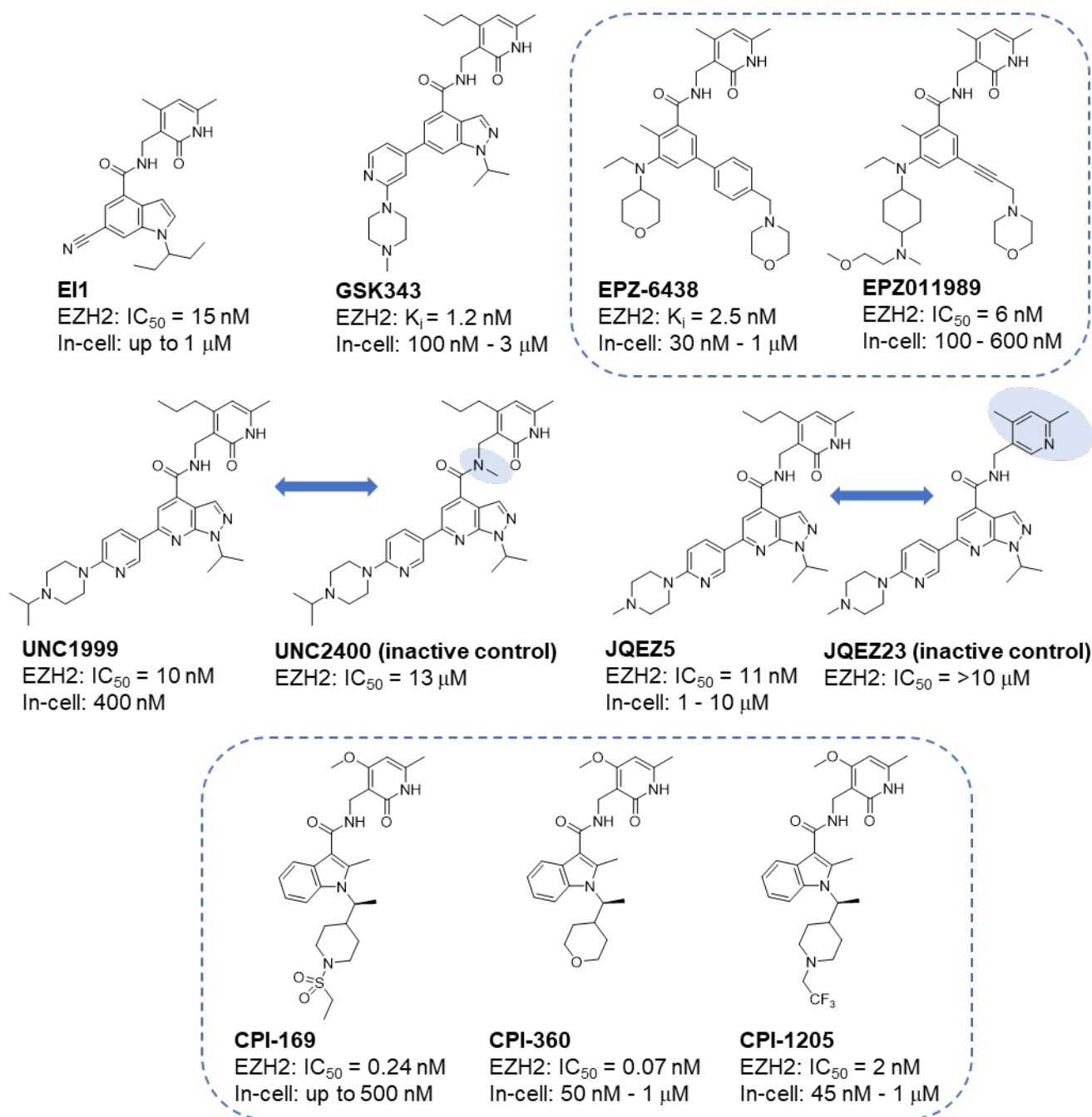
Supplementary Note 1. Reasons for exclusions of articles and eligibility criteria for inclusion of publications.

Reasons for exclusion

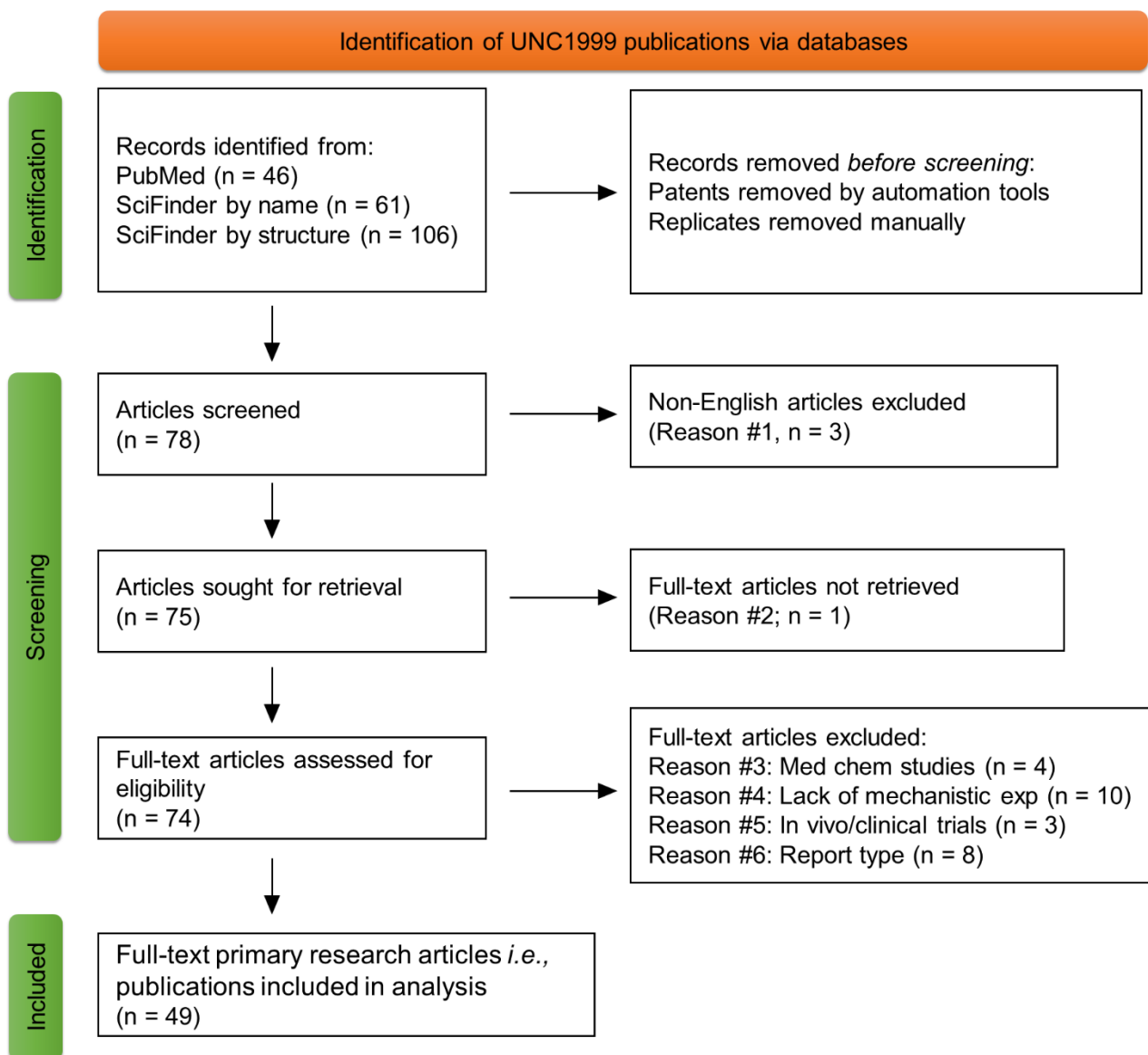
- 1) Articles not written in English.
- 2) Articles whose full-text were not available via University of Sydney library access.
- 3) Articles describing the discovery and characterisation of a given chemical probe, or medicinal chemistry/SAR articles using the probe as a lead compound.
- 4) Articles in which the chemical probe was used to generate chemical probe-resistant clones and/or studies lacking mechanistic experiments
- 5) Articles containing only *in vivo* (animal/human tissue) data and/or clinical trial articles.
- 6) Reviews, commentaries, editorials, letters to the editors, conference proceedings, pre-print and similar.

Eligibility criteria for inclusion

- 1) Publication presents at least one figure panel using the chemical probe in a cell-based assay



Supplementary Figure 1. Structures, biochemical potency (K_i/IC_{50}) and recommended in-cell concentration of EZH2 targeting chemical probes listed on the Chemical Probes Portal (www.chemicalprobes.org). Dashed lines group structurally related chemical probes that should not be used together as orthogonal tools (e.g., EPZ-6438 can be used as an orthogonal chemical probe with UNC1999, but not with EPZ011989). Bidirectional arrows link target-inactive analogues and shaded fields highlight the structural changes leading to decreased EZH2 targeting.



Supplementary Figure 2. PRISMA flow diagram summarising identification of publications using the EZH2 chemical probe UNC1999.

Supplementary Table 1. List of excluded articles using the EZH2 probe UNC1999.

| | Title (PMID) | Reason for exclusion |
|----|--|--|
| 1 | [Novel epigenetic therapies for multiple myeloma] (PMID: 33967157) | 1) Non-English publication |
| 2 | [Effects of histone methyltransferase inhibitors on the survival, apoptosis and cell cycle of Raji cells] (PMID: 31631594) | 1) Non-English publication |
| 3 | Effects of EZH2 inhibitor combined with cisplatin on proliferation and apoptosis of non-small cell lung cancer A549 cells (No PMID; DOI: 10.3969/j.issn.1005-9202.2016.23.029) | 1) Non-English publication |
| 4 | Development of a UPLC-MS/MS method for determination of a dual EZH1/2 inhibitor UNC1999 in rat plasma (PMID: 34841882) | 2) No access |
| 5 | ¹⁸ F-Labeled PET probe targeting enhancer of zeste homologue 2 (EZH2) for cancer imaging (PMID: 30891136) | 3) Development of [¹⁸ F]-labelled EZH2 probes |
| 6 | An orally bioavailable chemical probe of the lysine methyltransferases EZH2 and EZH1 (PMID: 23614352) | 3) Discovery of UNC1999 / UNC2400 |
| 7 | Structure-activity relationship studies for enhancer of zeste homologue 2 (EZH2) and enhancer of zeste homologue 1 (EZH1) inhibitors (PMID: 27468126) | 3) SAR of UNC1999 analogues |
| 8 | Identification of novel EZH2 inhibitors through pharmacophore-based virtual screening and biological assays (PMID: 27289323) | 3) SAR study of new EZH1/2 inhibitors. |
| 9 | Identification of novel Ebola virus inhibitors using biologically contained virus (PMID: 35337896) | 4) No mechanistic exp. - screen (>4000 compounds) for Ebola virus inhibitors, no follow up experiments with UNC1999. |
| 10 | Combined inhibition of JAK/STAT pathway and lysine-specific demethylase 1 as a therapeutic strategy in CSF3R/CEBPA mutant acute myeloid leukemia (PMID: 32471953) | 4) No mechanistic exp. - cell viability screen only |
| 11 | The BRD9/7 inhibitor TP-472 blocks melanoma tumor growth by suppressing ECM-mediated oncogenic signaling and inducing apoptosis (PMID: 34771678) | 4) No mechanistic exp. - cell viability screen only |
| 12 | Dissecting the role of novel EZH2 inhibitors in primary glioblastoma cell cultures: effects on proliferation, epithelial-mesenchymal transition, migration, and on the pro-inflammatory phenotype (PMID: 31791385) | 4) No mechanistic experiments |
| 13 | Dual inhibition of enhancer of zeste homolog 1/2 overactivates WNT signaling to deplete cancer stem cells in multiple myeloma (PMID: 30343511) | 4) No mechanistic experiments |
| 14 | BET-bromodomain and EZH2 inhibitor-treated chronic GVHD mice have blunted germinal centers with distinct transcriptomes (PMID: 35226736) | 4) No mechanistic experiments |
| 15 | Discovery of a first-in-class EZH2 selective degrader (PMID: 31819273) | 4) No mechanistic experiments |
| 16 | Cell panel profiling reveals conserved therapeutic clusters and differentiates the mechanism of action of different PI3K/mTOR, aurora kinase and EZH2 inhibitors (PMID: 27587489) | 4) No mechanistic experiments - 122 epigenetic inhibitors tested; no follow up |
| 17 | Permissive epigenomes endow reprogramming competence to transcriptional regulators (PMID: 32807969) | 4) No mechanistic experiments - 17 compounds identified as hits incl UNC1999; no follow up |
| 18 | Activity Comparison of Epigenetic Modulators against the Hemoprotzoan Parasites <i>Babesia divergens</i> and <i>Plasmodium falciparum</i> (PMID: 33599488) | 4) No mechanistic exp. - Parasites growth |
| 19 | The role of the histone methyltransferase EZH2 in liver inflammation and fibrosis in STAM NASH mice (PMID: 32370249) | 5) In vivo study |
| 20 | Enhancer of Zeste Homolog 2 inhibition stimulates bone formation and mitigates bone loss caused by ovariectomy in skeletally mature mice (PMID: 27758858) | 5) In vivo study |
| 21 | Fate mapping of human glioblastoma reveals an invariant stem cell hierarchy (PMID: 28854171) | 5) In vivo study |
| 22 | The miR-125a and miR-320c are potential tumor suppressor microRNAs epigenetically silenced by the polycomb repressive complex 2 in multiple myeloma (PMID: 28664185) | 6) Commentary |
| 23 | Discovery of selective inhibitors for lysine methyltransferases EZH2/EZH1 and SETD8 (No PMID, DOI or ISSN available, AN: 2015:1328182) | 6) Conference proceedings |
| 24 | Chemical probes for the lysine methyltransferases G9a and EZH2 (No PMID, DOI or ISSN available, AN: 2015:1328166) | 6) Conference proceedings |

| | | |
|----|---|---------------------------|
| 25 | Manipulation of chromatin to enhance CRISPR activity (No PMID, DOI or ISSN available, AN: 2017:1932488) | 6) Conference proceedings |
| 26 | Evaluating small molecule histone inhibitors with high resolution mass spectrometry and 3D cell cultures (No PMID, DOI or ISSN available, AN: 2016:294990) | 6) Conference proceedings |
| 27 | Histone modifications and active gene expression are associated with enhanced CRISPR activity in de-silenced chromatin (No PMID available, DOI: https://doi.org/10.1101/228601) | 6) Pre-print |
| 28 | Six years (2012-2018) of researches on catalytic EZH2 inhibitors: the boom of the 2-pyridone compounds (PMID: 30338896) | 6) Review |
| 29 | Targeting EZH2 and PRC2 dependence as novel anticancer therapy (PMID: 26027790) | 6) Review |

Supplementary Table 2. Overview of eligible publications using the EZH2 probe UNC1999 and compliance (in blue) with recommendations to use UNC1999 up to 400 nM (<https://www.chemicalprobes.org/unc1999?q=UNC1999>) or 3 μ M (<https://www.thesgc.org/chemical-probes/UNC1999>), validate results with the inactive compound UNC2400 and orthogonal EZH2 inhibitors. Citations are sourced from SciFinder (January 2023).

| | UNC1999 | UNC2400 | Orthogonal inhibitors | Title (PMID) | Cites |
|----|-----------------------|---------|--|--|-------|
| 1 | 0.1 μ M | No | GSK343, GSK126, EPZ005687, EPZ-6438 (100 nM) | ABCB1 and ABCG2 restrict the brain penetration of a panel of novel EZH2-Inhibitors (PMID: 25868794) | 46 |
| 2 | 0.1-1 μ M | No | None | EZH2 inhibition enhances the efficacy of an EGFR inhibitor in suppressing colon cancer cells (PMID: 25535899) | 37 |
| 3 | 0.1-5 μ M | No | GSK343 (5 μ M) | An inhibitor screen identifies histone-modifying enzymes as mediators of polymer-mediated transgene expression from plasmid DNA (PMID: 29964136) | 7 |
| 4 | 0.1-6 μ M | No | None | Increased EZH2 expression in prostate cancer is associated with metastatic recurrence following external beam radiotherapy (PMID: 31104332) | 20 |
| 5 | 0.25-1 μ M | No | None | Palmitate-triggered COX2/PGE2-related hyperinflammation in dual-stressed pdl fibroblasts is mediated by repressive H3K27 trimethylation (PMID: 35326406) | 1 |
| 6 | 0.5 μ M | No | None | Uropathogenic E. coli (UPEC) infection induces proliferation through enhancer of zeste homologue 2 (EZH2) (PMID: 26964089) | 7 |
| 7 | 0.5 - 3 μ M | Yes | GSK126 (2 μ M) | Selective inhibition of EZH2 and EZH1 enzymatic activity by a small molecule suppresses MLL-rearranged leukemia (PMID: 25395428) | 161 |
| 8 | 1 - 2 μ M | Yes | GSK343 (2 μ M) | Genome-wide profiling of histone H3 lysine 27 and lysine 4 trimethylation in multiple myeloma reveals the importance of Polycomb gene targeting and highlights EZH2 as a potential therapeutic target (PMID: 26755663) | 49 |
| 9 | 1 μ M | No | GSK126, EPZ-5687 (1 μ M) | Targeting EZH2-mediated methylation of histone 3 inhibits proliferation of pediatric acute monocytic leukemia cells in vitro (PMID: 33978549) | 3 |
| 10 | 1 μ M | No | GSK126 (1 μ M) | EZH1/2 inhibition augments the anti-tumor effects of sorafenib in hepatocellular carcinoma. (PMID: 34725436) | 9 |
| 11 | 1 μ M | No | None | NOTCH and EZH2 collaborate to repress PTEN expression in breast cancer (PMID: 33750924) | 7 |
| 12 | 1 μ M | No | GSK126 (1 μ M) | EZH1/2 inhibitors favor ILC3 development from human HSPC-CD34 + cells (PMID: 33467134) | 6 |
| 13 | 1 μ M | No | None | Contribution of DNA methylation and EZH2 in SRBC down-regulation in gastric cancer (PMID: 32676814) | 2 |
| 14 | 1 μ M | No | None | A distinct metabolic response characterizes sensitivity to EZH2 inhibition in multiple myeloma (PMID: 33579905) | 8 |
| 15 | 1 μ M | Yes | None | XIST loss impairs mammary stem cell differentiation and increases tumorigenicity through Mediator hyperactivation (PMID: 35597241) | 2 |
| 16 | 1 μ M | No | GSK343 (1 μ M) | TRACE generates fluorescent human reporter cell lines to characterize epigenetic pathways (PMID: 34963054) | 2 |
| 17 | 1 μ M | No | None | A mass spectrometry-based assay using metabolic labeling to rapidly monitor chromatin accessibility of modified histone proteins (PMID: 31541121) | 19 |
| 18 | 1 μ M & 4 μ M | No | None | EZH2 inhibition in multiple myeloma downregulates myeloma associated oncogenes and upregulates microRNAs with potential tumor suppressor functions (PMID: 28052011) | 39 |
| 19 | 1 μ M & 5 μ M | No | GSK126, EPZ6438 (1 - 5 μ M) | Mechanisms of resistance to EZH2 inhibitors in diffuse large B-cell lymphomas (PMID: 29572378) | 67 |

| | | | | | |
|----|-------------------------|-----|---|--|----|
| 20 | 1 μ M & 5 μ M | No | CPI-169 (40 μ M), CPI-1205, EII, EPZ-6438, SK126, GSK503, PF-06726304 (all 5 μ M) | Multiple pharmacological inhibitors targeting the epigenetic suppressor enhancer of zeste homolog 2 (exh2) accelerate osteoblast differentiation (PMID: 33940225) | 14 |
| 21 | 1.25-5 μ M | No | None | Polycomb EZH1 regulates cell cycle/5-fluorouracil sensitivity of neuroblastoma cells in concert with MYCN (PMID: 36052716) | 0 |
| 22 | 1-5 μ M | No | None | Histone methyltransferase inhibition has a cytotoxic impact on transformed mast cells: implications for mastocytosis (PMID: 32366397) | 1 |
| 23 | 1-50 μ M | No | GSK126, GSK343, EPZ-6438, EPZ011989, EII (1 - 50 μ M) | Chromatin remodeling controls Kaposi's sarcoma-associated herpesvirus reactivation from latency (PMID: 30212584) | 26 |
| 24 | 0.5-5 μ M | No | GSK343 (0.5 - 5 μ M) | Evaluation of EED inhibitors as a class of PRC-2 targeted small molecules for HIV latency reversal (PMID: 32366397) | 7 |
| 25 | 2-3 μ M | No | None | Mammary molecular portraits reveal lineage-specific features and progenitor cell vulnerabilities (PMID: 29921600) | 17 |
| 26 | 2 - 5 μ M | Yes | GSK343, GSK126, EPZ-6438 (2 - 3 μ M) | Small molecule epigenetic screen identifies novel EZH2 and HDAC inhibitors that target glioblastoma brain tumor-initiating cells (PMID: 27449082) | 26 |
| 27 | 2 - 6 μ M | No | GSK503 (4 - 10 μ M) | Overexpression of EZH2 in conjunctival melanoma offers a new therapeutic target (PMID: 29732557) | 12 |
| 28 | 2 - 10 μ M | No | GSK343, EPZ005687 (2-10 μ M) | EZH2-mediated epigenetic silencing of miR-29/miR-30 targets LOXL4 and contributes to tumorigenesis, metastasis, and immune microenvironment remodeling in breast cancer (PMID: 32754259) | 27 |
| 29 | 2 - 10 μ M | No | EPZ005687 (2 - 8 μ M) | Targeting EZH1/2 induces cell cycle arrest and inhibits cell proliferation through reactivation of p57 CDKN1C and TP53INP1 in mantle cell lymphoma (PMID: 31565482) | 6 |
| 30 | 2.5 μ M & 5 μ M | No | GSK343 (5-10 μ M) | EZH2 inhibitors transcriptionally upregulate cytotoxic autophagy and cytoprotective unfolded protein response in human colorectal cancer cells (PMID: 27648357) | 31 |
| 31 | 3 μ M | No | None | Inhibition of polycomb repressor complex 2 ameliorates neointimal hyperplasia by suppressing trimethylation of H3K27 in vascular smooth muscle cells (PMID: 31162630) | 9 |
| 32 | 3 μ M | Yes | None | Targeting bivalency de-represses Indian Hedgehog and inhibits self-renewal of colorectal cancer-initiating cells (PMID: 30926792) | 21 |
| 33 | 5 μ M | No | None | EZH2 inhibits autophagic cell death of aortic vascular smooth muscle cells to affect aortic dissection (PMID: 29416002) | 43 |
| 34 | 5 μ M | No | GSK126 (1.25-5 μ M) | Akt inhibition synergizes with polycomb repressive complex 2 inhibition in the treatment of multiple myeloma (PMID: 31571328) | 11 |
| 35 | 5 μ M | No | GSK126 (5 μ M) | Dual inhibition of EZH2 and EZH1 sensitizes PRC2-dependent tumors to proteasome inhibition (PMID: 28490465) | 45 |
| 36 | 5 μ M | No | None | Multicellular tumor spheroids combined with mass spectrometric histone analysis to evaluate epigenetic drugs (PMID: 28194967) | 24 |
| 37 | 5 μ M | No | None | Dual inhibition of H3K9me2 and H3K27me3 promotes tumor cell senescence without triggering the secretion of SASP (PMID: 35409271) | 1 |
| 38 | 5 μ M | No | GSK126 (5 μ M), | Sustained expression of FMR1 mRNA from reactivated fragile X syndrome alleles after treatment with small | 25 |

| | | | | | |
|---|-----------------|----------|-----------------------------------|--|----|
| | | | GSK343 (5 μ M) | molecules that prevent trimethylation of H3K27 (PMID: 27378697) | |
| 39 | 5 μ M | No | None | Engineered multivalent sensors to detect coexisting histone modifications in living stem cells (PMID: 29174541) | 26 |
| 40 | 5 μ M | Yes | None | Combinatorial anticancer drug screen identifies off-target effects of epigenetic chemical probes (PMID: 36084291) | 0 |
| 41 | 5 μ M | No | None | BRD4770 functions as a novel ferroptosis inhibitor to protect against aortic dissection (PMID: 35149187) | 11 |
| 42 | 10 μ M | No | None | Site-directed targeting of transcriptional activation-associated proteins to repressed chromatin restores CRISPR activity (PMID: 31967103) | 3 |
| 43 | 10 μ M | No | GSK126, GSK503, EPZ6438 (unclear) | EZH2-mediated H3K27me3 is a predictive biomarker and therapeutic target in uveal melanoma (PMID: 36276954) | 0 |
| 44 | 5 - 10 μ M | No | GSK343 (2.5 -10 μ M) | Enhanced calcium signal induces NK cell degranulation but inhibits its cytotoxic activity (PMID: 34911773) | 1 |
| 45 | 10 - 30 μ M | No | GSK343 (10 - 30 μ M) | Response and resistance to CDK12 inhibition in aggressive B-cell lymphomas (PMID: 34162179) | 1 |
| 46 | 15 μ M | No | None | MicroRNA-20a suppresses tumor proliferation and metastasis in hepatocellular carcinoma by directly targeting EZH1. (PMID: 34976797) | 4 |
| 47 | 100 μ M | No | None | EZH2 inhibition suppresses bladder cancer cell growth and metastasis via the JAK2/STAT3 signaling pathway (PMID: 31289569) | 21 |
| 48 | Not provided | No | None | EZH2 targeting to improve the sensitivity of acquired radio-resistance bladder cancer cells. (PMID: 34952334) | 3 |
| 49 | Not provided | No | None | SOX8 affects tumoral SPARC expression by regulating EZH2 to attenuate effectiveness of albumin-bound paclitaxel in PDAC (PMID: 35173526) | 1 |
| Compliance | | | | | |
| Fully: 18 (37%)^a | | 6 (12%) | 23 (47%) | | |
| Partially: 14 (29%)^b | | | | | |
| Non-Compliance | | | | | |
| 17 (35%) (total is 101% due to rounding up) | | 43 (88%) | 26 (53%) | | |

a Probe's concentration below the recommended in-cell maximum in all figures.

b Probe's concentration below the recommended in-cell maximum in some, but not all figures.

Supplementary Note 2. Citations for UNC1999 publications included in the systematic review.
Citations for 49 publications using UNC1999: 909

Citations for 32 publications with a compliant UNC1999 concentration: 689

Citations for 17 publications with a non-compliant UNC1999 concentration: 220

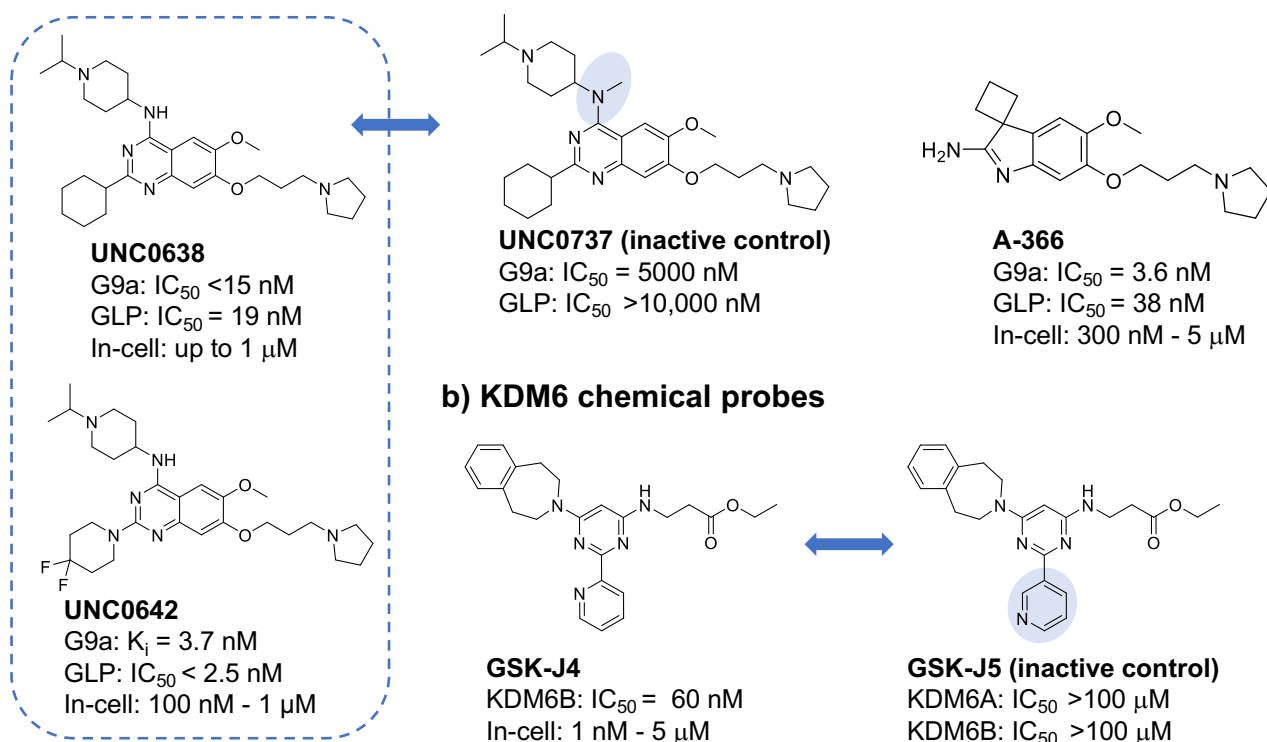
Citations for 6 publications using inactive compound UNC2400: 259

Citations for 43 publications not using inactive compound UNC2400: 650

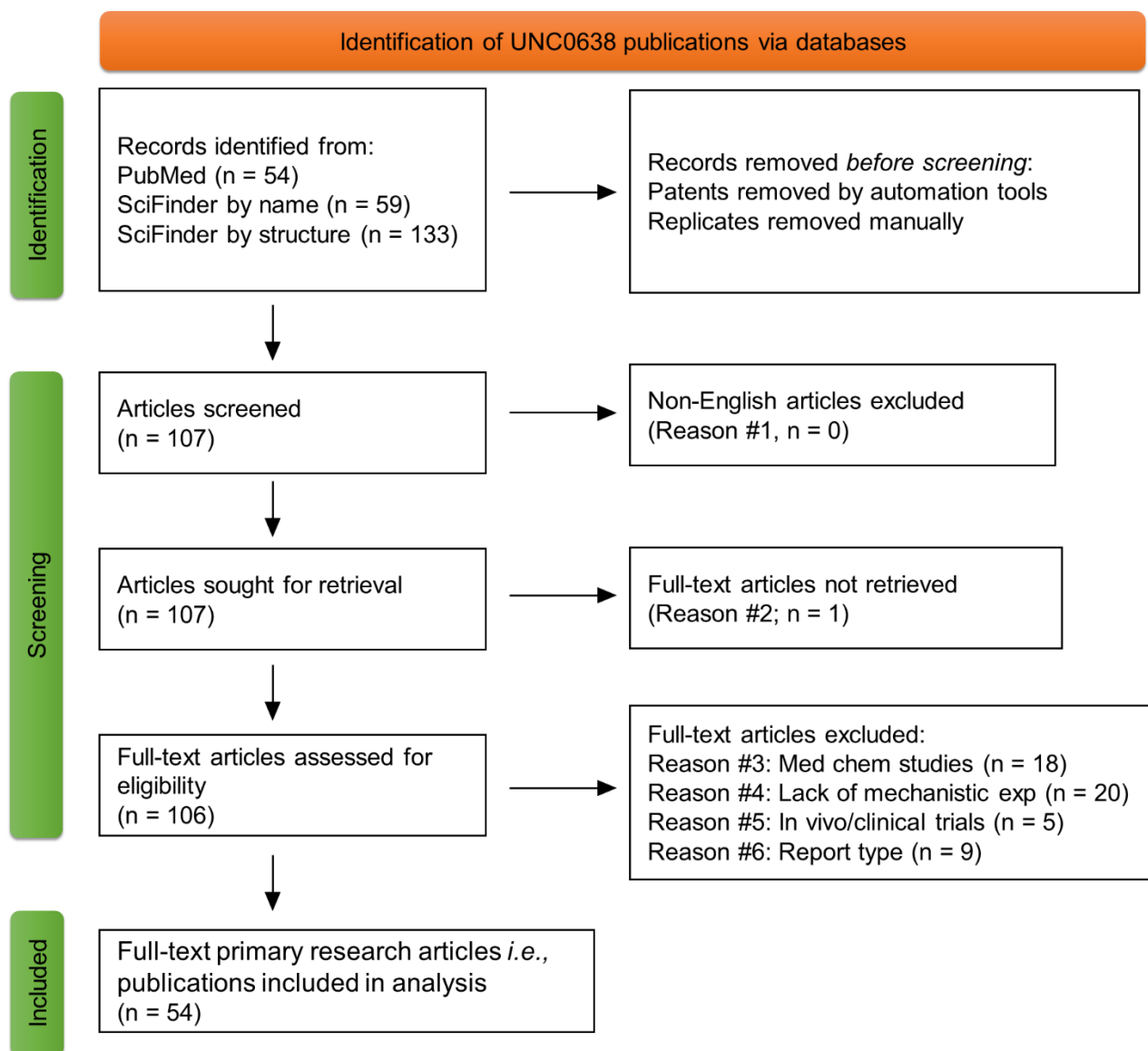
Citations for 23 publications using orthogonal inhibitors: 582

Citations for 26 publications not using orthogonal inhibitors: 327

a) G9a/GLP chemical probes



Supplementary Figure 3. Structures, biochemical potency (K_i/IC_{50}) and recommended in-cell concentrations of **a)** G9a/GLP and **b)** KDM6 chemical probes as listed on the Chemical Probes Portal (www.chemicalprobes.org). Dashed lines group structurally related chemical probes that should not be used together as orthogonal tools (*e.g.*, UNC0642 can be used as an orthogonal chemical probe with A-366, but not with UNC0638). Bidirectional arrows link target-inactive analogues and shaded fields highlight the structural changes leading to decreased G9a/GLP or KDM6 engagement.



Supplementary Figure 4. PRISMA flow diagram summarising identification of publications using the G9a/GLP chemical probe UNC0638.

Supplementary Table 3. List of excluded articles using the G9a/GLP probe UNC0638.

| Title (PMID) | Reason for exclusion |
|--|---|
| 1 The discovery of novel histone lysine methyltransferase G9a inhibitors (part 1): molecular design based on a series of substituted 2,4-diamino-7-aminoalkoxyquinazoline by molecular-docking-guided 3D quantitative structure-activity relationship studies (PMID: 24151879) | 2) No access |
| 2 A chemical probe selectively inhibits G9a and GLP methyltransferase activity in cells (PMID: 21743462) | 3) Discovery of UNC0638 |
| 3 Optimization of cellular activity of G9a inhibitors 7-aminoalkoxy-quinazolines (PMID: 217807990) | 3) Medicinal chemistry |
| 4 Structure-activity relationship studies of G9a-like protein (GLP) inhibitors (PMID: 28662962) | 3) Medicinal chemistry |
| 5 Properly substituted analogues of BIX-01294 lose inhibition of G9a histone methyltransferase and gain selective anti-DNA methyltransferase 3A activity (PMID: 24810902) | 3) Medicinal chemistry |
| 6 7-Aminoalkoxy-quinazolines from epigenetic focused libraries are potent and selective inhibitors of DNA methyltransferase 1 (PMID: 35566242) | 3) Medicinal chemistry |
| 7 Discovery of a potent and selective fragment-like inhibitor of methyllysine reader protein Spindlin 1 (SPIN1) (PMID: 31260300) | 3) Medicinal chemistry |
| 8 Discovery of the first-in-class G9a/GLP covalent inhibitors (PMID: 3573668) | 3) Medicinal chemistry |
| 9 Discovery of a potent histone deacetylase (HDAC) 3/6 selective dual inhibitor (PMID: 31627059) | 3) Medicinal chemistry |
| 10 Identification of novel quinazoline derivatives as potent antiplasmodial agents (PMID: 30366254) | 3) Medicinal chemistry |
| 11 Discovery of Reversible DNA Methyltransferase and Lysine Methyltransferase G9a Inhibitors with Antitumoral in Vivo Efficacy (PMID: 29953809) | 3) Medicinal chemistry |
| 12 Discovery of a novel chemotype of histone lysine methyltransferase EHMT1/2 (GLP/G9a) inhibitors: Rational design, synthesis, biological Evaluation, and co-crystal Structure (PMID:30753076) | 3) Medicinal chemistry |
| 13 Discovery of potent and selective inhibitors for G9a-like protein (GLP) lysine methyltransferase (PMID: 28135087) | 3) Medicinal chemistry |
| 14 Mimicking H3 substrate arginine in the design of G9a lysine methyltransferase inhibitors for cancer therapy: A computational study for structure-based drug design (PMID: 33718701) | 3) Medicinal chemistry |
| 15 Novel SAR for quinazoline inhibitors of EHMT1 and EHMT2 (PMID: 31350126) | 3) Medicinal chemistry |
| 16 Discovery, design and synthesis of 6H-anthra[1,9-cd]isoxazol-6-one scaffold as G9a inhibitor through a combination of shape-based virtual screening and structure-based molecular modification (PMID: 27720557) | 3) Medicinal chemistry |
| 17 A chemical tool for in vitro and in vivo precipitation of lysine methyltransferase G9a (PMID: 24443078) | 3) Medicinal chemistry |
| 18 Discovery of an in vivo chemical probe of the lysine methyltransferases G9a and GLP (PMID: 24102134) | 3) Medicinal chemistry |
| 19 Selective, small-molecule co-factor binding site inhibition of a Su(var)3-9, enhancer of Zeste, Trithorax domain containing lysine methyltransferase (PMID: 31415173) | 3) Medicinal chemistry |
| 20 An inhibitor screen identifies histone-modifying enzymes as mediators of polymer-mediated transgene expression from plasmid DNA (PMID: 29964136) | 4) No mechanistic exp. - dose-response screen only |
| 21 Identification of a novel autophagy-related prognostic signature and small molecule drugs for glioblastoma by bioinformatics (PMID: 35550147) | 4) No mechanistic exp. - Bioinformatic study |
| 22 Identification of novel quinoline inhibitor for EHMT2/G9a through virtual screening (PMID: 31756401) | 4) No mechanistic exp. - Computational study |
| 23 Strategy to target the substrate binding site of SET domain protein methyltransferases (PMID: 23410263) | 4) No mechanistic exp. - Computational study |
| 24 Detailed exploration around 4-aminoquinolines chemical space to navigate the lysine methyltransferase G9a and DNA methyltransferase biological spaces (PMID: 29890830) | 4) No mechanistic exp. - Computational study |
| 25 Efficient rescue of a newly classified Ebinur lake orthobunyavirus with GFP reporter and its application in rapid antiviral screening (PMID: 36150523) | 4) No mechanistic exp. - Dose response anti-viral screen only |

| | | |
|----|--|--|
| 26 | Bioluminescent cell-based NAD(P)/NAD(P)H assays for rapid dinucleotide measurement and inhibitor screening (PMID: 25506801) | 4) No mechanistic exp. - Dose-response screen only |
| 27 | TR-FRET cellular assays for interrogating posttranslational modifications of histone H3 (PMID: 21972037) | 4) No mechanistic exp. - Methodology study |
| 28 | Identification of six hub genes and analysis of their correlation with drug sensitivity in acute myeloid leukemia through bioinformatics (PMID: 35116245) | 4) No mechanistic exp. - no cell-based experiments |
| 29 | High-throughput brain activity mapping and machine learning as a foundation for systems Neuropharmacology (PMID: 30510233) | 4) No mechanistic exp. - no cell-based experiments |
| 30 | Polymyxins and quinazolines are LSD1/KDM1A inhibitors with unusual structural features (PMID: 27626075) | 4) No mechanistic exp. - no cell-based experiments |
| 31 | Phenotypic-screening generates active novel fetal globin-inducers that downregulate Bcl11a in a monkey model (PMID: 31751536) | 4) No mechanistic exp. - no cell-based experiments |
| 32 | Hypoxia induces HIF1 α -dependent epigenetic vulnerability in triple negative breast cancer to confer immune effector dysfunction and resistance to anti-PD-1 immunotherapy (PMID: 3580558) | 4) Probed not used |
| 33 | Visualizing nuclear RNAi activity in single living human cells (PMID: 29073029) | 4) Probed not used |
| 34 | Treatment of donor cells with recombinant KDM4D protein improves preimplantation development of cloned ovine embryos (PMID: 29766333) | 4) Probed not used |
| 35 | HIV signaling through CD4 and CCR5 activates Rho family GTPases that are required for optimal infection of primary CD4+ T cells (PMID: 28114951) | 4) No mechanistic exp. - dose-response viability |
| 36 | Genetically encoded molecular biosensors to image histone methylation in living animals (PMID: 25506787) | 4) No mechanistic exp. - Probe used for validating real-time methylation |
| 37 | Histone methyltransferase G9a inhibitor-loaded redox-responsive nanoparticles for pancreatic ductal adenocarcinoma therapy (PMID: 32729861) | 4) No mechanistic exp. - Nanoparticle delivery study |
| 38 | JAK1/2 and BCL2 inhibitors synergize to counteract bone marrow stromal cell-induced protection of AML (PMID: 28619982) | 4) No mechanistic exp. - probe used only in screen |
| 39 | Discovery of novel drug sensitivities in T-PLL by high-throughput ex vivo drug testing and mutation profiling (PMID: 28804127) | 4) No mechanistic exp. - probe used only in screen |
| 40 | An augmentation in histone demethylation at lysine nine residues elicits vision impairment following traumatic brain injury (PMID: 30790655) | 5) In vivo study |
| 41 | Inhibition of histone methyltransferase G9a attenuates liver cancer initiation by sensitizing DNA-damaged hepatocytes to p53-induced apoptosis (PMID: 33468997) | 5) In vivo study |
| 42 | Threshold inhibition of methyltransferase G9a/Glp exacerbates neuropathic hypersensitivity through mediating GRIN2B methylation (No PMID; DOI: 10.15354/si.19.ar910) | 5) In vivo study |
| 43 | Effects of environmental conditions on nephron number: 13emethyla maternal disease and epigenetic regulation in renal development (PMID: 33923831) | 5) Ex vivo study |
| 44 | Reduced and highly diverse peripheral HIV-1 reservoir in virally suppressed patients infected with non-B HIV-1 strains in Uganda (PMID: 35033105) | 5) Study in human cohort |
| 45 | Chemical probes for the lysine methyltransferases G9a and EZH2 (No PMID, DOI or ISSN available, AN: 2015:1328166) | 6) Conference proceeding |
| 46 | Stereoselective formation of gliotoxin isomers (No PMID, DOI or ISSN available, AN: 2014:379481) | 6) Conference proceeding |
| 47 | Discovery of a first-in-class G9a/GLP covalent inhibitor (No PMID, DOI or ISSN available, AN: 2022:3010552) | 6) Conference proceedings |
| 48 | Discovery of a potent and selective fragment-like inhibitor of SPIN1 (No PMID, DOI or ISSN available, AN: 2019:1501424) | 6) Conference proceedings |
| 49 | A chemical probe selectively inhibits G9a and GLP methyltransferase activity in cells [Erratum to document cited in CA155:320969] (No PMID available, DOI: 10.1038/nchembio0911-648c) | 6) Erratum |
| 50 | Small molecule inhibitors of G9a reactivate the maternal PWS genes in Prader-Willi-Syndrome patient derived neural stem cells and differentiated neurons (No PMID available, DOI: 10.1101/640938) | 6) Preprint |
| 51 | Chromatin looping as a target for altering erythroid gene expression (PMID: 26918894) | 6) Review |
| 52 | Chemical probes: sharpen your epigenetic tools (PMID: 21769094) | 6) Review |
| 53 | Regulation, genomics, and clinical characteristics of cuproptosis regulators in pancreatic cancer (PMID: 36387247) | 6) Review |

Supplementary Table 4. Overview of eligible publications using the G9a/GLP probe UNC0638 and compliance (in blue) with recommendations to use UNC0638 up to 250 nM (ref³²) and validate results with the inactive control compound UNC0737 and orthogonal G9a/GLP inhibitors. Citations are sourced from SciFinder (January 2023).

| | UNC0638 | UNC0737 | Orthogonal inhibitors | Title (PMID) | Cites |
|----|---------------------------------------|---------|--|--|-------|
| 1 | 1 nM - 1 μM Most assays: 100 nM | No | None | Effects of the histone methyltransferase inhibitor UNC0638 on histone H3K9 dimethylation of cultured ovine somatic cells and development of resulting early cloned embryos (PMID: 24467723) | 11 |
| 2 | 10 nM & 5 μM | No | None | α-Synuclein enhances histone H3 lysine-9 dimethylation and H3K9me2-dependent transcriptional responses (PMID: 27808254) | 35 |
| 3 | 50 nM - 250 nM | No | BIX01294 (14 nM - 10 μM) | EHMT1 and EHMT2 inhibition induces fetal hemoglobin expression (PMID: 26320100) | 69 |
| 4 | 100 nM | No | BIX01294 (5 μM) | Multiple histone lysine methyltransferases are required for the establishment and maintenance of HIV-1 latency (PMID: 28246360) | 77 |
| 5 | 100 nM - 250 nM | No | None | UNC0638 induces high levels of fetal hemoglobin expression in β-thalassemia/HbE erythroid progenitor cells (PMID: 32567028) | 7 |
| 6 | 100 nM, 200 nM & 3 μM | No | None | Interaction of BARD1 and HP1 is required for BRCA1 retention at sites of DNA damage (PMID: 25634209) | 70 |
| 7 | 0.1 - 0.5 μM | No | BIX01294 (0.1 - 1 μM) | Targeting p53 and histone methyltransferases restores exhausted CD8+ T cells in HCV infection (PMID: 32001678) | 38 |
| 8 | 0.12 μM | No | None | Estimating intraclonal heterogeneity and subpopulation changes from bulk expression profiles in CMap (PMID: 35688486) | 1 |
| 9 | 125 nM | No | None | HRI depletion cooperates with pharmacologic inducers to elevate fetal hemoglobin and reduce sickle cell formation (PMID: 32956454) | 10 |
| 10 | 150 nM | No | BIX01294 (500 nM) | Epigenetic regulation by G9a/GLP complex ameliorates amyloid-beta 1-42 induced deficits in long-term plasticity and synaptic tagging/capture in hippocampal pyramidal neurons (PMID: 28665013) | 25 |
| 11 | 150 nM | No | BIX01294 (500 nM) | Inhibition of G9a/GLP complex promotes long-term potentiation and synaptic tagging/capture in hippocampal CA1 pyramidal neurons (PMID: 27252354) | 16 |
| 12 | 250 nM | No | None | Catalytic inhibition of H3K9me2 writers disturbs epigenetic marks during bovine nuclear reprogramming (PMID: 32661262) | 3 |
| 13 | 250 nM | No | None | Dicer promotes genome stability via the bromodomain transcriptional co-activator BRD4 (PMID: 35194019) | 2 |
| 14 | 250 nM - 750 nM | No | None | SETDB1 mediated histone H3 lysine 9 methylation suppresses MLL-fusion target expression and leukemic transformation (PMID: 33054052) | 11 |
| 15 | 250 nM - 1 μM | No | UNC2249 (not provided) | A chromatin activity based chemoproteomic approach reveals a transcriptional repressome for gene-specific silencing (PMID: 25502336) | 20 |
| 16 | 250 nM - 4 μM | No | UNC0642 (4 μM) BIX01294 (10 μM) | Targeting the histone methyltransferase G9a activates imprinted genes and improves survival of a mouse model of Prader-Willi syndrome (PMID: 28024084) | 67 |
| 17 | 0.3 - 1 μM | No | None | Report and application of a tool compound data set (PMID: 29035535) | 5 |
| 18 | 300 nM - 20 μM | No | None | Targeting histone methyltransferase G9a inhibits growth and Wnt signaling pathway by epigenetically regulating HP1α and APC2 gene expression in non-small cell lung cancer (PMID: 30348169) | 42 |

| | | | | | |
|----|--------------------|-----|--|---|-----|
| 19 | 0.375 - 3 μ M | No | UNC0642 (2.5 - 10 μ M), BIX-01294 (1 - 2 μ M), A-366 (20 - 40 μ M) | Targeting euchromatic histone lysine methyltransferases sensitizes colorectal cancer to histone deacetylase inhibitors (PMID: 35666536) | 1 |
| 20 | 500 nM | No | None | Reactivation of endogenous retroviral elements via treatment with DNMT- and HDAC-inhibitors (PMID: 29633898) | 32 |
| 21 | 500 nM - 1 μ M | No | None | UNC0638, a G9a inhibitor, suppresses epithelial-mesenchymal transition-mediated cellular migration and invasion in triple negative breast cancer (PMID: 29207160) | 21 |
| 22 | 500 nM - 1 μ M | No | None | The methyltransferase G9a regulates HoxA9-dependent transcription in AML (PMID: 24532712) | 101 |
| 23 | 500 nM - 2 μ M | Yes | None | G9a/GLP-dependent histone H3K9me2 patterning during human hematopoietic stem cell lineage commitment (PMID: 23105005) | 98 |
| 24 | 0.5 - 2 μ M | No | BIX01294 (0.5 - 2 μ M) | A disproportionate impact of G9a methyltransferase deficiency on the X chromosome (PMID: 34168040) | 2 |
| 25 | 0.5 - 8 μ M | No | BIX01294 (0.5 - 4 μ M) | Degron protease blockade sensor to image epigenetic histone protein methylation in cells and living animals (PMID: 25489787) | 7 |
| 26 | 1 μ M | No | None | The combination of G9a histone methyltransferase inhibitors with erythropoietin protects heart against damage from acute myocardial infarction (PMID: 32774698) | 8 |
| 27 | 1 μ M | No | None | Transcriptional selectivity of epigenetic therapy in cancer (PMID: 27879268) | 39 |
| 28 | 1 μ M | No | A-366 (10 μ M) | G9a inhibition potentiates the anti-tumour activity of DNA double-strand break inducing agents by impairing DNA repair independent of p53 status (PMID: 27431310) | 28 |
| 29 | 1 μ M | No | UNC0642 (1 μ M) | Dual EZH2 and G9a inhibition suppresses multiple myeloma cell proliferation by regulating the interferon signal and IRF4-MYC axis (PMID: 33436557) | 23 |
| 30 | 1 μ M | No | UNC0642; A-366 (1 μ M), UNC0648 (1 - 10 μ M) | Dual G9A/EZH2 inhibition stimulates antitumor immune response in ovarian high-grade serous carcinoma (PMID: 35131874) | 6 |
| 31 | 1 μ M | No | None | Inhibition of G9a methyltransferase stimulates fetal hemoglobin production by facilitating LCR/ γ -globin looping (PMID: 25979948) | 54 |
| 32 | 1 - 10 μ M | No | UNC0631, BIX01294, UNC0642 (1 - 10 μ M) | Activity comparison of epigenetic modulators against the Hemoprotozoan parasites Babesia divergens and Plasmodium falciparum (PMID: 33599488) | 6 |
| 33 | 1.25 - 5 μ M | No | BIX01294 (0.5 - 5 μ M) | G9a/GLP targeting in MM promotes autophagy-associated apoptosis and boosts proteasome inhibitor-mediated cell death (PMID: 33938943) | 7 |
| 34 | 1.5 - 20 μ M | No | None | Histone methyltransferase G9a promotes the development of renal cancer through epigenetic silencing of tumor suppressor gene SPINK5 (PMID: 34336110) | 6 |
| 35 | 2 μ M | No | BIX01294 (2 - 10 μ M) | Inhibition of H3K9 methyltransferases G9a/GLP prevents ototoxicity and ongoing hair cell death (PMID: 23429292) | 33 |
| 36 | 2 μ M | No | BIX01294 (1 - 5 μ M) | Epigenetic inhibitors target multiple stages of Plasmodium falciparum parasites (PMID: 32047203) | 31 |

| | | | | | |
|-----------------------------------|-----------------|--------|---|---|----|
| 37 | 2 - 4 μ M | No | BIX01294 (2 - 5 μM) | HeLa TI cell-based assay as a new approach to screen for chemicals able to reactivate the expression of epigenetically silenced genes (PMID: 34115770) | 3 |
| 38 | 2 - 20 μ M | No | None | Histone deacetylase inhibitors containing a benzamide functional group and a pyridyl cap are preferentially effective human immunodeficiency virus-1 latency-reversing agents in primary resting CD4 T cells (PMID: 28113052) | 14 |
| 39 | 2.5 - 5 μ M | No | None | Deregulation of Wnt/ β -catenin signaling through genetic or epigenetic alterations in human neuroendocrine tumors (PMID: 23354304) | 60 |
| 40 | 2.5 - 5 μ M | No | None | G9a promotes invasion and metastasis of non-small cell lung cancer through enhancing focal adhesion kinase activation via NF- κ B signaling pathway (PMID: 33298547) | 11 |
| 41 | 3 μ M | No | None | Class I histone deacetylase inhibitors inhibit the retention of BRCA1 and 53BP1 at the site of DNA damage (PMID: 26053117) | 23 |
| 42 | 4 μ M | No | None | Epigenetic therapy combination of UNC0638 and CI-994 suppresses breast cancer via epigenetic remodeling of BIRC5 and GADD45A (PMID: 34798471) | 4 |
| 43 | 5 μ M | No | BIX01294 (0.5 - 2.5 μM) | Inhibition of euchromatic histone methyltransferase 1 and 2 sensitizes chronic myeloid leukemia cells to interferon treatment (PMID: 25079219) | 8 |
| 44 | 5 μ M | No | None | Inhibition of EHMT2 induces a robust antiviral response against foot-and-mouth disease and vesicular stomatitis virus infections in bovine cells (PMID: 26418342) | 7 |
| 45 | 5 μ M | No | None | Histone methyltransferase inhibition has a cytotoxic impact on transformed mast cells: implications for mastocytosis (PMID: 32366397) | 1 |
| 46 | 5 μ M | No | None | M33 condenses chromatin through nuclear body formation and methylation of both histone H3 lysine 9 and lysine 27 (PMID: 34274396) | 0 |
| 47 | 5 - 10 μ M | No | None | Targeting EHMT2 reverses EGFR-TKI resistance in NSCLC by epigenetically regulating the PTEN/AKT signaling pathway (PMID: 29374157) | 41 |
| 48 | 5 - 10 μ M | No | UNC0642 (unclear) BIX01294 (3 μM) | Increased efficacy of histone methyltransferase G9a inhibitors against MYCN-amplified neuroblastoma (PMID: 32537432) | 12 |
| 49 | 8 - 12 μ M | No | None | Generation of induced pluripotent stem cells from a female patient with a Xq27.3-q28 deletion to establish disease models and identify therapies (PMID: 32608992) | 3 |
| 50 | 10 μ M | No | None | Deletion of histone methyltransferase G9a suppresses mutant Kras-driven pancreatic carcinogenesis (PMID: 33099471) | 7 |
| 51 | 20 μ M | No | None | The SUV39H1 inhibitor chaetocin induces differentiation and shows synergistic cytotoxicity with other epigenetic drugs in acute myeloid leukemia cells (PMID: 25978433) | 57 |
| 52 | 5 - 640 μ g | No | BIX01294 (0.625 - 80.0 μg) | Threshold effect of G9a/Glp on peripheral nerve injury-induced hypersensitivity (PMID: 28814147) | 4 |
| 53 | Not provided | No | UNC0642, UNC0631 (not provided) | An EHMT2/NFYA-ALDH2 signaling axis modulates the RAF pathway to regulate paclitaxel resistance in lung cancer (PMID: 35477569) | 1 |
| 54 | Not provided | No | UNC0224, UNC0321 (not provided) | Engineering lineage potency and plasticity of stem cells using epigenetic molecules (PMID: 30389989) | 5 |
| Compliance | | | | | |
| Fully: 9 (17%)^a | | 1 (2%) | 23 (43%) | | |

| | | | | |
|---------------------------------------|----------|----------|--|--|
| Partially: 7 (13%)^b | | | | |
| Non-Compliance | | | | |
| 38 (70%) | 53 (98%) | 31 (57%) | | |

a Probe's concentration below the recommended in-cell maximum in all figures.

b Probe's concentration below the recommended in-cell maximum in some, but not all figures.

Supplementary Note 3. Citations for UNC0638 publications included in the systematic review.

Citations for 54 publications using UNC0638: 1,273

Citations for 16 publications with a compliant UN0638 concentration: 462

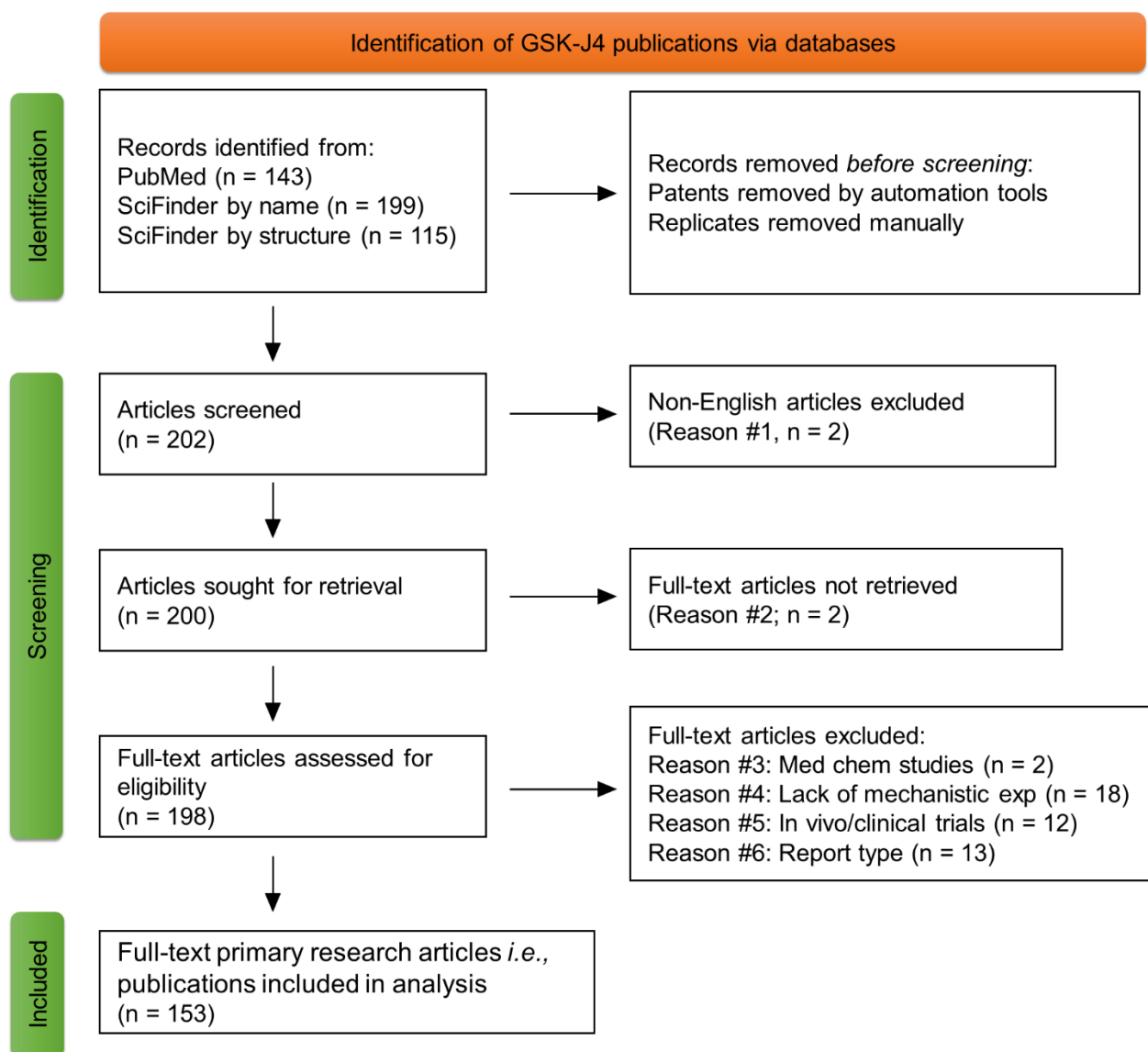
Citations for 38 publications with a non-compliant UNC0638 concentration: 811

Citations for 1 publication using inactive compound UNC0737: 98

Citations for 53 publications not using inactive compound UNC0737: 1,175

Citations for 23 publications using orthogonal G9a/GLP inhibitors: 489

Citations for 31 publications not using orthogonal G9a/GLP inhibitors: 784



Supplementary Figure 5. PRISMA flow diagram summarising identification of publications using the KDM6 chemical probe GSK-J4.

Supplementary Table 5. List of excluded articles using the KDM6 probe GSK-J4.

| | Title (PMID) | Reason for exclusion |
|----|--|--|
| 1 | Mechanism of alendronate sodium combined with LPS induced inflammatory responses in Macrophages (No PMID; DOI: 10.13241/j.cnki.pmb.2020.09.003) | 1) Non-English publication |
| 2 | Bioinformatics analysis of the clinical expression of APOC1 in papillary thyroid carcinoma (No PMID or DOI; ISSN: 1007-1520) | 1) Non-English publication |
| 3 | Forskolin potentiates the effects of GSKJ4 in human acute myeloid leukemia cells through protein kinase A pathway (No PMID or DOI; ISSN: 1105-4999) | 2) No access |
| 4 | Pharmaceutical interference of the EWS-FLI1-driven transcriptome by cotargeting H3K27ac and RNA polymerase activity in ewing sarcoma. (PMID: 34315769) | 2) No access |
| 5 | A selective jumonji H3K27 demethylase inhibitor modulates the proinflammatory macrophage response. (PMID: 22842901) | 3) GSK-J4 discovery |
| 6 | Design and discovery of new pyrimidine coupled nitrogen aromatic rings as chelating groups of JMJD3 inhibitors. (PMID: 26776360) | 3) Medicinal chemistry |
| 7 | The BRD9/7 inhibitor TP-472 blocks melanoma tumor growth by suppressing ECM-mediated oncogenic signaling and inducing apoptosis (PMID: 34771678) | 4) No mechanistic exp. |
| 8 | Identification of disulfiram as a potential antifungal drug by screening small molecular libraries (PMID: 33358402) | 4) No mechanistic exp.- Antifungal assays |
| 9 | The N6-methyladenosine-related gene BIRC5 as a prognostic biomarker correlated with cell migration and immune cell infiltrates in low grade glioma (PMID: 35309512) | 4) No mechanistic exp. - Bioinformatics study |
| 10 | Analysis of characteristic genes and ceRNA regulation mechanism of endometriosis based on full transcriptional sequencing (PMID: 35938015) | 4) No mechanistic exp. - Bioinformatics study |
| 11 | Effect of histone demethylase Jmjd3 on odontogenic differentiation of human dental pulp cells (PMID: 32208897) | 4) No GSK-J4 data |
| 12 | Differential kinase activity of ACVR1 G328V and R206H mutations with implications to possible TβRI cross-talk in diffuse intrinsic pontine glioma. (PMID: 32273545) | 4) No mechanistic exp. |
| 13 | HDAC inhibition enhances the in vivo efficacy of MEK inhibitor therapy in Uveal melanoma (PMID: 31227503) | 4) No mechanistic exp. – viability screen |
| 14 | Functionally defined therapeutic targets in diffuse intrinsic pontine glioma (PMID: 25939062) | 4) No mechanistic exp. |
| 15 | In silico identification of small molecules as new Cdc25 inhibitors through the correlation between chemosensitivity and protein expression pattern (PMID: 33918281) | 4) No mechanistic exp. |
| 16 | Discovery of novel drug sensitivities in T-PLL by high-throughput ex vivo drug testing and mutation profiling (PMID: 28804127) | 4) No GSK-J4 data |
| 17 | Mechanical stretch aggravates vascular smooth muscle cell apoptosis and vascular remodeling by downregulating EZH2 (PMID: 35985452) | 4) GSK-J4 not used in-cells |
| 18 | The memory of environmental chemical exposure in <i>C. elegans</i> is dependent on the jumonji demethylases <i>jmjd-2</i> and <i>jmjd-3/utx-1</i> (PMID: 29791850) | 4) No mechanistic exp. |
| 19 | Epigenetic reprogramming of H3K27me3 and DNA methylation during leaf-to-callus transition in peach (PMID: 35937864) | 4) No mechanistic exp. |
| 20 | Histone lysine demethylase inhibition reprograms prostate cancer metabolism and mechanics (PMID: 35944897) | 4) No mechanistic exp. |
| 21 | Systematic chemical and molecular profiling of MLL-rearranged infant acute lymphoblastic leukemia reveals efficacy of romidepsin (PMID: 27443263) | 4) No mechanistic exp. |
| 22 | Regulatory network analysis reveals the oncogenesis roles of feed-forward loops and therapeutic target in T-cell acute lymphoblastic leukemia (PMID: 30646895) | 4) No mechanistic exp. - Analytical research study |
| 23 | HIV signaling through CD4 and CCR5 activates Rho family GTPases that are required for optimal infection of primary CD4+ T cells (PMID: 28114951) | 4) No mechanistic exp. |
| 24 | Activity comparison of epigenetic Modulators against the Hemoprotozoan Parasites <i>Babesia divergens</i> and <i>Plasmodium falciparum</i> (PMID: 33599488) | 4) No mechanistic exp. |
| 25 | The histone demethylase KDM6B in the medial prefrontal cortex epigenetically regulates cocaine reward memory (PMID: 30165076) | 5) In vivo study |
| 26 | Activated Braf induces esophageal dilation and gastric epithelial hyperplasia in mice (PMID: 28973166) | 5) In vivo study |

| | | |
|----|--|-------------------------|
| 27 | Histone modification of pain-related gene expression in spinal cord neurons under a persistent postsurgical pain-like state by electrocautery (PMID: 34544461) | 5) In vivo study |
| 28 | Jmjd3 is involved in the susceptibility to depression induced by maternal separation via enhancing the neuroinflammation in the prefrontal cortex and hippocampus of male rats (PMID: 32084453) | 5) In vivo study |
| 29 | Upregulation of KDM6B contributes to lipopolysaccharide-induced anxiety-like behavior via modulation of VGLL4 in mice (PMID: 33865886) | 5) In vivo study |
| 30 | New BRAF knock-in mice provide a pathogenetic mechanism of developmental defects and a therapeutic approach in cardio-facio-cutaneous syndrome (PMID: 25035421) | 5) In vivo study |
| 31 | KDM6B epigenetically regulated-interleukin-6 expression in the dorsal root ganglia and spinal dorsal horn contributes to the development and maintenance of neuropathic pain following peripheral nerve injury in male rats (PMID: 34464689) | 5) In vivo study |
| 32 | IL-4 alleviates ischaemia-reperfusion injury by inducing kupffer cells M2 polarization via STAT6-JMJD3 pathway after rat liver transplantation. (PMID: 32258110) | 5) In vivo study |
| 33 | Histone demethylase UTX counteracts glucocorticoid deregulation of osteogenesis by modulating histone-dependent and -independent pathways (PMID: 28130569) | 5) In vivo study |
| 34 | Effects of GSK-J4 on JMJD3 Histone Demethylase in Mouse Prostate Cancer Xenografts (PMID: 35430567) | 5) In vivo study |
| 35 | Downregulation of interleukin-1 beta via Jmjd3 inhibition improves post-myocardial infarction depression (PMID: 35800354) | 5) In vivo study |
| 36 | Novel pharmacological inhibition of JMJD3 improves necrotizing enterocolitis by attenuating the inflammatory response and ameliorating intestinal injury (PMID: 35803318) | 5) In vivo study |
| 37 | An epigenetic therapy for diffuse intrinsic pontine gliomas. (PMID: 25473916) | 6) Comment |
| 38 | Inhibition of demethylases by GSK-J1/J4 (PMID: 25279926) | 6) Comment |
| 39 | Inhibition of demethylases by GSK-J1/J4 (PMID: 25279927) | 6) Comment reply |
| 40 | Functionally defined therapeutic targets in diffuse intrinsic pontine glioma [Erratum to document cited in CA163:294035] (PMID: 26151328) | 6) Erratum |
| 41 | Role of JMJD3 demethylase and its inhibitor GSK-J4 in regulation of MGMT, TRA2A, RPS6KA2, and U2AF1 genes in prostate cancer cell lines: (PMID: 32525734) | 6) Letter to the editor |
| 42 | Role of UTX histone demethylase in regulation of MGMT, TRA2A, U2AF1, and RPS6KA2 genes in prostate cancer cell lines (PMID: 33337267) | 6) Letter to the editor |
| 43 | JMJD3 promotes esophageal squamous cell carcinoma pathogenesis through epigenetic regulation of MYC (PMID: 32843613) | 6) Letter to the editor |
| 44 | GSK J4 is a Novel Neuroprotective Compound in Parkinson's Disease Model (No PMID, DOI or ISSN, AN: 2018:1273085) | 6) Dissertation |
| 45 | The role and prospect of JMJD3 in stem cells and cancer. (PMID: 31545292) | 6) Review |
| 46 | Neuroblastoma and histone demethylation. (PMID: 30646895) | 6) Review |
| 47 | Histone methylation: Achilles heel and powerful mediator of periodontal homeostasis (PMID: 32762486) | 6) Review |
| 48 | Structural genomics in drug discovery: an overview (no PMID; DOI: 10.4103/jpp.JPP_117_18) | 6) Review |
| 49 | Therapeutic potential of inhibiting histone 3 lysine 27 demethylases: a review of the literature (PMID: 35915507) | 6) Review |

Supplementary Table 6. Overview of eligible publications using the KDM6 probe GSK-J4 and compliance (in blue) with recommendations to use GSK-J4 up to 5 μ M (<https://www.chemicalprobes.org/gsk-j4?q=GSK-J4>) or up to 10 μ M (<https://www.thesgc.org/chemical-probes/GSKJ1>) and validate results with the inactive control compound GSK-J5. Citations are sourced from SciFinder (January 2023).

| | GSK-J4 | GSK-J5 | Title (PMID) | Cites |
|----|--------------------|--------|--|-------|
| 1 | 10 - 25 nM | No | The histone demethylase inhibitor GSK-J4 limits inflammation through the induction of a tolerogenic phenotype on DCs (PMID: 27528513) | 48 |
| 2 | 25 nM | No | The demethylase inhibitor GSK-J4 limits inflammatory colitis by promoting de novo synthesis of retinoic acid in dendritic cells (PMID: 33446666) | 5 |
| 3 | 50 nM | No | The H3K27me3-demethylase KDM6A is suppressed in breast cancer stem-like cells, and enables the resolution of bivalency during the mesenchymal-epithelial transition (PMID: 29029452) | 39 |
| 4 | 80 nM | No | The histone H3 lysine-27 demethylase Jmjd3 plays a critical role in specific regulation of Th17 cell differentiation (PMID: 25840993) | 68 |
| 5 | 100 nM | No | JMJD3 aids in reprogramming of bone marrow progenitor cells to hepatic phenotype through epigenetic activation of hepatic transcription factors (PMID: 28328977) | 7 |
| 6 | 0.1 - 0.5 μ M | No | Dual G9A/EZH2 inhibition stimulates antitumor immune response in ovarian high-grade serous carcinoma (PMID: 35131874) | 6 |
| 7 | 100 - 750 nM | No | Histone H3 lysine 27 trimethylation acts as an epigenetic barrier in porcine nuclear reprogramming (PMID: 26515777) | 53 |
| 8 | 0.1 - 1 μ M | No | Lysine demethylase inhibition protects pancreatic β cells from apoptosis and improves β -cell function (PMID: 28684291) | 15 |
| 9 | 0.1 - 2.5 μ M | No | KDM6B promotes activation of the oncogenic CDK4/6-pRB-E2F pathway by maintaining enhancer activity in MYCN-amplified neuroblastoma (PMID: 34893606) | 6 |
| 10 | 0.1 - 5 μ M | No | Jumonji domain containing-3 (JMJD3) inhibition attenuates IL-1 β -induced chondrocytes damage in vitro and protects osteoarthritis cartilage in vivo (PMID: 32394143) | 6 |
| 11 | 0.1 - 10 μ M | No | GSK-J4, a specific histone lysine demethylase 6A inhibitor, ameliorates lipotoxicity to cardiomyocytes via preserving H3K27 methylation and reducing ferroptosis (PMID: 35722096) | 0 |
| 12 | 175 nM | Yes | Jumonji inhibitors overcome radioresistance in cancer through changes in h3k4 methylation at double-strand breaks (PMID: 30355483) | 39 |
| 13 | 180 nM - 5 μ M | No | Combined targeting of mutant p53 and Jumonji family histone demethylase augments therapeutic efficacy of radiation in H3K27M DIPG (PMID: 31940975) | 15 |
| 14 | 200 nM | No | The repositioning of epigenetic probes/inhibitors identifies new anti-schistosomal lead compounds and chemotherapeutic targets (PMID: 31730617) | 16 |
| 15 | 250 nM | Yes | Inhibition of H3K27me3 demethylases promotes plasmablast formation (PMID: 34880105) | 0 |
| 16 | 250 - 500 nM | No | Therapeutic effect of a histone demethylase inhibitor in Parkinson's disease (PMID: 33116116) | 15 |
| 17 | 0.25 - 1 μ M | No | Adipocyte-mediated epigenomic instability in human T-ALL cells is cytotoxic and phenocopied by epigenetic-modifying drugs (PMID: 36060800) | 0 |
| 18 | 0.25 - 4 μ M | No | Impact of H3K27 demethylase inhibitor GSKJ4 on NSCLC cells alone and in combination with metformin (PMID: 27793936) | 25 |
| 19 | 0.5 - 1 μ M | No | Targeting of histone demethylases KDM5A and KDM6B inhibits the proliferation of temozolomide-resistant glioblastoma cells (PMID: 31238504) | 16 |
| 20 | 0.5 - 1 μ M | No | SAPCD2 promotes neuroblastoma progression by altering the subcellular distribution of E2F7 (PMID: 35197448) | 1 |
| 21 | 0.5 - 1.8 μ M | No | X-linked histone H3K27 demethylase Kdm6A regulates sexually dimorphic differentiation of hypothalamic neurons (PMID: 34633482) | 4 |

| | | | | |
|----|--------------------|-----|---|----|
| 22 | 0.5 - 1.9 μ M | No | The inhibitors of KDM4 and KDM6 histone lysine demethylases enhance the anti-growth effects of erlotinib and HS-173 in head and neck cancer cells (PMID: 34363938) | 4 |
| 23 | 0.5 - 2 μ M | No | GSKJ4, a selective Jumonji H3K27 demethylase inhibitor, effectively targets ovarian cancer stem cells (PMID: 26637876) | 45 |
| 24 | 0.5 - 2 μ M | No | SMARCA4 deficient tumours are vulnerable to KDM6A/UTX and KDM6B/JMJD3 blockade (PMID: 34262032) | 9 |
| 25 | 0.5 - 5 μ M | Yes | Inhibition of demethylase KDM6B sensitizes diffuse large B-cell lymphoma to chemotherapeutic drugs (PMID: 27742770) | 40 |
| 26 | 0.5 - 10 μ M | No | KDM6B counteracts EZH2-mediated suppression of IDFBP5 to confer resistance to PI3K/AKT inhibitor treatment in breast cancer (PMID: 29925528) | 29 |
| 27 | 500 nM | No | KDM6B overexpression activates innate immune signaling and impairs hematopoiesis in mice (PMID: 30275007) | 20 |
| 28 | 500 nM | No | Epigenetic remodeling through downregulation of polycomb repressive complex 2 mediates chemotherapy resistance in testicular germ cell tumors (PMID:31181810) | 15 |
| 29 | 600 nM - 1 μ M | Yes | Systematic identification of biomarker-driven drug combinations to overcome resistance (PMID: 35332332) | 1 |
| 30 | 1 μ M | No | H19-dependent transcriptional regulation of β 3 and β 4 integrins upon estrogen and hypoxia favors metastatic potential in prostate cancer (PMID: 31426484) | 14 |
| 31 | 1 μ M | No | Morphological screening of mesenchymal mammary tumor organoids to identify drugs that reverse epithelial-mesenchymal transition (PMID: 34253738) | 10 |
| 32 | 1 μ M | No | Cooperation between KDM6B overexpression and TET2 deficiency in the pathogenesis of chronic myelomonocytic leukemia (PMID: 35697791) | 0 |
| 33 | 1 μ M | No | Acquired resistance during adoptive cell therapy by transcriptional silencing of immunogenic antigens (PMID: 31413920) | 10 |
| 34 | 1 μ M | No | KDM6B is an androgen regulated gene and plays oncogenic roles by demethylating H3K27me3 at cyclin D1 promoter in prostate cancer (PMID: 33414463) | 16 |
| 35 | 1 μ M | No | Elevating H3K27me3 level sensitizes colorectal cancer to oxaliplatin (PMID: 31065671) | 30 |
| 36 | 1 μ M | No | Cystathionine- γ -lyase ameliorates the histone demethylase JMJD3-mediated autoimmune response in rheumatoid arthritis (PMID: 29844591) | 27 |
| 37 | 1 μ M | No | Histone H3K27 demethylase negatively controls the memory formation of antigen-stimulated CD8 + T cells (PMID: 30626691) | 10 |
| 38 | 1 μ M | No | Targeted inhibition of histone H3K27 demethylation is effective in high-risk neuroblastoma (PMID: 29769286) | 47 |
| 39 | 1 μ M | Yes | Taxane-platin-resistant lung cancers co-develop hypersensitivity to JumonjiC demethylase inhibitors (PMID: 28538184) | 56 |
| 40 | 1 μ M | No | HDAC8 prevents anthrax lethal toxin-induced cell cycle arrest through silencing PTEN in human monocytic THP-1 cells (PMID: 28509866) | 12 |
| 41 | 1 μ M | No | Histone demethylase JMJD3 downregulation protects against aberrant force-induced osteoarthritis through epigenetic control of NR4A1 (PMID: 35831280) | 0 |
| 42 | 1 - 2 μ M | No | Targeting histone acetylation dynamics and oncogenic transcription by catalytic P300/CBP inhibition (PMID: 34019788) | 22 |
| 43 | 1 - 2 μ M | No | Pharmacological targeting of KDM6A and KDM6B, as a novel therapeutic strategy for treating craniosynostosis in Saethre-Chotzen syndrome (PMID: 33298158) | 6 |
| 44 | 1 - 2.5 μ M | No | Pharmaceutical interference of the EWS-FLI1-driven transcriptome by cotargeting H3K27ac and RNA polymerase activity in ewing sarcoma (PMID: 34315769) | 4 |
| 45 | 1 - 3 μ M | No | HMGN1 plays a significant role in CRLF2 driven Down Syndrome leukemia and provides a potential therapeutic target in this high-risk cohort (PMID: 34857887) | 2 |
| 46 | 1 - 5 μ M | No | KDM6B-mediated histone demethylation of LDHA promotes lung metastasis of osteosarcoma (PMID: 33664867) | 9 |
| 47 | 1 - 5 μ M | No | KDM6B promotes ESCC cell proliferation and metastasis by facilitating C/EBP β transcription (PMID: 34001062) | 9 |

| | | | | |
|----|-----------------------------|-----|---|-----|
| 48 | 1 - 6 μ M | No | Radiosensitization by histone H3 demethylase inhibition in diffuse intrinsic pontine glioma (PMID: 31227500) | 28 |
| 49 | 1 - 10 μ M | No | Heterochromatin protein 1 γ deficiency decreases histone H3K27 methylation in mouse neurosphere neuronal genes (PMID: 31961023) | 1 |
| 50 | 1 - 10 μ M | No | Inhibition of the H3K27 demethylase UTX enhances the epigenetic silencing of HIV proviruses and induces HIV-1 DNA hypermethylation but fails to permanently block HIV reactivation (PMID: 34673825) | 8 |
| 51 | 1 - 10 μ M | No | The KDM inhibitor GSKJ4 triggers CREB downregulation via a protein kinase A and proteasome-dependent mechanism in human acute myeloid leukemia cells (PMID: 32582541) | 8 |
| 52 | 1 - 10 μ M | No | Screening of a neuronal cell model of tau pathology for therapeutic compounds (PMID: 30640040) | 5 |
| 53 | 1 & 10 μ M | No | Low HOX gene expression in PML-RAR α -positive leukemia results from suppressed histone demethylation (PMID: 29224413) | 10 |
| 54 | 1 - 10 μ M | No | An IFN γ /STAT1/JMJD3 axis induces ZEB1 expression and promotes aggressiveness in lung adenocarcinoma (PMID: 33771881) | 2 |
| 55 | 1 - 20 μ M | No | Histone demethylase Jmjd3 regulates the osteogenic differentiation and cytokine expressions of periodontal ligament cells (PMID: 35790358) | 0 |
| 56 | 1.25 - 5 μ M | No | Synergy of GSK-J4 with doxorubicin in KRAS-mutant anaplastic thyroid cancer (PMID: 32477122) | 5 |
| 57 | 1.25 - 10 μ M | No | Therapeutic potential of GSK-J4, a histone demethylase KDM6B/JMJD3 inhibitor, for acute myeloid leukemia (PMID: 29594337) | 48 |
| 58 | 1.3 - 5 μ M | No | A comprehensive study of epigenetic alterations in hepatocellular carcinoma identifies potential therapeutic targets (PMID: 30880225) | 53 |
| 59 | 1.8 μ M | Yes | Inhibition of KDM6 activity during murine ESC differentiation induces DNA damage (PMID: 26759175) | 21 |
| 60 | 2 μ M | Yes | Histone H3K27me3 demethylases regulate human Th17 cell development and effector functions by impacting on metabolism (PMID: 32123118) | 39 |
| 61 | 2 μ M | Yes | Contrasting roles of histone 3 lysine 27 demethylases in acute lymphoblastic leukaemia (PMID: 25132549) | 266 |
| 62 | 2 - 4 μ M | No | Expression pattern of histone lysine-specific demethylase 6B in gastric cancer (PMID: 33968207) | 0 |
| 63 | 2 - 5 μ M | No | AURKA suppresses leukemic THP-1 cell differentiation through inhibition of the KDM6B pathway (PMID: 29477140) | 14 |
| 64 | 2 - 5 μ M | No | The lysine demethylase KDM5B regulates islet function and glucose homeostasis (PMID: 31467927) | 8 |
| 65 | 2.5 - 5 μ M | No | Therapeutically targeting head and neck squamous cell carcinoma through synergistic inhibition of LSD1 and JMJD3 by TCP and GSK-J1 (PMID: 31848446) Note: this publication used mostly the non-cell permeable GSK-J1 | 18 |
| 66 | 2.5 - 5 μ M | No | Two old drugs, NVP-AEW541 and GSK-J4, repurposed against the Toxoplasma gondii RH strain (PMID: 32393321) | 6 |
| 67 | 2 - 8 μ M | No | JMJD3 suppresses tumor progression in oral tongue squamous cell carcinoma patients receiving surgical resection (PMID: 35855897) | 0 |
| 68 | 2 - 8 μ M | No | Overexpression of UTX promotes tumor progression in Oral tongue squamous cell carcinoma patients receiving surgical resection: a case control study (PMID: 34465286) | 2 |
| 69 | 2 & 8 μ M | No | The epigenetic regulation of OLIG2 by histone demethylase KDM6B in glioma cells (PMID: 35132566) | 0 |
| 70 | 2.5 - 10 μ M | No | H3K27me3 loss plays a vital role in CEMIP mediated carcinogenesis and progression of breast cancer with poor prognosis (PMID: 31846842) | 40 |
| 71 | 2.5 & 10 μ M | No | Histone demethylase KDM6B regulates human podocyte differentiation in vitro (PMID: 31138771) | 3 |
| 72 | 2 - 20 μ M | No | Inhibitor of H3K27 demethylase JMJD3/UTX GSK-J4 is a potential therapeutic option for castration resistant prostate cancer (PMID: 28977932) | 40 |
| 73 | 3 - 6 μ M | No | Pharmacologic inhibition of histone demethylation as a therapy for pediatric brainstem glioma (PMID: 25401693) | 294 |
| 74 | 3.53 & 3.93 & 22.87 μ M | No | A new metabolic gene signature in prostate cancer regulated by JMJD3 and EZH2 (PMID: 29805743) | 24 |

| | | | | |
|----|-------------------|-----|--|-------------|
| 75 | 3.75 - 30 μ M | Yes | The antischistosomal potential of GSK-J4, an H3K27 demethylase inhibitor: insights from molecular modeling, transcriptomics and in vitro assays (PMID: 32178714) | 10 |
| 76 | 4 μ M | No | Abnormally elevated EZH2-mediated H3K27me3 enhances osteogenesis in aortic valve interstitial cells by inhibiting SOCS3 expression (PMID: 36455343) | 4 |
| 77 | 4 μ M | No | Jmjd3 Mediates Neuropathic Pain by Inducing Macrophage Infiltration and Activation in Lumbar Spinal Stenosis Animal Model (PMID: 34948220) | 2 |
| 78 | 4 μ M | No | GSK-J4 induces cell cycle arrest and apoptosis via ER stress and the synergism between GSK-J4 and decitabine in acute myeloid leukemia KG-1a cells (PMID: 32514253) | 9 |
| 79 | 4 μ M | No | Histone demethylase UTX is a therapeutic target for diabetic kidney disease (PMID: 30516825) | 27 |
| 80 | 4 μ M | No | GSKJ4 protects mice against early sepsis via reducing proinflammatory factors and up-regulating MiR-146a (PMID: 30337925) | 25 |
| 81 | 4 μ M | No | Inhibition of the histone H3K27 demethylase UTX enhances tumor cell radiosensitivity (PMID: 29483212) | 22 |
| 82 | 4 μ M | No | Inhibiting KDM6A Demethylase Represses Long Non-Coding RNA Hotairm1 Transcription in MDSC During Sepsis (PMID: 35185915) | 3 |
| 83 | 4 & 8 μ M | No | The pharmacological role of histone demethylase JMJD3 inhibitor GSK-J4 on glioma cells (PMID: 28978140) | 31 |
| 84 | 5 μ M | No | Nanoparticle enhanced combination therapy for stem-like progenitors defined by single-cell transcriptomics in chemotherapy-resistant osteosarcoma (PMID: 32973147) | 17 |
| 85 | 5 μ M | No | Mucosal-associated invariant T cell effector function is an intrinsic cell property that can be augmented by the metabolic cofactor α -ketoglutarate (PMID: 33597151) | 3 |
| 86 | 5 μ M | No | Dual regulation of histone methylation by mTOR complexes controls glioblastoma tumor cell growth via EZH2 and SAM (PMID: 32366675) | 12 |
| 87 | 5 μ M | No | Nuclear pore protein NUP210 depletion suppresses metastasis through heterochromatin-mediated disruption of tumor cell mechanical response (PMID: 34903738) | 6 |
| 88 | 5 μ M | No | P53 affects epigenetic signature on SOCS1 promoter in response to TLR4 inhibition (PMID: 33476981) | 5 |
| 89 | 5 μ M | No | Structure of nascent chromatin is essential for hematopoietic lineage specification (PMID: 28402853) | 23 |
| 90 | 5 μ M | No | Fingolimod alleviates cognitive deficit in Type 2 diabetes by promoting microglial M2 polarization via the pSTAT3-jmjd3 axis (PMID: 36385233) | 0 |
| 91 | 5 μ M | No | Histone H3K27 methyltransferase EZH2 and demethylase JMJD3 regulate hepatic stellate cells activation and liver fibrosis (PMID: 33391480) | 24 |
| 92 | 5 μ M | No | Palmitate-TLR4 signaling regulates the histone demethylase, JMJD3, in macrophages and impairs diabetic wound healing (PMID: 32662520) | 18 |
| 93 | 5 μ M | Yes | Inhibition of histone H3K27 demethylases selectively modulates inflammatory phenotypes of natural killer cells (PMID: 29301935) | 49 |
| 94 | 5 - 10 μ M | No | Pharmacological inhibition of core regulatory circuitry liquid-liquid phase separation suppresses metastasis and chemoresistance in osteosarcoma (PMID: 34432948) | 9 |
| 95 | 5 - 10 μ M | No | PRC2 epigenetically silences Th1-type chemokines to suppress effector T-cell trafficking in colon cancer (PMID: 26567139) | 157 |
| 96 | 5 - 10 μ M | No | Development and validation of the TGx-HDACi transcriptomic biomarker to detect histone deacetylase inhibitors in human TK6 cells (PMID: 33770205) | 5 (Pub med) |
| 97 | 5 & 10 μ M | No | Oncogenic KRAS sensitizes lung adenocarcinoma to GSK-J4-induced metabolic and oxidative stress (PMID: 31506334) | 16 |
| 98 | 5 - 20 μ M | No | KDM6A and KDM6B: Altered expression in malignant pleural mesothelioma (PMID: 28197626) | 8 |
| 99 | 5 & 30 μ M | No | A KDM6 inhibitor potently induces ATF4 and its target gene expression through HRI activation and by UTX inhibition (PMID: 33633164) | 0 |

| | | | | |
|-----|------------------|-----|--|----|
| 100 | 6 μ M | No | Histone demethylase JMJD3 protects against renal fibrosis by suppressing TGF β and Notch signaling and preserving PTEN expression (PMID: 33456568) | 19 |
| 101 | 6 - 20 μ M | No | GSKJ4, an H3K27me3 demethylase inhibitor, effectively suppresses the breast cancer stem cells (PMID: 28823831) | 56 |
| 102 | 6 - 60 μ M | Yes | Disruption of the Plasmodium falciparum life cycle through transcriptional reprogramming by inhibitors of jumonji demethylases (PMID: 32272012) | 12 |
| 103 | 7.5 μ M | No | Inhibition of H3K27me3 demethylases attenuates asthma by reversing the shift in airway smooth muscle phenotype (PMID: 30084510) | 11 |
| 104 | 7 - 10 μ M | No | Inhibition of H3K27me3 histone demethylase activity prevents the proliferative regeneration of Zebrafish lateral line neuromasts (PMID: 28348517) | 12 |
| 105 | 7.5 - 20 μ M | No | Targeted inhibition of KDM6 histone demethylases eradicates tumor-initiating cells via enhancer reprogramming in colorectal cancer (PMID: 32929331) | 10 |
| 106 | 10 μ M | No | Increased H3K27 trimethylation contributes to cone survival in a mouse model of cone dystrophy (PMID: 35810394) | 0 |
| 107 | 10 μ M | Yes | Upregulation of H3K27 demethylase KDM6 during respiratory syncytial virus infection enhances proinflammatory responses and immunopathology (PMID: 31748348) | 17 |
| 108 | 10 μ M | No | Forskolin sensitizes human acute myeloid leukemia cells to H3K27me2/3 demethylases GSKJ4 inhibitor via protein kinase A (PMID: 30079022) | 11 |
| 109 | 10 μ M | No | Lysyl oxidase expression is regulated by the H3K27 demethylase Jmjd3 in tumor-associated M2-like macrophages (PMID: 32231406) | 4 |
| 110 | 10 μ M | Yes | KDM6B-dependent chromatin remodeling underpins effective virus-specific CD8+ T cell differentiation (PMID: 33730567) | 8 |
| 111 | 10 μ M | No | A transcriptomic dataset used to derive biomarkers of chemically induced histone deacetylase inhibition (HDACi) in human TK6 cells (PMID: 34036128) | 0 |
| 112 | 10 μ M | No | Inhibitors of Jumonji C domain-containing histone lysine demethylases overcome cisplatin and paclitaxel resistance in non-small cell lung cancer through APC/Cdh1-dependent degradation of CtIP and PAF15 (PMID: 35100078) | 1 |
| 113 | 10 μ M | No | Unlocking the recovery potential: JMJD3 inhibition-mediated SAPK/JNK signaling inactivation supports endogenous oligodendrocyte-lineage commitment post mammalian spinal cord injury (PMID: 33428096) | 0 |
| 114 | 10 μ M | No | Transcriptional repression of ER through hMAPK dependent histone deacetylation by class I HDACs (PMID: 25129342) | 12 |
| 115 | 10 μ M | No | JMJD3 downregulates IL4i1 aggravating lipopolysaccharide-induced acute lung injury via H3K27 and H3K4 demethylation (PMID: 36537648) | 0 |
| 116 | 10 μ M | No | Stretch-induced tenomodulin expression promotes tenocyte migration via F-actin and chromatin remodeling (PMID: 34066472) | 4 |
| 117 | 10 μ M | No | LncRNA H19 regulates macrophage polarization and promotes Freund's complete adjuvant-induced arthritis by upregulating KDM6A (PMID: 33540246) | 10 |
| 118 | 10 μ M | No | Effects of chronic stress on depressive-like behaviors and JMJD3 expression in the prefrontal cortex and hippocampus of C57BL/6 and ob/ob mice (PMID: 33340793) | 4 |
| 119 | 10 μ M | No | Histone demethylase Jmjd3 modulates osteoblast apoptosis induced by tumor necrosis factor-alpha through directly targeting RASSF5. (PMID: 31092054) | 4 |
| 120 | 10 μ M | No | Jmjd3 regulates inflammasome activation and aggravates DSS-induced colitis in mice (PMID: 31971317) | 21 |
| 121 | 10 μ M | Yes | Upregulation of H3K27 demethylase KDM6 during RSV infection enhances pro-inflammatory responses and immunopathology. (PMID: 31748348) | 17 |
| 122 | 10 μ M | No | Epigenetic profiling identifies LIF as a super-enhancer-controlled regulator of stem cell-like properties in osteosarcoma. (PMID: 31615908) | 20 |
| 123 | 10 μ M | No | Antiproliferative effect of the histone demethylase inhibitor GSK-J4 in chondrosarcomas. (PMID: 31241814) | 5 |

| | | | | |
|-----|----------------------------|-----|---|----|
| 124 | 10 μ M | No | Histone demethylase JMJD3 regulates fibroblast-like synoviocyte-mediated proliferation and joint destruction in rheumatoid arthritis. (PMID: 29481307) | 33 |
| 125 | 10 μ M | No | GSK-J4-mediated transcriptomic alterations in differentiating embryoid bodies. (PMID: 29047260) | 5 |
| 126 | 10 μ M | Yes | H3K27me3 demethylases regulate in vitro chondrogenesis and chondrocyte activity in osteoarthritis. (PMID: 27388528) | 23 |
| 127 | 10 μ M | No | Transcriptomic profiling and H3K27me3 distribution reveal both demethylase-dependent and independent regulation of developmental gene transcription in cell differentiation. (PMID: 26263556) | 13 |
| 128 | 10 μ M | No | Histone demethylation maintains Prdm14 and Tsix expression and represses xIst in embryonic stem cells. (PMID: 25993097) | 10 |
| 129 | 10 μ M | No | Combined action of FOXO1 and superoxide dismutase 3 promotes MDA-MB-231 cell migration (PMID: 35271779) | 1 |
| 130 | 10 μ M | No | JMJD3 inhibition protects against isoproterenol-induced cardiac hypertrophy by suppressing β -MHC expression. (PMID: 29753027) | 17 |
| 131 | 10 μ M | No | The histone demethylase KDM6B fine-tunes the host response to <i>Streptococcus pneumoniae</i> . (PMID: 33349663) | 7 |
| 132 | 10 μ M | Yes | Critical role of histone demethylase Jumonji domain-containing protein 3 in the regulation of neointima formation following vascular injury. (PMID: 29982434) | 24 |
| 133 | 10 μ M | No | RNA sequencing reveals resistance of TLR4 ligand-activated microglial cells to inflammation mediated by the selective jumonji H3K27 demethylase inhibitor. (PMID: 28747667) | 23 |
| 134 | 10 - 30 μ M | No | Inhibition of Histone H3 Lysine-27 Demethylase Activity Relieves Rheumatoid Arthritis Symptoms via Repression of IL6 Transcription in Macrophages (PMID: 35371061) | 1 |
| 135 | 20 μ M | No | Inhibition of H3K4 demethylation induces autophagy in cancer cell lines (PMID: 28800922) | 20 |
| 136 | 20 μ M | No | The TrxG complex mediates cytokine induced de novo enhancer formation in islets (PMID: 26505193) | 6 |
| 137 | 25 μ M | No | EZH2, JMJD3, and UTX epigenetically regulate hepatic plasticity inducing retro-differentiation and proliferation of liver cells. (PMID: 31285428) | 16 |
| 138 | 30 μ M | No | Lysine demethylase 6B regulates prostate cancer cell proliferation by controlling c-MYC expression. (PMID: 34862309) | 3 |
| 139 | 30 μ M | No | JMJD3 is involved in neutrophil membrane proteinase 3 overexpression during the hyperinflammatory response in early sepsis. (PMID: 29621735) | 10 |
| 140 | 35 μ M | No | A unique bipartite Polycomb signature regulates stimulus-response transcription during development (PMID: 33603234) | 9 |
| 141 | 30 - 50 μ M | No | Targeting P16INK4A in uterine serous carcinoma through inhibition of histone demethylation. (PMID: 30896884) | 3 |
| 142 | 30 - 60 μ M | No | Epigenomic regulation of schwann cell reprogramming in peripheral nerve injury. (PMID: 27581455) | 48 |
| 143 | 40 μ M | No | hsa-miR-199b-3p prevents the epithelial-mesenchymal transition and dysfunction of the renal tubule by regulating E-cadherin through targeting KDM6A in diabetic nephropathy. (PMID: 34257820) | 5 |
| 144 | 50 μ M | No | Inhibition of H3K27me3-specific histone demethylases JMJD3 and UTX blocks reactivation of herpes simplex virus 1 in trigeminal ganglion neurons. (PMID: 25552720) | 34 |
| 145 | 50 μ M | No | Lysine demethylase KDM6B regulates HIF-1 α -mediated systemic and cellular responses to intermittent hypoxia (PMID: 34297635) | 4 |
| 146 | 10 mM | No | The histone demethylase inhibitor GSK-J4 is a therapeutic target for the kidney fibrosis of diabetic kidney disease via DKK1 modulation (PMID: 36012674) | 0 |
| 147 | concentration not provided | No | UTX-1 regulates Tat-induced HIV-1 transactivation via changing the methylated status of histone H3 (PMID: 27671333) | 8 |
| 148 | concentration not provided | No | The fungal metabolite chaetocin is a sensitizer for pro-apoptotic therapies in glioblastoma (PMID: 31772153) | 11 |
| 149 | concentration not provided | No | Hypoxia induces HIF1 α -dependent epigenetic vulnerability in triple negative breast cancer to confer immune effector dysfunction and resistance to anti-PD-1 immunotherapy (PMID: 35840558) | 3 |

| | | | | |
|---|----------------------------|-----------|--|----|
| 150 | concentration not provided | No | Engineering lineage potency and plasticity of stem cells using epigenetic molecules (PMID: 30389989) | 5 |
| 151 | concentration not provided | No | KDM2B promotes cell viability by enhancing DNA damage response in canine hemangiosarcoma (PMID: 34023294) | 6 |
| 152 | concentration not provided | No | Activation of NFkB-JMJD3 signaling promotes bladder fibrosis via boosting bladder smooth muscle cell proliferation and collagen accumulation. (PMID: 31102789) | 8 |
| 153 | concentration not provided | No | Comprehensive profiling of JMJD3 in gastric cancer and its influence on patient survival. (PMID: 30696880) | 17 |
| Compliance | | | | |
| Fully below 5 μ M: 72 (47%) ^a | | 16 (11%) | | |
| Fully between 5 - 10 μ M: 52 (34%) ^b | | | | |
| Partially: 10 (7%) ^c | | | | |
| Non-Compliance | | | | |
| 19 (12%) | | 137 (89%) | | |

a Probe's concentration below the recommended 5 μ M (Chemical Probes Portal) in all figures.

b Probe's concentration above the recommended 5 μ M (Chemical Probes Portal) but below the recommended 10 μ M (SGC).

c Probe's concentration below the recommended 10 μ M SGC in-cell maximum in some but not all figures.

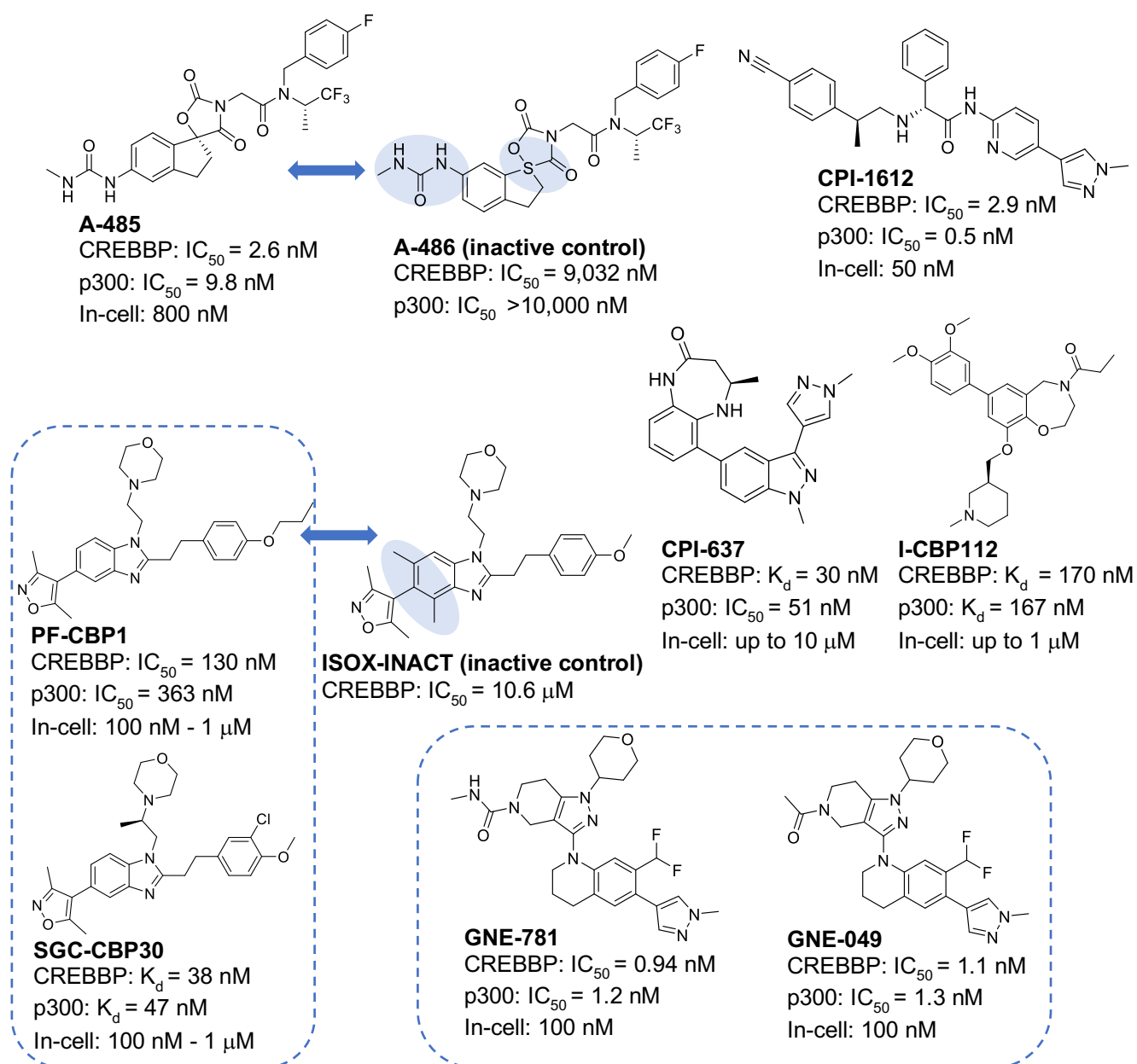
Supplementary Note 4. Citations for GSK-J4 publications included in the systematic review.
Citations for 153 publications using GSK-J4: 2,890

Citations for 134 publications with a compliant GSK-J4 concentration: 2,674

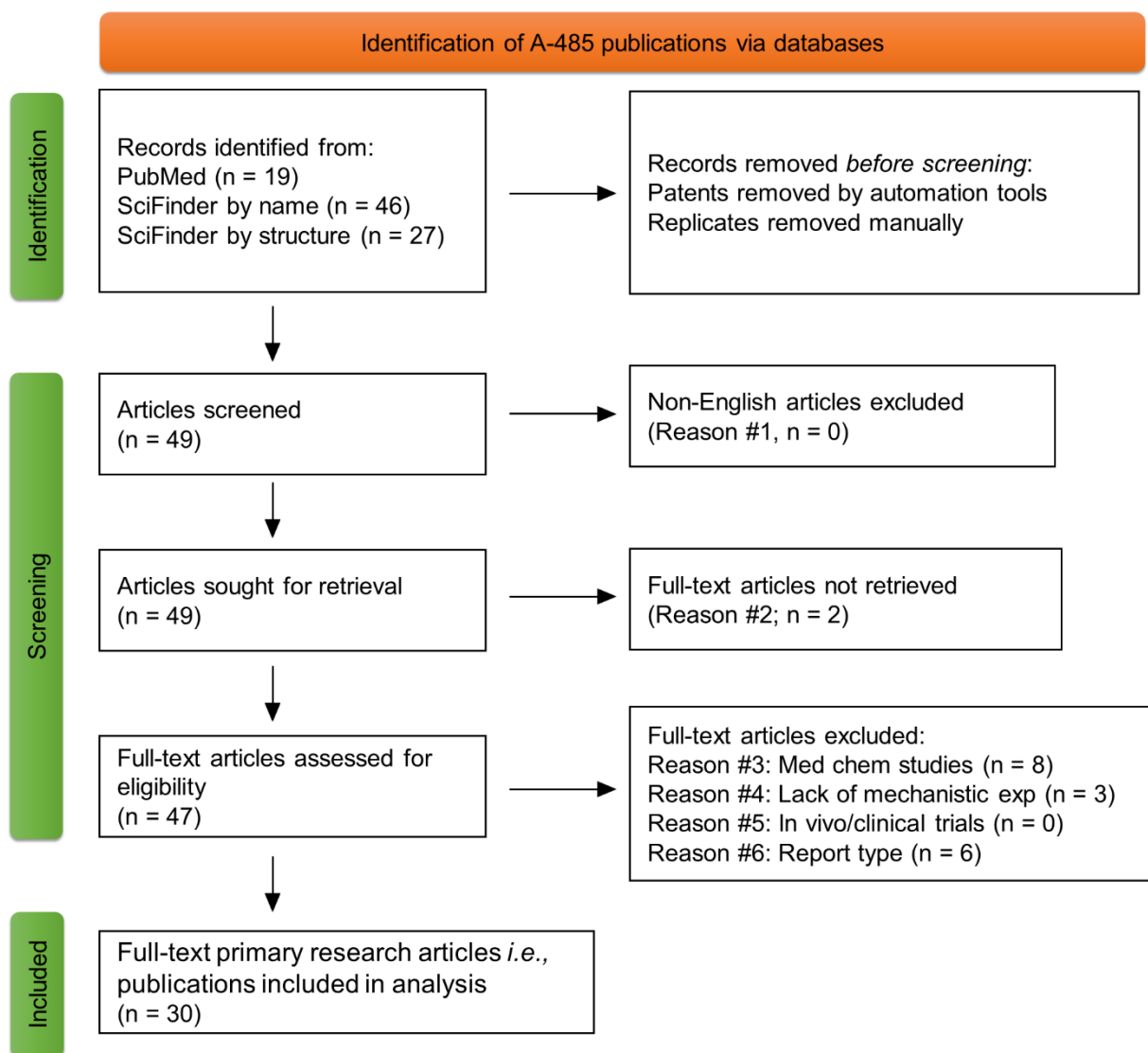
Citations for 19 publications with a non-compliant GSK-J4 concentration: 216

Citations for 16 publications using inactive compound GSK-J5: 622

Citations for 137 publications not using inactive compound GSK-J5: 2,268



Supplementary Figure 6. Structures, biochemical potency (K_d/IC_{50}) and recommended in-cell concentrations of CREBBP/p300 chemical probes as listed on the Chemical Probes Portal (www.chemicalprobes.org). Dashed lines group structurally related chemical probes that should not be used together as orthogonal tools (e.g., GNE-049 can be used as an orthogonal chemical probe with A-485, but not with GNE-781). Bidirectional arrows link target-inactive analogues and shaded fields highlight the structural changes leading to decreased CREBBP/p300 targeting.



Supplementary Figure 7. PRISMA flow diagram summarising identification of publications using CREBBP/p300 chemical probe A-485.

Note: Pubmed search retrieved 90 publications but includes any publication that writes ‘a 485’ (e.g., a 485 nm wavelength, a 485 amino acid-long length). These 90 publications were manually reviewed for publications referring to probe A-485.

Supplementary Table 7. List of excluded articles using the CREBBP/p300 probe A-485.

| | Title (PMID) | Reason for exclusion |
|----|---|--|
| 1 | Assays for validating histone acetyltransferase inhibitors (PMID: 32831305) | 2) No access |
| 2 | Report of the first international symposium on NUT carcinoma (PMID: 35417004) | 2) No access |
| 3 | Synthesis and biological evaluation of spirocyclic chromane derivatives as a potential treatment of prostate cancer (PMID: 34070610) | 3) A-485 lead optimization |
| 4 | Discovery of a selective catalytic p300/CBP inhibitor that targets lineage-specific tumours (PMID: 28953875) | 3) Discovery of A-485 |
| 5 | Discovery of a potent and selective covalent p300/CBP inhibitor (PMID: 34055218) | 3) Lead optimization |
| 6 | Discovery of spirohydantoin as selective, orally bioavailable inhibitors of p300/CBP histone acetyltransferases (PMID: 33631370) | 3) Lead optimization |
| 7 | Identification of ligand linkage vectors for the development of p300/CBP degraders (PMID: 35814928) | 3) Medicinal chemistry |
| 8 | Design, synthesis and biological evaluation of a novel spiro oxazolidinedione as potent p300/CBP HAT inhibitor for the treatment of ovarian cancer (PMID: 34801827) | 3) Medicinal chemistry study |
| 9 | Discovery of spiro oxazolidinediones as selective, orally bioavailable inhibitors of p300/CBP histone acetyltransferases (PMID: 29348807) | 3) Medicinal chemistry study |
| 10 | Combination targeting of the bromodomain and acetyltransferase active site of p300/CBP (PMID: 30924641) | 3) Study primarily employed A-485rs, a 1:1 diastereomeric mixture of A-485 |
| 11 | Dual-functional polyetheretherketone surface modification for regulating immunity and bone metabolism (no PMID; DOI: 10.1016/j.cej.2021.130806) | 4) No mechanistic exp.: A-485 loaded onto an activated PEEK surface |
| 12 | Inactivation of the CIC-DUX4 oncogene through P300/CBP inhibition, a therapeutic approach for CIC-DUX4 sarcoma (PMID: 34642317) | 4) No mechanistic exp. |
| 13 | Therapeutic targeting of ATR yields durable regressions in small cell lung cancers with high replication stress (PMID: 33848478) | 4) No mechanistic exp. |
| 14 | Another one (of the "undruggable" targets) bites the dust: Discovery of a potent and selective inhibitor of the histone acetyl transferase p300/CBP (PMID: 29244478) | 6) Commentary/Letter |
| 15 | Author Correction: Discovery of a selective catalytic p300/CBP inhibitor that targets lineage-specific tumours [Erratum to document cited in CA167:546652] (PMID: 29769713) | 6) Erratum |
| 16 | Targeting cancer epigenetic pathways with small-molecule compounds: Therapeutic efficacy and combination therapies (PMID: 34102228) | 6) Review |
| 17 | Histone acetyltransferases CBP/p300 in tumorigenesis and CBP/p300 inhibitors as promising novel anticancer agents (PMID: 35836809) | 6) Review article |
| 18 | Anti-cancer agents repurposed for p300-HAT binding (No PMID, DOI or ISSN, AN: 2022:3061564) | 6) Conference proceedings |
| 19 | Assay interference profiles of next-generation cell-active histone acetyltransferase inhibitors (No PMID, DPO or ISSN, AN: 2020:290416) | 6) Conference proceedings |

Supplementary Table 8. Overview of eligible publications using the CREBBP/p300 probe A-485 and compliance (in blue) with recommendations to use A-485 up to 800 nM (<https://www.chemicalprobes.org/485?q=A-485>; we consider publications using 1 μ M A-485 as compliant), validate results with the inactive control compound A-486 and orthogonal inhibitors. Citations are sourced from SciFinder (January 2023).

| | A-485 | A-486 | Orthogonal inhibitors | Title (PMID) | Cites |
|----|--------------------|-------|--|--|-------|
| 1 | 100 nM | No | GNE-781, dCBP-1 (both 100 nM) | Targeted degradation of the enhancer lysine acetyltransferases CBP and p300 (PMID: 33400925) | 36 |
| 2 | 100 nM - 1 μ M | No | GNE-049, SGC-CBP30 (0.1 - 10 μ M) | Domain-independent inhibition of CBP/p300 attenuates α -synuclein aggregation (PMID: 34110772) | 2 |
| 3 | 250 nM - 1 μ M | Yes | I-CBP112, SGC-CBP30 (10 μ M) | Therapeutic targeting of p300/CBP HAT domain for the treatment of NUT midline carcinoma (PMID: 32366905) | 19 |
| 4 | 0.25 - 2 μ M | No | None | H3K27 acetylation activated-CCS regulates autophagy and apoptosis of lung cancer by alleviating oxidative stress (PMID: 36402120) | 0 |
| 5 | 250 nM - 3 μ M | No | GNE-049 (0.25 - 1 μ M) | Pharmacological inhibition of CBP/p300 blocks estrogen receptor alpha function through suppressing enhancer H3K27 acetylation in luminal breast cancer (PMID:34199844) | 11 |
| 6 | 0.3 - 3 μ M | No | C646 (3 - 10 μ M) | Interplay between protein acetylation and ubiquitination controls MCL1 protein stability (PMID: 34758305) | 4 |
| 7 | 0.3 & 3 μ M | Yes | None | Targeting lineage-specific MITF pathway in human melanoma cell lines by A-485, the selective small-molecule inhibitor of p300/CBP (PMID: 30266801) | 37 |
| 8 | 500 nM | No | None | Histone acetylation dynamics modulates chromatin conformation and allele-specific interactions at oncogenic loci (PMID: 33972799) | 16 |
| 9 | 0.5 - 10 μ M | No | None | Integrative genomic profiling uncovers therapeutic targets of acral melanoma in Asian populations (PMID: 35294533) | 2 |
| 10 | 0.5 - 2 μ M | No | None | p300/CBP inhibitor A-485 inhibits the differentiation of osteoclasts and protects against osteoporotic bone loss (PMID: 33626422) | 3 |
| 11 | 0.8 μ M | No | SGC-CBP30 (1 μ M) I-CBP 112 (3 μ M) | The p300/CBP inhibitor A485 normalizes psoriatic fibroblast gene expression in vitro and reduces psoriasis-like skin inflammation in vivo (PMID: 36174717) | 0 |
| 12 | 1 μ M | No | A-241 (2 nM - 1 μ M) | Targeting histone acetylation dynamics and oncogenic transcription by catalytic P300/CBP inhibition (PMID: 34019788) | 22 |
| 13 | 1 μ M | Yes | CBP30 (0.5 μ M) I-CBP112 (1 μ M) | Bromodomain inhibition of the coactivators CBP/EP300 facilitate cellular reprogramming (PMID: 30962627) | 44 |
| 14 | 1 μ M | No | None | Targeted protein acetylation in cells using heterobifunctional molecules (PMID: 34592107) | 12 |
| 15 | 1-10 μ M | No | None | Merkel cell polyomavirus small T antigen is a viral transcription activator that is essential for viral genome maintenance (PMID: 36574443) | 0 |
| 16 | 1-20 μ M | No | None | Pharmacological targeting of CBP/p300 drives a redox/autophagy axis leading to senescence-induced growth arrest in non-small cell lung cancer cells (PMID: 36117234) | 0 |
| 17 | 1.25 - 5 μ M | No | None | The p300 inhibitor A-485 exerts antitumor activity in growth hormone pituitary adenoma (PMID: 35247260) | 2 |
| 18 | 2.2 - 20 μ M | No | SGC-CBP30, CPI-637 (2.2 - 20 μ M) | p300/CBP inhibitor A-485 alleviates acute liver injury by regulating macrophage activation and polarization (PMID: 31754401) | 27 |
| 19 | 3 μ M | No | None | CBP/p300 HAT maintains the gene network critical for β cell identity and functional maturity (PMID: 33980820) | 2 |
| 20 | 3 μ M | No | CPI-637, SGC-CBP30 (0.01 - 10 μ M) | P300/CBP inhibition sensitizes mantle cell lymphoma to PI3K δ inhibitor idelalisib (PMID: 33850273) | 4 |

| | | | | | |
|----------------------------|----------------|-------|--|---|-----|
| 21 | 3 μ M | No | None | Selective inhibition of CBP/p300 HAT by A-485 results in suppression of lipogenesis and hepatic gluconeogenesis (PMID: 32917859) | 10 |
| 22 | 3 μ M | No | Cmpd-R (3 μ M) I-CBP112 (5 μ M) | Time-resolved analysis reveals rapid dynamics and broad scope of the CBP/p300 acetylome (PMID: 29804834) | 176 |
| 23 | 3 μ M | No | None | TRPM3-induced gene transcription is under epigenetic control (PMID: 35890145) | 0 |
| 24 | 5 μ M | No | None | Histone modifications drive aberrant Notch3 expression/activity and growth in T-ALL (PMID: 31001470) | 25 |
| 25 | 5 - 20 μ M | No | None | A novel histone acetyltransferase inhibitor A485 improves sensitivity of non-small-cell lung carcinoma cells to TRAIL (PMID: 32173363) | 12 |
| 26 | 10 μ M | No | None | Promoter-specific changes in initiation, elongation, and homeostasis of histone H3 acetylation during CBP/p300 inhibition (PMID: 33704060) | 9 |
| 27 | 10 μ M | No | None | Large-scale RNAi screening uncovers therapeutic targets in the parasite <i>Schistosoma mansoni</i> (PMID: 32973031) | 26 |
| 28 | 10 μ M | No | CPI-637 (10 μ M) | Analysis and therapeutic targeting of the EP300 and CREBBP acetyltransferases in anaplastic large cell lymphoma and Hodgkin lymphoma (PMID: 36456744) | 0 |
| 29 | Not provided | No | None | Acetylation of histone 3 promotes miR-29a expression and downregulates STAT3 in sepsis (PMID: 34615595) | 0 |
| 30 | Unclear | No | None | Identification of potent inhibitors of SARS-CoV-2 infection by combined pharmacological evaluation and cellular network prioritization (PMID: 35992305) | 2 |
| Compliance | | | | | |
| 8 (27%)^a | | 3 | 12 (40%) | | |
| 8 (27%)^b | | (10%) | | | |
| Non-Compliance | | | | | |
| 14 (47%) | | 27 | 18 (60%) | | |
| | | (90%) | | | |

a Probe's concentration below the recommended in-cell maximum in all figures.

b Probe's concentration below the recommended in-cell maximum in some, but not all figures.

Supplementary Note 5. Citations for A-485 publications included in the systematic review.
Citations for 30 publications using A-485: 503

Citations for 16 publications with a compliant A-485 concentration: 208

Citations for 14 publications with a non-compliant A-485 concentration: 295

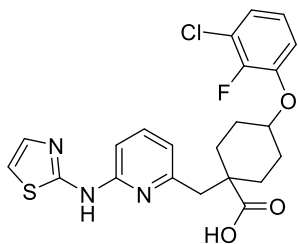
Citations for 3 publications using inactive compound A-486: 100

Citations for 27 publications not using inactive compound A-486: 403

Citations for 12 publications using orthogonal CREBBP/p300 inhibitors: 345

Citations for 18 publications not using orthogonal CREBBP/p300 inhibitors: 158

a) Aurora chemical probes



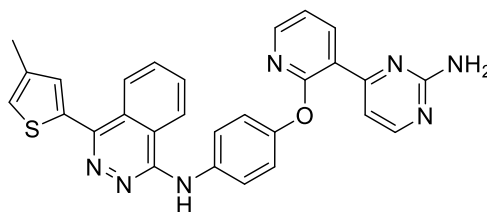
MK-5108

AURKA: IC_{50} = 0.064 nM

AURKB: IC_{50} = 14.1 nM

AURKC: IC_{50} = 12.1 nM

In-cell: 1 nM - 1 μ M



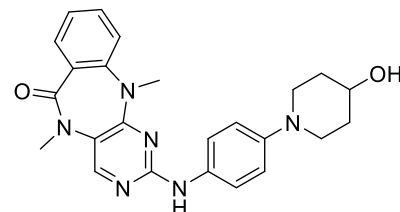
AMG900

AURKA: IC_{50} = 5 nM

AURKB: IC_{50} = 4 nM

AURKC: IC_{50} = 1 nM

In-cell: up to 100 nM



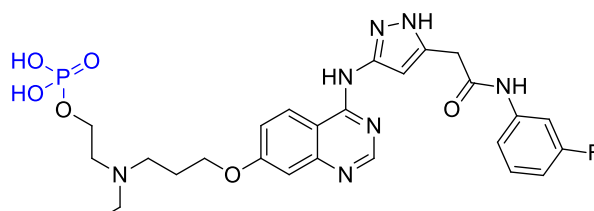
XMD-12

AURKA: IC_{50} = 5.6 nM

AURKB: IC_{50} = 18.4 nM

AURKC: IC_{50} = 24.6 nM

In-cell: up to 1 μ M

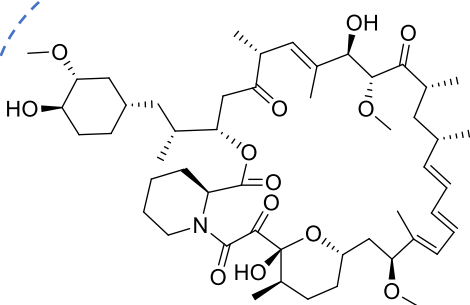


AZD1152 / AZD1152-HQPA (in black)

AURKB: K_i < 1 nM

In-cell: up to 100 nM

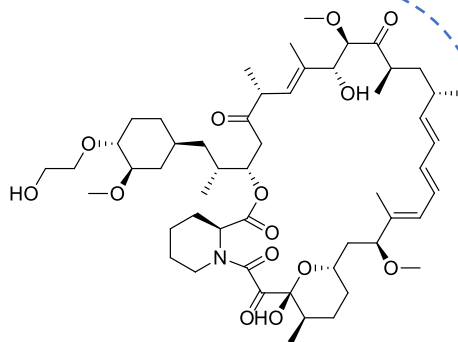
b) mTOR chemical probes



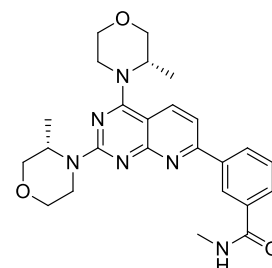
Rapamycin

mTOR: IC_{50} = 0.2 nM

In-cell: 1 nM - 200 nM



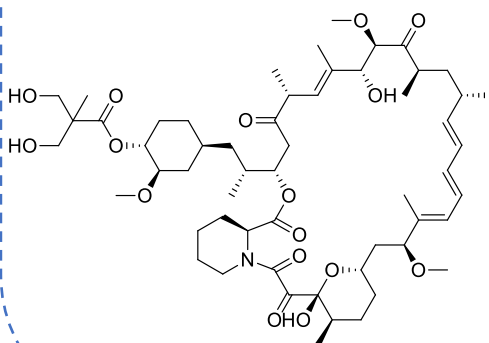
Everolimus



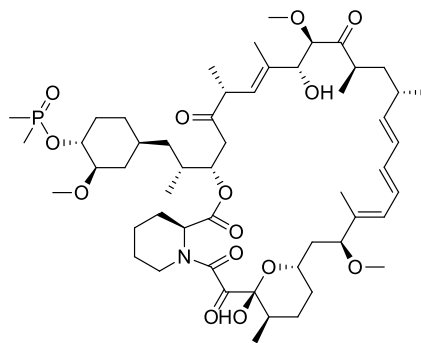
AZD2014

mTOR: IC_{50} = 2.8 nM

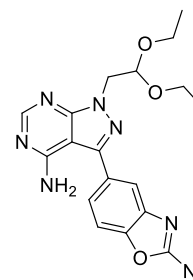
In-cell: 10 nM - 2 μ M



Temsirolimus



Ridaforolimus

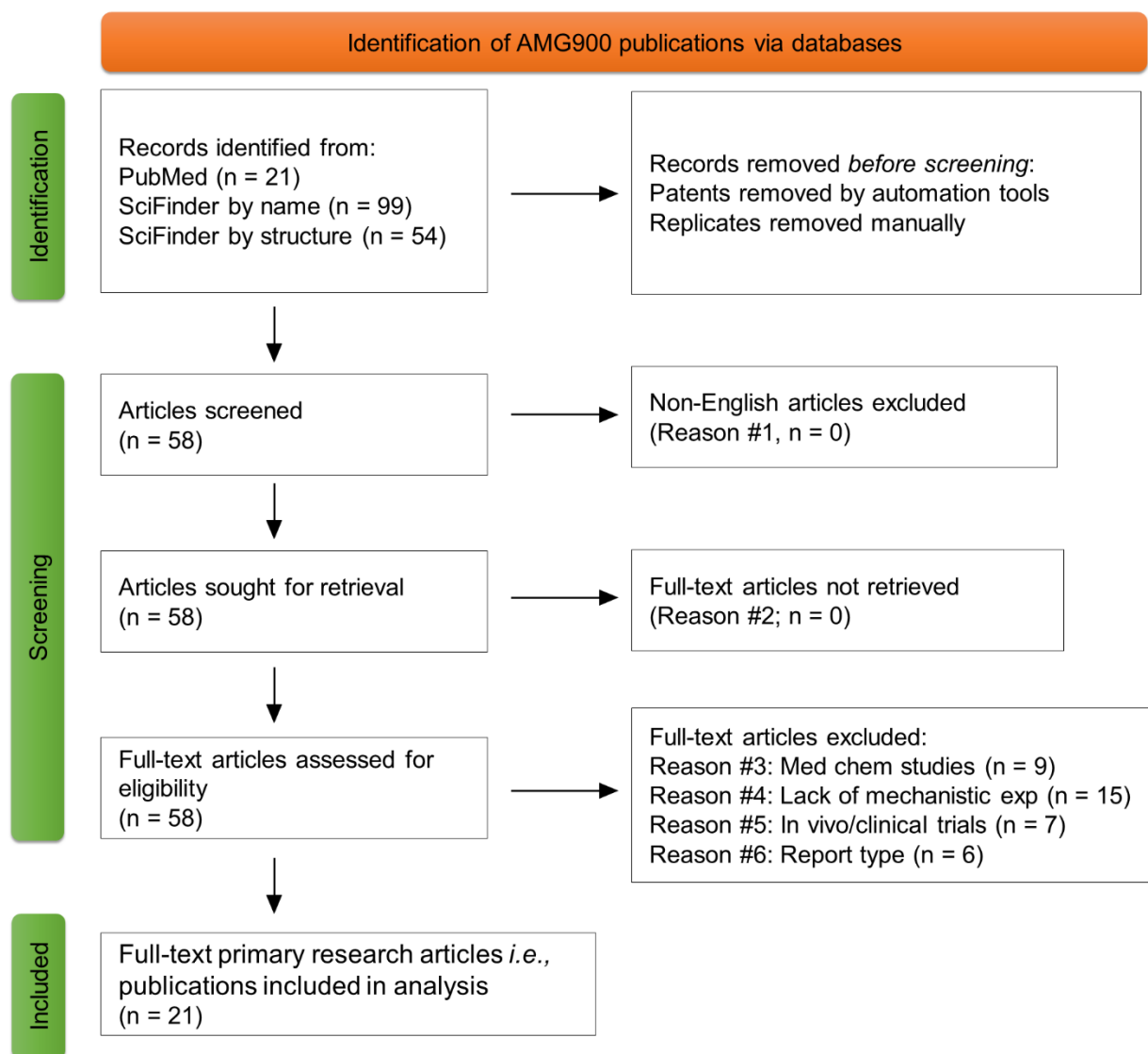


eCF309

mTOR: IC_{50} = 15 nM

In-cell: 20 nM - 50 nM

Supplementary Figure 8. Structures, biochemical potency (IC_{50}) and recommended in-cell concentrations of **a)** Aurora and **b)** mTOR chemical probes as listed on the Chemical Probes Portal (www.chemicalprobes.org). Note that everolimus, temsirolimus and ridaforolimus are not listed on the Chemical Probes Portal, but are included in the figure to demonstrate their structural similarity with rapamycin. Dashed lines group structurally related mTOR chemical probes that should not be used together as orthogonal tools.



Supplementary Figure 9. PRISMA flow diagram summarising identification of publications using Aurora kinase chemical probe AMG900.

Supplementary Table 9. List of excluded articles using the Aurora kinase targeting probe AMG900.

| Title (PMID) | Reason for exclusion |
|---|--|
| 1 In silico binding mode analysis (molecular docking studies) and absorption, distribution, metabolism and excretion prediction of some novel inhibitors of Aurora kinase A in clinical trials (No PMID; DOI: 10.14233/ajchem.2014.17175) | 3) Medicinal chemistry /Computational study |
| 2 Biologically relevant chemical space navigator: From patent and structure-activity relationship analysis to library acquisition and design (PMID: 23176522) | 3) Medicinal chemistry /Computational study |
| 3 Discovery of N-(4-(3-(2-aminopyrimidin-4-yl)pyridin-2-yloxy)phenyl)-4-(4-methylthiophen-2-yl)phthalazin-1-amine (AMG 900), a highly selective, orally bioavailable inhibitor of aurora kinases with activity against multidrug-resistant cancer cell lines (PMID: 25970324) | 3) Discovery of AMG900 |
| 4 A combined approach based on 3D pharmacophore and docking for identification of new aurora A kinase inhibitors (No PMID; DOI: 10.1007/s00044-013-0747-5) | 3) Medicinal chemistry / in silico study |
| 5 Quantitative conformational profiling of kinase inhibitors reveals origins of selectivity for Aurora kinase activation states (PMID: 30518564) | 3) Medicinal chemistry |
| 6 Optimization and biological evaluation of nicotinamide derivatives as Aurora kinase inhibitors (PMID: 31307762) | 3) Medicinal chemistry |
| 7 New affinity probe targeting VEGF receptors for kinase inhibitor selectivity profiling by chemical proteomics (PMID: 24712744) | 3) Medicinal chemistry |
| 8 SAR and evaluation of novel 5H-benzo[c][1,8]naphthyridin-6-one analogs as Aurora kinase inhibitors (PMID: 23570792) | 3) Medicinal chemistry |
| 9 In silico identification of strong binders of the SARS-CoV-2 receptor-binding domain (PMID: 33130279) | 3) Medicinal chemistry |
| 10 Real-time luminescence enables continuous drug-response analysis in adherent and suspension cell lines (PMID: 35443861) | 4) No mechanistic exp. - Assay protocol |
| 11 Synthetic lethality of RB1 and aurora A is driven by stathmin-mediated disruption of microtubule dynamics (PMID: 33037191) | 4) No mechanistic exp. - Dose response viability |
| 12 Modeling and targeting of erythroleukemia by hematopoietic genome editing (PMID: 33512458; DOI: 10.1182/blood.2020009103) | 4) Ex vivo study |
| 13 Activity comparison of epigenetic modulators against the Hemoprotozoan parasites Babesia divergens and Plasmodium falciparum (PMID: 33599488) | 4) No mechanistic exp. - Parasites growth |
| 14 Cell panel profiling reveals conserved therapeutic clusters and differentiates the mechanism of action of different PI3K/mTOR, aurora kinase and EZH2 inhibitors (PMID: 27587489) | 4) No mechanistic exp. |
| 15 The new paradigm of network medicine to analyze breast cancer phenotypes (PMID: 32932728) | 4) No mechanistic studies |
| 16 Aurora kinase A inhibition induces synthetic lethality in SMAD4-deficient colorectal cancer cells via spindle assembly checkpoint activation (PMID: 35393542) | 4) No mechanistic studies |
| 17 High-throughput compound screen reveals mTOR inhibitors as potential therapeutics to reduce (auto)antibody production by human plasma cells (PMID: 31621069) | 4) No mechanistic exp. with AMG900 |
| 18 Refinement of in vitro methods for identification of aldehyde oxidase substrates reveals metabolites of kinase inhibitors (PMID: 29615437) | 4) No mechanistic exp. - AMG900 metabolism |
| 19 Compound selectivity and target residence time of kinase inhibitors studied with surface plasmon resonance (PMID: 28043854) | 4) No mechanistic exp. – AMG900 kinetics |
| 20 RIPK1-dependent cell death: a novel target of the Aurora kinase inhibitor Tozasertib (VX-680) (PMID: 29434255) | 4) No mechanistic exp. |
| 21 Aneugen molecular mechanism assay: proof-of-concept with 27 reference chemicals (PMID: 31132080) | 4) No mechanistic exp. |
| 22 Interlaboratory evaluation of a multiplexed high information content in vitro genotoxicity assay (PMID: 28370322) | 4) No mechanistic exp. |
| 23 In vitro and in vivo pharmacokinetic characterizations of AMG 900, an orally bioavailable small molecule inhibitor of aurora kinases (PMID: 21294625) | 4) No mechanistic exp. |
| 24 Differential ABC transporter expression during hematopoiesis contributes to neutrophil-biased toxicity of Aurora kinase inhibitors (PMID: 36224199) | 4) No mechanistic exp. |
| 25 Definition of a novel cuproptosis-relevant lncRNA signature for uncovering distinct survival, genomic alterations, and treatment implications in lung adenocarcinoma (PMID: 36281357) | 5) Clinical data |

| | | |
|----|---|---------------------------|
| 26 | Experiments in the EpiDerm 3D skin in vitro model and minipigs in vivo indicate comparatively lower in vivo skin sensitivity of topically applied aneugenic compounds (PMID: 33481035) | 5) Clinical study |
| 27 | A phase 1, first-in-human study of AMG 900, an orally administered pan-Aurora kinase inhibitor, in adult patients with advanced solid tumors (PMID: 29980894) | 5) Clinical trial |
| 28 | A phase 1 study of AMG 900, an orally administered pan-aurora kinase inhibitor, in adult patients with acute myeloid leukemia (PMID: 28370201) | 5) Clinical trial |
| 29 | AMG 900, a potent inhibitor of aurora kinases causes pharmacodynamic changes in p-Histone H3 immunoreactivity in human tumor xenografts and proliferating mouse tissues (PMID: 25367255) | 5) In vivo study |
| 30 | LC-MS/MS bioanalytical method development for AMG 900: resolution of an isobaric interference in rodent in vivo studies (PMID: 23245248) | 5) In vivo study |
| 31 | Gender effects on rat metabolism of AMG 900, an orally available small molecule Aurora kinase inhibitor (PMID: 22022868) | 5) In vivo study |
| 32 | SnapShot: Kinase inhibitors II (PMID: 26000855) | 6) Abstract only |
| 33 | Discovery of AMG 900, a highly selective, orally bioavailable inhibitor of Aurora kinases with efficacy in preclinical antitumor models and activity against multidrug-resistant cancer cell lines (No PMID, DOI or ISSN, AN: 2014:1304450) | 6) Conference proceedings |
| 34 | Structural biology insight for the design of sub-type selective aurora kinase inhibitors (PMID: 25895501) | 6) Review |
| 35 | Phthalazinone scaffold: Emerging tool in the development of target based novel anticancer agents (PMID: 32767957) | 6) Review |
| 36 | Aurora kinase inhibitor patents and agents in clinical testing: an update (2011 - 2013) (PMID: 24965505) | 6) Review |
| 37 | Aurora kinase inhibition: a new light in the sky? (PMID: 26111271) | 6) Review |

Supplementary Table 10. Overview of eligible publications using Aurora kinase targeting probe AMG900 and compliance (in blue) with recommendations to use AMG900 up to 100 nM (<https://www.chemicalprobes.org/amg900?q=AMG-900>) and validate results with at least one orthogonal probe. Citations are sourced from SciFinder (January 2023).

| | AMG900 | Orthogonal inhibitors | Title (PMID) | Cites |
|----|--------------------|--|---|-------|
| 1 | 0 - 100 nM | None | Classification of in vitro genotoxicants using a novel multiplexed biomarker assay compared to the flow cytometric micronucleus test (PMID: 28940655) | 13 |
| 2 | 0.01 - 100 nM | Barasertib (0.05-500 nM), Hesperadin (1 nM-10 μ M) | A new imaging platform (iScreen) allows for the concurrent assessment of micronucleus induction and genotoxic mode of action in human A375 cells (PMID: 35703118) | 0 |
| 3 | 50 pM - 1 μ M | AZD1152-HQPA, MLN8054 (5 μ M) | Dual targeting of aurora kinases with AMG 900 exhibits potent preclinical activity against acute myeloid leukemia with distinct post-mitotic outcomes (PMID: 30266802) | 12 |
| 4 | 0.1 - 100 nM | None | An Aurora kinase inhibitor, AMG900, inhibits glioblastoma cell proliferation by disrupting mitotic progression (PMID: 30221846) | 8 |
| 5 | 0.15625 - 2.5 nM | Hesperadin (3 - 50 nM) VX680 (6.25-100 nM) | Aneugen versus clastogen evaluation and oxidative stress-related mode-of-action assessment of genotoxic compounds using the toxtracker reporter assay (PMID: 32617558) | 10 |
| 6 | 0.2 - 100 nM | Hesperadin (4 nM - 2 μ M), VX-680 (0.01 - 5 μ M) | TubulinTracker, a novel in vitro reporter assay to study intracellular microtubule dynamics, cell cycle progression, and aneugenicity (PMID: 35094094) | 2 |
| 7 | 0.2 - 100 nM | None | Image analysis of mechanistic protein biomarkers for the characterization of genotoxicants: Aneugens, clastogens, and reactive oxygen species inducers (No PMID; DOI: 10.1002/em.22374) | 1 |
| 8 | 0.5 nM - 1 μ M | AZD1152-HQPA, MK-5108 (0.5 nM - 1 μ M) | Preclinical evaluation of the Aurora kinase inhibitors AMG 900, AZD1152-HQPA, and MK-5108 on SW-872 and 93T449 human liposarcoma cells (PMID: 29197031) | 5 |
| 9 | 1 - 50 nM | None | Combining the pan-aurora kinase inhibitor AMG 900 with histone deacetylase inhibitors enhances antitumor activity in prostate cancer (PMID: 24989836) | 22 |
| 10 | 1.5 - 50 nM | None | AMG 900, a small-molecule inhibitor of aurora kinases, potentiates the activity of microtubule-targeting agents in human metastatic breast cancer models (PMID: 23990115) | 32 |
| 11 | 2.5 - 50 nM | None | The aurora kinase inhibitor AMG 900 increases apoptosis and induces chemosensitivity to anticancer drugs in the NCI-H295 adrenocortical carcinoma cell line (PMID: 28410270) | 15 |
| 12 | 2.5 - 50 nM | None | Antitumour activity of AMG 900 alone or in combination with histone deacetylase inhibitor SaHa on medulloblastoma cell lines (PMID: 26000978) | 5 |
| 13 | 2.5 - 160 nM | VX-680 (2.5 μ M), MLN8237 (0.1 - 2.5 μ M), AZD1152 (0.2 - 2.5 μ M) | 2-Phenoxy-3, 4'-bipyridine derivatives inhibit AURKB-dependent mitotic processes by disrupting its localization (PMID: 36413818) | 2 |
| 14 | 10 nM | None | AMG 900, pan-Aurora kinase inhibitor, preferentially inhibits the proliferation of breast cancer cell lines with dysfunctional p53 (PMID: 24091768) | 19 |
| 15 | 50 nM | ML8237 (50 nM) | Inhibition of Aurora kinase A activity enhances the antitumor response of beta-catenin blockade in human adrenocortical cancer cells (PMID: 33716050) | 4 |
| 16 | 50 nM | None | Preclinical evaluation of AMG 900, a novel potent and highly selective pan-aurora kinase inhibitor with activity in taxane-resistant tumor cell lines (PMID: 20935223) | 103 |
| 17 | 50 - 100 nM | None | Report and application of a tool compound data set (PMID: 29035535) | 5 |
| 18 | 300 nM | AT9283 (50 nM) | AT9283 exhibits antiproliferative effect on tyrosine kinase inhibitor-sensitive and -resistant chronic myeloid leukemia cells by inhibition of Aurora A and Aurora B (PMID: 33000229) | 2 |

| | | | | |
|-----------------------------|------------------------|--------------------------------|--|---|
| 19 | 3.435 - 13.74 μ M | Artesunate (12.6 - 50 μ M) | AMG900 as novel inhibitor of the translationally controlled tumor protein (PMID: 33259807) | 3 |
| 20 | 66.4 nM & 11.2 μ M | None | Pan Aurora Kinase Inhibitor: A Promising Targeted-Therapy in Dedifferentiated Liposarcomas With Differential Efficiency Depending on Sarcoma Molecular Profile (PMID: 32138169) | 8 |
| 21 | Unclear | VX680, PF03814735 (0 - 10 mM) | Biomarkers of DNA damage response improve in vitro micronucleus assays by revealing genotoxic mode of action and reducing the occurrence of irrelevant positive results (PMID: 34718711) | 0 |
| Compliance | | | | |
| 14 (67%)^a | | 10 (48%) | | |
| 4 (19%)^b | | | | |
| Non-Compliance | | | | |
| 3 (14%) | | 11 (52%) | | |

a Probe's concentration below the recommended in-cell maximum in all figures. *b* Probe's concentration below the recommended in-cell maximum in some, but not all figures.

Supplementary Note 6. Citations for AMG900 publications included in the systematic review.

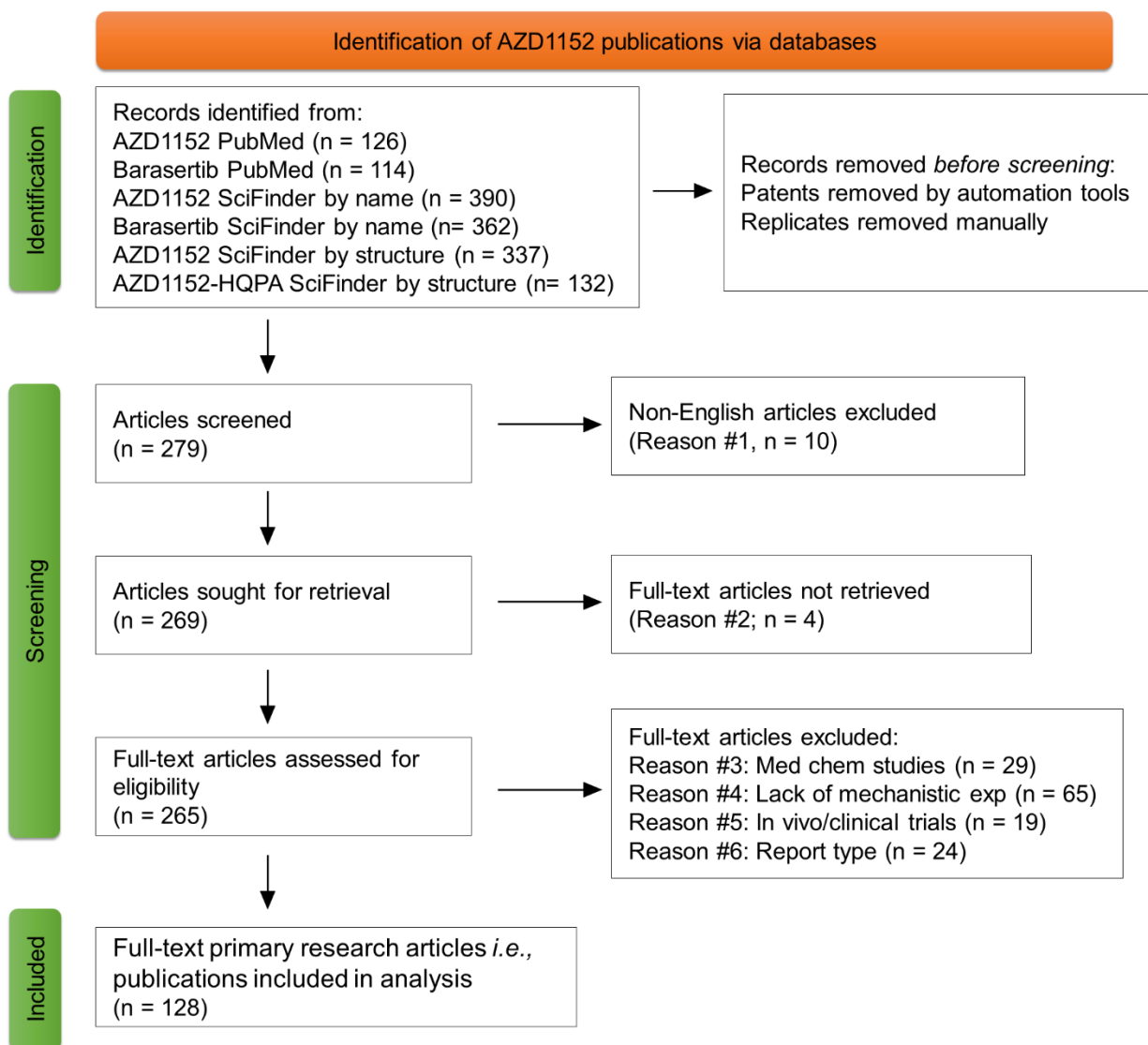
Citations for 21 publications using AMG900: 271

Citations for 18 publications with a compliant AMG900 concentration: 266

Citations for 3 publications with a non-compliant AMG900 concentration: 5

Citations for 10 publications using orthogonal Aurora kinase inhibitors: 40

Citations for 11 publications not using orthogonal Aurora kinase inhibitors: 231



Supplementary Figure 10. PRISMA flow diagram summarising identification of publications using Aurora kinases targeting chemical probe AZD1152.

Supplementary Table 11. List of excluded articles using the Aurora kinase probe AZD1152.

| | Title (PMID) | Reason for exclusion |
|----|--|--|
| 1 | Synthesis of Aurora-B kinase inhibitor AZD1152-HQPA (No PMID or DOI; ISSN: 1001-9677) | 1) Non-English |
| 2 | Inhibition effect of AZD1152-HQPA, a specific inhibitor of Aurora-B kinase, on human osteosarcoma cell line U2-OS cells (No PMID or DOI or ISSN, AN: 2011:420881) | 1) Non-English |
| 3 | Discovery of a novel hydrogen sulfide donor and the study of its structure activity relationship (No PMID; DOI: 10.16519/j.cnki.1004-311x.2018.02.0032) | 1) Non-English |
| 4 | The correlation between expression level of Aurora B and occurrence of cervical cancer (No PMID; DOI: 10.13417/j.gab.039.002367) | 1) Non-English |
| 5 | Localization and function of Aurora-B in pig (<i>Sus scrofa</i>) oocytes (No PMID; DOI: 10.3969/j.issn.1674-7968.2014.06.003) | 1) Non-English |
| 6 | Inhibitors of Aurora kinases (No PMID; DOI: 10.1016/j.pharma.2008.12.005) | 1) Non-English |
| 7 | Possibility of aurora kinase inhibitors for AML (No PMID or DOI; ISSN: 2185-582X) | 1) Non-English |
| 8 | Aurora kinase inhibitor (No PMID or DOI; ISSN: 0370-8241) | 1) Non-English |
| 9 | Management and novel drugs for older patients with acute myeloid leukemia (No PMID or DOI; ISSN: 2185-582X) | 1) Non-English |
| 10 | Effect of aurora kinase B inhibitor AZD1152 in the treatment of cisplatin-resistant ovarian carcinoma (PMID: 23531251) | 1) Non-English |
| 11 | Aurora kinase: A target for cancer therapy (No PMID or DOI; ISSN: 2230-9861) | 2) No access |
| 12 | In vitro sensitivity profiling of neuroblastoma cells against a comprehensive small molecule kinase inhibitor library to identify agents for future therapeutic studies (PMID: 27875952) | 2) No access |
| 13 | Exploring protein kinase inhibitors. Unveiling gemcitabine resistance in pancreatic cancer. Comments (No PMID; DOI: 10.1097/mpa.0b013e31823f3fcb) | 2) No access |
| 14 | Targeting Aurora kinases in cancer treatment (No PMID; DOI: 10.2174/138945011798829410) | 2) No access |
| 15 | Discovery, synthesis, and in vivo activity of a new class of pyrazoloquinazolines as selective inhibitors of aurora B kinase (PMID: 17373783) | 3) Discovery of AZD1152 |
| 16 | Structure-based drug design of novel aurora kinase A inhibitors: Structural basis for potency and specificity (PMID: 19140666) | 3) Medicinal Chemistry |
| 17 | Structure-based discovery and bioactivity evaluation of novel Aurora-A kinase inhibitors as anticancer agents via docking-based comparative intermolecular contacts analysis (dbCICA) (PMID: 33353031) | 3) Medicinal Chemistry |
| 18 | Epidermal growth factor receptor (EGFR) structure-based bioactive pharmacophore models for identifying next-generation inhibitors against clinically relevant EGFR mutations (PMID: 28303669) | 3) Medicinal Chemistry |
| 19 | Development of o-chlorophenyl substituted pyrimidines as exceptionally potent aurora kinase inhibitors (PMID: 22803810) | 3) Medicinal Chemistry |
| 20 | Quinazoline-benzimidazole hybrid as dual optical sensor for cyanide and Pb ²⁺ ions and Aurora kinase inhibitor (No PMID; DOI: 10.1016/j.jphotochem.2015.05.025) | 3) Medicinal Chemistry |
| 21 | Imidazo[4,5-b]pyridine derivatives as inhibitors of aurora kinases: Lead optimization studies toward the identification of an orally bioavailable preclinical development candidate (PMID: 20565112) | 3) Medicinal Chemistry |
| 22 | Facile identification of dual FLT3-Aurora A inhibitors: A computer-guided drug design approach (PMID: 24665000) | 3) Medicinal Chemistry |
| 23 | Identification of binding specificity-determining features in protein families (PMID: 22289061) | 3) Medicinal Chemistry |
| 24 | Discovery of SP-96, the first non-ATP-competitive Aurora kinase B inhibitor, for reduced myelosuppression (PMID: 32717530) | 3) Medicinal Chemistry |
| 25 | Identification of Aurora-A inhibitors by ligand and structure-based virtual screening (PMID: 27485892) | 3) Medicinal Chemistry |
| 26 | Discovery of <i>N</i> -(4-(3-(2-Aminopyrimidin-4-yl)pyridine-2-yloxy)phenyl)-4-(4-methylthiophen-2-yl)phthalazine-1-amine (AMG900), a highly selective, orally bioavailable inhibitor of Aurora kinases with activity against multidrug-resistant cancer cell lines (PMID: 25970324) | 3) Medicinal Chemistry – discovery of AMG900 |
| 27 | Ligand efficiency based approach for efficient virtual screening of compound libraries (PMID: 24960626) | 3) Medicinal Chemistry |

| | | |
|----|---|---|
| 28 | Selectivity data: Assessment, predictions, concordance, and implications (PMID: 23937569) | 3) Medicinal Chemistry |
| 29 | A specific pharmacophore model of Aurora B kinase inhibitors and virtual screening studies based on it (PMID: 19152640) | 3) Medicinal Chemistry |
| 30 | Structural studies of B-type Aurora kinase inhibitors using computational methods (PMID: 20139908) | 3) Medicinal Chemistry |
| 31 | Docking study and three-dimensional quantitative structure-activity relationship (3D-QSAR) analyses and novel molecular design of a series of 4-aminoquinazolines as inhibitors of Aurora B kinase (No PMID; DOI: 10.1002/cjoc.201180315) | 3) Medicinal Chemistry |
| 32 | Prediction of biological activity of Aurora-A kinase inhibitors by multilinear regression analysis and support vector machine (PMID: 21421314) | 3) Medicinal Chemistry |
| 33 | SAR and evaluation of novel 5 <i>H</i> -benzo[<i>c</i>][1,8]naphthyridine-6-one analogs as Aurora kinase inhibitors (PMID: 23570792) | 3) Medicinal Chemistry |
| 34 | Optimization and biological evaluation of nicotinamide derivatives as Aurora kinase inhibitors (PMID: 31307762) | 3) Medicinal Chemistry |
| 35 | Discovery of 7-aryl-substituted (1,5-naphthyridin-4-yl)ureas as Aurora kinase inhibitors (PMID: 24273104) | 3) Medicinal Chemistry |
| 36 | Discovery of selective aminothiazole Aurora kinase inhibitors (PMID: 18307303) | 3) Medicinal Chemistry |
| 37 | Probing the structural requirements of A-type Aurora kinase inhibitors using 3D-QSAR and molecular docking analysis (PMID: 21670994) | 3) Medicinal Chemistry |
| 38 | Analysis of kinase inhibitor selectivity using a thermodynamics-based partition index (PMID: 20459125) | 3) Medicinal Chemistry |
| 39 | Two-stage model-based design of cancer phase I dose escalation trials: evaluation using the phase I program of barasertib (AZD1152) (PMID: 21626115) | 3) Medicinal Chemistry |
| 40 | A novel cell-based, high-content assay for phosphorylation of Lats2 by Aurora A (PMID: 21788394) | 3) Medicinal Chemistry |
| 41 | Selective aurora kinase inhibitors identified using a taxol-induced checkpoint sensitivity screen (PMID: 21992004) | 3) Medicinal Chemistry |
| 42 | [14C]-AZD1152 drug substance manufacture: challenges of an IV-infusion dosed human mass balance study in patients (PMID: 27169761) | 3) Medicinal Chemistry |
| 43 | Discovery of novel GMPS inhibitors of <i>Candidatus Liberibacter Asiaticus</i> by structure based design and enzyme kinetics (PMID: 34203217) | 3) Medicinal Chemistry |
| 44 | RIPK1-dependent cell death: a novel target of the Aurora kinase inhibitor Tozasertib (VX-680) (PMID: 29434255) | 4) AZD-1152 not used |
| 45 | Biochemical characterization of GSK1070916, a potent and selective inhibitor of Aurora B and Aurora C kinases with an extremely long residence time (PMID: 19284385) | 4) AZD1152 not used in experiments |
| 46 | Preclinical Evaluation of AMG 900, a Novel Potent and Highly Selective Pan-Aurora Kinase Inhibitor with Activity in Taxane-Resistant Tumor Cell Lines (PMID: 20935223) | 4) AZD1152 used to generate resistant cell clones |
| 47 | Identification of genes that confer tumor cell resistance to the aurora B kinase inhibitor, AZD1152 (PMID: 19188929) | 4) AZD1152 used to generate resistant clones |
| 48 | Expression, purification, stability optimization and characterization of human Aurora B kinase domain from <i>E. coli</i> (PMID: 20699085) | 4) No mechanistic exp - focus on an Aurora B plasmid construct |
| 49 | CEP-32496: A novel orally active BRAF ^{V600E} inhibitor with selective cellular and in vivo antitumor activity (PMID: 22319199) | 4) No mechanistic exp with AZD1152 |
| 50 | Structure of Aurora B-INCENP in complex with barasertib reveals a potential trans-inhibitory mechanism (PMID: 24598913) | 4) No mechanistic exp - in silico study |
| 51 | Target inhibition networks: Predicting selective combinations of druggable targets to block cancer survival pathways (PMID: 24068907) | 4) No mechanistic exp - model-based prediction approach to drug discovery |
| 52 | A novel in situ hydrophobic ion pairing (HIP) formulation strategy for clinical product selection of a nanoparticle drug delivery system (PMID: 27001894) | 4) No mechanistic exp - nanoparticle delivery of AZD1152-HQPA |
| 53 | Measuring the rate of in-vitro drug release from polymeric nanoparticles by ¹⁹ F solution state NMR spectroscopy (PMID: 34400184) | 4) No mechanistic exp -- nanoparticle study |
| 54 | Evaluation of particle size techniques to support the development of manufacturing scale nanoparticles for application in pharmaceuticals (PMID: 32278922) | 4) No mechanistic exp - nanoparticle study |
| 55 | A quantitative analysis of kinase inhibitor selectivity (PMID: 18183025) | 4) No in-cell exp |

| | | |
|----|---|--|
| 56 | Chemical signatures and new drug targets for gametocytocidal drug development (PMID: 24434750) | 4) No mechanistic exp |
| 57 | CCT245718, a dual FLT3/Aurora A inhibitor overcomes D835Y-mediated resistance to FLT3 inhibitors in acute myeloid leukemia cells (PMID: 34446858) | 4) No mechanistic exp |
| 58 | A theoretical entropy score as a single value to express inhibitor selectivity (PMID: 21486481) | 4) No mechanistic exp |
| 59 | A new approach for prediction of tumor sensitivity to targeted drugs based on functional data (PMID: 23890326) | 4) No mechanistic exp |
| 60 | QSAR modelling of SARS-CoV M ^{pro} inhibitors identifies Sufugolix, Cenicriviroc, Proglumetacin, and other drugs as candidates for repurposing against SARS-CoV-2 (PMID: 33405340) | 4) No mechanistic exp |
| 61 | Explainable artificial intelligence for precision medicine in acute myeloid leukemia (PMID: 36248800) | 4) No mechanistic exp |
| 62 | Computationally predicting clinical drug combination efficacy with cancer cell line screens and independent drug action (PMID: 33203866) | 4) No mechanistic exp |
| 63 | Butyrophilin-like 9 expression is associated with outcome in lung adenocarcinoma (PMID: 34635082) | 4) No mechanistic exp |
| 64 | Machine learning models for the prediction of chemotherapy-induced peripheral neuropathy (PMID: 30617559) | 4) No mechanistic exp |
| 65 | Combining machine learning systems and multiple docking simulation packages to improve docking prediction reliability for network pharmacology (PMID: 24391846) | 4) No mechanistic exp |
| 66 | Using a gene network of pyroptosis to quantify the responses to immunotherapy and prognosis for neuroblastoma patients (PMID: 35401536) | 4) No mechanistic exp |
| 67 | A molecular case report: Functional assay of tyrosine kinase inhibitors in cells from a patient's primary renal cell carcinoma (PMID: 23192268) | 4) No mechanistic exp |
| 68 | Inhibition of Aurora-B kinase activity confers antitumor efficacy in preclinical mouse models of early and advanced gastrointestinal neoplasia (PMID: 22858681) | 4) No mechanistic exp – dose response in viability assays only |
| 69 | Aurora B kinase as a therapeutic target in acute lymphoblastic leukemia (PMID: 32144432) | 4) No mechanistic exp - Kinase inhibitor viability screen: 20-200 nM |
| 70 | Kinase pathway dependence in primary human leukemias determined by rapid inhibitor screening (PMID: 23087056) | 4) No mechanistic exp - Viability screen |
| 71 | Aneugen molecular mechanism assay: Proof-of-concept with 27 reference chemicals (PMID: 31132080) | 4) No mechanistic exp – toxicology study |
| 72 | IL15 agonists overcome the immunosuppressive effects of MEK inhibitors (PMID: 26980764) | 4) No mechanistic exp with AZD1152 |
| 73 | Profiling pathway-specific novel therapeutics in preclinical assessment for central nervous system atypical teratoid rhabdoid tumors (CNS ATRT): Favorable activity of targeting EGFR-ErbB2 signaling with lapatinib (PMID: 23375777) | 4) No mechanistic exp - dose-response viability screen with AZD1152 |
| 74 | JAK1/2 and BCL2 inhibitors synergize to counteract bone marrow stromal cell-induced protection of AML (PMID: 28619982) | 4) No mechanistic exp with AZD1152-HQPA |
| 75 | Identification of selective cytotoxic and synthetic lethal drug responses in triple negative breast cancer cells (PMID: 27165605) | 4) No mechanistic exp with AZD1152-HQPA |
| 76 | A high content clonogenic survival drug screen identifies MEK inhibitors as potent radiation sensitizers for KRAS mutant non-small-cell lung cancer (PMID: 24922006) | 4) No mechanistic exp with AZD1152-HQPA |
| 77 | Ex vivo drug response profiling detects recurrent sensitivity patterns in drug-resistant acute lymphoblastic leukemia (PMID: 28122742) | 4) No mechanistic exp with AZD1152-HQPA |
| 78 | System-level analysis of neuroblastoma tumor-initiating cells implicates AURKB as a novel drug target for neuroblastoma (PMID: 20651058) | 4) No mechanistic exp with AZD1152 |
| 79 | Comprehensive analysis of kinase inhibitor selectivity (PMID: 22037378) | 4) No mechanistic exp |
| 80 | A cell cycle progression-derived gene signature to predict prognosis and therapeutic response in hepatocellular carcinoma (PMID: 34721731) | 4) No mechanistic exp |
| 81 | RUNX1 mutations in blast-phase chronic myeloid leukemia associate with distinct phenotypes, transcriptional profiles, and drug responses (PMID: 32782381) | 4) No mechanistic exp |
| 82 | Pan-transcriptome-based candidate therapeutic discovery for idiopathic pulmonary fibrosis (PMID: 33167785) | 4) No mechanistic exp – analyses of gene expression signatures |
| 83 | BCL-XL blockage in TNBC models confers vulnerability to inhibition of specific cell cycle regulators (PMID: 34646365) | 4) No mechanistic exp with AZD1152-HQPA |

| | | |
|-----|---|--|
| 84 | Sarcoma cell line screen of oncology drugs and investigational agents identifies patterns associated with gene and microRNA expression (PMID: 26351324) | 4) No mechanistic exp with AZD1152-HQPA |
| 85 | Synthetic lethal interaction between the ESCRT paralog enzymes VPS4A and VPS4B in cancers harboring loss of chromosome 18q or 16q (PMID: 33326793) | 4) No mechanistic exp with AZD1152-HQPA |
| 86 | Epigenome-wide DNA methylation analysis of small cell lung cancer cell lines suggests potential chemotherapy targets (PMID: 32586373) | 4) No mechanistic exp - dose-response viability only |
| 87 | Aurora kinases in childhood acute leukemia: the promise of aurora B as therapeutic target (PMID: 22940834) | 4) No mechanistic exp - dose-response viability only |
| 88 | Identifying cancer driver genes from functional genomics screens (PMID: 32083704) | 4) No mechanistic exp - dose-response viability only |
| 89 | Aurora kinase B expression, its regulation and therapeutic targeting in human retinoblastoma (PMID: 33704359) | 4) No mechanistic exp - dose-response viability only |
| 90 | Imaging colon cancer response following treatment with AZD1152: a preclinical analysis of [18F]fluoro-2-deoxyglucose and 3'-deoxy-3'-[18F]fluorothymidine imaging (PMID: 21245090) | 4) No mechanistic exp - dose-response viability only |
| 91 | The target landscape of clinical kinase drugs (PMID: 29191878) | 4) No mechanistic exp - kinobead profiling |
| 92 | Optimizing therapeutic effect of Aurora b inhibition in acute myeloid leukemia with AZD2811 nanoparticles (PMID: 28292940) | 4) No mechanistic exp - nanoparticle delivery |
| 93 | Visualization of the distribution of nanoparticle-formulated AZD8211 in mouse tumour model using matrix-assisted laser desorption ionization mass spectrometry imaging (PMID: 32968211) | 4) No mechanistic exp - nanoparticle delivery |
| 94 | Multi-modal molecular imaging maps the correlation between tumor microenvironments and nanomedicine distribution (PMID: 35265205) | 4) No mechanistic exp - nanoparticle delivery |
| 95 | Real-time luminescence enables continuous drug-response analysis in adherent and suspension cell lines (PMID: 35443861) | 4) No mechanistic exp with AZD1152-HQPA |
| 96 | Data-driven exploration of selectivity and off-target activities of designated chemical probes (PMID: 30249057) | 4) No mechanistic exp - qualifying chemical probes |
| 97 | Activity comparison of epigenetic modulators against the Hemoprotozoan parasite Babesia divergens and Plasmodium falciparum (PMID: 33599488) | 4) No mechanistic exp. - Parasites growth |
| 98 | In vitro and in vivo evaluation of kinase and protease inhibitors against Trypanosoma evansi (PMID: 35751782) | 4) No mechanistic exp. - Parasites growth |
| 99 | Multiparametric cell-based assay for the evaluation of transcription inhibition by high-content imaging (PMID: 23307837) | 4) No mechanistic exp with AZD1152 |
| 100 | Predicting cell health phenotypes using image-based morphology profiling (PMID: 33534641) | 4) No mechanistic exp – HTS image-based cell viability |
| 101 | Analytical method considerations regarding carryover for monophosphate prodrugs for in vivo samples by liquid chromatography-tandem mass spectroscopy (PMID: 31395357) | 4) No mechanistic exp |
| 102 | High-throughput compound screening identifies navitoclax combined with irradiation as a candidate therapy for HPV-negative head and neck squamous cell carcinoma (PMID: 34285300) | 4) No mechanistic exp with AZD1152-HQPA |
| 103 | A panel of isogenic human cancer cells suggests a therapeutic approach for cancers with inactivated p53 (PMID: 19225112) | 4) No mechanistic exp with AZD1152 |
| 104 | Combined inhibition of XIAP and BCL2 drives maximal therapeutic efficacy in genetically diverse aggressive acute myeloid leukemia (PMID: 35121960) | 4) No mechanistic exp with AZD1152-HQPA |
| 105 | Integrative oncogene-dependency mapping identifies RIT1 vulnerabilities and synergies in lung cancer (PMID: 34373451) | 4) No mechanistic exp with AZD1152-HQPA |
| 106 | Patient-derived models of acquired resistance can identify effective drug combinations for cancer (PMID: 25394791) | 4) No mechanistic exp with AZD1152-HQPA |
| 107 | Viability fingerprint of glioblastoma cell lines: Roles of mitotic, proliferative, and epigenetic targets (PMID: 34645858) | 4) No mechanistic exp with AZD1152-HQPA |
| 108 | Targeting vcp enhances anticancer activity of oncolytic virus m1 in hepatocellular carcinoma (PMID: 28835517) | 4) No mechanistic exp with AZD1152-HQPA |

| | | |
|-----|---|----------------------|
| 109 | Experiments in the EpiDerm 3D skin in vitro model and minipigs in vivo indicate comparatively lower in vivo skin sensitivity of topically applied aneugenic compounds (PMID: 33481035) | 5) Clinical study |
| 110 | Clinical evaluation of AZD1152, an i.v. inhibitor of Aurora B kinase, in patients with solid malignant tumors (PMID: 20924078) | 5) Clinical trial |
| 111 | A Phase I study to assess the safety, pharmacokinetics and efficacy of barasertib (AZD1152), an Aurora B kinase inhibitor, in Japanese patients with advanced acute myeloid leukemia (PMID: 21565405) | 5) Clinical trial |
| 112 | Phase 1/2 study to assess the safety, efficacy, and pharmacokinetics of barasertib (AZD1152) in patients with advanced acute myeloid leukemia: (PMID: 21976672) | 5) Clinical trial |
| 113 | Phase I study of barasertib (AZD1152), a selective inhibitor of Aurora B kinase, in patients with advanced solid tumors (PMID: 22661287) | 5) Clinical trial |
| 114 | Phase I study of the Aurora B kinase inhibitor barasertib (AZD1152) to assess the pharmacokinetics, metabolism and excretion in patients with acute myeloid leukemia (PMID: 22864876) | 5) Clinical trial |
| 115 | Stage I of a phase 2 study assessing the efficacy, safety, and tolerability of barasertib (AZD1152) versus low-dose cytosine arabinoside in elderly patients with acute myeloid leukemia (PMID: 23605952) | 5) Clinical trial |
| 116 | Phase I study assessing the safety and tolerability of barasertib (AZD1152) with low-dose cytosine arabinoside in elderly patients with AML (PMID: 23763917) | 5) Clinical trial |
| 117 | A phase II trial of AZD1152 in relapsed/refractory diffuse large B-cell lymphoma (PMID: 25721307) | 5) Clinical trial |
| 118 | Biomarker-driven phase 2 umbrella trial study for patients with recurrent small cell lung cancer failing platinum-based chemotherapy (PMID: 32584426) | 5) Clinical trial |
| 119 | A comparative assessment of preclinical chemotherapeutic response of tumors using quantitative non-Gaussian diffusion MRI (PMID: 27919785) | 5) In vivo study |
| 120 | Simultaneous determination of AZD1152 (prodrug) and AZD1152-hydroxyquinazoline pyrazol anilide by reversed phase liquid chromatography (PMID: 19744901) | 5) In vivo study |
| 121 | The MEK1/2 inhibitor, selumetinib (AZD6244; ARRY-142886), enhances anti-tumour efficacy when combined with conventional chemotherapeutic agents in human tumour xenograft models (PMID: 22343622) | 5) In vivo study |
| 122 | Characterizing Tumor Response to Chemotherapy at Various Length Scales Using Temporal Diffusion Spectroscopy (PMID: 22911846) | 5) In vivo study |
| 123 | Aurora kinase inhibitor nanoparticles target tumors with favorable therapeutic index in vivo (PMID: 26865565) | 5) In vivo study |
| 124 | Salivary glands require Aurora Kinase B for regeneration after transient innate immune-mediated injury (PMID: 31383943) | 5) In vivo study |
| 125 | Modeling Dose and Schedule Effects of AZD2811 Nanoparticles Targeting Aurora B Kinase for Treatment of Diffuse Large B-cell Lymphoma (PMID: 30872381) | 5) In vivo study |
| 126 | Targeting aurora kinase B alleviates spinal microgliosis and neuropathic pain in a rat model of peripheral nerve injury (PMID: 31563141) | 5) In vivo study |
| 127 | Aurora-B knockdown inhibits osteosarcoma metastasis by inducing autophagy via the mTOR/ULK1 pathway (PMID: 33292257) | 5) In vivo study |
| 128 | Aurora kinase inhibitor AZD1152 negatively affects the growth and survival of HTLV-1-infected T lymphocytes in vitro [Retraction of document cited in CA154:351346] (No PMID; DOI: 10.1002/ijc.25178) | 6) Retracted |
| 129 | Phosphoproteomic analysis of Aurora kinase inhibition in monopolar cytokinesis [Erratum to document cited in CA163327364] (PMID: 26561005) | 6) Erratum |
| 130 | Correction: Bromodomain and extraterminal protein inhibition blocks growth of triple-negative breast cancers through the suppression of aurora kinases [Erratum to document cited in CA165:569636] (PMID: 32620694) | 6) Erratum |
| 131 | Effects of AZD1152, a selective Aurora B kinase inhibitor, on Burkitt's and Hodgkin's lymphomas [Erratum to document cited in CA154:556930] (No PMID; DOI: 10.1016/j.bcp.2011.07.098) | 6) Erratum |
| 132 | Therapeutic polymeric nanoparticles and the methods of making and using thereof: a patent evaluation of WO2015036792 (PMID: 27167102) | 6) Patent evaluation |
| 133 | Aurora kinase inhibitor AZD1152 negatively affects the growth and survival of HTLV-1-infected T lymphocytes in vitro (PMID: 20091867) | 6) Retracted |
| 134 | RETRACTED ARTICLE: Frequency of TP53 Mutations and its Impact on Drug Sensitivity in Acute Myeloid Leukemia? (PMID: 23543587) | 6) Retracted |

| | | |
|-----|---|-------------------------|
| 135 | Design strategies, SAR, and mechanistic insight of Aurora kinase inhibitors in cancer (PMID: 33934503) | 6) Review |
| 136 | Kinase Inhibitor 4 Minisymposium summary (PMID: 19589028) | 6) Review |
| 137 | Aurora kinase inhibitors as anti-cancer therapy (PMID: 20016367) | 6) Review |
| 138 | Novel agents and regimens for acute myeloid leukemia: 2009 ASH annual meeting highlights (PMID: 20416083) | 6) Review |
| 139 | Aurora kinase inhibitor patents and agents in clinical testing: an update (2011 - 2013) (PMID: 24965505) | 6) Review |
| 140 | Finding the optimal combination therapy for the treatment of newly diagnosed AML in older patients unfit for intensive therapy (PMID: 25577399) | 6) Review |
| 141 | Structural Biology Insight for the Design of Sub-type Selective Aurora Kinase Inhibitors (PMID: 25895501) | 6) Review |
| 142 | Aurora Kinase Inhibitors in Oncology Clinical Trials: Current State of the Progress (PMID: 26615129) | 6) Review |
| 143 | Advances in targeted therapy for osteosarcoma based on molecular classification (PMID: 34022396) | 6) Review |
| 144 | Are Accurins the cure for Aurora kinase inhibitors? (PMID: 26865564) | 6) Review |
| 145 | Novel drugs for older patients with acute myeloid leukemia (PMID: 25142817) | 6) Review |
| 146 | Targeting pan-essential genes in cancer: Challenges and opportunities (PMID: 33450197) | 6) Review |
| 147 | Aurora kinase inhibitors: a new class of drugs targeting the regulatory mitotic system (PMID: 20045785) | 6) Review |
| 148 | Emerging role of Aurora kinase inhibitors in chronic myeloid leukemia (No PMID; DOI: 10.3816/CLK.2007.n.025) | 6) Review |
| 149 | Aurora kinase inhibitors: Potential molecular-targeted drugs for gynecological malignant tumours (review) (PMID: 31798873) | 6) Review |
| 150 | SnapShot: Kinase inhibitors II (PMID: 26000855) | 6) Snapshot |
| 151 | NPM-ALK expression levels identify two distinct subtypes of pediatric anaplastic large cell lymphoma (PMID: 27773932) | 6) Letter to the editor |

Supplementary Table 12. Overview of eligible publications using Aurora kinase probe AZD1152 and compliance (in blue) with recommendations to use AZD1152 up to 100 nM (<https://www.chemicalprobes.org/azd1152?q=AZD1152>) and validate results with at least one orthogonal inhibitor.

| | AZD1152 | Orthogonal inhibitors | Title (PMID) | Cites |
|----|----------------|-----------------------------|--|-------|
| 1 | 75 pM - 300 pM | None | Aurora B expression modulates paclitaxel response in non-small cell lung cancer (PMID: 28095398) | 29 |
| 2 | 0.1 nM | None | Dicer promotes genome stability via the bromodomain transcriptional co-activator BRD4 (PMID: 35194019) | 2 |
| 3 | 0.5 - 25 nM | None | Overcoming cetuximab resistance in HNSCC: the role of AURKB and DUSP proteins (PMID: 25192874) | 44 |
| 4 | 2 nM - 63 nM | GSK1070916 (20 nM) | High-throughput chemical screening identifies focal adhesion kinase and Aurora kinase B inhibition as a synergistic treatment combination in Ewing sarcoma (PMID: 30979745) | 20 |
| 5 | 2 - 100 nM | None | AZD1152 negatively affects the growth of anaplastic thyroid carcinoma cells and enhances the effects of oncolytic virus dl922-947 (PMID: 21071467) | 31 |
| 6 | 2.5 nM - 40 nM | None | Significance of AZD1152 as a potential treatment against Aurora B overexpression in acute promyelocytic leukemia (PMID: 27091351) | 10 |
| 7 | 3 nM - 3 μM | None | Preclinical evaluation of M30 and M65 ELISAs as biomarkers of drug induced tumor cell death and antitumor activity (PMID: 18347133) | 52 |
| 8 | 5 - 20 nM | None | RING1B recruits EWSR1-FLI1 and cooperates in the remodeling of chromatin necessary for Ewing sarcoma tumorigenesis (PMID: 33097530) | 13 |
| 9 | 10 nM | None | Modeling the mitotic regulatory network identifies highly efficient anti-cancer drug combinations (PMID: 25418836) | 2 |
| 10 | 10 - 50 nM | None | Vitamins C and K3: A powerful redox system for sensitizing leukemia lymphocytes to everolimus and barasertib (PMID: 29491065) | 11 |
| 11 | 10 - 50 nM | None | Docosahexaenoic acid sensitizes leukemia lymphocytes to barasertib and everolimus by ROS-dependent mechanism without affecting the level of ROS and viability of normal lymphocytes (PMID: 27069145) | 18 |
| 12 | 10 - 50 nM | None | 2-Deoxy-D-glucose sensitizes cancer cells to barasertib and everolimus by ROS-independent mechanism(s) (PMID: 26637878) | 9 |
| 13 | 20 - 100 nM | None | Aurora B kinase regulates the postmitotic endoreduplication checkpoint via phosphorylation of the retinoblastoma protein at serine 780. (PMID: 19225156) | 73 |
| 14 | 50 nM | JNJ-7706621 (500 - 1500 nM) | Aurora kinase B is important for antiestrogen resistant cell growth and a potential biomarker for tamoxifen resistant breast cancer (PMID: 25885472) | 20 |
| 15 | 50 nM - 1 μM | MLN8237 (10 nM- 1 μM) | Selective inhibitors of aurora kinases inhibit proliferation, reduce cell viability and impair cell cycle progression in papillary thyroid carcinoma cells (PMID: 26753639) | 6 |
| 16 | 50 nM & 1 μM | JNJ-7706621 (0.5 - 1.5 μM) | Aurora kinase A and B as new treatment targets in aromatase inhibitor-resistant breast cancer cells (PMID: 25667100) | 29 |
| 17 | 60 nM | None | Enhanced radiosensitivity of androgen-resistant prostate cancer: AZD1152-mediated Aurora kinase B inhibition (PMID: 21222513) | 25 |
| 18 | 60 nM | None | Close correlation between MEK/ERK and Aurora-B signaling pathways in sustaining tumorigenic potential and radioresistance of gynecological cancer cell lines (PMID: 24189697) | 35 |

| | | | | |
|----|---------------------|--|--|----|
| 19 | 100 nM | None | Enhancing functional platelet release in vivo from in vitro-grown megakaryocytes using small molecule inhibitors (PMID: 29545255) | 14 |
| 20 | 100 nM | None | A novel therapeutic combination sequentially targeting Aurora B and Bcl-xL in hepatocellular carcinoma (PMID: 25524010) | 8 |
| 21 | 100 nM | MLN8237 (250 nM) | Bromodomain and extraterminal protein inhibition blocks growth of triple-negative breast cancers through the suppression of aurora kinases (PMID: 27650498) | 41 |
| 22 | 100 nM | MLN8237 (50 nM) | Chromosome oscillation promotes Aurora A-dependent Hec1 phosphorylation and mitotic fidelity (PMID: 33988677) | 10 |
| 23 | 100 nM | MLN8237 (100 nM), Scoulerine (2-20 μ M) | The phytochemical Scoulerine inhibits Aurora kinase activity to induce mitotic and cytokinetic defects (PMID: 34406008) | 4 |
| 24 | 100 nM - 1 μ M | MLN8237 (250 nM) | Effects of selective inhibitors of Aurora kinases on anaplastic thyroid carcinoma cell lines (PMID: 25074669) | 24 |
| 25 | 0.1 - 10 μ M | MLN8237 (0.5-10 μ M), ZM447439 (1 - 20 μ M) | A field guide to Aurora kinase inhibitors: an oocyte perspective (PMID: 36125382) | 0 |
| 26 | 200 nM | MLN8054 (250 nM) VX-680 (1000 nM) | Inhibition of Aurora B kinase sensitizes a subset of human glioma cells to TRAIL concomitant with induction of TRAIL-R2 (PMID: 19079141) | 26 |
| 27 | 200 nM | None | CNOT3 interacts with the Aurora B and MAPK/ERK kinases to promote survival of differentiating mesendodermal progenitor cells (PMID: 34613789) | 0 |
| 28 | 200 nM | VX680 (0.001-10 μ M), MLN8054 (0.001-5 μ M) | Bcl-XL represents a druggable molecular vulnerability during aurora B inhibitor-mediated polyploidization (PMID: 20616035) | 34 |
| 29 | 0.2 - 5 μ M | MLN8237 (100 nM - 5 μ M), LY3285668 (1 nM - 5 μ M) | Aurora A-selective inhibitor LY3295668 leads to dominant mitotic arrest, apoptosis in cancer cells, and shows potent preclinical antitumour efficacy (PMID: 31530649) | 21 |
| 30 | 250 nM - 1 μ M | MLN8237 (5 nM - 2 μ M) | Preclinical testing of selective Aurora kinase inhibitors on a medullary thyroid carcinoma-derived cell line (PMID: 26215279) | 5 |
| 31 | 400 nM | None | Histone H3 phosphorylation in GBM: a new rational to guide the use of kinase inhibitors in anti-GBM therapy (PMID: 25553095) | 21 |
| 32 | 500 nM - 10 μ M | None | AURKB promotes gastric cancer progression via activation of CCND1 expression (PMID: 31982864) | 24 |
| 33 | 0.5 - 50 μ M | None | Paradoxical implication of BAX/BAK in the persistence of tetraploid cells (PMID: 34725331) | 1 |
| 34 | 1 μ M | None | Aurora kinase B regulates axonal outgrowth and regeneration in the spinal motor neurons of developing zebrafish (PMID: 29468257) | 12 |
| 35 | 1 μ M | VX680 (400 nM) | Phosphoproteomic analysis of Aurora kinase inhibition in monopolar cytokinesis (PMID: 26270265) | 9 |
| 36 | 1 μ M | None | Aurora B induces epithelial-mesenchymal transition by stabilizing Snail1 to promote basal-like breast cancer metastasis (PMID: 31996785) | 7 |
| 37 | 1 μ M | MLN8237, SNS-314, AT9283, VX680, PHA-739358, PHA-680632, CYC116, CCT129202, ZM447439, JNJ-7706621, ENMD-2076, Aurora A Inhibitor 1 (1 μ M) | Aurora kinases as druggable targets in pediatric leukemia: Heterogeneity in target modulation activities and cytotoxicity by diverse novel therapeutic agents (PMID: 25048812) | 13 |

| | | | | |
|--|--|---|--|-----|
| | | hesperidin (0.1 - 1 μ M) | | |
| 38 | 3 - 7 μ M | None | Phosphorylation of histone H3 on Ser-10 by Aurora B is essential for chromosome condensation in porcine embryos during the first mitotic division (PMID: 28220245) | 5 |
| 39 | 5 μ M | ZM447439, MLN8054 (both 5 μ M) | Aurora B and C kinases regulate chromosome desynapsis and segregation during mouse and human spermatogenesis (PMID: 33172986) | 13 |
| 40 | 12.5 - 100 μ g/ml (21.3 - 170.3 μ M) | GSK-1070916, Hesperadin | Leishmania donovani Aurora kinase: A promising therapeutic target against visceral leishmaniasis (PMID: 27288586) | 12 |
| 41 | Unclear | MLN8237 (unclear), ZM447439 (0.25 - 4 μ M) | Evolution of resistance to Aurora kinase B inhibitors in leukemia cells (PMID: 22359551) | 11 |
| AZD1152-HQPA Orthogonal inhibitors Title (PMID) | | | | |
| 42 | 0.05 nM - 500 nM | AMG900 (0.01 - 100 nM), hesperadin (1 nM - 10 μ M) | A new imaging platform (iScreen) allows for the concurrent assessment of micronucleus induction and genotoxic mode of action in human A375 cells (PMID: 35703118) | 0 |
| 43 | 0.1 - 100 nM | MLN8237 (0.1 - 100 nM) | Suv420 enrichment at the centromere limits Aurora B localization and function (PMID: 34342353) | 3 |
| 44 | 0.3 nM - 150 nM | None | Aurora B kinase phosphorylates and instigates degradation of p53 (PMID: 22611192) | 117 |
| 45 | 0.5 nM - 200 nM | MLN8054, VX-680, MLN8237, MK-5108, MK-8745, ZM447439, hesperadin, GSK1070916 | A cell biologist's field guide to Aurora kinase inhibitors (PMID: 26732741) | 55 |
| 46 | 0.5 nM - 500 nM | None | Effects of AZD1152, a selective Aurora B kinase inhibitor, on Burkitt's and Hodgkin's lymphomas (PMID: 21371446) | 17 |
| 47 | 0.5 nM - 500 nM | Alisertib (0.5 - 500 nM) | Selective inhibition of Aurora A and B kinases effectively induces cell cycle arrest in t(8;21) acute myeloid leukemia (PMID: 31207577) | 6 |
| 48 | 500 pM - 1 μ M | AMG900, MK-5108 (0.5 - 1000 nM) | Preclinical evaluation of the Aurora kinase inhibitors AMG 900, AZD1152-HQPA, and MK-5108 on SW-872 and 93T449 human liposarcoma cells (PMID: 29197031) | 5 |
| 49 | 0.74 nM | Aurora A Inhibitor (6.8 nM), hesperidin (500 nM), JNJ-7706621 (18 nM), GSK1070916 (13 nM), ZM447439 (260 nM), PHA-680632 (270 nM) | Screening of compounds to identify novel epigenetic regulatory factors that affect innate immune memory in macrophages (PMID: 35115604) | 3 |
| 50 | 1 nM | None | Indomethacin promotes apoptosis in gastric cancer cells through concomitant degradation of Survivin and Aurora B kinase proteins (PMID: 24874838) | 13 |
| 51 | 1 nM | MLN8237 (5 nM) VX680 (2.5 nM) | The Aurora-kinase A Phe31-Ile polymorphism as possible predictor of response to treatment in head and neck squamous cell carcinoma (PMID: 29560108) | 6 |
| 52 | 1 - 10 nM | None | AZD1152, a novel and selective aurora B kinase inhibitor, induces growth arrest, apoptosis, and sensitization for tubulin depolymerizing agent or topoisomerase II inhibitor in human acute leukemia cells in vitro and in vivo (PMID: 17495131) | 217 |
| 53 | 1 - 100 nM | None | The selective Aurora B kinase inhibitor AZD1152 as a novel treatment for hepatocellular carcinoma (PMID: 19913935) | 53 |

| | | | | |
|----|---------------|---|--|----|
| 54 | 1 nM - 125 nM | None | Significance of Aurora B overexpression in hepatocellular carcinoma. Aurora B Overexpression in HCC. (PMID: 20799978) | 93 |
| 55 | 1 nM - 500 nM | None | The selective Aurora B kinase inhibitor AZD1152 is a potential new treatment for multiple myeloma (PMID: 18076711) | 50 |
| 56 | 2 nM - 30 µM | MLN8237 (0.1 - 0.5 µM), MK-5108 (5 nM - 33 µM), GSK1070916, VX680, PHA-739358 (5 nM-11.1 µM) | Loss of Aurora kinase signaling allows lung cancer cells to adopt endoreplication and form polyploid giant cancer cells that resist antimetabolic drugs (PMID: 33172929) | 13 |
| 57 | 2 nM - 100 nM | None | Barasertib (AZD1152), a small molecule Aurora B inhibitor, inhibits the growth of SCLC cell lines in vitro and in vivo (PMID: 27496133) | 57 |
| 58 | 3 - 100 nM | None | p53 is critical for the Aurora B kinase inhibitor-mediated apoptosis in acute myelogenous leukemia cells (PMID: 20013323) | 24 |
| 59 | 3 nM - 30 µM | None | Aurora B kinase inhibitor AZD1152: determinants of action and ability to enhance chemotherapeutics effectiveness in pancreatic and colon cancer (PMID: 21304529) | 49 |
| 60 | 4 nM - 5 µM | VX680, CYC116, ENMD-2076, MLN8054, PHA-739358 (all 0-5 µM) | A robust high-content imaging approach for probing the mechanism of action and phenotypic outcomes of cell-cycle modulators (PMID: 21216932) | 24 |
| 61 | 5 - 10 nM | None | Aurora kinase B inhibitor barasertib (AZD1152) inhibits glucose metabolism in gastric cancer cells (PMID: 30540594) | 7 |
| 62 | 5 - 100 nM | None | Inhibiting the Aurora B kinase potently suppresses repopulation during fractionated irradiation of human lung cancer cell lines (PMID: 22381900) | 20 |
| 63 | 5 - 500 nM | None | AZD1152-HQPA induces growth arrest and apoptosis in androgen-dependent prostate cancer cell line (LNCaP) via producing aneuploidy and polyploidy (PMID: 25277659) | 12 |
| 64 | 5 - 500 nM | None | Reactive oxygen species generation and increase in mitochondrial copy number: new insight into the potential mechanism of cytotoxicity induced by aurora kinase inhibitor, AZD1152-HQPA (PMID: 28639950) | 14 |
| 65 | 6.25 - 100 nM | MK5108, ZM447439 (both 250 nM - 10 µM), MLN8237 (50 - 1 µM) | P53 deficiency enhances mitotic arrest and slippage induced by pharmacological inhibition of Aurora kinases (PMID: 23955083) | 50 |
| 66 | 8 - 1000 nM | AMG900, MLN8237, CYC-116, SNS-314, PHA-739358, ENMD-984693, VX680, JNJ-7706621 (10 pM - 100 µM) | Aurora B kinase is a potent and selective target in MYCN-driven neuroblastoma (PMID: 26497213) | 35 |
| 67 | 10 nM | None | Epithelial cell transforming 2 and Aurora kinase B modulate formation of stress granule-containing transcripts from diverse cellular pathways in astrocytoma cells (PMID: 27106762) | 7 |
| 68 | 10 nM | VX680 (1 µM) | A mixed modality approach towards Xi reactivation for Rett syndrome and other X-linked disorders (PMID: 29282321) | 47 |

| | | | | |
|----|----------------|--|---|----|
| 69 | 10 - 20 nM | None | Aurora kinase inhibitor AZD1152 has an additional effect of platinum on a sequential application at the human ovarian cancer cell line SKOV3 (PMID: 23389245) | 8 |
| 70 | 10 - 50 nM | None | Divergent polypharmacology-driven cellular activity of structurally similar multi-kinase inhibitors through cumulative effects on individual targets (PMID: 31257184) | 10 |
| 71 | 10 - 50 nM | None | Inhibition of the pentose-phosphate pathway selectively sensitizes leukemia lymphocytes to chemotherapeutics by ROS-independent mechanism (PMID: 27793928) | 11 |
| 72 | 10 - 50 nM | None | Resveratrol modulates the redox-status and cytotoxicity of anticancer drugs by sensitizing leukemic lymphocytes and protecting normal lymphocytes (PMID: 31262901) | 14 |
| 73 | 10 - 50 nM | None | Synergistic cytotoxicity of melatonin and new-generation anticancer drugs against leukemia lymphocytes but not normal lymphocytes (PMID: 28011485) | 27 |
| 74 | 10 - 50 nM | Everolimus (5 μ M) | Effect of alpha-tocopheryl succinate on the cytotoxicity of anticancer drugs towards leukemia lymphocytes (PMID: 34969764) | 0 |
| 75 | 10 - 100 nM | None | The Aurora B kinase inhibitor AZD1152 sensitizes cancer cells to fractionated irradiation and induces mitotic catastrophe (PMID: 19755861) | 43 |
| 76 | 10 - 100 nM | None | The FLT3 internal tandem duplication mutation is a secondary target of the aurora B kinase inhibitor AZD1152-HQPA in acute myelogenous leukemia cells (PMID: 20159992) | 32 |
| 77 | 10 - 100 nM | MK-5108 (250 nM) | Co-inhibition of polo-like kinase 1 and Aurora kinases promotes mitotic catastrophe (PMID: 25871386) | 15 |
| 78 | 10 - 100 nM | None | Inhibition of Aurora-B suppresses osteosarcoma cell migration and invasion (PMID: 24520245) | 21 |
| 79 | 10 - 100 nM | None | The topoisomerase I poison CPT-11 enhances the effect of the aurora B kinase inhibitor AZD1152 both in vitro and in vivo (PMID: 19276280) | 31 |
| 80 | 10 & 100 nM | ZM447439 (10 - 1000 nM) | Effects of the aurora kinase inhibitors AZD1152-HQPA and ZM447439 on growth arrest and polyploidy in acute myeloid leukemia cell lines and primary blasts (PMID: 18367484) | 79 |
| 81 | 10 - 300 nM | VX680 (10 - 200 nM), MLN8237 (10 - 50 nM) | Genome-wide CRISPR screen uncovers a synergistic effect of combining Haspin and Aurora kinase B inhibition (PMID: 32300176) | 9 |
| 82 | 10 - 1000 nM | None | Inhibitor of Aurora kinase B induces differentially cell death and polyploidy via DNA damage response pathways in neurological malignancy: Shedding new light on the challenge of resistance to AZD1152-HQPA (PMID: 25752998) | 17 |
| 83 | 10 - 5 μ M | None | A peptide-based positron emission tomography probe for in vivo detection of caspase activity in apoptotic cells (PMID: 24573549) | 13 |
| 84 | 10 - 5 μ M | Tozasertib, VX-680, PHA-739358, PHA-680632, Aurora A Kinase, MLN-8054 (0.01-5 μ M) | Phenotypic fingerprinting of small molecule cell cycle kinase inhibitors for drug discovery (PMID: 20161832) | 16 |
| 85 | 12.5 nM | MLN8237 (62.5 nM) MK-5108 (125 nM) | Salt-inducible kinase 3 is a novel mitotic regulator and a target for enhancing antimitotic therapeutic-mediated cell death (PMID: 24743732) | 14 |
| 86 | 12.5 - 100 nM | None | Analysis of Aurora B kinase in non-Hodgkin lymphoma (PMID: 19823168) | 33 |
| 87 | 15 - 25 nM | None | Aurora B inhibitor barasertib and cytarabine exert a greater-than-additive cytotoxicity in acute myeloid leukemia cells (PMID: 23557198) | 21 |

| | | | | |
|-----|-------------------------------------|-----------------------------|--|----|
| 88 | 16 nM | None | Relapse-associated AURKB blunts the glucocorticoid sensitivity of B cell acute lymphoblastic leukemia (PMID: 30733284) | 21 |
| 89 | 20 - 105 nM | None | Antineoplastic effects of an Aurora B kinase inhibitor in breast cancer (PMID: 20175926) | 72 |
| 90 | 20 - 400 nM | ZM447439 (1 μ M) | Enhancement of radiation response in p53-deficient cancer cells by the Aurora-B kinase inhibitor AZD1152 (PMID: 18084327) | 76 |
| 91 | 20 nM - 1 μ M | ZM447439 (2 μ M) | Mitotic slippage and the subsequent cell fates after inhibition of Aurora B during tubulin-binding agent-induced mitotic arrest (PMID: 29196757) | 25 |
| 92 | 25 - 800 nM | None | Sequential treatment with aurora B inhibitors enhances cisplatin-mediated apoptosis via c-Myc (PMID: 25411027) | 5 |
| 93 | 25 nM - 10 μ M | None | Aurora kinase B/C inhibition impairs malignant glioma growth in vivo (PMID: 22382783) | 30 |
| 94 | 30 & 300 nM | None | Aurora kinase B inhibition reduces the proliferation of metastatic melanoma cells and enhances the response to chemotherapy (PMID: 25623468) | 33 |
| 95 | 42 nM - 1 μ M | None | Differential ABC transporter expression during hematopoiesis contributes to neutrophil-biased toxicity of Aurora kinase inhibitors (PMID: 36224199) | 0 |
| 96 | 50 nM | GSK6000063A (150 nM) | Pharmacological inhibition of aurora-A but not aurora-B impairs interphase microtubule dynamics. (PMID: 19395863) | 16 |
| 97 | 50 nM | None | Selective targeting of cancerous mitochondria and suppression of tumor growth using redox-active treatment adjuvant (PMID: 33204397) | 8 |
| 98 | 50 nM | Alisertib (200 nM) | Combined TRIP13 and aurora kinase inhibition induces apoptosis in human papillomavirus-driven cancers (PMID: 35972731) | 1 |
| 99 | 50 - 200 nM | S49076 (0.35 μ M) | AURKB as a target in non-small cell lung cancer with acquired resistance to anti-EGFR therapy (PMID: 31000705) | 68 |
| 100 | 50 - 500 nM | None | Aurora B is regulated by the mitogen-activated protein kinase/extracellular signal-regulated kinase (MAPK/ERK) signaling pathway and is a valuable potential target in melanoma cells (PMID: 22767597) | 60 |
| 101 | 100 nM | None | In vitro evaluation of a combination treatment involving anticancer agents and an aurora kinase B inhibitor (PMID: 27895801) | 4 |
| 102 | 100 nM | None | Mechanism of action and therapeutic efficacy of Aurora kinase B inhibition in MYC overexpressing medulloblastoma (PMID: 25739120) | 19 |
| 103 | 100 nM | None | Human genome-wide RNAi screen reveals host factors required for enterovirus 71 replication (PMID: 27748395) | 33 |
| 104 | 100 nM (most assays) 50 - 200 nM | None | Aurora B is dispensable for megakaryocyte polyploidization, but contributes to the endomitotic process (PMID: 20548097) | 35 |
| 105 | 100 & 1000 nM | None | AZD1152 rapidly and negatively affects the growth and survival of human acute myeloid leukemia cells in vitro and in vivo (PMID: 19366807) | 61 |
| 106 | 0.12 - 6 μ M | None | Inhibition of Aurora kinase B activity disrupts development and differentiation of salivary glands (PMID: 33462217) | 3 |
| 107 | 125 nM - 2 μ M | MLN8237 (0.125 - 2 μ M) | Inhibition of BRD4 triggers cellular senescence through suppressing Aurora kinases in oesophageal cancer cells (PMID: 32954665) | 3 |
| 108 | 150 - 250 nM | None | Aurora B prevents aneuploidy via MAD2 during the first mitotic cleavage in oxidatively damaged embryos (PMID: 31264311) | 3 |
| 109 | 200 nM | MK5108 (5 μ M) | MPS1 inhibition primes immunogenicity of KRAS-LKB1 mutant lung cancer (PMID: 36150391) | 2 |

| | | | | |
|-----|---------------------------|--|---|-----|
| 110 | 250 - 1000 nM | None | The potential contribution of microRNAs in anti-cancer effects of Aurora kinase inhibitor (AZD1152-HQPA) (PMID: 30051358) | 3 |
| 111 | 300 nM | None | AZD1152, a selective inhibitor of Aurora B kinase, inhibits human tumor xenograft growth by inducing apoptosis (PMID: 17575233) | 300 |
| 112 | 300 nM | VX680, MLN8237 (300 nM) | Recurrent 8q24 rearrangement in blastic plasmacytoid dendritic cell neoplasm: association with immunoblastoid cytology, MYC expression, and drug response (PMID: 29795241) | 24 |
| 112 | 300 nM | None | BRAFV600E induces reversible mitotic arrest in human melanocytes via microRNA-mediated suppression of AURKB (PMID: 34812139) | 8 |
| 113 | 300 nM - 1 μ M | None | P-glycoprotein and breast cancer resistance protein in acute myeloid leukaemia cells treated with the aurora-B kinase inhibitor barasertib-hQPA (PMID: 21679421) | 14 |
| 114 | 500 nM | None | Janus face-like effects of Aurora B inhibition: antitumoral mode of action versus induction of aneuploid progeny (PMID: 27515963) | 6 |
| 115 | 0.5 - 1 μ M | 22 Aurora kinase inhibitors (all 1 μ M) | Chemical genetic screens identify kinase inhibitor combinations that target anti-apoptotic proteins for cancer therapy (PMID: 29608269) | 10 |
| 116 | 1 μ M | MLN8237, VX680, hesperidin, PHA-680632, PHA-739358, SNS-314, CYC116, TAK-901, AMG900 (all 1 μ M) | High-throughput compound screen reveals mTOR inhibitors as potential therapeutics to reduce (auto)antibody production by human plasma cells (PMID: 31621069) | 9 |
| 117 | 1 μ M | None | Cytofluorometric assessment of cell cycle progression (PMID: 23296653) | 5 |
| 118 | 1 μ M | ZM-447439, hesperidin, PHA-739358, PHA-680632, CCT129202, CYC116, VX680, Aurora A Inhibitor I, MLN8237 (all 1 μ M) | A chemical screening approach to identify novel key erythroid enucleation (PMID: 26569102) | 8 |
| 119 | 1 - 5 μ M | VX680 (0 - 10 μ M) | Canine osteosarcoma cells exhibit resistance to aurora kinase inhibitors (PMID: 23410058) | 3 |
| 120 | 1 - 5 μ M | None | Inhibition of aurora kinase B attenuates fibroblast activation and pulmonary fibrosis (PMID: 32761869) | 14 |
| 121 | 1.6 μ M - 250 μ M | None | Effect of the drug transporters ABCG2, Abcg2, ABCB1 and ABCC2 on the disposition, brain accumulation and myelotoxicity of the aurora kinase B inhibitor barasertib and its more active form barasertib-hydroxy-QPA (PMID: 23315030) | 19 |
| 122 | 2 - 4 μ M | None | Aurora B inhibitor barasertib prevents meiotic maturation and subsequent embryo development in pig oocytes (PMID: 26993175) | 9 |
| 123 | 5 μ M | AMG 900 (1 - 100 nM) MLN8054 (5 μ M) | Dual targeting of Aurora kinases with AMG 900 exhibits potent preclinical activity against acute myeloid leukemia with distinct post-mitotic outcomes (PMID: 30266802) | 12 |
| 124 | 5 μ M | None | ALKBH5-mediated m6A-demethylation of USP1 regulated T-cell acute lymphoblastic leukemia cell glucocorticoid resistance by Aurora B (PMID: 34169564) | 11 |
| 125 | Not provided | ZM447439 | Hypersensitivity to aurora kinase inhibitors in cells resistant against platinum- containing anticancer agents (PMID: 24521151) | 9 |

| | | | | |
|-----------------------------|--------------|----------------------------------|---|---|
| 126 | Not provided | None | PLK1 and AURKB phosphorylate surviving differentially to affect proliferation in racially distinct triple-negative breast cancer (PMID: 36627281) | 0 |
| 127 | Unclear | None | Low-dose-rate irradiation suppresses the expression of cell-cycle-related genes, resulting in modification of sensitivity to anti-cancer drugs (PMID: 35159310) | 1 |
| 128 | Unclear | VX680, MLN8237 (Conc unclear) | Nf1-mutant tumors undergo transcriptome and kinome remodeling after inhibition of either mTOR or MEK (PMID: 32847978) | 1 |
| Compliance | | | | |
| 55 (43%)^a | | 50 (39%) | | |
| 33 (26%)^b | | | | |
| Non-Compliance | | | | |
| 40 (31%) | | 78 (61%) | | |

a Probe's concentration below the recommended in-cell maximum in all figures.

b Probe's concentration below the recommended in-cell maximum in some, but not all figures.

Supplementary Note 7. Citations for AZD1152 publications included in the systematic review.

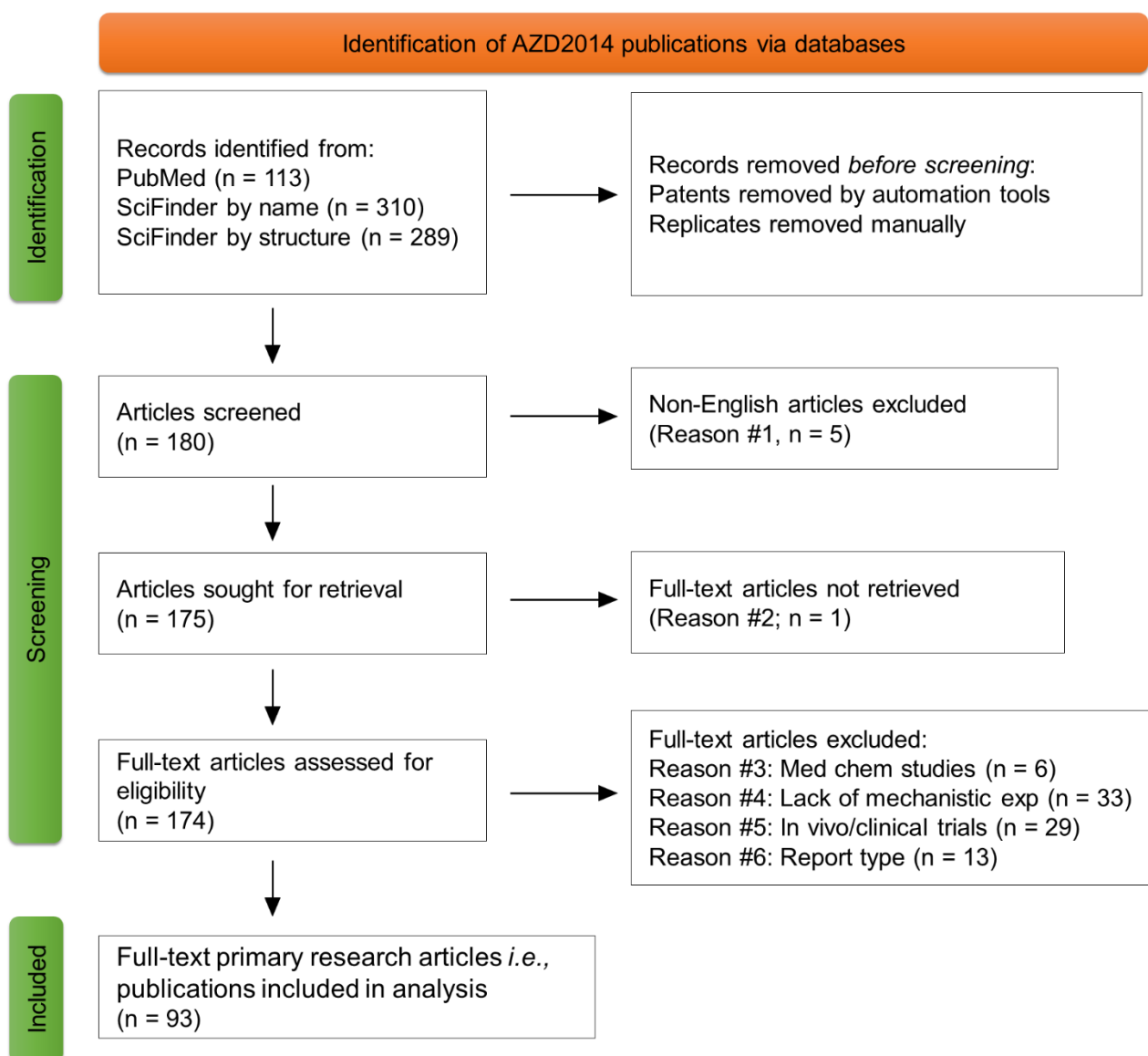
Citations for 128 publications using AZD1152/AZD1152-HQPA: 3,189

Citations for 88 publications with a compliant AZD1152/AZD1152-HQPA concentration: 2,507

Citations for 40 publications with a non-compliant AZD1152/AZD1152-HQPA concentration: 682

Citations for 50 publications using orthogonal Aurora kinase inhibitors: 935

Citations for 78 publications not using orthogonal Aurora kinase inhibitors: 2,254



Supplementary Figure 11. PRISMA flow diagram summarising identification of publications using mTOR chemical probe AZD2014.

Supplementary Table 13. List of excluded articles using the mTOR probe AZD2014.

| | Title (PMID) | Reason for exclusion |
|----|---|--|
| 1 | The dual mTORC1/2 inhibitor AZD2014 inhibits acute graft rejection in a rat liver transplantation model (PMID: 35527497) | 1) Non-English publication |
| 2 | Antitumor effects of AZD2014, a dual mTORC1/2 inhibitor, against human hepatocellular carcinoma xenograft in nude mice (PMID: 34308856) | 1) Non-English publication |
| 3 | Effect of mTOR inhibitor AZD2014 on proliferation of hepatoma HCC cells (No PMID; DOI: 10.3969/j.issn.1004-616x.2020.06.007) | 1) Non-English publication |
| 4 | Dual mTORC1/2 inhibitor AZD2014 inhibits proliferation of HCCLM3 cells through induction of autophagy (No PMID or DOI; ISSN: 0577-7402) | 1) Non-English publication |
| 5 | Optimization of synthesis process of 2-amino-6-chloronatenic acidnic acid (No PMID or DOI; ISSN: 1007-1865) | 1) Non-English publication |
| 6 | Combination vistusertib and anastrozole shows benefit in endometrial cancer (PMID: 35593584) | 2) No access to full article |
| 7 | Optimization of potent and selective dual mTORC1 and mTORC2 inhibitors: The discovery of AZD8055 and AZD2014 (PMID: 23375793) | 3) Discovery of AZD2014 |
| 8 | Design and development of tetrahydro-quinoline derivatives as dual mTOR-C1/C2 inhibitors for the treatment of lung cancer (PMID: 33280832) | 3) Medicinal chemistry |
| 9 | Practical synthesis of Vistusertib (AZD2014), an ATP competitive mTOR inhibitor (no PMID; DOI: 10.1016/j.tetlet.2019.151333) | 3) Medicinal chemistry |
| 10 | A conformational restriction strategy for the identification of a highly selective pyrimido-pyrrolooxazine mTOR inhibitor (PMID: 31465220) | 3) Medicinal chemistry |
| 11 | 4-(Difluoromethyl)-5-(4-((3 <i>R</i> ,5 <i>S</i>)-3,5-dimethylmorpholino)-6-((<i>R</i>)-3-methylmorpholino)-1,3,5-triazin-2-yl)pyridin-2-amine (PQR626), a potent, orally available, and brain-penetrant mTOR inhibitor for the treatment of neurological disorders (PMID: 33166139) | 3) Medicinal chemistry |
| 12 | Design, synthesis and antitumor evaluation of novel quinazoline analogs in hepatocellular carcinoma cell: Molecular docking study (PMID: 20599299) | 3) Medicinal chemistry |
| 13 | 3D Cell-based high-content screening (HCS) using a micropillar and microwell chip platform (PMID: 29889500) | 4) Analytical chemistry/no mechanistic exp. |
| 14 | Discovery of novel autophagy inhibitors and their sensitization abilities for vincristine-resistant esophageal cancer cell line Eca109/VCR (PMID: 32207878) | 4) No mechanistic exp. |
| 15 | Chemical proteomics reveals ferrochelatase as a common off-target of kinase inhibitors (PMID: 26863403) | 4) No mechanistic exp. |
| 16 | Exploiting evolutionary steering to induce collateral drug sensitivity in cancer (PMID: 32317663) | 4) AZD2014 not used |
| 17 | CC-223 inhibits human head and neck squamous cell carcinoma cell growth (PMID: 29402408) | 4) AZD2014 not used |
| 18 | RAPTOR up-regulation contributes to resistance of renal cancer cells to PI3K-mTOR inhibition (PMID: 29389967) | 4) Dose response only |
| 19 | Drug repurposing for paracoccidioidomycosis through a computational chemogenomics framework (PMID: 31244810) | 4) No mechanistic exp. |
| 20 | Validation of a rapid liquid chromatography tandem mass spectrometric method for the quantitative analysis of vistusertib (PMID: 34735991) | 4) No mechanistic exp. - Methodology study |
| 21 | Rituximab (anti-CD20)-modified AZD-2014-encapsulated nanoparticles killing of B lymphoma cells (PMID: 30198340) | 4) No mechanistic exp. - Nano-carrier study |
| 22 | Synergistic drug combinations and machine learning for drug repurposing in chordoma (PMID: 32737414) | 4) No <i>in vitro</i> experiments |
| 23 | Noninvasive MRI native T1 mapping detects response to MYCN-targeted therapies in the Th-MYCN model of neuroblastoma (PMID: 32595135) | 4) No <i>in vitro</i> experiments |
| 24 | Identification of selective cytotoxic and synthetic lethal drug responses in triple negative breast cancer cells (PMID: 27165605) | 4) No mechanistic exp. - cell viability screen |
| 25 | Palbociclib-based high-throughput combination drug screening identifies synergistic therapeutic options in HPV-negative head and neck squamous cell carcinoma (PMID: 35546399) | 4) No mechanistic exp. using AZD2014 |
| 26 | Ponatinib, lestaurtinib, and mTOR/PI3K inhibitors are promising repurposing candidates against <i>Entamoeba histolytica</i> (PMID: 34871094) | 4) No mechanistic exp. using AZD2014 |
| 27 | Sensitivity to PI3K and AKT inhibitors is mediated by divergent molecular mechanisms in subtypes of DLBCL (PMID: 28202458) | 4) No mechanistic exp. using AZD2014 |

| | | |
|----|---|---|
| 28 | Drug repurposing screening identifies bortezomib and panobinostat as drugs targeting cancer associated fibroblasts (CAFs) by synergistic induction of apoptosis (PMID: 29349597) | 4) No mechanistic exp. using AZD2014 |
| 29 | High-throughput dynamic BH3 profiling may quickly and accurately predict effective therapies in solid tumors (PMID: 32546544) | 4) No mechanistic exp. using AZD2014 |
| 30 | Selective colony area method for heterogeneous patient-derived tumor cell lines in anti-cancer drug screening system (PMID: 30995234) | 4) No mechanistic exp. using AZD2014 |
| 31 | Drug efficacy comparison of 3D forming and preforming sphere models with a micropillar and microwell chip platform (PMID: 30753787) | 4) No mechanistic exp. using AZD2014 |
| 32 | Drug-dependent morphological transitions in spherical and worm-like polymeric micelles define stability and pharmacological performance of micellar drugs (PMID: 34841670) | 4) No mechanistic exp. - micelle drug delivery system |
| 33 | Identification and analysis of DNA methylation-driven signatures for prognostic and immune microenvironments evaluation in hepatocellular carcinoma (PMID: 36299585) | 4) No mechanistic exp. using AZD2014 |
| 34 | JAK1/2 and BCL2 inhibitors synergize to counteract bone marrow stromal cell-induced protection of AML (PMID: 28619982) | 4) No mechanistic exp. using AZD2014 |
| 35 | Enhanced MAPK signaling drives ETS1-mediated induction of miR-29b leading to downregulation of TET1 and changes in epigenetic modifications in a subset of lung SCC (PMID: 26776158) | 4) No mechanistic exp. using AZD2014 |
| 36 | Molecular taxonomy of systemic lupus erythematosus through data-driven patient stratification: molecular endotypes and cluster-tailored drugs (No PMID: DOI: 10.3389/fimmu.2022.860726) | 4) No mechanistic exp. using AZD2014 |
| 37 | Machine learning models for the prediction of chemotherapy-induced peripheral neuropathy (PMID: 30617559) | 4) No mechanistic exp. using AZD2014 |
| 38 | Extra-virgin olive oil contains a metabolo-epigenetic inhibitor of cancer stem cells (PMID: 29452350) | 4) No mechanistic exp. using AZD2014 |
| 39 | Reconciling selectivity trends from a comprehensive kinase inhibitor profiling campaign with known activity data (PMID: 30023860) | 4) No mechanistic exp. using AZD2014 |
| 40 | Ex vivo modelling of drug efficacy in a rare metastatic urachal carcinoma (PMID: 32576176) | 4) No mechanistic exp. using AZD2014 |
| 41 | Sustained mTORC1 activity during palbociclib-induced growth arrest triggers senescence in ER+ breast cancer cells (PMID: 33356791) | 4) No mechanistic exp. using AZD2014 |
| 42 | Context-dependent intravital imaging of therapeutic response using intramolecular FRET biosensors (PMID: 28435000) | 4) No mechanistic exp. using AZD2014 |
| 43 | Establishment and characterization of 18 human colorectal cancer cell lines (PMID: 32321971) | 4) No mechanistic exp. using AZD2014 |
| 44 | A cell-based high-throughput screen identifies inhibitors that overcome P-glycoprotein (Pgp)-mediated multidrug resistance (PMID: 32484843) | 4) No mechanistic exp. using AZD2014 |
| 45 | Pre-clinical activity of combined LSD1 and mTORC1 inhibition in MLL-translocated acute myeloid leukaemia (PMID: 31780813) | 4) No mechanistic exp. using AZD2014 |
| 46 | AKT/mTORC2 inhibition activates FOXO1 function in CLL cells reducing B-cell receptor-mediated survival (PMID: 30559170) | 5) AZD2014 used <i>in vivo</i> |
| 47 | Safety and efficacy of the mTOR inhibitor, vistusertib, combined with anastrozole in patients with hormone receptor-positive recurrent or metastatic endometrial cancer (PMID: 35551299) | 5) Clinical publication |
| 48 | Comprehensive genome profiling in patients with metastatic non-small cell lung cancer: the precision medicine phase 2 randomized SAFIR02-Lung trial (PMID: 35802649) | 5) Clinical study |
| 49 | A phase I study investigating AZD8186, a potent and selective inhibitor of PI3K β/δ , in patients with advanced solid tumors (PMID: 35247924) | 5) Clinical study |
| 50 | First-in-child phase I/II study of the dual mTORC1/2 inhibitor vistusertib (AZD2014) as monotherapy and in combination with topotecan-temozolomide in children with advanced malignancies: arms E and F of the AcSé-ESMART trial (PMID: 34543871) | 5) Clinical study |
| 51 | A phase 1/2 study of the combination of acalabrutinib and vistusertib in patients with relapsed/refractory B-cell malignancies (PMID: 34269152) | 5) Clinical study |
| 52 | An adaptive, biomarker-directed platform study of durvalumab in combination with targeted therapies in advanced urothelial cancer (PMID: 33941921) | 5) Clinical study |
| 53 | Prospective experimental treatment of colorectal cancer patients based on organoid drug responses (PMID: 33887686) | 5) Clinical study |

| | | |
|----|---|--------------------|
| 54 | Biomarker-driven phase 2 umbrella trial study for patients with recurrent small cell lung cancer failing platinum-based chemotherapy (PMID: 32584426) | 5) Clinical study |
| 55 | A phase I study of vistusertib (dual mTORC1/2 inhibitor) in patients with previously treated glioblastoma multiforme: a CCTG study (PMID: 31707687) | 5) Clinical study |
| 56 | Fulvestrant plus vistusertib vs fulvestrant plus everolimus vs fulvestrant alone for women with hormone receptor-positive metastatic breast cancer: The MANTA phase 2 randomized clinical trial (PMID: 31465093) | 5) Clinical study |
| 57 | A phase II study to assess the safety and efficacy of the dual mTORC1/2 inhibitor vistusertib in relapsed, refractory DLBCL (PMID: 31385336) | 5) Clinical study |
| 58 | Tumor genomic profiling guides patients with metastatic gastric cancer to targeted treatment: The VIKTORY umbrella trial (PMID: 31315834) | 5) Clinical study |
| 59 | Phase I study of orally administered 14 Carbon-isotope labelled-vistusertib (AZD2014), a dual TORC1/2 kinase inhibitor, to assess the absorption, metabolism, excretion, and pharmacokinetics in patients with advanced solid malignancies (PMID: 30758651) | 5) Clinical study |
| 60 | Vistusertib (dual m-TORC1/2 inhibitor) in combination with paclitaxel in patients with high-grade serous ovarian and squamous non-small-cell lung cancer (PMID: 30016392) | 5) Clinical study |
| 61 | Rapamycin-insensitive companion of mTOR (RICTOR) amplification defines a subset of advanced gastric cancer and is sensitive to AZD2014-mediated mTORC1/2 inhibition (PMID: 28028034) | 5) Clinical study |
| 62 | A randomised phase 2 study of AZD2014 versus everolimus in patients with VEGF-refractory metastatic clear cell renal cancer (PMID: 26364551) | 5) Clinical study |
| 63 | A Phase 1 study of ADI-PEG20 (pegargiminase) combined with cisplatin and pemetrexed in ASS1- negative metastatic uveal melanoma (PMID: 35466524) | 5) Clinical study |
| 64 | Ribosome biogenesis-based predictive biomarkers in endocrine therapy (Anastrozole) combined with mTOR inhibitor (Vistusertib) in endometrial cancer: translational study from the VICTORIA trial in collaboration with the GINECO group (PMID: 36370117) | 5) Clinical study |
| 65 | Aberrant cholesterol metabolic signaling impairs antitumor immunosurveillance through natural killer T cell dysfunction in obese liver (PMID: 35595819) | 5) In vivo study |
| 66 | Quantitation of vistusertib by UHPLC-MS/MS in rat plasma and its application to a pharmacokinetic study (PMID: 34470474) | 5) In vivo study |
| 67 | The mTORC1 inhibitor rapamycin and the mTORC1/2 inhibitor AZD2014 impair the consolidation and persistence of contextual fear memory (PMID: 32601986) | 5) In vivo study |
| 68 | Combined mTOR/MEK inhibition prevents proliferation and induces apoptosis in NF2-mutant tumors (PMID: 31298338) | 5) In vivo study |
| 69 | Allosteric and ATP-competitive inhibitors of mTOR effectively suppress tumor progression-associated epithelial-mesenchymal transition in the kidneys of Tsc2 ^{+/-} mice (PMID: 31207499) | 5) In vivo study |
| 70 | Comparative toxicity evaluation of targeted anticancer therapeutics in embryonic zebrafish and sea urchin models (PMID: 30587022) | 5) In vivo study |
| 71 | Combination of dual mTORC1/2 inhibition and immune-checkpoint blockade potentiates anti-tumour immunity (PMID: 30221055) | 5) In vivo study |
| 72 | Selumetinib-based therapy in uveal melanoma patient-derived xenografts (PMID: 29774094) | 5) In vivo study |
| 73 | In vivo E2F reporting reveals efficacious schedules of MEK1/2-CDK4/6 targeting and mTOR-S6 resistance mechanisms (PMID: 29496664) | 5) In vivo study |
| 74 | First-in-human pharmacokinetic and pharmacodynamic study of the dual m-TORC 1/2 inhibitor, AZD2014 (PMID: 25805799) | 5) In vivo study |
| 75 | Mastering the complex targeted therapy for non-small cell lung cancer (PMID: 32857949) | 6) Commentary |
| 76 | Learning from BISCAY: The future of biomarker-based trial design in bladder cancer (PMID: 34256907) | 6) Commentary |
| 77 | Correction to: Combination of mTORC1/2 inhibitor vistusertib plus fulvestrant in vitro and in vivo targets oestrogen receptor-positive endocrine-resistant breast cancer (PMID: 32005287) | 6) Correction |
| 78 | Overcoming resistance to mTOR inhibition for enhanced strategies in clinical trials (PMID: 23631743) | 6) Editorial piece |
| 79 | MEDI-573, alone or in combination with mammalian target of rapamycin inhibitors, targets the insulin-like growth factor pathway in sarcomas [Erratum to document cited in CA162:419021] (PMID: 26039569) | 6) Erratum |

| | | |
|----|---|-----------|
| 80 | One size doesn't fit all in Ph-like ALL (PMID: 28082291) | 6) Letter |
| 81 | mTOR signaling and potential therapeutic targeting in meningioma (PMID: 35216092) | 6) Review |
| 82 | Evolution of PIKK family kinase inhibitors: A new age cancer therapeutics (PMID: 32114443) | 6) Review |
| 83 | Combined strategies with poly-(ADP-Ribose)-polymerase (PARP) inhibitors for the treatment of ovarian cancer: A literature review (PMID: 31374917) | 6) Review |
| 84 | mTOR deregulation in oral cavity squamous cell carcinoma (PMID: 28730764) | 6) Review |
| 85 | Ibrutinib inhibition of Bruton protein-tyrosine kinase (BTK) in the treatment of B cell neoplasms (PMID: 27641927) | 6) Review |
| 86 | Catalytic mammalian target of rapamycin inhibitors as antineoplastic agents (PMID: 25747970) | 6) Review |
| 87 | Time now to TORC the TORC? New developments in mTOR pathway inhibition in lymphoid malignancies (PMID: 24842496) | 6) Review |

Supplementary Table 14. Overview of eligible publications using the mTOR probe AZD2014 and compliance (in blue) with recommendations to use AZD2014 up to 2 μ M (<https://www.chemicalprobes.org/azd2014?q=AZD2014>) and orthogonal mTOR inhibitors. Citations are sourced from SciFinder (January 2023).

| | AZD2014 | Orthogonal inhibitors | Title (PMID) | Cites |
|----|-------------------|---|--|-------|
| 1 | 0.1 - 100 nM | AZD8055, INK128 (0.1 - 100 nM) | RICTOR amplification identifies a subgroup in small cell lung cancer and predicts response to drugs targeting mTOR (PMID: 27863413) | 34 |
| 2 | 1 - 100 nM | None | Inhibition of Bcl-2 potentiates AZD-2014-induced anti-head and neck squamous cell carcinoma cell activity (PMID: 27343560) | 10 |
| 3 | 1 - 100 nM | None | Dramatic suppression of colorectal cancer cell growth by the dual mTORC1 and mTORC2 inhibitor AZD-2014 (PMID: 24309100) | 42 |
| 4 | 1 nM - 1 μ M | INK-128, rapamycin, torin1 (1 nM - 1 μ M), everolimus (1 μ M) | HSP90 inhibitors induce GPNMB cell-surface expression by modulating lysosomal positioning and sensitize breast cancer cells to glembatumumab vedotin (PMID: 35110681) | 1 |
| 5 | 2.5 - 500 nM | AZD8055 (250 nM), Torin2, rapamycin (both 500 nM) | Antiviral drug screen identifies DNA-damage response inhibitor as potent blocker of SARS-CoV-2 replication (PMID: 33784499) | 43 |
| 6 | 3 - 300 nM | Rapamycin (20 nM - 1 μ M) | A high-throughput kinome screen reveals serum/glucocorticoid-regulated kinase 1 as a therapeutic target for NF2-deficient meningiomas (PMID: 26219339) | 37 |
| 7 | 3 nM - 1 μ M | Everolimus (1 - 500 nM) | AZD2014, an inhibitor of mTORC1 and mTORC2, is highly effective in ER+ breast cancer when administered using intermittent or continuous schedules (PMID: 26358751) | 90 |
| 8 | 4 - 250 nM | Everolimus (0 - 10 μ M), AZD8055 (0 - 100 nM), BEZ235 (0 - 100 nM) | A genome-scale CRISPR screen identifies the ERBB and mTOR signaling networks as key determinants of response to PI3K inhibition in pancreatic cancer (PMID: 32371585) | 8 |
| 9 | 10 nM | None | mTOR inhibition sensitizes human hepatocellular carcinoma cells to resminostat (PMID: 27311860) | 9 |
| 10 | 10 nM | Everolimus (0.1 - 100 nM), AZD8055 (10 nM), KU-0063794 (100 nM) | Potential of growth inhibitory responses of the mTOR inhibitor everolimus by dual mTORC1/2 inhibitors in cultured breast cancer cell lines (PMID: 26148118) | 28 |
| 11 | 10 nM | Rapamycin (10 ng/mL) | Rapamycin induces mitogen-activated protein (MAP) kinase phosphatase-1 (MKP-1) expression through activation of protein kinase B and mitogen-activated protein kinase kinase pathways (PMID: 24126911) | 43 |
| 12 | 10 -100 nM | Rapamycin (100 nM) | AZD2014, a dual mTOR inhibitor, attenuates cardiac hypertrophy in vitro and in vivo (PMID: 34674743) | 0 |
| 13 | 10 nM - 1 μ M | Rapamycin (10 nM - 1 μ M) | Potent antitumour of the mTORC1/2 dual inhibitor AZD2014 in docetaxel-sensitive and docetaxel-resistant castration-resistant prostate cancer cells (PMID: 33507584) | 7 |
| 14 | 10 nM - 1 μ M | Rapamycin (10 nM - 1 μ M) | Dramatic antitumor effects of the dual mTORC1 and mTORC2 inhibitor AZD2014 in hepatocellular carcinoma (PMID: 25628925) | 44 |
| 15 | 10 nM - 1 μ M | Everolimus, NVP-BEZ235, rapamycin (0.1 nM - 1 μ M), OSI-027 (10 nM - 1 μ M) | Long-term acquired everolimus resistance in pancreatic neuroendocrine tumours can be overcome with novel PI3K-AKT-mTOR inhibitors (PMID: 26978006) | 57 |
| 16 | 20 - 500 nM | None | 18 F-meta-fluorobenzylguanidine (18 F-mFBG) to monitor changes in norepinephrine transporter expression in response to therapeutic intervention in neuroblastoma models (PMID: 33262374) | 3 |
| 17 | 20 - 500 nM | None | F-metafluorobenzylguanidine (18F-mFBG) to monitor changes in norepinephrine transporter expression in response to therapeutic intervention in neuroblastoma models (PMID: 33262374) | 3 |

| | | | | |
|----|--------------------|---|---|-----|
| 18 | 25 nM | Rapamycin, everolimus, temsirolimus (1 - 5 μ M) | SARS-CoV-2 infection rewires host cell metabolism and is potentially susceptible to mTORC1 inhibition (PMID: 33767183) | 56 |
| 19 | 25 nM - 1 μ M | None | An mTORC1/2 dual inhibitor, AZD2014, acts as a lysosomal function activator and enhances gemtuzumab ozogamicin-induced apoptosis in primary human leukemia cells (PMID: 31286402) | 12 |
| 20 | 30 - 300 nM | None | Intermittent high-dose scheduling of AZD8835, a novel selective inhibitor of PI3K α and PI3K δ , demonstrates treatment strategies for PIK3CA-dependent breast cancers (PMID: 26839307) | 34 |
| 21 | 50 - 100 nM | Rapamycin, everolimus (10 - 250 nM) | Pre-clinical evaluation of AZD-2014, a novel mTORC1/2 dual inhibitor, against renal cell carcinoma (PMID: 25444920) | 90 |
| 22 | 50 - 500 nM | Rapamycin, AZD8055 (50 - 500 nM) | Synergistic anti-tumor effect of mTOR inhibitors with irinotecan on colon cancer cells (PMID: 31627299) | 15 |
| 23 | 50 - 500 nM | None | Targeting mantle cell lymphoma metabolism and survival through simultaneous blockade of mTOR and nuclear transporter exportin-1 (PMID: 28388555) | 6 |
| 24 | 50 nM - 1 μ M | RAD001 (50 nM - 1 μ M) | mTORC1/2 inhibitor served as a more ideal agent against the growth of mouse lymphocytic leukemia both in vitro and in vivo (PMID: 31519585) | 3 |
| 25 | 50 nM - 10 μ M | None | mTORC2 signaling drives the development and progression of pancreatic cancer (PMID: 27758884) | 51 |
| 26 | 100 nM | None | Combination of mTORC1/2 inhibitor vistusertib plus fulvestrant in vitro and in vivo targets oestrogen receptor-positive endocrine-resistant breast cancer (PMID: 31801615) | 5 |
| 27 | 100 nM | None | Targeting autophagy to modulate cell survival: a comparative analysis in cancer, normal and embryonic cells (PMID: 28664293) | 10 |
| 28 | 100 nM | None | AZD2014 radiosensitizes oral squamous cell carcinoma by inhibiting AKT/mTOR axis and inducing G1/G2/M cell cycle arrest (PMID: 27031247) | 15 |
| 29 | 100 nM | AZD8055 (100 nM) | Kinome RNAi screens reveal synergistic targeting of mTOR and FGFR1 pathways for treatment of lung cancer and HNSCC (PMID: 26359452) | 46 |
| 30 | 100 nM | Everolimus (100 nM), rapamycin (25 nM), WYE-125132 (100 nM) | Screening reveals sterol derivatives with pro-differentiation, pro-survival, or potent cytotoxic effects on oligodendrocyte progenitor cells (PMID: 34232635) | 3 |
| 31 | 100 nM | None | An mTOR and DNA-PK dual inhibitor CC-115 hinders non-small cell lung cancer cell growth (PMID: 35717530) | 1 |
| 32 | 100 nM | None | mTOR inhibition amplifies the anti-lymphoma effect of PI3K β / δ blockage in diffuse large B-cell lymphoma (PMID: 36352190) | 0 |
| 33 | 100 nM | Everolimus (1 μ M) | Methuosis contributes to Jaspine-B-induced cell death (PMID: 35806262) | 0 |
| 34 | 100 nM | Rapamycin (100 nM) | ADCK1 is a potential therapeutic target of osteosarcoma (PMID: 36371387) | 0 |
| 35 | 100 nM | Everolimus, temsirolimus, rapamycin, OSI-027, INK-128, vortalisib, palomid 529, VS-5584, gedatolisib, ICSN3250 (all 100 nM) | mTOR inhibition via displacement of phosphatidic acid induces enhanced cytotoxicity specifically in cancer cells (PMID: 30054335) | 11 |
| 36 | 100 - 300 nM | None | Potential of the dual mTOR kinase inhibitor AZD2014 to overcome paclitaxel resistance in anaplastic thyroid carcinoma (PMID: 29790111) | 13 |
| 37 | 100 - 800 nM | AZD8055 (50 - 400 nM) | Inducing and exploiting vulnerabilities for the treatment of liver cancer (PMID: 31578521) | 148 |

| | | | | |
|----|------------------|---|--|----|
| 38 | 100 - 1000 nM | None | Combined inhibition of mTOR and CDK4/6 is required for optimal blockade of E2F function and long term growth inhibition in estrogen receptor positive breast cancer (PMID: 29483206) | 90 |
| 39 | 0.1 μM - 5 μM | None | Dual mTORC1/2 inhibitor AZD2014 diminishes myeloid-derived suppressor cells accumulation in ovarian cancer and delays tumor growth (PMID: 34560229) | 2 |
| 40 | 0.1 - 10 μM | None | Landscapes of cellular phenotypic diversity in breast cancer xenografts and their impact on drug response (PMID: 33790302) | 16 |
| 41 | 0.1 - 10 μM | Rapamycin (10 - 100 nM) | Investigation of the novel mTOR inhibitor AZD2014 in neuronal ischemia (PMID: 31100427) | 5 |
| 42 | 0.125 - 1 μM | None | The novel combination of dual mTOR inhibitor AZD2014 and pan-PIM inhibitor AZD1208 inhibits growth in acute myeloid leukemia via HSF pathway suppression (PMID: 26473447) | 28 |
| 43 | 200 nM | Rapamycin (200 nM) | Inhibition of mTORC1/C2 signaling improves anti-leukemia efficacy of JAK/STAT blockade in CRLF2 rearranged and/or JAK driven Philadelphia chromosome-like acute B-cell lymphoblastic leukemia (PMID: 29487712) | 27 |
| 44 | 200 nM | OSI-027, AZD-8055 (200 nM) | MHY1485 ameliorates UV-induced skin cell damages via activating mTOR-Nrf2 signaling (PMID: 28061443) | 8 |
| 45 | 200 nM | None | Synergistic induction of apoptosis by combination of BTK and dual mTORC1/2 inhibitors in diffuse large B cell lymphoma (PMID: 24970801) | 39 |
| 46 | 200 nM | Torin1 (500 nM) | SHMT2 inhibition disrupts the TCF3 transcriptional survival program in Burkitt lymphoma (PMID: 34624079) | 7 |
| 47 | 200 nM | BEZ235 (200 nM), rapamycin (100 nM), torin1 & MLN-0128 (200 nM) | PIK3CA mutations enable targeting of a breast tumor dependency through mTOR-mediated MCL-1 translation (PMID: 27974663) | 36 |
| 48 | 200 - 400 nM | Rapamycin (200 nM) | Mechanisms underlying synergy between DNA topoisomerase I-targeted drugs and mTOR kinase inhibitors in NF1-associated malignant peripheral nerve sheath tumors (PMID: 31444410) | 12 |
| 49 | 200 - 500 nM | Everolimus (100 - 400 nM), sapanisertib (100 - 400 nM) | Impact of baseline culture conditions of cancer organoids when determining therapeutic response and tumor heterogeneity (PMID: 35338174) | 3 |
| 50 | 250 nM | None | Identification of differential PI3K pathway target dependencies in T-cell acute lymphoblastic leukemia through a large cancer cell panel screen (PMID: 26989080) | 16 |
| 51 | 250 nM | Everolimus (100 nM) | Transforming growth factor-β (TGF-β) induces the expression of chondrogenesis-related genes through TGF-β receptor II (TGFRII)-AKT-mTOR signaling in primary cultured mouse precartilaginous stem cells (PMID: 24946212) | 18 |
| 52 | 250 nM | None | Chemo-protective and regenerative effects of diarylheptanoids from the bark of black alder (<i>Alnus glutinosa</i>) in human normal keratinocytes (PMID: 26162555) | 13 |
| 53 | 300 nM | Rapamycin (20 nM) | mTOR kinase inhibition disrupts neuregulin 1-ERBB3 autocrine signaling and sensitizes NF2-deficient meningioma cellular models to IGF1R inhibition (PMID: 33273014) | 1 |
| 54 | 300 nM | None | Combination therapy with mTOR kinase inhibitor and dasatinib as a novel therapeutic strategy for vestibular schwannoma (PMID: 32144278) | 8 |
| 55 | 300 nM | Rapamycin (20 nM) | EPH receptor signaling as a novel therapeutic target in NF2-deficient meningioma (PMID: 29982664) | 14 |
| 56 | 300 nM | Everolimus (0 - 50 μM) | Diverse resistance mechanisms to the third-generation ALK inhibitor lorlatinib in alk-rearranged lung cancer (PMID: 31585938) | 63 |
| 57 | 0.316 μM - 10 μM | Everolimus (50 nM - 5 μM) | Preclinical analysis of MTOR complex 1/2 inhibition in diffuse intrinsic pontine glioma (PMID: 29207163) | 16 |
| 58 | 450 nM - 10 μM | BEZ235 (1.13 - 10 μM) | Implementation of a multiplex and quantitative proteomics platform for assessing protein lysates using DNA-barcoded antibodies (PMID: 29531020) | 13 |
| 59 | 500 nM | Rapamycin (500 nM) | Therapeutic enhancement of verteporfin-mediated photodynamic therapy by mTOR inhibitors (PMID: 31769520) | 3 |

| | | | | |
|----|--------------------------------------|---|---|----|
| 60 | 500 nM | AZD8186 (250 nM) | Combined inhibition of PI3K β and mTOR inhibits growth of PTEN-null tumors (PMID: 30097489) | 10 |
| 61 | 500 nM | Rapamycin (100 nM) | Intravital imaging to monitor therapeutic response in moving hypoxic regions resistant to PI3K pathway targeting in pancreatic cancer (PMID: 29898401) | 50 |
| 62 | 500 nM | Rapamycin (30 nM) | MEDI-573, alone or in combination with mammalian target of rapamycin inhibitors, targets the insulin-like growth factor pathway in sarcomas (PMID: 25193511) | 18 |
| 63 | 500 nM | Everolimus, LY294002 (500 nM) | Keratinocyte growth factor protects endometrial cells from oxygen glucose deprivation/re-oxygenation via activating Nrf2 signaling (PMID: 29709474) | 22 |
| 64 | 500 nM - 1 μ M | Rapamycin (20 nM), torin1 (250 nM), rapalink-1 (5 nM) | Reciprocal effects of mTOR inhibitors on pro-survival proteins dictate therapeutic responses in tuberous sclerosis complex (PMID: 36388985) | 0 |
| 65 | 0.5 - 1 μ M | None | Evaluation of the combination of the dual m-TORC1/2 inhibitor vistusertib (AZD2014) and paclitaxel in ovarian cancer models (PMID: 29371953) | 15 |
| 66 | 0.5 - 1 μ M | None | FBW7 suppression leads to SOX9 stabilization and increased malignancy in medulloblastoma (PMID: 27625374) | 39 |
| 67 | 0.5 - 2 μ M | Rapamycin (11.9 nM) | Influence of the novel ATP-competitive dual mTORC1/2 inhibitor AZD2014 on immune cell populations and heart allograft rejection (PMID: 28885497) | 10 |
| 68 | 0.8 μ M or 3.6 μ M (unclear) | AZD8055, WYE-125132 (0.8 μ M or 3.6 μ M) | Pyrimidine inhibitors synergize with nucleoside analogues to block SARS-CoV-2 (PMID: 35130559) | 45 |
| 69 | 1 μ M | None | Inhibiting mTOR activity using AZD2014 increases autophagy in the mouse cerebral cortex (PMID: 33794244) | 5 |
| 70 | 1 μ M | BEZ235 (0.5 μ M) | Synergistic effects of combination therapy with AKT and mTOR inhibitors on bladder cancer cells (PMID: 32325639) | 6 |
| 71 | 1 μ M | None | Enhanced autocrine FGF19/FGFR4 signaling drives the progression of lung squamous cell carcinoma, which responds to mTOR inhibitor AZD2104 (PMID: 32111983) | 14 |
| 72 | 1 μ M | Everolimus, rapamycin (1 - 5 μ M) | Repurposing of mTOR complex inhibitors attenuates MCL-1 and sensitizes to PARP inhibition (PMID: 30201826) | 11 |
| 73 | 1 μ M | None | BEZ235 (PIK3/mTOR inhibitor) overcomes pazopanib resistance in patient-derived refractory soft tissue sarcoma cells (PMID: 27267837) | 9 |
| 74 | 1 μ M | Rapamycin (10 nM) | Phosphorylated ribosomal S6 (p-rpS6) as a post-treatment indicator of HER2 signalling targeted drug resistance (PMID: 26329528) | 7 |
| 75 | 1 μ M | Torin1 (250 nM), rapamycin (50 nM) | Macropinocytosis renders a subset of pancreatic tumor cells resistant to mTOR inhibition (PMID: 32101748) | 16 |
| 76 | 1 μ M | None | High-risk neuroblastoma with NF1 loss of function is targetable using SHP2 inhibition (PMID: 35905710) | 1 |
| 77 | 1 μ M | GDC0980 (10 μ M) | Colon cancer organoids using monoclonal organoids established in four different lesions of one cancer patient reveal tumor heterogeneity and different real-time responsiveness to anti-cancer drugs (PMID: 35691158) | 1 |
| 78 | 1 μ M | Rapamycin (100 nM) | Dual blockade of the PI3K/Akt/mTOR pathway inhibits posttransplant Epstein-Barr virus B cell lymphomas and promotes allograft survival (PMID: 30549430) | 12 |
| 79 | 1 - 4 μ M | None | The mTORC1/mTORC2 inhibitor AZD2014 enhances the radiosensitivity of glioblastoma stem-like cells (PMID: 24311635) | 76 |
| 80 | 1 - 5 μ M | Rapamycin (2 - 8 μ M) | Synergistic Effects between mTOR Complex 1/2 and Glycolysis Inhibitors in Non-Small-Cell Lung Carcinoma Cells (PMID: 26176608) | 15 |
| 81 | 5 μ M | None | Unspliced X-box-binding protein 1 (XBP1) protects endothelial cells from oxidative stress through interaction with histone deacetylase 3 (PMID: 25190803) | 60 |

| | | | | |
|-----------------------------|----------------|---|---|----|
| 82 | 5 μ M | None | Atractylenolide I inhibits colorectal cancer cell proliferation by affecting metabolism and stemness via AKT/mTOR signaling (PMID: 32135457) | 20 |
| 83 | 7 - 11 μ M | Rapamycin (10 μ M) INK128 (7 - 16 μ M) | Directly imaging the localisation and photosensitization properties of the pan-mTOR inhibitor, AZD2014, in living cancer cells (PMID: 33142217) | 2 |
| 84 | 10 μ M | Rapamycin, OSI-027, AZD8055 (0.1 - 10 μ M) | Prolonged tau clearance and stress vulnerability rescue by pharmacological activation of autophagy in tauopathy neurons (PMID: 32591533) | 53 |
| 85 | 10 μ M | Everolimus, rapamycin (10 μ M) | Somatic mutation profiling of vulvar cancer: Exploring therapeutic targets (PMID: 29980281) | 29 |
| 86 | 20 μ M | Everolimus, BEZ235, XL765, PF-05212384 (20 μ M) | High throughput 3D cell migration assay using micropillar/microwell chips (PMID: 36014542) | 0 |
| 87 | Not clear | GDC-0349 (5 - 500 nM), rapamycin (100 nM) | GDC-0349 inhibits non-small cell lung cancer cell growth (PMID: 33154352) | 12 |
| 88 | Not provided | None | PI3k inhibitors (BKM120 and BYL719) as radiosensitizers for head and neck squamous cell carcinoma during radiotherapy (PMID: 33471836) | 6 |
| 89 | Not provided | None | Integrated pharmaco-proteogenomics defines two subgroups in isocitrate dehydrogenase wild-type glioblastoma with prognostic and therapeutic opportunities (PMID: 32620753) | 23 |
| 90 | Not provided | None | MiR-99a enhances the radiation sensitivity of non-small cell lung cancer by targeting mTOR (PMID: 29614485) | 43 |
| 91 | Not provided | None | Overproduction of IGF-2 drives a subset of colorectal cancer cells, which specifically respond to an anti-IGF therapeutic antibody and combination therapies (PMID: 27399333) | 17 |
| 92 | Unclear | None | Insights into significance of combined inhibition of MEK and mTOR signalling output in KRAS mutant non-small-cell lung cancer (PMID: 27441499) | 9 |
| 93 | Unclear | AZD8055, everolimus | Dynamic BH3 profiling identifies active BH3 mimetic combinations in non-small cell lung cancer (PMID: 34315868) | 4 |
| Compliance | | | | |
| 71 (76%)^a | | 56 (60%) | | |
| 9 (10%)^b | | | | |
| Non-Compliance | | | | |
| 13 (14%) | | 37 (40%) | | |

a Probe's concentration below the recommended in-cell maximum in all figures.

b Probe's concentration below the recommended in-cell maximum in some, but not all figures.

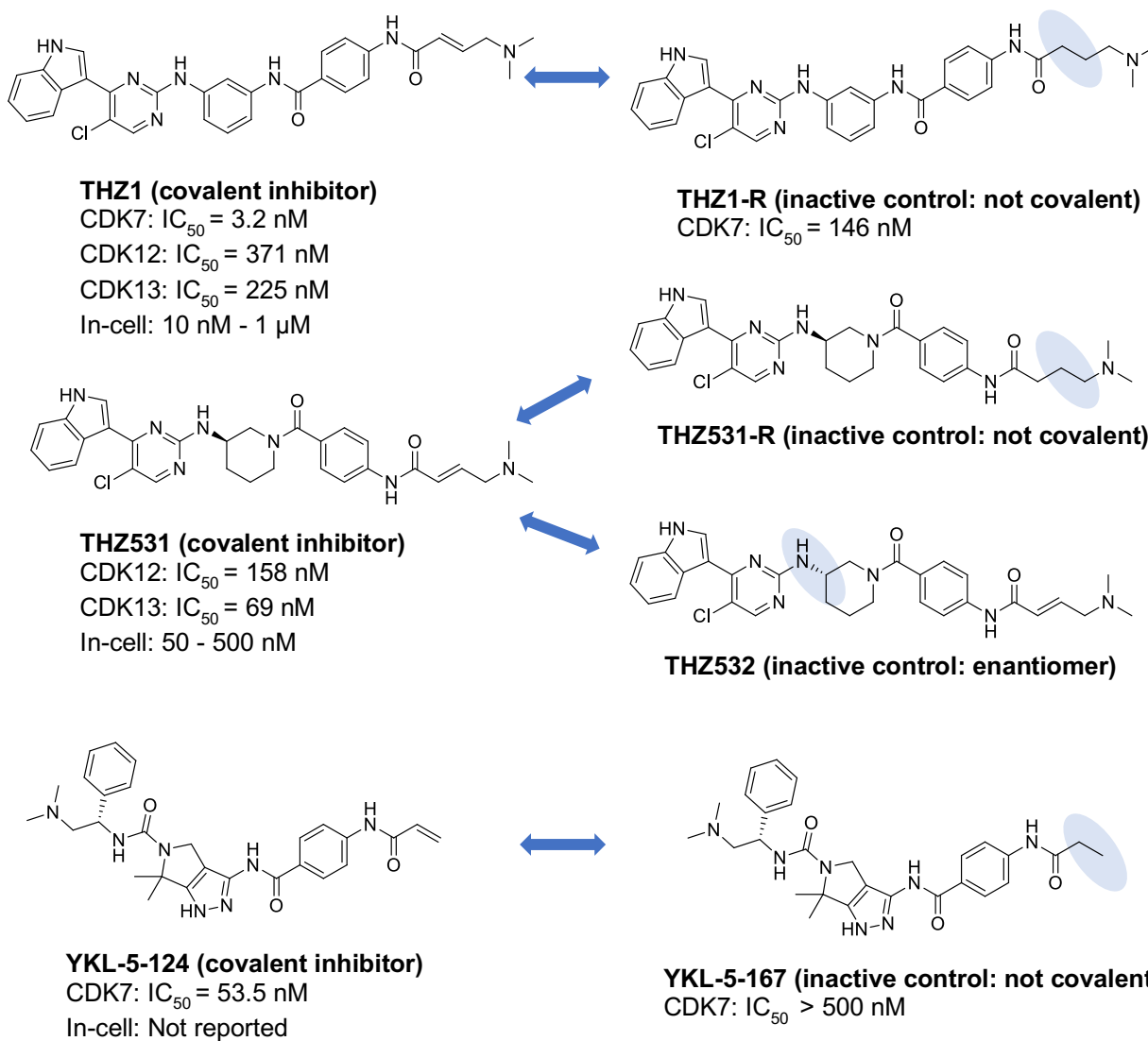
Supplementary Note 8. Citations for AZD2014 publications included in the systematic review.
Citations for 93 publications using AZD2014: 2,076

Citations for 80 publications with a compliant AZD2014 concentration: 1,798

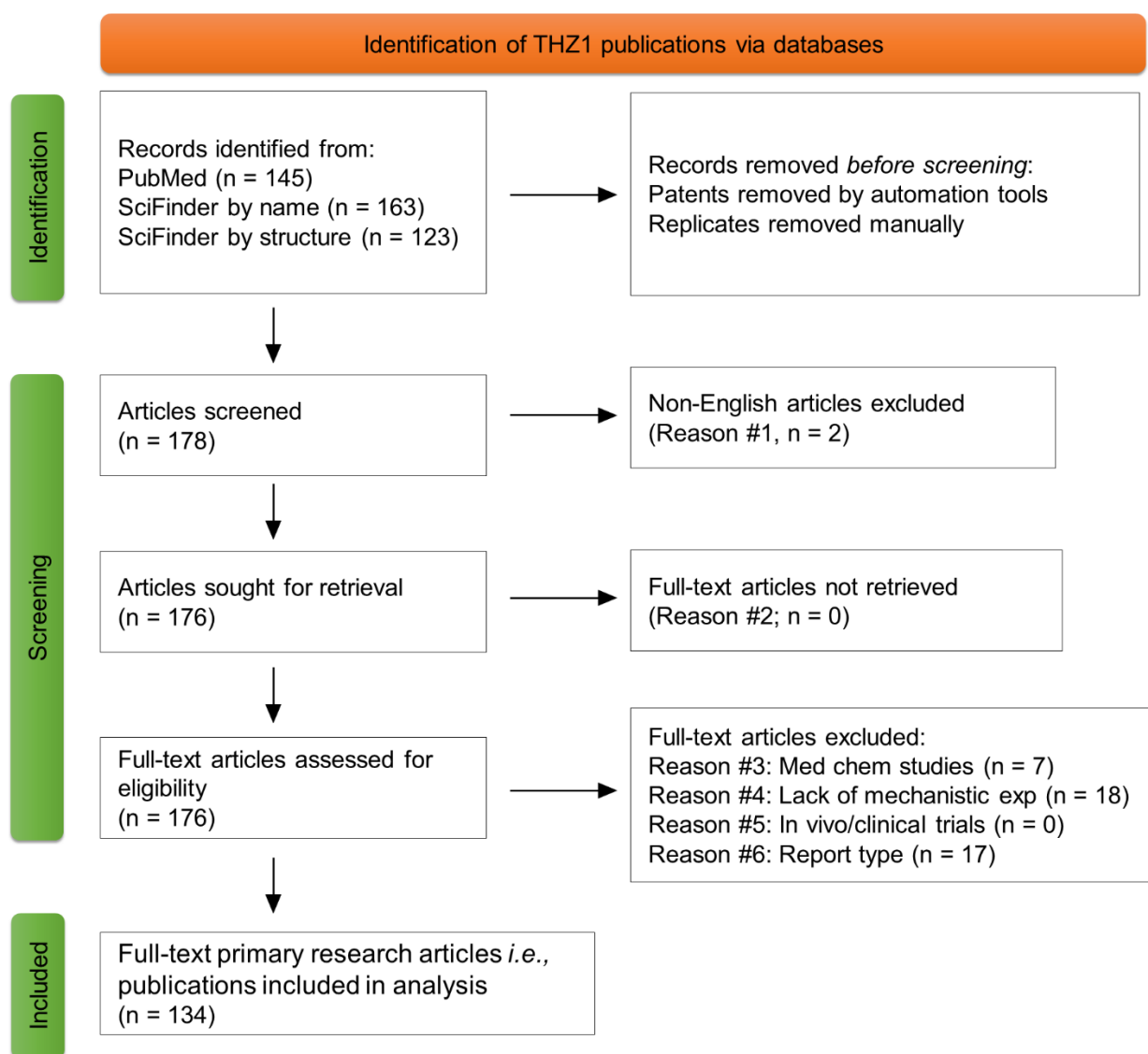
Citations for 13 publications with a non-compliant AZD2014 concentration: 278

Citations for 56 publications using orthogonal mTOR inhibitors: 1,313

Citations for 37 publications not using orthogonal mTOR inhibitors: 763



Supplementary Figure 12. Structures, biochemical potency (IC_{50}) and recommended in-cell concentrations of chemical probes targeting CDK7 and CDK12/13 as listed on the Chemical Probes Portal (www.chemicalprobes.org) and the Nathanael Gray Lab website (<https://graylab.stanford.edu/probe-resources/>). Bidirectional arrows link target-inactive analogues and shaded fields highlight the structural changes leading to decreased CDK7/12/13 targeting.



Supplementary Figure 13. PRISMA flow diagram summarising identification of publications using CDK7 chemical probe THZ1.

Note: Pubmed/SciFinder search keyword: THZ1 and “THZ-1”, respectively (maximises number of papers retrieved). Pubmed search retrieved 145 publications including any publication that writes ‘THz’ (e.g., 0.3 THz - 1 THz range, $55 \times 10^3 \text{ s}^{-1} \text{ THz-1 mW}^{-1}$). These 145 publications were manually reviewed for publications referring to the probe THZ1. SciFinder keyword search retrieved 166 publications including any publication that writes ‘THz’ (e.g., 0.3 THz - 1 THz range, $55 \times 10^3 \text{ s}^{-1} \text{ THz-1 mW}^{-1}$). These 166 publications were manually reviewed for publications referring to the probe THZ1.

Supplementary Table 15. List of excluded articles using the CDK7 probe THZ1.

| | Title (PMID) | Reason for exclusion |
|----|--|---|
| 1 | [Extracting THz absorption coefficient spectrum based on accurate determination of sample thickness] (PMID: 22715781) | 1) Non-English |
| 2 | CDK7 inhibitor THZ1 increases the radiosensitivity of human glioma cell line U251 (No PMID or DOI; ISSN: 1671-7554) | 1) Non-English |
| 3 | Targeting transcription regulation in cancer with a covalent CDK7 inhibitor (PMID: 25043025) | 3) Discovery of THZ1 & THZ1-R |
| 4 | Partitioning of cancer therapeutics in nuclear condensates (PMID: 32822580) | 3) Fluorescently modified THZ1 |
| 5 | Identification of CDK7 inhibitors from natural sources using pharmacoinformatics and molecular dynamics simulations (PMID: 34572383) | 3) Medicinal chemistry |
| 6 | Synthesis and biological evaluation of new C-12(α/β)-(N-) sulfamoyl-phenylamino-14-deoxy-andrographolide derivatives as potent anti-cancer agents (PMID: 28527822) | 3) Medicinal chemistry |
| 7 | Discovery of Novel N-(5-(Pyridin-3-yl)-1H-indazol-3-yl)benzamide derivatives as potent cyclin-dependent kinase 7 inhibitors for the treatment of autosomal dominant polycystic kidney disease (PMID: 36384292) | 3) Medicinal chemistry |
| 8 | Leveraging gas-phase fragmentation pathways for improved identification and selective detection of targets modified by covalent probes (PMID: 28193034) | 3) Medicinal chemistry |
| 9 | Discovery and characterization of SY-1365, a selective, covalent inhibitor of CDK7 (PMID: 31064851) | 3) SAR analysis |
| 10 | Quantifying CDK inhibitor selectivity in live cells (PMID: 32488087) | 4) No mechanistic exp.-cell viability & dose response only |
| 11 | Measurement and models accounting for cell death capture hidden variation in compound response (PMID: 32312951) | 4) No mechanistic exp.-cell viability & dose response only |
| 12 | Multiplexed and reproducible high content screening of live and fixed cells using Dye Drop (PMID: 36376301) | 4) No mechanistic exp. - dose response viability and cell cycle |
| 13 | The cryoelectron microscopy structure of the human CDK-activating kinase (PMID: 32855301) | 4) No mechanistic exp.-crystallography study |
| 14 | Nanomaterial-facilitated cyclin-dependent kinase 7 inhibition suppresses gallbladder cancer progression via targeting transcriptional addiction (PMID: 34405985) | 4) Nanoparticle delivery of THZ1 |
| 15 | Targeting super-enhancers via nanoparticle-facilitated BRD4 and CDK7 inhibitors synergistically suppresses pancreatic ductal adenocarcinoma (PMID: 32274304) | 4) Nanoparticle delivery of THZ1 |
| 16 | Design and characterization of telecentric f- θ scanning lenses for broadband terahertz frequency systems (PMID: 33344001) | 4) THZ1 not used |
| 17 | Vanadium dioxide-assisted broadband absorption and linear-to-circular polarization conversion based on a single metasurface design for the terahertz wave (PMID: 33114874) | 4) THZ1 not used |
| 18 | Non-perturbing THZ generation at the Tsinghua University Accelerator Laboratory 31 MeV electron beamline (PMID: 30278713) | 4) THZ1 not used |
| 19 | A single-crystal source of path-polarization entangled photons at non-degenerate wavelengths (PMID: 18575538) | 4) THZ1 not used |
| 20 | Narrowband polarization-entangled photon pairs distributed over a WDM link for qubit networks (PMID: 19547007) | 4) THZ1 not used |
| 21 | Computational drug repositioning identifies potentially active therapies for chordoma (PMID: 33017025) | 4) THZ1 not used in mechanistic assays |
| 22 | Overcoming resistance to the THZ series of covalent transcriptional CDK inhibitors (PMID: 29276047) | 4) THZ1 used to generate resistant cell clones |
| 23 | Patient-derived models recapitulate heterogeneity of molecular signatures and drug response in pediatric high-grade glioma (PMID: 34215733) | 4) Used in dose-response screen, no further experiments |
| 24 | Therapeutic targeting of ATR yields durable regressions in small cell lung cancers with high replication stress (PMID: 33848478) | 4) Used in dose-response screen, no further experiments |

| | | |
|----|--|---|
| 25 | Modeling and targeting of erythroleukemia by hematopoietic genome editing (PMID: 33512458) | 4) Used in dose-response screen, no further experiments |
| 26 | Refinement of in vitro methods for identification of aldehyde oxidase substrates reveals metabolites of kinase inhibitors (PMID: 29615437) | 4) Used in dose-response screen, no further experiments |
| 27 | Functionally active cyclin-dependent kinase 9 is essential for porcine reproductive and respiratory syndrome virus subgenomic RNA synthesis (PMID: 33990004) | 4) Used in screen, no further experiments |
| 28 | Androgen receptor interaction with mediator complex is enhanced in castration-resistant prostate cancer by CDK7 phosphorylation of MED1 (PMID: 31676563) | 6) Commentary |
| 29 | Collapsing the tumor ecosystem: Preventing adaptive response to treatment by inhibiting transcription (PMID: 29311224) | 6) Commentary |
| 30 | No driver behind the wheel? Targeting transcription in cancer (PMID: 26406367) | 6) Commentary |
| 31 | Revisiting the function of CDK7 in transcription by virtue of a recently described TFIID kinase inhibitor (PMID: 26295956) | 6) Commentary |
| 32 | Treating transcriptional addiction in small cell lung cancer (PMID: 25490443) | 6) Commentary |
| 33 | Inhibit globally, act locally: CDK7 inhibitors in cancer therapy (PMID: 25117707) | 6) Commentary |
| 34 | Highly selective purine based covalent CDK12 inhibitors. (No PMID, DOI or ISSN, AN: 2018:1503628) | 6) Conference abstract |
| 35 | Corrigendum: THZ1 targeting CDK7 suppresses STAT transcriptional activity and sensitizes T-cell lymphomas to BCL2 inhibitors (PMID: 28218232) | 6) Corrigendum |
| 36 | A CRISPR screen identifies CDK7 as a therapeutic target in hepatocellular carcinoma (PMID: 29507396) | 6) Letter to the editor |
| 37 | Comprehensive survey of CDK inhibitor selectivity in live cells with energy transfer probes (No PMID or DOI; ISSN: 2573-2293) | 6) Preprint |
| 38 | Advances in targeted therapy for osteosarcoma based on molecular classification (PMID: 34022396) | 6) Review |
| 39 | Cyclin-dependent kinase 7 inhibitor THZ1 in cancer therapy (PMID: 31891127) | 6) Review |
| 40 | The essential and multifunctional TFIID complex (PMID: 29664212) | 6) Review |
| 41 | Targeting bromodomain and extraterminal proteins in breast cancer (PMID: 29154989) | 6) Review |
| 42 | Nucleotide excision repair and transcriptional regulation: TFIID and beyond (PMID: 27294439) | 6) Review |
| 43 | Strategically targeting MYC in cancer (PMID: 27081479) | 6) Review |
| 44 | CDK7 Inhibitors in cancer therapy: The sweet smell of success? (PMID: 32150405) | 6) Review |

Supplementary Table 16. Overview of eligible publications using the CDK7/12/13 probe THZ1 and compliance (in blue) with recommendations to use THZ1 up to 1 μ M (<https://www.chemicalprobes.org/thz1?q=THZ1>), to validate data with an inactive control molecule THZ1-R and orthogonal inhibitors. Citations are sourced from SciFinder (January 2023), unless stated otherwise.

| | THZ1 | THZ1-R | Orthogonal inhibitors | Title (PMID) | Cites |
|----|---------------------|--------|---|---|-------|
| 1 | 0.1-500 nM | No | YKL-5-124, SY0351 (0.1 - 500 nM) | Transcriptional CDK inhibitors as potential treatment option for testicular germ cell tumors (PMID: 35406461) | 0 |
| 2 | 0.1 nM - 1 μ M | No | dinaciclub (CDK1/2/5/9), palbociclib (CDK4/6) | Characterizing CDK8/19 inhibitors through a NF κ B-dependent cell-based assay (PMID: 31590445) | 7 |
| 3 | 0.2 - 10 nM | No | THZ2 (40 - 240 nM) YKL-5-124 (50 nM) CT7001 (50 nM) | Transcriptional control of DNA repair networks by CDK7 regulates sensitivity to radiation in MYC-driven medulloblastoma (PMID: 33910002) | 12 |
| 4 | 0.78 - 800 nM | No | None | Selective Inhibitors of Autophagy Reveal New Link between the Cell Cycle and Autophagy and Lead to Discovery of Novel Synergistic Drug Combinations (PMID: 36469692) | 0 |
| 5 | 1 - 100 nM | No | None | SQLE inhibition suppresses the development of pancreatic ductal adenocarcinoma and enhances its sensitivity to chemotherapeutic agents in vitro (PMID: 35552960) | 0 |
| 6 | 1 - 13 nM | No | None | Targeting CDK7 reverses tamoxifen resistance through regulating stemness in ER+ breast cancer (PMID: 35000145) | 1 |
| 7 | 1 - 13 nM | No | None | Blockade of CDK7 reverses endocrine therapy resistance in breast cancer (PMID: 32340192) | 8 |
| 8 | 1 - 200 nM | No | BS-181 (0.1 - 20 μ M) | Therapeutic rationale to target highly expressed CDK7 conferring poor outcomes in triple-negative breast cancer (PMID: 28455421) | 60 |
| 9 | 1 - 250 nM | Yes | YKL-1-116 (0.1 - 5 μ M) | Targeting transcription in heart failure via CDK7/12/13 inhibition (PMID: 35896549) | 0 |
| 10 | 1 nM - 1 μ M | No | None | CDK7 inhibition synergizes with topoisomerase I inhibition in small cell lung cancer cells by inducing ubiquitin-mediated proteolysis of RNA polymerase II (PMID: 35830858) | 1 |
| 11 | 1.56 - 50 nM | No | None | A combination strategy targeting enhancer plasticity exerts synergistic lethality against BETi-resistant leukemia cells (PMID: 32029739) | 27 |
| 12 | 2 nM - 6.25 μ M | Yes | THZ2 (333 nM) | CDK7-dependent transcriptional addiction in triple-negative breast cancer (PMID: 26406377) | 30 |
| 13 | 3.125 nM - 200 nM | Yes | None | CDK7 inhibition is a novel therapeutic strategy against GBM both in vitro and in vivo (PMID: 30532595) | 19 |
| 14 | 4 - 32 nM | No | None | Combination therapy with the CDK7 inhibitor and the tyrosine kinase inhibitor exerts synergistic anticancer effects against MYCN-amplified neuroblastoma (PMID: 32086952) | 18 |
| 15 | 5 - 10 nM | No | None | Trib1 promotes acute myeloid leukemia progression by modulating the transcriptional programs of Hoxa9 (PMID: 32730594) | 17 |
| 16 | 5 - 20 nM | No | Dinaciclub (CDK1/2/5/9; 5 - 20 nM); palbociclib (CDK4/6; 1 μ M) | The individual effects of cyclin-dependent kinase inhibitors on head and neck cancer cells-A systematic analysis (PMID: 34063457) | 1 |
| 17 | 5 nM - 1 μ M | No | Palbociclib (CDK4/6); | Transcriptional targeting of oncogene addiction in medullary thyroid cancer (PMID: 30135308) | 15 |

| | | | | | |
|----|----------------|----|---|--|-----|
| | | | dinaciclub (CDK1/2/5/9) | | |
| 18 | 10 - 20 nM | No | Abemaciclib (CDK4/6, 0.1 - 1 µM), dinaciclub (CDK1/2/5/9, 1 - 5 nM) | Preclinical head and neck squamous cell carcinoma models for combined targeted therapy approaches (PMID: 35626088) | 0 |
| 19 | 10 - 50 nM | No | None | Myeloma-specific superenhancers affect genes of biological and clinical relevance in myeloma (PMID: 33579893) | 5 |
| 20 | 10 - 50 nM | No | Flavopiridol (broad-spectrum CDK inhibitor) | Elevation of effective p53 expression sensitizes wild-type p53 breast cancer cells to CDK7 inhibitor THZ1 (PMID: 36058938) | 0 |
| 21 | 10 - 100 nM | No | YPN-005 (10 - 100 nM) | Discovery of a novel CDK7 inhibitor YPN-005 in small cell lung cancer (PMID: 34224696) | 3 |
| 22 | 10 - 100 nM | No | None | CDK7 is a reliable prognostic factor and novel therapeutic target in epithelial ovarian cancer (PMID: 31776040) | 10 |
| 23 | 10 - 100 nM | No | YKL-1-116 (25 - 800 nM) | Activation of the p53 transcriptional program sensitizes cancer cells to Cdk7 inhibitors (PMID: 29020632) | 51 |
| 24 | 10 - 160 nM | No | None | Pharmaceutical interference of the EWS-FLI1-driven transcriptome by cotargeting H3K27ac and RNA polymerase activity in Ewing Sarcoma (PMID: 34315769) | 4 |
| 25 | 10 - 200 nM | No | None | Transcriptional dependencies in diffuse intrinsic pontine glioma (PMID: 28434841) | 181 |
| 26 | 10 - 250 nM | No | None | CDK7 inhibition suppresses super-enhancer-linked oncogenic transcription in MYCN-driven cancer (PMID: 25416950) | 394 |
| 27 | 10 - 500 nM | No | YKL-5-125 (1 - 500 nM) | BET and CDK inhibition reveal differences in the proliferation control of sympathetic ganglion neuroblasts and adrenal chromaffin cells (PMID: 35681734) | 0 |
| 28 | 10 nM - 500 nM | No | YKL-1-116 (0.5 - 20 µM), THZ531 (50 nM - 5 µM) | Targeting MYC dependency in ovarian cancer through inhibition of CDK7 and CDK12/13 (PMID: 30422115) | 90 |
| 29 | 10 nM - 1 µM | No | None | Efficacy of the CDK7 inhibitor on EMT-associated resistance to 3rd generation EGFR-TKIs in non-small cell lung cancer cell lines (PMID: 33287368) | 9 |
| 30 | 10 - 1000 nM | No | None | Cdk7 is required for activity-dependent neuronal gene expression, long-lasting synaptic plasticity and long-term memory (PMID: 29163040) | 10 |
| 31 | 10 nM - 1 µM | No | None | Tumors with TSC mutations are sensitive to CDK7 inhibition through NRF2 and glutathione depletion (PMID: 31506280) | 12 |
| 32 | 10 nM - 1 µM | No | None | Carrier-free multifunctional nanomedicine for intraperitoneal disseminated ovarian cancer therapy (PMID: 35193583) | 5 |
| 33 | 10 nM - 1 µM | No | None | Inhibition of cyclin-dependent kinase 7 suppresses human hepatocellular carcinoma by inducing apoptosis (PMID: 30145799) | 16 |
| 34 | 10 nM - 5 µM | No | None | Genomic modelling of the ESR1 Y537S mutation for evaluating function and new therapeutic approaches for metastatic breast cancer (PMID: 27748765) | 101 |
| 35 | 10 µM | No | LDC4297 (10 µM) milciclib (10 µM) | A high-throughput screen identifies that CDK7 activates glucose consumption in lung cancer cells (PMID: 31784510) | 15 |

| | | | | | |
|----|---------------------------------------|-----|----------------------------------|---|-----|
| 36 | 10 nM - 6.25 μ M; 100 & 250 nM | No | None | CDK7 inhibition is effective in all the subtypes of breast cancer: Determinants of response and synergy with EGFR inhibition (PMID: 32155786) | 16 |
| 37 | 12.5 - 100 nM | No | LDC4297 (2.5 - 5 μ M) | Targeting mutated p53 dependency in triple-negative breast cancer cells through CDK7 inhibition (PMID: 34109118) | 4 |
| 38 | 12.5 - 200 nM | No | None | CDK7 blockade suppresses super-enhancer-associated oncogenes in bladder cancer (PMID: 33905040) | 2 |
| 39 | 12.5 - 25 nM | No | None | Combinational therapeutic targeting of BRD4 and CDK7 synergistically induces anticancer effects in head and neck squamous cell carcinoma (PMID: 31765738) | 27 |
| 40 | 12.5 - 250 nM | No | THZ2 | Systematic characterization of recurrent genomic alterations in cyclin-dependent kinases reveals potential therapeutic strategies for cancer treatment (PMID: 32668240) | 13 |
| 41 | 12.5 - 250 nM | No | None | Super enhancer inhibitors suppress MYC driven transcriptional amplification and tumor progression in osteosarcoma (PMID: 29644114) | 66 |
| 42 | 12.5 nM - 1 μ M | Yes | CT7001 (125 nM - 5 μ M) | CDK7 inhibition suppresses aberrant hedgehog pathway and overcomes resistance to smoothed antagonists (PMID: 31182587) | 15 |
| 43 | 13 - 175 nM | No | None | CDK7 inhibition augments response to multidrug chemotherapy in pancreatic cancer (PMID: 35945614) | 0 |
| 44 | 20 - 80 nM | No | TZH531 & THZ531R (50 - 500 nM) | EWS/FLI confers tumor cell synthetic lethality to CDK12 inhibition in Ewing sarcoma (PMID: 29358035) | 80 |
| 45 | 20 - 200 nM | No | None | Targeting CDK7 suppresses super enhancer-linked inflammatory genes and alleviates CAR T cell-induced cytokine release syndrome (PMID: 33397398) | 9 |
| 46 | 20 - 500 nM | No | None | Targeting CDK7 increases the stability of Snail to promote the dissemination of colorectal cancer (PMID: 30451989) | 29 |
| 47 | 20 - 500 nM | No | None | High MITF expression is associated with super-enhancers and suppressed by CDK7 inhibition in melanoma (PMID: 29408204) | 32 |
| 48 | 25 - 50 nM | No | None | Inhibition of retinoic acid receptor α phosphorylation represses the progression of triple-negative breast cancer via transactivating miR-3074-5p to target DHRS3 (PMID: 33902658) | 2 |
| 49 | 25 - 100 nM | No | None | THZ1 targeting CDK7 suppresses c-KIT transcriptional activity in gastrointestinal stromal tumours (PMID: 36076237) | 0 |
| 50 | 25 - 200 nM | No | None | Super-enhancer-associated MEIS1 promotes transcriptional dysregulation in Ewing sarcoma in co-operation with EWS-FLI1 (PMID: 30496486) | 35 |
| 51 | 25 - 250 nM | No | None | SOX9 interacts with FOXC1 to activate MYC and regulate CDK7 inhibitor sensitivity in triple-negative breast cancer (PMID: 32398735) | 16 |
| 52 | 25 - 300 nM | No | None | Targeting super-enhancer-associated oncogenes in oesophageal squamous cell carcinoma (PMID: 27196599) | 134 |
| 53 | 25 - 400 nM | No | None | Characterization of super-enhancer-associated functional lncRNAs acting as ceRNAs in ESCC (PMID: 32460441) | 12 |
| 54 | 25 - 400 nM | Yes | ICEC0942 (CDK7, 1 - 2.5 μ M) | CDK7 inhibitor THZ1 inhibits MCL1 synthesis and drives cholangiocarcinoma apoptosis in | 25 |

| | | | | | |
|----|----------------------|-----|--|---|-----|
| | | | | combination with BCL2/BCL-XL inhibitor ABT-263 (PMID: 31399555) | |
| 55 | 25 - 500 nM | No | None | Super-enhancer landscape reveals leukemia stem cell reliance on X-box binding protein 1 as a therapeutic vulnerability (PMID: 34550724) | 7 |
| 56 | 25 - 600 nM | Yes | Flavopiridol (600 nM) | Targeting transcriptional addictions in small cell lung cancer with a covalent CDK7 inhibitor (PMID: 25490451) | 295 |
| 57 | 25 - 800 nM | No | None | Covalent CDK7 inhibitor THZ1 inhibits myogenic differentiation (PMID: 30210638) | 5 |
| 58 | 25 nM - 1 μ M | No | YKL-5-124 (25 - 400 nM) | Synergistic anti-tumor effect of combining selective CDK7 and BRD4 inhibition in neuroblastoma (PMID: 35198433) | 2 |
| 59 | 30 - 60 nM | No | None | Natural compound library screening identifies Sanguinarine chloride for the treatment of SCLC by upregulating CDKN1A (PMID: 35066462) | 0 |
| 60 | 30 - 500 nM | No | None | Super-enhancer-driven metabolic reprogramming promotes cystogenesis in autosomal dominant polycystic kidney disease (PMID: 32694829) | 11 |
| 61 | 31.25 nM - 1 μ M | No | YKL-5-124 (62 nM - 19 μ M) THZ531 (31 nM - 1 μ M) | Development of a selective CDK7 covalent inhibitor reveals predominant cell-cycle phenotype (PMID: 30905681) | 69 |
| 62 | 32 - 64 nM | No | None | JMJD6 is a tumorigenic factor and therapeutic target in neuroblastoma (PMID: 31346162) | 48 |
| 63 | 35 nM | No | None | TBX2 is a neuroblastoma core regulatory circuitry component enhancing MYCN/FOXM1 reactivation of DREAM targets (PMID: 30451831) | 48 |
| 64 | 40 nM - 5 μ M | Yes | None | A chemoproteomic strategy for direct and proteome-wide covalent inhibitor target-site identification (PMID: 30518210) | 48 |
| 65 | 50 nM | No | None | An integrative multi-omics approach uncovers the regulatory role of CDK7 and CDK4 in autophagy activation induced by silica nanoparticles (PMID: 32397800) | 12 |
| 66 | 50 nM | No | Dinaciclib (25 nM) | Synthetic lethality of PARP inhibitors in combination with MYC blockade is independent of BRCA status in triple negative breast cancer (PMID: 29180466) | 74 |
| 67 | 50 - 75 nM | No | THZ2, SY-1365 | TGF- β /activin signaling promotes CDK7 inhibitor resistance in triple-negative breast cancer cells through upregulation of multidrug transporters (PMID: 34481843) | 1 |
| 68 | 50 - 100 nM | No | Alvocidib (CDK9, 100 - 200 nM); dinaciclib (CDK9, 25 - 100 nM) | Vulnerability of drug-resistant EML4-ALK rearranged lung cancer to transcriptional inhibition (PMID: 32558295) | 7 |
| 69 | 50 - 100 nM | No | None | CDK7 inhibitor suppresses tumor progression through blocking the cell cycle at the G2/M phase and inhibiting transcriptional activity in cervical cancer (PMID: 30962695) | 16 |
| 70 | 50 - 100 nM | No | None | THZ1 reveals CDK7-dependent transcriptional addictions in pancreatic cancer (PMID: 30692639) | 30 |
| 71 | 50 - 100 nM | No | None | THZ1 suppresses human non-small-cell lung cancer cells in vitro through interference with cancer metabolism (PMID: 30446732) | 27 |
| 72 | 50 - 100 nM | No | Flavopiridol (pan-CDK, 50 nM) | Cyclin-dependent kinase 7 (CDK7)-mediated phosphorylation of the CDK9 activation loop promotes P-TEFb assembly with Tat and proviral HIV reactivation (PMID: 29743242) | 29 |

| | | | | | |
|----|-------------------|----|--|---|-------------|
| 73 | 50 - 100 nM | No | None | ER stress signaling promotes the survival of cancer "persister cells" tolerant to EGFR tyrosine kinase inhibitors (PMID: 29259014) | 62 |
| 74 | 50 - 100 nM | No | None | Inhibition of MYC suppresses programmed cell death ligand-1 expression and enhances immunotherapy in triple-negative breast cancer (PMID: 36583862) | 0 (Pub med) |
| 75 | 50 - 100 nM | No | None | Enhancer RNA commits osteogenesis via microRNA-3129 expression in human bone marrow-derived mesenchymal stem cells (PMID: 36114571) | 0 |
| 76 | 50 - 200 nM | No | None | CDK7 inhibitor THZ1 enhances antiPD-1 therapy efficacy via the p38 α /MYC/PD-L1 signaling in non-small cell lung cancer (PMID: 32690037) | 29 |
| 77 | 50 - 200 nM | No | None | Inhibition of super enhancer downregulates the expression of KLF5 in basal-like breast cancers (PMID: 31360115) | 18 |
| 78 | 50 - 200 nM | No | None | Antitumor effects of a covalent cyclin-dependent kinase 7 inhibitor in colorectal cancer (PMID: 30694816) | 5 |
| 79 | 50 - 200 nM | No | THZ531 (250 - 750 nM) | CDK9 activity is critical for maintaining MDM4 overexpression in tumor cells (PMID: 32934219) | 16 |
| 80 | 50 - 250 nM | No | None | Inhibition of the transcriptional kinase CDK7 overcomes therapeutic resistance in HER2-positive breast cancers (PMID: 31462705) | 33 |
| 81 | 50 - 250 nM | No | None | BCL2 amplicon loss and transcriptional remodeling drives ABT-199 resistance in B cell lymphoma models (PMID: 31085176) | 41 |
| 82 | 50 - 300 nM | No | None | Disruption of TFIIH activities generates a stress gene expression response and reveals possible new targets against cancer (PMID: 32543350) | 2 |
| 83 | 50 - 400 nM | No | None | The covalent CDK7 inhibitor THZ1 potently induces apoptosis in multiple myeloma cells in vitro and in vivo (PMID: 31358538) | 31 |
| 84 | 50 - 400 nM | No | Flavopiridol (pan-CDK, 400 nM); dinaciclib (CDK1/2/5/9, 25 nM) | The CDK7 inhibitor THZ1 alters RNA polymerase dynamics at the 5' and 3' ends of genes (PMID: 30805632) | 19 |
| 85 | 50 - 500 nM | No | None | Suppression of angiogenesis by targeting cyclin-dependent kinase 7 in human umbilical vein endothelial cells and renal cell carcinoma: An in vitro and in vivo study (PMID: 31752390) | 8 |
| 86 | 50 - 500 nM | No | None | Targeting super-enhancer-driven oncogenic transcription by CDK7 inhibition in anaplastic thyroid carcinoma (PMID: 30924726) | 33 |
| 87 | 50 - 500 nM | No | None | Suppression of adaptive responses to targeted cancer therapy by transcriptional repression (PMID: 29054992) | 65 |
| 88 | 50 - 500 nM | No | YKL-5-124, THZ531 (100 nM) | Blocking CDK7-mediated NOTCH1-cMYC signaling attenuates cancer stem cell activity in anaplastic thyroid cancer (PMID: 35822558) | 0 |
| 89 | 50 - 800 nM | No | None | Anti-tumor drug THZ1 suppresses TGF β 2-mediated EMT in lens epithelial cells via Notch and TGF β /Smad signaling pathway (PMID: 31333795) | 10 |
| 90 | 50 nM - 1 μ M | No | None | Epigenetic targeting of Mcl-1 is synthetically lethal with Bcl-xL/Bcl-2 inhibition in model systems of glioblastoma (PMID: 32752193) | 10 |
| 91 | 50 nM - 1 μ M | No | None | CDK7 inhibition as a promising therapeutic strategy for lung squamous cell carcinomas with a SOX2 amplification (PMID: 30838525) | 11 |

| | | | | | |
|-----|-------------------|-----|-------------------------------|--|----|
| 92 | 50 nM - 1 μ M | No | dinaciclub, flavopiridol | Preclinical efficacy and molecular mechanism of targeting CDK7-dependent transcriptional addiction in ovarian cancer (PMID: 28572168) | 48 |
| 93 | 62.5 - 100 nM | No | None | CDK7/GRP78 signaling axis contributes to tumor growth and metastasis in osteosarcoma (PMID: 36042349) | 0 |
| 94 | 100 nM | No | None | Identification of four enhancer-associated genes as risk signature for diffuse glioma patients (PMID: 34462884) | 2 |
| 95 | 100 nM | No | CYC065 (CDK2/9, 3 μ M) | Transcriptional CDK inhibitors, CYC065 and THZ1 promote Bim-dependent apoptosis in primary and recurrent GBM through cell cycle arrest and Mcl-1 downregulation (PMID: 34344865) | 3 |
| 96 | 100 nM | No | CYC065 (CDK2/9, 3 μ M) | Transcriptional CDK inhibitors CYC065 and THZ1 induce apoptosis in glioma stem cells derived from recurrent GBM (PMID: 34066147) | 2 |
| 97 | 100 nM | No | None | Pharmacological inhibition of CDK7 by THZ1 impairs tumor growth in p53-mutated HNSCC (PMID: 33503275) | 2 |
| 98 | 100 nM | No | None | Modulation of the Pol II CTD phosphorylation code by Rac1 and Cdc42 small GTPases in cultured human cancer cells and its implication for developing a synthetic-lethal cancer therapy (PMID: 32143485) | 2 |
| 99 | 100 nM | No | None | Aberrant super-enhancer landscape in human hepatocellular carcinoma (PMID: 30723918) | 53 |
| 100 | 100 nM | No | None | Essential role of endogenous prolactin and CDK7 in estrogen-induced upregulation of the prolactin receptor in breast cancer cells (PMID: 28423697) | 12 |
| 101 | 100 nM | No | None | Super enhancer-regulated LINC00094 (SERLOC) upregulates the expression of MMP-1 and MMP-13 and promotes invasion of cutaneous squamous cell carcinoma (PMID: 36010973) | 0 |
| 102 | 100 - 150 nM | No | None | Therapeutic targeting of CDK7 suppresses tumor progression in intrahepatic cholangiocarcinoma (PMID: 32174795) | 10 |
| 103 | 100 - 200 nM | No | None | CDK7 regulates organ size and tumor growth by safeguarding the Hippo pathway effector Yki/Yap/Taz in the nucleus (PMID: 31857346) | 32 |
| 104 | 100 - 200 nM | No | None | The covalent CDK7 inhibitor THZ1 enhances temsirolimus-induced cytotoxicity via autophagy suppression in human renal cell carcinoma (PMID: 31812697) | 16 |
| 105 | 100 - 200 nM | Yes | dinaciclub (10 nM) | CDK7 inhibition suppresses castration-resistant prostate cancer through MED1 inactivation (PMID: 31466944) | 42 |
| 106 | 100 - 200 nM | No | None | Cyclin-dependent kinase 7 is a therapeutic target in high-grade glioma (PMID: 28504693) | 46 |
| 107 | 100 - 300 nM | No | None | Enhancer profiling identifies critical cancer genes and characterizes cell identity in adult T-cell leukemia (PMID: 28978570) | 52 |
| 108 | 100 - 300 nM | No | None | Phosphoproteomics of primary cells reveals druggable kinase signatures in ovarian cancer (PMID: 28355574) | 67 |
| 109 | 100 - 500 nM | No | None | Super-enhancers promote transcriptional dysregulation in nasopharyngeal carcinoma (PMID: 28951465) | 69 |
| 110 | 100 - 500 nM | No | None | CDK7 inhibitor THZ1 induces the cell apoptosis of B-cell acute lymphocytic leukemia by perturbing cellular metabolism (PMID: 33889549) | 5 |

| | | | | | |
|-----|-------------------|-----|---|--|-------------|
| 111 | 0.1 - 1 μ M | No | Compound 919278 (0.01 - 10 μ M) | CDK12-mediated transcriptional regulation of noncanonical NF- κ B components is essential for signaling (PMID: 30065029) | 18 |
| 112 | 0.1 - 1.6 μ M | No | None | CDK7 inhibition by THZ1 suppresses cancer stemness in both chemo-naïve and chemoresistant urothelial carcinoma via the hedgehog signaling pathway (PMID: 33741425) | 4 |
| 113 | 0.2 - 5 μ M | No | None | Reimagining high-throughput profiling of reactive cysteines for cell-based screening of large electrophile libraries (PMID: 33398154) | 50 |
| 114 | 200 nM | No | None | Converged DNA damage response renders human hepatocellular carcinoma sensitive to CDK7 inhibition (PMID: 35406486) | 0 |
| 115 | 200 nM | No | None | Gene expression profile of THZ1-treated nasopharyngeal carcinoma cell lines indicates its involvement in the inhibition of the cell cycle (PMID: 35116274) | 0 |
| 116 | 200 nM | No | None | Inhibition of CDK7 bypasses spindle assembly checkpoint via premature cyclin B degradation during oocyte meiosis (PMID: 27693251) | 7 |
| 117 | 200 nM | No | None | Cyclin-dependent kinase 7 (CDK7) expression in human hepatocellular carcinoma: association with HCC progression, prognosis and cell proliferative capacity (No PMID; DOI: 10.21037/tcr.2018.04.15) | 1 |
| 118 | 200 nM | No | None | Phosphatase PP2A enhances MCL-1 protein half-life in multiple myeloma cells (PMID: 33658484) | 5 |
| 119 | 250 nM | No | HY-126251 (CDK9; 5 μ M) | Targeting triple-negative breast cancer with combination therapy of EGFR CAR T cells and CDK7 inhibition (PMID: 33875483) | 19 |
| 120 | 250 nM | No | THZ531 (1 μ M), Palbociclib (1 μ M), flavopiridol (10 - 200 nM) | Dynamic regulation of P-TEFb by 7SK snRNP is integral to the DNA damage response to regulate chemotherapy sensitivity (PMID: 36034227) | 0 |
| 121 | 250 nM | No | None | Modulating Androgen Receptor-Driven Transcription in Prostate Cancer with Selective CDK9 Inhibitors (PMID: 33086052) | 27 |
| 122 | 250 - 500 nM | No | None | THZ1, a covalent CDK7 inhibitor, enhances gemcitabine-induced cytotoxicity via suppression of Bcl-2 in urothelial carcinoma (PMID: 33520367) | 2 |
| 123 | 250 - 500 nM | Yes | SNS-032 | THZ1 targeting CDK7 suppresses STAT transcriptional activity and sensitizes T-cell lymphomas to BCL2 inhibitors (PMID: 28134252) | 63 |
| 124 | 400 nM | No | ICEC0942 (1 μ M) | ABC-transporter upregulation mediates resistance to the CDK7 inhibitors THZ1 and ICEC0942 (PMID: 31530935) | 10 |
| 125 | 0.5 - 1 μ M | No | SNS-032 (500 nM) | Pharmacological targeting of TFIIH suppresses KRAS mutant pancreatic ductal adenocarcinoma and synergizes with TRAIL (PMID: 35819261) | 0 (Pub med) |
| 126 | 0.5 - 1 μ M | No | THZ531 (0.01 pM - 10 mM) | Small-molecule targeting of brachyury transcription factor addiction in chordoma (PMID: 30664779) | 70 |
| 127 | 0.5 - 1 μ M | No | None | Global and transcription-coupled repair of 8-oxoG is initiated by nucleotide excision repair proteins (PMID: 35190564) | 3 |
| 128 | 1 μ M | No | THZ531 (0.1 - 1 μ M) | CDK7 is a component of the integrated stress response regulating SNAT2 (SLC38A2)/System A adaptation in response to cellular amino acid deprivation (PMID: 30857869) | 5 |

| | | | | | |
|------------------------------|----------------------------|-----------|----------|---|-----|
| 129 | 1 μ M | No | None | Human TFIIH kinase CDK7 regulates transcription-associated chromatin modifications (PMID: 28768201) | 83 |
| 130 | 1 μ M | No | None | THZ1 reveals roles for Cdk7 in co-transcriptional capping and pausing (PMID: 26257281) | 112 |
| 131 | 1 μ M | No | None | CtIP-dependent nascent RNA expression flanking DNA breaks guides the choice of DNA repair pathway (PMID: 36085345) | 0 |
| 132 | 1 μ M & 10 μ M | No | None | TFIIE orchestrates the recruitment of the TFIIH kinase module at promoter before release during transcription (PMID: 31064989) | 21 |
| 133 | concentration not provided | No | None | Transcription without XPB establishes a unified helicase-independent mechanism of promoter opening in eukaryotic gene expression (PMID: 28157507) | 47 |
| 134 | concentration not provided | No | None | Systematic analysis of drug vulnerabilities conferred by tumor suppressor loss (PMID: 31189115) | 14 |
| Compliance | | | | | |
| 124 (93%)^a | | 9 (7%) | 42 (31%) | | |
| 7 (5%)^b | | | | | |
| Non-Compliance | | | | | |
| 3 (2%) | | 125 (93%) | 92 (69%) | | |

a Probe's concentration below the recommended in-cell maximum in all figures.

b Probe's concentration below the recommended in-cell maximum in some, but not all figures.

Supplementary Note 9. Citations for THZ1 publications included in the systematic review.

Citations for 134 publications using THZ1: 3,785

Citations for 131 publications with a compliant THZ1 concentration: 3,709

Citations for 3 publications with a non-compliant THZ1 concentration: 76

Citations for 9 publications using inactive compound THZ1-R: 537

Citations for 125 publications not using inactive compound THZ1-R: 3,248

Citations for 42 publications using orthogonal inhibitors: 1,213

Citations for 92 publications not using orthogonal inhibitors: 2,572

Chapter 4

Pharmacological
evaluation of QC6352 in
glioblastoma cells

4.1. Introduction

The KDM4 family of lysine demethylases, encompassing five distinct enzymes from KDM4A to KDM4E, are important machinery in the regulation of epigenetic modifications¹. KDM4A-E are primarily known for their role in demethylating H3K9me3/me2, while KDM4A-C also shows activity demethylating H3K36me3/2²²³. The KDM4 enzymes either activate or repress transcription depending on the targeted lysine residue. H3K9 methylation is considered a repressive state for gene expression, often seen as a marker of senescence, thus in this context the KDM4 family function to activate gene expression. However, the opposite is true for H3K36 methylation which is considered important for activating the expression of DNA damage repair proteins and therefore KDM4 acts in a gene-repressing role¹.

In various cancer types, the dependency on individual KDM4 members varies. For example, in breast cancer cells, the knockdown of KDM4A leads to increased H3K9me3 marks at the EGFR promoter, which correlates with reduced tumour growth, while knockdown of KDM4B/C/D does not yield the same effect²¹⁰. In gastric cancer, KDM4B is specifically implicated in tumour progression as a key regulatory of c-Jun activity²²⁴. Enhanced cellular proliferation and migration were caused by IL-8 gene activation when demethylating H3K9me3/me2 at the IL-8 promoter²²⁴. Conversely, KDM4C knockdown in prostate cancer cells significantly inhibited cell viability by inhibiting Akt signalling²²⁵. KDM4D knockdown inhibited proliferation in acute myeloid leukemia (AML) by reducing MCL-1 expression controlled by H3K9me3 expression²²⁶. Finally, there are currently no studies that has focused on the function of KDM4E in cancer cells, and furthermore its gene expression is thought to be too low to significantly contribute to the chromatin methylation state²²⁷.

In glioblastoma, KDM4A has been shown to promote cell growth by upregulating PDK1 which activates the Akt-MTOR pathway²²⁸. Moreover, KDM4B knockdown also inhibited glioblastoma proliferation and survival by downregulating the oncogene MYC²²⁹ and KDM4C was shown to also increase MYC expression as well as suppress the expression of the tumour suppressor p53 and also maintaining stemness^{125,230}. Lastly, KDM4D was shown to accumulate at sites of DNA damage in glioblastoma cells in a PARP1-dependent manner. and assist in the repair of single strand breaks²³¹. Depletion of KDM4D sensitised the cells to DNA damage induced by ionising radiation and found to assist in the repair of single- and double-strand breaks²³¹.

There are few KDM4 inhibitors currently available to study the selective inhibition of KDM4 in cells²³². When comparing the KDM4 inhibitor selectivity profiles within the KDM family, QC6352 selectively inhibits KDM4A-D ($IC_{50} = 35 - 104$ nM) compared to KDM5B ($IC_{50} = 750$ nM) and KDM2A-B, KDM3A-B, or KDM6A-B inhibition ($IC_{50} > 10$ μ M)^{209,210}. Conversely, the broad-spectrum 2-OG inhibitor, IOX1, inhibits KDM4A-E at the high nanomolar range ($IC_{50} = 200 - 600$ nM) but also KDM3A and KDM6A-B ($IC_{50} = 0.14 - 1.1$ μ M)²³³. The selectivity profile for ML324 has not been fully investigated currently, but has demonstrated inhibition of KDM4E ($IC_{50} = 920$ nM)²³⁴ and KDM4B at ($IC_{50} = 4.9$ μ M)²³⁵ while B3 inhibits KDM4A-D with its IC_{50} ranging from 0.1 - 1 μ M²³⁶.

Out of these inhibitors, QC6352 is the only KDM4 inhibitor with sufficient potency, selectivity, and efficacy to be accepted as a chemical probe. Currently, there are only four publications investigating the role of the KDM4 family in cancer cells using QC6352. Metzger et al. showed that QC6352 decreased the viability of breast cancer stem cells by inhibiting specifically KDM4A leading to decreased EGFR expression²¹⁰. Moreover, Wang et al. found that QC6352 induced senescence in *TP53*-mutated gastric cancer cells by inhibiting KDM4C leading to repressed SP1-CDK2 signalling which allowed the senescence-targeting agent, SSK1, to effectively eliminate the cells²³⁷. In a study by Singh et al., rhabdomyosarcoma cells were dependent on KDM4B for tumour growth and QC6352 treatment eliminated the cancer cells and had no effect on non-cancerous muscle cells²³⁸. Lastly, renal tumour cells treated with QC6352 or siKDM4A were arrested in the S-phase caused by DNA double-strand breaks and impaired ribosome biogenesis²³⁹.

Our preliminary phenotypic screening of a library of epigenetic inhibitors (**Figure 1.5**) identified that QC6352 treatment significantly inhibited cell viability in glioblastoma stem cells. However, none of these studies comprehensively validated KDM4 as a cancer target, lacking orthogonal experiments and assays. This chapter aims to demonstrate the therapeutic potential of KDM4 inhibitors and validate KDM4 as the primary target for QC6352's mechanism of action in glioblastoma cells.

4.2. Results

4.2.1. Efficacy of KDM4 inhibitors in glioblastoma stem cells

To compare the biochemical activities of the structurally analogous KDM4 inhibitors, KDM4 inhibitory activity (IC_{50}) of QC6352, ML324, NCGC00244536 (also labelled as B3), and IOX1 were determined and compared against one another. In previous literature, the KDM4 inhibitors demonstrated inhibition within the range of 10 nM - 920 nM^{209,234,236,240} (**Figure 4.1a**), but inconsistent methodologies prevented direct comparison of their potencies. In this study, the inhibitors were assessed under uniform conditions in a biochemical KDM4A inhibition assay using AlphaScreen technology.

Dose-inhibition curves were constructed after incubating purified KDM4A protein with varying concentrations of inhibitor (2 nM - 100 μ M). The potency of the inhibitors was evaluated by comparing the extent of KDM4A inhibition to the baseline activity observed in the absence of inhibitors (set as 100%) (**Figure 4.1b**). The results revealed comparable KDM4A inhibition for QC6352, ML324, and IOX1, ranging from 78 nM - 404 nM. In contrast, B3 exhibited no detectable KDM4A inhibition at concentrations up to 20 μ M.

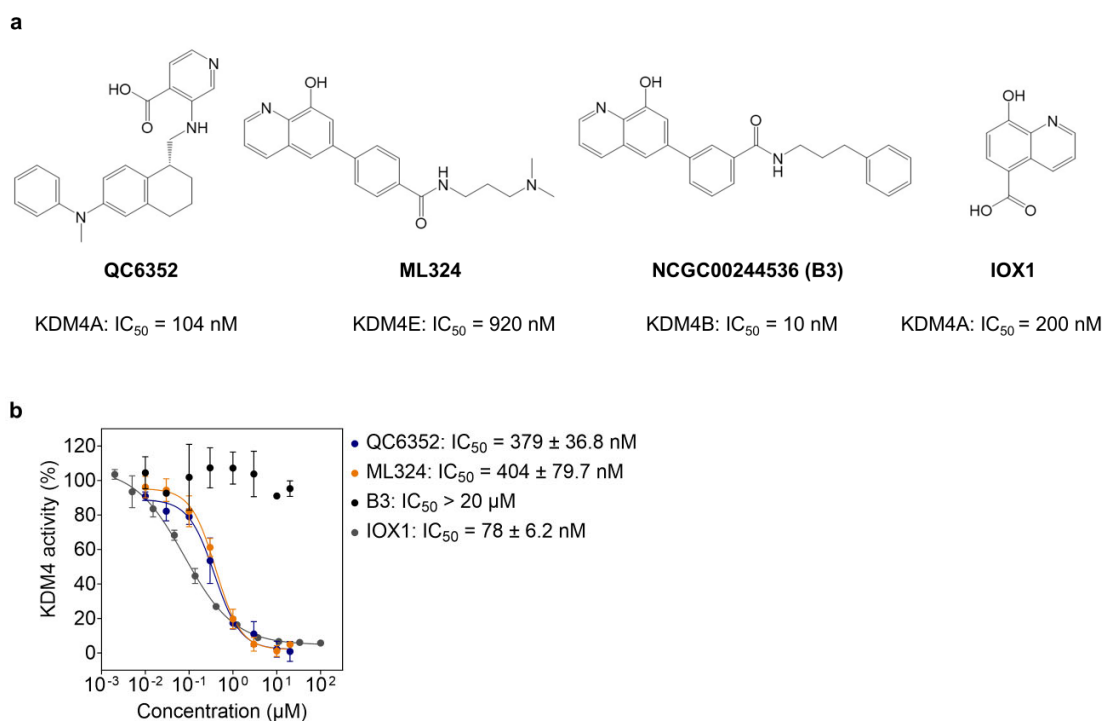


Figure 4.1. Biochemical potency of KDM4 inhibitors. a) Structures and reported IC_{50} values of the KDM4 inhibitors QC6352, ML324, NCGC00244536 (B3), and IOX1. **b)** KDM4A dose-inhibition curves determined with the AlphaScreen assay. IC_{50} values were determined by a four-parameter nonlinear analysis and mean \pm SEM ($n = 2$ for B3; $n = 3$ for ML324, QC6352, and IOX1). IOX1 data were generated by Ramzi Abbassi, PhD thesis 2021.

After confirming that KDM4A activity was inhibited by QC6352, antiproliferative efficacy was further explored. Cell viability, clonogenic, and spheroid growth assays were performed in various glioblastoma stem cell lines. The efficacy of QC6352 was assessed using the GRcalculator, a tool that accounts for the growth rate of each cell line, allowing for a more accurate comparison of the effects of different compounds across various cell lines²⁴¹. Generating GR dose-response curves and GR metrics, such as GR₅₀, GR_{max}, and h_{GR}, provides a standardised measure of cell sensitivity to the inhibitors²⁴¹.

The efficacy of QC6352 was evaluated in HW1 and GBM6 glioblastoma stem cell lines (**Figure 4.2a**), extending existing data obtained in RKI1, FPW1, SB2, and JK2 cells (Ramzi Abbassi, PhD thesis 2021; Jacinda Holtsmark, Honours thesis 2023). QC6352 demonstrated similar potency between HW1 and RKI1 cells, with GR₅₀ values of 135 nM and 98 nM, respectively. QC6352 treatment in all other tested cell lines showed a GR₅₀ value of less than 30 nM. Furthermore, QC6352 showed a cytotoxic efficacy in FPW1 cells (GR_{max} = -0.2) and cytostatic efficacy in the remaining cell lines, with GR_{max} between 0 in JK2 cells and 0.4 in HW1 cells. Across all tested cell lines, the Hill coefficient (indicator of cell-to-cell heterogeneity and sensitivity) was similar (h_{GR} = 1.2 - 1.6). Complementing these findings, clonogenic assays were also performed using HW1 and GBM6 cells treated with QC6352 for 10 days, showing significantly less confluency compared to untreated cells already at the lowest tested concentration of 5 nM (HW1: 5.4%, GBM6: 19.6%) (**Figure 4.2b-c**).

FPW1 and RKI1 stem cell lines were chosen for further experiments. To assess the recovery of glioblastoma cells from QC6352's cytostatic effects, FPW1 and RKI1 cells were treated with QC6352 for 10 days, followed by a 10-day drug-free period, known as a 'drug holiday' (**Figure 4.3a**). After 10 days of treatment, FPW1 and RKI1 cells showed a decrease in confluency compared to untreated, starting at 5 nM QC6352 (FPW1: 30%, RKI1: 53%). Following the drug holiday, the confluency of cells treated at 5 nM and 10 nM recovered to levels comparable to untreated cells, while cells treated with 50 nM and 100 nM did not recover to more than 25% confluency (**Figure 4.3b**).

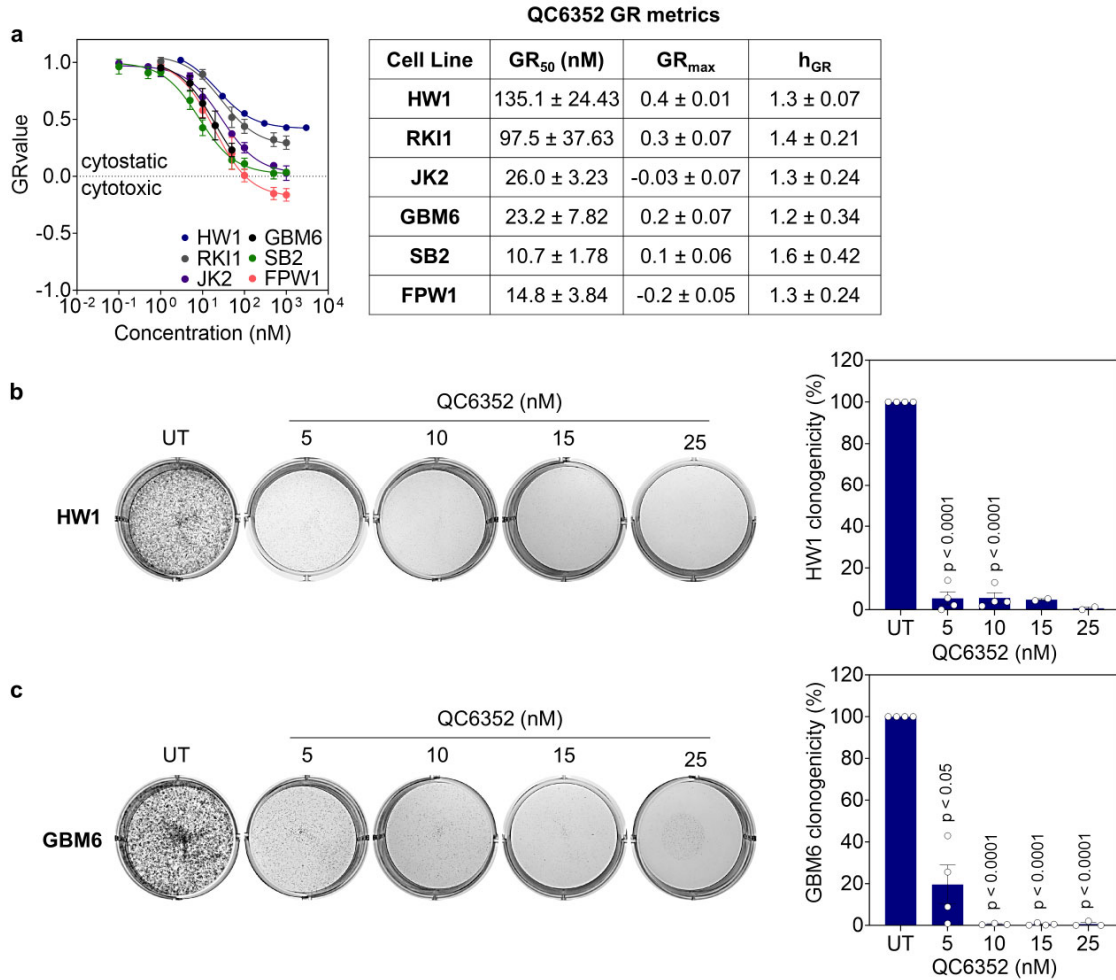


Figure 4.2. Efficacy and potency of QC6352 in glioblastoma stem cell lines. **a**) GR dose-response curves and GR metrics for QC6352 in glioblastoma stem cell lines treated for 5 days. Data represents the mean ± SEM (n = 3 - 5). **b - c**) Representative images of HW1 and GBM6 cells treated with QC6352 for 10 days, data represents the mean ± SEM (n = 2 - 4). One-sample t-tests were performed for each concentration with three or more replicates compared to 100%, and p-values were adjusted using Bonferroni's correction for multiple comparisons.

To investigate QC6352's antiproliferative effects in a disease-relevant tumour model, FPW1 and RKI1 cells were cultured into spheroids and treated with QC6352 for 14 days at concentrations of 0, 50, and 100 nM. Spheroid growth was assessed by measuring the circumference on Day 0, Day 7, and Day 14. Untreated FPW1 spheroids exhibited a 2.0-fold growth by Day 14, while treatment with QC6352 at 50 nM and 100 nM reduced growth to 1.5-fold and 1.4-fold, respectively (**Figure 4.4a**). Conversely, untreated RKI1 spheroids grew 6.3-fold by Day 14, but this growth was limited to 2.4-fold and 2.0-fold with 50 nM and 100 nM QC6352 treatment, respectively (**Figure 4.4b**). These results indicate that QC6352 effectively inhibits spheroid growth at concentrations of 50 nM and 100 nM.

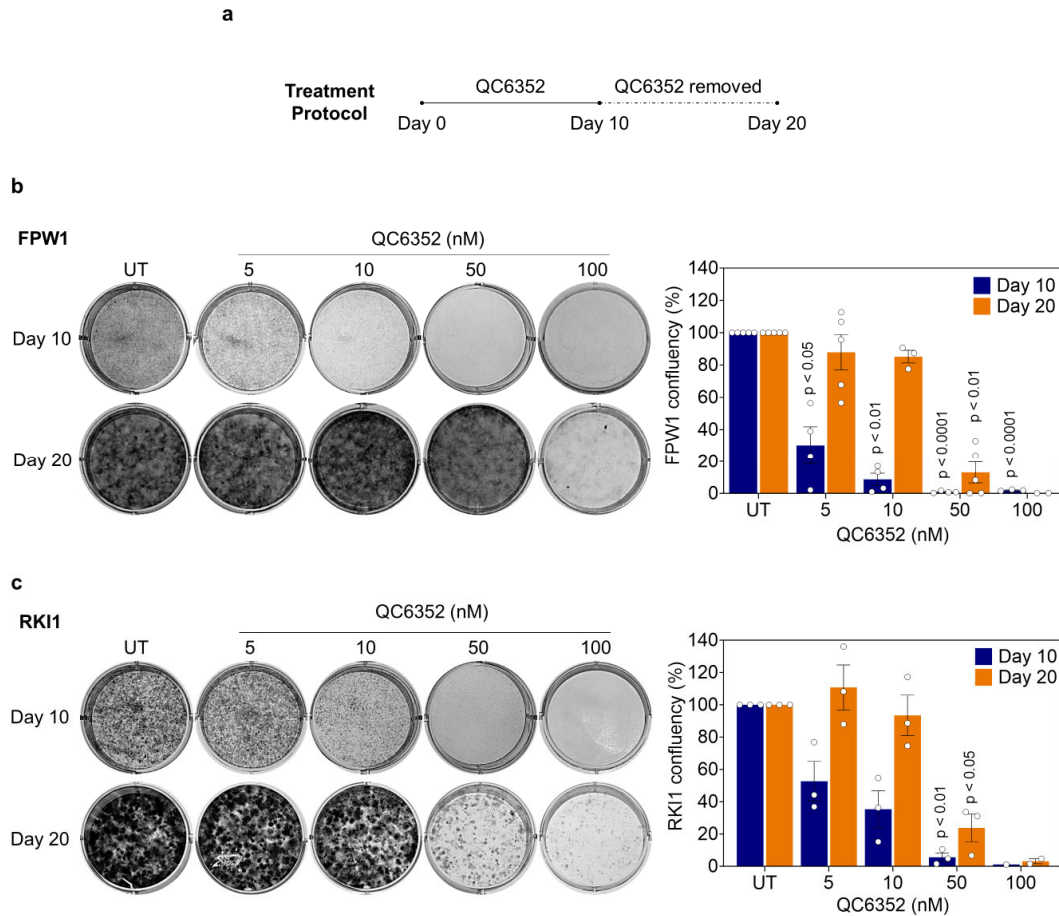


Figure 4.3. Efficacy of QC6352 in FPW1 and RK11 cells followed by drug holidays. **a)** Schematic diagram illustrating the ‘drug-holiday’ treatment protocol. **b)** Representative images in FPW1 (n = 2 - 5) and **c)** RK11 (n = 1 - 3) stem cell lines after 10 days of QC6352 treatment followed by an additional 10-day recovery in drug holiday. Quantifications are presented as mean \pm SEM. One-sample t-tests were performed for each concentration with three or more replicates compared to 100%. All p-values were adjusted using Bonferroni’s correction for multiple comparisons.

The potential role of KDM4 in glioblastoma cell proliferation was investigated by treating cells with the orthogonal KDM4 inhibitors ML324, B3, and IOX1 for 10 days. Surprisingly, all cell lines treated with ML324, B3, and IOX1 showed no significant change in confluency at all tested concentrations (**Figure 4.5**). Additionally, the effects of QC6352, ML324, and B3 on the viability of normal human astrocytes were also examined. Up to concentrations of 1 μ M, no significant alterations in astrocyte viability were detected. However, at a concentration of 100 μ M, all three KDM4 inhibitors exhibited complete cytotoxic efficacy, as indicated by a GR value of -1 (**Figure 4.6**). Thus, while ML324, B3, and IOX1 did not affect glioblastoma proliferation, QC6352, ML324, and B3 were found to exert cytotoxic effects on normal human astrocytes between concentrations of 1 μ M and 100 μ M. Cytotoxicity at 100 μ M may be due to many factors as, at this concentration, the compounds are likely to interfere with numerous targets and pathways.

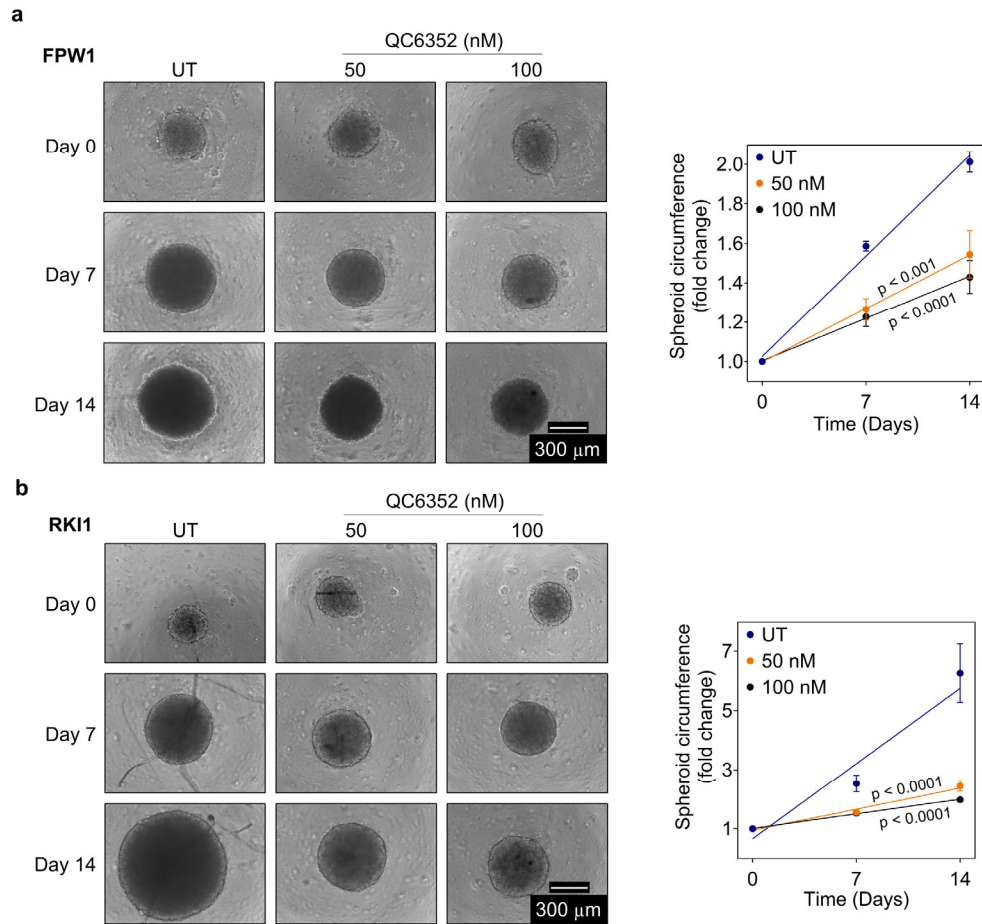


Figure 4.4. Antiproliferative efficacy of QC6352 in glioblastoma spheroids. Representative images and quantification of **a**) FPW1 ($n = 3 - 4$) and **b**) RKI1 ($n = 2 - 3$) spheroids size (circumference) following QC6352 treatment. Data are presented as mean \pm SEM. Simple linear regression analysis, followed by one-way ANOVA with Bonferroni's correction for multiple comparisons was used to determine significant changes in spheroid growth rate compared to untreated.

In summary, these findings support the antiproliferative efficacy of QC6352 in glioblastoma stem cells at concentrations up to 100 nM, without affecting the viability of normal human astrocytes at concentrations below 1 μ M. Through cell viability, clonogenic, and spheroid growth assays, QC6352 consistently inhibited cell growth, a response not observed with orthogonal KDM4 inhibitors ML324, B3, or IOX1. This is despite the findings that QC6352, ML324, and IOX1 exhibited comparable potencies in the AlphaScreen assay. Notably, QC6352-treated cells failed to recover during drug holidays at concentrations of 50 nM and above, suggesting a sustained efficacy after the removal of the drug.

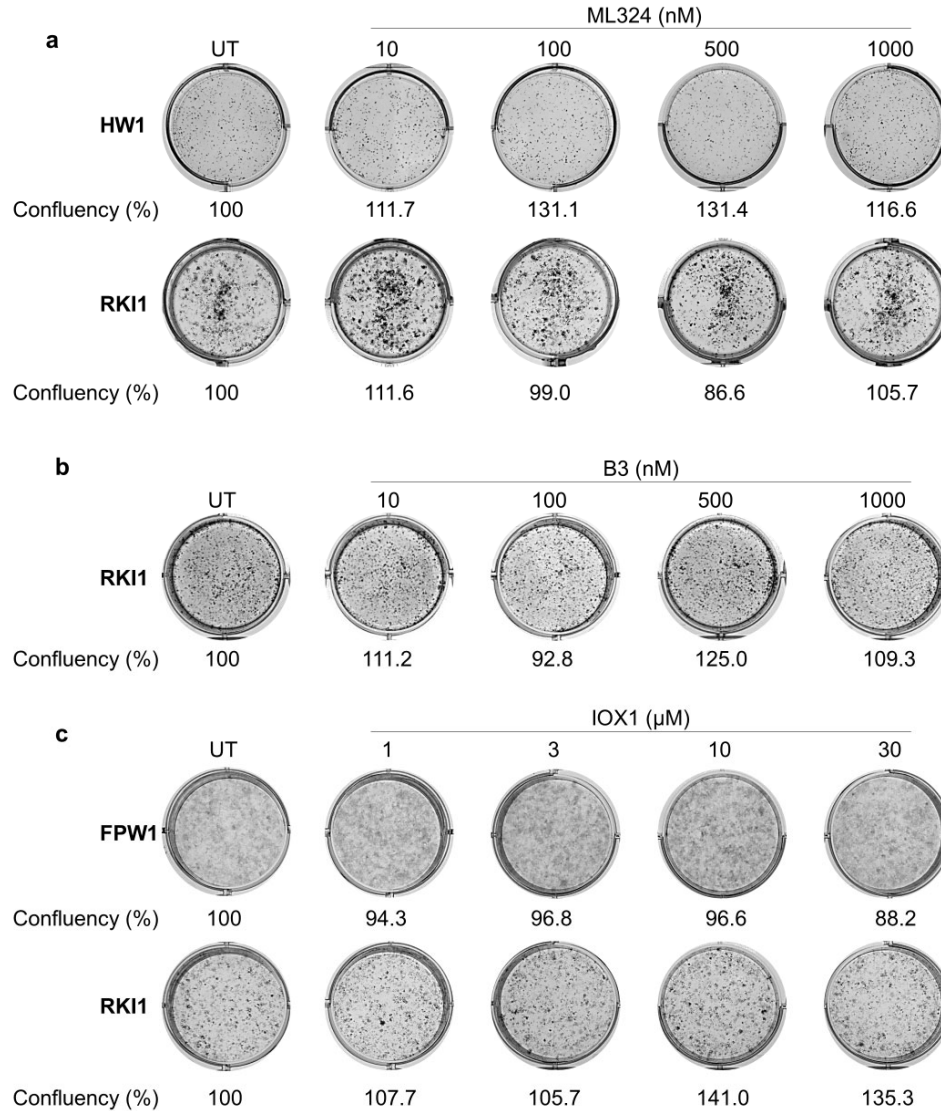


Figure 4.5. Efficacy of orthogonal KDM4 inhibitors in glioblastoma stem cells. Representative images of **a)** HW1 and RKI1 cells treated with ML324 (n = 2 - 4), **b)** RKI1 cells were treated with B3 (n = 2) and **c)** FPW1 and RKI1 cells treated with IOX1 (n = 2 - 3) for 10 days. Quantification is displayed below the representative images as mean confluency relative to untreated (UT).

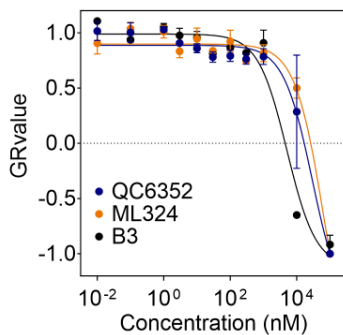


Figure 4.6. Efficacy of KDM4 inhibitors in normal human astrocytes. GR dose-response curves for glioblastoma stem cell lines treated with QC6352, ML324, and B3 for 5 days. Data represents the mean \pm SEM (n = 2 - 3).

4.2.2. QC6352 influences cellular processes related to growth and survival

With the antiproliferative effects of QC6352 established (Figures 4.1 - 4.6), attention was directed to understanding the underlying mechanism of action, beginning with the investigation of QC6352's impact on cell cycle arrest. Changes in the transcript levels of genes essential for cell cycle progression were assessed by RT-qPCR analysis of FPW1 cells treated with QC6352 at concentrations of 0, 100, and 500 nM for 5 and 7 days. Normalisation was performed using *GAPDH*, *ACTB1*, and *rRNA S18*, and fold-changes from untreated cells (set at 1) were calculated and expressed on a \log_2 scale. Consistency across all housekeeping genes led to the selection of *GAPDH* for representative data presentation. The analysis targeted genes representing different cell cycle phases: *MCM5*²⁴² and *ORC1*²⁴³ (S phase), *BUB1*²⁴⁴ (M phase), *NEK2*²⁴⁵ (G2/M transition), and *CCNA2*²⁴⁶ (G1/S and G2/M transition). Of all the tested genes involved in cell cycle progression, *NEK2* was significantly upregulated by 1.5-fold at Day 5 (Figure 4.7a) while *MCM5* and *ORC1* were significantly upregulated by 2.3- to 3.6-fold at Day 7 (Figure 4.7b). All remaining tested genes showed no significant difference in the presence of QC6352 for 5 and 7 days.

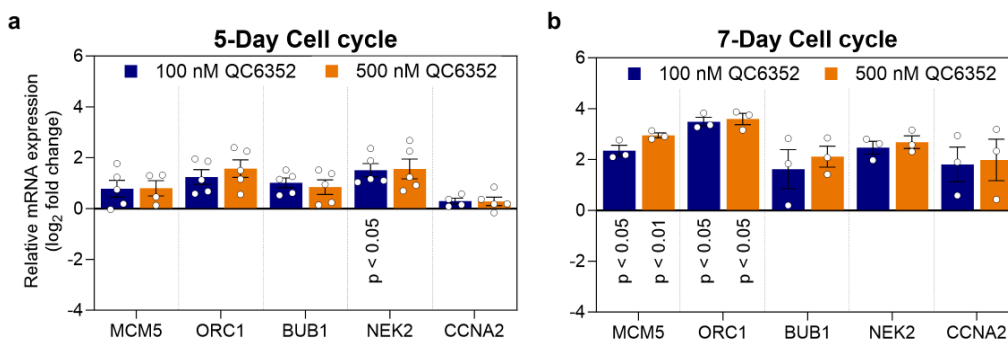


Figure 4.7. Cell cycle gene expression in QC6352-treated FPW1 cells. a - b) FPW1 cells received QC6352 treatment (0, 100, and 500 nM) for 5 and 7 days. Cell cycle gene expression, assessed via RT-qPCR, is displayed as Log_2 fold change relative to untreated, normalised to *GAPDH*. Data represents mean \pm SEM (n = 3 - 5). Paired t-tests were conducted for each gene prior to normalisation to show significant changes compared to untreated, with p-values were adjusted using Bonferroni's correction for multiple comparisons.

Cell cycle progression was further examined in A172 cells using the Fluorescence Ubiquitination Cell Cycle Indicator (FUCCI) system which visualises the distinct cell cycle stages through the expression of fluorescently tagged fusion proteins²⁴⁷. During the G0/G1 phase, the mKO2-hCdt1(30/120) fusion protein is expressed. This protein consists of the red fluorescent protein mKO2 fused to Chromatin licensing and DNA replication factor 1 (CDT1). In the S-G2-M phase, the mAG-hGem(1/110) fusion protein is expressed, consisting of the green fluorescent protein mAG fused to Geminin (Gem). The intermediate G1-S phase is

characterised by the co-expression of both fusion proteins, resulting in an orange fluorescence due to the overlapping expression of the red and green fluorescent proteins (**Figure 4.8a**).

A172-FUCCI cells were treated with QC6352 at the concentrations 0, 50, 100, and 500 nM and observed every 4 hours for changes in confluency and cell cycle progression using IncuCyte live cell imaging and analysis. Interestingly, there was no significant change in confluency between treated and untreated cells for 3 days after treatment, suggesting a delayed antiproliferative efficacy (**Figure 4.8b**). Specifically, after 5 days the confluency of untreated cells had increased by 6.7-fold while the confluency of cells treated with 50, 100, and 500 nM QC6352 had increased between 3.6- to 4.7-fold. Cell cycle analysis of A172-FUCCI cells in the presence of QC6352 at 50, 100, and 500 nM revealed a cell cycle arrest at the G0/G1 cell cycle phase. This was represented by an increase in the percentage of cells in the G0/G1 phase, ranging from 18 - 20% at Day 0, rising to 53 - 56% at Day 3, and reaching 76 - 77% at Day 5. In contrast, the percentage of untreated cells in the G0/G1 phases was 22% at Day 0, 33% at Day 3, and 37% at Day 5 (**Figure 4.8c**).

In response to the observed G0/G1 cell cycle arrest during treatment with QC6352, it was determined if cellular senescence was involved. Specific genes associated with senescence, defined as the irreversible cell cycle arrest²⁴⁸, were examined, namely, *CDKNIA*²⁴⁹, *CDKNIB*²⁵⁰, *DEC2*²⁵¹, *NR2F1*²⁵¹, *PML*²⁵², and *YPEL3*²⁵³. Transcript levels were evaluated using RT-qPCR and analysed using a log₂ scale. At Day 5, there was a significant upregulation in the genes *CDKNIA*, *CDKNIB*, *DEC2*, and *NR2F1*, with fold changes ranging from 0.6 to 1.9 (**Figure 4.9a**). By contrast, at Day 7, only *CDKNIA* continued to be upregulated, while *NR2F1* became downregulated (**Figure 4.9b**), suggesting a potential change in transcriptional activity between these timepoints.

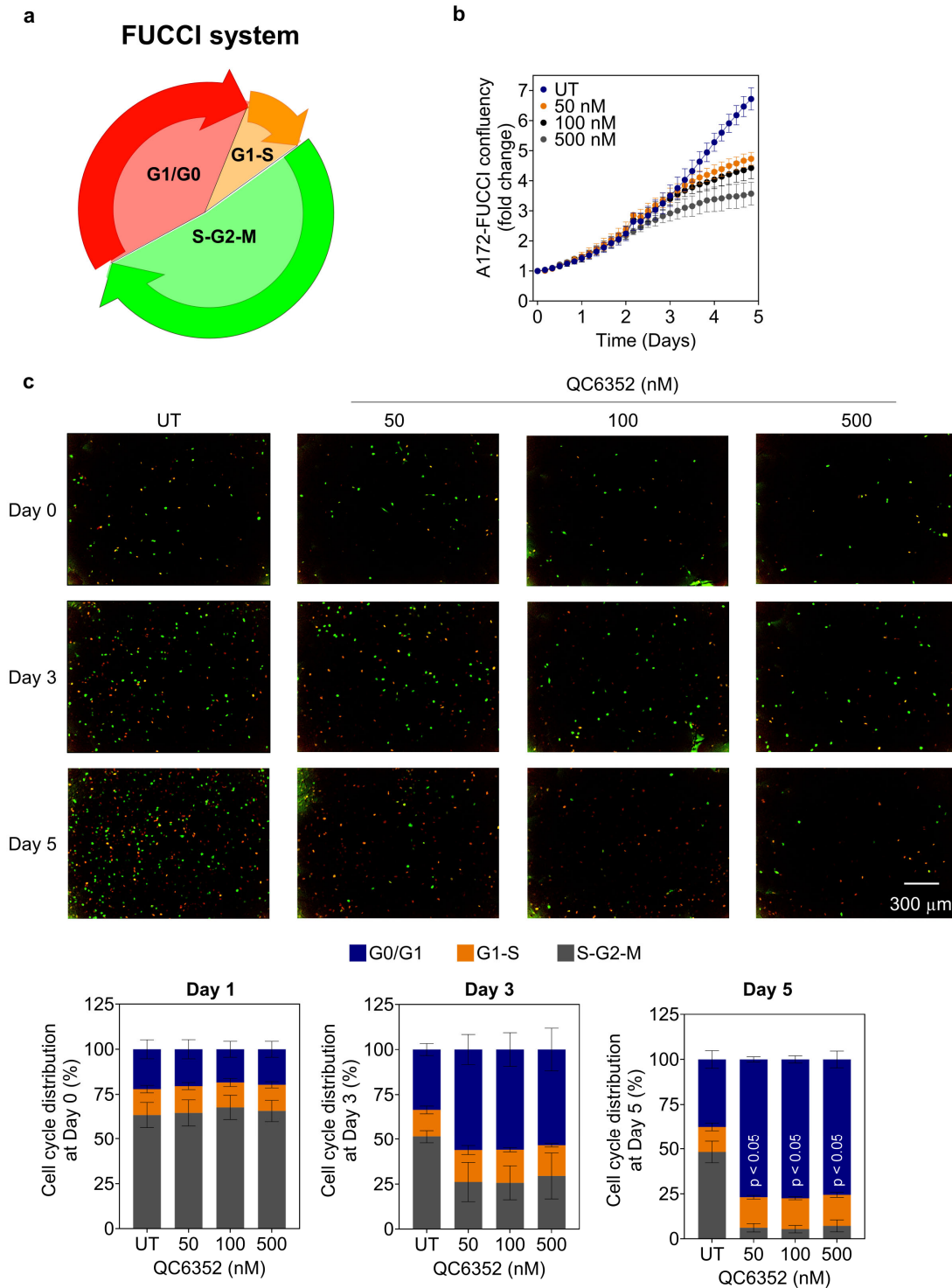


Figure 4.8. Cell cycle analysis in A172-FUCCI cells. **a)** Schematic illustrating the fluorescing colours representing different cell cycle phases visualised using the FUCCI system. **b)** Live cell imaging of A172-FUCCI cells ($n = 3$) treated with QC6352 at 0, 50, 100, and 500 nM for 5 days. **c)** Representative images and quantification of confluency (phase-contrast), G0/G1 (red), G1-S (orange) and S-G2-M (green) are shown at Day 0, Day 3, and Day 5. Data was obtained from three independent experiments conducted in triplicate, with four images taken per well. Data are presented as mean \pm SEM. Paired t-tests were performed for all concentrations and timepoints compared to untreated and p-values were adjusted using Bonferroni's correction for multiple comparisons.

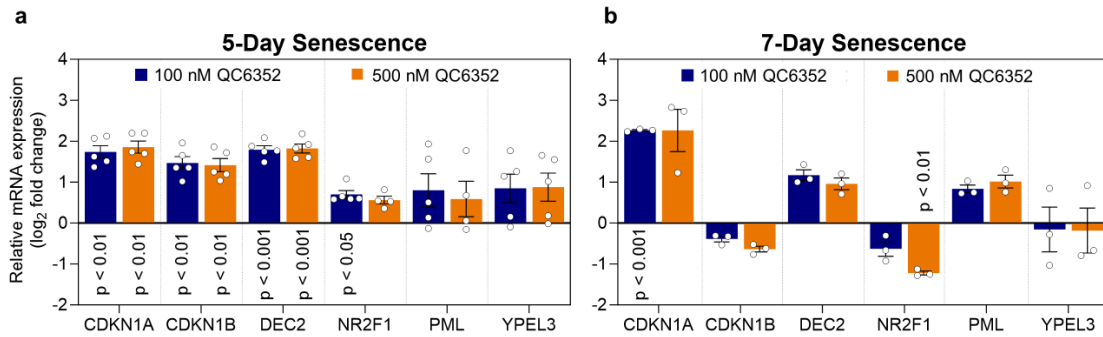


Figure 4.9. Senescence-associated gene expression in QC6352-treated FPW1 cells. a - b) FPW1 cells were subjected to QC6352 treatment (0, 100, and 500 nM) for 5 and 7 days. Senescence-associated gene expression, evaluated via RT-qPCR, is shown as log₂ fold change relative to untreated (UT), normalised to *GAPDH*. Data represents mean \pm SEM (n = 3 - 5). Paired t-tests were performed for each gene before normalisation compared to untreated and p-values were adjusted using Bonferroni's correction for multiple comparisons.

To confirm senescence following QC6352 treatment, FPW1 and RKI1 cells were stained for β -galactosidase expression. This enzyme's expression is known to be elevated in senescent cells and is therefore commonly used as marker of senescence²⁵⁴. Untreated FPW1 and RKI1 cells showed baseline senescent cell populations of 4% and 3%, respectively. Treatment with QC6352 at 50 nM did not affect FPW1 cells but increased the RKI1 senescent cell percentage to 11%. At 100 nM, QC6352 induced senescence in 35% of FPW1 cells (**Figure 4.10a**) and 14% of RKI1 cells (**Figure 4.10b**).

In summary, QC6352 treatment led to the upregulation of S phase-related genes in FPW1 cells and induced G0/G1 arrest in A172-FUCCI cells. This was accompanied by an increase in senescence-associated genes and β -galactosidase expression. Notably, treatment with 100 nM QC6352 only elevated β -galactosidase expression in 31% of FPW1 cells and 11% of RKI1 cells, reflecting a variable response wherein only a subset of cells presented markers of senescence.

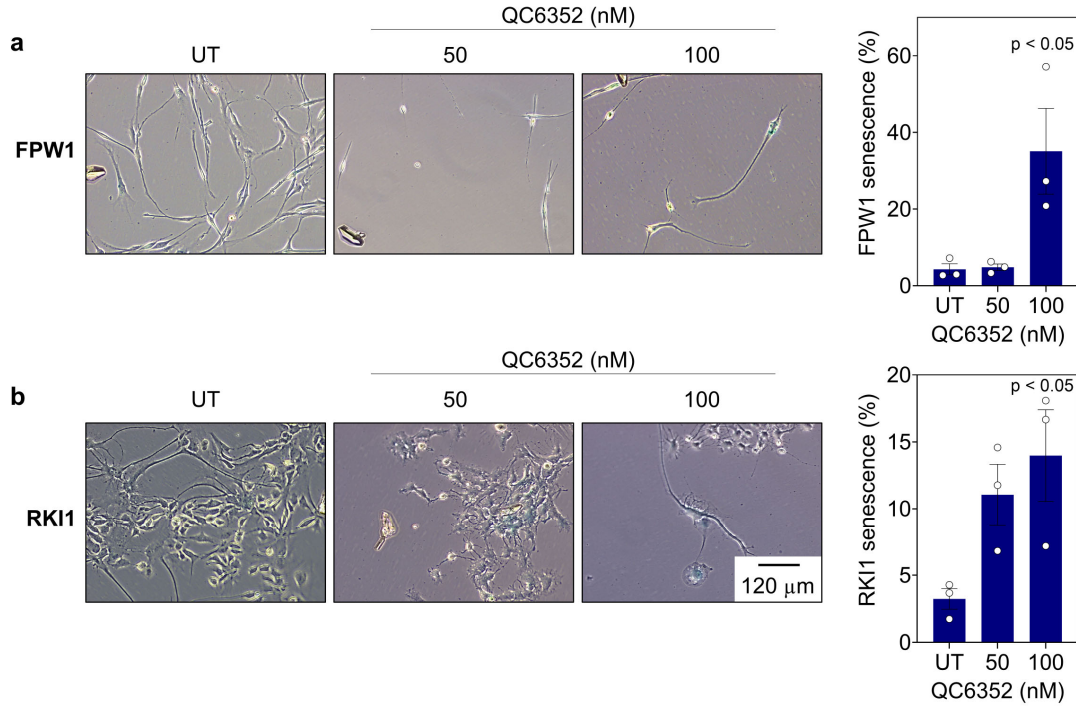


Figure 4.10. Senescence-associated protein expression in QC6352-treated FPW1 and RKI1 cells. a) FPW1 and b) RKI1 cells treated with QC6352 (0, 50, 100 nM) for 10 days and stained for β -galactosidase expression. Representative images were taken from three independent experiments and quantification shows the percentage of cells expressing β -galactosidase within the cell population for each treatment group. One-way ANOVA was performed to find significant changes compared to untreated, and p-values were adjusted using Bonferroni's correction for multiple comparisons.

To extend the analysis of QC6352's mechanisms in glioblastoma cells, the focus next shifted to the apoptotic pathway. Transcript levels of the pro-apoptotic genes *BAX*²⁵⁵, *PMAIP1*²⁵⁶, and *FOXO3*²⁵⁷, were quantified by RT-qPCR following 5 and 7 days of treatment with QC6352 and expressed on a log₂ scale. On Day 5, all three genes showed significant upregulation: 1.5-, 1.2-, and 1.3-fold increases at 100 nM and 1.6-, 1.7-, 1.9-fold increases at 500 nM (**Figure 4.11a**). By contrast, only *FOXO3* levels significantly changed on Day 7, exhibiting a 1.5- and 1.6-fold decrease at both concentrations, respectively (**Figure 4.11b**).

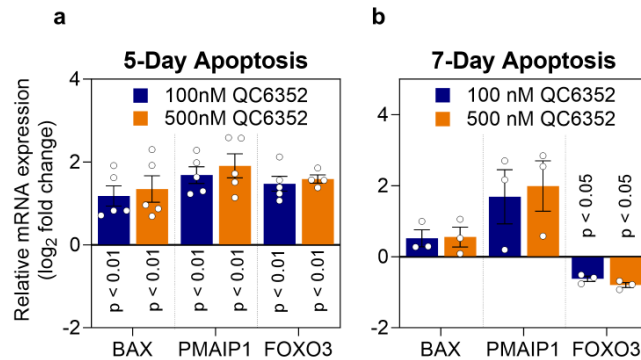


Figure 4.11. Apoptosis-associated gene expression in QC6352-treated FPW1 cells. a - b) FPW1 cells were treated with QC6352 (0, 100, and 500 nM) for 5 and 7 days. *BAX*, *PMAIP1* and *FOXO3* gene expression, measured via RT-qPCR, is presented as Log₂ fold change relative to untreated (UT), normalised to *GAPDH*. Data represents mean ± SEM (n = 3 - 5). Paired t-tests were conducted for each gene before normalisation compared to untreated and p-values were adjusted using Bonferroni's correction for multiple comparisons.

The effect of QC6352 on cell survival was subsequently investigated by analysing the extracellular presentation of the apoptosis marker phosphatidylserine using an InCuCyte Annexin V Red Reagent. Normally, phosphatidylserine is an intracellular component of the cell membrane that is released extracellularly during apoptosis²⁵⁸. Annexin V, which binds to phosphatidylserine²⁵⁹, was conjugated to a red fluorophore in the InCuCyte Annexin V Red Reagent. In the presence of apoptotic cells, the reagent fluoresces red, allowing for the detection of apoptosis. FPW1 and RKI1 cells were treated with QC6352 for a duration of 10 days, and apoptosis was measured as fluorescent intensity relative to cell confluency and compared against untreated cells (set as 1). FPW1 cells exhibited an 8-fold and 28-fold increase in apoptosis at 50 nM and 100 nM of QC6352, respectively (**Figure 4.12a**). RKI1 cells showed less apoptosis, with a 3-fold change at 50 nM and a 4-fold change at 100 nM (**Figure 4.12b**).

To assess if QC6352 induces differentiation in the glioblastoma stem cells, RT-qPCR was utilised and analysed using a log₂ scale to determine the expression of specific lineage-associated genes. Increased *GFAP* expression is associated with the astrocytic lineage²⁶⁰, while *MBP* and *OLIG2* are expressed in the oligodendrocyte lineage²⁶¹, and *TUBB2A* and *TUBB3* are indicative of the neuronal lineage²⁶². In the presence of QC6352 at 100 nM and 500 nM for 5 days, only *MBP* was significantly upregulated by 3.8-fold at 100 nM and 3.9-fold at 500 nM (**Figure 4.13a**). In contrast, after 7 days of treatment, only *GFAP* was downregulated by 5.5-fold at 100 and 500 nM (**Figure 4.13b**). Collectively, the findings indicate that QC6352 promotes differentiation into the oligodendrocyte lineage while inhibiting differentiation into the astrocytic lineage.

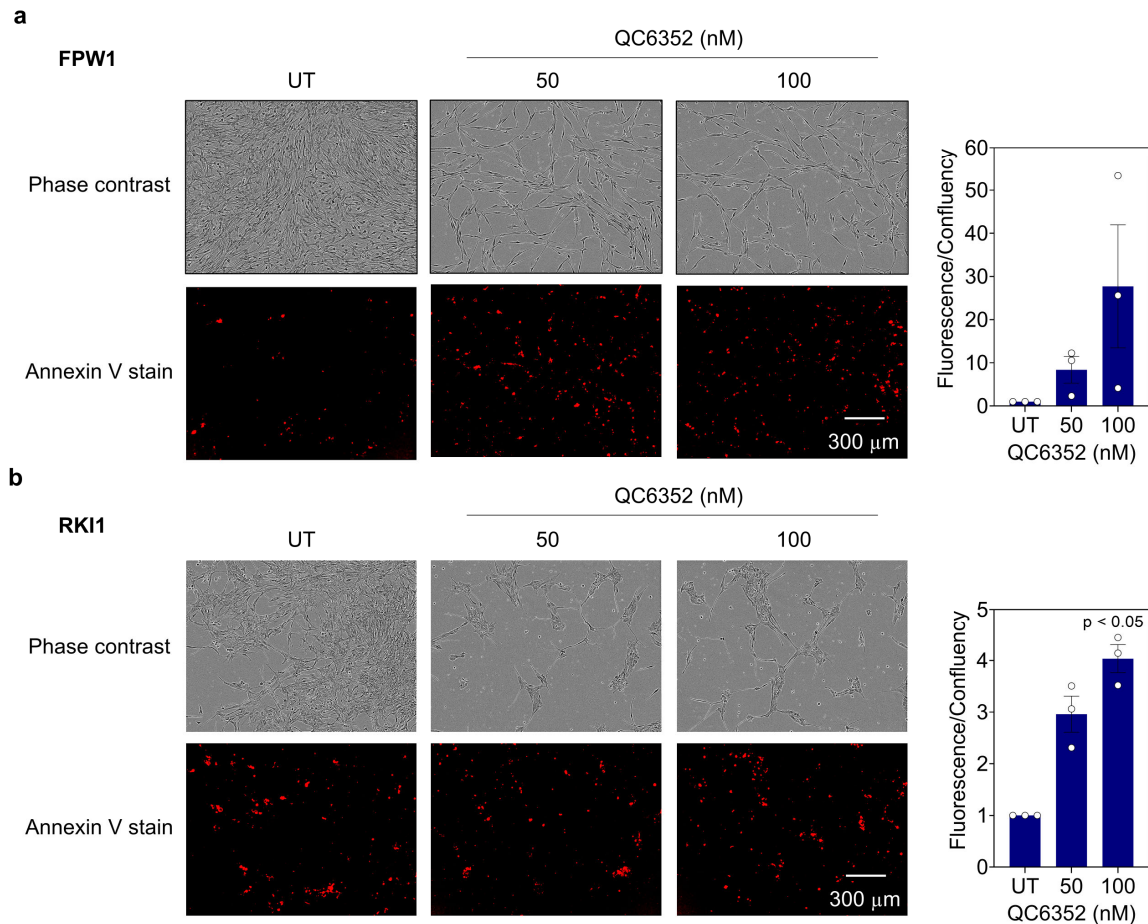


Figure 4.12. Apoptosis-associated protein expression in QC6352-treated in FPW1 and RKI1 cells. **a - b** Live cell imaging of apoptosis in FPW1 and RKI1 cells post 10-day QC6352 treatment at 0, 50, and 100 nM. Apoptosis visualised using IncuCyte Annexin V Red Reagent in triplicate, with four images taken per well. Data represents mean \pm SEM ($n = 3$). One-sample t-tests performed for each concentration compared to a fold change of 1, and p-values were adjusted using Bonferroni's correction for multiple comparisons.

To confirm the effect of QC6352 on differentiation, GFAP expression and β III-tubulin protein expression were next examined in FPW1 cells by immunofluorescence. In untreated cells, both proteins exhibited uniform basal expression. However, 10-day QC6352 treatment revealed a bifurcated response: a subset of cells displayed elevated expression of both proteins (represented by increased fluorescence), while the remainder exhibited reduced expression (**Figure 4.14**). The heterogeneity of the treated cell populations prevented accurate quantification of protein expression, necessitating a qualitative analysis.

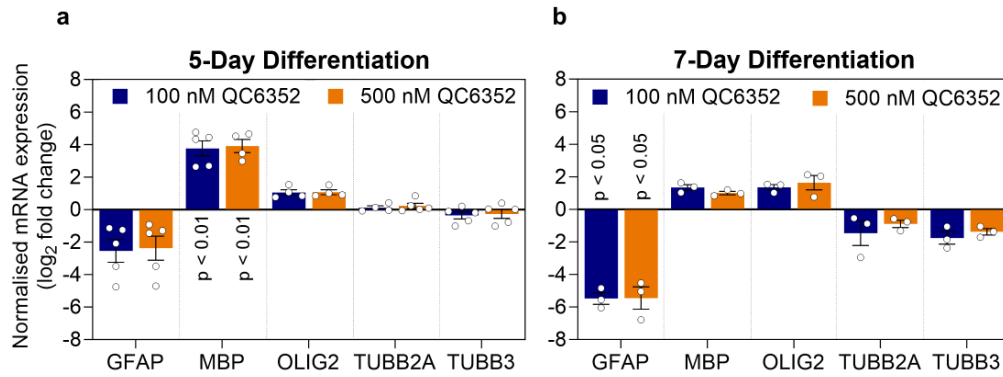


Figure 4.13. Differentiation-associated gene expression in QC6352-treated FPW1 cells. a - b) FPW1 cells treated with QC6352 at 0, 100, and 500 nM for 5 and 7 days. Expression of differentiation genes assessed by RT-qPCR, presented as Log₂ fold change relative to untreated (UT), normalised to *GAPDH*. Data represents mean \pm SEM (n = 3 - 5). Paired t-tests performed for each gene prior to normalisation compared to untreated, and p-values were adjusted using Bonferroni's correction for multiple comparisons.

To investigate if glioblastoma stem cells become more stem-like in the presence of QC6352, changes in the expression of genes associated with stemness, specifically, *NES*, *SOX2* and *SOX9*²⁶³, were investigated using RT-qPCR analysis, followed by changes in the protein expression of SOX9. The results showed a similar pattern to that observed when analysing changes in genes associated with differentiation in the presence of QC6352. After 5 days, cells treated at 100 nM and 500 nM revealed *SOX2* was significantly upregulated (100 nM: 0.7-fold; 500 nM: 0.8-fold) (**Figure 4.15a**). Moreover, after 7 days, *SOX2* became significantly downregulated at 500 nM (-1.1-fold) and *SOX9* was significantly downregulated (100 nM: 1.1-fold decrease; 500 nM: 1.5-fold decrease) (**Figure 4.15b**). Western blot analysis of RKI1 cells treated with QC6352 for 7 days revealed a significant 0.6-fold decrease in the protein expression of SOX9 (**Figure 4.15c**).

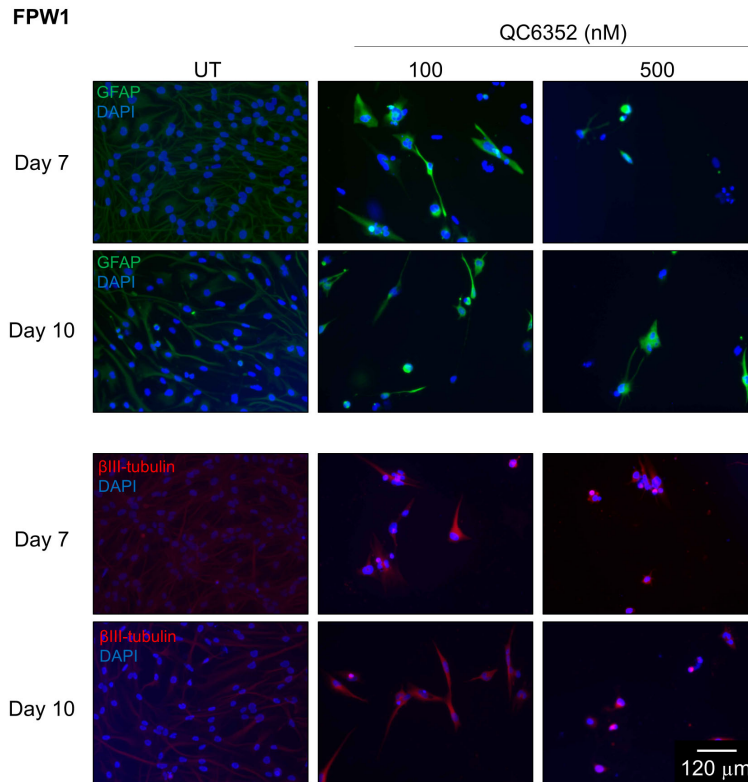


Figure 4.14. Differentiation status in QC6352-treated FPW1 cells. Immunofluorescence imaging of FPW1 cells treated with QC6352 at concentrations 0, 50, and 100 nM for 7 and 10 days. Cells were fixed and stained with DAPI (blue) and Alexa Fluor 488-labeled antibodies specific to GFAP (green) and β III-tubulin (red). Representative images from three independent experiments are shown.

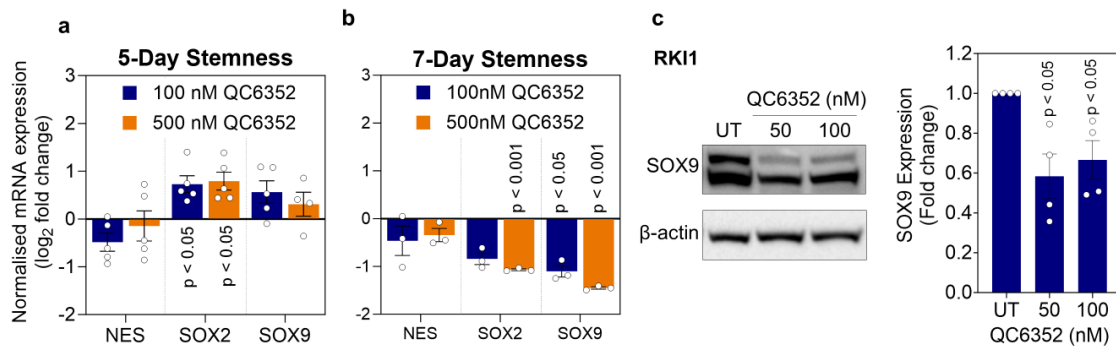


Figure 4.15. Expression of stemness markers in QC6352-treated FPW1 and RKI1 cells. **a - b)** FPW1 cells were treated with QC6352 (0, 100, and 500 nM) for 5 and 7 days. Stemness-related gene expression, assessed via RT-qPCR, is shown as Log_2 fold change relative to untreated (UT), normalised to *GAPDH*. Data represents mean \pm SEM ($n = 3 - 5$). Paired t-tests were performed for each gene before normalisation compared to untreated, with p-values adjusted using Bonferroni's correction. **c)** Western blot analysis with representative images of the expression of SOX9 and β -actin (30 μg of total protein) in RKI1 cells treated with QC6352 at concentrations 0, 50 and 100 nM for 10 days ($n = 4$). Data are expressed as mean \pm SEM. Statistical significance was assessed using one-sample t-tests compared to a fold change of 1 and p-values were adjusted using Bonferroni's correction.

To summarise, the findings thus far have demonstrated the effects of QC6352 in glioblastoma cells. Specifically, a G0/G1 arrest was observed in A172-FUCCI cells after 3 days of treatment, while S-phase-related genes were upregulated in FPW1 cells after 5 and 7 days of treatment. Treatment with QC6352 also identified subpopulations of senescent and apoptotic cells. Moreover, QC6352 induced a mixed response in gene expression changes related to differentiation and stemness, leading to the emergence of distinct subpopulations of differentiated cells. A significant decrease in both mRNA and protein levels of the stemness marker SOX9 was also observed after seven days of QC6352 treatment, suggesting a shift in the overall cell population towards a differentiated phenotype. Individually, each identified phenotype may not have a substantial impact on the overall cell proliferation rate, but since these phenotypes are occurring in combination with one another this leads to a pronounced antiproliferative effect.

4.2.3. KDM4 expression and localisation in glioblastoma stem cells

Initial findings suggest that KDM4 may not be a critical target in QC6352's mechanism of action, as indicated by the lack of efficacy of orthogonal KDM4 inhibitors ML324, B3, and IOX1 (**Figure 4.5**). Before examining whether KDM4 contributes to QC6352's mechanism of action, gene expression profiling was conducted to determine if KDM4 expression significantly differs from other genes important for histone post-translational modifications. Commonly, genes with higher expression levels are essential for proliferation and survival²⁶⁴. The expression of genes responsible for histone methylation (*KMT1-8*), demethylation (*KDMI-8*), acetylation (*KATI-8*), and deacetylation (*HDAC1-11*) were retrieved from RNA sequencing dataset of 12 glioblastoma stem cell lines used in our laboratory²¹³ (**Figure 4.16**). Gene expression was quantified as normalised read counts calculated as Fragments Per Kilobase of transcript per Million mapped reads (FPKM). Genes were ranked by their mean expression across all glioblastoma stem cell lines, and the cell lines were ranked by their median expression across the gene panel. *KDM4A-D* were ranked 36th, 39th, 57th, and 67th, respectively, and *KDM4E* gene expression was undetectable. The cell lines PB1, SJH1, SB2b, and HW1 showed higher *KDM4A-D* expression levels, ranging from 33 - 1046 FPKM. In contrast, the remaining cell lines exhibited minimal *KDM4A-D* expression, all less than 125 FPKM. These findings show that the KDM4 family is the least expressed KDM member and is less expressed than over 50% of all other examined histone-modifying genes.

KDM4 localisation was next investigated in FPW1 and RKI1 cells. Localisation is important for understanding the function of KDM4, as it dictates the site of its activity within the cell. To investigate this, immunofluorescence and Western blotting of subcellular fractionations were conducted, however, these methods yielded inconsistent results. Immunofluorescence showed nuclear and cytoplasmic localisation for KDM4A-E (**Figure 4.17a-b**), while Western blotting showed enrichment in the nuclear sample fractions for KDM4A-C (**Figure 4.17c**). The discrepancy between the two methods likely arises from the extensive non-specific antibody binding shown in the Western blot results. Unlike immunofluorescence, Western blotting offers a more refined distinction between specific and non-specific antibody interactions by enabling separation based on molecular weight.

In summary, gene expression profiling showed KDM4 was minimally expressed in glioblastoma stem cell lines and less expressed compared to other *KDM*, *KMT*, *HDAC* and *KAT* gene families. Our findings showed KDM4 protein localisation primarily in the nucleus of RKI1 cells. However, due to the noticeable non-specificity identified from the KDM4-targeting antibodies, additional experiments should be conducted using more specific KDM4-targeting antibodies to confirm and validate the obtained results.

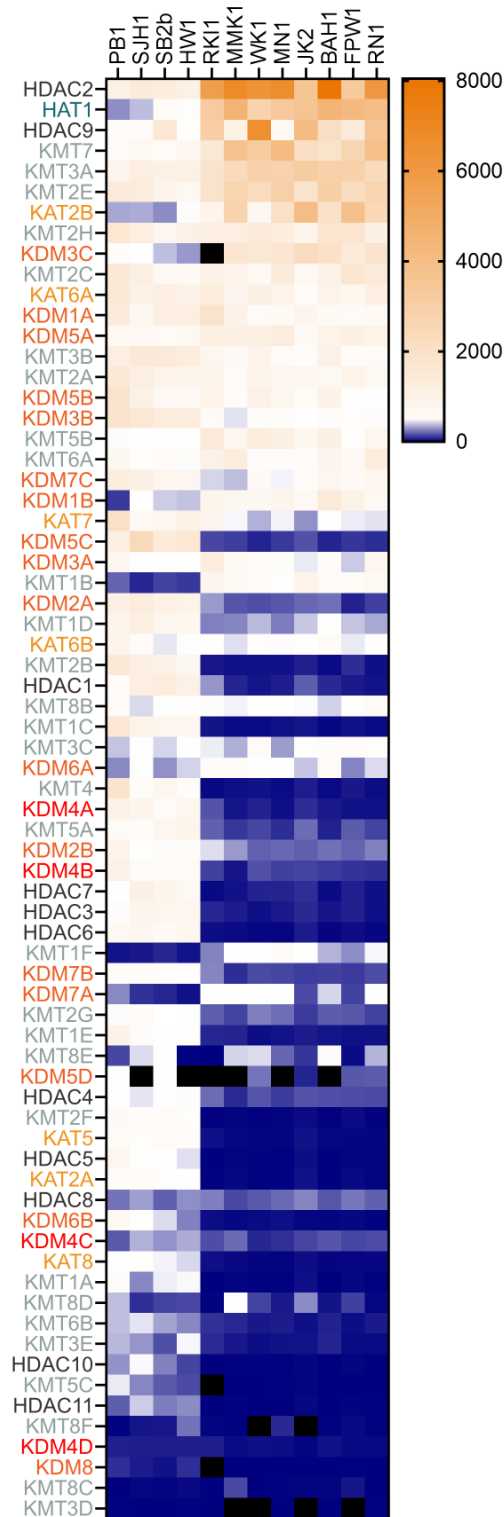


Figure 4.16. Gene expression of histone-modifying enzymes in glioblastoma stem cell lines. Heatmap showcases gene expression across epigenetic families: HDAC (dark blue), KAT (turquoise), KMT (light blue), and KDM (KDM4 in red; other KDM genes in orange). Cell lines ranked by descending median expression; genes ranked by descending average expression. Undetectable gene expression is marked in black. Data obtained from publicly available RNA sequencing²¹³.

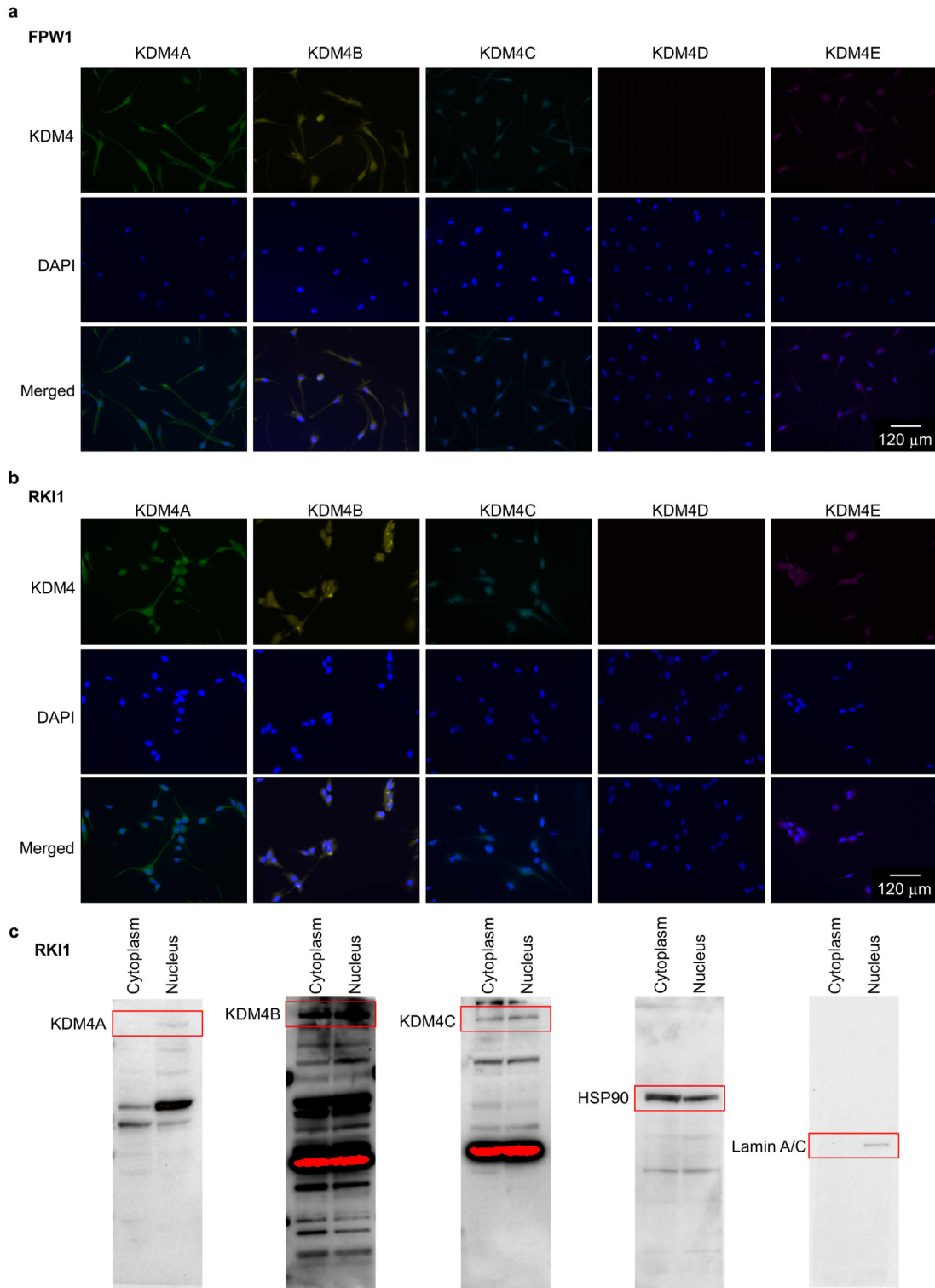


Figure 4.17. KDM4 localisation in FPW1 and RKI1 cells. a - b) Immunofluorescence imaging of FPW1 and RKI1 cells fixed and stained with DAPI (blue) and Alexa Fluor 488-labeled antibodies specific to KDM4A (green), KDM4B (yellow), KDM4C (aqua), KDM4D (brown), and KDM4E (purple). Representative images from three experiments are shown. **c)** Western blot protein samples were fractionated into nuclear and cytoplasmic proteins (n = 3) and probed for KDM4A (121 kDa), KDM4B (121 kDa), KDM4C (120 kDa), HSP90 (90 kDa), and Lamin A/C (74 kDa). A red box outlines the expected molecular weight for the targeted protein.

4.2.4. Target modulation by KDM4 inhibitors in glioblastoma stem cells

To gain insights into the mechanism of action of QC6352, the modulation of its primary target, KDM4, was assessed²⁰⁹. Target modulation refers to the process in which a bioactive molecule interacts with its intended biological target, inducing a measurable change in the target's activity or function²⁶⁵. This modulation underpins the observed phenotype and is often quantified by observing downstream functional outcomes²⁶⁶. In the context of QC6352, target modulation can be determined by increased methylation of the KDM4 sites of action, H3K9me3 and H3K36me3²⁶⁷. However, it is important to note that the changes in methylation could also be due to an indirect effect.

First, immunofluorescence was conducted in FPW1 cells treated with QC6352 at concentrations of 0, 50, 100, and 500 nM for 72 hours to identify any changes in the abundance of H3K9me3 and H3K36me3. However, the cells were too heterogenous to accurately compare changes in the methylation status (**Figure 4.18**). When observing changes in the levels of H3K9me3 in each cell individually, untreated fluorescent intensity was highly variable, ranging from 26 - 196 units, while cells treated with 50 nM - 500 nM QC6352 showed no significant change, ranging from 26 - 219 units. Furthermore, the mean fluorescence value across all cells remained relatively stable, with untreated cells exhibiting a mean value of 87 units, compared to 82 - 95 units in the treated cells.

The levels of H3K36me3 showed similar fluorescent intensity in untreated cells, ranging from 30 - 182 units, and fluorescent intensity in treated cells ranged from 26 - 219 units. However, despite the variation, the mean values from each treatment condition displayed a dose-dependent increase in trimethylation with untreated fluorescence showing a mean value of 63 units while 50 nM, 100 nM, and 500 nM QC6352 presented mean values of 82, 88, and 95 units, respectively (**Figure 4.18**).

To confirm the changes in H3K9me3 and H3K36me3 levels after QC6352 treatment, cell histones were extracted and subjected to Western blotting. A significant increase in both H3K9me3 and H3K36me3 was observed in cells treated with 10 nM QC6352 (**Figure 4.19**). H3K9me3 expression levels in cells treated with 10, 50, and 100 nM QC6352 increased by 1.4-, 1.8-, and 1.6-fold respectively compared to untreated cells. H3K36me3 expression levels showed a larger fold change than H3K9me3 expression levels when normalised to untreated cells. H3K36me3 expression levels in cells treated with 10, 50, and 100 nM QC6352 increased by 2.7-, 3.2-, and 4.1-fold, respectively, compared to untreated cell H3K36me3 abundance.

Additionally, orthogonal KDM4 inhibitors ML324 and B3 were tested for target modulation. The analysis showed a non-significant 1.5- and 1.7-fold change in H3K9me3 levels at 1 and 5 μ M, respectively (**Figure 4.20a**). When examining H3K36me3 abundance, 5 μ M of ML324 resulted in a 3-fold increase. At similar concentrations, B3 had no change on H3K9me3 or H3K36me3 levels up to 5 μ M (**Figure 4.20b**).

Taken together, target modulation of KDM4 inhibitors QC6352, ML324, B3 was examined in FPW1 and RKI1 cells by analysing changes in the abundance of H3K9me3 and H3K36me3. Immunofluorescence in FPW1 cells showed a variable methylation status. Despite this, a noticeable increase in H3K36me3 levels was noted after QC6352 treatment. Western blotting supported this, indicating a smaller increase in H3K9me3 abundance. In RKI1 cells, a minor, non-significant increase in H3K9me3 levels was observed for both QC6352 and ML324 but not B3. Additionally, a 5 μ M concentration of ML324 resulted in a significant increase in H3K36me3 levels. These preliminary findings suggest that QC6352 and ML324 show some level of target modulation, but further studies are needed to confirm whether these are direct effects of KDM4 inhibition or the result of off-target interactions.

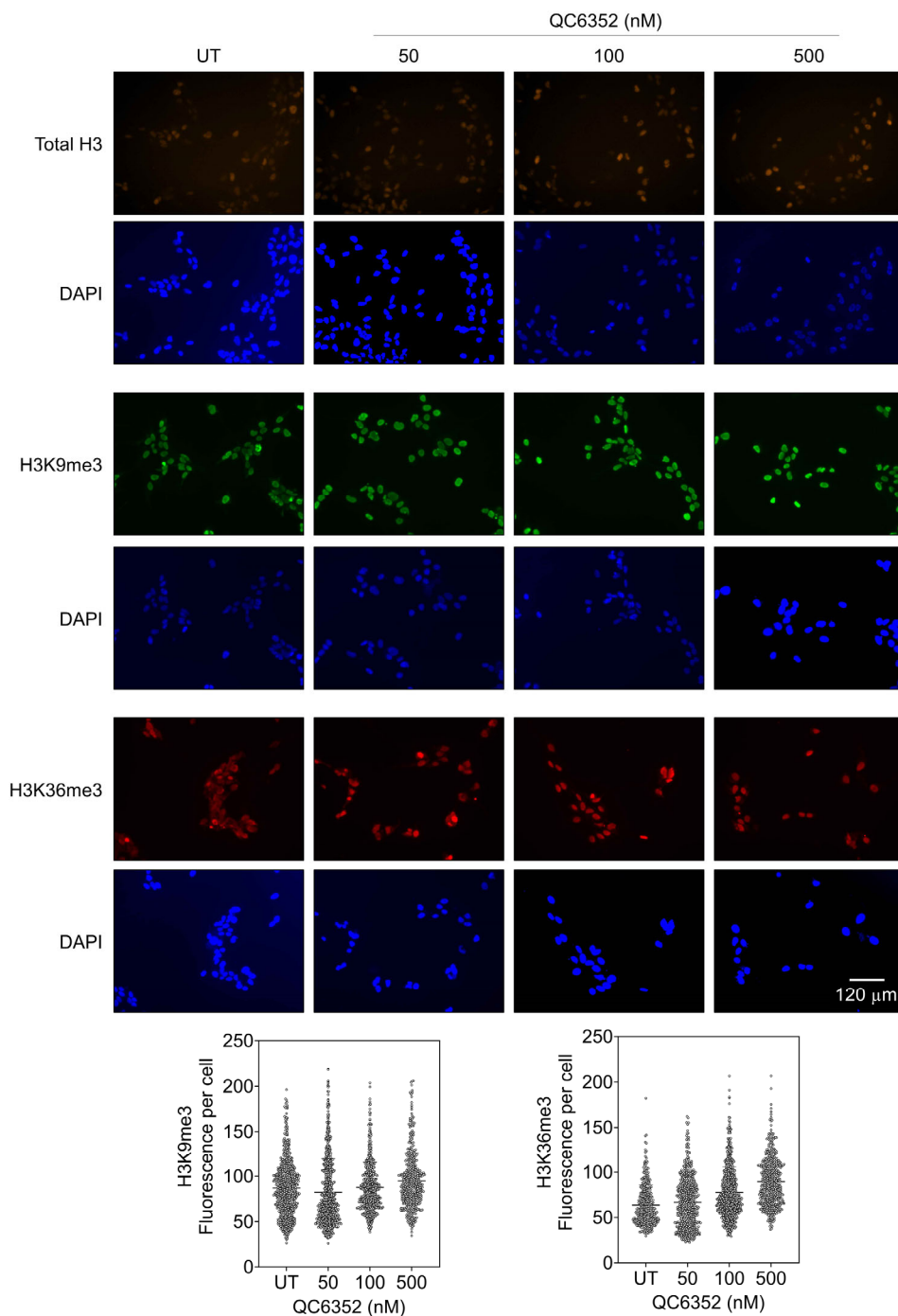


Figure 4.18. Heterogeneous H3K9 and H3K36 trimethylation in FPW1 cells. Immunofluorescence imaging of FPW1 cells treated with QC6352 at concentrations 0, 50, 100, and 500 nM for 72 hours. Cells were fixed and stained with DAPI (blue) and Alexa Fluor 488-labeled antibodies specific to Total H3 (orange), H3K9me3 (green), and H3K36me3 (red). Representative images showing individual cell fluorescence, and mean fluorescence from three experiments are displayed.

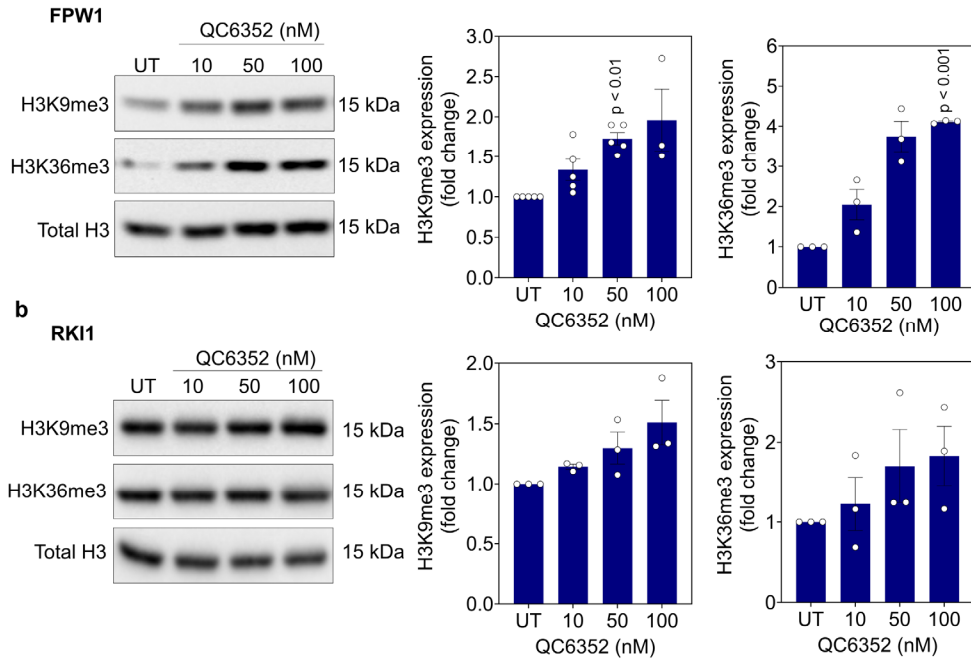


Figure 4.19. H3K9 and H3K36 trimethylation status in QC6352-treated FPW1 and RKI1 cells. a - b) Western blot analysis of H3K9 and H3K36 trimethylation in FPW1 and RKI1 cells treated with QC6352 (0, 10, 50, 100 nM) for 72 hours ($n = 3 - 5$) using 1 μg of histone protein. Data expressed as mean \pm SEM. Statistical significance assessed using one-sample t-tests compared to a fold change of 1 with p-values adjusted using Bonferroni's correction for multiple comparisons.

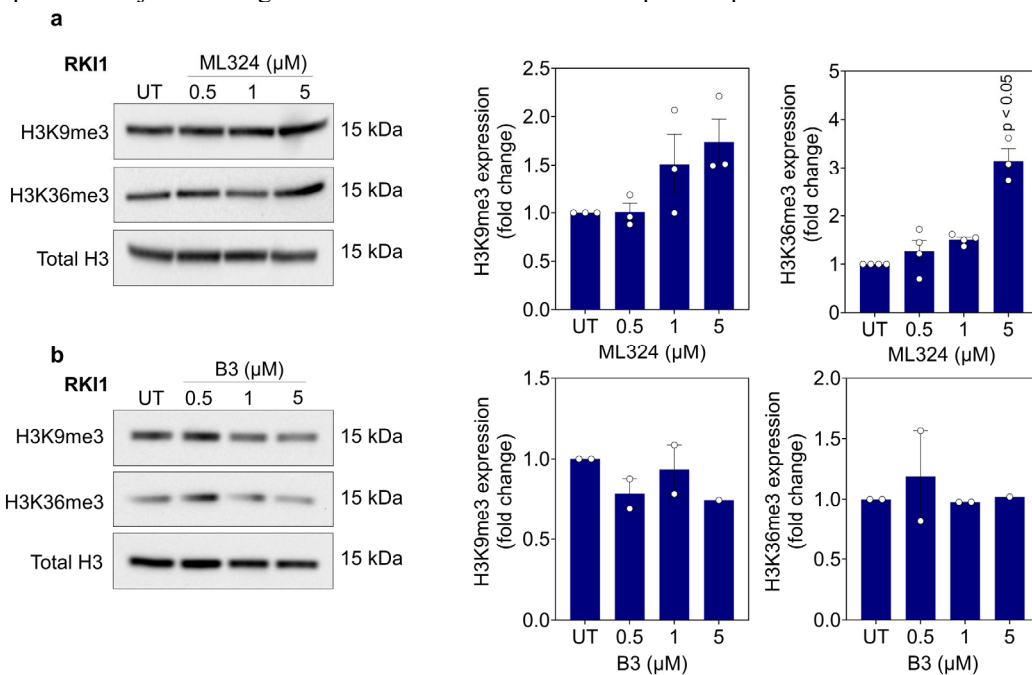


Figure 4.20. H3K9 and H3K36 trimethylation status in ML324- and B3-treated RKI1 cells. a - b) Western blot analysis of H3K9 and H3K36 trimethylation in RKI1 cells treated with ML324 or B3 (0, 0.5, 1, 5 μM) for 72 hours ($n = 3 - 5$) using 1 μg of histone protein. Data expressed as mean \pm SEM normalised to total H3. Statistical significance assessed using one-sample t-tests compared to a fold change of 1 with p-values adjusted using Bonferroni's correction for multiple comparisons.

4.2.5. Impact of KDM4 knockdown on proliferation and H3K9 trimethylation

To further investigate the role of KDM4 in glioblastoma cell proliferation and histone methylation, siRNA knockdowns of KDM4A-D were performed in A172 cells. KDM4E, however, was not investigated since its expression levels were undetectably low in glioblastoma stem cell lines (**Figure 4.16**). The efficacy of the knockdown was validated using RT-qPCR, with all changes in mRNA levels compared against a scramble siRNA control at the same time points using a log₂ scale. In each single knockdown of *KDM4A-D*, the entire KDM4 family was evaluated for changes in mRNA expression firstly to identify the effectiveness of the knockdown, and secondly, to observe any indications of redundancy or compensation in the remaining KDM4 family gene expression. Each isoform was knocked down using two individual siRNAs.

The initial set of siRNAs targeting KDM4A-D (siKDM4A-D_1) resulted in a significant reduction in mRNA levels for their respective targets: between 1.1- to 2.5-fold compared to the scramble control at Day 1 (**Figure 4.21a**). However, these knockdowns were no longer significant at Day 4. In contrast, the second set of siRNAs (siKDM4A-D_2) decreased mRNA levels for their respective targets by 1.1- to 4.1-fold at Day 1 and 1.1- to 3.3-fold at Day 4 (**Figure 4.21b**). Interestingly, non-targeted KDM4 isoforms did not exhibit significant mRNA changes, suggesting that these isoforms do not compensate for the targeted inhibition at the mRNA level in glioblastoma cells.

Subsequent analysis examined the impact of KDM4 knockdown on A172 cell proliferation rate, as measured by changes in confluency over a 3-day period using IncuCyte live cell imaging and analysis. Cells subjected to the scramble siRNA control exhibited a 7.1-fold increase in confluency, while cells subjected to siKDM4A-C_1 showed similar growth rates, with 6.9-, 7.2-, and 7.4-fold increases, respectively. In contrast, cells incubated with siKDM4D_1 displayed a slower proliferation rate, with only a 3.3-fold change in confluency (**Figure 4.22a**). When examining the effects of siKDM4A-D_2, the scramble control showed a 7.4-fold increase in confluency, whereas siKDM4A_2 exhibited a reduced 3.4-fold increase. siKDM4B-D_2 showed growth rates similar to the scramble control, with 7-, 7.5-, and 6-fold increases in confluency (**Figure 4.22b**). Given that at least one siRNA treatment for each KDM4 isoform did not significantly change cell confluency over time, the data collectively suggest that individual knockdowns of KDM4 isoforms do not have a marked impact on glioblastoma cell proliferation. The reduced proliferation observed in siKDM4D_1 and

siKDM4A_2-treated cells may be due to off-target effects, underscoring the need for validation with multiple siRNA sets.

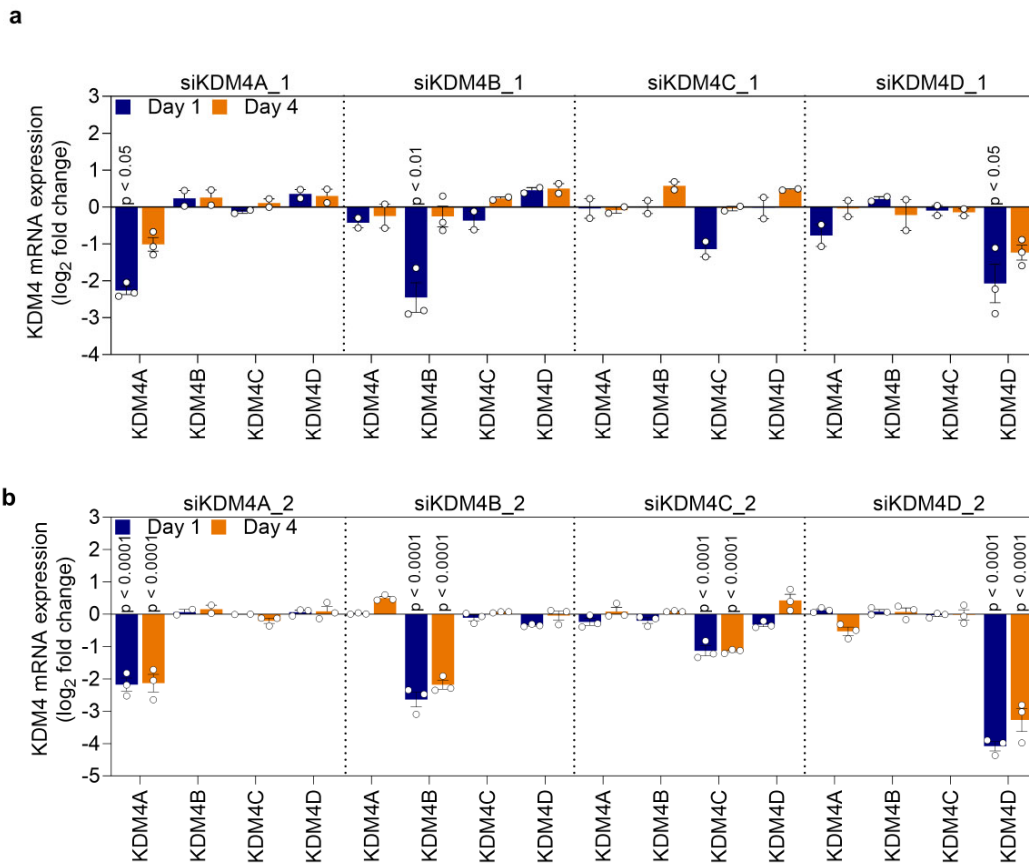


Figure 4.21. siRNA validation of KDM4A-D knockdown. a - b) A172 cells were treated with two independent sets of siRNAs targeting KDM4A-D for 1 and 4 days. Gene expression changes were assessed via RT-qPCR and shown as Log₂ fold change relative to scramble control, normalised to *GAPDH*. Data represents mean ± SEM (n = 2 - 3). One-way ANOVA was performed to assess significant changes compared to untreated with p-values adjusted using Bonferroni's correction for multiple comparisons.

The impact of KDM4 knockdown on histone methylation was next analysed using Western blotting. A172 cells were subjected to siRNAs targeting KDM4A-D for 3 days. The abundance of H3K9me3 was then compared against cells incubated with a scramble control. Cells subjected to siKDM4A-C_1 showed no change, ranging from 0.7- to 1.1-fold change (**Figure 4.22c**). Surprisingly, cells incubated with siKDM4D_1 resulted in a 0.2-fold decrease in H3K9me3 levels compared to the scramble control. This finding contradicts the expected increase in H3K9me3 levels typically associated with demethylase inhibition and suggests that the observed decrease may be attributed to off-target effects. In support of this, an orthogonally targeted siRNA, siKDM4D_2, did not replicate this decrease in H3K9me3 levels (**Figure 4.22d**).

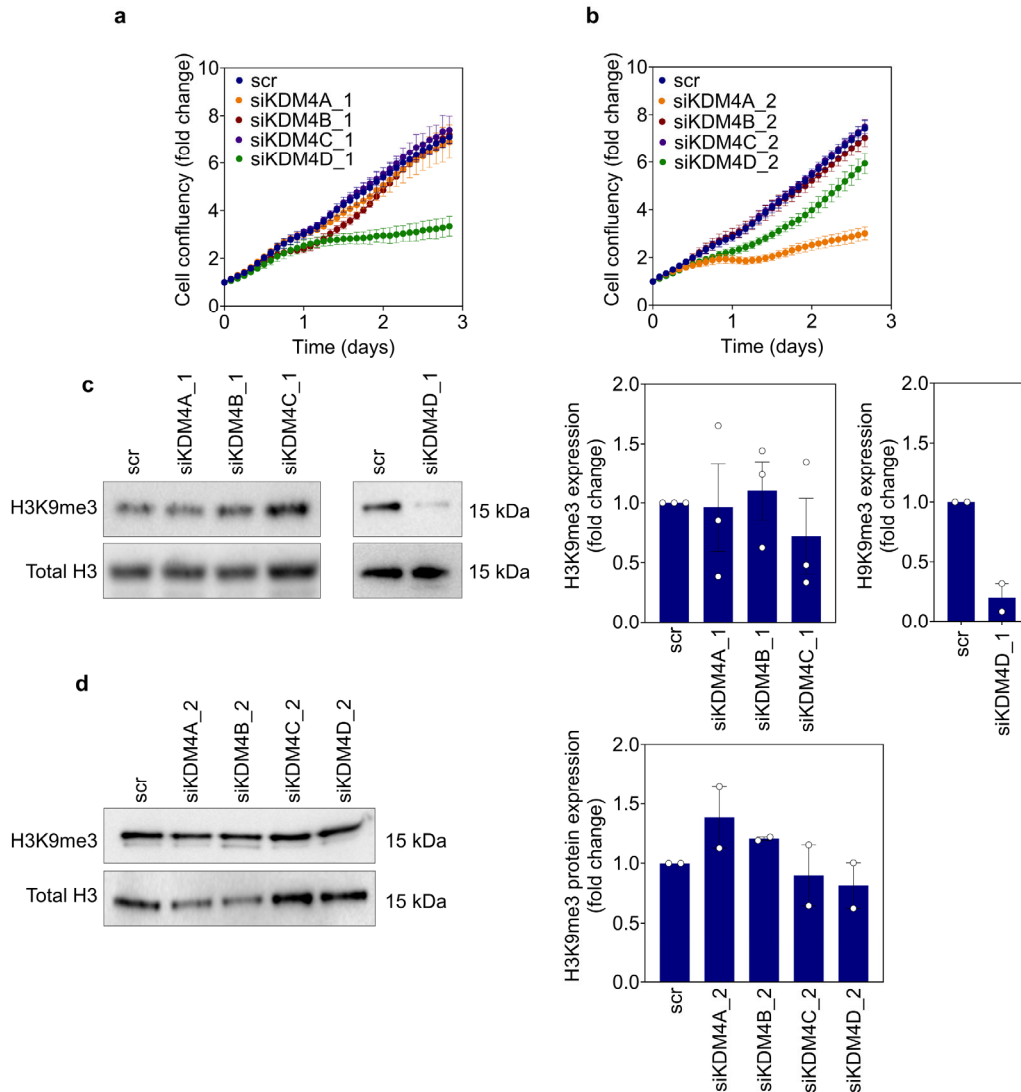


Figure 4.22. Phenotypic response to siKDM4A-D knockdown. **a - b**) Live cell imaging of A172 cells ($n = 2 - 3$). Cells were incubated with 5 nM orthogonal siRNA targeting KDM4A-D and quantification of confluency was analysed every 2 hours. **c - d**) Representative images of a Western blot analysis of H3K9me3 and total H3 following siRNA knockdown of KDM4A-D. Quantifications are presented as mean \pm SEM normalised to total H3. One-sample t-tests were performed for all Western blot conditions with three replicates compared to a fold change of 1 and p-values were adjusted using Bonferroni's correction for multiple comparisons.

Taken together, individual knockdown of KDM4A-D showed no significant effect in A172 proliferation or H3K9 trimethylation status. **Figure 4.21** validates that both siKDM4_1 and siKDM4_2 have on-target activity since they consistently reduce the gene expression of their respective target. However, there is not enough evidence to determine if this off-target effect is present in the first set of siRNAs or the second set and to determine this, further experiments are required.

4.2.6. Impact of KDM4A overexpression on glioblastoma cells

Within the glioblastoma stem cell lines, *KDM4A* exhibits the highest mean expression level in the KDM4 family. However, the expression levels of *KDM4A-D* are comparably low, with 11 other KDM isoforms demonstrating higher gene expression across the entire panel of glioblastoma stem cell lines (**Figure 4.16**). To investigate the impact of KDM4A overexpression, the lentiviral KDM4A overexpression vector, under the control of the *CMV* promoter, was transduced into A172 cells at a Multiplicity of Infection (MOI) of 1. An MOI of 1 ensures that, on average, one lentiviral particle to infect one cell. This MOI was chosen to increase KDM4A expression while minimising potential disruptions to essential genes caused by interrupting their open reading frames²⁶⁸. KDM4A overexpression was subsequently validated by Western blotting. Despite the overexpression, no significant changes were observed in histone methylation status, proliferation rate, or in QC6352 efficacy compared to control A172 cells (**Figure 4.23a-c**). To further investigate, A172 overexpression was repeated with an MOI range of 1 - 25, further increasing KDM4A expression levels²⁶⁹. However, at the highest tested MOI of 25 (A172-KDM4A-MOI25), no significant changes were also observed in H3K9me3 abundance, proliferation rate, or QC6352 efficacy (**Figure 4.24a-d**).

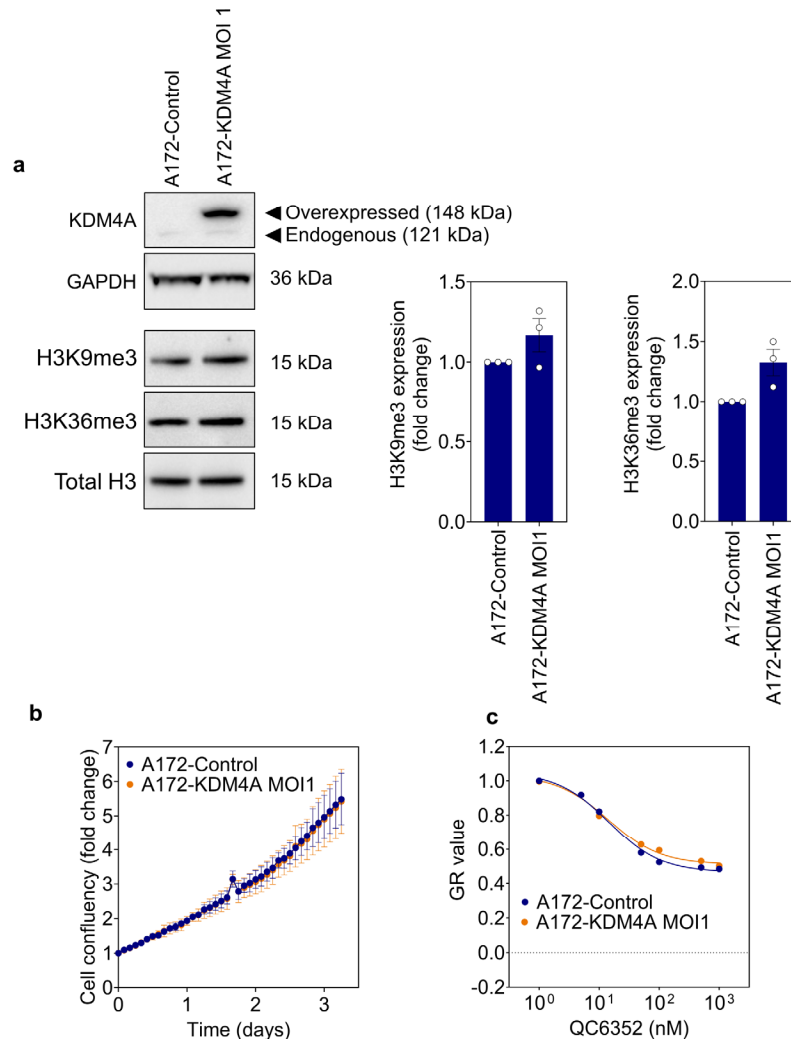


Figure 4.23. Phenotypic response and QC6352 efficacy of KDM4A overexpression at MOI1. a) Western blot analysis comparing KDM4A, GAPDH, H3K9me3, H3K36me3, and total H3 levels in A172-KDM4A MOI1 or left untransduced (A172-Control). Endogenous (121 kDa) and overexpressed KDM4A (148 kDa) bands are labelled. **b)** Live cell imaging of confluency over time in A172-Control and A172-KDM4A MOI1 cells. **c)** GR dose-response curves for A172-Control and A172-KDM4A MOI1 cells, treated with QC6352 for 5 days. Data presented as mean \pm SEM ($n = 3$). Statistical significance for Western blot data assessed using one-sample t-tests compared to a fold change of 1. For live cell imaging, two-way ANOVA followed by Bonferroni's correction for multiple comparisons.

To investigate the target modulation of KDM4 inhibitors QC6352 and ML324 in A172 cells overexpressing KDM4A, Western blotting was conducted to examine changes in the abundance of H3K9me3 and H3K36me3 in the presence of the KDM4 inhibitors QC6352 (100 nM) and ML324 (1 μ M) for 72 hours. These concentrations were chosen as they increased histone methylation in FPW1 and RKI1 cells (**Figure 4.19 - 4.20**). In both untransduced and KDM4A-overexpressing A172 cells, the abundance of H3K9me3 and H3K36me3 did not significantly change in the presence of QC6352 (1.3- to 2.5-fold) or ML324 (0.6- to 1.3-fold) (**Figure 4.25**).

Finally, to investigate the potential molecular mechanisms underlying the stable H3K9me3 levels in A172-KDM4A cells, we examined the gene expression alterations in the KDM and KMT families using an MOI of 1. Cells were screened using RT-qPCR and analysed as a log₂ scale to observe changes in the mRNA expression of KDMs and KMTs compared to untransduced A172s. The screen confirmed a 1.5-fold increase in *KDM4A* expression in overexpressed cells. However, no significant changes were identified in the mRNA expression of all other KDMs and KMTs (**Figure 4.26**).

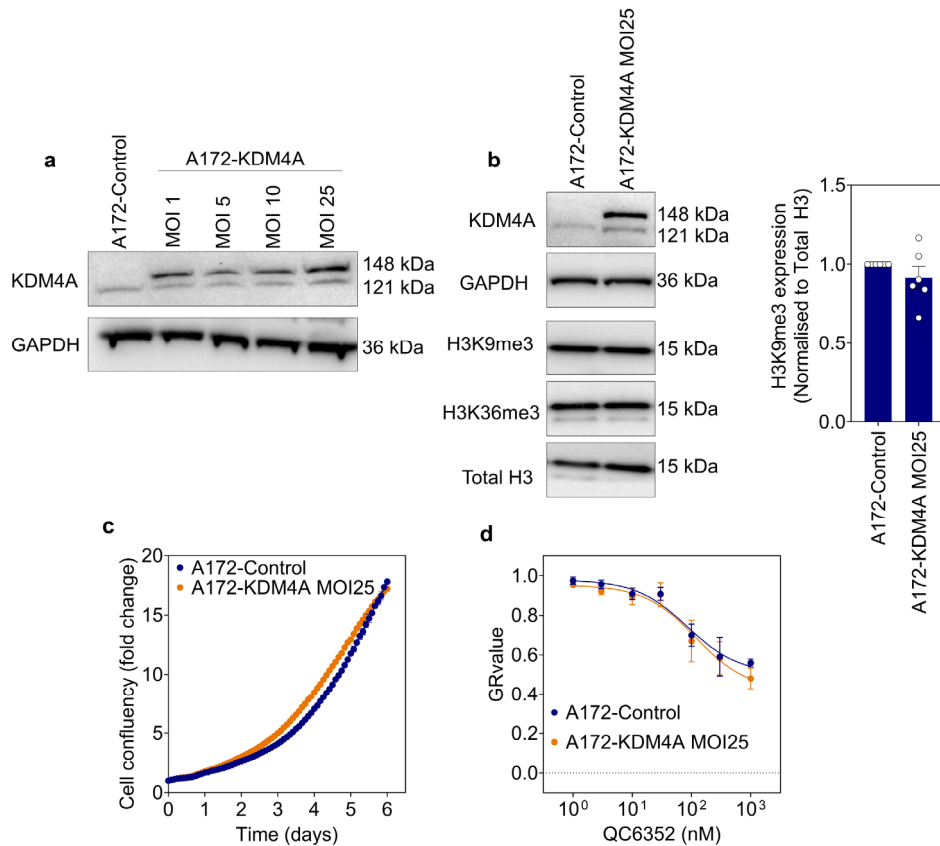


Figure 4.24. Phenotypic response and QC6352 efficacy of KDM4A overexpression at MOI25. **a)** Western blot analysis comparing KDM4A and GAPDH expression in A172-KDM4A MOI1-25 **b)** Western blot for KDM4A, GAPDH, H3K9me3, H3K36me3, and Total H3 levels in A172-KDM4A MOI1 or left untransduced (A172-Control). **c)** Live cell imaging of cell confluency over time in A172-Control and A172-KDM4A MOI25 cells **d)** GR dose-response curves for A172-Control and A172-KDM4A MOI25 cells, treated with QC6352 for 5 days. Data presented as mean \pm SEM. Statistical significance for Western blot data assessed using one-sample t-tests compared to a fold change of 1. For live cell imaging, two-way ANOVA followed by Bonferroni's correction for multiple comparisons.

In summary, lentiviral-mediated overexpression was conducted in A172 cells at an MOI of 1 to explore the role of KDM4A in glioblastoma at elevated expression levels. Although the

overexpression was successfully validated through Western blotting and RT-qPCR, it did not induce significant changes in histone methylation, cell proliferation, or target modulation. This observation remained consistent even when the overexpression was repeated at an MOI of 25. Furthermore, mRNA screening of KDM4A overexpressed cells revealed a 1.5-fold increase in KDM4A expression but no significant changes in other KDM or KMT genes. These collective observations suggest that, in the context of glioblastoma, KDM4A's role in cell proliferation and histone methylation may be limited, warranting further investigation into the significance of the additional KDM4B-E isoforms.

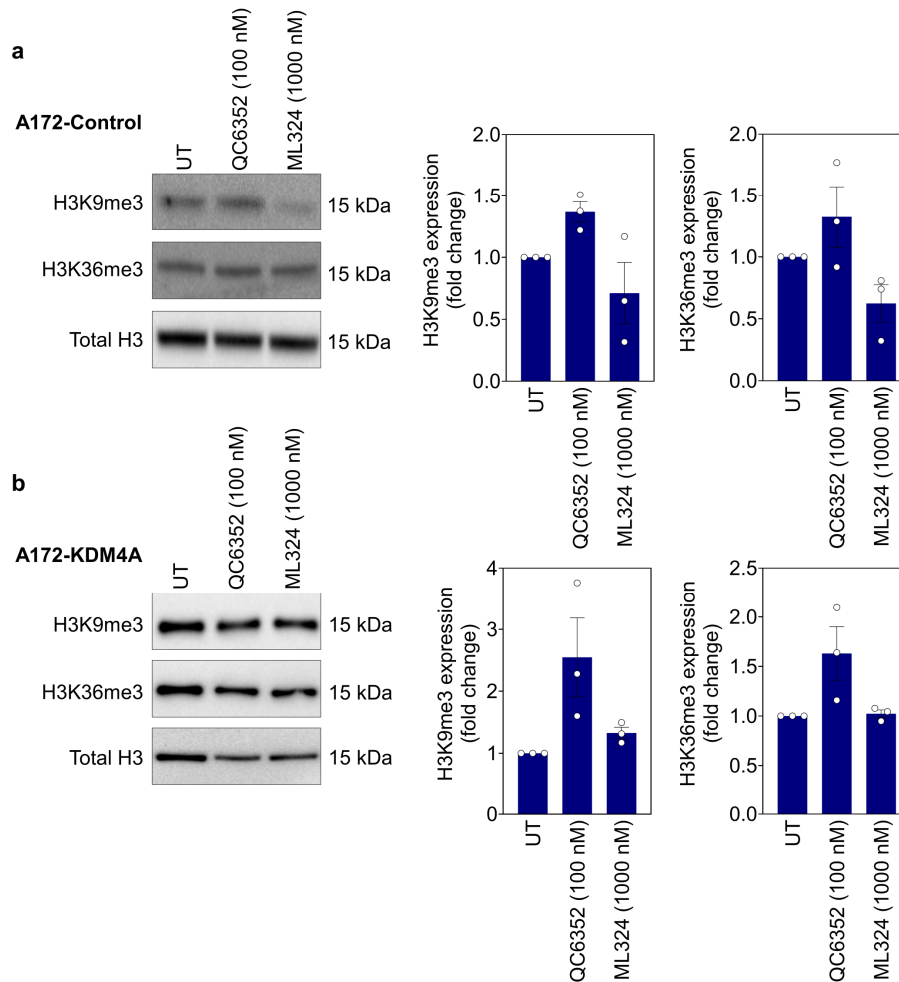


Figure 4.25. H3K9 and H3K36 trimethylation in A172-KDM4A overexpressing cells. a - b) Western blot analysis of H3K9me3, H3K36me3, and Total H3 in A172 cells with or without KDM4A overexpression at MOI 25. Cells were either untreated or treated with QC6352 (100 nM) or ML324 (1000 nM). Quantifications are mean \pm SEM and statistical analysis was performed using a one-sample t-test compared to a fold change of 1 and p-values were adjusted using Bonferroni's correction for multiple comparisons.

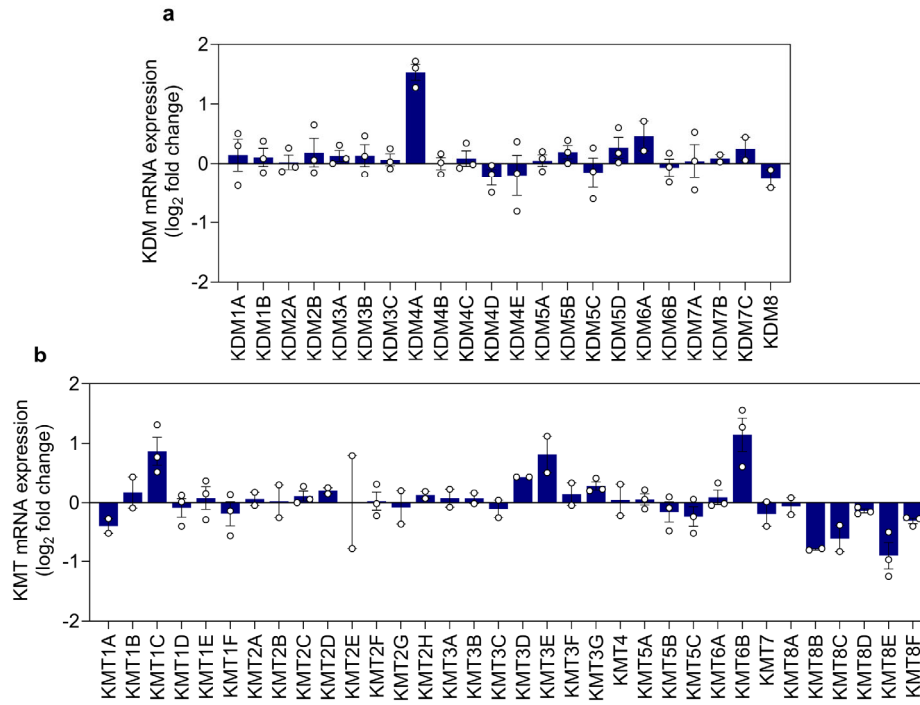


Figure 4.26. Gene expression of KDM and KMT families in A172-KDM4A overexpressing cells. RT-qPCR analysis of **a)** KDM and **b)** KMT gene expression in A172-KDM4A cells compared to an untransduced control. Data presented as mean \pm SEM.

4.3. Discussion

The findings presented in this chapter investigated the mechanism-of-action of QC6352 in glioblastoma cells. We first established the antiproliferative efficacy of QC6352 compared to the orthogonal KDM4 inhibitors ML324, B3 and IOX1. Despite all KDM4 inhibitors exhibiting a comparable efficacy in the biochemical inhibition of KDM4A activity, QC6352 distinctly suppressed cellular proliferation at concentrations starting from 5 nM; a significant inhibitory response that was not replicated by other KDM4 inhibitors, even at concentrations in the micromolar range. In other studies, the antiproliferative effect of QC6352 on breast cancer stem cells was demonstrated with an EC_{50} of 3.4 nM²¹⁰. Moreover, B3 has been shown to inhibit proliferation starting at 1 μ M in prostate cells²³⁶, while ML324 reduced colony formation at a starting concentration of 2.5 μ M in a clonogenic assay in the hepatocarcinoma cell lines²⁷⁰, and IOX1 reduced colony formation at 25 μ M in the colorectal carcinoma cells²⁷¹. Further experiments need to be conducted to determine why compound B3 failed to inhibit KDM4A. This includes verification of B3 structure by NMR, investigating its potency in KDM4B-E inhibition assays as well as testing target engagement/target modulation in cells.

Investigation into QC6352's mechanism of action revealed that a 5-day treatment induced G0/G1 cell cycle arrest. This supports a similar cell cycle analysis finding showing G1 cell cycle arrest after knocking down KDM4A in myoblasts²⁷². However, the findings from another study identified an S-phase cell cycle arrest in head and neck cancer cell lines after treatment with ML324²⁷³ and another study found that KDM4C regulates cell cycle genes essential for S- and M-phase progression²⁷⁴. These findings may indicate that cell cycle arrest may occur at different stages of the cell cycle depending on the KDM4 isoform and cancer type investigated. Additionally, our findings showed a subset of the cell population treated with QC6352 exhibited increased markers for senescence, apoptosis, differentiation, and stemness. KDM4 inhibition has been implicated in all of these markers wherein KDM4A inhibition caused apoptosis and senescence in lung cancer cells²⁷⁵, while loss of KDM4B caused senescence in osteoclasts²⁷⁶, and KDM4C was shown to be essential to maintain stemness in glioblastoma initiating cells¹²⁵. Interestingly, knockdown of KDM4A in IMR90 cells and KDM4B in oral bone mesenchymal stem cells lead to an approximate 35% increase in senescence^{276,277}. A similar percentage of senescence was also identified in our experiments within the QC6352-treated FPW1 cells, but to a lesser extent in the RKI1 cells, suggesting a resistance mechanism in these cells. Moreover, temozolomide is known to induce senescence in a much higher percentage of the cell population with Beltzig et al. showing up to 90% at 50

μM^{278} . Therefore, further experiments are necessary to understand the role of KDM4 in glioblastoma to elucidate whether the phenotypic effects induced by QC6352 are due to KDM4 inhibition similar to other cancer cell types and also why only a subpopulation of the cells are induced into senescence.

The characterisation of KDM4 began with gene expression profiling, which indicated a lower mean KDM4A-D gene expression compared to the majority of KDM, KMT, HDAC and KAT genes across a panel of glioblastoma stem cell lines. Interestingly, an earlier comprehensive transcriptomics analysis of KDM gene expression in gastric cancer cells identified many similarities in the relative gene expressions between the KDM family members⁸⁷. For instance, KDM4D and KDM8 were the least expressed in cell types and the majority of KDM genes had higher expression than the entire KDM4 family⁸⁷.

The non-specific binding of KDM4 antibodies resulted in misleading localisation by immunofluorescence. In-house validation of the antibodies was not performed as at this stage of the project, as the data indicated an irrelevance of KDM4 activity in glioblastoma. Hence, we rather focused on the identification of the target underlying QC6253's efficacy. Western blotting displayed nuclear localisation of KDM4A-C when analysing bands at the expected molecular weight. This agrees with current literature findings that KDM4 is localised to the nucleus of cells primarily due to their JmjN, PHD, or Tudor domains^{279,280}. Further, the target modulation of KDM4 inhibitors were investigated to find changes in the methylation status of the KDM4 sites of action, H3K9me3 and H3K36me3. Immunofluorescence and Western blotting revealed significantly elevated levels of H3K36me3 in FPW1 cells after QC6352 treatment. Moreover, RKI1 cells treated with both QC6352 and ML324 showed similar increases in H3K9me3 and H3K36me3 levels. These increases were also noted in studies using ML324 in myoblast cells and QC6352 in breast cancer stem cells^{210,272}.

To further understand the significance of KDM4 in glioblastoma, we used siRNA knockdown of KDM4A-D and lentiviral overexpression of KDM4A in A172 cells. Interestingly, when using two orthogonally targeting siRNAs for each KDM4 member, some knockdowns resulted in significant decrease in cell viability which was not replicated in the orthogonally targeting siRNA. Without a reproducible phenotypic effect, it was concluded that the decrease in cell viability was due to off-target effects. In agreement with this, many studies have identified a lack of selectivity in siRNA knockdown experiments. This highlights the importance of using orthogonally-targeting molecular probes to ensure unbiased conclusions. Interestingly, other studies have noted knockdown of KDM4A decreased viability and

increased H3K9me3 abundance in nasopharyngeal carcinoma cells²⁸¹, breast cancer stem cells²¹⁰, and prostate cancer cells²⁸². This could mean that KDM4A is important in some cell types but not others. Future experiments using sgRNA would be highly beneficial to confirm the results shown here as sgRNA is notably more selective and can induce complete knockout of the gene to allow studying the long-term effects of KDM4 inhibition.

Additionally, overexpression of KDM4A did not alter QC6352 efficacy or target modulation compared to untransduced A172 cells. It is well known that overexpressing a protein usually confers resistance to compounds targeting that protein while partially knocking down that same protein confers sensitivity to the compound. Therefore, KDM4A does not seem to be important for glioblastoma cell proliferation or QC6352 antiproliferative action. More research should be undertaken to identify potential redundancies in the remaining KDM4 isoforms in order to explain why the overexpression of a single KDM4 isoform had no effect. Another approach would be to investigate the effect of reliably knocking down or knocking out all KDM4 isoforms at once to examine QC6352 antiproliferative efficacy for signs of sensitisation.

Lastly, we conducted an RT-qPCR screen in A172 cells overexpressing KDM4A to uncover potential changes in the gene expression of KDMs and KMTs. Such changes could explain why the methylation status of the cells did not change. This investigation revealed no significant changes in the gene expression of any KDM or KMT genes, with the exception of the overexpressed KDM4A. The two most likely explanations for the lack of change in methylation status is either that KDM4A activity is not physiologically relevant for histone methylation or that the activity is negatively regulated to maintain a homeostatic histone methylation. Since other studies have shown KDM4A is highly important in certain cancer types for regulating H3K9me3 and H3K36me3 abundance²⁸³, it is more likely that the activity of the KDMs and KMTs are regulated by post-translational modifications²⁸⁴. For instance, it is known that KDMs have more than 20 phosphorylation sites which can affect their activity²⁸⁵. Therefore, future experiments are required to further elucidate the post-translational modifications regulating KDM and KMT activity. These may also provide insights into why some KDMs are more important in some cell types compared to others.

In conclusion, this chapter aimed to validate KDM4 as the primary target of QC6352 causing an antiproliferative effect. However, the orthogonally targeting KDM4 inhibitor, ML324, and KDM4 knockdown and KDM4A overexpression could not produce the same effect (**Figure 4.27**). QC6352 caused cell cycle arrest, apoptosis and differentiation but the

evidence obtained does not support KDM4 as the primary target for QC6352. More experiments in target identification are necessary to deconvolute the proteins targeted by QC6352 which are essential for the viability of glioblastoma cells.

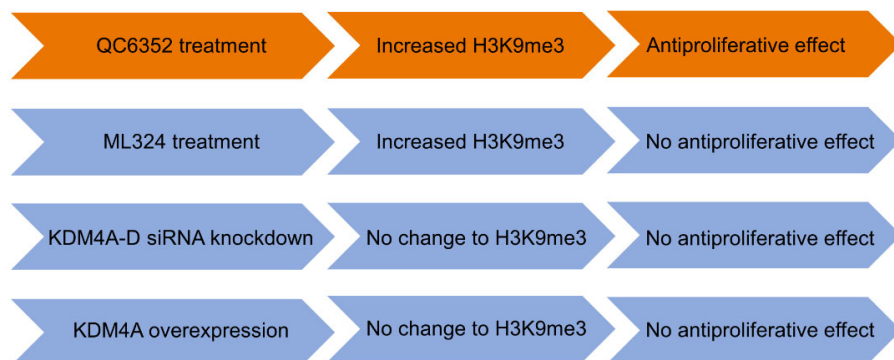


Figure 4.27. Summary of findings from Chapter 4. Based on all experiments conducted in this chapter, QC6352 treatment in glioblastoma cell lines increased H3K9me3 abundance and had an antiproliferative efficacy. These phenotypic effects were not repeated in any other condition including treatment with an orthogonal compound or manipulation of the KDM4 protein expression.

Chapter 5

Investigating the
mechanism of action of
QC6352

5.1. Introduction

QC6352 is designed as a KDM4 inhibitor and there are currently no known off-target proteins with comparable potency to the KDM4 family²¹⁰. However, the findings from Chapter 4 question whether KDM4 is important for the viability of glioblastoma cells, with KDM4A-D knockdown and KDM4A overexpression showing no effect on cell viability and histone methylation in A172 cells. Thus, further investigation was necessary to confirm the importance of KDM4 in glioblastoma cells and to potentially identify QC6352's target(s) underlying its antiproliferative efficacy. These investigations employed four state-of-the-art orthogonal methodologies: genome-wide CRISPR-Cas9 loss-of-function screen, proteome-wide mass spectrometry-based CETSA, transcriptome-wide RNA-sequencing, and the Connectivity Map (CMap) L1000 Query analysis.

5.1.1. CRISPR-Cas9 loss-of-function screens

CRISPR-Cas9 gene-editing technology can induce precise changes to the DNA of organisms²⁸⁶. It consists of a nuclease protein (Cas9) complexed with a synthetic guide RNA (sgRNA) which together induce double-stranded DNA breaks at a specific genomic locus dictated by the specific coding sequence of the sgRNA²⁸⁷. Double-stranded breaks can be correctly repaired via homology directed repair in the late S-G2 cell cycle phase where a sister chromatid can be used as a repair template²⁸⁸. More commonly, however, double-strand breaks are repaired through non-homologous end joining, an error prone repair mechanism that results in insertion and/or deletions that impair gene function²⁸⁸. Furthermore, CRISPR-Cas9 knockout of a gene is an inherently stochastic process, in which some sgRNAs will fail to cut their target, cause an in-frame mutation which may leave protein function partially intact, or introduce a mutation which completely ablates protein function²⁸⁹. Therefore, CRISPR-Cas9 loss-of-function results in a population of cells ranging from total or partial loss of function mutations, to completely conserved function²⁹⁰.

The basic research application of CRISPR-Cas9 genome editing has allowed efficient interrogation of the functions of individual genes²⁹¹. The ability to perform functional genome-wide screens has been greatly enhanced by use of CRISPR-Cas9, particularly when compared to earlier genetic perturbation technologies such as RNA interference (RNAi)²⁹². In particular, RNAi suffers from high off-target effects and incomplete knockdown, resulting in reduced sensitivity and specificity compared to CRISPR²⁹². The ability of CRISPR to generate complete

gene knock-out provides a more biologically robust system to interrogate mutant phenotypes, with low noise, and minimal off-target effects²⁸⁷.

The sgRNA lentiviral library used, called the Toronto Knock-out (TKO) v3, targets approximately 18,000 human protein-coding genes with 71,090 guides optimised for efficient gene editing²⁹³. The transduced cells are then cultured, with the abundance of sgRNAs over time quantified by RNA sequencing, providing a readout to assess dropout or enrichment of cells. CRISPR knock-out libraries can be harnessed for a variety of investigations including to identify genes that cause changes to cellular fitness, moderate drug efficacy, regulate protein expression, or are required for a certain pathway function and cellular state²⁹⁴. In this chapter, a fitness screen was conducted in RKII cells to identify fitness genes, which increase or decrease viability^{214,295,296}.

Fitness genes increasing cell fitness are also known as dependency genes²⁹⁷, while fitness genes which decrease cell fitness are also known as proliferation-suppressor genes^{296,298} (**Table 5.1**). Dependency genes can be further classified into core dependency genes^{214,295,296}, common to all cell types, and selective dependency genes^{214,295,296}, which are specific to a certain cell lineage²⁹⁶. Selective gene dependencies offer greater potential as targets for cancer treatment, as targeting core gene dependencies will likely result in adverse side effects and/or systematic toxicity²⁹⁹. To distinguish between core and selective gene dependencies, each gene must be scaled based on the frequency of dependency across cell lineages. Broad Institute's Dependency Map (DepMap) portal contains the probability of dependency for all genes in 1095 cancer cell lines from the Cancer Cell Line Encyclopedia (CCLE)³⁰⁰. For each gene, the mean probability of dependency is calculated using probabilities across all cancer cell lines from the CCLE. Additionally, chemogenetic screens are commonly used to identify genes which act to decrease or increase the efficacy of a compound, known as sensitising and resistance genes respectively. Positive selection screens are conducted by using a high concentration of QC6352 on CRISPR-Cas9 transduced cells to identify gene knockouts which decrease QC6352 efficacy and therefore normally act sensitising genes. Moreover, negative selection screens identify gene knockouts which increase QC6352 efficacy and therefore normally act as resistance genes.

Chronos is a modern bioinformatic analysis package developed in 2021 which is designed to effectively interpret CRISPR-Cas9 data and identify significant changes to cell fitness in response to gene deletions²¹⁴. The package utilises a mechanistic modelling approach, using positive controls (*i.e.* core gene dependencies) and negative controls (*i.e.* non-expressed

genes) as reference points to enhance the accuracy of its predictions²¹⁴. Additionally, Empirical Bayesian statistical methods are commonly used to analyse CRISPR-Cas9 screens and have proven highly effective at identifying significant changes in the abundance of sgRNAs over time³⁰¹. Limma is an additional bioinformatic analysis package²¹⁵. Limma utilises a broad suite of statistical models known as “linear models” in conjunction with the powerful Empirical Bayesian statistical methods as an effective analysis methodology for the CRISPR-Cas9 fitness and chemogenetic screens^{215,302}.

Table 5.1. CRISPR-Cas9 screen glossary. A list of relevant terminologies and definitions commonly used in publications performing CRISPR-Cas9 genetic screens.

| | |
|---|--|
| Cell fitness | The ability of the cells to survive, grow and proliferate. |
| Fitness gene | A gene which either increase or decreases cell fitness. |
| Dependency gene | A fitness gene which reduces cell growth when knocked out. |
| Mean probability of dependency | The average probability of dependency for a given gene across all Cancer Cell Line Encyclopedia (CCLE) lineages. |
| Core dependency gene | A dependency gene which is commonly essential to all cell lineages. |
| Selective dependency gene | A dependency gene which is not common to all cancer lineages. |
| Proliferation-suppressor gene | A gene which inhibits cell viability and therefore increase proliferation when knocked out. |
| Chemogenetic screen | A screen which combines compound treatment with CRISPR-Cas9 loss-of-function, usually used to identify genes that enhance or suppress the phenotypic effect of the compound. |
| Positive selection screen | A chemogenomic screen where CRISPR-Cas9 transduced cells are treated with a high concentration of a compound. Cells contain genes causing sensitivity to the compound and so cells in which these genes are knocked out will outgrow the rest of the cell population and are therefore positively selected. |
| Sensitising gene | A gene which, when knocked out, reduces cell sensitivity to the compound. Thus, it is a gene that is necessary for the compound’s mechanism of action. |
| Negative selection screen | A chemogenomic screen where CRISPR-Cas9 transduced cells are treated with a low concentration of a compound. Cells contain genes causing resistance to the compound and so cells in which these genes are knocked out will drop out from the cell population and are therefore negatively selected. |
| Resistance gene | A gene which, when knocked out, increases cell sensitivity to the compound. Thus, it is a gene that is causing resistance to the compound’s mechanism of action. |
| EC ₂₀ /EC ₉₀ efficacy score | Chronos scores for EC ₂₀ -treated or EC ₉₀ -treated cells subtracted from the Chronos scores for untreated cells. These scores represent the change in compound efficacy due to gene knockouts. Positive scores indicate reduced efficacy, and negative scores represents enhanced efficacy. |

5.1.2. Mass-spectrometry based cellular thermal shift assay

Cellular Thermal Shift Assay (CETSA) is based on the principle that each protein unfolds, denatures, or ‘melts’ at a specific temperature due to its inherent thermal stability, determined by the protein’s structural conformation^{303,304}. The binding of a compound to a protein usually enhances its thermal stability, resulting in a detectable shift of melting temperature (T_m)³⁰⁵. While there are many methodologies incorporating CETSA, the two most commonly used label-free methods are intact-cell CETSA and lysed-cell CETSA³⁰⁶ (**Figure 5.1**). In intact-cell CETSA, cells are first treated with a compound, allowing for compound-protein binding under normal cellular conditions. This approach enables the detection of direct compound-protein binding as well as indirect effects, such as inhibited protein-protein interactions, detectable through the destabilisation of a particular protein³⁰⁷. Lysed-cell CETSA involves lysing cells prior to treatment with a compound, which disrupts normal protein activity. This prevents the detection of destabilised proteins but also allows the compound to bind to its targets without needing to cross the cell membrane or interact with protein complexes³⁰⁶.

To quantify stabilisation of a protein of interest, Western blotting with target-specific antibodies is commonly used. Mass spectrometry-based quantification of protein expression offers a proteome-wide approach to identify all proteins stabilised by the compound³⁰⁸. To effectively identify significant protein stabilisation and destabilisation when utilising mass spectrometry, the thermal proteome profiling (TPP) package can be used to analyse the proteome data in the R coding environment³⁰⁸. The TPP package creates stability profiles for each protein were identified by calculating melting points from melt curves based on the protein stabilisation as temperature increases. Changes in melting points between treatment conditions can then identify compound-protein stabilisations associated with compound binding or destabilisations associated with disrupted protein-protein interactions³⁰⁹. One such study successfully used the TPP package to analyse MS-CETSA data and identify 54 binding partners of the multikinase inhibitor staurosporine, 30 binding partners of the kinase inhibitor GSK3182571, and 4 binding partners of the Abl inhibitor dasatinib³⁰⁸.

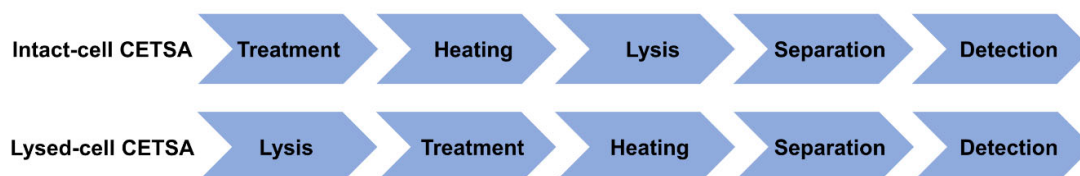


Figure 5.1. Schematic of CETSA methods. An illustrative detailing of the methodology and key differences in the intact-cell and lysed-cell CETSA methodologies.

5.1.3. RNA-sequencing and L1000 Query analysis

RNA-sequencing technology has revolutionised transcriptome-wide analysis of cellular gene expression in recent years by allowing a high throughput, sensitive, and accurate quantification of complementary DNA (cDNA) with a high dynamic range and minimal background noise³¹⁰. First, cell mRNA is extracted and reverse transcribed into cDNA, sequenced, and aligned to a reference genome to produce quantified expression levels for every gene in the cell genome. RNA-sequencing is often used as an important tool in the drug discovery process for target identification and to understand a compound's mechanism of action³¹¹. For instance, *SI00A4* was identified as an immunotherapy target in glioblastoma by comparing highly expressed genes in both immune and glioblastoma cells using single-cell RNA sequencing³¹². Furthermore, when assessing the changes in gene expression between cells treated with a compound compared to untreated, upregulations in genes with a common pathway or function can be identified using pathway analysis programs such as the Ingenuity Pathway Analysis (IPA)³¹³. One such study used RNA sequencing and IPA to uncover the mechanism of action of the compound celastrol to upregulate the farnesoid X receptor (FXR) signalling pathway, and inhibiting the nuclear factor-kappa B (NF- κ B) and p53 signalling pathways which reduced cholestatic liver injury in mice³¹⁴.

In an effort to provide more advanced tools for target identification through RNA sequencing, an initiative was led by the Library of Integrated Network-Based Cellular Signatures (LINCS) program to create a database of characteristic gene expression changes when cells were treated with various compounds³¹⁵. This allows the gene expression changes induced by a compound with an unknown mechanism of action to be correlated against the gene expression changes induced by compounds with known mechanisms of action. This database, known as the Connectivity Map (CMap) now contains over 1,000,000 profiles of key gene expression changes in cells treated with chemical and molecular modulators³¹⁵. To minimise the extensive costs necessary for genome-wide RNA sequencing for so many profiles, a methodology known as the L1000 was established which chose 1058 of the most important transcripts to be probed instead of the entire genome³¹⁵. By using the Query search tool to correlate gene expression profiles against the CMap database, the compound CCT020312 which was identified as a G1/S checkpoint activator by a phenotypic screening, was correlated to 15-delta prostaglandin J2 which is known to trigger EIF2A phosphorylation through EIF2AK3/PERK³¹⁶. Additional experiments validated the same mechanism of action for CCT020312 which increased EIF2A phosphorylation leading to G1/S cell cycle arrest.

5.2. Results

5.2.1. Genome-wide CRISPR-Cas9 screen data quality validation

To identify fitness genes modulating RKI1 cell proliferation and survival, a loss-of-function CRISPR-Cas9 fitness screen was undertaken. Targeted gene knockouts were induced using the CRISPR-Cas9 system and single-guide RNA (sgRNA) Toronto Knock Out v3 (TKOv3) library, containing 71,090 uniquely-tagged sgRNAs targeting 18,049 protein-coding genes. The library, along with a puromycin-resistance gene for selection, was packaged into lentiviral particles and transduced into RKI1 cells. A multiplicity of infection (MOI) of 0.3 was selected to ensure that each cell was transduced with only one viral particle on average and therefore the effects of single gene knockouts could be accurately analysed³¹⁷. To ensure each sgRNA maintained a robust representation in the cell population, a minimum of 300 copies of each sgRNA was transduced into the initial cell population. Following transduction, cells were selected with puromycin (2 µg/mL) to eliminate non-transduced cells.

In addition to the fitness screen, CRISPR-Cas9 chemogenetic screens were conducted by treating transduced RKI1 cells with QC6352 to identify genes important for QC6352's mechanism of action. Specifically, a positive selection screen was established by treating cells with QC6352 at the EC₉₀ concentration to identify sensitising genes (*i.e.*, genes that enhance QC6352 efficacy)³¹⁸. When sensitising genes are knocked out, the gene can no longer provide sensitisation to QC6352 and thus the cells continue to grow during treatment. Additionally, a negative selection screen was conducted where cells are treated with QC6352 at the EC₂₀ concentration to identify resistance genes (*i.e.*, genes that reduce QC6352 efficacy)³¹⁹. When a resistance gene is knocked out, the antiproliferative effect of QC6352 is enhanced.

To find the optimal concentration of QC6352 for the chemogenomic screens, RKI1 cells were first transduced with control lentiviral particles and treated with QC6352 (3 - 100 nM, 10 days). The EC₂₀ (25 nM) and EC₉₀ (70 nM) calculated from the cell viability assay were used as the high and low concentrations of QC6352 for positive and negative selection screens, respectively (**Figure 5.2a**). The fitness screen was focused on in **Section 5.2.2.** and the chemogenetic screens were focused on in **Section 5.2.3.** Overall, harvesting occurred immediately post-selection (Day 0), with additional harvests taking place approximately every two cell doublings. During Days 15 - 20 and Days 26 - 31, cells were treated with QC6352 at concentrations corresponding to the EC₂₀ and EC₉₀ values (**Figure 5.2b-c**). The Chronos

analysis package was used to analyse changes in QC6352 efficacy in response to gene knockouts across a 26-day period.

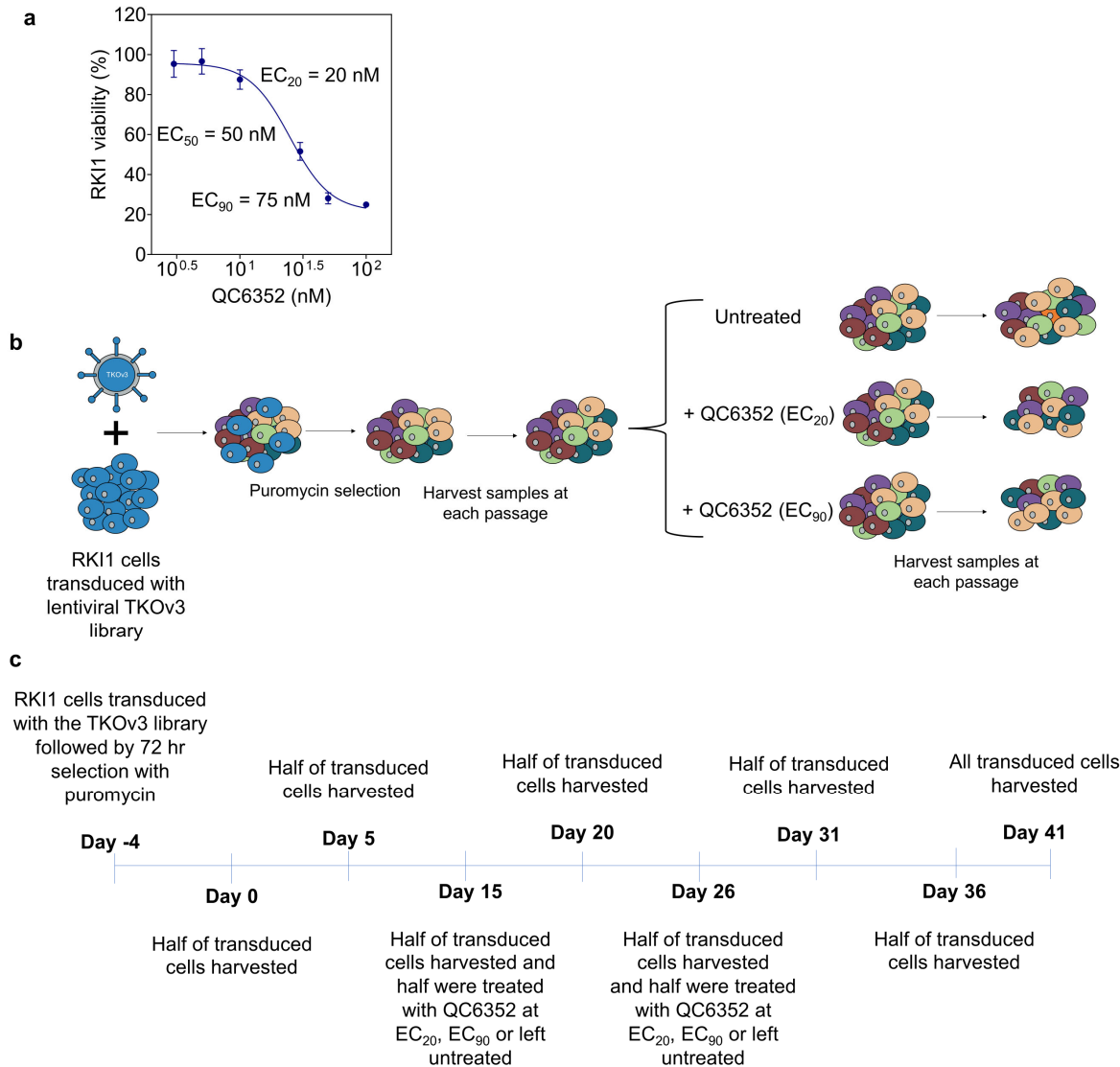


Figure 5.2. Workflow of CRISPR-Cas9 fitness and chemogenomic screens . a) QC6352 dose-response curve (10 days treatment) in RK11 cells transduced with an empty lentiviral vector. Data represents the mean \pm SEM ($n = 2$). EC_{50} value was determined using a nonlinear regression analysis, EC_{20} and EC_{90} values were calculated using the EC_{50} and Hill slope. **b)** Summary of CRISPR-Cas9 combined fitness and chemogenomic screens. **c)** Experimental timeline for transduction, harvesting, and QC6352 treatment in the CRISPR-Cas9 screen.

To obtain an overall understanding of the variation within the dataset, read counts were normalised and assessed with a principal component analysis (PCA), which quantitatively visualises and interprets the largest variations within the dataset³²⁰. The overall largest variation in the dataset, labelled as PC1, accounts for 26% of the total variance and represent the genetic drift between replicate 1 and replicate 2. This was defined by both replicates being positioned

at the extreme ends of the x-axis (**Figure 5.3a**). Consistently, PC2, which accounted for total 19% of the variation, illustrated the change in read counts over time, with Day 0 and Day 41 data points situated on opposite ends of the y-axis. Subsequent variations, including PC3 (8.2%), PC4 (6.4%), PC5 (5.6%), and PC6 (4.6%), corresponded to shifts in read counts due to treatment conditions in each replicate (**Figure 5.3b-c**). In total, the first six principal components represented 69.8% of the total variance in the CRISPR-Cas9 fitness screen dataset, highlighting its complexity and underscoring the necessity for advanced bioinformatic analysis.

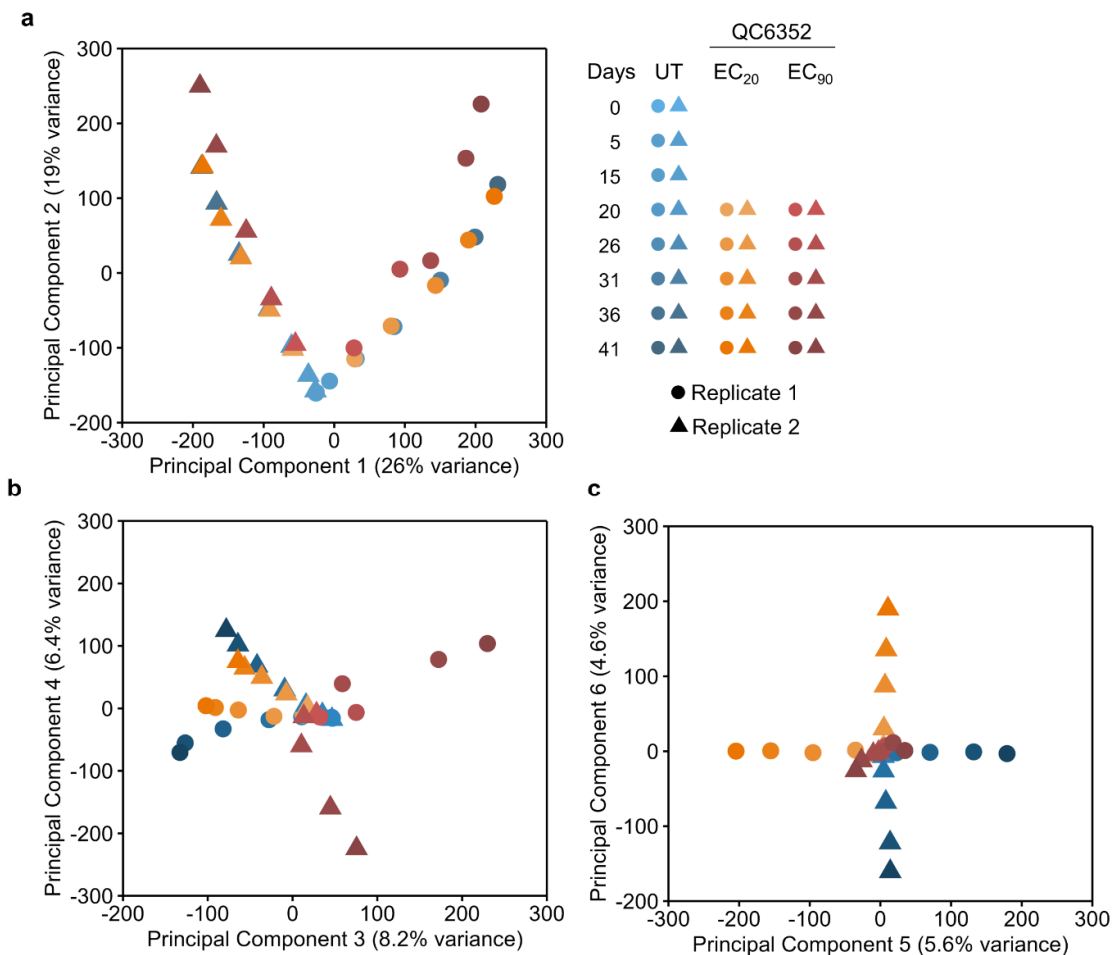


Figure 5.3. Principal component analysis of the CRISPR-Cas9 screen. a - c) RKII cells were transduced with the TKOv3 sgRNA library and normalised gene counts were categorised into their respective timepoints, replicates and treatment conditions. Variations in the dataset were quantified using a principal component analysis and plotted on arbitrary scales to show relative changes in variance over time.

5.2.2. Genome-wide CRISPR-Cas9 fitness screen in RKI1 glioblastoma cells

Since the Chronos analysis does not provide statistical significance, a threshold is commonly used for Chronos scores to differentiate between fitness and non-fitness genes²¹⁴. Chronos scores less than -0.5 were taken as gene dependencies while Chronos scores greater than 0.5 were taken as proliferation-suppressor genes. The analysis identified 3359 fitness genes in total (**Figure 5.4a**). 1927 selective gene dependencies were identified, the top 5 of which were *SOX2*, *DRD5*, *METTL2A*, *SOX9*, and *CENPO* (**Figure 5.4b**). *SOX2* and *SOX9* are transcription factors regulating stemness²⁹⁹, while *DRD5* is a dopamine receptor that activate the phospholipase C (PLC) signalling³²¹. *METTL2A* is a methyltransferase involved in the methylation of tRNA for improved stability and protein translation³²². Lastly, *CENPO* is a kinetochore which plays a role in the regulation of mitosis, particularly in spindle assembly and chromosome segregation³²³.

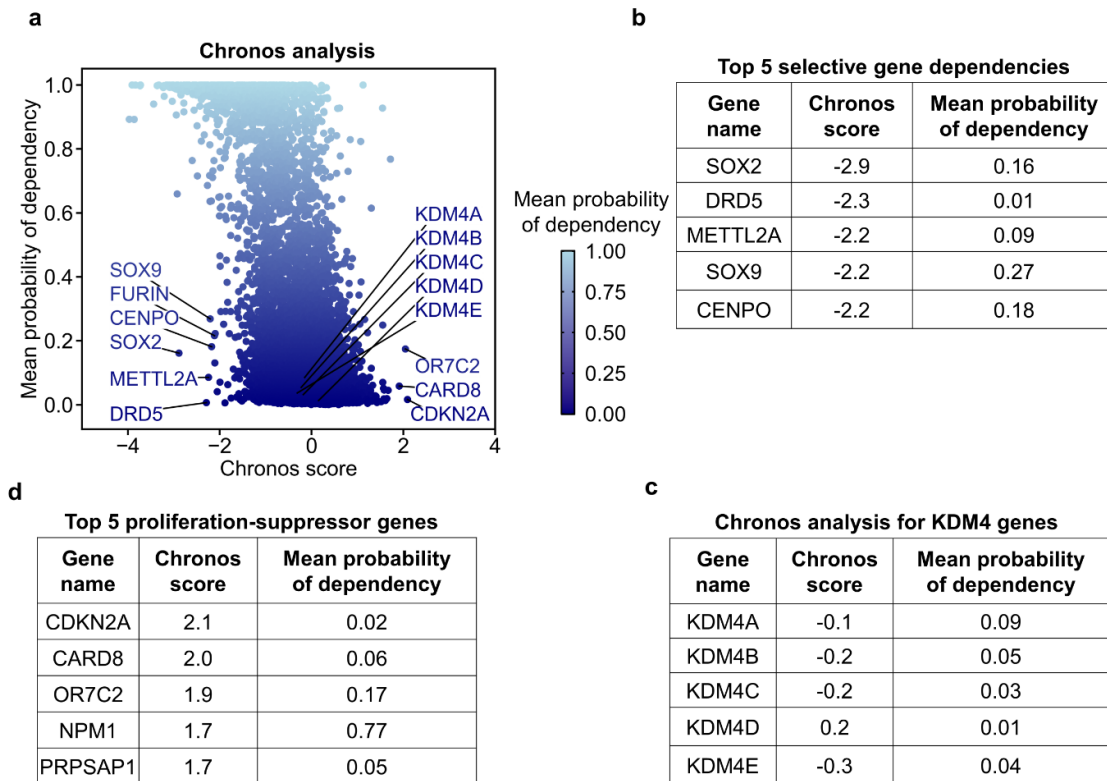


Figure 5.4. RKI1 fitness genes identified by Chronos analysis. **a)** RKI1 cells were transduced with the TKOv3 sgRNA library and analysed using the Chronos package. Each data point represents an individual gene knockout. Mean probability of dependency was calculated from 1095 cell lines in the Cancer Cell Line Encyclopedia (CCLE) obtained from the Dependency Map (DepMap) portal. **b)** Top 5 gene knockouts with the lowest Chronos scores (selective gene dependencies). **c)** Top 5 gene knockouts with the highest Chronos scores (proliferation-suppressor genes). **d)** Chronos analysis of the change in cell fitness when knocking out the KDM4 family.

In addition, 1432 proliferation-suppressor genes were identified and the top 5 were *CDKN2A*, *CARD8*, *OR7C2*, *NPM1*, and *PRPSAP1* (**Figure 5.4c**). These results should be given a certain level of caution since the Chronos analysis software was created with the intention to identify gene dependencies and is therefore not optimised to find proliferation-suppressor genes²⁹⁸. However, *CDKN2A* is a well-established tumour suppressor which regulates G1 cell cycle progression³²⁴, suggesting that Chronos can identify proliferation-suppressor genes with a certain level of accuracy. *CARD8* functions as an inflammasome sensor that can trigger caspase-1-dependent pyroptosis, a form of cell death involved in inflammatory responses³²⁵. *OR7C2*, classified as a G-protein coupled receptor, is traditionally known as an olfactory receptor and its role in suppressing proliferation is a particularly novel finding³²⁶. *NPM1* is noted for its dual function; it acts as a proto-oncogene by such roles as facilitating ribosome biogenesis for protein synthesis and cell growth²¹. *NPM1* also acts as a tumour suppressor through the stabilisation of p53 and the degradation of oncoproteins like c-MYC, cyclin E, Notch, and c-jun^{327,328}. Finally, *PRPSAP1* is hypothesised to play a regulatory role in the synthesis of purines and pyrimidines for DNA replication and proliferation³²⁹ and so functions to limit the resources necessary for proliferation.

Importantly, the knockout of the KDM4 family did not substantially change cell fitness, as evidenced by their Chronos scores, which ranged from -0.3 to 0.2 (**Figure 5.4d**). To assess cell fitness upon KDM4 knockout in other cancer cell lineages, Chronos scores from the DepMap database for all CCLE lineages were used to generate Tukey's box plots (**Figure 5.5**). Within the KDM4 family, only *KDM4A* and *KDM4C* were identified as gene dependencies in 6 and 4 cancer cell lines, respectively, indicated by a Chronos score less than -0.5. This suggests that, overall, the KDM4 isoforms are not important for cell fitness, however, this analysis cannot determine the possibility of redundancy between the KDM4 isoforms. For instance, individual knockout of each family member has no effect but a combined knockdown of two or more members greatly reduces cell fitness³³⁰. Further experiments are necessary to investigate the functional effect of simultaneously knocking out several KDM4 isoforms.

To validate the RKI1 fitness genes identified through the Chronos analysis, a parallel analysis was conducted using the Limma package. To ensure comparability between the Chronos and Limma analyses, the same mean probability of dependency threshold of 0.4 was taken. Additionally, only gene knockouts with an adjusted p-value less than 0.05, and a log₂ fold change in cell fitness greater than 3 or less than -3 relative to the cell population was included in the analysis. Through Limma analysis, 1259 genes were identified as RKI1 fitness

genes (**Figure 5.6a**); of these, 1107 were selective gene dependencies (**Figure 5.6b**), while the remaining 152 were proliferation-suppressor genes (**Figure 5.6c**). Similar to the Chronos analysis, no member of the KDM4 family was identified as a fitness gene with \log_2 fold changes in cell fitness over time ranging between 1.8 to -2.2 (**Figure 5.6d**).

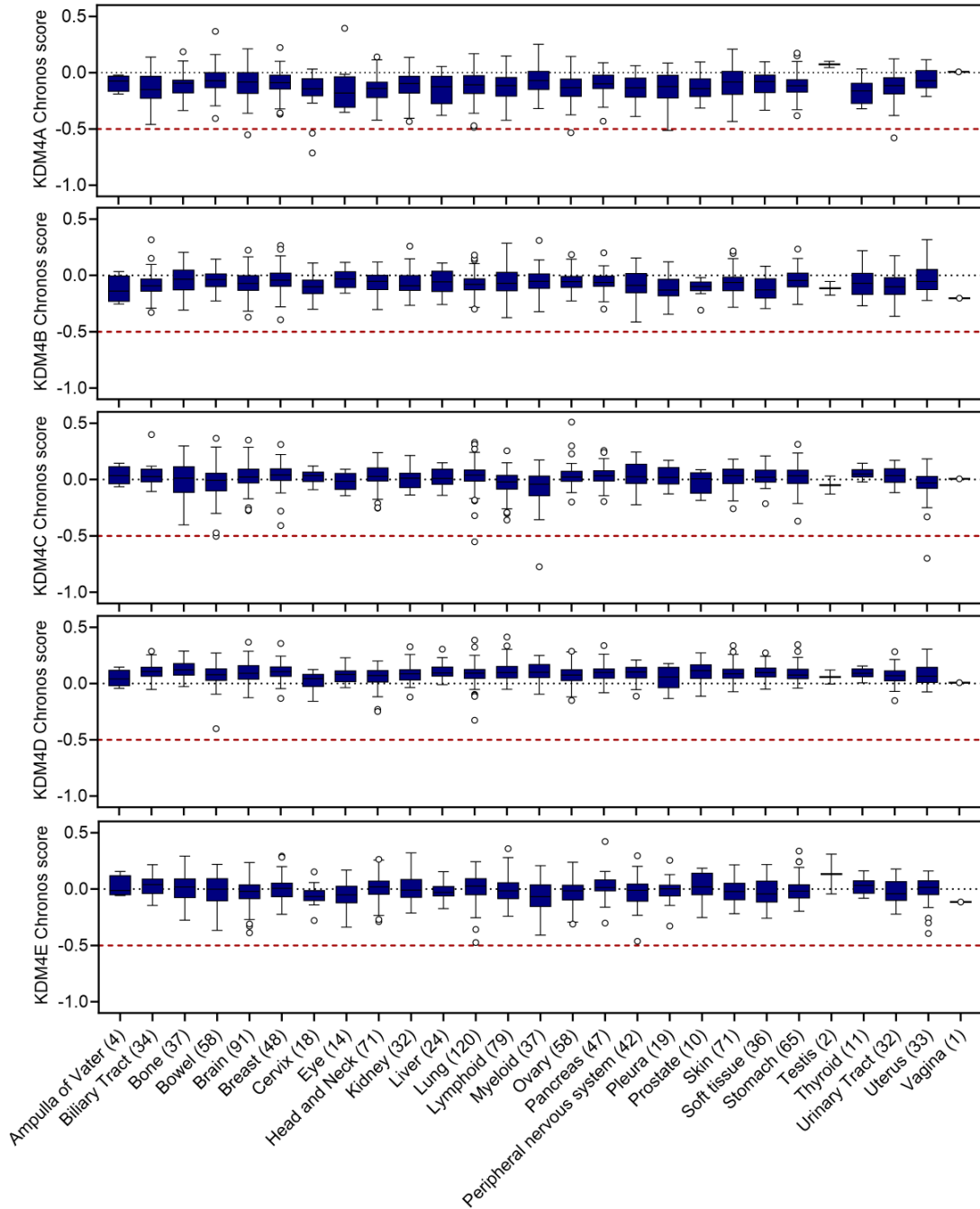


Figure 5.5. KDM4 dependency genes in the CCLE. Tukey's box plots displaying Chronos scores for KDM4 knockout in 1095 cancer cell lines. Cell lines are categorised into their respective tissue types with the number of cell lines in parentheses. Data was sourced using the "23Q2 + Score" dataset

obtained from the DepMap portal. Cell lines with a Chronos score < -0.5 (red dashed line) show KDM4 dependency genes.

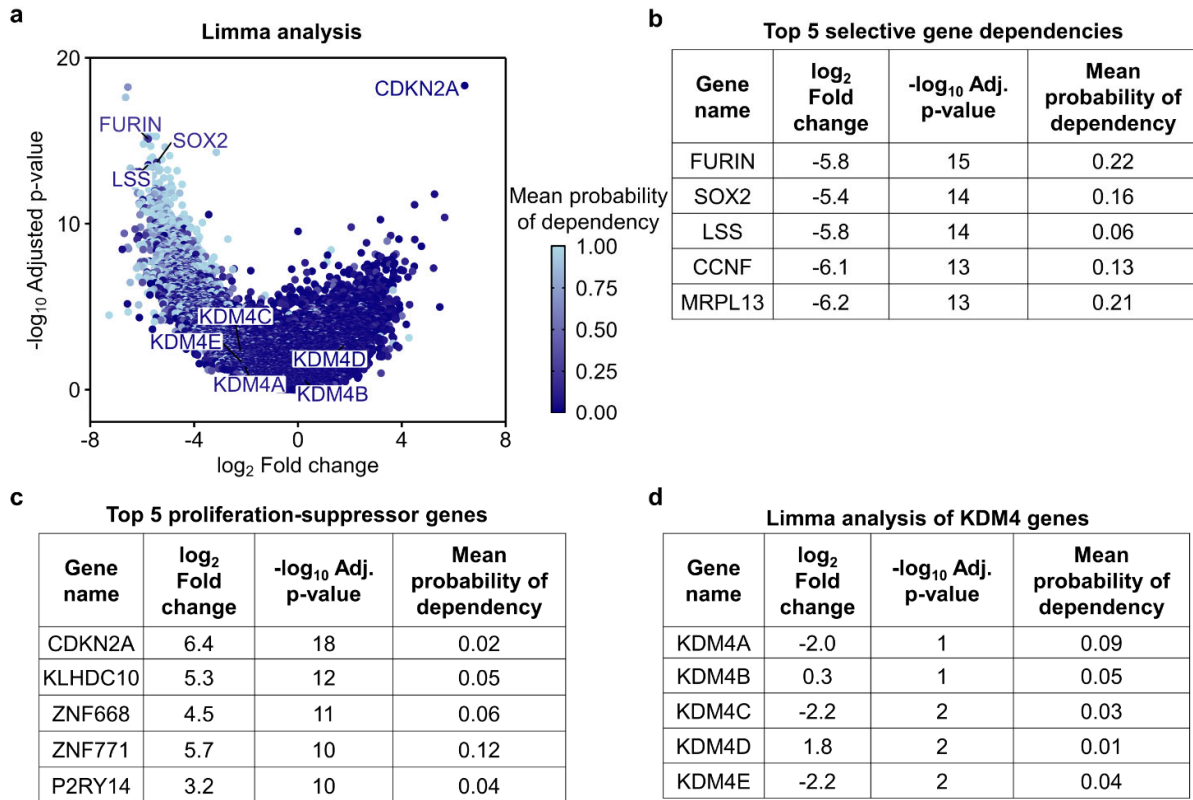


Figure 5.6. RKI1 fitness genes identified by Limma analysis. **a)** RKI1 cells were transduced with the TKOv3 sgRNA library and analysed using the Limma package. Each data point represents an individual gene knockout. Mean probability of dependency was calculated from 1095 cell lines in the CCLE obtained from the DepMap portal. **b)** Top 5 gene knockouts with the lowest log₂ fold change (selective gene dependencies). **c)** Top 5 gene knockouts with the highest log₂ fold change (proliferation-suppressor genes). **d)** Limma analysis of the change in cell fitness when knocking out the KDM4 family. For each sgRNA, p-values were calculated using Empirical Bayes moderated statistics, adjusted for multiple testings using the Benjamini-Hochberg method, and combined for each gene using the Lancaster method.

To integrate the individual genes into broader cellular processes, the results obtained using the Chronos and Limma packages were analysed with the Ingenuity Pathway Analysis (IPA) software. A pathway's significance was determined based on a p-value threshold of < 0.05 , and a Z-score less than -2 (strong association with dependency genes) or greater than 2 (strong association with proliferation-suppression)^{215,302}. The IPA clustering of Chronos fitness genes revealed a dependency of RKI1 cells on the myelination signalling pathway (**Figure 5.7a**). In simpler terms, deletion of genes within this pathway reduced RKI1 cell fitness. Myelination signalling is a broad term covering multiple proliferative pathways such as PI3K/Akt/mTOR, Erk1/MAPK and Ca²⁺/Calcineurin/NFATC³³¹. Moreover, gene knockouts

related to generic transcription, which are genes involved in RNA-polymerase II function, were identified as proliferation suppressor genes. Generic transcription broadly categorises families such as NOTCH, histone deacetylases, oestrogen receptors, retinoid X receptors, androgen receptor, and zinc finger proteins which all affect RNA polymerase II activity and have been implicated in a role suppressing cell growth^{332,333}.

Signalling pathways associated with fitness genes identified through the Limma analysis showed a noticeable difference compared to the IPA of Chronos results, except for the myelination signalling pathway, remaining the most significant pathway (**Figure 5.7b**). Additionally, gene knockouts in the retinoid acid receptor (RAR) activation pathway decreased cell fitness, implicating RAR activation as essential for cell fitness. To improve the reliability of the identified signalling pathways, a pathway analysis was performed using the 1013 overlapping fitness genes identified in both Chronos and Limma analyses (**Figure 5.7c-d**). Using this approach, myelination signalling, and retinoic acid receptor activation were identified as pathways most significantly associated with RKI1 cell fitness.

In summary, a CRISPR-Cas9 fitness screen combined with Chronos and Limma analyses confirmed that individual KDM4A-E knockouts are not crucial for RKI1 cell fitness, in agreement with almost all cell lines from the CCLE analysed by Chronos. The two most significantly associated pathways identified in both Chronos and Limma analyses were myelination signalling and retinoid acid receptor activation suggesting that proteins involved in these pathways could be promising targets for the development of novel therapies against glioblastoma.

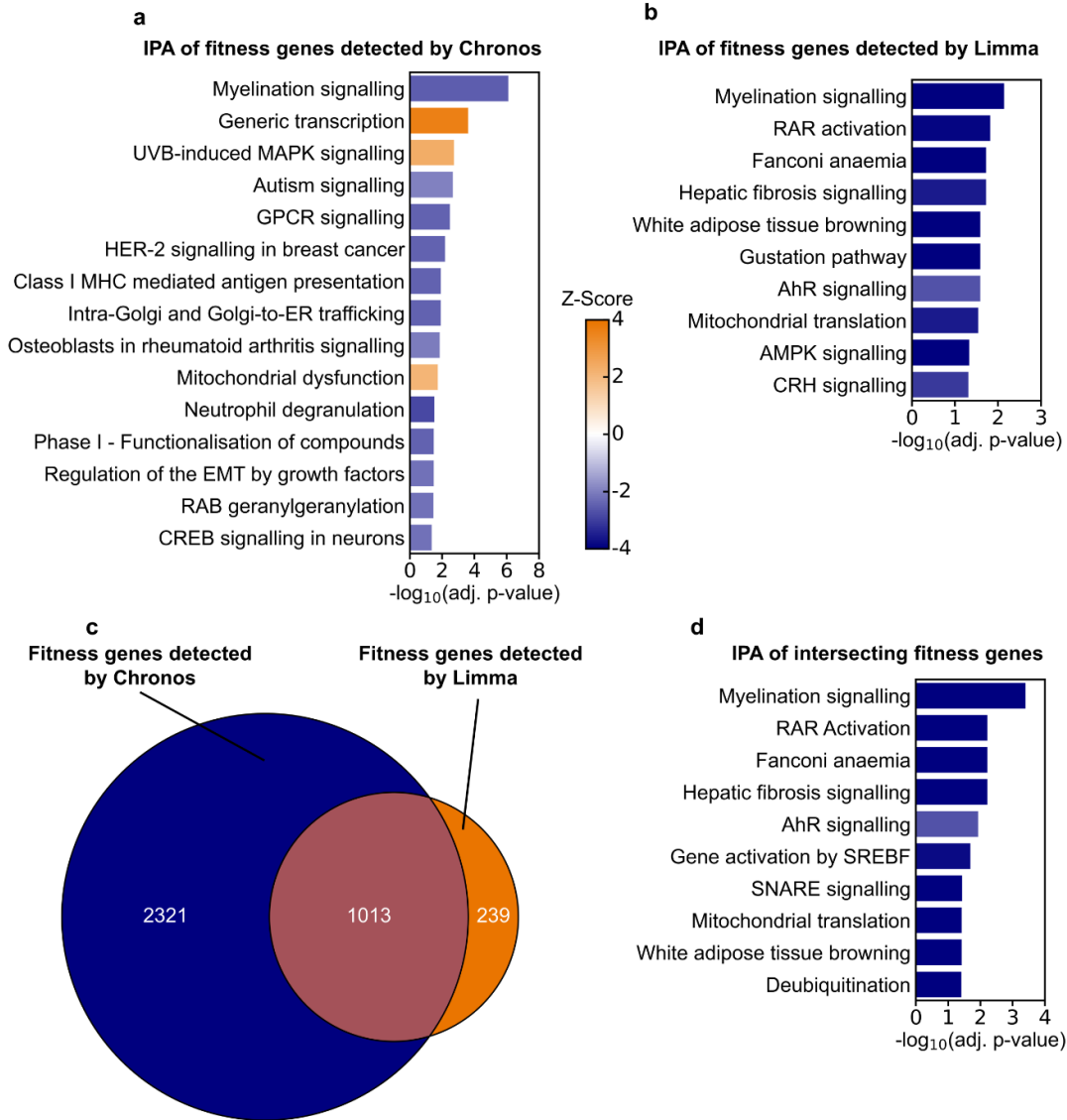


Figure 5.7. Ingenuity Pathway Analysis of fitness genes. a - b) Ingenuity Pathway Analysis of fitness genes identified using the Chronos and Limma packages. **c - d)** Venn diagram and Ingenuity Pathway Analysis of the intersecting fitness genes detected in both analyses. Statistical significance for relevant pathways was determined using a Fisher’s exact test adjusted for multiple testing using the Benjamini-Hochberg method. A Z-score greater than 2 denotes pathways involving the proliferation-suppressor genes while pathways with a Z-score less than -2 represented pathways involving the selective gene dependencies.

5.2.3. Identification of resistance and sensitising genes for QC6352 efficacy

Parallel with the loss-of-function screen, chemogenetic screens were conducted using high concentrations of QC6352 in a positive selection screen to identify sensitising genes and low concentrations of QC6352 were used to perform a negative selection screen to identify resistance genes. To ensure there is no systematic bias, Chronos scores of untreated cells were correlated with Chronos scores of EC₉₀- or EC₂₀-treated cells. A strong linear correlation³³⁴ was identified in both the positive selection ($r = 0.86$; $p < 2.2 \times 10^{-16}$) (**Figure 5.8a**) and negative selection screens ($r = 0.91$; $p < 2.2 \times 10^{-16}$) (**Figure 5.8b**). This indicates a consistent association between scores across treated and untreated conditions, confirming that changes in the untreated cell fitness does not skew QC6352 efficacy measurements. Additionally, the average difference in Chronos score for all gene knockouts in both the positive and negative screens was 0.00, indicating no systematic bias in each screen. Therefore, these results ensure that the differences between Chronos scores in treated and untreated cell populations accurately reflect the modulation in QC6352 efficacy. In subsequent analyses, the difference in Chronos score between EC₉₀- and EC₂₀-treated cells and untreated cells are termed the EC₉₀ and EC₂₀ efficacy scores, respectively.

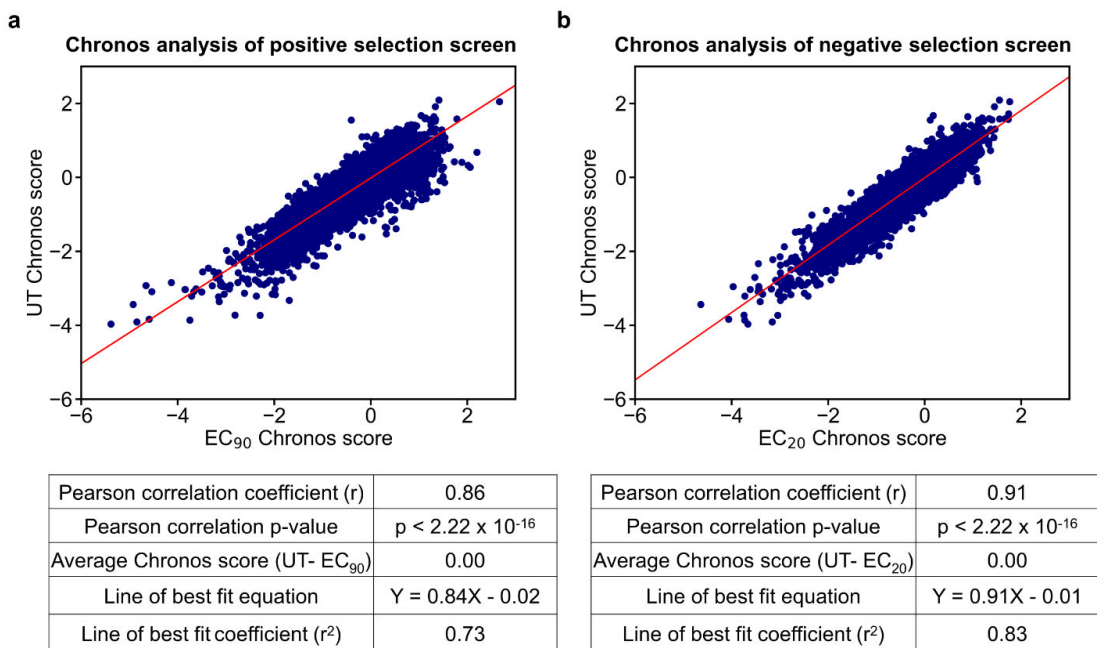


Figure 5.8. Comparison of Chronos scores between treatment groups. TKOv3-transduced RKII cells were left untreated (UT) or treated with QC6352 at EC₂₀ or EC₉₀. Each treatment condition was analysed using the Chronos package and Chronos scores from UT cells were compared against Chronos scores from **a**) EC₂₀-treated cells and **b**) EC₉₀-treated cells. Each correlation was assessed by computing a Pearson correlation coefficient. A line of best fit (shown in red) was generated using the least squares method.

To minimise the occurrence of false positives, gene knockouts that produced contradictory efficacy scores between the positive and negative selection screens were excluded. As such, for the positive selection screen, EC₉₀ efficacy scores greater than 0.5 and EC₂₀ efficacy scores greater than 0 indicate sensitising genes. In the negative selection screen, EC₉₀ efficacy scores less than 0 and EC₂₀ efficacy scores less than -0.5 indicate resistance genes. Using these thresholds, 887 genes in total were identified (**Figure 5.9a**).

Of these, 609 were identified as sensitising genes enhancing QC6352 efficacy (**Figure 5.9b**) and the top 5 with the highest EC₉₀ efficacy scores were *UGT1A5*, *TLN1*, *ACTL6A*, *RBMXL1*, and *CEP152*. *UGT1A5* is a UDP-glucuronosyltransferase which attaches glucuronic acid to lipophilic molecules to facilitate excretion from the body³³⁵, while *TLN1* is a scaffold protein important for integrin signalling which activates the Raf/Mek/Erk pathway in a FAK1-dependent manner³³⁶. *ACTL6A* encodes a member of the actin-related protein family necessary for ATP-dependent chromatin-remodelling and neural progenitor stem cell proliferation³³⁷. *RBMXL1* is a retrogene which promotes the transcriptional activity of the CBX5 locus which binds to H3K9 methylation³³⁸ and *CEP152* is essential for centrosome duplication together with Plk4 and other proteins from the CEP family³³⁹.

In the negative selection screen, 278 were identified as resistance genes suppressing QC6352 efficacy. The top 5 with the lowest EC₂₀ efficacy scores were *PRPSAP1*, *OSGEP*, *MT2A*, *MYC*, *WDR77* (**Figure 5.9c**). *PRPSAP1* was identified in the fitness screen as one of the top 5 proliferation-suppressor genes essential for the regulation of purines and pyrimidines synthesis³⁴⁰, while *OSGEP* are fundamental for proper protein synthesis³⁴¹. *MT2A* regulates the cellular concentration of trace metal ions which are essential for cell growth³⁴² and *MYC* is a well-known transcription factor activating many growth-related genes³⁴³. Lastly, *WDR77* is a core component of the methylosome, a complex involved in the methylation of arginine residues which plays a role in proliferation and survival³⁴⁴.

Although none of the KDM4 members met the threshold criteria in the positive and negative selection screens (**Figure 5.9d**), KDM4C was found marginally below the threshold, with an EC₉₀ efficacy score of -0.03 and an EC₂₀ efficacy score of -0.48. Since QC6352 was developed as a KDM4 inhibitor with the highest specificity towards KDM4C, these results could indicate that KDM4C might contribute to the antiproliferative efficacy of QC6352, in addition to additional unknown target/s. Finally, Ingenuity Pathway Analysis of the 887 genes important for QC6352 efficacy identified 13 pathways (**Figure 5.9e**). Interestingly, all

pathways were related to either mitosis, transcription, RNA processing, or translation suggesting that these biological processes are essential for QC6352’s mechanism of action.

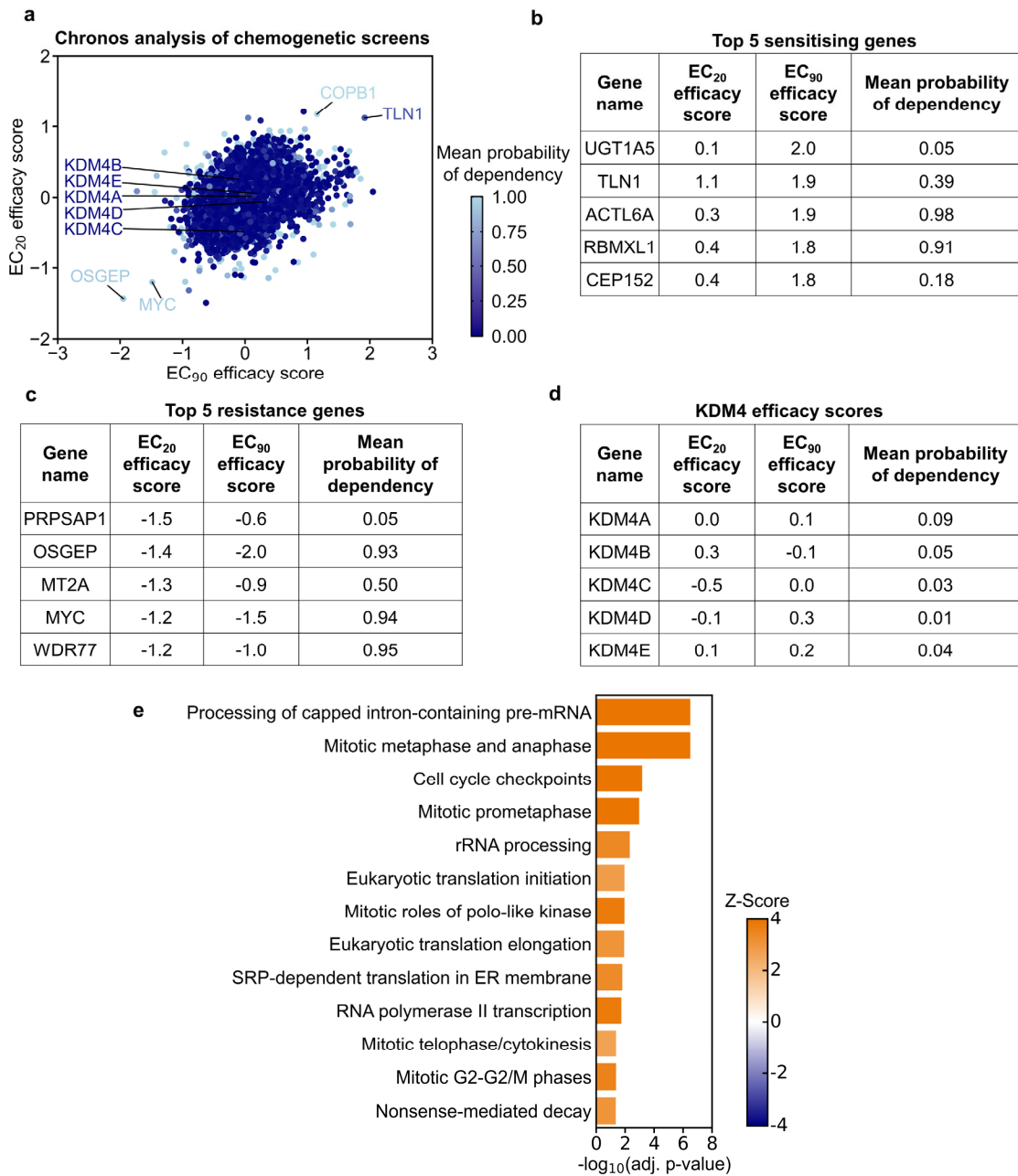


Figure 5.9. QC6352 sensitising and resistance genes identified by Chronos analysis. **a)** TKOv3-transduced RKI1 cells were treated with QC6352 at EC₂₀ or EC₉₀ and analysed using the Chronos package. **b)** Top 5 gene knockouts with the highest EC₉₀ efficacy scores (sensitising genes). **c)** Top 5 gene knockouts with the lowest EC₂₀ efficacy scores (resistance genes). **d)** Chronos analysis of the change in cell fitness when knocking out the KDM4 family. **e)** Significant pathways for QC6352 efficacy identified using Ingenuity Pathway Analysis. A Z-score greater than 2 denotes pathways involving the sensitising genes while pathways with a Z-score less than -2 represented pathways involving the resistance genes.

Limma analysis of the chemogenetic screen did not find significant changes in QC6352 efficacy when cells were treated at EC₂₀ ($-\log_{10}$ adjusted p-value < 1.3). Thus, Limma could not be used to assess changes in QC6352 efficacy upon gene knockouts (**Figure 5.10**). In summary, the CRISPR-Cas9 screen incorporated chemogenetic positive and negative selection screens to find important genes for the antiproliferative efficacy of QC6352. A total of 887 genes were found to modulate the efficacy of QC6352. Notably, the genes essential for QC6352's action were primarily associated with key proliferation processes such as mitosis, transcription, RNA processing, and translation. Validation of these pathways may assist in uncovering the mechanism of action of QC6352.

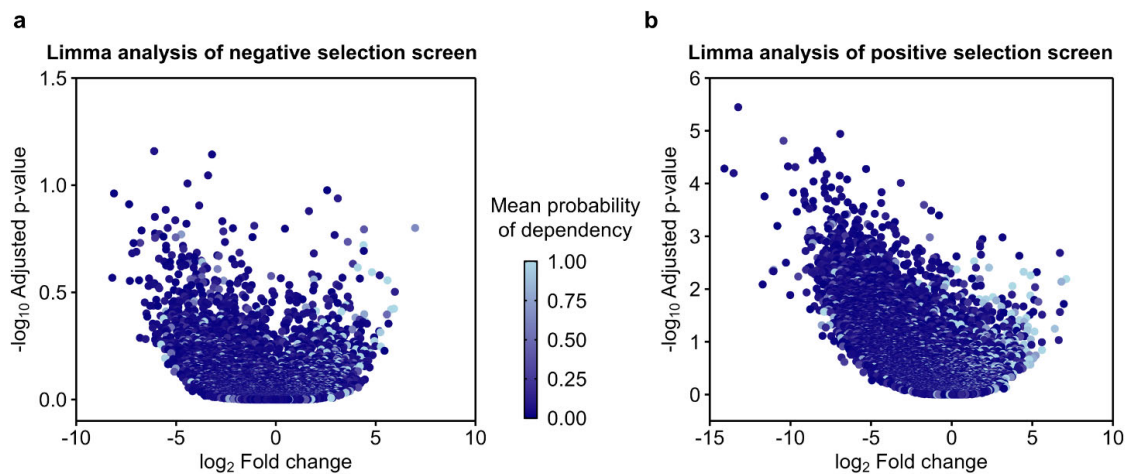


Figure 5.10. Limma analysis of gene knockouts modulating QC6352 efficacy. TKOv3-transduced RK11 cells were treated with QC6352 at **a)** EC₂₀ or **b)** EC₉₀ and analysed using the Limma package. Each data point represents an individual gene knockout. Mean probability of dependency was calculated from 1095 cell lines in the CCLE obtained from the DepMap portal. For each sgRNA, p-values were calculated using Empirical Bayes moderated statistics, adjusted for multiple testings using the Benjamini-Hochberg method, and combined for each gene using the Lancaster method.

5.2.4. Identification of proteins stabilised by QC6352 using Cellular Thermal Shift Assay

CETSA methodology was next utilised as an orthogonal approach to identifying the binding partners of QC6352 and compared against the KDM4 inhibitor ML324. Since KDM4A is minimally expressed in glioblastoma cells (**Figure 4.17**), a cell line overexpressing KDM4A was necessary to visualise KDM4A by Western blotting. Therefore, to confirm if KDM4A is thermally stabilised by QC6352 and ML324, lysed-cell CETSA was performed in A172 cells overexpressing KDM4A (**Figure 5.11a**). QC6352 exhibited a minor, statistically insignificant, increase in KDM4A thermal stability ($T_m = 48.7^\circ\text{C}$) compared to the vehicle ($T_m = 45.6^\circ\text{C}$) while ML324 did not increase KDM4A thermal stability ($T_m = 44.3^\circ\text{C}$). To ensure each sample

was heated, GAPDH was used as a loading control which showed uniform melting (**Figure 5.11b**).

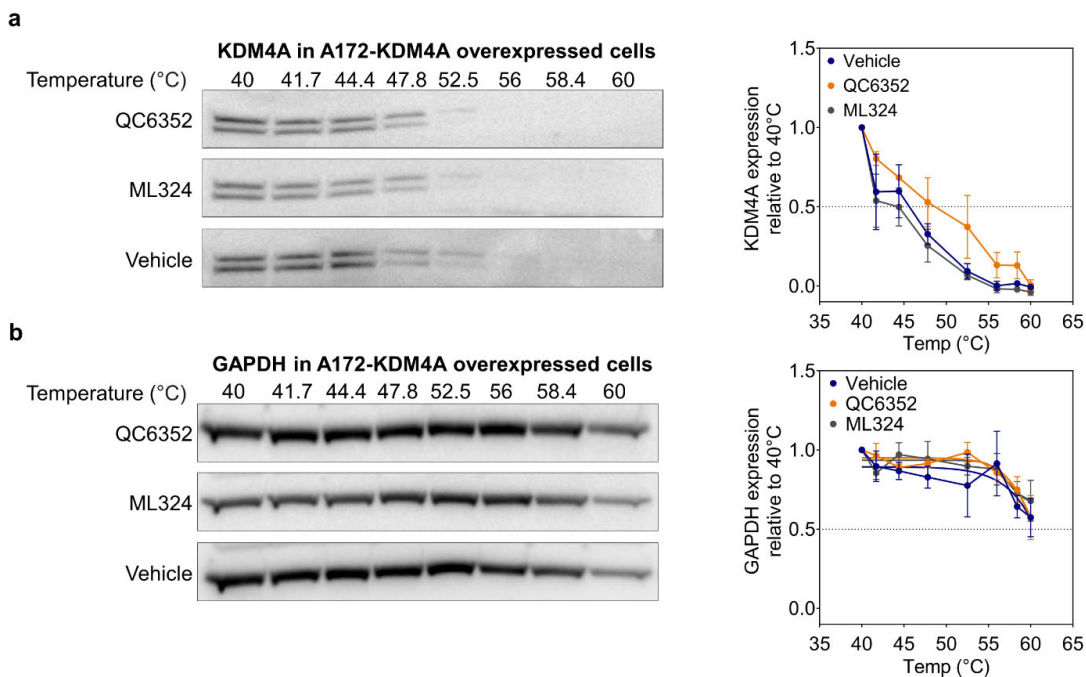


Figure 5.11. KDM4A stabilisation by QC6352 and ML324. a - b) Lysed-cell CETSA was performed by lysing A172 cells overexpressing KDM4A and incubating cell lysates with 100 μ M QC6352, ML324, or DMSO (Vehicle). Incubated lysates were heated from 40 - 60°C and unmelting protein expression was visualised using Western blotting. Quantifications are mean \pm SEM (n = 3 - 4) relative to the lowest tested temperature (40°C).

To validate the sample preparation protocol used for all CETSA experiments, the Akt inhibitor MK2206, was used as a positive control to detect Akt stabilisation³⁴⁵. Stabilisation of Akt was assessed in FPW1 lysates treated with MK2206 (**Figure 4.2**). In the presence of MK2206, Akt was greatly stabilised, exhibiting a T_m value greater than 60°C compared to a T_m of 47.8°C in the presence of the vehicle (**Figure 5.12a**). These findings validate the lysed-cell CETSA protocol used in our hands. However, no KDM4A stabilisation was found in lysates incubated with QC6352 or ML324 (**Figure 5.11a**), which could be explained by several hypotheses. A likely explanation is that the semi-quantitative Western blotting-based quantification may be unable to identify subtle changes in T_m between vehicle and treated samples, or less likely, that both compounds are unable to bind in a cellular context.

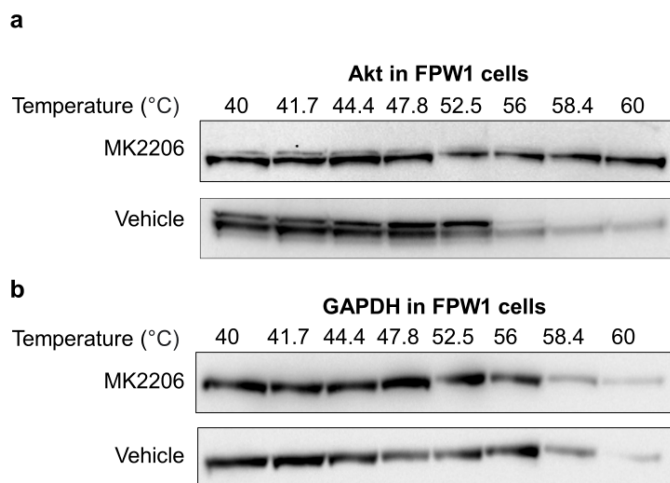


Figure 5.12. Akt stabilisation by MK2206. a - b) Lysed-cell CETSA was performed by lysing FPW1 cells and incubating cell lysates with 20 μ M MK2206 or DMSO (Vehicle). Incubated lysates were heated from 40 - 60°C and unmelted protein expression was visualised using Western blotting. Representative images are shown for two independent experiments.

5.2.5. QC6352 and ML324 target identification using intact-cell MS-CETSA

To increase the sensitivity and throughput in measuring protein stabilisation by QC6352 or ML324, mass spectrometry was utilised³⁴⁶. Intact-cell MS-CETSA was performed using FPW1 cells incubated with either 20 μ M QC6352, ML324, or the vehicle control for 5 hours. Two independent experiments were conducted in which intact cells were subjected to a range of heating temperatures (40 - 60°C) and lysed for mass spectrometry analysis.

In the first experiment, QC6352-incubated samples showed a total of 8 significantly stabilised proteins while in the second experiment only one protein, ISG15, was significantly stabilised (**Figure 5.13a**). Similarly, there were 3 significantly destabilised proteins identified in experiment 1 and 9 significantly destabilised proteins in experiment 2 (**Figure 5.13b**). No protein was identified as significantly stabilised or destabilised in both experiments. Furthermore, only 3 proteins, DCK, LARS2, and PACSIN3 had identifiable melting points in all treatment conditions in both experiments.

In the ML324-incubated samples, the first experiment detected 13 significantly stabilised proteins while the second experiment only found 5 significantly stabilised proteins. However, none of these 18 proteins was stabilised by ML324 in both experiments (**Figure 5.14a**). Surprisingly, there were no significantly destabilised proteins in experiment 1 and 7 significantly destabilised proteins in experiment 2 (**Figure 5.14b**). Similar to the QC6352-incubated samples, many protein melting points could not be detected in both experiments and only ARMT1 had a detectable melting point in all treatment conditions for both experiments.

Additionally, only 4 members of the KDM family (KDM1A, KDM2A, KDM3B, and KDM5B) were detected overall, and none were significantly stabilised or destabilised by QC6352 or ML324.

| a Significantly QC6352-stabilised proteins | | | | | b Significantly QC6352-destabilised proteins | | | | |
|--|--------------------------------|------------------|--------------------------------|------------------|--|--------------------------------|------------------|--------------------------------|------------------|
| Protein name | Experiment 1 ΔT_m (°C) | $-\log_{10}$ FDR | Experiment 2 ΔT_m (°C) | $-\log_{10}$ FDR | Protein name | Experiment 1 ΔT_m (°C) | $-\log_{10}$ FDR | Experiment 2 ΔT_m (°C) | $-\log_{10}$ FDR |
| CDC123 | 10.9 | 4.12 | - | - | NOS1AP | -16.6 | 4.84 | - | - |
| KANK2 | 9.8 | 3.19 | - | - | DCTN1 | -6.0 | 2.04 | - | - |
| TERF2 | 9.2 | 2.74 | - | - | DOCK5 | -11.3 | 2.04 | - | - |
| COMMD3-BMI1 | 8.7 | 2.43 | - | - | LIG3 | 2.0 | 0.32 | -9.8 | 5.51 |
| UBE2G2 | 8.5 | 2.30 | - | - | DCK | -2.8 | 0.09 | -9.5 | 5.40 |
| RPP14 | 8.2 | 2.11 | - | - | ZYG11B | -0.1 | 0 | -8.5 | 4.30 |
| PAFAH1B2 | 8.0 | 2.04 | - | - | SNTB1 | 0.1 | 0 | -8.4 | 4.19 |
| TRAPPC2L | 3.9 | 2.04 | - | - | SMEK1 | - | - | -7.5 | 3.31 |
| ISG15 | - | - | 9.9 | 3.87 | SMYD5 | - | - | -7.4 | 3.31 |
| | | | | | ACSS2 | 3.9 | - | -6.3 | 2.25 |
| | | | | | LARS2 | -0.0 | 0 | -5.9 | 1.89 |
| | | | | | PACSIN3 | 1.0 | 0.04 | -5.5 | 1.60 |

Figure 5.13. Proteome-wide screen of QC6352 binding partners using intact-cell MS-CETSA. Intact-cell MS-CETSA was performed by incubating FPW1 cell lysates with 20 μ M QC6352 or DMSO (Vehicle). Treated cells were heated from 40 - 60°C prior to lysis and unmelted protein abundance was quantified using mass spectrometry. Significantly **a**) stabilised or **b**) destabilised proteins were identified by comparing changes in melting point (ΔT_m) between QC6352 and Vehicle using the TPP-TR package in R. All p-values were calculated using the robust Z-score method and adjusted for the false discovery rate (FDR) using the Benjamini-Hochberg method. Bolded proteins were identified in all treatment groups for both experiments.

| a Significantly ML324-stabilised proteins | | | | | b Significantly ML324-destabilised proteins | | | | |
|---|--------------------------------|------------------|--------------------------------|------------------|---|--------------------------------|------------------|--------------------------------|------------------|
| Protein name | Experiment 1 ΔT_m (°C) | $-\log_{10}$ FDR | Experiment 2 ΔT_m (°C) | $-\log_{10}$ FDR | Protein name | Experiment 1 ΔT_m (°C) | $-\log_{10}$ FDR | Experiment 2 ΔT_m (°C) | $-\log_{10}$ FDR |
| VPS8 | 7.5 | 3.07 | - | - | TOM1 | -8.2 | 3.07 | -13.8 | - |
| KANK2 | 7.0 | 2.95 | - | - | UBAP1 | -7.0 | 2.17 | - | - |
| SRP54 | 6.9 | 2.95 | - | - | CDK9 | -11.3 | 2.17 | - | - |
| INADL | 6.7 | 2.76 | - | - | HNRNPA3 | -6.6 | 1.90 | - | - |
| CKM | 5.8 | 2.06 | - | - | VWA9 | -10.0 | 1.53 | - | - |
| ZNF598 | 3.6 | 1.94 | - | - | HNRNPLL/ HNRPLL | -9.7 | 1.48 | - | - |
| ATIC | 3.5 | 1.90 | - | - | PALLD | -5.8 | 1.38 | - | - |
| CA8 | 3.4 | 1.85 | -0.03 | 0.10 | | | | | |
| MLST8 | 3.1 | 1.49 | - | - | | | | | |
| ADNP | 3.1 | 1.48 | - | - | | | | | |
| SQSTM1 | 3.1 | 1.48 | - | - | | | | | |
| ASPSCR1 | 4.7 | 1.42 | -7.2 | - | | | | | |
| NRF1 | 4.6 | 1.34 | - | - | | | | | |
| GSTM4 | - | - | 7.7 | 2.73 | | | | | |
| RQCD1 | -2.42 | - | 8.1 | 2.73 | | | | | |
| ARMT1 | -0.62 | 0.01 | 7.3 | 2.53 | | | | | |
| ISG15 | 2.01 | 0.26 | 6.9 | 2.39 | | | | | |
| CA2 | -0.01 | 0.02 | 5.4 | 1.44 | | | | | |

Figure 5.14. Proteome-wide screen of ML324 binding partners using intact-cell MS-CETSA. Intact-cell MS-CETSA was performed by incubating FPW1 cells with 20 μ M ML324 or DMSO (Vehicle). Treated cells were heated from 40 - 60°C prior to lysis and unmelted protein abundance was quantified using mass spectrometry. Significantly **a)** stabilised or **b)** destabilised proteins were identified by comparing changes in melting point (ΔT_m) between ML324 and Vehicle using the TPP-TR package in R. All p-values were calculated using the robust Z-score method and adjusted for the false discovery rate (FDR) using the Benjamini-Hochberg method. Bolded proteins were identified in all treatment groups for both experiments.

Overall, out of the total 46 significantly stabilised/destabilised proteins identified from QC6352- and ML324-incubated samples in individual experiments, only ARMT1, PACSIN3, DCK, and LARS2 provided complete melting curves and quantifiable melting temperatures in both experiments. Averaging the protein abundance at each temperature created a more robust representation of their respective melt curves (**Figure 5.15**). However, when assessing the melt curves of average values, QC6352 destabilised, only deoxycytidine kinase (DCK, $T_m = 47.7^\circ\text{C}$) compared to vehicle control ($T_m = 55.7^\circ\text{C}$). DCK phosphorylates 2'-deoxycytidine to form deoxycytidine monophosphate, which is converted to deoxycytidine triphosphate for DNA synthesis and repair³⁴⁷. Therefore, it is possible that QC6352 indirectly prevents protein-protein interactions involving DCK, thereby reducing DCK's thermal stability in cells. However, due to the significant variability observed between replicates in the CETSA results, additional validation is essential to confirm the potential interaction between QC6352 and DCK.

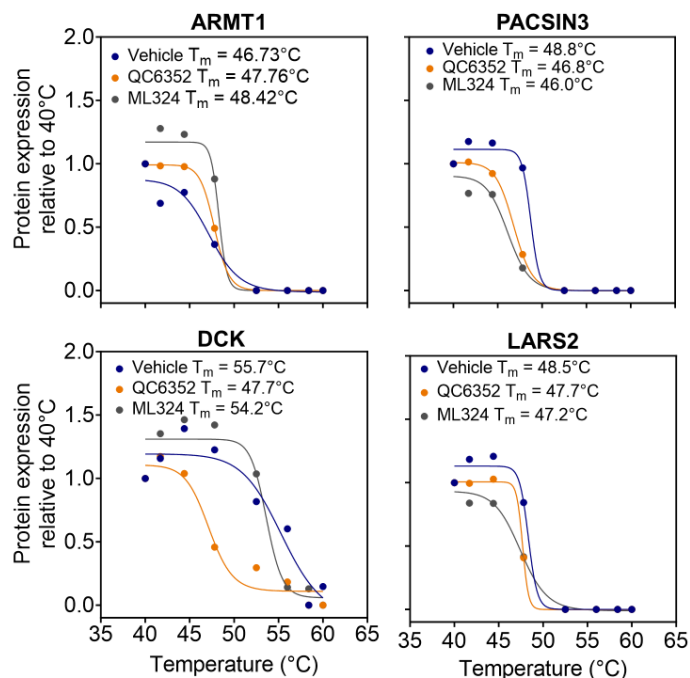


Figure 5.15. Melt curves of significant binding partners using intact-cell MS-CETSA. Intact-cell MS-CETSA was performed by incubating FPW1 cells with 20 μM QC6352, ML324 or DMSO (Vehicle). Treated cells were heated from 40 - 60°C prior to lysis and unmelted protein abundance was quantified using mass spectrometry. Protein abundance was averaged for all proteins identified as significant in at least one treatment condition and detected in all treatment conditions for both experiments and were fitted with a four-parameter nonlinear regression melt curve. The data represents mean protein abundance relative to the lowest temperature (40°C).

5.2.6. QC6352 and ML324 target identification using lysed-cell MS-CETSA

Given the lack of reproducibility when using live-cell MS-CETSA, a more simplified lysed-cell MS-CETSA was conducted in FPW1 cells in three independent experiments. The Akt inhibitor MK2206, was used as a positive control to detect Akt stabilisation. Intriguingly, only one member of the KDM family was detected, KDM1A, which showed no significant stabilisation when incubated with QC6352, ML324, or MK2206. Analysis of lysates incubated with QC6352 identified 13, 7, and 13 significantly stabilised proteins in each experiment (**Figure 5.16**). However, no protein was stabilised in more than one experiment. Similarly, MS analysis of lysates incubated with ML324 identified 0, 7, and 7 significantly stabilised proteins in each experiment (**Figure 5.17**), whereas MK2206 significantly stabilised 4, 3, and 15 proteins in each experiment (**Figure 5.18**). However, no protein was stabilised in more than one experiment and Akt was not identified as a significantly stabilised protein in MK2206-incubated lysates.

Significantly QC6352-stabilised proteins

| Protein name | Experiment 1 ΔT_m (°C) | $-\log_{10}$ FDR | Experiment 2 ΔT_m (°C) | $-\log_{10}$ FDR | Experiment 3 ΔT_m (°C) | $-\log_{10}$ FDR |
|-----------------|-----------------------------------|---------------------|-----------------------------------|---------------------|-----------------------------------|---------------------|
| MAN2B2 | 9.6 | 4.02 | 5.5 | - | -5.6 | - |
| PTGR2 | 7.8 | 2.27 | -0.9 | - | 7.3 | - |
| GEMIN5 | 7.3 | 1.90 | 3.0 | 0.02 | -5.3 | - |
| NOVA1 | 7.7 | 1.74 | - | - | 0.75 | - |
| EIF4A3 | 6.8 | 1.65 | 4.3 | 0.45 | -4.9 | - |
| GOPC | 6.8 | 1.64 | 6.7 | - | -2.2 | - |
| C9orf64 | 6.7 | 1.58 | 0.25 | 0.00 | 5.9 | 0.61 |
| UMPS | 7.0 | 1.40 | - | - | -0.6 | - |
| RTKN | 6.4 | 1.40 | - | - | - | - |
| NAGLU | 6.2 | 1.39 | -2.8 | 0.10 | 5.5 | 0.74 |
| GSTM2 | 6.1 | 1.39 | 1.4 | 0.00 | 0.3 | - |
| UROS | 6.2 | 1.39 | 4.1 | 0.42 | - | - |
| CMTR1 | 6.1 | 1.39 | - | - | - | - |
| MDH1 | - | - | 9.6 | 3.21 | -4.6 | - |
| PAFAH1B3 | -2.0 | - | 8.4 | 2.20 | -0.5 | 0.00 |
| PBLD | -4.2 | - | 8.0 | 2.03 | 6.5 | - |
| TACO1 | -6.4 | 1.80 | 8.0 | 2.03 | - | - |
| PLD3 | 1.9 | 0.00 | 7.8 | 1.95 | 2.1 | - |
| SUB1 | - | - | 9.5 | 1.79 | - | - |
| GAA | - | - | 6.9 | 1.41 | -0.9 | - |
| PCYT1A/B | -0.7 | - | - | - | 11.6 | 3.58 |
| FAT3 | - | - | - | - | 11.2 | 3.56 |
| AK6/TAF9 | 2.9 | - | -1.8 | - | 9.6 | 2.23 |
| GNAS | 2.4 | - | 1.2 | 0.00 | 9.4 | 2.20 |
| PRPSAP2 | -3.9 | - | 0.2 | - | 8.5 | 2.14 |
| GUK1 | -0.6 | - | -2.3 | 0.4 | 8.9 | 1.95 |
| WIPI2 | -0.7 | - | - | - | 7.9 | 1.83 |
| OSBPL3 | -2.0 | 0.08 | - | - | 8.5 | 1.76 |
| DHX9 | 0.7 | 0 | 4.6 | 0.52 | 7.4 | 1.63 |
| AP3B1 | 4.2 | 0.50 | - | - | 8.1 | 1.63 |
| PDLIM7 | - | - | 17.5 | - | 7.7 | 1.45 |
| WDR92 | -5.5 | 1.39 | 1.3 | 0.00 | 7.6 | 1.36 |
| EPN1 | - | - | - | - | 7.4 | 1.32 |

Figure 5.16. Proteome-wide screen of QC6352 binding partners using lysed-cell MS-CETSA. Lysed-cell CETSA was performed by lysing FPW1 cells and incubating cell lysates with 20 μ M QC6352 or DMSO (Vehicle). Incubated lysates were heated from 40 - 60°C and unmelted protein abundance was quantified using mass spectrometry. Significantly stabilised proteins in at least one of three experiments were identified by comparing changes in melting point (ΔT_m) between QC6352 and Vehicle using the TPP-TR package in R. All p-values were calculated using the robust Z-score method and adjusted for the false discovery rate (FDR) using the Benjamini-Hochberg method. Bolded proteins were identified in all treatment groups for all three experiments.

Significantly ML324-stabilised proteins

| Protein name | Experiment 1 ΔT_m (°C) | $-\log_{10}$ FDR | Experiment 2 ΔT_m (°C) | $-\log_{10}$ FDR | Experiment 3 ΔT_m (°C) | $-\log_{10}$ FDR |
|-----------------|-----------------------------------|---------------------|-----------------------------------|---------------------|-----------------------------------|---------------------|
| MDH1 | - | - | 14.6 | 4.87 | -2.6 | - |
| PBLD | - | - | 11.0 | 2.46 | -3.6 | - |
| NNMT | -2.3 | - | 10.7 | 2.31 | -1.7 | - |
| PLAA | - | - | 10.6 | 2.31 | 0.2 | - |
| PPIG | 6.3 | - | 9.7 | 1.88 | -3.4 | 0.01 |
| CALM1/2 | - | - | 9.2 | 1.83 | - | - |
| SUB1 | - | - | 8.6 | 1.48 | - | - |
| ATP6V1G1 | -8.9 | - | -1.6 | - | 11.0 | 2.93 |
| CCT6B | -1.0 | - | - | - | 14.4 | 2.93 |
| TWF1 | -4.2 | - | 1.0 | - | 14.1 | 2.93 |
| LUC7L2 | -4.1 | - | - | - | 9.9 | 2.22 |
| ZC3H14 | 4.5 | - | -6.8 | - | 11.2 | 1.60 |
| PEF1 | -4.0 | 0.00 | 6.7 | - | 11.4 | 1.60 |
| MYO6 | -2.6 | 0.00 | -0.6 | - | 10.9 | 1.56 |

Figure 5.17. Proteome-wide screen of ML324 binding partners using lysed-cell MS-CETSA. Lysed-cell CETSA was performed by lysing FPW1 cells and incubating cell lysates with 20 μ M ML324 or DMSO (Vehicle). Incubated lysates were heated from 40 - 60°C and unmelted protein abundance was quantified using mass spectrometry. Significantly stabilised proteins in at least one of three experiments were identified by comparing changes in melting point (ΔT_m) between ML324 and Vehicle using the TPP-TR package in R. All p-values were calculated using the robust Z-score method and adjusted for the false discovery rate (FDR) using the Benjamini-Hochberg method. Bolded proteins were identified in all treatment groups for all three experiments.

Overall, 62 proteins were identified as significantly stabilised in samples treated with QC6352, ML324, or MK2206 compared to the vehicle. However, only 15 of these proteins had detectable melting points in all treatment groups for all 3 experiments. The protein abundance was averaged at each temperature to assess the changes in melt curves more robustly (**Figure 5.19**). Only Phospholipase D3 (PLD3) showed stabilisation by QC6352. The function of PLD3 is currently unclear with some researchers showing activity cleaving phosphatidylcholine phosphatidic acid and choline to regulate PI4P5K and mTOR pathways³⁴⁸. However, others argue that PLD3 is not a phospholipase but instead a 5' exonuclease which digests ssDNA³⁴⁹. Further research could unveil a novel function of PLD3 in glioblastoma proliferation by validating PLD3 as a potential target for QC6352 action. However, the lack of Akt stabilisation by MK2206 in MS-CETSA experiments, despite stabilisation in Western blotting CETSA (**Figure 5.12**), raises questions on the robustness of the MS-CETSA results. Given that the stabilisation of Akt by MK2206 was not detected, it is plausible that the proteins stabilised by QC6352 may also have been missed.

Significantly MK2206-stabilised proteins

| Protein name | Experiment 1 ΔT_m (°C) | $-\log_{10}$ FDR | Experiment 2 ΔT_m (°C) | $-\log_{10}$ FDR | Experiment 3 ΔT_m (°C) | $-\log_{10}$ FDR |
|--------------|-----------------------------------|---------------------|-----------------------------------|---------------------|-----------------------------------|---------------------|
| ARHGAP35 | 11.0 | 1.70 | - | - | 2.0 | 0 |
| GOPC | 10.8 | 1.66 | - | - | -5.9 | - |
| KLHDC4 | 10.0 | 1.36 | - | - | - | - |
| SH2D4A | 9.7 | 1.36 | - | - | - | - |
| TSNAX_DISC1 | - | - | 15.1 | 4.60 | - | - |
| GAA | - | - | 14.5 | 4.37 | 4.2 | - |
| RNH1 | -2.1 | 0.01 | 12.0 | 2.82 | -1.9 | 0 |
| ARL8A/B | -2.7 | - | 10.3 | - | 14.9 | 3.57 |
| SRR | 0.3 | 0.01 | -0.0 | 0.00 | 10.9 | 3.05 |
| MAP1LC3A | - | - | -5.0 | - | 13.6 | 3.05 |
| ERO1L | 2.4 | - | 0.6 | 0.00 | 10.5 | 2.92 |
| VRK1 | -3.2 | - | - | - | 13.0 | 2.82 |
| PRPSAP2 | -2.0 | - | -0.5 | - | 10.1 | 2.75 |
| TUBB8 | - | - | -3.1 | 0.14 | 12.6 | 2.71 |
| EPN1 | - | - | - | - | 10.0 | 2.71 |
| RIC8A | 3.8 | 0.03 | - | - | 10.9 | 1.88 |
| PLOD2 | -11.9 | - | 0.8 | - | 10.7 | 1.86 |
| NEU1 | 2.8 | - | - | - | 8.5 | 1.86 |
| CNOT1 | 1.6 | 0.01 | - | - | 10.4 | 1.73 |
| DDX39A | -6.1 | - | 7.9 | - | 8.0 | 1.66 |
| PDE6D | -4.2 | - | - | - | 9.9 | 1.51 |
| EEF1A2 | - | - | -4.6 | - | 9.7 | 1.43 |

Figure 5.18. Proteome-wide screen of MK2206 binding partners using lysed-cell MS-CETSA. Lysed-cell CETSA was performed by lysing FPW1 cells and incubating cell lysates with 20 μ M MK2206 or DMSO (Vehicle). Incubated lysates were heated from 40 - 60°C and unmelted protein abundance was quantified using mass spectrometry. Significantly stabilised proteins in at least one of three experiments were identified by comparing changes in melting point (ΔT_m) between MK2206 and Vehicle using the TPP-TR package in R. All p-values were calculated using the robust Z-score method and adjusted for the false discovery rate (FDR) using the Benjamini-Hochberg method. Bolded proteins were identified in all treatment groups for all three experiments.

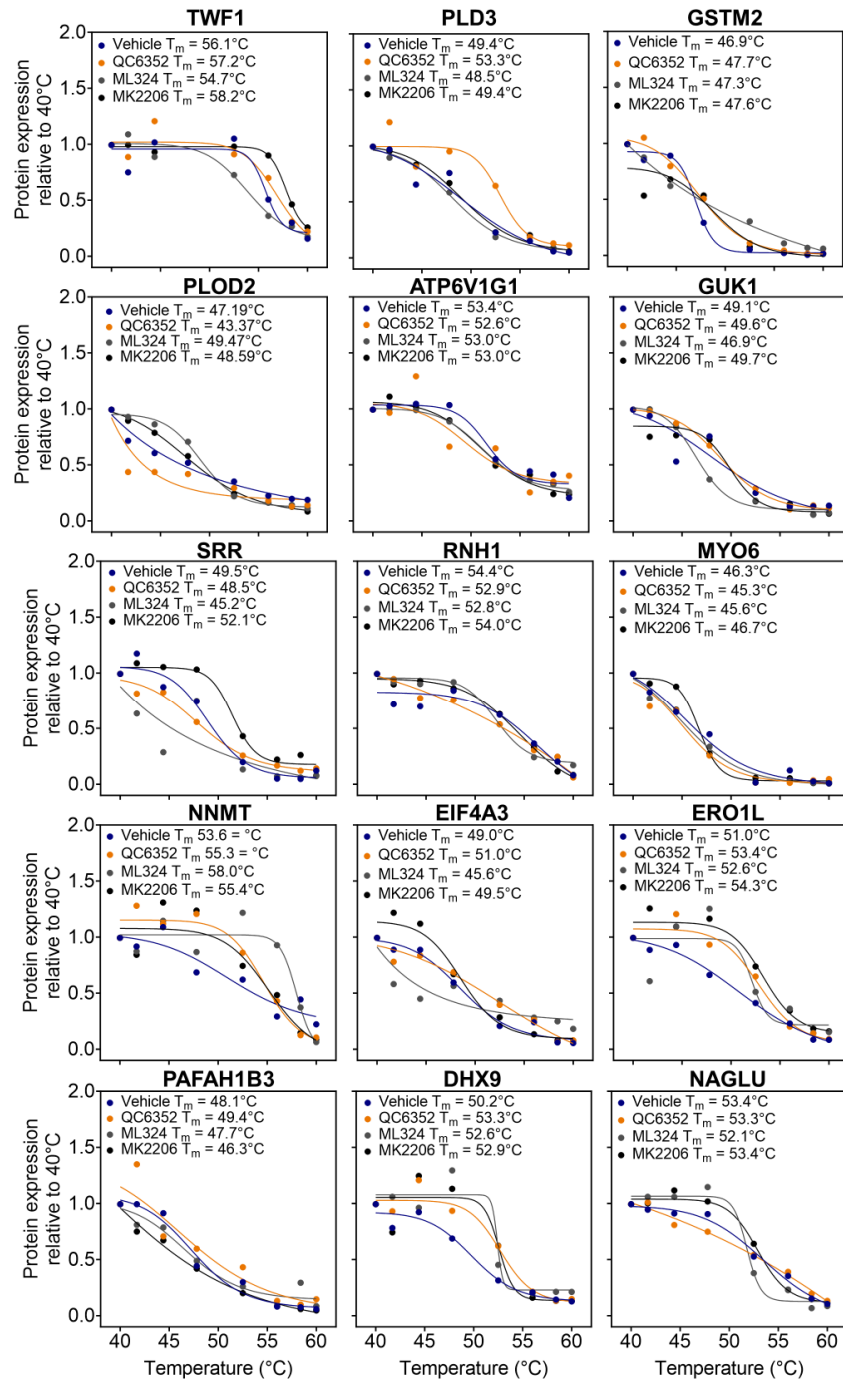


Figure 5.19. Melt curves of significant binding partners identified with lysed-cell MS-CETSA. Lysed-cell CETSA was performed by lysing FPW1 cells and incubating cell lysates with 20 μM QC6352, ML324, MK2206 or DMSO (Vehicle). Incubated lysates were heated from 40 - 60°C and unmelted protein abundance was quantified using mass spectrometry. Protein abundance was averaged for all proteins identified as significant in at least one treatment condition and detected in all treatment conditions for both experiments and were fitted with a four-parameter nonlinear regression melt curve. The data represents mean protein abundance relative to the lowest temperature (40°C).

5.2.7. Validation of the MS-CETSA results

To evaluate the performance and limitations of the MS-CETSA results, a frequency distribution analysis was conducted. Data from both the intact-cell (**Figure 5.20a**) and lysed-cell (**Figure 5.20b**) MS-CETSA experiments were compared with an intact-cell MS-CETSA study by Franken et al.³⁰⁹ (**Figure 5.20c**). This study was used to benchmark the expected variance and sensitivity of the MS-CETSA methodology. The analysis revealed a 3-fold higher standard deviation in our intact-cell MS-CETSA, with almost 3000 fewer proteins identified in both experiments compared to the study by Franken et al.³⁰⁹. The lysed-cell MS-CETSA data was slightly less variable and slightly more sensitive in comparison to the intact-cell MS-CETSA, showing a 2-fold higher standard deviation, with approximately 2600 fewer proteins detected in total compared to the study by Franken et al.³⁰⁹. Overall, the results show that considerably less proteins were detected in our analyses, and with much higher variability compared to the Franken et al. study³⁰⁹, which likely contributed to the lack of significant changes in protein stabilisation and lack of reproducibility between experiments.

The source of this variation could potentially originate from differences in the cell lines and compounds used in comparison to the Franken et al. study³⁰⁹. However, this seems unlikely since the cells were lysed prior to heating, and the vehicle controls yielded results similar to the treated lysates. A more plausible explanation for the variability lies in the methodological differences. In our study, lysates were analysed individually using mass spectrometry without TMT-labels, whereas Franken et al. utilised TMT-labelling for simultaneous analysis of all samples, a technique aimed at minimising batch effect variations. To conclusively determine the precise cause of the observed discrepancies in findings compared to the Franken et al. study³⁰⁹, further troubleshooting experiments are required.

In summary, the CETSA protocol was validated in FPW1 cells by confirming Akt stabilisation using MK2206. However, QC6352 and ML324 failed to significantly stabilise KDM4A in A172 cells overexpressing KDM4A. Intact-cell MS-CETSA identified DCK as potentially destabilised by QC6352 while lysed-cell MS-CETSA identified PLD3 as a potential binding partner of QC6352. However, both results were lacking the sensitivity and accuracy to effectively identify changes in thermal stability. Specifically, both methods were found to detect substantially less proteins and with greater variation between experiments compared to publicly available MS-CETSA data³⁰⁹. Nevertheless, validation of the involvement of DCK and PLD3 in QC6352's mechanism of action could be beneficial.

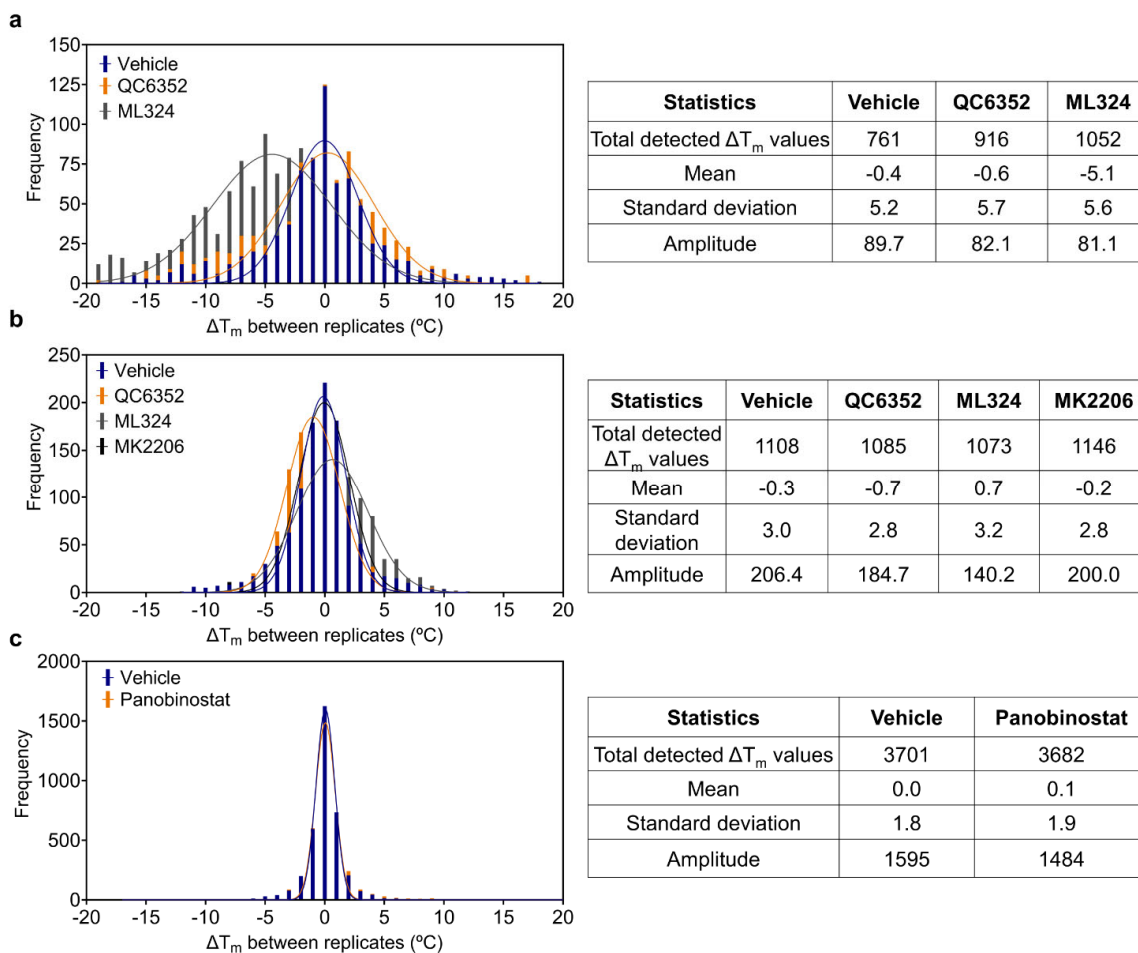


Figure 5.20. Variability and sensitivity comparison between MS-CETSA data. Frequency distribution comparing the change in melting points (ΔT_m) between replicates in **a**) intact-cell MS-CETSA **b**) lysed-cell MS-CETSA and **c**) published MS-CETSA data from Franken et al. 2015, Nature Protocols³⁰⁹. Melting point temperatures were rounded to the nearest integer and non-linear regression analysis was performed to generate gaussian curves and descriptive statistics for each treatment condition.

5.2.8. RNA sequencing of QC6352-treated glioblastoma cells

To further understand the mechanisms of action of QC6352, a transcriptomics analysis was conducted in FPW1 cells treated with QC6352 for 1, 3, and 5 days and compared against untreated cells. Significant differentially expressed genes (DEGs) were identified by taking genes with an adjusted p-value smaller than 0.05 and \log_2 fold change greater than 0.5 or less than -0.5. After 1 day of treatment with QC6352, 106 DEGs were found, with 60% of genes being downregulated (**Figure 5.21a**). Among the most significantly affected genes, many are uncharacterised or classified as pseudogenes. Notably, the gene encoding a phosphatase regulatory subunit, *PPP1R10*, known for modulating protein phosphatase 1 (PP1) activity in the nucleus³⁵⁰, was the most significantly downregulated gene. After 3 days of treatment, the number of DEGs increased to 1553, with 52% downregulated (**Figure 5.21b**). The most significantly downregulated gene was *COLEC12*, which is implicated in inflammatory processes but its exact function remains under investigation³⁵¹. Moreover, the most significantly upregulated gene was *CD68*, primarily expressed in the brain by activated phagocytic microglia, suggesting an immune response by the cells when treated with QC6352.

After 5 days of QC6352 treatment, there were 1705 DEGs, with 46% downregulated (**Figure 5.21c**). *FOS* was the most significantly downregulated gene which assists in cell proliferation, differentiation and survival³⁵², while *MFAP4* was the most significantly upregulated gene and is involved in cell adhesion and proliferation by integrin signalling³⁵³. These changes in gene expression in QC6352-treated FPW1 cells highlight a shift in cellular transcriptional activity over time, indicating that QC6352 induces a complex dysregulation of the transcriptome involving genes with diverse functions.

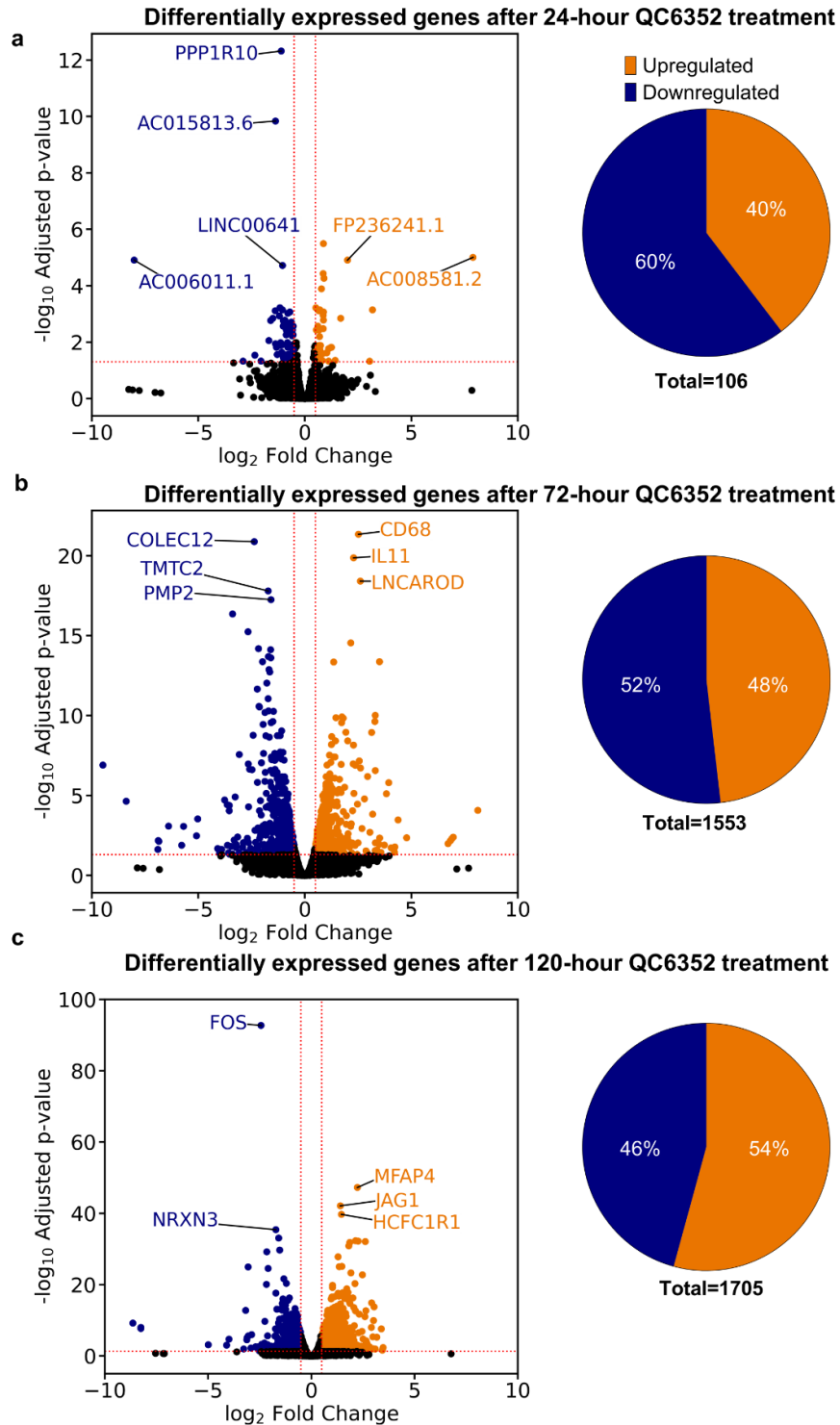


Figure 5.21. Differential gene expression in QC6352-treated FPW1 cells. FPW1 cells were treated with QC6352 (100 nM) for **a**) 1 (n = 3), **b**) 3 (n = 2), or **c**) 5 days (n = 3) and gene expression was compared against untreated cells using RNA-sequencing. Genes with a $-\log_{10}$ adjusted p-value >1.3 and a \log_2 fold change greater than 0.5 (orange) or less than -0.5 (blue) were taken as differentially expressed genes. Statistical significance was calculated using the Wald test and adjusted using the Benjamini-Hochberg method.

5.2.9. Pathway analysis of QC6352-treated glioblastoma cells

To understand the overall changes in signalling pathways induced by QC6352, Ingenuity Pathway Analysis was performed on differentially expressed genes at each timepoint. An adjusted p-value of 0.05 and a Z-score greater than 2 or less than -2 was taken as a threshold for significant pathway involvement and significant pathway activity modulation, respectively. Surprisingly, after 1 day of QC6352 treatment, there were no pathways identified with significantly altered activity after adjusting the p-value for multiple comparisons using the Benjamini Hochberg method. After 3 days of QC6352 treatment (**Figure 5.22a**), the DEGs mapped to processes such as mitotic metaphase and anaphase, cell cycle checkpoints, mitotic prometaphase, and rRNA processing, sharing similarity to the pathways found in the CRISPR compound sensitivity screen and related to cell cycle regulation and RNA processing (**Figure 5.9**). The most significant pathways changing after 5 days of QC6352 treatment (**Figure 5.22b**) were the pulmonary fibrosis idiopathic signalling pathway which encompasses TGF β ³⁵⁴, Wnt³⁵⁵, PI3K/Ras³⁵⁶, and NOTCH³⁵⁷ signalling pathways. Interestingly, 55 of the 60 pathways significantly altered by QC6352 showed increased activity despite QC6352's antiproliferative effects on cancer cells. This corroborates with the previous qPCR analysis which showed an upregulation in cell cycle genes (**Figure 4.8**).

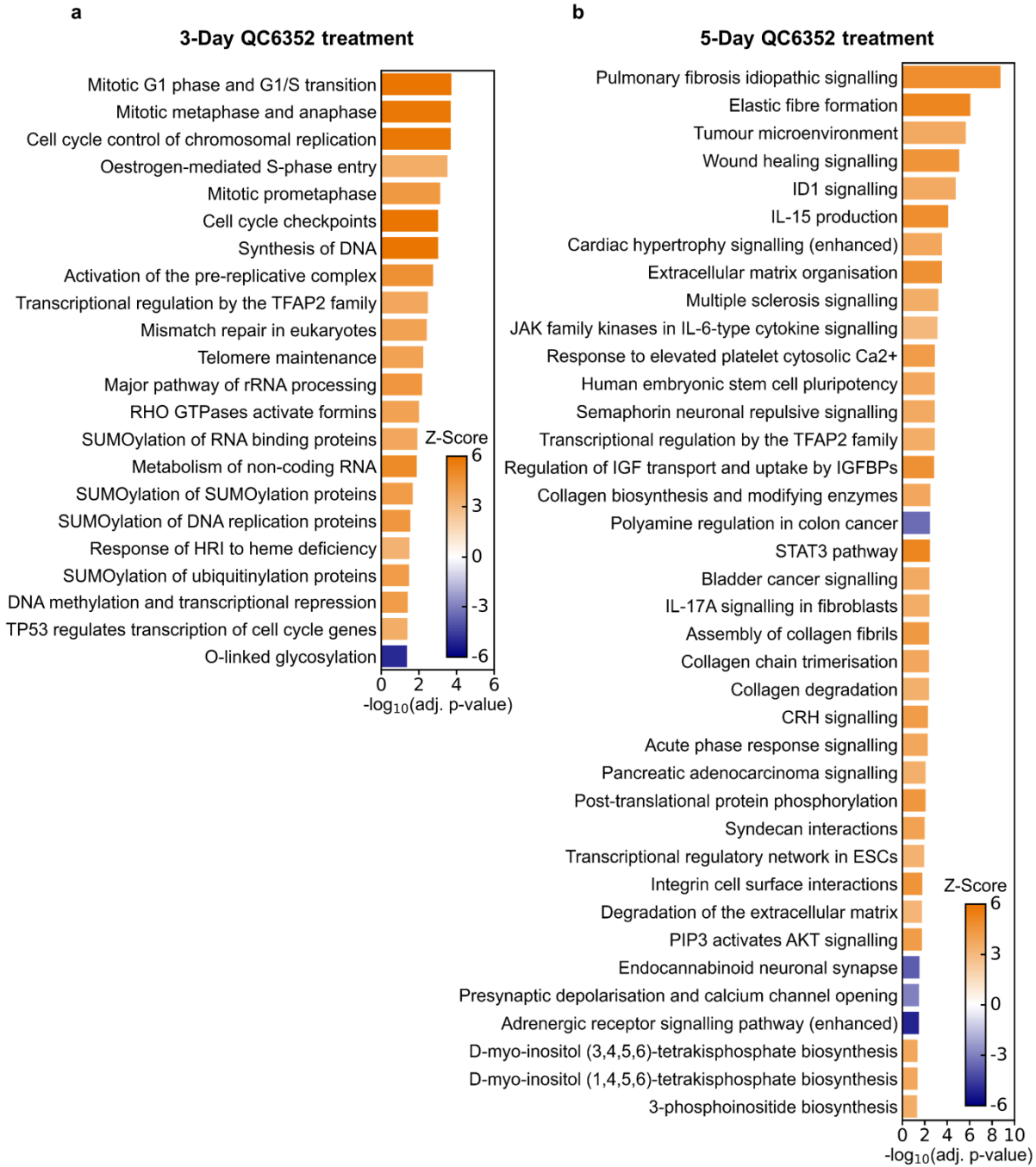


Figure 5.22. Ingenuity Pathway Analysis of DGEs in QC6352-treated FPW1 cells. FPW1 cells were treated with QC6352 (100 nM) for **a**) 3 or **b**) 5 days and Ingenuity Pathway Analysis was conducted on differentially expressed genes. Statistical significance for relevant pathways was determined using a Fisher’s exact test adjusted for multiple testing using the Benjamini-Hochberg method. A Z-score greater than 2 denotes increased pathway activity while a Z-score less than -2 represented decreased pathway activity.

5.2.10. Analysis of QC6352 gene signature with the Connectivity Map L1000 Query analysis

To further understand potential targets and a mechanism of action for QC6352, the RNA-sequencing data was compared against the RNA-sequencing DEGs from approximately 5,000 small-molecule compounds, and 3,000 genetic reagents that induce unique gene expression profiles known as “gene signatures”. This comparison was facilitated by listing and contrasting the top 150 upregulated and 150 downregulated genes from each QC6352 treatment time point with the Connectivity Map (CMap; Build 2) database using the ‘L1000 Query’ tool³¹⁵. This comparison aimed to identify substances, termed perturbagens, that exhibit gene expression signatures positively or negatively correlating with those induced by QC6352. Perturbagens with highly similar expression signatures to QC6352 potentially share similar targets and mechanisms of action³⁵⁸. For each treatment timepoint, a significance threshold for the false discovery rate (FDR) greater than 0.05 was used. Additionally, a Transcriptional Activity Score (TAS) of 0.2 or higher was taken to identify perturbagens representing reliable and robust gene expression profiles within the CMap database³⁵⁹.

The top 5 gene expression profiles most similar to QC6352-treated FPW1 cells were tabulated after 1, 3, and 5 days of treatment. As a positive control of our approach, the top 5 gene expression profiles positively correlating with a PI3K-mTOR inhibitor BEZ235 were also investigated (**Figure 5.23a**)³⁶⁰. The top 5 compounds with gene expression profiles most similar to BEZ235 were all PI3K-mTOR inhibitors. In contrast, compounds with the most similar gene expression profiles to QC6352 were not uniform and targeted different proteins for each time point (**Figure 5.23b-d**), with the exception of brequinar. Brequinar, targeting dihydroorotate dehydrogenase (DHODH)³⁶¹, was identified as having a similar gene expression profile in two different cell lines compared to 1-day QC6352-treated FPW1 cells. DHODH is essential for the *de novo* pyrimidine synthesis pathway³⁶², which is essential for rapidly proliferative cells due to the increased demand for fundamental components for DNA and RNA synthesis^{362,363}. However, it seems unlikely that DHODH is a target of QC6352 since the CRISPR fitness screen did not identify DHODH as a dependency gene. Furthermore, knockout of DHODH did not significantly modulate QC6352 efficacy in the compound sensitivity screen. Additionally, the IPA of QC6352-treated cells determined increased activity in DNA synthesis which contradicts if QC6352 were to inhibit DHODH.

a

Top 5 positively correlating gene expression profiles compared to 1-day BEZ235-treated cells

| Compound | Treatment duration (hours) | Treatment concentration (μM) | Target(s) | Transcriptional activation score (TAS) | $-\log_{10}\text{FDR}$ | Normalised connectivity score |
|-------------|----------------------------|---|---------------|--|------------------------|-------------------------------|
| PF-05212384 | 24 | 2.5 | MTOR and PI3K | 0.62 | 4.99 | 2.44 |
| GDC-0980 | 24 | 2.22 | MTOR and PI3K | 0.57 | 4.02 | 2.35 |
| OSI-027 | 24 | 10 | MTOR | 0.54 | 3.88 | 2.31 |
| Voxtalisib | 24 | 10 | MTOR and PI3K | 0.49 | 3.85 | 2.30 |
| NVP-BEZ235 | 24 | 10 | MTOR and PI3K | 0.60 | 3.83 | 2.29 |

b

Top 5 positively correlating gene expression profiles compared to 1-day QC6352-treated cells

| Compound | Treatment duration (hours) | Treatment concentration (μM) | Target(s) | Transcriptional activation score (TAS) | $-\log_{10}\text{FDR}$ | Normalised connectivity score |
|----------------|----------------------------|---|----------------|--|------------------------|-------------------------------|
| Brivanib | 24 | 10 | VEGFR and FGFR | 0.23 | 2.11 | 1.95 |
| BRD-K63750851 | 24 | 10 | IMPDH1/2 | 0.4 | 1.88 | 1.89 |
| Brequinar | 24 | 3.33 | DHODH | 0.4 | 1.75 | 1.83 |
| Brequinar | 24 | 4 | DHODH | 0.53 | 1.74 | 1.82 |
| Periplocymarin | 6 | 10 | Na/K-ATPase | 0.49 | 1.72 | 1.81 |

c

Top 5 positively correlating gene expression profiles compared to 3-day QC6352-treated cells

| Compound | Treatment duration (hours) | Treatment concentration (μM) | Target(s) | Transcriptional activation score (TAS) | $-\log_{10}\text{FDR}$ | Normalised connectivity score |
|----------------------|----------------------------|---|-----------|--|------------------------|-------------------------------|
| CYT-997 | 24 | 0.74 | Tubulin | 0.72 | 3.28 | 2.19 |
| Fdcyd | 24 | 0.08 | DNMT | 0.55 | 2.85 | 2.07 |
| Olmesartan-medoxomil | 24 | 0.04 | AGTR1 | 0.65 | 2.79 | 2.04 |
| KF-38789 | 6 | 10 | SELP | 0.36 | 2.69 | 1.98 |
| VU-0365114-2 | 6 | 10 | CHRM5 | 0.41 | 2.67 | 1.97 |

d

Top 5 positively correlating gene expression profiles compared to 5-day QC6352-treated cells

| Compound | Treatment duration (hours) | Treatment concentration (μM) | Target(s) | Transcriptional activation score (TAS) | $-\log_{10}\text{FDR}$ | Normalised connectivity score |
|---------------|----------------------------|---|---------------|--|------------------------|-------------------------------|
| Rigosertib | 24 | 10 | PLK1 and MCL1 | 0.54 | 3.22 | 1.94 |
| LY-2090314 | 24 | 10 | GSK3B | 0.70 | 2.89 | 1.85 |
| BRD-K43796186 | 24 | 10 | EGFR | 0.23 | 2.86 | 1.85 |
| KF-38789 | 6 | 10 | SELP | 0.36 | 2.84 | 1.83 |
| Vincristine | 6 | 10 | Tubulin | 0.29 | 2.80 | 1.82 |

Figure 5.23. Compounds with gene signatures positively correlating with QC6352-treated cells. **a)** An L1000 Query search using DEGs from A2058 cells treated with BEZ235 for 1 day showing compounds with the top 5 most similar gene signatures, sourced from the CMap database. **b - d)** Top 5 compounds with the most similar gene signatures compared to the gene signatures of FPW1 cells treated with QC6352 (100 nM) for 1, 3, and 5 days. Only compounds with a Transcriptional Activity Score (TAS) of 0.2 or higher are listed.

The IPA analysis of QC6352 gene signatures identified a noticeable increase in the activity of many pathways (**Figure 5.22**). It was therefore postulated that QC6352 may be activating a certain pathway and hence that the DEGs induced by QC6352 treatment may more closely resemble an activating compound instead of an inhibitor. The top 5 gene expression profiles negatively correlating to QC6352-treated FPW1 cells was tabulated for each treatment timepoint as well as a reference example dataset of the top 5 gene signatures expression profiles negatively correlating to the BEZ235 inhibitor targeting PI3K and MTOR (**Figure 5.24**). The Raf/Mek/Erk signalling pathway was identified as negatively correlating with the gene expression profile of QC6352-treated FPW1 cells in 1 - 4 of the top 5 compounds for the 3 timepoints. The results indicate that the list of genes upregulated by QC6352 treatment matches the list of genes downregulated by several Raf/Mek inhibitors and the list of genes downregulated by QC6352 matched the list of genes upregulated by the same MEK inhibitors. QC6352 activity therefore appears to be activating the Raf/Mek/Erk signalling pathway, although this pathway is essential for survival, prolonged activation is known to cause G0/G1 cell cycle arrest (**Figure 4.9**)^{364,365}.

In summary, the gene expression profile of QC6352 was compared against other compounds using the CMap database and L1000 query tool. The PI3K/MTOR inhibitor BEZ235 example dataset was included as an internal control which revealed that the BEZ235 gene signature closely matches five other PI3K/MTOR inhibitors. In contrast, the gene expression profile of QC6352 matched inhibitors with a variety of targets and mechanisms of action, making it challenging to pinpoint a clear mechanism of action for QC6352. Notably, the DHODH inhibitor brequinar's gene signature closely matched that of QC6352 in two separate cell lines. However, brequinar appears unlikely to contribute to QC6352's antiproliferative effect as DHODH was not identified as a fitness gene and did not modulate QC6352 efficacy when knocked out. Furthermore, when identifying compounds that produced gene signatures opposite to those of QC6352, targets frequently identified were from the Raf/Mek/Erk pathway. Additionally, members of this pathway including *RASGRP1*, *RAF1*, and *MAPKAPK2*, were found in the CRISPR compound sensitivity screen to decrease the efficacy of QC6352 when knocked out. This suggests that these genes are crucial for the mechanism of action of QC6352.

a

Top 5 negatively correlating gene expression profiles compared to 1-day BEZ235-treated cells

| Compound | Treatment duration (hours) | Treatment concentration (μM) | Target(s) | Transcriptional activation score (TAS) | $-\log_{10}\text{FDR}$ | Normalised connectivity score |
|----------------------|----------------------------|---|-----------|--|------------------------|-------------------------------|
| Dolastatin-10 | 24 | 10 | Tubulin | 0.73 | 15.65 | -2.22 |
| CC-401 | 24 | 10 | JNK | 0.5 | 15.65 | -2.11 |
| MLN-4924 | 24 | 0.37 | NAE1 | 0.53 | 15.65 | -2.06 |
| CYT-997 | 24 | 0.74 | Tubulin | 0.72 | 15.65 | -2.05 |
| Olmesartan-medoxomil | 24 | 0.04 | AGTR1 | 0.59 | 15.65 | -2.05 |

b

Top 5 negatively correlating gene expression profiles compared to 1-day QC6352-treated cells

| Compound | Treatment duration (hours) | Treatment concentration (μM) | Target(s) | Transcriptional activation score (TAS) | $-\log_{10}\text{FDR}$ | Normalised connectivity score |
|-------------|----------------------------|---|-------------------------|--|------------------------|-------------------------------|
| RAF-265 | 24 | 10 | RAF and VEGFR | 0.2 | 15.65 | -1.84 |
| AT-9283 | 24 | 0.04 | AUKA/B, JAK2/3, and ABL | 0.25 | 15.65 | -1.76 |
| ABT-737 | 6 | 10 | BCL2 | 0.34 | 15.65 | -1.72 |
| Azacitidine | 24 | 3.33 | DNMT1/3A | 0.21 | 15.65 | -1.72 |
| Ledipasvir | 24 | 10 | NS5A | 0.33 | 15.65 | -1.71 |

c

Top 5 negatively correlating gene expression profiles compared to 3-day QC6352-treated cells

| Compound | Treatment duration (hours) | Treatment concentration (μM) | Target(s) | Transcriptional activation score (TAS) | $-\log_{10}\text{FDR}$ | Normalised connectivity score |
|------------|----------------------------|---|-----------|--|------------------------|-------------------------------|
| PD-0325901 | 6 | 10 | MEK/ERK | 0.25 | 15.65 | -2.06 |
| MEK-162 | 24 | 2.22 | MEK | 0.73 | 15.65 | -2.02 |
| Trametinib | 24 | 3.33 | MEK | 0.74 | 15.65 | -2.00 |
| UNC-0321 | 24 | 10 | KMT1C | 0.61 | 15.65 | -2.00 |
| Ro-4987655 | 24 | 0.25 | MEK | 0.77 | 15.65 | -1.98 |

d

Top 5 negatively correlating gene expression profiles compared to 5-day QC6352-treated cells

| Compound | Treatment duration (hours) | Treatment concentration (μM) | Target(s) | Transcriptional activation score (TAS) | $-\log_{10}\text{FDR}$ | Normalised connectivity score |
|--------------|----------------------------|---|-----------|--|------------------------|-------------------------------|
| H-89 | 24 | 10 | PKA | 0.48 | 15.65 | -1.80 |
| D-4476 | 24 | 10 | TGFB1 | 0.31 | 15.65 | -1.76 |
| Fostamatinib | 24 | 1.11 | SYK | 0.25 | 15.65 | -1.74 |
| SGI-1776 | 24 | 10 | PIM | 0.27 | 15.65 | -1.73 |
| GW-5074 | 24 | 10 | RAF | 0.22 | 15.65 | -1.71 |

Figure 5.24. Compounds with gene signatures negatively correlating with QC6352-treated cells.

a) An L1000 Query search using DEGs from A2058 cells treated with BEZ235 for 1 day showing compounds with the top 5 negatively correlating DEGs, sourced from the CMap database. **b - d)** Top 5 compounds with gene signatures negatively correlating with QC6352 gene signature (100 nM) for 1, 3, and 5 days. Only compounds with a Transcriptional Activity Score (TAS) of 0.2 or higher are listed.

5.3. Discussion

Phenotypic screens are useful for identifying new drugs by testing a library of compounds and detecting which of those compounds have a desired phenotypic effect¹⁸³. A key step in phenotypic drug discovery is the deconvolution of a compound's mechanism of action, which includes identifying the target(s) impacted to induce the phenotypic effect¹⁸³. The overall aim of this chapter was to determine the target(s) of QC6352 that contribute to its antiproliferative efficacy. Target deconvolution often requires orthogonal mechanistic investigations to fully understand the mechanism of action of the compound and so in this study CRISPR-Cas9, MS-CETSA, RNA-sequencing, and L1000 Query analysis were performed and compared to understand QC6352's antiproliferative effect.

5.3.1. Novel fitness genes affecting glioblastoma cell viability

QC6352 was developed as a KDM4 inhibitor²⁰⁹ but the importance of KDM4 in glioblastoma proliferation was questioned after siRNA knockdown and KDM4A overexpression showed no changes to cell growth or histone methylation status. Furthermore, the CRISPR-Cas9 fitness screen revealed that KDM4 isoforms are not essential for the viability of the RKI1 glioblastoma stem cell line, confirming results discussed in Chapter 4. Instead, the fitness screen identified new potential drug targets for glioblastoma with *SOX2*, *DRD5*, *METTL2A*, *SOX9*, and *CENPO* knockouts causing the largest decrease in cell fitness.

Our analysis is corroborated by previous research, wherein the well-known SOX transcription factor family of stemness regulators was identified as essential genes in a loss-of-function CRISPR-Cas9 fitness screen using glioblastoma stem cells³⁶⁶. In contrast, our identification of *DRD5* as a selective dependency gene is a particularly interesting finding, since it has not been identified in any other cancer cell line within the DepMap portal²⁹⁷. However, the dopamine receptor family has been implicated in the cell viability of numerous cancer types, with DRD1-5 inhibition by antagonists causing increased cell viability in colorectal cancers and decreased cell viability in glioblastoma³⁶⁷. Post-transcriptional m3C RNA methylation, a function of m3C methyltransferase proteins such as *METTL2A/B*, *METTL6*, *METTL8*, has received considerable interest in recent years as an important epitranscriptomic mark for cancer proliferation and survival³⁶⁸. The identification of *METTL2A* as a top selective dependency gene in our CRISPR-Cas9 fitness screen agrees with the current findings in the literature³⁶⁹. Furthermore, our findings also identified *METTL2B* as a selective dependency gene, suggesting that both *METTL2A/B* but not *METTL6* or *METTL8* are crucial

for glioblastoma stem cells. Finally, *CENPO* has been identified as an important gene for gastric and lung cancer cells, where knockdown of *CENPO* caused cell cycle arrest and apoptosis and this study agrees with the importance of *CENPO* in the arrest of glioblastoma cells^{370,371}. Currently, there are no pharmacological inhibitors targeting *CENPO*³⁷², however, future research using a target-based screen could uncover a novel compound with therapeutic potential, since many studies have shown *CENPO* to be a target for cancer cells.

Interestingly, the DRD2 antagonist, *ONC201*, shares a history that seems to parallel the findings presented here for *QC6352*. *ONC201* was originally identified through phenotypic screening as an activator of TNF-Related Apoptosis Inducing Ligand (TRAIL), demonstrating efficacy in inducing apoptosis and halting the cell cycle in colorectal cancer cells³⁷³. Subsequent observations, however, revealed TRAIL-independent mechanisms of apoptosis and cell cycle arrest, raising questions about the involvement of an off-target protein in the observed phenotypic effects³⁷⁴. Further research unveiled that *ONC201* functions as a selective antagonist of the dopamine receptor D2 (DRD2), a discovery that significantly reshaped the understanding of its antiproliferative effects and established DRD2 as a novel target for glioblastoma cells³⁷⁵. In a similar vein, *QC6352* was initially conceptualised and developed as a KDM4 inhibitor. Yet, our emerging evidence suggests that its mechanism of action might be influenced by additional off-target proteins.

Moreover, the CRISPR-Cas9 fitness screen also identified *CDKN2A*, *CARD8*, *OR7C2*, *NPM1*, and *PRPSAP1* as proliferation-suppressor genes, increasing RK11 viability when knocked down. These results are similar to another CRISPR-Cas9 loss-of-function fitness screen which identified known tumour suppressors such as *TP53* and *CDKN1A*²⁹⁸. Moreover, in our findings, *CDKN2A* and *NPM1* are known to regulate cell proliferation while *CARD8*, *OR7C2*, and *PRPSAP1* have lesser-known roles in regulating cancer cell fitness. It is known that the mechanism of action for some chemotherapies is an increase in the gene expression of tumour suppressors which consequently arrests the cells and initiates apoptosis. For instance, Wang et al., 2006, performed a target-based screen involving 2,000 small molecule compounds to identify activators of p53 transcription³⁷⁶. Several molecules were discovered from the screen which induced p53 gene expression, cell cycle arrest, and apoptosis in HCT116 colonic cancer cell line³⁷⁶. Therefore, future novel compounds could upregulate the potential tumour suppressors *CARD8*, *OR7C2*, or *PRPSAP1* and act as a novel mechanism of action, thereby providing a therapeutic target in cancer cells.

5.3.2. QC6352 target identification

RNA-sequencing was conducted to look at the change in transcriptomics in cells treated with QC6352 and identified a substantial activation of pathways involved in proliferation and survival. The RNA-sequencing data was analysed using the L1000 Query tool to identify compounds and/or targets with gene signatures similar to the one obtained with QC6352. The L1000 Query analysis revealed that QC6352 activates the MAPK pathway after 3 days of treatment. Although activation of MAPK signalling is essential for cell survival and cell cycle progression³⁷⁷, it has also been shown that sustained activation of MAPK signalling causes G0/G1 cell cycle arrest and apoptosis³⁷⁸.

Using the information from the L1000 Query analysis, we re-analysed the CRISPR-Cas9 screens to see if MAPK signalling genes were identified. When comparing over 3000 genes identified as important for RKI1 viability against over 500 genes identified as important for QC6352 efficacy, only 194 overlapping genes identified in both screens were considered. We found that genes both important for cell fitness and QC6352 efficacy included many MAPK signalling genes as well as pathways which are known to modulate MAPK activity such as Integrin, WNT, and G-protein coupled receptor signalling. Thus, the CRISPR-Cas9 screen results support the notion that MAPK signalling is an important part of QC6352's mechanism of action, since any inhibition of MAPK signalling either directly or indirectly reduced the efficacy of QC6352.

Kinases and phosphatases are the most prominent regulators of the MAPK signalling pathway. Therefore, QC6352 could either activate kinase(s) or inhibit phosphatase(s) in order to sustain activation of MAPK signalling. However, activation of proteins often requires specific and precise modifications, such as phosphorylation, conformational changes, or allosteric modulation³⁷⁹. For example, UCL-TRO-1938 is the first small molecule PI3K α activator. It acts in part by allosterically repositioning the activation loop of PI3K α to facilitate PI3K signalling in cells³⁸⁰. However, given that QC6352 was designed as a KDM4 inhibitor it is more plausible (although not certain) for QC6352 to inhibit, rather than activate a targeted protein. Hence, it is hypothesised that QC6352 could inhibit a phosphatase. When we narrow our search to phosphatases, PP5 was the only phosphatase that was found to be both essential for RKI1 fitness and QC6352 efficacy. Additionally, PP5 directly (via dephosphorylation) inhibits Raf activity which is necessary to activate MEK and Erk to regulate cell cycle progression³⁸¹. Intriguingly, the gene *RAF1* was identified in the CRISPR-Cas9 screen as essential for RKI1 fitness and QC6352 efficacy (**Figure 5.25a**).

5.3.3. Protein phosphatase 5 as a potential target of QC6352

PP5 is a member of the serine/threonine family of phosphoprotein phosphatase (PPP). While ubiquitously expressed in all mammalian tissue, PP5 has relatively high expression particularly in brain³⁸². PP5 contains a catalytic domain at its C-terminus and a regulatory tetratricopeptide repeat (TPR) domain at the N-terminus³⁸³. PP5 is unique among the PPP family due to its low basal activity which is regulated by the TPR domain³⁸⁴. When in an inactive state, the TPR domain covers the catalytic domain. Binding to HSP90 or polyunsaturated fatty acids triggers a conformational change which uncovers the catalytic domain thereby activating the phosphatase activity³⁸³. As well as regulating Raf, PP5 also dephosphorylates (*i.e.*, deactivates) several other kinases, most notably the proapoptotic Apoptosis Signal-Regulating kinase 1 (ASK1), the Ataxia Telangiectasia Mutated (ATM) kinase, the Ataxia Telangiectasia and Rad3-Related (ATR) kinase, as well as the prominent tumour suppressor p53⁸².

The activation of these PP5 substrates closely resembles the phenotypic responses observed upon QC6352 treatment and supports the hypothesis that QC6352 inhibits PP5 activity. Specifically, the PP5 substrates induce G0/G1 cell cycle arrest and apoptosis when activated, particularly Raf and ASK1 which contribute to the sustained activation of MAPK signalling identified in the L1000 Query analysis³⁸¹. In further support of this hypothesis, PP5 was found essential for glioblastoma proliferation, with siRNA knockdown of PP5 inhibiting proliferation and colony formation, via sustained MAPK activation causing G0/G1 cell cycle arrest³⁸⁵. Similar phenotypes were found when inhibiting PP5 in a variety of other cancer models^{383,386}. Furthermore, high expression of PP5 in patients with low-grade and high-grade gliomas correlated with lower survival rates (**Figure 5.25b**). Inhibitors targeting PP5 include Ro 90-7501³⁸⁷, which binds to a variety of receptors as well as the catalytic domain of PP5, and LB-100, a PP2A/PP5 inhibitor currently in phase II clinical trials for glioblastoma³⁸⁸. Recently, a novel selective PP5 inhibitor named Compound P053 was tested in renal cancer cells and significantly reduced cell viability³⁸⁹.

In summary, by integrating the findings from four orthogonal target identification methodologies, MAPK signalling was found to be activated and PP5 identified as a potential target of QC6352. Future experiments warrant validation of these findings and validation of PP5 as a target of QC6352. If QC6352 is confirmed to target PP5 at similar concentrations to the KDM4 family, this could become a confounding factor for future KDM4-focused investigations using QC6352. In this case, QC6352 could only be used in model systems where

PP5 has no importance such as in cell types where PP5 is not expressed or not activated. At the time of writing, QC6352 is the only chemical probes targeting the KDM4 family and as such there is a need for novel potent and selective KDM4 inhibitors.

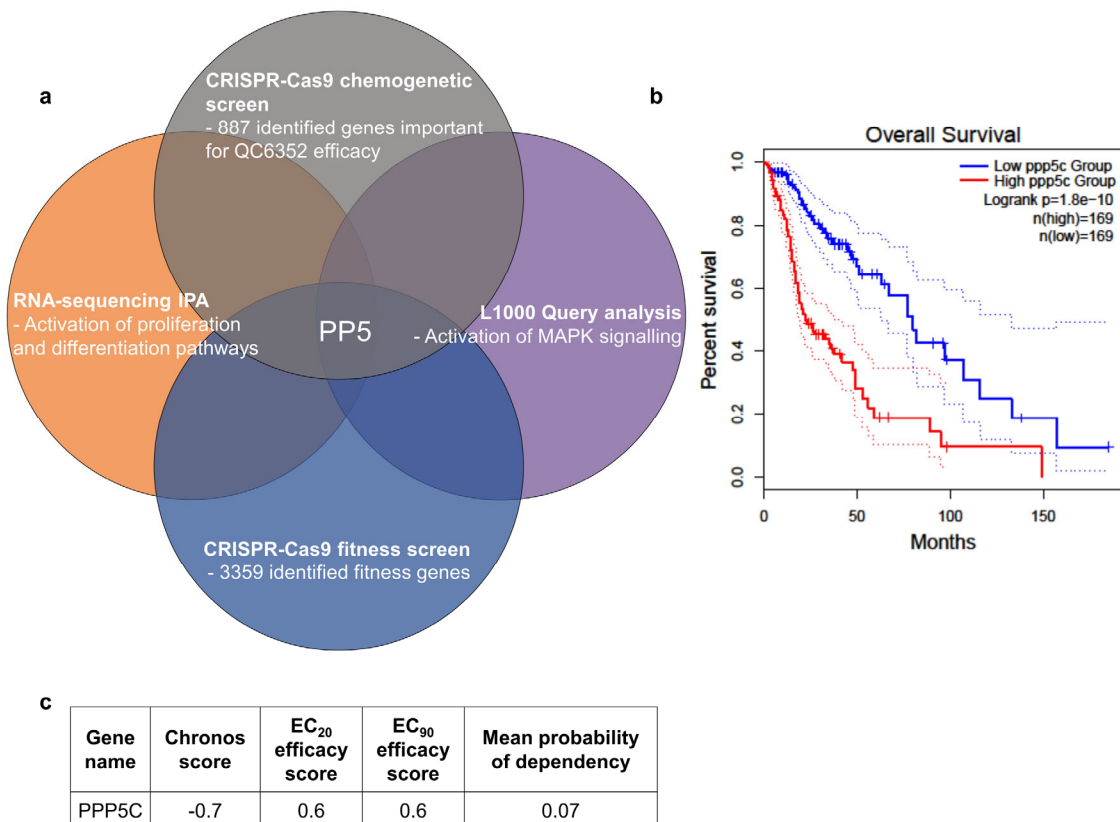


Figure 5.25. Identification of protein phosphatase 5 (PP5) as a potential target of QC6352. a) Venn diagram schematic illustrating the combination of orthogonal findings which suggest PP5 as a target of QC6352. **b)** Survival plot of patients diagnosed with glioblastoma with low or high expression levels of PP5 (sourced from GEPIA). **c)** Chronos analysis of PPP5C from the CRISPR-Cas9 fitness screen (Chronos score) and chemogenetic screens (EC₂₀ and EC₉₀ efficacy score).

Exploration of hydrazine-based small molecules as metal chelators for KDM4 inhibition

Received 00th February 202x,
Accepted 00th February 202x

Angus J. Saxton,^a Jayden Sterling,^b Michael P. Hamilton,^a Ramzi H. Abbassi,^b Lenka Munoz,^{b*} and Jennifer R. Baker^{a*}

DOI: 10.1039/x0xx00000x

KDM4 has promising potential in targeted cancer therapies, due to decreased cellular proliferation in cancer cells observed with knockdown of individual KDM genes. Given this potential, there is a significant demand for novel KDM4 inhibitors. Several effectively potent inhibitors have been reported, however issues with poor solubility, membrane permeability and toxicity profiles, as well as limited selectivity towards individual KDM4 isoforms, has limited their effect. The hydrazine moiety has been demonstrated as an effective metal chelator, and some initial research suggests that incorporating this functionality into small molecule inhibitors may improve their affinity. Here we report an investigation into their continued potential as KDM4A inhibitors. A total of 81 hydrazine-containing compounds were prepared via a condensation between either formyl benzoic acid or methyl formylbenzoate, and a range of hydrazine or benzoylhydrazono reagents. Molecular modelling studies were conducted, with the hydrazine group chelating the catalytic metal ion effectively in the most active compound in this work, the *p*-isopropyl hydrazine **72**.

Introduction

Post-translational modifications to histones such as acetylation, methylation, and phosphorylation contribute to chromatin formation and stabilisation, gene transcription, and DNA repair by facilitating the recruitment of transcription factors and repair proteins to DNA.^{1,2} As a result, histone modifications exhibit diverse influences on gene expression and genomic differentiation. The installation and removal of histone modifications are mediated by a variety of enzymatic families, dysregulation of which have been increasingly associated with aberrant transcriptional activity and genomic instability.³ Accordingly, significant interest has been generated regarding such enzymes as contributing factors to the development and progression of inherited and acquired autoimmune,^{4,5} neurodegenerative,^{6,7} and metabolic⁸ disorders. Furthermore, anomalous expression of histone-modifying enzymes is also regularly observed in cancers^{9,10} and speculated to contribute to oncogenesis via chromatin disruption and proto-oncogene overexpression, making these enzymes clinically relevant cancer biomarkers and potential targets for therapeutic intervention.

The methylation of different histone lysine substrates has been associated with both transcriptional activation and

repression.^{3,11} Histone lysine methylation is regulated in part by the histone lysine demethylase (KDM) family of proteins. Depletion of chromatin methylation as a result of KDM overexpression is frequently observed in a broad variety of cancers, most prominently, but not limited to, haematopoietic and solid breast, lung, colorectal, and glial cancers.^{10,12} Eight KDM subfamilies (KDM1-8) have been categorised on the basis of their conserved catalytic and noncatalytic domains and their histone lysine substrate specificities. KDM1 contains a flavin adenine dinucleotide-dependent amine oxidase domain that catalyses the removal of mono-methyl (me1) and di-methyl (me2) post-translational modifications (PTMs) at the histone H3 lysine 4 (H3K4) and histone H3 lysine 9 (H3K9) residues.³ KDM2-8 contain 2-oxoglutarate-dependent Jumonji C domains that catalyse the removal of di-methyl (me2) and tri-methyl (me3) PTMs from certain histone H3 and H4 lysine residues. Each subfamily exhibits distinct substrate specificities and selectivities due to the presence of additional noncatalytic domains responsible for chromatin binding and lysine methylation recognition. For instance, Jumonji N domains are responsible for KDM dimerisation,¹³ while Tudor and PHD zinc-finger domains are responsible for the methylation state recognition of bound histone lysine residues.^{14,15} CXXC and C5HC2 zinc-finger domains are responsible for chromatin and DNA binding,¹⁶ while F-box domains are responsible for interacting with polycomb repressive complexes resulting in altered chromatin conformation.¹⁷ Finally, ARID, leucine-rich repeat, and tetratricopeptide repeat domains are collectively responsible for non-specific protein and DNA binding.¹⁸ Within the Jumonji C domain, catalytic activity is initiated by the generation of an iron(III) superoxide complex from the iron(II) centre and molecular oxygen, followed by intramolecular

^a Chemistry, School of Environmental and Life Sciences, The University of Newcastle, Callaghan, New South Wales 2308, Australia.

^b Charles Perkins Centre and School of Medical Sciences, Faculty of Medicine and Health, The University of Sydney, Sydney, New South Wales 2006, Australia.

* L.M.: lenka.munoz@sydney.edu.au

* J.R.B.: jennifer.r.baker@newcastle.edu.au

Electronic Supplementary Information (ESI) available: [details of any supplementary information available should be included here]. See DOI: 10.1039/x0xx00000x

oxidative decarboxylation of the 2-oxoglutarate cofactor. Homolytic cleavage of the resulting succinyl peroxide ligand generates a highly reactive iron(IV) oxo species which then hydroxylates an ϵ -*N*-methylated lysine to produce a hemiaminal via oxygen rebound. Elimination of this hemiaminal intermediate produces a mono-demethylated lysine and formaldehyde as a byproduct.¹⁹ Hydroxylation through this mechanism proceeds via radical proton abstraction which allows for the demethylation of ϵ -*N*-trimethylated lysines.²⁰

The KDM4 subfamily consists of four proteins KDM4A-D and two pseudogenes KDM4E/F. KDM4A-C demethylate the histone substrates H3K9me2/me3 and H3K36me2/me3, whereas KDM4D, and KDM4E/F when ectopically expressed, preferentially demethylate H3K9me2/me3. Knockdown of individual KDM4 genes is generally well tolerated in mice studies and embryonic stem cell lethality is only observed in at least a double knockout between KDM4A-C.²¹ These factors, combined with the overlap in their histone substrates, suggest that KDM4A-D demonstrate redundant demethylation functionality in healthy cells. In contrast, knockdown of individual KDM4 genes in cancer cells is associated with decreased cellular proliferation, and numerous studies have identified abnormal KDM4 levels in human tumour specimens and immortalised cancer cell lines. Recent literature has focused on elucidating specific mechanisms through which KDM4 overexpression may contribute to cancer progression. For example, KDM4 isoforms bind to androgen receptors and regulate H3K9 methylation in prostate-specific antigen promoter regions. Depletion of H3K9me2/me3 stimulates the transcription of prostate-specific antigen, resulting in increased proteolysis in the extracellular fluid of prostate epithelial cells, which is speculated to disrupt cellular adhesion leading to prostate cancer tumourigenesis and metastasis.^{22,23} KDM4 overexpression has also been observed in endometrial cancer due to the downregulated transcription of other androgen receptor target genes such as *CDKN1B* and *c-Myc*.^{24,25} Depletion of H3K9me3 in the MCL-1 promoter region by KDM4 is associated with chemoresistance,²⁶ and activation of ATR and ATM kinases as a result of KDM4-mediated chromatin remodelling is associated with acquired resistance to platin-based chemotherapeutics in non-small cell lung cancers.²⁷ KDM4C/D overexpression activates PI3K/AKT and HIF/VEGF signalling by upregulating AKT/*c-Myc* and HIF-1 expression respectively leading to inhibited apoptosis and stimulated angiogenesis in lung and breast cancers by promoting the differentiation of cancer stem-like cells to endothelial cells.²⁸⁻³⁰ Altered Wnt and Notch signalling as a result of H3K9 demethylation in multiple Wnt and Notch target promoter regions by KDM4 has been observed to promote angiogenesis and self-renewal in cancer stem-like cells.^{31,32}

Given the promising potential of KDM4 targeting in cancer therapy, there is a significant demand for KDM4 inhibitors. Several KDM inhibitor scaffolds have been reported, however, many contain problematic moieties leading to poor solubility, membrane permeability, and toxicity profiles which limit their usage in *in vivo* and clinical studies.³³ Representative compounds frequently employed in KDM4 inhibitory assays

(**Figure 1**) include *N*-oxalylglycine (**1**), lutidinic acid (**2**), QC6352 (**3**),³⁴ and ML324 (**4**).³⁵ Hydroxamic acids such as vorinostat (**5**) developed as histone deacetylase inhibitors also frequently exhibit moderate KDM inhibitory activity through bidentate chelation of the iron(II) centre in the active site.^{36,37} Daminozide (**6**) and related compounds containing 1,1-dimethylhydrazine functional groups demonstrate similar chelating behaviour and selectivity towards KDM2/7, however, they are also significantly genotoxic.³⁷ Compounds containing unsubstituted hydrazides such as 2-(1*H*-tetrazol-5-yl)acetohydrazide (**7**) possess improved physicochemical properties compared to carboxylic acid-based inhibitors and moderate inhibitory activity.³⁸ Substituted hydrazide JIB-04 (**8**) has also been shown to exhibit KDM4/5 inhibitory activity.³⁹

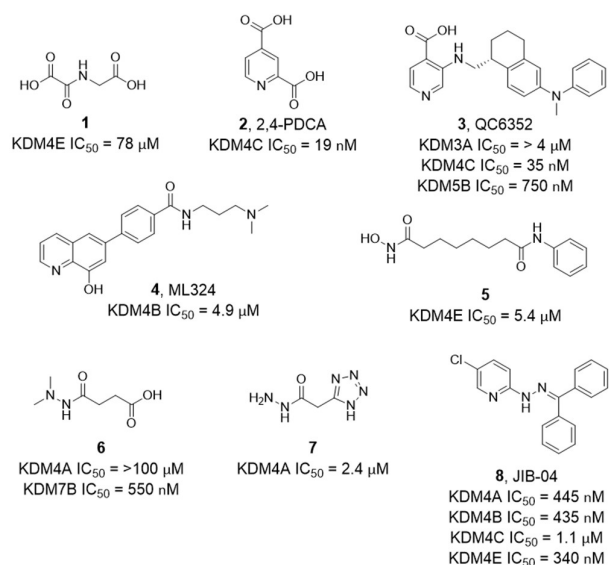


Figure 1. Select KDM4 inhibitors *N*-oxalylglycine (**1**), lutidinic acid (**2**), QC6352 (**3**), ML324 (**4**), and example hydroxamic acid or hydrazine-based KDM4 ligands (**5-7**) including JIB-04 (**8**), and some reported IC₅₀ values.

The KDM catalytic site is hydrophilic and highly conserved between subfamilies and isoforms, both of which are significant challenges for small-molecule drug discovery.⁴⁰ Competitive KDM inhibitors typically mimic the interactions of **1**, a catalytically inert analogue of the native 2-oxoglutarate cofactor, or **2** with the iron(II) centre and key residues in the binding pocket. Several lead compounds based on fragments **1** and **2** fail to demonstrate cellular efficacy despite exhibiting *in vitro* potency, however, **3** is cell-permeable and 7 to 40 times more selective for KDM4 and its isoforms over the other KDM subfamilies.³⁴ Co-crystal structures of **3** reveal pyridine nitrogen coordination to the iron(II) centre and carboxylate H-bond interactions with neighbouring tyrosine and lysine residues, emulating the binding mode of **2**. 8-Hydroxyquinoline derivatives form bidentate coordinate interactions with the iron(II) centre similarly to **2**, and **4** exhibits moderate cell permeability but poor selectivity.³⁵ Hydrazine-containing functional groups are regularly employed in metal chelators and demonstrate inhibitory activity against

KDMs;^{39,41} however, exploration of these scaffolds as KDM4 inhibitors has primarily been restricted to terminal unsubstituted hydrazines and hydrazides.^{37,38} Some compounds containing related functional groups such as hydrazones have been identified as hits as part of larger quantitative high throughput screening screens, although structural elaboration and structure-activity relationship analysis was not performed in favour of other scaffolds.³⁵ Herein, we report a protocol for the facile synthesis and purification of hydrazones and *N*-acylhydrazones, the screening of an exploratory library of compounds, and a preliminary evaluation of these moieties as alternative iron-chelating scaffolds to **1** and **2** for future KDM4 ligand development.

Results and discussion

KDM4A Inhibition Assay

As AlphaScreen beads, biotinylated peptides, and IgG antibodies differ between batches, individual assay components were validated under conditions adapted from a previously published study.⁴² LC-MS analysis of biotinylated H3K9me3 peptide confirmed the expected molecular mass (2764.2 g/mol). Dot blot analysis of biotinylated H3K9me3 peptide revealed that the H3K9me1 antibody failed to generate any signal, whereas the H3K9me2 antibody showed concentration-dependent cross-reactivity against the H3K9me3 peptide. However, the reactivity of the H3K9me3 antibody to the H3K9me3 peptide was superior at every concentration

(Figure 2a). To demonstrate the specificity of the H3K9me2 antibody used in the assay, biotinylated H3K9me2 and H3K9me3 peptides were titrated with AlphaScreen beads and H3K9me2 antibody. At concentrations up to 1 μ M, the H3K9me2 peptide consistently generated a stronger signal than the H3K9me3 peptide (Figure 2b).

RapidFire mass spectrometry confirmed the expected molecular mass of the recombinant KDM4A enzyme (44 kDa) and the time-dependent demethylation of the H3K9me3 peptide (Figure 2c). Having verified the structural and functional integrities of the recombinant KDM4A, the biotinylated H3K9me2 and H3K9me3 peptides, and the H3K9me2 antibody, the KDM4A inhibition assay was performed using 3 nM KDM4A and 30 nM H3K9me3 to determine IC₅₀ values for established pan-KDM inhibitors **2** and IOX1 and KDM4-selective inhibitor **3**. Our IC₅₀ values for **2** and IOX1 were comparable to previously published data, however, **3** exhibited a nearly tenfold loss of inhibitory potency compared to previously determined values (Figure 2d). Given that the published values were obtained in a KDM4 inhibitory assay using 0.02% w/v BSA as a blocking agent whereas we used 0.1% w/v BSA, the BSA concentration was adjusted, and the inhibitors were re-tested. Reducing the BSA concentration to 0.02% w/v decreased the observed IC₅₀ values of all three inhibitors (Figure 2e). Given the impact of BSA on the potency of KDM4 inhibitors in this assay, subsequent assays were carried out at 1:10 KDM4a/H3K9me3 ratio using 0.2% BSA in the buffer.

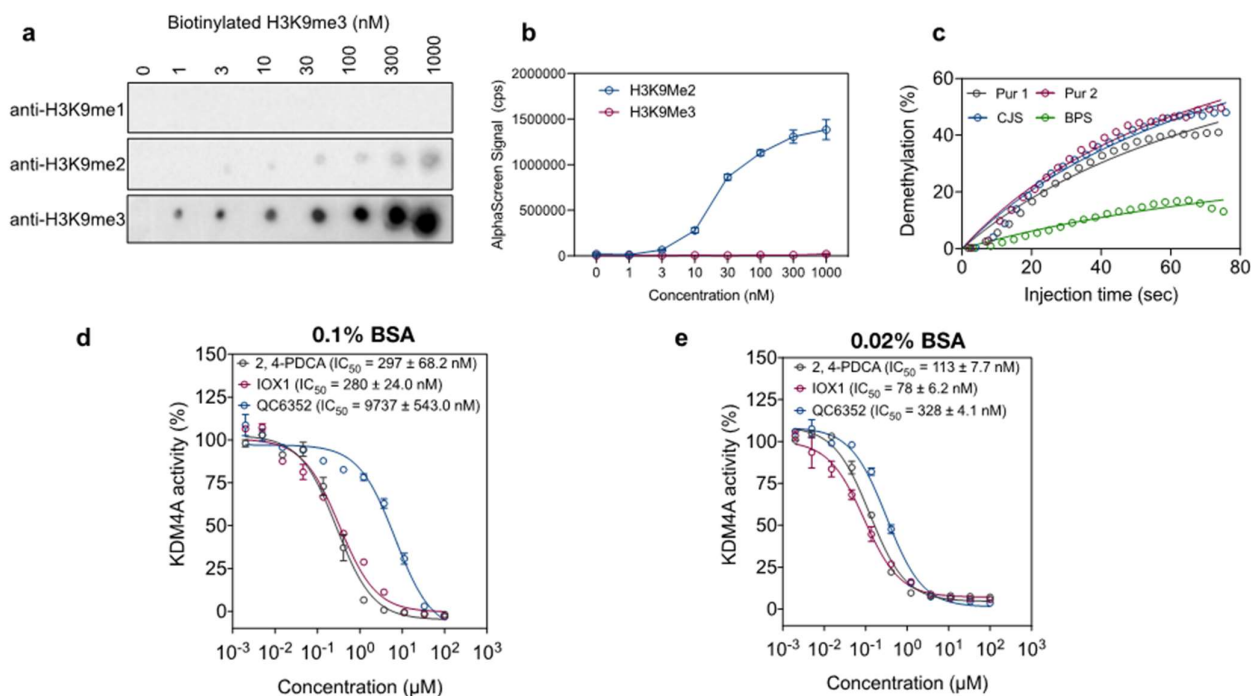


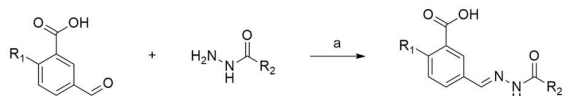
Figure 2. (a) Dot blots of biotinylated H3K9me3 droplets using antibodies against mono-, di- and tri-methylated H3K9. (b) AlphaScreen beads were incubated with H3K9me2 antibody and increasing concentration of biotinylated H3K9me2 and H3K9me3 peptides. Data are mean \pm SEM of two independent experiments. (c) Recombinant KDM4A was incubated with biotinylated H3K9me3 in the presence of cofactors Fe²⁺, L-ascorbic acid and 2-oxoglutarate. Extracted ion chromatograms for the trimethylated substrate and dimethylated product were integrated using the RapidFire Integrator software (Agilent). (d-e) Dose-response curves and IC₅₀ values for KDM4 inhibitors determined in the in-house KDM4A Inhibition assays using AlphaScreen platform. Data are mean \pm SEM (n = 3-6).

Synthesis and testing of novel analogues

An initial library (Library 1) of *N*-acylated 3-(benzoylhydrazono)benzoic acids **9-41** was generated from the condensation of 3-formylbenzoic acid with a series of arylhydrazides (**Scheme 1**). Several analogues bearing additional substituents on the 6-position were also prepared (**17, 18, 26, 27, 28, 29**). The availability of starting reagents, as well as simple isolation and purification, led to a large library of initial analogues. The inhibitory activity of all analogues was determined using the KDM4A AphaScreen assay (**Table 1**), with QC6352 and ML324 used as positive controls in each experiment.

The halogenated arylhydrazide analogues **13-20** demonstrated the most significant inhibition of KDM4A activity, and **14** (*m*-chlorophenyl, 63% residual KDM4 activity @ 20 μ M) and **16** (*p*-bromophenyl, 57% residual KDM4 activity @ 20 μ M) analogues were particularly favoured over other halogenated derivatives in different positions. The (*m*-pyridyl)-analogue **28** (57% residual KDM4 activity @ 20 μ M) also exhibited notable inhibition compared to the rest of **Table 1** and was favoured over the corresponding (*o*-pyridyl) **31** and (*p*-pyridyl) **25** isomers (74% and 106% residual KDM4 activity @ 20 μ M, respectively). Para-substituted lipophilic groups such as **35** (*p*-dimethylamino)phenyl], **37** (*p*-*tert*-butyl)phenyl] and **38** (*p*-trifluoromethyl)phenyl]) exhibited moderate KDM4A inhibition at 20 μ M (75%, 72%, 61% respectively), however, the closely related [*p*-(isopropyl)phenyl] **34** and [*p*-(trifluoromethoxy)phenyl] **41** groups were inactive (~100% residual activity @ 20 μ M). The effect of the 6-fluoro and 6-hydroxy substituents on inhibitory activity varied; both **29** and **30** were less active than the unmodified **28** (*m*-pyridyl, 59% > 83% (fluoro), 70% (hydroxy) whereas **17** (*p*-bromo, 6-hydroxy, 37% residual KDM4 activity @ 20 μ M) was significantly more active than **16** (unmodified, 57%) and **18** (6-fluoro, 78%) was significantly less so.

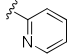
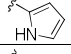
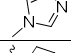

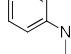
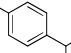
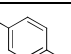
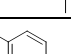
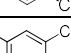
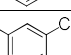
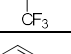
The remaining heterocyclic analogues demonstrated varied effects, from inactive (**21, 22, 25, 33**, >99% residual KDM4 activity @ 20 μ M) to moderately poor inhibition (**10-12, 23, 24, 31, 32, 35**, 60-89% residual KDM4 activity @ 20 μ M). The addition of lipophilic moieties also gave little results of note, with the *p*-*tert*-butyl **37** demonstrating moderate inhibitory activity, while the adamantane **34** and *p*-isopropyl **36** offered little to no KDM4A inhibition (**37**, 72%; **34**, 92%; **36**, 101% residual KDM4 activity @ 20 μ M). A further 5 heterocyclic-containing analogues demonstrated no inhibitory activity (**S1-S5**, supplementary data).



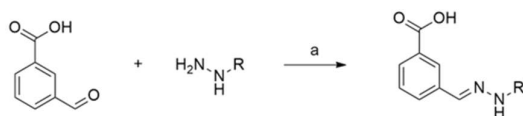
Scheme 1. Synthesis of analogues **9-41**. Reagents and conditions: (a) Ethanol, μ wave 200 W, 120 $^{\circ}$ C, 20 min or ethanol, 50-100 $^{\circ}$ C, 19 h.

Table 1. KDM4A activity in the presence of Library 1 analogues **9-41**. Results are mean for two independent KDM4A AlphaScreen assays. QC6352 (**3**) and ML342 (**4**) data are shown for comparison.

| Analogue | R ₁ | R ₂ | KDM4A activity at 20 μ M | KDM4A activity at 1 μ M |
|---------------|----------------|---------------------------|------------------------------|-----------------------------|
| QC6352 | | | 0.2% | 34% |
| ML342 | | | 5% | 21% |
| 9 | H | NH ₂ | 84% | 66% |
| 10 | H | <i>p</i> -OMe | 89% | 106% |
| 11 | H | <i>m</i> -OMe | 73% | 99% |
| 12 | H | <i>o</i> -OMe | 72% | 84% |
| 13 | H | <i>p</i> -Cl | 103% | 102% |
| 14 | H | <i>m</i> -Cl | 63% | 81% |
| 15 | H | <i>o</i> -Cl | 90% | 102% |
| 16 | H | <i>p</i> -Br | 57% | 67% |
| 17 | HO | <i>p</i> -Br | 37% | 72% |
| 18 | F | <i>p</i> -Br | 78% | 96% |
| 19 | H | <i>m</i> -Br | 87% | 104% |
| 20 | H | <i>o</i> -Br | 77% | 78% |
| 21 | H | <i>p</i> -NO ₂ | 99% | 100% |
| 22 | H | <i>p</i> -OH | 126% | 127% |
| 23 | H | <i>m</i> -OH | 88% | 91% |
| 24 | H | <i>o</i> -OH | 60% | 94% |
| 25 | H | <i>p</i> -pyridyl | 106% | 114% |
| 26 | HO | <i>m</i> -pyridyl | 79% | 93% |
| 27 | F | <i>o</i> -pyridyl | 82% | 78% |
| 28 | H | <i>m</i> -pyridyl | 59% | 70% |
| 29 | HO | <i>p</i> -pyridyl | 70% | 81% |
| 30 | F | <i>o</i> -pyridyl | 83% | 85% |

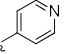
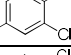
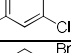
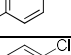
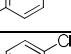
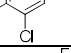
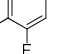
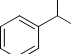
| Analogue | R ₁ | R ₂ | KDM4A activity at 20 μM | KDM4A activity at 1 μM |
|----------|----------------|---|-------------------------|------------------------|
| 31 | H |  | 74% | 82% |
| 32 | H |  | 71% | 85% |
| 33 | H |  | 103% | 112% |
| 34 | H |  | 92% | 84% |
| 35 | H |  | 75% | 82% |
| 36 | H |  | 101% | 125% |
| 37 | H |  | 72% | 89% |
| 38 | H |  | 61% | 85% |
| 39 | H |  | 105% | 68% |
| 40 | H |  | 66% | 80% |
| 41 | H |  | 125% | 128% |

To explore the importance of the benzoylhydrazono carbonyl oxygen, a series of *N*-aryl 3-(hydrazonomethyl)benzoic acids **42-49** (Library 2) was generated from the condensation of 3-formylbenzoic acid with a more focused series of arylhydrazines (Scheme 2). While the (*p*-bromophenyl) arylhydrazine analogue **45** demonstrated essentially no KDM4A inhibition (Table 2, 93% residual KDM4 activity @ 20 μM), replacement of the bromine with a chlorine in **46** resulted in the greatest decrease in KDM4 activity in this library (56% residual KDM4 activity @ 20 μM). Additional substituents in the other chlorinated compounds **43** (*m*-chloro-*p*-methylphenyl), **44** (*m,p*-dichlorophenyl) and **47** (*o,p*-dichlorophenyl) proved slightly detrimental to KDM4A inhibitory activity (65%, 75%, 56% residual KDM4 activity @ 20 μM respectively), while replacement of the chlorines with fluorine in **48** resulted in slightly poorer inhibitory effect (66% residual KDM4 activity @ 20 μM). Addition of a lipophilic functionality, such as the *p*-isopropyl **49**, gave poorer inhibition than much of Table 2 at 85% residual KDM4A activity (@ 20 μM): this was, however, improved over its Table 1 counterpart (**36**, inactive).



Scheme 2. Synthesis of analogues **47-53**. Reagent and conditions: (a) Ethanol, 50-100 °C, 19 h, 0-1.0 eq. sodium hydroxide.

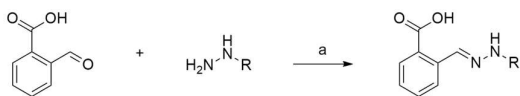
Table 2. KDM4A activity in the presence of Library 2 analogues **42-49**. Results are mean for two independent KDM4A AlphaScreen assays.

| Analogue | R | KDM4A activity at 20 μM | KDM4A activity at 1 μM |
|----------|---|-------------------------|------------------------|
| 42 |  | 119% | 118% |
| 43 |  | 65% | 85% |
| 44 |  | 75% | 84% |
| 45 |  | 93% | 82% |
| 46 |  | 56% | 82% |
| 47 |  | 71% | 77% |
| 48 |  | 66% | 78% |
| 49 |  | 85% | 105% |

To further explore this scaffold and determine the effect of the 2-substituted hydrazine position, a library (Library 3) of *N*-substituted 2-(hydrazonomethyl)benzoic acids **50-69** was generated from condensation of 2-formylbenzoic acid with a series of some matched arylhydrazines and arylbenzohydrazides (Scheme 3). Analysis of the compounds in Table 3 indicated almost overall negligible inhibitory activity, as well as poorer inhibitory activity than the matched 3-(hydrazonomethyl)benzoic acids. Some differing trends as with Table 1 were observed: the *m*-bromo analogue **51** exhibited improved inhibitory activity over the *p*-bromo variant **50** (88% > 114% residual KDM4 activity @ 20 μM), and the *p*-pyridyl **52** proved marginally more effective than the *m*-pyridyl **53** (84% > 99% residual KDM4 activity @ 20 μM). Of the remaining nitrogen-containing groups, the pyrrole **58** and methyl-1*H*-imidazole **59** exhibited no inhibitory activity. One noted exception amongst the arylhydrazines was the *p*-isopropyl analogue **55**: comparison with its 3-substituted partner **49** uncovered improved activity with the 2-substituted analogue **55** (69% > 85% residual KDM4 activity @ 20 μM). Adding additional lipophilic bulk in the form of the *p*-*tert*-butyl **57**, meanwhile, gave poorer inhibitory effect (85% residual KDM4 activity @ 20 μM).

Varied results were observed with the benzoylhydrazono analogues **62-69**: when compared to the respective 3-(hydrazonomethyl)benzoic acids (Table 1), both the *m*-bromo **64** and *p*-bromo **65** analogues exhibited poorer inhibitory activity than their matched partners **19** and **16** from Table 1 (**64**, 89% residual KDM4 activity @ 20 μM, **19**, 87%; **65**, 100%; **16**, 57%). Conversely, both the *p*-chloro **66** and the *p*-isopropyl **69** exhibited slightly improved inhibitory activity over their respective Table 1 entries **13** and **36** (**66**, 90% residual KDM4 activity @ 20 μM, **13**, 103%; **69**, 79%; **36**, 101%). With the

exception of the 4-hydroxyphenylpropanoyl **60** (80% residual KDM4 activity @ 20 μ M), the remaining Library 3 entries exhibited poor to no KDM4A inhibition.



Scheme 3. Synthesis of analogues **50-69**. Reagents and conditions: (a) Ethanol, 50-100 $^{\circ}$ C, 19 h, 0-1.0 eq. sodium hydroxide.

Table 3. KDM4A activity in the presence of Library 3 analogues **50-69**. Results are mean for two independent KDM4A AlphaScreen assays.

| Analogue | R | KDM4A activity at 20 μ M | KDM4A activity at 1 μ M |
|-----------|---|------------------------------|-----------------------------|
| 50 | | 114% | 94% |
| 51 | | 88% | 93% |
| 52 | | 84% | 80% |
| 53 | | 99% | 95% |
| 54 | | 104% | 99% |
| 55 | | 69% | 92% |
| 56 | | 98% | 101% |
| 57 | | 85% | 78% |
| 58 | | 93% | 100% |
| 59 | | 113% | 104% |
| 60 | | 80% | 89% |
| 61 | | 94% | 90% |
| 62 | | 98% | 95% |
| 63 | | 92% | 93% |
| 64 | | 89% | 94% |
| 65 | | 100% | 94% |
| 67 | | 82% | 88% |

| Analogue | R | KDM4A activity at 20 μ M | KDM4A activity at 1 μ M |
|-----------|---|------------------------------|-----------------------------|
| 68 | | 91% | 84% |
| 69 | | 79% | 107% |

With varied results observed for **Tables 1-3**, a general trend began to be observed: the addition of an electron-withdrawing moiety in the para-position led to improved inhibitor activity, in the 3-substituted (hydrazonomethyl)benzoic acids, for both the benzohydrazides and the hydrazine analogues over the 2-substituted examples (p-bromo, **16** > **65**; **45** > **50**). With electron-donating groups in the para-position, however, the 3-substituted (hydrazonomethyl)benzoic acids were favoured, in both the benzohydrazides and the hydrazine analogues, over the 3-substituted examples (p-isopropyl, **69** > **36**; **55** > **49**) (**Figure 3**).

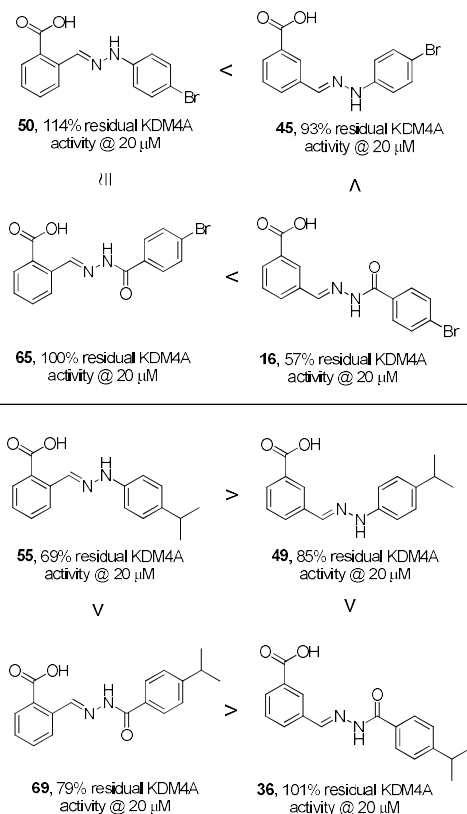


Figure 3. Varied effects were observed with the Library 1-3 analogues, dependent on the electron donating-or-withdrawing nature of the substituents. The 3-substituted position was preferred for the electron-withdrawing p-bromine analogues, while the 2-position was preferred for the electron-donating p-isopropyl analogues.

Further analysis of a selection of these analogues was conducted via molecular modelling (Molecular Operating Environment, (MOE) software suite, Chemical Computing Group, Montreal, Canada). Utilising an existing co-liganded crystal structure (pdb 5VGI),³⁴ the 2-substituted benzohydrazides **50** and **55**, and the 3-substituted analogues **45** and **49**, were docked within the enzymatic binding site to determine if differences in interactions and binding poses contributed to the observed differences in KDM4A inhibitory activity. As can be seen in **Figure 4**, interactions with both the metal ion and residues within the binding site help to rationalize these differences in inhibitory effects. The *p*-bromo analogues **65** (**Figure 4a**) and **16** (**Figure 4b**) both chelate the active site nickel, however **65** forms a bidentate interaction with the carboxylic acid, while **16** only interacts with the carbonyl oxygen of the acid group. While the bidentate chelation is the only interaction observed with **65**, **16** also forms hydrogen bonds between the carboxylic acid oxygen and serine 288 and asparagine 198, as well as a hydrogen bonding interaction between the hydrazinyl N-H with aspartic acid 135, and a water-mediated hydrogen bond between the benzoylhydrazine carbonyl oxygen and lysine 241. These additional interactions observed with analogue **16** help reinforce the slightly improved inhibitory ability of analogue **16** over analogue **65**. (Ligand interaction maps in supplementary data).

Similarly, observation of the predicted binding poses of *p*-isopropyl analogues **69** (**Figure 4c**) and **36** (**Figure 4d**) supported the improved inhibitory activity of **69** over **36**. Examination of the pose of **69** shows a bidentate chelation of the catalytic site metal ion and the carboxylic acid, as well as a water-mediated interaction between the benzoylhydrazide carbonyl oxygen and alanine 186. Compound **36**, meanwhile, only forms a single chelation with the metal atom, and a hydrogen bond between the carbonyl oxygen and asparagine 198. Additionally, water-mediated hydrogen bonds between the benzoylhydrazine carbonyl oxygen and lysine 241 and alanine 186. The formation of only a monodentate chelation with **36**, compared to the bidentate chelation observed with **69**, helps rationalise the improved inhibitory activity of **69**.

To determine if these activity trends continued with the reduction of the hydrogen-bonding or metal-chelating capability of the acid group, a selection of methyl esters (Library 4) were prepared. Beginning with a selection of the 3-substituted benzoylhydrazones and hydrazides investigated previously (**Tables 1** and **2**), reaction of the methyl 3-formylbenzoate with a range of benzohydrazides or hydrazones afforded analogues **70-81**. Three ethyl ester variants were also prepared (**82-84**) (**Table 4**).

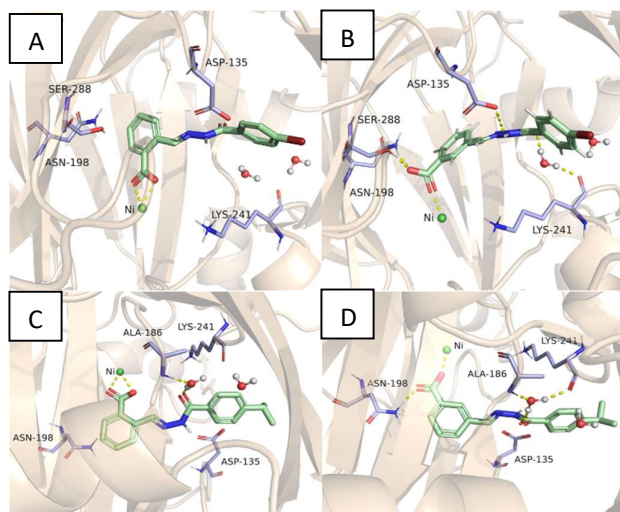
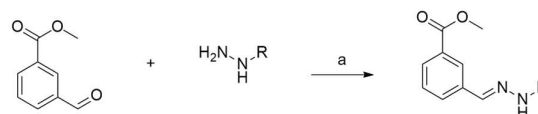


Figure 4. Molecular modelling studies, performed in Molecular Operating Environment, demonstrate the preferred pose for select analogues from Libraries 2 and 3. A) 2-substituted *p*-bromo **65** is observed to chelate the metal ion via a bidentate interaction with the carboxylic acid; B) 3-substituted *p*-bromo **16** chelates the metal ion via the carbonyl oxygen of the acid group, as well as hydrogen bonding interactions between the carboxylic acid proton and serine 288 and asparagine 198. A water-mediated interaction between the benzoylhydrazide carbonyl oxygen and lysine 241, as well as a hydrogen bond between the hydrazinyl N-H and aspartic acid 135 are also observed; C) The 2-substituted *p*-isopropyl **69** chelates the metal ion in a bidentate manner with the carboxylic acid, as well as a water mediated interaction between the benzoylhydrazide carbonyl oxygen and alanine 186; D) 3-substituted *p*-isopropyl **36** forms similar metal ion interactions as **65**, as well as water-mediated hydrogen bonds between the benzoylhydrazide carbonyl oxygen and lys241 and alanine 186.

To determine if these activity trends continued with the reduction of the hydrogen-bonding or metal-chelating capability of the acid group, a selection of methyl esters (Library 4) were prepared. Beginning with a selection of the 3-substituted benzoylhydrazones and hydrazides investigated previously (**Tables 1** and **2**), reaction of the methyl 3-formylbenzoate with a range of benzohydrazides or hydrazones afforded analogues **70-81**. Three ethyl ester variants were also prepared (**82-84**) (**Table 4**).

Analysis of these results demonstrated, surprisingly, that the best results to date were afforded with the methyl ester analogues. Specifically, the *p*-bromo (**70**) and *p*-isopropyl (**72**) gave improved activity over the free acid counterparts **45** and **49** (**70**, 56% > **45**, 93%; **72**, 39% > **49**, 85% residual KDM4 activity @ 20 μ M). The respective ethyl esters, meanwhile, exhibited poorer inhibitory effect: the *p*-bromo **84** was inactive, while the *p*-isopropyl **82** allowed KDM4A to retain 69% residual activity, over the 39% exhibited by the methyl ester **72** (@ 20 μ M). The remaining Library 4 methyl esters all demonstrated reduced KDM4A inhibition over their Library 2 free acid counterparts.



Scheme 4. Synthesis of analogues **70-84**. Reagents and conditions: (a) Ethanol, μ wave 200 W, 120 $^{\circ}$ C, 20 min or ethanol/methanol, 50-100 $^{\circ}$ C, 4-19 h, 0-1.0 eq. sodium hydroxide.

Table 4. KDM4A activity in the presence of Library 4 analogues **70-84**. Results are mean for two independent KDM4A AlphaScreen assays.

| Analogue | R ₁ | R ₂ | KDM4A activity at 20 μ M | KDM4A activity at 1 μ M |
|-----------|----------------|----------------|------------------------------|-----------------------------|
| 70 | Me | | 56% | 83% |
| 71 | Me | | 80% | 83% |
| 72 | Me | | 39% | 83% |
| 73 | Me | | 76% | 74% |
| 74 | Me | | 90% | 92% |
| 75 | Me | | 81% | 92% |
| 76 | Me | | 77% | 86% |
| 77 | Me | | 71% | 80% |
| 78 | Me | | 63% | 74% |
| 79 | Me | | 73% | 67% |
| 80 | Me | | 91% | 90% |
| 81 | Me | | 79% | 75% |
| 82 | Et | | 69% | 79% |
| 83 | Et | | 113% | 110% |

To further investigate the observed differences between the free acids, methyl and ethyl esters, molecular modelling analysis on selected compounds from Table 4 demonstrated a shift in binding mode, compared to the previously discussed free acid moieties. Masking of the acid with an ester resulted in the hydrazine functionality instead chelating the metal atom in the binding site (**Figure 4**). Both the *p*-bromo **70** and *p*-isopropyl **72** analogues demonstrated a similar binding mode, with the major interaction observed for both between the hydrazine N-atom and the Ni ion, with a further hydrogen bonding interaction between the carbonyl oxygen and lysine-241 (**Figure 5a-b**). The *p*-isopropyl ethyl ester analogue **82**, however, was shifted further from the Ni atom, with no major interactions observed (**Figure 5c**). An overlay of the *p*-isopropyl free acid **49**, the methyl ester **72** and ethyl ester **82** (**Figure 5d**) demonstrates that the **72** (blue) and **82** (green) variants lay in a very similar

fashion in the KDM4A binding site, with the ethyl ester shifted slightly, with no interactions with either the metal ion in the binding site, or residues, observed. The free acid **49** (pink), however, due to its bidentate interactions with the nickel atom, occupies a different binding mode.

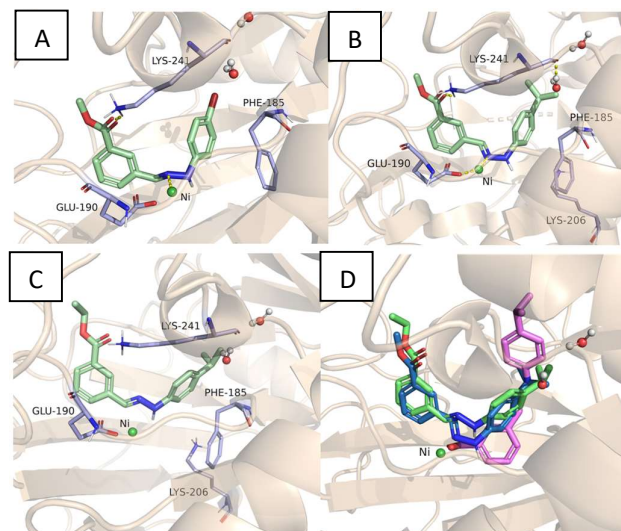


Figure 5. Molecular modelling studies, performed in Molecular Operating Environment, demonstrate the preferred pose for select analogues from Library 4. A) *p*-bromo **70** is observed to chelate the metal ion via the hydrazinyl tertiary nitrogen, and forms a hydrogen bond with lysine 241; B) *p*-isopropyl **72** demonstrates a similar binding mode as **70**; C) The ethyl ester variant *p*-isopropyl **82** occupies a similar binding pose to **72**, but no interactions are observed; D) An overlay of the *p*-isopropyl analogues **49** (free acid, (pink), methyl ester **72** (blue) and ethyl ester **82** (green).

Conclusions

The KDM4 subfamily, in particular KDM4A-D, have been associated with a range of human diseases and conditions, due to the depletion of chromatin methylation in these conditions. Inhibition of these epigenetic modifiers are therefore attractive disease targets. Our recent studies have focussed on KDM4A. The binding site of KDM4A is occupied by an iron(II) atom: chelation of this ion represents an effective inhibitory strategy. Hydrazines have been demonstrated as metal chelators in the literature, and in this work, we sought to investigate their continued potential as KDM4A inhibitors. Four libraries comprising 81 hydrazide or benzoylhydrazono analogues were synthesised via a condensation between either formyl benzoic acid or methyl formylbenzoate and a range of hydrazine or benzoylhydrazono reagents. A KDM4A AlphaScreen was established to assess these analogues for their KDM4A inhibitory activity.

Beginning with 3-formylbenzoic acid, as well as the 6-hydroxy-3-formyl and 6-fluoro-3-formylbenzoic acids, and a range of arylhydrazides, Library 1 explored a selection of halogenated, lipophilic and heterocyclic-containing analogues. Of these, the halogenated analogues demonstrated the most promising KDM4A inhibitory activity. Of particular note were the *p*-bromo **16**, as well as the 6-hydroxy variant, **17**, which both demonstrated <60% residual KDM4A activity @ 20 μ M ligand concentration. The *m*-pyridyl **28** and *p*-trifluoromethyl **38** were

also observed to demonstrate ~60% residual KDM4A activity @ 20 μ M ligand concentration. To explore the effect of removal of the benzoylhydrazine carbonyl oxygen, a focused library (Library 2) of arylhydrazines were prepared. Of these, the only entry that exhibited <60% residual KDM4A activity was the *p*-chloro **46** (56% @ 20 μ M). The *p*-bromo functionality (compound **45**), the most active amongst Library 1, was essentially inactive (93% residual KDM4A activity).

Library 3 investigated the 2-formylbenzoic acid-based analogues. A selection of benzoylhydrazines and arylhydrazines were synthesised, with almost negligible inhibitory activity, for the majority of Library 3: as well as poorer inhibitory activity than the matched 3-(hydrazonomethyl)benzoic acids. Of these analogues, the only entries that demonstrated any inhibition of note were the *p*-isopropyl hydrazine analogue **55** and the matched *p*-isopropyl benzohydrazine **69**, with 69% and 79% residual KDM4A activity @ 20 μ M, respectively.

Molecular modelling analysis of select *p*-bromo and *p*-isopropyl analogues from Libraries **1** and **3**, to attempt to rationalise some differing trends that were observed. The *p*-bromo Library **1** **16** proved to have improved inhibitory effect than its Library 3 counterpart **65**, while the opposite was observed for the *p*-isopropyl analogues **36** and **69**. Analysis of the preferred binding poses supported these observations, with **16** and **69** observed to form more favourable interactions with both the catalytic site metal ion, and surrounding residues, than their counterparts **65** and **36**.

The final selection of compounds prepared, Library 4, were designed to explore the effect of reducing the metal-chelating capacity of the carboxylic acid group by esterifying with either a methyl or ethyl ester. Here, surprisingly, the best overall activity to date was reported. The *p*-isopropyl arylhydrazine **72** demonstrated effective inhibitory of KDM4A, with 39% residual KDM4A activity @ 20 μ M ligand concentration. The *p*-bromo **70** also proved moderately effective, with 56% residual KDM4A activity noted. Molecular modelling analysis was observed to show that these analogues adopted a differing confirmation within the KDM4A active site. With the carboxylic acid less able to effectively chelate the metal ion, the hydrazine moiety instead formed interactions within the binding site. These observations lend weight towards the effective use of hydrazines as metal chelators for KDM4A inhibition, and further work is encouraged to incorporate this moiety into targeted inhibitory compounds.

Experimental

Materials

KDM4A activity was measured using the AlphaScreen General IgG detection kit supplied by PerkinElmer Life Sciences (catalogue number 6760617C). Biotinylated H3K9me2 peptide was supplied by AnaSpec (catalogue number AS-64359-025). Biotinylated H3K9me3 peptide was supplied by AnaSpec (catalogue number AS-64360-025). Anti-H3K9me2 mouse IgG was supplied by Abcam (catalogue number Ab1220). HEPES was supplied by Gibco Life Technologies (catalogue number 11344041). BSA was supplied by Sigma-Aldrich (catalogue number A7030). Tween 20 was supplied by Sigma-Aldrich (catalogue number P1379). Ammonium iron(II) sulfate hexahydrate was supplied by Sigma-Aldrich (catalogue number

12304). Disodium 2-oxoglutarate dihydrate was supplied by Sigma-Aldrich (catalogue number K3752). L-ascorbic acid was supplied by Sigma-Aldrich (catalogue number A5960). EDTA was supplied by Fisher Scientific (catalogue number BP120). Sodium chloride was supplied by Avantor (catalogue number 27810.364). Western blot detection was performed using the Immobilon Western HRP Substrate Luminol-Peroxidase kit supplied by Merck Millipore (catalogue number WBKLS0500). Compounds were diluted and dispensed using an Integra ViaFlo 16-Channel Electronic Pipette (catalogue number 4642) and plated in triplicate. The AlphaScreen assay was performed in white 384-well ProxiPlates supplied by PerkinElmer Life Sciences (catalogue number 6008280). QC6352 was supplied by MedChemExpress (catalogue number HY-104048). ML324 was supplied by MedChemExpress (catalogue number HY-12725).

KDM4A Production

The construct encoding KDM4A residues 1-359, kindly provided by Prof. Paul Brennan (University of Oxford, UK), was used to produce recombinant KDM4A at the Sydney Analytical core facility. The construct was amplified by PCR from an expressed sequence tag (EST) clone and cloned into pNIC289-Bsa4. The expression plasmid was transformed into a phage-resistant derivative of *E. coli* BL21 (DE3) carrying the pRARE2 plasmid. 12 L of TB media containing kanamycin (50 μ g/mL) and chloramphenicol (34 μ g/mL) were inoculated with overnight culture (5 mL/L) and grown at 37 °C in baffled flasks. Expression was induced with isopropyl β -D-1-thiogalactopyranoside (0.2 mM) at $A_{600} = 0.8$ and allowed to continue for 18 h at 18 °C. Bacterial cells were then collected by centrifugation and frozen at -80 °C. Frozen cell pellets were thawed and resuspended in lysis buffer consisting of HEPES (50 mM, pH 7.5), sodium chloride (500 mM), imidazole (20 mM), TCEP (0.5 mM), PMSF (0.5 mM), and benzonase (15 units/mL). Cells were disrupted by high-pressure homogenisation followed by sonication and cell debris was removed by centrifugation.

Recombinant KDM4A was purified by nickel-affinity (1 mL HisTrap FF crude) and size-exclusion chromatography (120 mL HiLoad 16/60 Superdex 200) on an AKTExpress system. The supernatant was loaded onto the nickel-affinity column (0.8 mL/min), washed with 10 column volumes of lysis buffer and 50 column volumes of lysis buffer containing imidazole (40 mM), and eluted with lysis buffer containing imidazole (250 mM). The A_{280} peak was collected and loaded onto the gel filtration column (1 mL/min) in HEPES (10 mM, pH 7.5), sodium chloride (500 mM), glycerol (5% v/v), and TCEP (0.5 mM). EDTA (1 mM) was added to pool fractions overnight. The protein was exchanged in HEPES (10 mM, pH 7.5), sodium chloride (500 mM), glycerol (5% v/v), and TCEP (0.5 mM), concentrated to 25 mg/mL, flash frozen in liquid nitrogen, and stored at -80 °C.

Following gel filtration and dialysis, a fraction of the protein was further purified using an anion exchange column (5 mL HiTrap Q HP) developed with a gradient of 50-500 mM sodium chloride in Tris-HCl (50 mM). The protein was exchanged in HEPES (10 mM, pH 7.5), sodium chloride (500 mM), glycerol (5% v/v), and TCEP (0.5 mM), concentrated to 13 mg/mL, flash frozen in liquid nitrogen, and stored at -80 °C.

H3K9me3 Peptide Validation by Dot Blots

1 μL droplets of biotinylated H3K9me3 peptide were blotted on an activated PVDF membrane and incubated with primary antibodies in 5% w/v BSA in TBST overnight. Membranes were blocked with 5% w/v BSA in TBST, incubated with primary antibodies for H3K9me1, H3K9me2, and H3K9me3 peptides in 5% w/v BSA in TBST overnight at 4 °C, and with secondary antibodies for 1 h at room temperature. Membranes were then washed with TBST (3 x 10 min) before incubation with streptavidin-HRP. Detection was performed using the Bio-Rad ChemiDoc MP Imaging System.

KDM4A Catalytic Activity Assessment by RapidFire Mass Spectrometry

An assay buffer consisting of MES (50 mM), sodium chloride (50 mM), and TCEP (1 mM) was prepared in Milli-Q water and pH adjusted to 7.00. 500 μL of assay buffer containing KDM4A (188 nM) was transferred into wells of a 96-deep-well polypropylene block, and the enzyme reaction was initiated by the addition of 100 μL of assay buffer containing biotinylated H3K9me3 peptide (60 μM), ammonium iron(II) sulfate hexahydrate (60 μM), disodium 2-oxoglutarate dihydrate (60 μM), and L-ascorbic acid (600 μM). The deep-well block was transferred to an Agilent RapidFire RF360 high-throughput sampling robot connected to a 6530 Accurate-Mass Q-TOF LC/MS system operating in positive-ion mode. Samples were aspirated under vacuum for 400 ms and applied to a C4 solid-phase extraction cartridge. The solid-phase extraction was washed to remove non-volatile buffer salts with water containing 0.1% v/v formic acid using a flow rate of 1.5 mL/min for 6 s, and peptides were eluted with a mobile phase of 0.85:0.15 v/v mixture of acetonitrile and water containing 0.1% v/v formic acid using a flow rate of 1.25 mL/min for 6 s. The cartridge was re-equilibrated with water for 500 ms. This cycle of aspiration, aqueous washing, organic elution, and re-equilibration was repeated every 3.5 min for 75 min. Ion chromatogram data were extracted for the +6 charge state for the H3K9me3 substrate and the H3K9me2 product, and peak-area data for extracted ion chromatograms were integrated using RapidFire Integrator software. The fractional conversion of H3K9me2 substrate to H3K9me1 product was calculated as a percentage of change in peptide peak areas. Demethylation was plotted over time for each of the enzymes tested and Kinetic curves were fitted using GraphPad Prism v8.0.

KDM4A AlphaScreen Biochemical Assays.

An assay buffer consisting of HEPES (50 mM, pH 7.5), BSA (0.02% w/v), and Tween 20 (0.01% v/v) was prepared in Milli-Q water, pH adjusted to 7.50, and filtered through a sterilised 0.2 μm filter. The detection stock solution consisting of streptavidin donor beads (80 $\mu\text{g}/\text{mL}$), Protein A acceptor beads (80 $\mu\text{g}/\text{mL}$), and anti-H3K9me2 mouse IgG (120 ng/mL) was prepared in assay buffer and preincubated at room temperature in the dark for 1 h. The cofactor stock solution consisting of ammonium iron(II) sulfate hexahydrate (2 μM), disodium 2-oxoglutarate dihydrate (200 μM), and L-ascorbic acid (200 μM) was prepared

in assay buffer. H3K9me2 and H3K9me3 peptide stock solutions were prepared from the cofactor stock solution additionally containing either biotinylated H3K9me2 (60 nM) or biotinylated H3K9me3 (60 nM). The enzyme stock solution consisting of KDM4A (12 nM) was prepared in assay buffer. The stop solution consisting of EDTA (30 mM) and sodium chloride (800 mM) was prepared in assay buffer. Compound stock solutions were prepared at 20 mM in anhydrous DMSO and diluted in assay buffer to generate dilution series ranging in concentration from 0.04-80 μM .

2.5 μL of diluted compounds were combined with 2.5 μL of enzyme stock directly in plate wells followed by centrifugation at 1000 rpm for 1 min and preincubation at room temperature for 15 min. The enzyme reaction was initiated by the addition of 5 μL of biotinylated H3K9me3 peptide stock followed by centrifugation at 1000 rpm for 1 min and incubation at room temperature for 20 min. The enzyme reaction was halted by the addition of 5 μL of stop solution followed by addition of 5 μL of detection stock and centrifugation at 1000 rpm for 1 min. Plates were sealed and incubated at room temperature in the dark for 2 h. AlphaScreen signals were measured using either a Tecan INFINITE M1000 Pro plate reader or a Tecan Spark 20M plate reader with the AlphaScreen module, an excitation wavelength of 680 nm, a detection range of 520-620 nm, an excitation time of 100 ms, an integration time of 300 ms, a settle time of 0 ms, and temperature correction. Percentage enzyme activity was calculated relative to negative (enzymeless) and positive (uninhibited) wells. Correct functioning of the detection system was validated by the inclusion of additional control wells containing only cofactors and only H3K9me2 and inhibited wells containing QC6352 or ML324.

Computational Chemistry

Computational visualisation, protein preparation, and docking were performed in Molecular Operating Environment 2020.0901 using unaltered Amber10:EHT forcefield parameters. An existing KDM4A-ligand cocrystal structure (PDB 5VGI) was prepared using the Structure Preparation tool and all water molecules exterior to the catalytic site were deleted. Docking placement was constrained to a set of alpha spheres generated within 5 Å of the cocrystallised ligand atoms, calculated using the Triangle Matcher method, and scored using the London dG scoring function. Docking placement refinement was calculated using the Induced Fit method and scored using the GBVI/WSA dG scoring function. S scores and RMSD values were evaluated to select the preferred docked ligand conformations. Final images were prepared in Pymol 2.5.2.

Chemistry

Commercially available starting materials, reagents, and anhydrous solvents were supplied by Sigma-Aldrich or AK Scientific and used without further purification. Microwave-assisted reactions were performed using a Biotage Initiator+. Organic solvent extracts were dried under reduced pressure using Büchi or Heidolph rotary evaporators. Normal-phase flash column chromatography was performed on a Biotage Isolera purification system using solid-loaded Biotage Sfär cartridges

and Merck silica gel 60 (230-400 mesh). Thin-layer chromatography was performed using Merck Millipore TLC silica gel 60 F₂₅₄ pre-coated aluminium plates and visualised by UV (254 and 280 nm). Melting points were recorded in open capillaries on a Büchi Melting Point M-565. Infrared spectra were recorded using a Perkin-Elmer Spectrum Two FT-IR Spectrometer with a scan range of 450-4000 cm⁻¹ and a resolution of 2 cm⁻¹. All peaks are reported in cm⁻¹.

NMR Analysis

¹H, ¹³C, and ¹⁹F NMR spectra were acquired on either a Bruker Avance III 400 MHz spectrometer or a Bruker Avance III 600 MHz spectrometer. NMR samples were prepared as solutions in deuterated dimethyl sulfoxide (DMSO-*d*₆) or deuterated methanol (methanol-*d*₄) supplied by Cambridge Isotope Laboratories. Chemical shifts (δ) were recorded in parts per million and referenced against the internal solvent or standard peaks. ¹⁹F chemical shifts were referenced against a trifluoroacetic acid standard. Coupling constants (*J*) were measured in Hertz. NMR assignments were determined through the interpretation of one-dimensional and two-dimensional spectra. Multiplicities are denoted as singlet (s), broad singlet (bs), doublet (d), doublet of doublets (dd), triplet (t), quartet (q), triplet of doublets (td), doublet of triplets (dt) and multiplet (m). Peaks are listed in order of decreasing chemical shift in the following format: chemical shift (multiplicity, coupling constant, integration).

In solution, *N*-acylhydrazones exist in equilibrium between the syn-periplanar and anti-periplanar conformers which may interconvert through rotation of the amide bond.⁴³ Full NMR data corresponding to the anti-periplanar conformer, the major conformer observed in solution, are quoted. Full NMR data corresponding to the minor syn-periplanar conformer are also quoted, denoted with an asterisk (*), where the relative proportion by ¹H NMR integration was observed to exceed 10%.

UPLC-MS Analysis

UPLC-MS analysis was performed on an Agilent Technologies 1260 Infinity LC system and diode array detector coupled to a 6210 Quadrupole UPLC/MS fitted with a dual electrospray ionisation source. Analytical separation was performed at 40 °C on an Agilent Technologies ZORBAX RRHD SB-C18 column (2.1 mm × 50 mm, 1.8 μ m particle size) using a 0.4 mL.min⁻¹ flow rate and timed isocratic elutions. All methods used a primary mobile phase of water containing 0.1% v/v formic acid (Solvent A) and a secondary mobile phase of 9:1 v/v mixture of acetonitrile and water containing 0.1% v/v formic acid (Solvent B).

Author Contributions

AJS, MPH and JRB synthesized the analogues examined. RHA established the KDM4A AlphaScreen assay. JS and AJS conducted all biological assays and analysis. JRB and AJS conducted all modelling experiments and analysis. LM and

JRB conceived the project and obtained funding. Manuscript draft by JRB, AJS and LM. All authors involved in evolving manuscript discussion, proof reading and editing.

Conflicts of interest

There are no conflicts to declare.

Acknowledgements

This work was funded by NHMRC Ideas grant APP2003150. The authors kindly thank Anthony Turner and Chris Schofield for help and guidance with establishing the KDM4 AlphaScreen assay. APS is the recipient of a University of Newcastle Higher Degree Scholarship. JS and RHA are recipients of XXXX. Funding from the Hunter Medical Research Institute's Precision Medicine Research Program is gratefully acknowledged.

References

- 1 B. Strahl and C. Allis, *Nature*, 2000, **403**, 41–45. doi.org/10.1038/47412
- 2 A. Bannister and T. Kouzarides, *Cell Res.*, 2011, **21**, 381–395. doi.org/10.1038/cr.2011.22
- 3 J. C. Black, C. van Rechem, and J. R. Whetstone, *Mol. Cell*, 2012, **48**, 491–507. doi.org/10.1016/j.molcel.2012.11.006
- 4 Y. Araki, and T. Mimura, *Mediators Inflamm.*, 2017, **2017**, 2608605. doi.org/10.1155/2017/2608605
- 5 A. E. A. Surace and C. M. Hedrich, *Front. Immunol.*, 2019, **10**, 1525. doi.org/10.3389/fimmu.2019.01525
- 6 A. Berson, R. Nativio, S. L. Berger and N. M. Bonini, *Trends Neurosci.*, 2018, **41**, 587–598. doi.org/10.1016/j.tins.2018.05.005
- 7 S. A. Bennett, R. Tanaz, S. N. Cobos and M. P. Torrente, *Transl. Res.*, 2019, **204**, 19–30. doi.org/10.1016/j.trsl.2018.10.002
- 8 Y. L. Wu, Z. J. Lin, C. C. Li, X. Lin, S. K. Shan, B. Guo, M. H. Zheng, F. Li, L. Q. Yuan and Z. H. Li, *Sig. Transduct. Target. Ther.*, 2023, **8**, 98. doi.org/10.1038/s41392-023-01333-7
- 9 Z. Zhao and A. Shilatifard, *Genome Biol.*, 2019, **20**, 245. doi.org/10.1186/s13059-019-1870-5
- 10 Y. Yang, M. Zhang and Y. Wang, *J. Natl. Cancer Inst.*, 2022, **2**, 277–290. doi.org/10.1016/j.jncc.2022.09.002
- 11 P. Hublitz, M. Albert and A. Peters, *Int. J. Dev. Biol.*, 2009, **53**, 335–354. doi.org/10.1387/ijdb.082717ph
- 12 J. Sterling, S. Menezes, R. Abbassi and L. Munoz, *Int. J. Cancer*, 2020, **148**, 2375–2388. doi.org/10.1002/ijc.33375
- 13 M. Levin, M. Stark and Y. G. Assaraf, *Oncotarget* 2018, **9**, 16861–16882. doi.org/10.18632/oncotarget.24717
- 14 Y. Jiang, L. Liu, W. Shan and Z. Yang, *Mol. Oncol.*, 2015, **10**, 292–302. doi.org/10.1016/j.molonc.2015.10.013
- 15 R. Sanchez and M. Zhou, *Trends Biochem. Sci.*, 2011, **36**, 364–372. doi.org/10.1016/j.tibs.2011.03.005
- 16 N. P. Blackledge, J. C. Zhou, M. Y. Tolstorukov, A. M. Farcas, P. J. Park and R. J. Klose, *Mol. Cell*, 2010, **38**, 179–190. doi.org/10.1016/j.molcel.2010.04.009
- 17 T. Vacík, D. Lađinović and I. Raška, *Nucleus*, 2018, **9**, 431–441. doi.org/10.1080/19491034.2018.1498707
- 18 A. Patsialou, D. Wilsker and E. Moran, *Nucleic Acids Res.*, 2005, **33**, 66–80. doi.org/10.1093/nar/gki145
- 19 E. Flashman L. M. Hoffart, R. B. Hamed, J. M. Bollinger Jr., C. Krebs and C. J. Schofield, *FEBS J.*, 2010, **277**, 4089–4099. doi.org/10.1111/j.1742-4658.2010.07804.x

- 20 R. Ramanan, S. S. Chaturvedi, N. Lehnert, C. J. Schofield, T. G. Karabencheva-Christova and C. Z. Christov, *Chem. Sci.*, 2020, **36**, 9950–9961. doi.org/10.1039/d0sc03713c
- 21 M. T. Pedersen, S. M. Kooistra, A. Radziszewska, A. Laugesen, J. V. Johansen, D. G. Hayward, J. Nilsson, K. Agger and K. Helin, *EMBO J.*, 2016, **35**, 1550–1564. doi.org/10.15252/embj.201593317
- 22 S. Shin and R. Janknecht, *Res. Commun.*, 2007, **359**, 742–746. doi.org/10.1016/j.bbrc.2007.05.179
- 23 J. M. Mattsson, S. Ravela, C. Hekim, M. Jonsson, J. Malm, A. Närvänen, U. H. Stenman and H. Koistinen, *PLoS One*, 2014, **9**, e107819. doi.org/10.1371/journal.pone.0107819
- 24 M. T. Qiu, Q. Fan, Z. Zhu, S. Y. Kwan, L. Chen, J. H. Chen, Z. L. Ying, Y. Zhou, W. Gu, L. H. Wang, W. W. Cheng, J. Zeng, X. P. Wan, S. Mok, K. K. Wong and W. Bao, *Oncotarget*, 2015, **6**, 31702–31720. doi.org/10.18632/oncotarget.5165
- 25 M. J. Wu, C. J. Chen, T. Y. Lin, Y. Y. Liu, L. L. Tseng, M. L. Cheng, C. P. Chuu, H. K. Tsai, W. L. Kuo, H. J. Kung and W. C. Wang, *Theranostics*, 2021, **11**, 7779–7796. doi.org/10.7150/thno.58729
- 26 W. Wu, X. Cao and L. Mo, *Am. J. Transl. Res.*, 2021, **13**, 2308–2319. PMID: 34017391
- 27 L. Duan, R. E. Perez, P. D. Chastain II, T. M. Mathew, D. R. Bijukumar and C. G. Maki, *Oncogene*, 2019, **38**, 5643–5657. doi.org/10.1038/s41388-019-0814-6
- 28 C. Y. Lin, B. J. Wang, B. C. Chen, J. C. Tseng, S. S. Jiang, K. K. Tsai, Y. Y. Shen, C. H. Yuh, Z. L. Sie, W. C. Wang, H. J. Kung and C. P. Chuu, *Cancers (Basel)*, 2019, **11**, 1785. doi.org/10.3390/cancers11111785
- 29 W. Luo, R. Chang, J. Zhong, A. Pandey and G. L. Semenza, *Proc. Natl. Acad. Sci. U.S.A.*, 2012, **109**, E3367–E3376. doi.org/10.3390/cancers11111785
- 30 L. Wu, K. K. Wary, S. Revskoy, X. Gao, K. Tsang, Y. A. Komarova, J. Rehman and A. B. Malik, *Stem Cell Rep.*, 2015, **5**, 10–21. doi.org/10.1016/j.stemcr.2015.05.016
- 31 Y. Chen, R. Fang, C. Yue, G. Chang, P. Li, Q. Guo, J. Wang, A. Zhou, S. Zhang, G. N. Fuller, X. Shi and S. Huang, *Cancer Res.*, 2020, **80**, 1049–1063. doi.org/10.1158/0008-5472.CAN-19-1229
- 32 Y. Deng, M. Li, M. Zhuo, P. Guo, Q. Chen, P. Mo, W. Li, and C. Yu, *J. Biol. Chem.*, 2021, **296**, 100121. doi.org/10.1074/jbc.RA120.015335
- 33 S. Baby, D. G. Valapil and Shankaraiah, *Drug Discov. Today*, 2021, **26**, 1841–1856. doi.org/10.1016/j.drudis.2021.05.015
- 34 Y. K. Chen, T. Bonaldi, A. Cuomo, J. R. Del Rosario, D. J. Hosfield, T. Kanouni, S. C. Kao, C. Lai, N. A. Lobo, J. Matuszkiewicz, A. McGeehan, S. M. O'Connell, L. Shi, J. A. Stafford, R. K. Stansfield, J. M. Veal, M. S. Weiss, N. Y. Yuen and M. B. Wallace, *ACS Med. Chem. Lett.*, 2017, **8**, 869–874. doi.org/10.1021/acsmchemlett.7b00220
- 35 O. N. F. King, X. S. Li, M. Sakurai, A. Kawamura, N. R. Rose, S. S. Ng, A. M. Quinn, G. Rai, B. T. Mott, P. Beswick R. J. Klose, U. Oppermann, A. Jadhav, T. D. Heightman, D. J. Maloney, C. J. Schofield and A. Simeonov, *PLoS One*, 2010, **5**, e15535. doi.org/10.1371/journal.pone.0015535
- 36 R. Lilloco, M. G. Sobral, N. Stesco and T. M. Lakowski, *J. Proteomics*, 2016, **133**, 125–133. doi.org/10.1016/j.jprot.2015.12.018
- 37 T. Suzuki, H. Ozasa, Y. Itoh, P. Zhan, H. Sawada, K. Mino, L. Walport, R. Ohkubo, A. Kawamura, M. Yonezawa, Y. Tsukada, A. Tumber, H. Nakagawa, M. Hasegawa, R. Sasaki, T. Mizukami, C. J. Schofield and N. Miyata, *J. Med. Chem.*, 2013, **56**, 7222–7231. doi.org/10.1021/jm400624b
- 38 P. H. Małeckı, N. Rürger, M. Roatsch, O. Krylova, A. Link, M. Jung, U. Heinemann and M. S. Weiss, *ChemMedChem*, 2019, **14**, 1828–1839. doi.org/10.1002/cmdc.201900441
- 39 L. Wang, J. Chang, D. Varghese, M. Dellinger, S. Kumar, A. M. Best, J. Ruiz, R. Bruick, S. Peña-Llopis, J. Xu, D. J. Babinski, D. E. Frantz, R. A. Brekken, A. M. Quinn, A. Simeonov, J. Easmon and E. D. Martinez, *Nat. Commun.*, 2013, **4**, 2035. doi.org/10.1038/ncomms3035
- 40 J. Yoo, Y. H. Jeon, H. Y. Cho, S. W. Lee, G. W. Kim, D. H. Lee and S. H. Kwon, *Cancers (Basel)*, 2020, **12**, 1098. doi.org/10.3390/cancers12051098
- 41 V. Sorna, E. R. Theisen, B. Stephens, S. L. Warner, D. J. Bearss, H. Vankayalapati and S. Sharma, *J. Med. Chem.*, 2013, **56**, 9496–9508. doi.org/10.1021/jm400870h
- 42 V. Bavetsias, R. M. Lanigan, G. F. Ruda, B. Atrash, M. G. McLaughlin, A. Tumber, N. Y. Mok, Y. L. Bihan, S. Dempster, K. J. Boxall, F. Jeganathan, S. B. Hatch, P. Savitsky, S. Velupillai, T. Krojer, K. S. England, J. Sejberg, C. Thai, A. Donovan, A. Pal, G. Scozzafava, J. M. Bennett, A. Kawamura, C. Johansson, A. Szykowska, C. Gileadi, N. A. Burgess-Brown, F. von Delft, U. Oppermann, Z. Walters, J. Shipley, F. I. Raynaud, S. M. Westaway, R. K. Prinjha, O. Fedorov, R. Burke, C. J. Schofield, I. M. Westwood, C. Bountra, S. Müller, R. L. M. van Montfort, P. E. Brennan and J. Blagg, *J. Med. Chem.* 2016, **59**, 1388–1409. doi.org/10.1021/acs.jmedchem.5b01635
- 43 L. I. Socea, S. F. Barbuceanu, E. M. Pahontu, A. C. Dumitru, G. M. Nitulescu, R. C. Sfetea and T. V. Apostol, *Molecules*, 2022, **27**, 8719. doi.org/10.3390/molecules27248719

Chapter 7

Final conclusions

Researchers have frequently highlighted the critical role of chemical probes in preclinical mechanistic studies. Ensuring the correct use of chemical probes by using the appropriate controls early in the drug discovery process is vital for accurate target identification and validation^{208,393}. In **Chapter 3**, we uncovered less than half of reviewed publications used orthogonal or inactive controls and only a mere 4% of eligible publications correctly incorporated all three recommendations where possible. The results from publications not following these recommendations are insufficiently robust and present potentially biased results with misleading conclusions, such as attributing the phenotypic effects of a compound to the incorrect protein. Ultimately, such conclusions are revealed during clinical trials when the drug candidate fails to provide the necessary efficacy^{394,395}.

Additionally, **Chapter 4** demonstrated that the chemical probe QC6352 induced a G0/G1 cell cycle arrest in glioblastoma cells at the low nanomolar concentrations. However, neither the orthogonal KDM4 inhibitor ML324 nor the knockdown of KDM4A-D replicated this cytostatic effect, casting doubt on KDM4's role in glioblastoma viability and its relevance to QC6352's effects. This was further investigated in **Chapter 5** where the mechanisms of action of QC6352 were explored. These findings agreed that inhibiting the KDM4 subtypes individually had no effect on glioblastoma viability or QC6352 efficacy; however, the research identified significant genes essential for glioblastoma viability and QC6352 efficacy. Importantly, PP5 was potentially implicated in the inhibited cell viability caused by QC6352 treatment. In sum, these chapters firstly showed the importance of proper target validation to prevent misidentification of a compound's mechanism of action, and secondly identified a potential off-target of QC6352 which must be accounted for in future mechanistic studies.

7.1. A robustness crisis in the use of chemical probes

Concerns regarding the misuse of chemical probes have been prominently raised by many within the chemical biology community. These concerns highlight instances where probes were either utilised incorrectly or inadequately validated at the time of their development³⁹⁶. Although no other publication has surveyed the percentage of misuse, our systematic review to date was the first to quantify and confirm what experts in the field have been claiming. Moreover, this specific issue of chemical probe misuse underscores a broader challenge in the scientific field. Our findings resonate with the broader concerns expressed by experts about the integrity and reliability of scientific research³⁹⁷⁻³⁹⁹.

Cognitive bias is one of the most important factors influencing the integrity and reliability of research, impacting experimental design, data analysis, and the conclusions presented in their studies⁴⁰⁰. Identified decades ago, bias contributes significantly to the multifaceted reproducibility crisis. This crisis was initially highlighted by Ioannidis in 2005, where it was suggested in a theoretical analysis that the majority of research findings are false, primarily blaming insufficient statistical power and bias in their analyses³⁹⁷. A later survey conducted by Baker in 2016 showed that 75% of research groups reported being unable to replicate findings from other research groups⁴⁰¹. Furthermore, a study by Errington et al. in 2021 repeated a total of 50 preclinical experiments in the field of cancer biology and was only able to reproduce 46% of described effects from the findings³⁹⁸. After the problem was identified, a set of best practices were formulated and followed by the scientific community, the problem appears to be rectifying with publications like Protzko et al. in 2023 now showing a very high reproducibility rate in studies that have followed these best practices laid out for social science research⁴⁰².

Such advancements are similarly achievable in the domain of chemical probe usage, where the inherent bias does not necessarily cause irreproducibility in the purest definition of the word. Our study highlights instead a tangential ‘robustness crisis’, centred on biased conclusions derived from incomplete preclinical studies that fail to adhere to the proper controls recommended by expert chemical biologists, thus leading to a pronounced lack of robustness. The critical issue with these conclusions is that, due to the absence of recommended controls, the incorrect protein or protein function is being associated with a particular phenotype. These studies are then used as the foundations for drug design and lead identification⁴⁰³. The consequence is years of research and millions of dollars to produce a candidate drug that was always destined to fail in clinical trials⁴⁰⁴ (**Figure 7.1**).

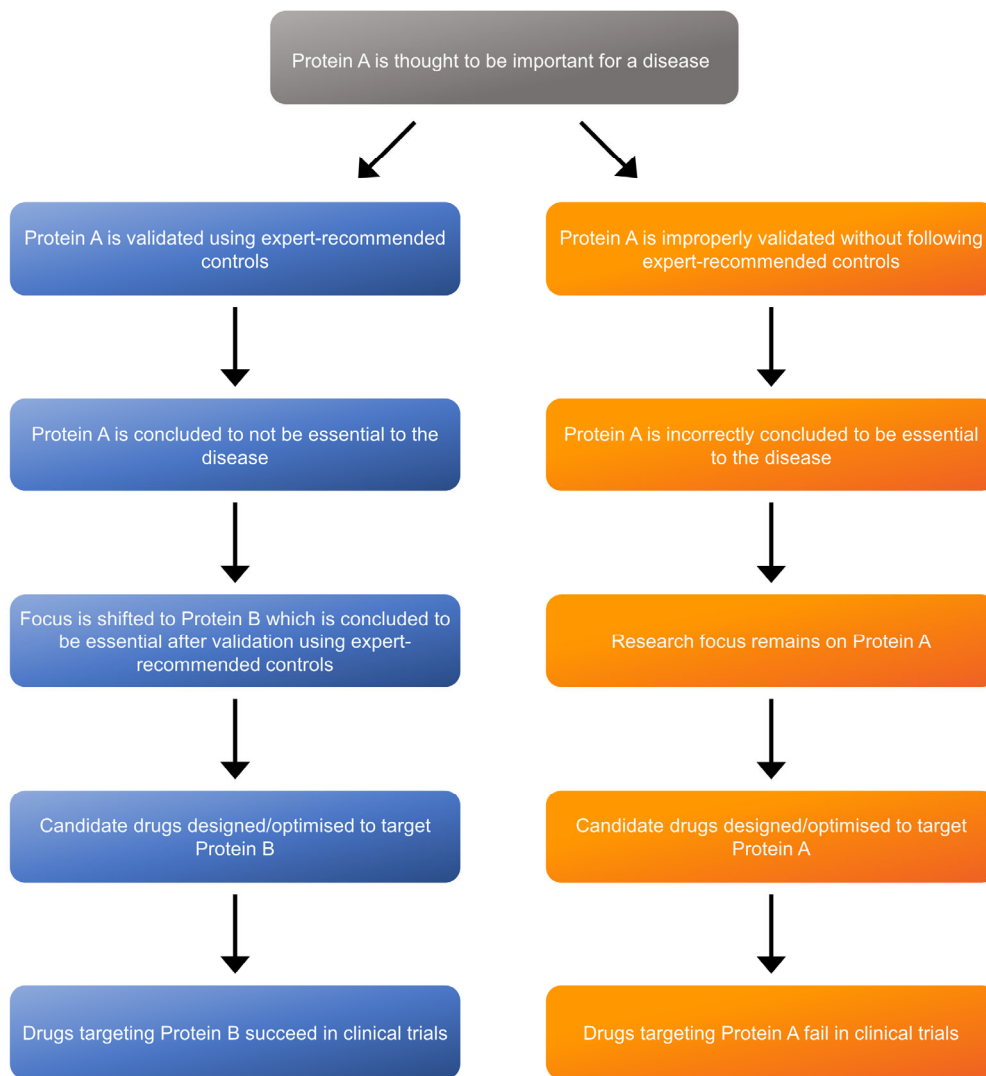


Figure 7.1. Proper and improper chemical probe use in the drug discovery process. The pathway in blue illustrates a successful drug discovery process following the recommended controls while the pathway in orange illustrates an unsuccessful drug discovery process that did not follow the recommended controls.

Glioblastoma research already faces a multitude of challenges. When considering that many preclinical mechanistic studies may be presenting incorrect results, it explains why it has been 19 years since there has been any improvement in glioblastoma therapy⁴⁰⁵. However, based on our findings, improvements can already be seen in some areas of chemical probe usage such as the surprisingly high percentage of compliance using the recommended concentration compared to what was expected. Further improvements can be made by educating the scientific community on the ‘how’ and ‘why’ for chemical probe proper usage.

One of the most effective ways to educate scientists is to create a simple and robust set of rules that can be easily explained, understood, and disseminated to current- and next-generation of scientists. To assist in this, we propose the ‘rule of two’ which details that studies using chemical probes at the very minimum should be paired with either an orthogonal probe or inactive control (preferably both if available) and must all be used at the recommended concentrations. While such a rule has not been made regarding chemical probe use prior to our study, a similar rule has been followed for siRNA knockdown experiments⁴⁰⁶. Since the early 2000’s, a scramble siRNA negative control is commonly used in conjunction with orthogonally targeting siRNA molecules to provide robust findings limiting the chance of misleading results. The education of the scientific community in the importance of controlling for potential off-target effect from siRNA knockdown studies provides an optimistic view of the future of chemical probe usage and our paper serves as a small step towards a universal acknowledgement of the limitations of chemical probe selectivity.

7.2. QC6352: another compound with relevant off-targets

Chapter 4 and **Chapter 5** resulted in two major findings: firstly, that KDM4 is likely not to be essential for glioblastoma proliferation and survival, and secondly, that PP5 is likely to be essential instead (**Figure 7.2**). Previous studies have already implicated PP5 as a potential therapeutic target for several cancer types, including glioblastoma, and our findings are in support of this³⁸⁵. Despite the large number of identified compounds targeting PP5, these modulators still require improved selectivity, cell permeability, or efficacy⁴⁰⁷. If QC6352 is validated and endorsed as a bone-fide PP5 inhibitor, it would, to the best of our knowledge, be the only membrane-permeable PP5 inhibitor to our knowledge that is efficacious in the low nanomolar range⁴⁰⁸. Not only would this provide useful information in regards to structure-activity relationship studies but would also assist in identifying the pharmacological structures necessary for efficient inhibition of PP5.

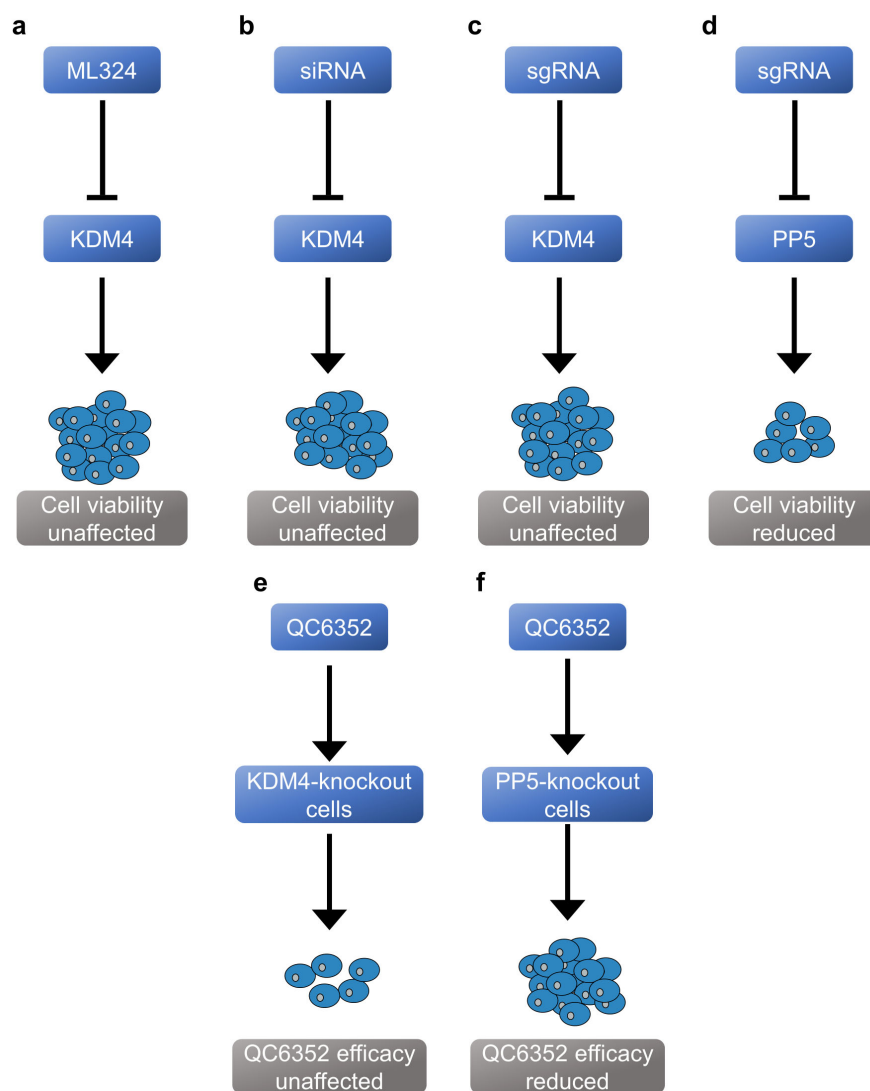


Figure 7.2. Summary of findings from Chapters 4 and 5. **a)** The KDM4 inhibitor ML324, **b)** the KDM4-targeting siRNA molecules, and **c)** KDM4-targeting sgRNA molecules had no effect on glioblastoma cell viability. **d)** CRISPR-Cas9 sgRNA-mediated PP5 loss-of-function reduced glioblastoma viability. **e)** QC6352 antiproliferative efficacy was not reduced when treating KDM4-knockout cells but **f)** QC6352 antiproliferative efficacy was reduced when treating PP5-knockout cells.

With this newfound knowledge of the mechanism of action of QC6352, it is important to return to the four papers earlier publications focusing on QC6352 to see how our findings challenge or compliment their results. As discussed previously, QC6352 is the only chemical probe targeting KDM4 and has no inactive control or orthogonal probe available, making robust target validation challenging. A common solution is to use multiple RNAi molecules and if the findings are the same. If so, this increases the probability that the effects are on-target⁴⁰⁶. In the four mechanistic studies using QC6352, only Singh et al.²³⁸ used multiple RNAi molecules in addition to QC6352 treatment which increases the validity of their findings. In

the other studies, Pichavaram et al.⁴⁰⁹ only used one set of KDM4 siRNA molecules while Wang et al.²³⁷ did not use orthogonal molecular probes or chemical inhibitors alongside QC6352 for confirmation. Despite this, Wang et al. claimed KDM4C was solely responsible for the induced senescence. Unfortunately, this is a biased conclusion made from incomplete results. Moreover, not only do orthogonal molecular probes or chemical inhibitors need to be included but they need to be used in a way that does not promote off-targeting themselves. Metzger et al.²¹⁰ used adenovirus shKDM4A-D constructs to show that only KDM4A reduced breast cancer stem cell viability. However, the cells were transduced at an MOI of 150 or 300 which raises questions about the specificity of the RNAi at such a high MOI⁴¹⁰. In summary, these mechanistic studies employing QC6352 seem to carry biased conclusions to varying degrees but these conclusions should not be dismissed. Further studies using multiple orthogonally-targeting RNAi molecules are required to confirm or dispute their results. It is entirely possible that the mechanism of action identified in QC6352-treated glioblastoma cells may not translate to other cancer cell types at all and different KDM4 family members could still be important for other cancers driven by entirely different signalling pathways.

QC6352 is but one of potentially hundreds of examples of a compound that has a mischaracterised mechanism of action³⁹⁵. Another example, OTS167 was developed as a highly potent and efficacious MELK inhibitor based on early preclinical mechanistic studies which found that MELK was essential for proliferation and survival using siRNA and small molecule inhibitors⁴¹¹. However, this finding was disproven by Lin et al. in 2019³⁹⁵ using CRISPR-Cas9 knockout to firstly show MELK was dispensable for proliferation in 13 different cancer cell lines and secondly that OTS167 efficacy was not affected by MELK knockout. It is easy to see how crucial mischaracterisations such as this often lead to the development of highly selective and efficacious drug candidates with favourable pharmacokinetics but, in reality, have a completely irrelevant target that has no clinical effect on tumour progression.

Moreover, a study by Antolin et al. in 2020 reviewed the kinase selectivity profile of four clinical PARP inhibitors: niraparib, rucaparib, olaparib, and talazoparib. Niraparib inhibits DYRK1A and DYRK1B while rucaparib inhibits CDK16, PIM3, and DYRK1B with potencies easily achievable with clinical doses. Overall, the four clinical PARP inhibitors have distinct side-effect profiles (including several adverse effects) which are thought to be due at least in part by their unique pharmacological profiles. Therefore, the drug candidate's affinity, selectivity, and pharmacokinetics might not be optimised for the unintended off-target leading to toxicity, which might limit the drug's dosage to levels below those required for efficacy. A

concerningly high 96% of drug candidates fail in clinical trials due to a lack of efficacy and severe side effects that risk patient safety and likely caused by biased conclusions serving as the foundation for drug discovery^{412,413}.

7.3. Concluding remarks and future directions

There is still much work left to be done based on our findings. While this thesis was able to assess chemical probe misuse, cast doubt on the importance of KDM4 in the mechanism of QC6352, and hypothesise PP5 as a relevant off-target, these findings nevertheless require further validations. In terms of the quantification of chemical probe use, only eight chemical probes were assessed targeting either kinase or epigenetic proteins. Continuing this assessment on additional chemical probes targets in other areas of research may complement these novel findings. However, a more compelling study would be a follow-up 5-year systematic review to review the latest publications released using the same chemical probes to identify any improvements in using the recommended concentration, orthogonal probe, and inactive control. Only by assessing the trend over time can we see whether their use is improving or not.

Many studies have identified the importance of KDM4 in a variety of cancer types other than glioblastoma. Further studies could investigate the possible redundant role of the KDM4 family using molecules that effectively inhibit all members¹⁰⁹. While multiple RNAi molecules could potentially fill this role, the combined use of four or more molecules would lead to many off-targets. Alternatively, selective small molecule inhibitors could be used such as the novel hydrazine-based KDM4 inhibitors generated in **Chapter 6**. After further structural optimisations, the compounds should be evaluated for cellular efficacy and selectivity and if satisfactory could fulfill the role left behind by QC6352.

Lastly, PP5 has not been validated as a target of QC6352 and at this point in time can only be viewed as a potential target based on the combination of results obtained from orthogonal experiments. A direct biochemical assay should be conducted to assess the binding and/or inhibition of PP5 by QC6352. Meanwhile, the identification of MAPK activation has been observed only through the transcriptomic analysis of FPW1 cells treated with QC6352 and it is essential for further studies to confirm these findings at the protein level. Alternatively, the most fundamental approaches to test whether PP5 is important for the mechanism of action of QC6352 is to knockdown PP5 using such methods as RNAi, or to engineer glioblastoma

cells without a functional PP5 using CRISPR-Cas9 technology and to assess the efficacy of QC6352 in multiple cell lines.

A common theme throughout this thesis is the importance of a well-validated and properly controlled study to ensure the accuracy of the findings. Throughout this thesis, we found that few publications are following the expert recommendations for chemical probe use in their entirety. We also showed that QC6352 is yet another chemical compound with relevant off-target effects that complicate its mechanism of action. The antiproliferative efficacy of QC6352 was likely found to be through PP5 inhibition rather than its KDM4 efficacy in glioblastoma cells. Finally, we discovered novel KDM4 inhibitors that could potentially be used as a substitute for QC6352 which may offer greater selectivity and potency towards KDM4 after additional structural optimisations. Accurate and non-biased conclusions made in fundamental mechanistic studies serve as the foundation for the drug discovery process and often dictate the outcome when a drug candidate enters clinical trials²¹⁹. If there is any realistic hope of obtaining improved therapies for the treatment of glioblastoma, it is crucial that the foundational research surrounding the novel target is derived from robust and well-controlled experiments.

Chapter 8

References

- 1 Sterling, J., Menezes, S. V., Abbassi, R. H. & Munoz, L. Histone lysine demethylases and their functions in cancer. *Int. J. Cancer* **148**, 2375-88 (2021)
- 2 Sterling, J., Baker, J. R., McCluskey, A. & Munoz, L. Systematic literature review reveals suboptimal use of chemical probes in cell-based biomedical research. *Nat. Comm.* **14**, 3228 (2023)
- 3 Hassanzadeh, S., Jalessi, M., Jameie, S. B., Khanmohammadi, M., Bagher, Z., Namjoo, Z. & Davachi, S. M. More attention on glial cells to have better recovery after spinal cord injury. *Biochem Biophys. Rep.* **25**, 100905 (2021)
- 4 Zong, H., Parada, L. F. & Baker, S. J. Cell of origin for malignant gliomas and its implication in therapeutic development. *Cold Spring Harb. Perspect. Biol.* **7** (2015)
- 5 Ostrom, Q. T., Price, M., Neff, C., Cioffi, G., Waite, K. A., Kruchko, C. & Barnholtz-Sloan, J. S. CBTRUS statistical report: Primary brain and other central nervous system tumors diagnosed in the United States in 2016-2020. *Neuro. Oncol.* **25**, iv1-iv99 (2023)
- 6 Louis, D. N., Perry, A., Wesseling, P., Brat, D. J., Cree, I. A., Figarella-Branger, D., Hawkins, C., Ng, H. K., Pfister, S. M., Reifenberger, G., Soffietti, R., Von Deimling, A. & Ellison, D. W. The 2021 WHO classification of tumors of the central nervous system: A summary. *Neuro. Oncol.* **23**, 1231-51 (2021)
- 7 Wang, W., Zhao, Y., Teng, L., Yan, J., Guo, Y., Qiu, Y., Ji, Y., Yu, B., Pei, D., Duan, W., Wang, M., Wang, L., Duan, J., Sun, Q., Wang, S., Duan, H., Sun, C., Guo, Y., Luo, L., Guo, Z., Guan, F., Wang, Z., Xing, A., Liu, Z., Zhang, H., Cui, L., Zhang, L., Jiang, G., Yan, D., Liu, X., Zheng, H., Liang, D., Li, W., Li, Z. C. & Zhang, Z. Neuropathologist-level integrated classification of adult-type diffuse gliomas using deep learning from whole-slide pathological images. *Nat. Comm.* **14**, 6359 (2023)
- 8 Bader, J. M., Deigendesch, N., Misch, M., Mann, M., Koch, A. & Meissner, F. Proteomics separates adult-type diffuse high-grade gliomas in metabolic subgroups independent of 1p/19q codeletion and across IDH mutational status. *Cell. Rep. Med.* **4**, 100877 (2023)
- 9 Han, S., Liu, Y., Cai, S. J., Qian, M., Ding, J., Larion, M., Gilbert, M. R. & Yang, C. IDH mutation in glioma: Molecular mechanisms and potential therapeutic targets. *Br. J. Cancer* **122**, 1580-9 (2020)
- 10 Kayabolen, A., Yilmaz, E. & Bagci-Onder, T. IDH mutations in glioma: Double-edged sword in clinical applications? *Biomedicines* **9** (2021)
- 11 Schaff, L. R. & Mellinghoff, I. K. Glioblastoma and other primary brain malignancies in adults: A review. *JAMA* **329**, 574-87 (2023)
- 12 Hertler, C., Felsberg, J., Gramatzki, D., Le Rhun, E., Clarke, J., Soffietti, R., Wick, W., Chinot, O., Ducray, F., Roth, P., McDonald, K., Hau, P., Hottinger, A. F., Reijneveld,

- J., Schnell, O., Marosi, C., Glantz, M., Darlix, A., Lombardi, G., Krex, D., Glas, M., Reardon, D. A., Van Den Bent, M., Lefranc, F., Herrlinger, U., Razis, E., Carpentier, A. F., Phillips, S., Ruda, R., Wick, A., Tabouret, E., Meyronet, D., Maura, C. A., Rushing, E., Rapkins, R., Bumes, E., Hegi, M., Weyerbrock, A., Aregawi, D., Gonzalez-Gomez, C., Pellerino, A., Klein, M., Preusser, M., Bendszus, M., Golfopoulos, V., Von Deimling, A., Gorlia, T., Wen, P. Y., Reifenberger, G. & Weller, M. Long-term survival with IDH wildtype glioblastoma: First results from the eternity brain tumor funders' collaborative consortium (eortc 1419). *Eur. J. Cancer* **189**, 112913 (2023)
- 13 Jovcevska, I., Kocevar, N. & Komel, R. Glioma and glioblastoma - how much do we (not) know? *Mol. Clin. Oncol.* **1**, 935-41 (2013)
- 14 Singh, N., Miner, A., Hennis, L. & Mittal, S. Mechanisms of temozolomide resistance in glioblastoma - a comprehensive review. *Cancer Drug Resist.* **4**, 17-43 (2021)
- 15 Du, K., Xia, Q., Sun, J. & Feng, F. Visible light and glutathione dually responsive delivery of a polymer-conjugated temozolomide intermediate for glioblastoma chemotherapy. *ACS Appl. Mater. Interfaces* **13**, 55851-61 (2021)
- 16 Ortiz, R., Perazzoli, G., Cabeza, L., Jiménez-Luna, C., Luque, R., Prados, J. & Melguizo, C. Temozolomide: An updated overview of resistance mechanisms, nanotechnology advances and clinical applications. *Curr. Neuropharmacol.* **19**, 513-37 (2021)
- 17 Fuchs, R. P., Isogawa, A., Paulo, J. A., Onizuka, K., Takahashi, T., Amunugama, R., Duxin, J. P. & Fujii, S. Crosstalk between repair pathways elicits double-strand breaks in alkylated DNA and implications for the action of temozolomide. *Elife* **10** (2021)
- 18 Aasland, D., Gotzinger, L., Hauck, L., Berte, N., Meyer, J., Effenberger, M., Schneider, S., Reuber, E. E., Roos, W. P., Tomacic, M. T., Kaina, B. & Christmann, M. Temozolomide induces senescence and repression of DNA repair pathways in glioblastoma cells via activation of ATR-CHK1, p21, and NF-KappaB. *Cancer Res.* **79**, 99-113 (2019)
- 19 Van Den Boogaard, W. M. C., Komninos, D. S. J. & Vermeij, W. P. Chemotherapy side-effects: Not all DNA damage is equal. *Cancers (Basel)* **14** (2022)
- 20 Torgovnick, A. & Schumacher, B. DNA repair mechanisms in cancer development and therapy. *Front. Genet.* **6**, 157 (2015)
- 21 Butler, M., Pongor, L., Su, Y. T., Xi, L., Raffeld, M., Quezado, M., Trepel, J., Aldape, K., Pommier, Y. & Wu, J. MGMT status as a clinical biomarker in glioblastoma. *Trends Cancer* **6**, 380-91 (2020)
- 22 Egaña, L., Auzmendi-Iriarte, J., Andermatten, J., Villanua, J., Ruiz, I., Elua-Pinin, A., Aldaz, P., Querejeta, A., Sarasqueta, C., Zubia, F., Matheu, A. & Samprón, N.

- Methylation of MGMT promoter does not predict response to temozolomide in patients with glioblastoma in Donostia hospital. *Sci. Rep.* **10**, 18445 (2020)
- 23 Kotecha, R., Odia, Y., Khosla, A. A. & Ahluwalia, M. S. Key clinical principles in the management of glioblastoma. *JCO Oncol. Pract.* **19**, 180-9 (2023)
- 24 Seelig, A. The role of size and charge for blood-brain barrier permeation of drugs and fatty acids. *J. Mol. Neurosci.* **33**, 32-41 (2007)
- 25 Kadry, H., Noorani, B. & Cucullo, L. A blood-brain barrier overview on structure, function, impairment, and biomarkers of integrity. *Fluids Barriers CNS* **17**, 69 (2020)
- 26 Heffron, T. P. Small molecule kinase inhibitors for the treatment of brain cancer. *J. Med. Chem.* **59**, 10030-66 (2016)
- 27 Brown, N. F., Carter, T. J., Ottaviani, D. & Mulholland, P. Harnessing the immune system in glioblastoma. *Br. J. Cancer* **119**, 1171-81 (2018)
- 28 Fucikova, J., Kepp, O., Kasikova, L., Petroni, G., Yamazaki, T., Liu, P., Zhao, L., Spisek, R., Kroemer, G. & Galluzzi, L. Detection of immunogenic cell death and its relevance for cancer therapy. *Cell Death Dis.* **11**, 1013 (2020)
- 29 Hiam-Galvez, K. J., Allen, B. M. & Spitzer, M. H. Systemic immunity in cancer. *Nat. Rev. Cancer* **21**, 345-59 (2021)
- 30 Luksik, A. S., Yazigi, E., Shah, P. & Jackson, C. M. Car T cell therapy in glioblastoma: Overcoming challenges related to antigen expression. *Cancers (Basel)* **15** (2023)
- 31 Yabo, Y. A., Niclou, S. P. & Golebiewska, A. Cancer cell heterogeneity and plasticity: A paradigm shift in glioblastoma. *Neuro. Oncol.* **24**, 669-82 (2022)
- 32 Eisenbarth, D. & Wang, Y. A. Glioblastoma heterogeneity at single cell resolution. *Oncogene* **42**, 2155-65 (2023)
- 33 Woodward, A. A., Urbanowicz, R. J., Naj, A. C. & Moore, J. H. Genetic heterogeneity: Challenges, impacts, and methods through an associative lens. *Genet. Epidemiol.* **46**, 555-71 (2022)
- 34 Tong, M., Deng, Z., Zhang, X., He, B., Yang, M., Cheng, W. & Liu, Q. New insights from the widening homogeneity perspective to target intratumor heterogeneity. *Cancer Commun. (Lond)* **38**, 17 (2018)
- 35 Liu, J., Dang, H. & Wang, X. W. The significance of intertumor and intratumor heterogeneity in liver cancer. *Exp. Mol. Med.* **50**, e416-e (2018)

- 36 Verhaak, R. G., Hoadley, K. A., Purdom, E., Wang, V., Qi, Y., Wilkerson, M. D., Miller, C. R., Ding, L., Golub, T., Mesirov, J. P., Alexe, G., Lawrence, M., O'Kelly, M., Tamayo, P., Weir, B. A., Gabriel, S., Winckler, W., Gupta, S., Jakkula, L., Feiler, H. S., Hodgson, J. G., James, C. D., Sarkaria, J. N., Brennan, C., Kahn, A., Spellman, P. T., Wilson, R. K., Speed, T. P., Gray, J. W., Meyerson, M., Getz, G., Perou, C. M. & Hayes, D. N. Integrated genomic analysis identifies clinically relevant subtypes of glioblastoma characterized by abnormalities in PDGFRA, IDH1, EGFR, and NF1. *Cancer Cell* **17**, 98-110 (2010)
- 37 Wang, Q., Hu, B., Hu, X., Kim, H., Squatrito, M., Scarpace, L., Decarvalho, A. C., Lyu, S., Li, P., Li, Y., Barthel, F., Cho, H. J., Lin, Y. H., Satani, N., Martinez-Ledesma, E., Zheng, S., Chang, E., Sauv e, C. G., Olar, A., Lan, Z. D., Finocchiaro, G., Phillips, J. J., Berger, M. S., Gabrusiewicz, K. R., Wang, G., Eskilsson, E., Hu, J., Mikkelsen, T., Depinho, R. A., Muller, F., Heimberger, A. B., Sulman, E. P., Nam, D. H. & Verhaak, R. G. W. Tumor evolution of glioma-intrinsic gene expression subtypes associates with immunological changes in the microenvironment. *Cancer Cell* **32**, 42-56 (2017)
- 38 An, Z., Aksoy, O., Zheng, T., Fan, Q.-W. & Weiss, W. A. Epidermal growth factor receptor and EGFRvIII in glioblastoma: Signaling pathways and targeted therapies. *Oncogene* **37**, 1561-75 (2018)
- 39 Pan, P. C. & Magge, R. S. Mechanisms of EGFR resistance in glioblastoma. *Int. J. Mol. Sci.* **21** (2020)
- 40 Sadida, H. Q., Abdulla, A., Marzooqi, S. A., Hashem, S., Macha, M. A., Akil, A. S. A. & Bhat, A. A. Epigenetic modifications: Key players in cancer heterogeneity and drug resistance. *Transl. Oncol.* **39**, 101821 (2024)
- 41 Neftel, C., Laffy, J., Filbin, M. G., Hara, T., Shore, M. E., Rahme, G. J., Richman, A. R., Silverbush, D., Shaw, M. L., Hebert, C. M., Dewitt, J., Gritsch, S., Perez, E. M., Gonzalez Castro, L. N., Lan, X., Druck, N., Rodman, C., Dionne, D., Kaplan, A., Bertalan, M. S., Small, J., Pelton, K., Becker, S., Bonal, D., Nguyen, Q.-D., Servis, R. L., Fung, J. M., Mylvaganam, R., Mayr, L., Gojo, J., Haberler, C., Geyeregger, R., Czech, T., Slavic, I., Nahed, B. V., Curry, W. T., Carter, B. S., Wakimoto, H., Brastianos, P. K., Batchelor, T. T., Stemmer-Rachamimov, A., Martinez-Lage, M., Frosch, M. P., Stamenkovic, I., Riggi, N., Rheinbay, E., Monje, M., Rozenblatt-Rosen, O., Cahill, D. P., Patel, A. P., Hunter, T., Verma, I. M., Ligon, K. L., Louis, D. N., Regev, A., Bernstein, B. E., Tirosh, I. & Suv a, M. L. An integrative model of cellular states, plasticity, and genetics for glioblastoma. *Cell* **178**, 835-49 (2019)
- 42 Johnson, A. L., Lattera, J. & Lopez-Bertoni, H. Exploring glioblastoma stem cell heterogeneity: Immune microenvironment modulation and therapeutic opportunities. *Front. Oncol.* **12**, 995498 (2022)
- 43 Du, P. & Wu, J. Hallmarks of totipotent and pluripotent stem cell states. *Cell Stem Cell* (2024)

- 44 Shi, W., Liao, Y., Willis, S. N., Taubenheim, N., Inouye, M., Tarlinton, D. M., Smyth, G. K., Hodgkin, P. D., Nutt, S. L. & Corcoran, L. M. Transcriptional profiling of mouse B cell terminal differentiation defines a signature for antibody-secreting plasma cells. *Nat. Immunol.* **16**, 663-73 (2015)
- 45 Jögi, A., Vaapil, M., Johansson, M. & Pählman, S. Cancer cell differentiation heterogeneity and aggressive behavior in solid tumors. *Ups. J. Med. Sci.* **117**, 217-24 (2012)
- 46 De Silva, M. I., Stringer, B. W. & Bardy, C. Neuronal and tumourigenic boundaries of glioblastoma plasticity. *Trends Cancer* **9**, 223-36 (2023)
- 47 Doualle, C., Gouju, J., Nouari, Y., Wery, M., Guittonneau, C., Codron, P., Rousseau, A., Saulnier, P., Eyer, J. & Letournel, F. Dedifferentiated cells obtained from glioblastoma cell lines are an easy and robust model for mesenchymal glioblastoma stem cells studies. *Am. J. Cancer Res.* **13**, 1425-42 (2023)
- 48 Gupta, P. B., Fillmore, C. M., Jiang, G., Shapira, S. D., Tao, K., Kuperwasser, C. & Lander, E. S. Stochastic state transitions give rise to phenotypic equilibrium in populations of cancer cells. *Cell* **146**, 633-44 (2011)
- 49 Prager, B. C., Bhargava, S., Mahadev, V., Hubert, C. G. & Rich, J. N. Glioblastoma stem cells: Driving resilience through chaos. *Trends Cancer* **6**, 223-35 (2020)
- 50 Shah, S., Philipp, L.-M., Giaimo, S., Sebens, S., Traulsen, A. & Raatz, M. Understanding and leveraging phenotypic plasticity during metastasis formation. *npj Syst. Biol. Appl.* **9**, 48 (2023)
- 51 Burrell, R. A., Mcgranahan, N., Bartek, J. & Swanton, C. The causes and consequences of genetic heterogeneity in cancer evolution. *Nature* **501**, 338-45 (2013)
- 52 Chen, H. M., Nikolic, A., Singhal, D. & Gallo, M. Roles of chromatin remodelling and molecular heterogeneity in therapy resistance in glioblastoma. *Cancers (Basel)* **14** (2022)
- 53 Chaligne, R., Gaiti, F., Silverbush, D., Schiffman, J. S., Weisman, H. R., Kluegel, L., Gritsch, S., Deochand, S. D., Gonzalez Castro, L. N., Richman, A. R., Klughammer, J., Biancalani, T., Muus, C., Sheridan, C., Alonso, A., Izzo, F., Park, J., Rozenblatt-Rosen, O., Regev, A., Suvà, M. L. & Landau, D. A. Epigenetic encoding, heritability and plasticity of glioma transcriptional cell states. *Nat. Genet.* **53**, 1469-79 (2021)
- 54 Shu, F., Xiao, H., Li, Q.-N., Ren, X.-S., Liu, Z.-G., Hu, B.-W., Wang, H.-S., Wang, H. & Jiang, G.-M. Epigenetic and post-translational modifications in autophagy: Biological functions and therapeutic targets. *Signal Transduct. Target. Ther.* **8**, 32 (2023)

- 55 Lee, D., Yang, J. & Kim, S. Learning the histone codes with large genomic windows and three-dimensional chromatin interactions using transformer. *Nat. Comm.* **13**, 6678 (2022)
- 56 Gillette, T. G. & Hill, J. A. Readers, writers, and erasers: Chromatin as the whiteboard of heart disease. *Circ. Res.* **116**, 1245-53 (2015)
- 57 Lee, H. T., Oh, S., Ro, D. H., Yoo, H. & Kwon, Y. W. The key role of DNA methylation and histone acetylation in epigenetics of atherosclerosis. *J. Lipid Atheroscler.* **9**, 419-34 (2020)
- 58 Bardani, E., Kallemini, P., Tselika, M., Katsarou, K. & Kalantidis, K. Spotlight on plant bromodomain proteins. *Biology (Basel)* **12** (2023)
- 59 Gibney, E. R. & Nolan, C. M. Epigenetics and gene expression. *Heredity* **105**, 4-13 (2010)
- 60 Husmann, D. & Gozani, O. Histone lysine methyltransferases in biology and disease. *Nat. Struct. Mol. Biol.* **26**, 880-9 (2019)
- 61 Liu, M., Espinosa-Diez, C., Mahan, S., Du, M., Nguyen, A. T., Hahn, S., Chakraborty, R., Straub, A. C., Martin, K. A., Owens, G. K. & Gomez, D. H3K4 di-methylation governs smooth muscle lineage identity and promotes vascular homeostasis by restraining plasticity. *Dev. Cell* **56**, 2765-82 (2021)
- 62 Crouch, J., Shvedova, M., Thanapaul, R., Botchkarev, V. & Roh, D. Epigenetic regulation of cellular senescence. *Cells* **11** (2022)
- 63 Juan, A. H., Wang, S., Ko, K. D., Zare, H., Tsai, P. F., Feng, X., Vivanco, K. O., Ascoli, A. M., Gutierrez-Cruz, G., Krebs, J., Sidoli, S., Knight, A. L., Pedersen, R. A., Garcia, B. A., Casellas, R., Zou, J. & Sartorelli, V. Roles of H3K27me2 and H3K27me3 examined during fate specification of embryonic stem cells. *Cell Rep.* **17**, 1369-82 (2016)
- 64 Sun, Z., Zhang, Y., Jia, J., Fang, Y., Tang, Y., Wu, H. & Fang, D. H3K36me3, message from chromatin to DNA damage repair. *Cell Biosci.* **10**, 9 (2020)
- 65 Yuan, J., Pu, M., Zhang, Z. & Lou, Z. Histone H3-K56 acetylation is important for genomic stability in mammals. *Cell Cycle* **8**, 1747-53 (2009)
- 66 Fu, H., Maunakea, A. K., Martin, M. M., Huang, L., Zhang, Y., Ryan, M., Kim, R., Lin, C. M., Zhao, K. & Aladjem, M. I. Methylation of histone H3 on lysine 79 associates with a group of replication origins and helps limit DNA replication once per cell cycle. *PLoS Genet.* **9**, e1003542 (2013)

- 67 Jørgensen, S., Schotta, G. & Sørensen, C. S. Histone H4 lysine 20 methylation: Key player in epigenetic regulation of genomic integrity. *Nucleic Acids Res.* **41**, 2797-806 (2013)
- 68 Faundes, V., Newman, W. G., Bernardini, L., Canham, N., Clayton-Smith, J., Dallapiccola, B., Davies, S. J., Demos, M. K., Goldman, A., Gill, H., Horton, R., Kerr, B., Kumar, D., Lehman, A., Mckee, S., Morton, J., Parker, M. J., Rankin, J., Robertson, L., Temple, I. K. & Banka, S. Histone lysine methylases and demethylases in the landscape of human developmental disorders. *Am. J. Hum. Genet.* **102**, 175-87 (2018)
- 69 Bhat, K. P., Ümit Kaniskan, H., Jin, J. & Gozani, O. Epigenetics and beyond: Targeting writers of protein lysine methylation to treat disease. *Nat. Rev. Drug Discov.* **20**, 265-86 (2021)
- 70 Perillo, B., Tramontano, A., Pezone, A. & Migliaccio, A. LSD1: More than demethylation of histone lysine residues. *Exp. Mol. Med.* **52**, 1936-47 (2020)
- 71 Gaweska, H. & Fitzpatrick, P. F. Structures and mechanism of the monoamine oxidase family. *Biomol. Concepts* **2**, 365-77 (2011)
- 72 Hosseini, A. & Minucci, S. A comprehensive review of lysine-specific demethylase 1 and its roles in cancer. *Epigenomics* **9**, 1123-42 (2017)
- 73 Klose, R. J., Kallin, E. M. & Zhang, Y. JmjC-domain-containing proteins and histone demethylation. *Nat. Rev. Genet.* **7**, 715-27 (2006)
- 74 Horton, J. R., Engstrom, A., Zoeller, E. L., Liu, X., Shanks, J. R., Zhang, X., Johns, M. A., Vertino, P. M., Fu, H. & Cheng, X. Characterization of a linked jumonji domain of the KDM5/JARID1 family of histone H3 lysine 4 demethylases. *J. Biol. Chem.* **291**, 2631-46 (2016)
- 75 Shen, J. & Spruck, C. F-box proteins in epigenetic regulation of cancer. *Oncotarget* **8**, 110650-5 (2017)
- 76 Hyun, K., Jeon, J., Park, K. & Kim, J. Writing, erasing and reading histone lysine methylations. *Exp. Mol. Med.* **49**, e324 (2017)
- 77 Hou, H. & Yu, H. Structural insights into histone lysine demethylation. *Curr. Opin. Struct. Biol.* **20**, 739-48 (2010)
- 78 Zheng, Y., Hsu, F. N., Xu, W., Xie, X. J., Ren, X., Gao, X., Ni, J. Q. & Ji, J. Y. A developmental genetic analysis of the lysine demethylase KDM2 mutations in drosophila melanogaster. *Mech. Dev.* **133**, 36-53 (2014)
- 79 Tsukada, Y., Ishitani, T. & Nakayama, K. I. Kdm7 is a dual demethylase for histone H3 lys 9 and lys 27 and functions in brain development. *Genes Dev.* **24**, 432-7 (2010)

- 80 Klein, B. J., Piao, L., Xi, Y., Rincon-Arano, H., Rothbart, S. B., Peng, D., Wen, H., Larson, C., Zhang, X., Zheng, X., Cortazar, M. A., Peña, P. V., Mangan, A., Bentley, D. L., Strahl, B. D., Groudine, M., Li, W., Shi, X. & Kutateladze, T. G. The histone-H3K4-specific demethylase KDM5B binds to its substrate and product through distinct PHD fingers. *Cell Rep.* **6**, 325-35 (2014)
- 81 Liu, X. & Secombe, J. The histone demethylase kdm5 activates gene expression by recognizing chromatin context through its PHD reader motif. *Cell Rep.* **13**, 2219-31 (2015)
- 82 Su, Z., Wang, F., Lee, J. H., Stephens, K. E., Papazyan, R., Voronina, E., Krautkramer, K. A., Raman, A., Thorpe, J. J., Boersma, M. D., Kuznetsov, V. I., Miller, M. D., Taverna, S. D., Phillips, G. N., Jr. & Denu, J. M. Reader domain specificity and lysine demethylase-4 family function. *Nat Comm.* **7**, 13387 (2016)
- 83 Hillringhaus, L., Yue, W. W., Rose, N. R., Ng, S. S., Gileadi, C., Loenarz, C., Bello, S. H., Bray, J. E., Schofield, C. J. & Oppermann, U. Structural and evolutionary basis for the dual substrate selectivity of human KDM4 histone demethylase family. *J. Biol. Chem.* **286**, 41616-25 (2011)
- 84 Wang, Y. & Shen, Z. Unmasking the mammalian set domain-containing protein 4. *NAR Cancer* **4**, zcac021 (2022)
- 85 Thinnes, C. C., England, K. S., Kawamura, A., Chowdhury, R., Schofield, C. J. & Hopkinson, R. J. Targeting histone lysine demethylases - progress, challenges, and the future. *Biochim Biophys. Acta.* **1839**, 1416-32 (2014)
- 86 Yang, Y., Zhang, M. & Wang, Y. The roles of histone modifications in tumorigenesis and associated inhibitors in cancer therapy. *J. Natl. Cancer Inst.* **2**, 277-90 (2022)
- 87 Zhang, H., Wang, H., Ye, L., Bao, S., Zhang, R., Che, J., Luo, W., Yu, C. & Wang, W. Comprehensive transcriptomic analyses identify KDM genes-related subtypes with different TME infiltrates in gastric cancer. *BMC Cancer* **23**, 454 (2023)
- 88 Harris, W. J., Huang, X., Lynch, J. T., Spencer, G. J., Hitchin, J. R., Li, Y., Ciceri, F., Blaser, J. G., Greystoke, B. F., Jordan, A. M., Miller, C. J., Ogilvie, D. J. & Somerville, T. C. The histone demethylase KDM1A sustains the oncogenic potential of MLL-AF9 leukemia stem cells. *Cancer Cell* **21**, 473-87 (2012)
- 89 Sun, G., Alzayady, K., Stewart, R., Ye, P., Yang, S., Li, W. & Shi, Y. Histone demethylase LSD1 regulates neural stem cell proliferation. *Mol. Cell Biol.* **30**, 1997-2005 (2010)
- 90 Li, W., Sun, G., Yang, S., Qu, Q., Nakashima, K. & Shi, Y. Nuclear receptor TLX regulates cell cycle progression in neural stem cells of the developing brain. *Mol. Endocrinol.* **22**, 56-64 (2008)

- 91 Saccà, C. D., Gorini, F., Ambrosio, S., Amente, S., Faicchia, D., Matarese, G., Lania, L. & Majello, B. Inhibition of lysine-specific demethylase LSD1 induces senescence in glioblastoma cells through a HIF-1 α -dependent pathway. *Biochim. Biophys. Acta* **1862**, 535-46 (2019)
- 92 Ellis, L. & Loda, M. Lsd1: A single target to combat lineage plasticity in lethal prostate cancer. *Proc. Natl. Acad. Sci. U. S. A.* **115**, 4530-1 (2018)
- 93 Liu, C., Liu, L., Chen, X., Cheng, J., Zhang, H., Zhang, C., Shan, J., Shen, J. & Qian, C. LSD1 stimulates cancer-associated fibroblasts to drive NOTCH3-dependent self-renewal of liver cancer stem-like cells. *Cancer Res.* **78**, 938-49 (2018)
- 94 Cao, C., Vasilatos, S. N., Bhargava, R., Fine, J. L., Oesterreich, S., Davidson, N. E. & Huang, Y. Functional interaction of histone deacetylase 5 (HDAC5) and lysine-specific demethylase 1 (LSD1) promotes breast cancer progression. *Oncogene* **36**, 133-45 (2017)
- 95 Hayami, S., Kelly, J. D., Cho, H. S., Yoshimatsu, M., Unoki, M., Tsunoda, T., Field, H. I., Neal, D. E., Yamaue, H., Ponder, B. A., Nakamura, Y. & Hamamoto, R. Overexpression of LSD1 contributes to human carcinogenesis through chromatin regulation in various cancers. *Int. J. Cancer* **128**, 574-86 (2011)
- 96 Augert, A., Eastwood, E., Ibrahim, A. H., Wu, N., Grunblatt, E., Basom, R., Liggitt, D., Eaton, K. D., Martins, R., Poirier, J. T., Rudin, C. M., Milletti, F., Cheng, W. Y., Mack, F. & Macpherson, D. Targeting NOTCH activation in small cell lung cancer through LSD1 inhibition. *Sci. Signal.* **12** (2019)
- 97 Katz, T. A., Vasilatos, S. N., Harrington, E., Oesterreich, S., Davidson, N. E. & Huang, Y. Inhibition of histone demethylase, LSD2 (KDM1B), attenuates DNA methylation and increases sensitivity to DNMT inhibitor-induced apoptosis in breast cancer cells. *Breast Cancer Res. Treat.* **146**, 99-108 (2014)
- 98 Hu, J., Sun, T., Wang, H., Chen, Z., Wang, S., Yuan, L., Liu, T., Li, H. R., Wang, P., Feng, Y., Wang, Q., Mclendon, R. E., Friedman, A. H., Keir, S. T., Bigner, D. D., Rathmell, J., Fu, X. D., Li, Q. J., Wang, H. & Wang, X. F. MiR-215 is induced post-transcriptionally via HIF-Drosha complex and mediates glioma-initiating cell adaptation to hypoxia by targeting KDM1B. *Cancer Cell* **29**, 49-60 (2016)
- 99 Wagner, K. W., Alam, H., Dhar, S. S., Giri, U., Li, N., Wei, Y., Giri, D., Cascone, T., Kim, J. H., Ye, Y., Multani, A. S., Chan, C. H., Erez, B., Saigal, B., Chung, J., Lin, H. K., Wu, X., Hung, M. C., Heymach, J. V. & Lee, M. G. KDM2A promotes lung tumorigenesis by epigenetically enhancing ERK1/2 signaling. *J. Clin. Invest.* **123**, 5231-46 (2013)

- 100 He, J., Kallin, E. M., Tsukada, Y. & Zhang, Y. The H3K36 demethylase JHDM1B/KDM2B regulates cell proliferation and senescence through p15(Ink4b). *Nat. Struct. Mol. Biol.* **15**, 1169-75 (2008)
- 101 He, J., Nguyen, A. T. & Zhang, Y. KDM2B/JHDM1B, an H3K36me2-specific demethylase, is required for initiation and maintenance of acute myeloid leukemia. *Blood* **117**, 3869-80 (2011)
- 102 Staberg, M., Rasmussen, R. D., Michaelsen, S. R., Pedersen, H., Jensen, K. E., Villingshøj, M., Skjoth-Rasmussen, J., Brennum, J., Vitting-Seerup, K., Poulsen, H. S. & Hamerlik, P. Targeting glioma stem-like cell survival and chemoresistance through inhibition of lysine-specific histone demethylase KDM2B. *Mol. Oncol.* **12**, 406-20 (2018)
- 103 Wade, M. A., Jones, D., Wilson, L., Stockley, J., Coffey, K., Robson, C. N. & Gaughan, L. The histone demethylase enzyme KDM3A is a key estrogen receptor regulator in breast cancer. *Nucleic Acids Res.* **43**, 196-207 (2015)
- 104 Ramadoss, S., Guo, G. & Wang, C. Y. Lysine demethylase KDM3A regulates breast cancer cell invasion and apoptosis by targeting histone and the non-histone protein p53. *Oncogene* **36**, 47-59 (2017)
- 105 Saraç, H., Morova, T., Pires, E., Mccullagh, J., Kaplan, A., Cingöz, A., Bağci-Onder, T., Önder, T., Kawamura, A. & Lack, N. A. Systematic characterization of chromatin modifying enzymes identifies KDM3B as a critical regulator in castration resistant prostate cancer. *Oncogene* **39**, 2187-201 (2020)
- 106 Lynch, J. R., Salik, B., Connerty, P., Vick, B., Leung, H., Pijning, A., Jeremias, I., Spiekermann, K., Trahair, T., Liu, T., Haber, M., Norris, M. D., Woo, A. J., Hogg, P., Wang, J. & Wang, J. Y. JMJD1C-mediated metabolic dysregulation contributes to HOXA9-dependent leukemogenesis. *Leukemia* **33**, 1400-10 (2019)
- 107 Agger, K., Nishimura, K., Miyagi, S., Messling, J.-E., Rasmussen, K. D. & Helin, K. The KDM4/JMJD2 histone demethylases are required for hematopoietic stem cell maintenance. *Blood* **134**, 1154-8 (2019)
- 108 Pedersen, M. T., Kooistra, S. M., Radzisheuskaya, A., Laugesen, A., Johansen, J. V., Hayward, D. G., Nilsson, J., Agger, K. & Helin, K. Continual removal of H3K9 promoter methylation by JMJD2 demethylases is vital for esc self-renewal and early development. *EMBO J.* **35**, 1550-64 (2016)
- 109 Agger, K., Miyagi, S., Pedersen, M. T., Kooistra, S. M., Johansen, J. V. & Helin, K. JMJD2/KDM4 demethylases are required for expression of IL3RA and survival of acute myeloid leukemia cells. *Genes Dev* **30**, 1278-88 (2016)

- 110 Peng, K., Kou, L., Yu, L., Bai, C., Li, M., Mo, P., Li, W. & Yu, C. Histone demethylase JMJD2D interacts with β -catenin to induce transcription and activate colorectal cancer cell proliferation and tumor growth in mice. *Gastroenterology* **156**, 1112-26 (2019)
- 111 Katoh, M. & Katoh, M. Identification and characterization of JMJD2 family genes in silico. *Int. J. Oncol.* **24**, 1623-8 (2004)
- 112 Yang, G. J., Ko, C. N., Zhong, H. J., Leung, C. H. & Ma, D. L. Structure-based discovery of a selective KDM5A inhibitor that exhibits anti-cancer activity via inducing cell cycle arrest and senescence in breast cancer cell lines. *Cancers (Basel)* **11** (2019)
- 113 Oser, M. G., Sabet, A. H., Gao, W., Chakraborty, A. A., Schinzel, A. C., Jennings, R. B., Fonseca, R., Bonal, D. M., Booker, M. A., Flaifel, A., Novak, J. S., Christensen, C. L., Zhang, H., Herbert, Z. T., Tolstorukov, M. Y., Buss, E. J., Wong, K. K., Bronson, R. T., Nguyen, Q. D., Signoretti, S. & Kaelin, W. G., Jr. The KDM5A/RBP2 histone demethylase represses notch signaling to sustain neuroendocrine differentiation and promote small cell lung cancer tumorigenesis. *Genes Dev.* **33**, 1718-38 (2019)
- 114 Tumber, A., Nuzzi, A., Hookway, E. S., Hatch, S. B., Velupillai, S., Johansson, C., Kawamura, A., Savitsky, P., Yapp, C., Szykowska, A., Wu, N., Bountra, C., Strain-Damerell, C., Burgess-Brown, N. A., Ruda, G. F., Fedorov, O., Munro, S., England, K. S., Nowak, R. P., Schofield, C. J., La Thangue, N. B., Pawlyn, C., Davies, F., Morgan, G., Athanasou, N., Müller, S., Oppermann, U. & Brennan, P. E. Potent and selective KDM5 inhibitor stops cellular demethylation of H3K4me3 at transcription start sites and proliferation of MM1S myeloma cells. *Cell Chem. Biol.* **24**, 371-80 (2017)
- 115 Roesch, A., Mueller, A. M., Stempf, T., Moehle, C., Landthaler, M. & Vogt, T. RBP2-H1/JARID1B is a transcriptional regulator with a tumor suppressive potential in melanoma cells. *Int. J. Cancer* **122**, 1047-57 (2008)
- 116 Shen, H., Xu, W., Guo, R., Rong, B., Gu, L., Wang, Z., He, C., Zheng, L., Hu, X., Hu, Z., Shao, Z. M., Yang, P., Wu, F., Shi, Y. G., Shi, Y. & Lan, F. Suppression of enhancer overactivation by a RACK7-histone demethylase complex. *Cell* **165**, 331-42 (2016)
- 117 Rondinelli, B., Rosano, D., Antonini, E., Frenquelli, M., Montanini, L., Huang, D., Segalla, S., Yoshihara, K., Amin, S. B., Lazarevic, D., The, B. T., Verhaak, R. G., Futreal, P. A., Di Croce, L., Chin, L., Cittaro, D. & Tonon, G. Histone demethylase JARID1C inactivation triggers genomic instability in sporadic renal cancer. *J. Clin. Invest.* **125**, 4625-37 (2015)
- 118 Li, N., Dhar, S. S., Chen, T. Y., Kan, P. Y., Wei, Y., Kim, J. H., Chan, C. H., Lin, H. K., Hung, M. C. & Lee, M. G. JARID1D is a suppressor and prognostic marker of prostate cancer invasion and metastasis. *Cancer Res.* **76**, 831-43 (2016)
- 119 Ezponda, T., Dupéré-Richer, D., Will, C. M., Small, E. C., Varghese, N., Patel, T., Nabet, B., Popovic, R., Oyer, J., Bulic, M., Zheng, Y., Huang, X., Shah, M. Y., Maji, S., Riva, A., Occhionorelli, M., Tonon, G., Kelleher, N., Keats, J. & Licht, J. D.

- UTX/KDM6A loss enhances the malignant phenotype of multiple myeloma and sensitizes cells to EZH2 inhibition. *Cell Rep.* **21**, 628-40 (2017)
- 120 Ler, L. D., Ghosh, S., Chai, X., Thike, A. A., Heng, H. L., Siew, E. Y., Dey, S., Koh, L. K., Lim, J. Q., Lim, W. K., Myint, S. S., Loh, J. L., Ong, P., Sam, X. X., Huang, D., Lim, T., Tan, P. H., Nagarajan, S., Cheng, C. W., Ho, H., Ng, L. G., Yuen, J., Lin, P. H., Chuang, C. K., Chang, Y. H., Weng, W. H., Rozen, S. G., Tan, P., Creasy, C. L., Pang, S. T., McCabe, M. T., Poon, S. L. & Teh, B. T. Loss of tumor suppressor KDM6A amplifies PRC2-regulated transcriptional repression in bladder cancer and can be targeted through inhibition of EZH2. *Sci. Transl. Med.* **9** (2017)
- 121 Wu, Q., Tian, Y., Zhang, J., Tong, X., Huang, H., Li, S., Zhao, H., Tang, Y., Yuan, C., Wang, K., Fang, Z., Gao, L., Hu, X., Li, F., Qin, Z., Yao, S., Chen, T., Chen, H., Zhang, G., Liu, W., Sun, Y., Chen, L., Wong, K. K., Ge, K., Chen, L. & Ji, H. In vivo CRISPR screening unveils histone demethylase UTX as an important epigenetic regulator in lung tumorigenesis. *Proc. Natl. Acad. Sci. U. S. A.* **115**, e3978-e86 (2018)
- 122 Yang, L., Zha, Y., Ding, J., Ye, B., Liu, M., Yan, C., Dong, Z., Cui, H. & Ding, H.-F. Histone demethylase KDM6B has an anti-tumorigenic function in neuroblastoma by promoting differentiation. *Oncogenesis* **8**, 3 (2019)
- 123 Cheng, Y., He, C., Wang, M., Ma, X., Mo, F., Yang, S., Han, J. & Wei, X. Targeting epigenetic regulators for cancer therapy: Mechanisms and advances in clinical trials. *Sig. Transduct. Target. Ther.* **4**, 62 (2019)
- 124 Lee, K. H., Hong, S., Kang, M., Jeong, C. W., Ku, J. H., Kim, H. H. & Kwak, C. Histone demethylase KDM7A controls androgen receptor activity and tumor growth in prostate cancer. *Int. J. Cancer* **143**, 2849-61 (2018)
- 125 Mallm, J. P., Windisch, P., Biran, A., Gal, Z., Schumacher, S., Glass, R., Herold-Mende, C., Meshorer, E., Barbus, M. & Rippe, K. Glioblastoma initiating cells are sensitive to histone demethylase inhibition due to epigenetic deregulation. *Int. J. Cancer* **146**, 1281-92 (2020)
- 126 Zhu, G., Liu, L., She, L., Tan, H., Wei, M., Chen, C., Su, Z., Huang, D., Tian, Y., Qiu, Y., Liu, Y. & Zhang, X. Elevated expression of histone demethylase PHF8 associates with adverse prognosis in patients of laryngeal and hypopharyngeal squamous cell carcinoma. *Epigenomics* **7**, 143-53 (2015)
- 127 Pappa, S., Padilla, N., Iacobucci, S., Vicioso, M., Álvarez De La Campa, E., Navarro, C., Marcos, E., De La Cruz, X. & Martínez-Balbás, M. A. PHF2 histone demethylase prevents DNA damage and genome instability by controlling cell cycle progression of neural progenitors. *Proc. Natl. Acad. Sci. U. S. A.* **116**, 19464-73 (2019)
- 128 Lee, K. H., Park, J. W., Sung, H. S., Choi, Y. J., Kim, W. H., Lee, H. S., Chung, H. J., Shin, H. W., Cho, C. H., Kim, T. Y., Li, S. H., Youn, H. D., Kim, S. J. & Chun, Y. S.

- PHF2 histone demethylase acts as a tumor suppressor in association with p53 in cancer. *Oncogene* **34**, 2897-909 (2015)
- 129 Hsia, D. A., Tepper, C. G., Pochampalli, M. R., Hsia, E. Y., Izumiya, C., Huerta, S. B., Wright, M. E., Chen, H. W., Kung, H. J. & Izumiya, Y. Kdm8, a H3K36me2 histone demethylase that acts in the cyclin A1 coding region to regulate cancer cell proliferation. *Proc. Natl. Acad. Sci. U. S. A.* **107**, 9671-6 (2010)
- 130 Youn, M. Y., Yokoyama, A., Fujiyama-Nakamura, S., Ohtake, F., Minehata, K., Yasuda, H., Suzuki, T., Kato, S. & Imai, Y. JMJD5, a jumonji c (JmjC) domain-containing protein, negatively regulates osteoclastogenesis by facilitating NFATC1 protein degradation. *J. Biol. Chem.* **287**, 12994-3004 (2012)
- 131 Del Rizzo, P. A., Krishnan, S. & Trievel, R. C. Crystal structure and functional analysis of JMJD5 indicate an alternate specificity and function. *Mol. Cell Biol.* **32**, 4044-52 (2012)
- 132 Wang, H., Zhou, X., Wu, M., Wang, C., Zhang, X., Tao, Y., Chen, N. & Zang, J. Structure of the JmjC-domain-containing protein JMJD5. *Acta Crystallogr. D Biol. Crystallogr.* **69**, 1911-20 (2013)
- 133 Liu, H., Wang, C., Lee, S., Deng, Y., Wither, M., Oh, S., Ning, F., Dege, C., Zhang, Q., Liu, X., Johnson, A. M., Zang, J., Chen, Z., Janknecht, R., Hansen, K., Marrack, P., Li, C. Y., Kappler, J. W., Hagman, J. & Zhang, G. Clipping of arginine-methylated histone tails by JMJD5 and JMJD7. *Proc. Natl. Acad. Sci. U. S. A.* **114**, E7717-e26 (2017)
- 134 Shen, J., Xiang, X., Chen, L., Wang, H., Wu, L., Sun, Y., Ma, L., Gu, X., Liu, H., Wang, L., Yu, Y. N., Shao, J., Huang, C. & Chin, Y. E. JMJD5 cleaves monomethylated histone H3 n-tail under DNA damaging stress. *EMBO Rep.* **18**, 2131-43 (2017)
- 135 Wilkins, S. E., Islam, M. S., Gannon, J. M., Markolovic, S., Hopkinson, R. J., Ge, W., Schofield, C. J. & Chowdhury, R. JMJD5 is a human arginyl C-3 hydroxylase. *Nat. Comm.* **9**, 1180 (2018)
- 136 Harris, W. J., Huang, X., Lynch, J. T., Spencer, G. J., Hitchin, J. R., Li, Y., Ciceri, F., Blaser, J. G., Greystoke, B. F., Jordan, A. M., Miller, C. J., Ogilvie, D. J. & Somerville, T. C. P. The histone demethylase KDM1A sustains the oncogenic potential of MLL-AF9 leukemia stem cells. *Cancer Cell* **21**, 473-87 (2012)
- 137 Saccà, C. D., Gorini, F., Ambrosio, S., Amente, S., Faicchia, D., Matarese, G., Lania, L. & Majello, B. Inhibition of lysine-specific demethylase LSD1 induces senescence in glioblastoma cells through a HIF-1 α -dependent pathway. *Biochim. Biophys. Acta. Gene Regul. Mech.* **1862**, 535-46 (2019)

- 138 Liu, C., Liu, L., Chen, X., Cheng, J., Zhang, H., Zhang, C., Shan, J., Shen, J. & Qian, C. LSD1 stimulates cancer-associated fibroblasts to drive NOTCH3-dependent self-renewal of liver cancer stem-like cells. *Cancer Res.* **78**, 938-49 (2018)
- 139 Hayami, S., Kelly, J. D., Cho, H.-S., Yoshimatsu, M., Unoki, M., Tsunoda, T., Field, H. I., Neal, D. E., Yamaue, H., Ponder, B. a. J., Nakamura, Y. & Hamamoto, R. Overexpression of LSD1 contributes to human carcinogenesis through chromatin regulation in various cancers. *Int. J. Cancer* **128**, 574-86 (2011)
- 140 Augert, A., Eastwood, E., Ibrahim, A. H., Wu, N., Grunblatt, E., Basom, R., Liggitt, D., Eaton, K. D., Martins, R., Poirier, J. T., Rudin, C. M., Milletti, F., Cheng, W.-Y., Mack, F. & Macpherson, D. Targeting NOTCH activation in small cell lung cancer through LSD1 inhibition. *Sci. Signal.* **12**, eaau2922 (2019)
- 141 Wagner, K. W., Alam, H., Dhar, S. S., Giri, U., Li, N., Wei, Y., Giri, D., Cascone, T., Kim, J.-H., Ye, Y., Multani, A. S., Chan, C.-H., Erez, B., Saigal, B., Chung, J., Lin, H.-K., Wu, X., Hung, M.-C., Heymach, J. V. & Lee, M. G. KDM2A promotes lung tumorigenesis by epigenetically enhancing ERK1/2 signaling. *J. Clin. Invest.* **123**, 5231-46 (2013)
- 142 Staberg, M., Rasmussen, R. D., Michaelsen, S. R., Pedersen, H., Jensen, K. E., Villingshøj, M., Skjoth-Rasmussen, J., Brennum, J., Vitting-Seerup, K., Poulsen, H. S. & Hamerlik, P. Targeting glioma stem-like cell survival and chemoresistance through inhibition of lysine-specific histone demethylase KDM2B. *Mol. Oncol.* **12**, 406-20 (2018)
- 143 He, J., Nguyen, A. T. & Zhang, Y. Kdm2b/jhdm1b, an H3K36me2-specific demethylase, is required for initiation and maintenance of acute myeloid leukemia. *Blood* **117**, 3869-80 (2011)
- 144 Peng, K., Su, G., Ji, J., Yang, X., Miao, M., Mo, P., Li, M., Xu, J., Li, W. & Yu, C. Histone demethylase JMJD1A promotes colorectal cancer growth and metastasis by enhancing WNT/ β -catenin signaling. *J. Biol. Chem.* **293**, 10606-19 (2018)
- 145 Fan, L., Zhang, F., Xu, S., Cui, X., Hussain, A., Fazli, L., Gleave, M., Dong, X. & Qi, J. Histone demethylase JMJD1A promotes alternative splicing of AR variant 7 (AR-V7) in prostate cancer cells. *Proc. Nat. Acad. Sci. U.S.A* **115**, E4584-E93 (2018)
- 146 Dalvi, M. P., Wang, L., Zhong, R., Kollipara, R. K., Park, H., Bayo, J., Yenerall, P., Zhou, Y., Timmons, B. C., Rodriguez-Canales, J., Behrens, C., Mino, B., Villalobos, P., Parra, E. R., Suraokar, M., Pataer, A., Swisher, S. G., Kalhor, N., Bhanu, N. V., Garcia, B. A., Heymach, J. V., Coombes, K., Xie, Y., Girard, L., Gazdar, A. F., Kittler, R., Wistuba, Ii, Minna, J. D. & Martinez, E. D. Taxane-platin-resistant lung cancers co-develop hypersensitivity to jumonjiC demethylase inhibitors. *Cell Rep.* **19**, 1669-84 (2017)

- 147 Agger, K., Miyagi, S., Pedersen, M. T., Kooistra, S. M., Johansen, J. V. & Helin, K. JMJD2/KDM4 demethylases are required for expression of IL3RA and survival of acute myeloid leukemia cells. *Genes Dev.* **30**, 1278-88 (2016)
- 148 Metzger, E., Stepputtis, S. S., Strietz, J., Preca, B.-T., Urban, S., Willmann, D., Allen, A., Zenk, F., Iovino, N., Bronsert, P., Proske, A., Follo, M., Boerries, M., Stickeler, E., Xu, J., Wallace, M. B., Stafford, J. A., Kanouni, T., Maurer, J. & Schüle, R. KDM4 inhibition targets breast cancer stem-like cells. *Cancer Res.* **77**, 5900-12 (2017)
- 149 Wu, M.-C., Cheng, H.-H., Yeh, T.-S., Li, Y.-C., Chen, T.-J., Sit, W. Y., Chuu, C.-P., Kung, H.-J., Chien, S. & Wang, W.-C. KDM4B is a coactivator of c-JUN and involved in gastric carcinogenesis. *Cell Death Dis.* **10**, 68 (2019)
- 150 Chen, Y., Fang, R., Yue, C., Chang, G., Li, P., Guo, Q., Wang, J., Zhou, A., Zhang, S., Fuller, G. N., Shi, X. & Huang, S. Wnt-induced stabilization of KDM4C is required for wnt/ β -catenin target gene expression and glioblastoma tumorigenesis. *Cancer Res.* **80**, 1049-63 (2020)
- 151 Lin, C.-Y., Wang, B.-J., Chen, B.-C., Tseng, J.-C., Jiang, S. S., Tsai, K. K., Shen, Y.-Y., Yuh, C. H., Sie, Z.-L., Wang, W.-C., Kung, H.-J. & Chuu, C.-P. Histone demethylase KDM4C stimulates the proliferation of prostate cancer cells via activation of AKT and c-MYC. *Cancers (Basel)* **11**, 1785 (2019)
- 152 Yang, G.-J., Ko, C.-N., Zhong, H.-J., Leung, C.-H. & Ma, D.-L. Structure-based discovery of a selective KDM5A inhibitor that exhibits anti-cancer activity via inducing cell cycle arrest and senescence in breast cancer cell lines. *Cancers (Basel)* **11**, 92 (2019)
- 153 Sharma, S. V., Lee, D. Y., Li, B., Quinlan, M. P., Takahashi, F., Maheswaran, S., McDermott, U., Azizian, N., Zou, L., Fischbach, M. A., Wong, K. K., Brandstetter, K., Wittner, B., Ramaswamy, S., Classon, M. & Settleman, J. A chromatin-mediated reversible drug-tolerant state in cancer cell subpopulations. *Cell* **141**, 69-80 (2010)
- 154 Vinogradova, M., Gehling, V. S., Gustafson, A., Arora, S., Tindell, C. A., Wilson, C., Williamson, K. E., Guler, G. D., Gangurde, P., Manieri, W., Busby, J., Flynn, E. M., Lan, F., Kim, H. J., Odate, S., Cochran, A. G., Liu, Y., Wongchenko, M., Yang, Y., Cheung, T. K., Maile, T. M., Lau, T., Costa, M., Hegde, G. V., Jackson, E., Pitti, R., Arnott, D., Bailey, C., Bellon, S., Cummings, R. T., Albrecht, B. K., Harmange, J. C., Kiefer, J. R., Trojer, P. & Classon, M. An inhibitor of KDM5 demethylases reduces survival of drug-tolerant cancer cells. *Nat. Chem. Biol.* **12**, 531-8 (2016)
- 155 Banelli, B., Carra, E., Barbieri, F., Würth, R., Parodi, F., Pattarozzi, A., Carosio, R., Forlani, A., Allemanni, G., Marubbi, D., Florio, T., Daga, A. & Romani, M. The histone demethylase KDM5A is a key factor for the resistance to temozolomide in glioblastoma. *Cell Cycle* **14**, 3418-29 (2015)

- 156 Wong, S. H., Goode, D. L., Iwasaki, M., Wei, M. C., Kuo, H. P., Zhu, L., Schneidawind, D., Duque-Afonso, J., Weng, Z. & Cleary, M. L. The H3K4-methyl epigenome regulates leukemia stem cell oncogenic potential. *Cancer Cell* **28**, 198-209 (2015)
- 157 Roesch, A., Mueller, A. M., Stempf, T., Moehle, C., Landthaler, M. & Vogt, T. Rbp2-H1/JARID1B is a transcriptional regulator with a tumor suppressive potential in melanoma cells. *Int. J. Cancer* **122**, 1047-57 (2008)
- 158 Roesch, A., Vultur, A., Bogeski, I., Wang, H., Zimmermann, K. M., Speicher, D., Korbel, C., Laschke, M. W., Gimotty, P. A., Philipp, S. E., Krause, E., Patzold, S., Villanueva, J., Krepler, C., Fukunaga-Kalabis, M., Hoth, M., Bastian, B. C., Vogt, T. & Herlyn, M. Overcoming intrinsic multidrug resistance in melanoma by blocking the mitochondrial respiratory chain of slow-cycling JARID1B(high) cells. *Cancer Cell* **23**, 811-25 (2013)
- 159 Liu, X., Zhang, S.-M., Mcgeary, M. K., Krykbaeva, I., Lai, L., Jansen, D. J., Kales, S. C., Simeonov, A., Hall, M. D., Kelly, D. P., Bosenberg, M. W. & Yan, Q. KDM5B promotes drug resistance by regulating melanoma-propagating cell subpopulations. *Mol. Cancer Ther.* **18**, 706-17 (2019)
- 160 Shen, H., Xu, W., Guo, R., Rong, B., Gu, L., Wang, Z., He, C., Zheng, L., Hu, X., Hu, Z., Shao, Z.-M., Yang, P., Wu, F., Shi, Y. G., Shi, Y. & Lan, F. Suppression of enhancer overactivation by a RACK7-histone demethylase complex. *Cell* **165**, 331-42 (2016)
- 161 Rondinelli, B., Rosano, D., Antonini, E., Frenquelli, M., Montanini, L., Huang, D., Segalla, S., Yoshihara, K., Amin, S. B., Lazarevic, D., The, B. T., Verhaak, R. G., Futreal, P. A., Di Croce, L., Chin, L., Cittaro, D. & Tonon, G. Histone demethylase JARID1C inactivation triggers genomic instability in sporadic renal cancer. *J. Clin. Invest.* **125**, 4625-37 (2015)
- 162 Li, N., Dhar, S. S., Chen, T. Y., Kan, P. Y., Wei, Y., Kim, J. H., Chan, C. H., Lin, H. K., Hung, M. C. & Lee, M. G. JARID1D is a suppressor and prognostic marker of prostate cancer invasion and metastasis. *Cancer Res.* **76**, 831-43 (2016)
- 163 Arseneault, M., Monlong, J., Vasudev, N. S., Laskar, R. S., Safisamghabadi, M., Harnden, P., Egevad, L., Nourbehesht, N., Panichnantakul, P., Holcatova, I., Brisuda, A., Janout, V., Kollarova, H., Foretova, L., Navratilova, M., Mates, D., Jinga, V., Zaridze, D., Mukeria, A., Jandaghi, P., Brennan, P., Brazma, A., Tost, J., Scelo, G., Banks, R. E., Lathrop, M., Bourque, G. & Riazalhosseini, Y. Loss of chromosome Y leads to down regulation of KDM5D and KDM6C epigenetic modifiers in clear cell renal cell carcinoma. *Sci. Rep.* **7**, 44876 (2017)
- 164 Kim, J.-H., Sharma, A., Dhar, S. S., Lee, S.-H., Gu, B., Chan, C.-H., Lin, H.-K. & Lee, M. G. UTX and MLL4 coordinately regulate transcriptional programs for cell proliferation and invasiveness in breast cancer cells. *Cancer Res.* **74**, 1705-17 (2014)

- 165 Watanabe, S., Shimada, S., Akiyama, Y., Ishikawa, Y., Ogura, T., Ogawa, K., Ono, H., Mitsunori, Y., Ban, D., Kudo, A., Yamaoka, S., Tanabe, M. & Tanaka, S. Loss of KDM6A characterizes a poor prognostic subtype of human pancreatic cancer and potentiates HDAC inhibitor lethality. *Int. J. Cancer* **145**, 192-205 (2019)
- 166 Van Der Meulen, J., Sanghvi, V., Mavrakis, K., Durinck, K., Fang, F., Matthijssens, F., Rondou, P., Rosen, M., Pieters, T., Vandenberghe, P., Delabesse, E., Lammens, T., De Moerloose, B., Menten, B., Van Roy, N., Verhasselt, B., Poppe, B., Benoit, Y., Taghon, T., Melnick, A. M., Speleman, F., Wendel, H. G. & Van Vlierberghe, P. The H3K27me3 demethylase UTX is a gender-specific tumor suppressor in T-cell acute lymphoblastic leukemia. *Blood* **125**, 13-21 (2015)
- 167 Andricovich, J., Perkail, S., Kai, Y., Casasanta, N., Peng, W. & Tzatsos, A. Loss of KDM6A activates super-enhancers to induce gender-specific squamous-like pancreatic cancer and confers sensitivity to bet inhibitors. *Cancer Cell* **33**, 512-26 (2018)
- 168 Gozdecka, M., Meduri, E., Mazan, M., Tzelepis, K., Dudek, M., Knights, A. J., Pardo, M., Yu, L., Choudhary, J. S., Metzakopian, E., Iyer, V., Yun, H., Park, N., Varela, I., Bautista, R., Collord, G., Dovey, O., Garyfallos, D. A., De Braekeleer, E., Kondo, S., Cooper, J., Göttgens, B., Bullinger, L., Northcott, P. A., Adams, D., Vassiliou, G. S. & Huntly, B. J. P. UTX-mediated enhancer and chromatin remodeling suppresses myeloid leukemogenesis through noncatalytic inverse regulation of ETS and GATA programs. *Nat. Genet.* **50**, 883-94 (2018)
- 169 Liao, B. B., Sievers, C., Donohue, L. K., Gillespie, S. M., Flavahan, W. A., Miller, T. E., Venteicher, A. S., Herbert, C. H., Carey, C. D., Rodig, S. J., Shareef, S. J., Najm, F. J., Van Galen, P., Wakimoto, H., Cahill, D. P., Rich, J. N., Aster, J. C., Suvà, M. L., Patel, A. P. & Bernstein, B. E. Adaptive chromatin remodeling drives glioblastoma stem cell plasticity and drug tolerance. *Cell Stem Cell* **20**, 233-46 (2017)
- 170 Yang, L., Zha, Y., Ding, J., Ye, B., Liu, M., Yan, C., Dong, Z., Cui, H. & Ding, H. F. Histone demethylase KDM6B has an anti-tumorigenic function in neuroblastoma by promoting differentiation. *Oncogenesis* **8**, 3 (2019)
- 171 Lee, K.-H., Hong, S., Kang, M., Jeong, C. W., Ku, J. H., Kim, H.-H. & Kwak, C. Histone demethylase KDM7A controls androgen receptor activity and tumor growth in prostate cancer. *Int. J. Cancer* **143**, 2849-61 (2018)
- 172 Mallm, J.-P., Windisch, P., Biran, A., Gal, Z., Schumacher, S., Glass, R., Herold-Mende, C., Meshorer, E., Barbus, M. & Rippe, K. Glioblastoma initiating cells are sensitive to histone demethylase inhibition due to epigenetic deregulation. *Int. J. Cancer* **146**, 1281-92 (2020)
- 173 Zhu, G., Liu, L., She, L., Tan, H., Wei, M., Chen, C., Su, Z., Huang, D., Tian, Y., Qiu, Y., Liu, Y. & Zhang, X. Elevated expression of histone demethylase PHF8 associates with adverse prognosis in patients of laryngeal and hypopharyngeal squamous cell carcinoma. *Epigenomics* **7**, 143-53 (2015)

- 174 Pappa, S., Padilla, N., Iacobucci, S., Vicioso, M., Campa, E. Á. D. L., Navarro, C., Marcos, E., Cruz, X. D. L. & Martínez-Balbás, M. A. PHF2 histone demethylase prevents DNA damage and genome instability by controlling cell cycle progression of neural progenitors. *Proc. Nat. Acad. Sci. U.S.A.* **116**, 19464-73 (2019)
- 175 Lee, K. H., Park, J. W., Sung, H. S., Choi, Y. J., Kim, W. H., Lee, H. S., Chung, H. J., Shin, H. W., Cho, C. H., Kim, T. Y., Li, S. H., Youn, H. D., Kim, S. J. & Chun, Y. S. PHF2 histone demethylase acts as a tumor suppressor in association with p53 in cancer. *Oncogene* **34**, 2897-909 (2015)
- 176 Hsia, D. A., Tepper, C. G., Pochampalli, M. R., Hsia, E. Y. C., Izumiya, C., Huerta, S. B., Wright, M. E., Chen, H.-W., Kung, H.-J. & Izumiya, Y. KDM8, a H3K36me2 histone demethylase that acts in the cyclin A1 coding region to regulate cancer cell proliferation. *Proc. Nat. Acad. Sci. U.S.A.* **107**, 9671-6 (2010)
- 177 Zhao, Z., Sun, C., Li, F., Han, J., Li, X. & Song, Z. Overexpression of histone demethylase JMJD5 promotes metastasis and indicates a poor prognosis in breast cancer. *Int. J. Clin. Exp. Path.* **8**, 10325-34 (2015)
- 178 Wang, H.-J., Pochampalli, M., Wang, L.-Y., Zou, J. X., Li, P.-S., Hsu, S.-C., Wang, B.-J., Huang, S.-H., Yang, P., Yang, J. C., Chu, C.-Y., Hsieh, C.-L., Sung, S.-Y., Li, C.-F., Tepper, C. G., Ann, D. K., Gao, A. C., Evans, C. P., Izumiya, Y., Chuu, C.-P., Wang, W.-C., Chen, H.-W. & Kung, H.-J. KDM8/JMJD5 as a dual coactivator of ar and PKM2 integrates AR/EZH2 network and tumor metabolism in CRPC. *Oncogene* **38**, 17-32 (2019)
- 179 Hughes, J. P., Rees, S., Kalindjian, S. B. & Philpott, K. L. Principles of early drug discovery. *Br. J. Pharmacol.* **162**, 1239-49 (2011)
- 180 Manchado, E., Huang, C. H., Tasdemir, N., Tschaharganeh, D. F., Wilkinson, J. E. & Lowe, S. W. A pipeline for drug target identification and validation. *Cold Spring Harb. Symp. Quant. Biol.* **81**, 257-67 (2016)
- 181 Swinney, D. C. Phenotypic vs. Target-based drug discovery for first-in-class medicines. *Clin. Pharmacol. Ther.* **93**, 299-301 (2013)
- 182 Sadri, A. Is target-based drug discovery efficient? Discovery and “off-target” mechanisms of all drugs. *J. Med. Chem.* **66**, 12651-77 (2023)
- 183 Zheng, W., Thorne, N. & Mckew, J. C. Phenotypic screens as a renewed approach for drug discovery. *Drug Discov. Today* **18**, 1067-73 (2013)
- 184 Yang, Y., Adelstein, S. J. & Kassis, A. I. Target discovery from data mining approaches. *Drug Discov. Today* **14**, 147-54 (2009)

- 185 Salame, N., Fooks, K., El-Hachem, N., Bikorimana, J.-P., Mercier, F. E. & Rafei, M. Recent advances in cancer drug discovery through the use of phenotypic reporter systems, connectivity mapping, and pooled CRISPR screening. *Front. Pharmacol.* **13** (2022)
- 186 Hart, T., Chandrashekhar, M., Aregger, M., Steinhart, Z., Brown, Kevin r., Macleod, G., Mis, M., Zimmermann, M., Fradet-Turcotte, A., Sun, S., Mero, P., Dirks, P., Sidhu, S., Roth, Frederick p., Rissland, Olivia s., Durocher, D., Angers, S. & Moffat, J. High-resolution CRISPR screens reveal fitness genes and genotype-specific cancer liabilities. *Cell* **163**, 1515-26 (2015)
- 187 Chanchal, D. K., Chaudhary, J. S., Kumar, P., Agnihotri, N. & Porwal, P. CRISPR-based therapies: Revolutionizing drug development and precision medicine. *Curr. Gene Ther.* (2024)
- 188 Kampmann, M., Bassik, M. C. & Weissman, J. S. Integrated platform for genome-wide screening and construction of high-density genetic interaction maps in mammalian cells. *Proc. Nat. Acad. Sci. U.S.A.* **110**, E2317-E26 (2013)
- 189 Wu, F., Zhou, Y., Li, L., Shen, X., Chen, G., Wang, X., Liang, X., Tan, M. & Huang, Z. Computational approaches in preclinical studies on drug discovery and development. *Front Chem* **8**, 726 (2020)
- 190 Jorgensen, W. L. Efficient drug lead discovery and optimization. *Acc. Chem. Res.* **42**, 724-33 (2009)
- 191 Al-Awadhi, F. H., Gao, B., Rezaei, M. A., Kwan, J. C., Li, C., Ye, T., Paul, V. J. & Luesch, H. Discovery, synthesis, pharmacological profiling, and biological characterization of brintonamides A-E, novel dual protease and GPCR modulators from a marine cyanobacterium. *J. Med. Chem.* **61**, 6364-78 (2018)
- 192 Galloway, W. R. J. D., Isidro-Llobet, A. & Spring, D. R. Diversity-oriented synthesis as a tool for the discovery of novel biologically active small molecules. *Nat. Comm.* **1**, 80 (2010)
- 193 Harris, C. J., Hill, R. D., Sheppard, D. W., Slater, M. J. & Stouten, P. F. The design and application of target-focused compound libraries. *Comb. Chem. High Throughput Screen.* **14**, 521-31 (2011)
- 194 Wassermann, A. M., Camargo, L. M. & Auld, D. S. Composition and applications of focus libraries to phenotypic assays. *Front. Pharmacol.* **5** (2014)
- 195 Wilson, B. a. P., Thornburg, C. C., Henrich, C. J., Grkovic, T. & O'keefe, B. R. Creating and screening natural product libraries. *Nat. Prod. Rep.* **37**, 893-918 (2020)
- 196 Atanasov, A. G., Zotchev, S. B., Dirsch, V. M., Orhan, I. E., Banach, M., Rollinger, J. M., Barreca, D., Weckwerth, W., Bauer, R., Bayer, E. A., Majeed, M., Bishayee, A.,

- Bochkov, V., Bonn, G. K., Braidy, N., Bucar, F., Cifuentes, A., D'onofrio, G., Bodkin, M., Diederich, M., Dinkova-Kostova, A. T., Efferth, T., El Bairi, K., Arkells, N., Fan, T.-P., Fiebich, B. L., Freissmuth, M., Georgiev, M. I., Gibbons, S., Godfrey, K. M., Gruber, C. W., Heer, J., Huber, L. A., Ibanez, E., Kijjoo, A., Kiss, A. K., Lu, A., Macias, F. A., Miller, M. J. S., Mocan, A., Müller, R., Nicoletti, F., Perry, G., Pittalà, V., Rastrelli, L., Ristow, M., Russo, G. L., Silva, A. S., Schuster, D., Sheridan, H., Skalicka-Woźniak, K., Skaltsounis, L., Sobarzo-Sánchez, E., Bredt, D. S., Stuppner, H., Sureda, A., Tzvetkov, N. T., Vacca, R. A., Aggarwal, B. B., Battino, M., Giampieri, F., Wink, M., Wolfender, J.-L., Xiao, J., Yeung, A. W. K., Lizard, G., Popp, M. A., Heinrich, M., Berindan-Neagoe, I., Stadler, M., Daglia, M., Verpoorte, R., Supuran, C. T. & The International Natural Product Sciences, T. Natural products in drug discovery: Advances and opportunities. *Nat. Rev. Drug Discov.* **20**, 200-16 (2021)
- 197 Carbery, A., Skyner, R., Von Delft, F. & Deane, C. M. Fragment libraries designed to be functionally diverse recover protein binding information more efficiently than standard structurally diverse libraries. *J. Med. Chem.* **65**, 11404-13 (2022)
- 198 Li, Q. Application of fragment-based drug discovery to versatile targets. *Front. Mol. Biosci.* **7** (2020)
- 199 Corsello, S. M., Bittker, J. A., Liu, Z., Gould, J., Mccarren, P., Hirschman, J. E., Johnston, S. E., Vrcic, A., Wong, B., Khan, M., Asiedu, J., Narayan, R., Mader, C. C., Subramanian, A. & Golub, T. R. The drug repurposing hub: A next-generation drug library and information resource. *Nat. Med.* **23**, 405-8 (2017)
- 200 Begley, C. G., Ashton, M., Baell, J., Bettess, M., Brown, M. P., Carter, B., Charman, W. N., Davis, C., Fisher, S., Frazer, I., Gautam, A., Jennings, M. P., Kearney, P., Keeffe, E., Kelly, D., Lopez, A. F., MCGuckin, M., Parker, M. W., Rayner, C., Roberts, B., Rush, J. S. & Sullivan, M. Drug repurposing: Misconceptions, challenges, and opportunities for academic researchers. *Sci. Transl. Med.* **13**, eabd5524 (2021)
- 201 Miller, F. G. & Dickert, N. W. The limits and hazards of clinical equipoise on cardiology study design and conduct. *JAMA Cardiol.* **3**, 791-2 (2018)
- 202 Hughes, R. E., Elliott, R. J. R., Dawson, J. C. & Carragher, N. O. High-content phenotypic and pathway profiling to advance drug discovery in diseases of unmet need. *Cell Chem. Biol.* **28**, 338-55 (2021)
- 203 Vincent, F., Nueda, A., Lee, J., Schenone, M., Prunotto, M. & Mercola, M. Phenotypic drug discovery: Recent successes, lessons learned and new directions. *Nat. Rev. Drug Discov.* **21**, 899-914 (2022)
- 204 Priest, B. T. & Erdemli, G. Phenotypic screening in the 21st century. *Front. Pharmacol.* **5** (2014)
- 205 Antolin, A. A., Sanfelice, D., Crisp, A., Villasclaras fernandez, E., Mica, I. L., Chen, Y., Collins, I., Edwards, A., Müller, S., Al-Lazikani, B. & Workman, P. The chemical

- probes portal: An expert review-based public resource to empower chemical probe assessment, selection and use. *Nucleic Acids Res.* **51**, D1492-D502 (2023)
- 206 Arrowsmith, C. H., Audia, J. E., Austin, C., Baell, J., Bennett, J., Blagg, J., Bountra, C., Brennan, P. E., Brown, P. J., Bunnage, M. E., Buser-Doepner, C., Campbell, R. M., Carter, A. J., Cohen, P., Copeland, R. A., Cravatt, B., Dahlin, J. L., Dhanak, D., Edwards, A. M., Frederiksen, M., Frye, S. V., Gray, N., Grimshaw, C. E., Hepworth, D., Howe, T., Huber, K. V. M., Jin, J., Knapp, S., Kotz, J. D., Kruger, R. G., Lowe, D., Mader, M. M., Marsden, B., Mueller-Fahrnow, A., Müller, S., O'hagan, R. C., Overington, J. P., Owen, D. R., Rosenberg, S. H., Ross, R., Roth, B., Schapira, M., Schreiber, S. L., Shoichet, B., Sundström, M., Superti-Furga, G., Taunton, J., Toledo-Sherman, L., Walpole, C., Walters, M. A., Willson, T. M., Workman, P., Young, R. N. & Zuercher, W. J. The promise and peril of chemical probes. *Nat. Chem. Biol.* **11**, 536-41 (2015)
- 207 Blagg, J. & Workman, P. Choose and use your chemical probe wisely to explore cancer biology. *Cancer Cell* **32**, 9-25 (2017)
- 208 Mader, M. M., Rudolph, J., Hartung, I. V., Uehling, D., Workman, P. & Zuercher, W. Which small molecule? Selecting chemical probes for use in cancer research and target validation. *Cancer Discov.* **13**, 2150-65 (2023)
- 209 Chen, Y. K., Bonaldi, T., Cuomo, A., Del Rosario, J. R., Hosfield, D. J., Kanouni, T., Kao, S. C., Lai, C., Lobo, N. A., Matuszkiewicz, J., Mcgeehan, A., O'connell, S. M., Shi, L., Stafford, J. A., Stansfield, R. K., Veal, J. M., Weiss, M. S., Yuen, N. Y. & Wallace, M. B. Design of KDM4 inhibitors with antiproliferative effects in cancer models. *ACS Med. Chem. Lett.* **8**, 869-74 (2017)
- 210 Metzger, E., Stepputtis, S. S., Strietz, J., Preca, B. T., Urban, S., Willmann, D., Allen, A., Zenk, F., Iovino, N., Bronsert, P., Proske, A., Follo, M., Boerries, M., Stickeler, E., Xu, J., Wallace, M. B., Stafford, J. A., Kanouni, T., Maurer, J. & Schule, R. KDM4 inhibition targets breast cancer stem-like cells. *Cancer Res.* **77**, 5900-12 (2017)
- 211 Shapovalov, V., Kopanitsa, L., Pruteanu, L. L., Ladds, G. & Bailey, D. S. Transcriptomics-based phenotypic screening supports drug discovery in human glioblastoma cells. *Cancers (Basel)* **13** (2021)
- 212 Hoque, M., Abbassi, R. H., Froio, D., Man, J., Johns, T. G., Stringer, B. W., Day, B. W., Pajic, M., Kassiou, M. & Munoz, L. Changes in cell morphology guide identification of tubulin as the off-target for protein kinase inhibitors. *Pharmacol. Res.* **134**, 166-78 (2018)
- 213 Stringer, B. W., Day, B. W., D'souza, R. C. J., Jamieson, P. R., Ensbey, K. S., Bruce, Z. C., Lim, Y. C., Goasdoue, K., Offenhauser, C., Akgul, S., Allan, S., Robertson, T., Lucas, P., Tolleson, G., Campbell, S., Winter, C., Do, H., Dobrovic, A., Inglis, P. L., Jeffree, R. L., Johns, T. G. & Boyd, A. W. A reference collection of patient-derived cell line and xenograft models of proneural, classical and mesenchymal glioblastoma. *Sci. Rep.* **9**, 4902 (2019)

- 214 Dempster, J. M., Boyle, I., Vazquez, F., Root, D. E., Boehm, J. S., Hahn, W. C., Tsherniak, A. & Mcfarland, J. M. Chronos: A cell population dynamics model of CRISPR experiments that improves inference of gene fitness effects. *Genome Biol.* **22**, 343 (2021)
- 215 Ritchie, M. E., Phipson, B., Wu, D., Hu, Y., Law, C. W., Shi, W. & Smyth, G. K. Limma powers differential expression analyses for RNA-sequencing and microarray studies. *Nucleic Acids Res.* **43**, e47 (2015)
- 216 Savitski, M. M., Reinhard, F. B. M., Franken, H., Werner, T., Savitski, M. F., Eberhard, D., Molina, D. M., Jafari, R., Dovega, R. B., Klaeger, S., Kuster, B., Nordlund, P., Bantscheff, M. & Drewes, G. Tracking cancer drugs in living cells by thermal profiling of the proteome. *Science* **346**, 1255784 (2014)
- 217 Emmerich, C. H., Gamboa, L. M., Hofmann, M. C. J., Bonin-Andresen, M., Arbach, O., Schendel, P., Gerlach, B., Hempel, K., Bernal, A., Dirnagl, U. & Parnham, M. J. Improving target assessment in biomedical research: The got-it recommendations. *Nat. Rev. Drug Discov.* **20**, 64-81 (2021)
- 218 Bunnage, M. E., Gilbert, A. M., Jones, L. H. & Hett, E. C. Know your target, know your molecule. *Nat. Chem. Biol.* **11**, 368-72 (2015)
- 219 Licciardello, M. P. & Workman, P. The era of high-quality chemical probes. *RSC Med. Chem.* **13**, 1446-59 (2022)
- 220 Lowe, D. *Chemical probes, used and misused*, 2023).
- 221 Mullard, A. Massive misuse of chemical probes undermines the utility of these tools. *Nat. Rev. Drug Discov.* **22**, 611 (2023)
- 222 Knapp, S. & Müller, S. Improving data quality in chemical biology. *Nat. Chem. Biol.* **19**, 1301-2 (2023)
- 223 Zhang, B., Long, Q., Wu, S., Xu, Q., Song, S., Han, L., Qian, M., Ren, X., Liu, H., Jiang, J., Guo, J., Zhang, X., Chang, X., Fu, Q., Lam, E. W., Campisi, J., Kirkland, J. L. & Sun, Y. KDM4 orchestrates epigenomic remodeling of senescent cells and potentiates the senescence-associated secretory phenotype. *Nat. Aging* **1**, 454-72 (2021)
- 224 Wu, M. C., Cheng, H. H., Yeh, T. S., Li, Y. C., Chen, T. J., Sit, W. Y., Chuu, C. P., Kung, H. J., Chien, S. & Wang, W. C. KDM4B is a coactivator of c-JUN and involved in gastric carcinogenesis. *Cell Death Dis.* **10**, 68 (2019)
- 225 Lin, C. Y., Wang, B. J., Chen, B. C., Tseng, J. C., Jiang, S. S., Tsai, K. K., Shen, Y. Y., Yuh, C. H., Sie, Z. L., Wang, W. C., Kung, H. J. & Chuu, C. P. Histone demethylase KDM4C stimulates the proliferation of prostate cancer cells via activation of AKT and c-MYC. *Cancers (Basel)* **11** (2019)

- 226 Wu, W., Cao, X. & Mo, L. Overexpression of KDM4D promotes acute myeloid leukemia cell development by activating MCL-1. *Am. J. Transl. Res.* **13**, 2308-19 (2021)
- 227 Lee, D. H., Kim, G. W., Jeon, Y. H., Yoo, J., Lee, S. W. & Kwon, S. H. Advances in histone demethylase KDM4 as cancer therapeutic targets. *FASEB J.* **34**, 3461-84 (2020)
- 228 Li, M., Cheng, J., Ma, Y., Guo, H., Shu, H., Huang, H., Kuang, Y. & Yang, T. The histone demethylase JMJD2A promotes glioma cell growth via targeting AKT-MTOR signaling. *Cancer Cell Int.* **20**, 101 (2020)
- 229 Wang, Z., Cai, H., Li, Z., Sun, W., Zhao, E. & Cui, H. Histone demethylase KDM4B accelerates the progression of glioblastoma via the epigenetic regulation of MYC stability. *Clin. Epigenetics* **15**, 192 (2023)
- 230 Lee, D. H., Kim, G. W., Yoo, J., Lee, S. W., Jeon, Y. H., Kim, S. Y., Kang, H. G., Kim, D. H., Chun, K. H., Choi, J. & Kwon, S. H. Histone demethylase KDM4C controls tumorigenesis of glioblastoma by epigenetically regulating p53 and c-MYC. *Cell Death Dis.* **12**, 89 (2021)
- 231 Khoury-Haddad, H., Guttmann-Raviv, N., Ipenberg, I., Huggins, D., Jeyasekharan, A. D. & Ayoub, N. PARP1-dependent recruitment of KDM4D histone demethylase to DNA damage sites promotes double-strand break repair. *Proc. Nat. Acad. Sci. U.S.A.* **111**, E728-E37 (2014)
- 232 Chin, Y. W. & Han, S. Y. KDM4 histone demethylase inhibitors for anti-cancer agents: A patent review. *Expert Opin. Ther. Pat.* **25**, 135-44 (2015)
- 233 Hopkinson, R. J., Tumber, A., Yapp, C., Chowdhury, R., Aik, W., Che, K. H., Li, X. S., Kristensen, J. B. L., King, O. N. F., Chan, M. C., Yeoh, K. K., Choi, H., Walport, L. J., Thinnis, C. C., Bush, J. T., Lejeune, C., Rydzik, A. M., Rose, N. R., Bagg, E. A., McDonough, M. A., Krojer, T. J., Yue, W. W., Ng, S. S., Olsen, L., Brennan, P. E., Oppermann, U., Müller, S., Klose, R. J., Ratcliffe, P. J., Schofield, C. J. & Kawamura, A. 5-carboxy-8-hydroxyquinoline is a broad spectrum 2-oxoglutarate oxygenase inhibitor which causes iron translocation. *Chem. Sci.* **4**, 3110-7 (2013)
- 234 Rai, G., Kawamura, A., Tumber, A., Liang, Y., Vogel, J. L., Arbuckle, J. H., Rose, N. R., Dexheimer, T. S., Foley, T. L., King, O. N., Quinn, A., Mott, B. T., Schofield, C. J., Oppermann, U., Jadhav, A., Simeonov, A., Kristie, T. M. & Maloney, D. J. *Probe reports from the nih molecular libraries program* (2010).
- 235 Kirkpatrick, J. E., Kirkwood, K. L. & Woster, P. M. Inhibition of the histone demethylase KDM4B leads to activation of KDM1A, attenuates bacterial-induced pro-inflammatory cytokine release, and reduces osteoclastogenesis. *Epigenetics* **13**, 557-72 (2018)

- 236 Duan, L., Rai, G., Roggero, C., Zhang, Q. J., Wei, Q., Ma, S. H., Zhou, Y., Santoyo, J., Martinez, E. D., Xiao, G., Raj, G. V., Jadhav, A., Simeonov, A., Maloney, D. J., Rizo, J., Hsieh, J. T. & Liu, Z. P. KDM4/JMJD2 histone demethylase inhibitors block prostate tumor growth by suppressing the expression of AR and bmyb-regulated genes. *Chem. Biol.* **22**, 1185-96 (2015)
- 237 Wang, K., Gong, Z., Chen, Y., Zhang, M., Wang, S., Yao, S., Liu, Z., Huang, Z. & Fei, B. KDM4C-mediated senescence defense is a targetable vulnerability in gastric cancer harboring TP53 mutations. *Clin. Epigenetics* **15**, 163 (2023)
- 238 Singh, S., Abu-Zaid, A., Jin, H., Fang, J., Wu, Q., Wang, T., Feng, H., Quarni, W., Shao, Y., Maxham, L., Abdolvahabi, A., Yun, M. K., Vaithiyalingam, S., Tan, H., Bowling, J., Honnell, V., Young, B., Guo, Y., Bajpai, R., Pruett-Miller, S. M., Grosveld, G. C., Hatley, M., Xu, B., Fan, Y., Wu, G., Chen, E. Y., Chen, T., Lewis, P. W., Rankovic, Z., Li, Y., Murphy, A. J., Easton, J., Peng, J., Chen, X., Wang, R., White, S. W., Davidoff, A. M. & Yang, J. Targeting KDM4 for treating PAX3-FOXO1-driven alveolar rhabdomyosarcoma. *Sci. Transl. Med.* **14**, eabq2096 (2022)
- 239 Pichavaram, P., Jablonowski, C. M., Fang, J., Fleming, A. M., Gil, H. J., Boghossian, A. S., Rees, M. G., Ronan, M. M., Roth, J. A., Morton, C. L., Zambetti, G. P., Davidoff, A. M., Yang, J. & Murphy, A. J. Oncogenic cells of renal embryonic lineage sensitive to the small molecule inhibitor QC6352 display depletion of KDM4 levels and disruption of ribosome biogenesis. *Mol. Cancer Ther.* (2023)
- 240 King, O. N. F., Li, X. S., Sakurai, M., Kawamura, A., Rose, N. R., Ng, S. S., Quinn, A. M., Rai, G., Mott, B. T., Beswick, P., Klose, R. J., Oppermann, U., Jadhav, A., Heightman, T. D., Maloney, D. J., Schofield, C. J. & Simeonov, A. Quantitative high-throughput screening identifies 8-hydroxyquinolines as cell-active histone demethylase inhibitors. *PLoS One* **5**, e15535 (2010)
- 241 Hafner, M., Niepel, M., Chung, M. & Sorger, P. K. Growth rate inhibition metrics correct for confounders in measuring sensitivity to cancer drugs. *Nat. Methods* **13**, 521-7 (2016)
- 242 Wang, J., Amin, A., Cheung, M. H., Shi, L. & Liang, C. Targeted inhibition of the expression of both MCM5 and MCM7 by miRNA-214 impedes DNA replication and tumorigenesis in hepatocellular carcinoma cells. *Cancer Lett.* **539**, 215677 (2022)
- 243 Wang, B. & Song, J. Structural basis for the ORC1-cyclin A association. *Protein Sci.* **28**, 1727-33 (2019)
- 244 Fischer, E. S., Yu, C. W. H., Hevler, J. F., Mclaughlin, S. H., Maslen, S. L., Heck, A. J. R., Freund, S. M. V. & Barford, D. Juxtaposition of BUB1 and CDC20 on phosphorylated MAD1 during catalytic mitotic checkpoint complex assembly. *Nat. Comm.* **13**, 6381 (2022)

- 245 Naro, C., Barbagallo, F., Chieffi, P., Bourgeois, C. F., Paronetto, M. P. & Sette, C. The centrosomal kinase NEK2 is a novel splicing factor kinase involved in cell survival. *Nucleic Acids Res.* **42**, 3218-27 (2014)
- 246 Liao, C., Li, S. Q., Wang, X., Muhlrads, S., Bjartell, A. & Wolgemuth, D. J. Elevated levels and distinct patterns of expression of A-type cyclins and their associated cyclin-dependent kinases in male germ cell tumors. *Int. J. Cancer* **108**, 654-64 (2004)
- 247 Fischer, L. & Thievensen, I. FUCCI reporter gene-based cell cycle analysis. *Methods Mol. Biol.* **2644**, 371-85 (2023)
- 248 Di Micco, R., Krizhanovsky, V., Baker, D. & D'adda Di Fagagna, F. Cellular senescence in ageing: From mechanisms to therapeutic opportunities. *Nat. Rev. Mol. Cell Biol.* **22**, 75-95 (2021)
- 249 Xing, J., Chen, K., Gao, S., Pousse, M., Ying, Y., Wang, B., Chen, L., Wang, C., Wang, L., Hu, W., Lu, Y., Gilson, E. & Ye, J. Protein phosphatase 2A activators reverse age-related behavioral changes by targeting neural cell senescence. *Aging Cell* **22** (2023)
- 250 Alza, L., Nager, M., Visa, A., Canti, C. & Herreros, J. FAK inhibition induces glioblastoma cell senescence-like state through p62 and p27. *Cancers (Basel)* **12** (2020)
- 251 Sun, D., Singh, D. K., Carcamo, S., Filipescu, D., Khalil, B., Huang, X., Miles, B. A., Westra, W., Sproll, K. C., Hasson, D., Bernstein, E. & Aguirre-Ghiso, J. A. MacroH2A impedes metastatic growth by enforcing a discrete dormancy program in disseminated cancer cells. *Sci. Adv.* **8**, eabo0876 (2022)
- 252 Zhang, R., Poustovoitov, M. V., Ye, X., Santos, H. A., Chen, W., Daganzo, S. M., Erzberger, J. P., Serebriiskii, I. G., Canutescu, A. A., Dunbrack, R. L., Pehrson, J. R., Berger, J. M., Kaufman, P. D. & Adams, P. D. Formation of macroH2A-containing senescence-associated heterochromatin foci and senescence driven by ASF1A and HIRA. *Dev. Cell* **8**, 19-30 (2005)
- 253 Kelley, K. D., Miller, K. R., Todd, A., Kelley, A. R., Tuttle, R. & Berberich, S. J. YPEL3, a p53-regulated gene that induces cellular senescence. *Cancer Res.* **70**, 3566-75 (2010)
- 254 Cai, Y., Zhou, H., Zhu, Y., Sun, Q., Ji, Y., Xue, A., Wang, Y., Chen, W., Yu, X., Wang, L., Chen, H., Li, C., Luo, T. & Deng, H. Elimination of senescent cells by beta-galactosidase-targeted prodrug attenuates inflammation and restores physical function in aged mice. *Cell Res.* **30**, 574-89 (2020)
- 255 Gsottberger, F., Meier, C., Ammon, A., Parker, S., Wendland, K., George, R., Petkovic, S., Mellenthin, L., Emmerich, C., Lutzny-Geier, G., Metzler, M., Mackensen, A., Chandramohan, V. & Muller, F. Targeted inhibition of protein synthesis renders cancer cells vulnerable to apoptosis by unfolded protein response. *Cell Death Dis.* **14**, 561 (2023)

- 256 Fidyk, K., Pastorczak, A., Cyran, J., Crump, N. T., Goral, A., Madzio, J., Muchowicz, A., Poprzeczko, M., Domka, K., Komorowski, L., Winiarska, M., Harman, J. R., Siudakowska, K., Graczyk-Jarzynka, A., Patkowska, E., Lech-Maranda, E., Mlynarski, W., Golab, J., Milne, T. A. & Firczuk, M. Potent, p53-independent induction of NOXA sensitizes MLL-rearranged B-cell acute lymphoblastic leukemia cells to venetoclax. *Oncogene* **41**, 1600-9 (2022)
- 257 Guan, H., Song, L., Cai, J., Huang, Y., Wu, J., Yuan, J., Li, J. & Li, M. Sphingosine kinase 1 regulates the AKT/FOXO3A/BIM pathway and contributes to apoptosis resistance in glioma cells. *PLoS One* **6**, e19946 (2011)
- 258 Kira, A., Tatsutomi, I., Saito, K., Murata, M., Hattori, I., Kajita, H., Muraki, N., Oda, Y., Satoh, S., Tsukamoto, Y., Kimura, S., Onoue, K., Yonemura, S., Arakawa, S., Kato, H., Hirashima, T. & Kawane, K. Apoptotic extracellular vesicle formation via local phosphatidylserine exposure drives efficient cell extrusion. *Dev. Cell* **58**, 1282-98 (2023)
- 259 Lee, S. H., Meng, X. W., Flatten, K. S., Loegering, D. A. & Kaufmann, S. H. Phosphatidylserine exposure during apoptosis reflects bidirectional trafficking between plasma membrane and cytoplasm. *Cell Death Differ* **20**, 64-76 (2013)
- 260 Laso-Garcia, F., Casado-Fernandez, L., Piniella, D., Gomez-De Frutos, M. C., Arizaga-Echebarria, J. K., Perez-Mato, M., Alonso-Lopez, E., Otero-Ortega, L., Bravo, S. B., Chantada-Vazquez, M. D. P., Avendano-Ortiz, J., Lopez-Collazo, E., Lumbreras-Herrera, M. I., Gamez-Pozo, A., Fuentes, B., Diez-Tejedor, E., Gutierrez-Fernandez, M. & Alonso De Lecinana, M. Circulating extracellular vesicles promote recovery in a preclinical model of intracerebral hemorrhage. *Mol. Ther. Nucleic Acids* **32**, 247-62 (2023)
- 261 Sun, J., Wang, W., Ma, Q., Pan, X., Zhai, H., Wang, J., Han, Y., Li, Y. & Wang, Y. Necrostatin-1S suppresses RIPK1-driven necroptosis and inflammation in periventricular leukomalacia neonatal mice. *Neurochem. Res.* (2023)
- 262 De Gendt, K., Denolet, E., Willems, A., Daniels, V. W., Clinckemalie, L., Denayer, S., Wilkinson, M. F., Claessens, F., Swinnen, J. V. & Verhoeven, G. Expression of TUBB3, a beta-tubulin isotype, is regulated by androgens in mouse and rat sertoli cells. *Biol. Reprod.* **85**, 934-45 (2011)
- 263 Laga, A. C., Zhan, Q., Weishaupt, C., Ma, J., Frank, M. H. & Murphy, G. F. SOX2 and nestin expression in human melanoma: An immunohistochemical and experimental study. *Exp. Dermatol.* **20**, 339-45 (2011)
- 264 Shao, X., Lv, N., Liao, J., Long, J., Xue, R., Ai, N., Xu, D. & Fan, X. Copy number variation is highly correlated with differential gene expression: A pan-cancer study. *BMC Med. Genet.* **20** (2019)

- 265 Ward, C. S., Venkatesh, H. S., Chaumeil, M. M., Brandes, A. H., Vancrinkinge, M., Dafni, H., Sukumar, S., Nelson, S. J., Vigneron, D. B., Kurhanewicz, J., James, C. D., Haas-Kogan, D. A. & Ronen, S. M. Noninvasive detection of target modulation following phosphatidylinositol 3-kinase inhibition using hyperpolarized ^{13}C magnetic resonance spectroscopy. *Cancer Res.* **70**, 1296-305 (2010)
- 266 Fuentes, E. Modulation of glycoprotein vi and its downstream signaling pathways as an antiplatelet target. *Int. J. Mol. Sci.* **23** (2022)
- 267 Sterling, J., Menezes, S. V., Abbassi, R. H. & Munoz, L. Histone lysine demethylases and their functions in cancer. *Int. J. Cancer* (2020)
- 268 Shearer, R. F. & Saunders, D. N. Experimental design for stable genetic manipulation in mammalian cell lines: Lentivirus and alternatives. *Genes Cells* **20**, 1-10 (2015)
- 269 Lee, C. I., Kohn, D. B., Ekert, J. E. & Tarantal, A. F. Morphological analysis and lentiviral transduction of fetal monkey bone marrow-derived mesenchymal stem cells. *Mol. Ther.* **9**, 112-23 (2004)
- 270 Kim, S. Y., Hwang, S., Lee, B. R., Hong, J. A., Sung, Y. H. & Kim, I. Inhibition of histone demethylase KDM4 by ML324 induces apoptosis through the unfolded protein response and BIM upregulation in hepatocellular carcinoma cells. *Chem. Biol. Interact.* **353**, 109806 (2022)
- 271 Hoyle, R. G., Wang, H., Cen, Y., Zhang, Y. & Li, J. IOX1 suppresses Wnt target gene transcription and colorectal cancer tumorigenesis through inhibition of KDM3 histone demethylases. *Mol. Cancer Ther.* **20**, 191-202 (2021)
- 272 Zhu, Q., Liang, F., Cai, S., Luo, X., Duo, T., Liang, Z., He, Z., Chen, Y. & Mo, D. KDM4A regulates myogenesis by demethylating H3K9me3 of myogenic regulatory factors. *Cell Death Dis.* **12**, 514 (2021)
- 273 Kleszcz, R., Skalski, M., Krajka-Kuzniak, V. & Paluszczak, J. The inhibitors of KDM4 and KDM6 histone lysine demethylases enhance the anti-growth effects of erlotinib and HS-173 in head and neck cancer cells. *Eur. J. Pharm. Sci.* **166**, 105961 (2021)
- 274 Zhao, E., Ding, J., Xia, Y., Liu, M., Ye, B., Choi, J. H., Yan, C., Dong, Z., Huang, S., Zha, Y., Yang, L., Cui, H. & Ding, H. F. KDM4C and ATF4 cooperate in transcriptional control of amino acid metabolism. *Cell Rep.* **14**, 506-19 (2016)
- 275 Yang, G., Li, C., Tao, F., Liu, Y., Zhu, M., Du, Y., Fei, C., She, Q. & Chen, J. The emerging roles of lysine-specific demethylase 4A in cancer: Implications in tumorigenesis and therapeutic opportunities. *Genes Dis.* **11**, 645-63 (2024)
- 276 Deng, P., Chang, I., Wang, J., Badreldin, A. A., Li, X., Yu, B. & Wang, C. Y. Loss of KDM4B impairs osteogenic differentiation of OMSCs and promotes oral bone aging. *Int. J. Oral Sci.* **14**, 24 (2022)

- 277 Mallette, Frédérick a. & Richard, S. JMJD2A promotes cellular transformation by blocking cellular senescence through transcriptional repression of the tumor suppressor CHD5. *Cell Rep.* **2**, 1233-43 (2012)
- 278 Beltzig, L., Christmann, M. & Kaina, B. Abrogation of cellular senescence induced by temozolomide in glioblastoma cells: Search for senolytics. *Cells* **11** (2022)
- 279 Kupershmit, I., Khoury-Haddad, H., Awwad, S. W., Guttmann-Raviv, N. & Ayoub, N. KDM4C (GASC1) lysine demethylase is associated with mitotic chromatin and regulates chromosome segregation during mitosis. *Nucleic Acids Res.* **42**, 6168-82 (2014)
- 280 Klose, R. J., Yamane, K., Bae, Y., Zhang, D., Erdjument-Bromage, H., Tempst, P., Wong, J. & Zhang, Y. The transcriptional repressor JHDM3A demethylates trimethyl histone H3 lysine 9 and lysine 36. *Nature* **442**, 312-6 (2006)
- 281 Zhao, J., Li, B., Ren, Y., Liang, T., Wang, J., Zhai, S., Zhang, X., Zhou, P., Zhang, X., Pan, Y., Gao, F., Zhang, S., Li, L., Yang, Y., Deng, X., Li, X., Chen, L., Yang, D. & Zheng, Y. Histone demethylase KDM4A plays an oncogenic role in nasopharyngeal carcinoma by promoting cell migration and invasion. *Exp. Mol. Med.* **53**, 1207-17 (2021)
- 282 Wang, L. Y., Hung, C. L., Chen, Y. R., Yang, J. C., Wang, J., Campbell, M., Izumiya, Y., Chen, H. W., Wang, W. C., Ann, D. K. & Kung, H. J. KDM4A coactivates E2F1 to regulate the PDK-dependent metabolic switch between mitochondrial oxidation and glycolysis. *Cell Rep.* **16**, 3016-27 (2016)
- 283 Cascante, A., Klum, S., Biswas, M., Antolin-Fontes, B., Barnabe-Heider, F. & Hermanson, O. Gene-specific methylation control of H3K9 and H3K36 on neurotrophic BDNF versus astroglial GFAP genes by KDM4A/C regulates neural stem cell differentiation. *J. Mol. Biol.* **426**, 3467-77 (2014)
- 284 Toffolo, E., Rusconi, F., Paganini, L., Tortorici, M., Pilotto, S., Heise, C., Verpelli, C., Tedeschi, G., Maffioli, E., Sala, C., Mattevi, A. & Battaglioli, E. Phosphorylation of neuronal lysine-specific demethylase 1LSD1/KDM1A impairs transcriptional repression by regulating interaction with corepressors and histone deacetylases HDAC1/2. *J. Neurochem.* **128**, 603-16 (2014)
- 285 Karakatsanis, N. M., Hamey, J. J. & Wilkins, M. R. Taking me away: The function of phosphorylation on histone lysine demethylases. *Trends Biochem. Sci.* (2024)
- 286 Tsai, H. H., Kao, H. J., Kuo, M. W., Lin, C. H., Chang, C. M., Chen, Y. Y., Chen, H. H., Kwok, P. Y., Yu, A. L. & Yu, J. Whole genomic analysis reveals atypical non-homologous off-target large structural variants induced by CRISPR-Cas9-mediated genome editing. *Nat. Comm.* **14**, 5183 (2023)

- 287 Chavez, M., Chen, X., Finn, P. B. & Qi, L. S. Advances in CRISPR therapeutics. *Nat. Rev. Nephrol.* **19**, 9-22 (2023)
- 288 Nambiar, T. S., Billon, P., Diedenhofen, G., Hayward, S. B., Taglialatela, A., Cai, K., Huang, J. W., Leuzzi, G., Cuella-Martin, R., Palacios, A., Gupta, A., Egli, D. & Ciccia, A. Stimulation of CRISPR-mediated homology-directed repair by an engineered RAD18 variant. *Nat. Comm.* **10**, 3395 (2019)
- 289 Gandhi, S., Piacentino, M. L., Vieceli, F. M. & Bronner, M. E. Optimization of CRISPR/Cas9 genome editing for loss-of-function in the early chick embryo. *Dev. Biol.* **432**, 86-97 (2017)
- 290 Liu, Q., Yang, F., Zhang, J., Liu, H., Rahman, S., Islam, S., Ma, W. & She, M. Application of CRISPR/Cas9 in crop quality improvement. *Int. J. Mol. Sci.* **22** (2021)
- 291 A CRISPR-based system for temporal, combinatorial gene knockout in mice. *Nat. Immunol.* **25**, 15-6 (2024)
- 292 Unniyampurath, U., Pilankatta, R. & Krishnan, M. N. RNA interference in the age of CRISPR: Will CRISPR interfere with RNAi? *Int. J. Mol. Sci.* **17**, 291 (2016)
- 293 Novak, L. C., Chou, J., Colic, M., Bristow, C. A. & Hart, T. Pickles v3: The updated database of pooled in vitro CRISPR knockout library essentiality screens. *Nucleic Acids Res.* **51**, D1117-D21 (2023)
- 294 Liu, J.-Q. & Li, T. CRISPR-Cas9-mediated loss-of-function screens. *Front. Life Sci.* **12**, 1-13 (2019)
- 295 Hart, T., Chandrashekhar, M., Aregger, M., Steinhart, Z., Brown, K. R., Macleod, G., Mis, M., Zimmermann, M., Fradet-Turcotte, A., Sun, S., Mero, P., Dirks, P., Sidhu, S., Roth, F. P., Rissland, O. S., Durocher, D., Angers, S. & Moffat, J. High-resolution CRISPR screens reveal fitness genes and genotype-specific cancer liabilities. *Cell* **163**, 1515-26 (2015)
- 296 Yu, S., Wang, H., Gao, J., Liu, L., Sun, X., Wang, Z., Wen, P., Shi, X., Shi, J., Guo, W. & Zhang, S. Identification of context-specific fitness genes associated with metabolic rearrangements for prognosis and potential treatment targets for liver cancer. *Front. Genet.* **13**, 863536 (2022)
- 297 Tsherniak, A., Vazquez, F., Montgomery, P. G., Weir, B. A., Kryukov, G., Cowley, G. S., Gill, S., Harrington, W. F., Pantel, S., Krill-Burger, J. M., Meyers, R. M., Ali, L., Goodale, A., Lee, Y., Jiang, G., Hsiao, J., Gerath, W. F. J., Howell, S., Merkel, E., Ghandi, M., Garraway, L. A., Root, D. E., Golub, T. R., Boehm, J. S. & Hahn, W. C. Defining a cancer dependency map. *Cell* **170**, 564-76 e16 (2017)
- 298 Lenoir, W. F., Morgado, M., Deweirdt, P. C., Mclaughlin, M., Griffith, A. L., Sangree, A. K., Feeley, M. N., Esmacili Anvar, N., Kim, E., Bertolet, L. L., Colic, M., Dede, M.,

- Doench, J. G. & Hart, T. Discovery of putative tumor suppressors from CRISPR screens reveals rewired lipid metabolism in acute myeloid leukemia cells. *Nat. Comm.* **12**, 6506 (2021)
- 299 Rocha, C. R. R., Reily Rocha, A., Molina Silva, M., Rodrigues Gomes, L., Teatin Latancia, M., Andrade Tomaz, M., De Souza, I., Karolynne Seregni Monteiro, L. & Menck, C. F. M. Revealing temozolomide resistance mechanisms via genome-wide CRISPR libraries. *Cells* **9** (2020)
- 300 Barretina, J., Caponigro, G., Stransky, N., Venkatesan, K., Margolin, A. A., Kim, S., Wilson, C. J., Lehár, J., Kryukov, G. V., Sonkin, D., Reddy, A., Liu, M., Murray, L., Berger, M. F., Monahan, J. E., Morais, P., Meltzer, J., Korejwa, A., Jane-Valbuena, J., Mapa, F. A., Thibault, J., Bric-Furlong, E., Raman, P., Shipway, A., Engels, I. H., Cheng, J., Yu, G. K., Yu, J., Aspesi, P., Jr., De Silva, M., Jagtap, K., Jones, M. D., Wang, L., Hatton, C., Palessandolo, E., Gupta, S., Mahan, S., Sougnez, C., Onofrio, R. C., Liefeld, T., Macconail, L., Winckler, W., Reich, M., Li, N., Mesirov, J. P., Gabriel, S. B., Getz, G., Ardlie, K., Chan, V., Myer, V. E., Weber, B. L., Porter, J., Warmuth, M., Finan, P., Harris, J. L., Meyerson, M., Golub, T. R., Morrissey, M. P., Sellers, W. R., Schlegel, R. & Garraway, L. A. The cancer cell line encyclopedia enables predictive modelling of anticancer drug sensitivity. *Nature* **483**, 603-7 (2012)
- 301 Kim, E. & Hart, T. Improved analysis of CRISPR fitness screens and reduced off-target effects with the BAGEL2 gene essentiality classifier. *Genome Med.* **13**, 2 (2021)
- 302 Smyth, G. K. Linear models and empirical bayes methods for assessing differential expression in microarray experiments. *Stat. Appl. Genet. Mol. Biol.* **3**, Article3 (2004)
- 303 Ishii, T., Okai, T., Iwatani-Yoshihara, M., Mochizuki, M., Unno, S., Kuno, M., Yoshikawa, M., Shibata, S., Nakakariya, M., Yogo, T. & Kawamoto, T. CETSA quantitatively verifies in vivo target engagement of novel RIPK1 inhibitors in various biospecimens. *Sci. Rep.* **7**, 13000 (2017)
- 304 Simon, G. M., Niphakis, M. J. & Cravatt, B. F. Determining target engagement in living systems. *Nat. Chem. Biol.* **9**, 200-5 (2013)
- 305 Schurmann, M., Janning, P., Ziegler, S. & Waldmann, H. Small-molecule target engagement in cells. *Cell Chem. Biol.* **23**, 435-41 (2016)
- 306 Tolvanen, T. A. Current advances in CETSA. *Front Mol. Biosci.* **9**, 866764 (2022)
- 307 Nagasawa, I., Muroi, M., Kawatani, M., Ohishi, T., Ohba, S. I., Kawada, M. & Osada, H. Identification of a small compound targeting PKM2-regulated signaling using 2D gel electrophoresis-based proteome-wide CETSA. *Cell Chem. Biol.* **27**, 186-96 (2020)
- 308 Savitski, M. M., Reinhard, F. B., Franken, H., Werner, T., Savitski, M. F., Eberhard, D., Martinez Molina, D., Jafari, R., Dovega, R. B., Klaeger, S., Kuster, B., Nordlund,

- P., Bantscheff, M. & Drewes, G. Tracking cancer drugs in living cells by thermal profiling of the proteome. *Science* **346**, 1255784 (2014)
- 309 Franken, H., Mathieson, T., Childs, D., Sweetman, G. M., Werner, T., Togel, I., Doce, C., Gade, S., Bantscheff, M., Drewes, G., Reinhard, F. B., Huber, W. & Savitski, M. M. Thermal proteome profiling for unbiased identification of direct and indirect drug targets using multiplexed quantitative mass spectrometry. *Nat. Protoc.* **10**, 1567-93 (2015)
- 310 Wang, Z., Gerstein, M. & Snyder, M. Rna-seq: A revolutionary tool for transcriptomics. *Nat. Rev. Genet.* **10**, 57-63 (2009)
- 311 Van De Sande, B., Lee, J. S., Mutasa-Gottgens, E., Naughton, B., Bacon, W., Manning, J., Wang, Y., Pollard, J., Mendez, M., Hill, J., Kumar, N., Cao, X., Chen, X., Khaladkar, M., Wen, J., Leach, A. & Ferran, E. Applications of single-cell RNA sequencing in drug discovery and development. *Nat. Rev. Drug Discov.* **22**, 496-520 (2023)
- 312 Abdelfattah, N., Kumar, P., Wang, C., Leu, J. S., Flynn, W. F., Gao, R., Baskin, D. S., Pichumani, K., Ijare, O. B., Wood, S. L., Powell, S. Z., Haviland, D. L., Parker Kerrigan, B. C., Lang, F. F., Prabhu, S. S., Huntoon, K. M., Jiang, W., Kim, B. Y. S., George, J. & Yun, K. Single-cell analysis of human glioma and immune cells identifies S100A4 as an immunotherapy target. *Nat. Comm.* **13**, 767 (2022)
- 313 Battaglin, F., Baca, Y., Millstein, J., Yang, Y., Xiu, J., Arai, H., Wang, J., Ou, F. S., Innocenti, F., Mumenthaler, S. M., Jayachandran, P., Kawanishi, N., Lenz, A., Soni, S., Algaze, S., Zhang, W., Khoukaz, T., Roussos Torres, E., Seeber, A., Abraham, J. P., Lou, E., Philip, P. A., Weinberg, B. A., Shields, A. F., Goldberg, R. M., Marshall, J. L., Venook, A. P., Korn, W. M. & Lenz, H. J. CCR5 and CCL5 gene expression in colorectal cancer: Comprehensive profiling and clinical value. *J Immunother. Cancer* **12** (2024)
- 314 Zhao, Q., Liu, F., Cheng, Y., Xiao, X. R., Hu, D. D., Tang, Y. M., Bao, W. M., Yang, J. H., Jiang, T., Hu, J. P., Gonzalez, F. J. & Li, F. Celastrol protects from cholestatic liver injury through modulation of SIRT1-FXR signaling. *Mol. Cell Proteomics* **18**, 520-33 (2019)
- 315 Subramanian, A., Narayan, R., Corsello, S. M., Peck, D. D., Natoli, T. E., Lu, X., Gould, J., Davis, J. F., Tubelli, A. A., Asiedu, J. K., Lahr, D. L., Hirschman, J. E., Liu, Z., Donahue, M., Julian, B., Khan, M., Wadden, D., Smith, I. C., Lam, D., Liberzon, A., Toder, C., Bagul, M., Orzechowski, M., Enache, O. M., Piccioni, F., Johnson, S. A., Lyons, N. J., Berger, A. H., Shamji, A. F., Brooks, A. N., Vrcic, A., Flynn, C., Rosains, J., Takeda, D. Y., Hu, R., Davison, D., Lamb, J., Ardlie, K., Hogstrom, L., Greenside, P., Gray, N. S., Clemons, P. A., Silver, S., Wu, X., Zhao, W. N., Read-Button, W., Wu, X., Haggarty, S. J., Ronco, L. V., Boehm, J. S., Schreiber, S. L., Doench, J. G., Bittker, J. A., Root, D. E., Wong, B. & Golub, T. R. A next generation connectivity map: L1000 platform and the first 1,000,000 profiles. *Cell* **171**, 1437-52 (2017)

- 316 Stockwell, S. R., Platt, G., Barrie, S. E., Zoumpoulidou, G., Te Poele, R. H., Aherne, G. W., Wilson, S. C., Sheldrake, P., McDonald, E., Venet, M., Soufy, C., Elustondo, F., Rigoreau, L., Blagg, J., Workman, P., Garrett, M. D. & Mitnacht, S. Mechanism-based screen for G1/S checkpoint activators identifies a selective activator of EIF2AK3/PERK signalling. *PLoS One* **7**, e28568 (2012)
- 317 Bock, C., Datlinger, P., Chardon, F., Coelho, M. A., Dong, M. B., Lawson, K. A., Lu, T., Maroc, L., Norman, T. M., Song, B., Stanley, G., Chen, S., Garnett, M., Li, W., Moffat, J., Qi, L. S., Shapiro, R. S., Shendure, J., Weissman, J. S. & Zhuang, X. High-content CRISPR screening. *Nat. Rev. Methods Primers* **2** (2022)
- 318 Zhang, Z., Zhang, M., Zhou, J. & Wang, D. Genome-wide CRISPR screening reveals ADCK3 as a key regulator in sensitizing endometrial carcinoma cells to MPA therapy. *Br. J. Cancer* **129**, 601-11 (2023)
- 319 Castells-Roca, L., Tejero, E., Rodriguez-Santiago, B. & Surrallés, J. CRISPR screens in synthetic lethality and combinatorial therapies for cancer. *Cancers (Basel)* **13** (2021)
- 320 Greenacre, M., Groenen, P. J. F., Hastie, T., D'enza, A. I., Markos, A. & Tuzhilina, E. Principal component analysis. *Nat. Rev. Methods Primers* **2**, 100 (2022)
- 321 Undieh, A. S. Pharmacology of signaling induced by dopamine D(1)-like receptor activation. *Pharmacol. Ther.* **128**, 37-60 (2010)
- 322 Kleiber, N., Lemus-Diaz, N., Stiller, C., Heinrichs, M., Mai, M. M., Hackert, P., Richter-Dennerlein, R., Hobartner, C., Bohnsack, K. E. & Bohnsack, M. T. The RNA methyltransferase METTL8 installs M(3)C(32) in mitochondrial tRNAs(thr/ser(UCN)) to optimise tRNA structure and mitochondrial translation. *Nat. Comm.* **13**, 209 (2022)
- 323 Nguyen, A. L., Fadel, M. D. & Cheeseman, I. M. Differential requirements for the CENP-O complex reveal parallel PLK1 kinetochore recruitment pathways. *Mol. Biol. Cell* **32**, 712-21 (2021)
- 324 Jiao, Y., Feng, Y. & Wang, X. Regulation of tumor suppressor gene CDKN2A and encoded p16-Ink4A protein by covalent modifications. *Biochemistry (Mosc.)* **83**, 1289-98 (2018)
- 325 Linder, A., Bauernfried, S., Cheng, Y., Albanese, M., Jung, C., Keppler, O. T. & Hornung, V. CARD8 inflammasome activation triggers pyroptosis in human T cells. *EMBO J.* **39**, e105071 (2020)
- 326 Rouquier, S., Taviaux, S., Trask, B. J., Brand-Arpon, V., Van Den Engh, G., Demaille, J. & Giorgi, D. Distribution of olfactory receptor genes in the human genome. *Nat. Genet.* **18**, 243-50 (1998)
- 327 Khan, I. & Gartel, A. L. The antagonistic duality of NPM1 mutations in AML. *Blood Adv.* **6**, 4028-30 (2022)

- 328 Di Matteo, A., Franceschini, M., Paiardini, A., Grottesi, A., Chiarella, S., Rocchio, S., Di Natale, C., Marasco, D., Vitagliano, L., Travaglini-Allocatelli, C. & Federici, L. Structural investigation of nucleophosmin interaction with the tumor suppressor FBW7 γ . *Oncogenesis* **6**, e379 (2017)
- 329 Yang, Y., Song, L., Huang, X., Feng, Y., Zhang, Y., Liu, Y., Li, S., Zhan, Z., Zheng, L., Feng, H. & Li, Y. PRPS1-mediated purine biosynthesis is critical for pluripotent stem cell survival and stemness. *Aging* **13**, 4063-78 (2021)
- 330 O'neil, N. J., Bailey, M. L. & Hieter, P. Synthetic lethality and cancer. *Nat. Rev. Genet.* **18**, 613-23 (2017)
- 331 Castelnovo, L. F., Bonalume, V., Melfi, S., Ballabio, M., Colleoni, D. & Magnaghi, V. Schwann cell development, maturation and regeneration: A focus on classic and emerging intracellular signaling pathways. *Neural Regen. Res.* **12**, 1013-23 (2017)
- 332 Malik, S. & Roeder, R. G. Dynamic regulation of pol II transcription by the mammalian mediator complex. *Trends Biochem. Sci.* **30**, 256-63 (2005)
- 333 Maston, G. A., Evans, S. K. & Green, M. R. Transcriptional regulatory elements in the human genome. *Annu. Rev. Genomics Hum. Genet.* **7**, 29-59 (2006)
- 334 Schober, P., Boer, C. & Schwarte, L. A. Correlation coefficients: Appropriate use and interpretation. *Anesth. Analg.* **126**, 1763-8 (2018)
- 335 Chen, J., Zheng, H., Zeng, S., Xie, C., Li, X., Yan, T., Gong, X., Lu, L., Qi, X., Wang, Y., Hu, M., Zhu, L. & Liu, Z. Profiles and gender-specifics of UDP-glucuronosyltransferases and sulfotransferases expressions in the major metabolic organs of wild-type and efflux transporter knockout FVB mice. *Mol. Pharm.* **14**, 2967-76 (2017)
- 336 Latour, Y. L., Allaman, M. M., Barry, D. P., Smith, T. M., Williams, K. J., Mcnamara, K. M., Jacobse, J., Goettel, J. A., Delgado, A. G., Piazuelo, M. B., Zhao, S., Gobert, A. P. & Wilson, K. T. Epithelial TALIN-1 protects mice from citrobacter rodentium-induced colitis by restricting bacterial crypt intrusion and enhancing T cell immunity. *Gut Microbes* **15**, 2192623 (2023)
- 337 Bao, X., Tang, J., Lopez-Pajares, V., Tao, S., Qu, K., Crabtree, G. R. & Khavari, P. A. ACTL6A enforces the epidermal progenitor state by suppressing SWI/SNF-dependent induction of KLF4. *Cell Stem Cell* **12**, 193-203 (2013)
- 338 Prieto, C., Nguyen, D. T. T., Liu, Z., Wheat, J., Perez, A., Gourkanti, S., Chou, T., Barin, E., Velleca, A., Rohwetter, T., Chow, A., Taggart, J., Savino, A. M., Hoskova, K., Dhodapkar, M., Schurer, A., Barlowe, T. S., Vu, L. P., Leslie, C., Steidl, U., Rabadan, R. & Kharas, M. G. Transcriptional control of CBX5 by the RNA binding

- proteins RBMX and RBMXL1 maintains chromatin state in myeloid leukemia. *Nat. Cancer* **2**, 741-57 (2021)
- 339 Park, S. Y., Park, J. E., Kim, T. S., Kim, J. H., Kwak, M. J., Ku, B., Tian, L., Murugan, R. N., Ahn, M., Komiya, S., Hojo, H., Kim, N. H., Kim, B. Y., Bang, J. K., Erikson, R. L., Lee, K. W., Kim, S. J., Oh, B. H., Yang, W. & Lee, K. S. Molecular basis for unidirectional scaffold switching of human PLK4 in centriole biogenesis. *Nat. Struct. Mol. Biol.* **21**, 696-703 (2014)
- 340 Gandia, M., Fernandez-Toral, J., Solanellas, J., Dominguez-Ruiz, M., Gomez-Rosas, E., Del Castillo, F. J., Villamar, M., Moreno-Pelayo, M. A. & Del Castillo, I. Mutations in PRPS1 causing syndromic or nonsyndromic hearing impairment: Intrafamilial phenotypic variation complicates genetic counseling. *Pediatr. Res.* **78**, 97-102 (2015)
- 341 Ali Alghamdi, M., Benabdelkamel, H., Masood, A., Saheb Sharif-Askari, N., Hachim, M. Y., Alsheikh, H., Hamad, M. H., Salih, M. A., Bashiri, F. A., Alhasan, K., Kashour, T., Guatibonza Moreno, P., Schroder, S., Karageorgou, V., Bertoli-Avella, A. M., Alkhalidi, H., Jamjoom, D. Z., Alorainy, I. A., Alfadda, A. A. & Halwani, R. Genomic, proteomic, and phenotypic spectrum of novel O-sialoglycoprotein endopeptidase variant in four affected individuals with galloway-mowat syndrome. *Front. Genet.* **13**, 806190 (2022)
- 342 Sekovanic, A., Jurasovic, J., Piasek, M., Pasalic, D., Orct, T., Grgec, A. S., Stasenko, S., Cakanic, K. B. & Jazbec, A. Metallothionein 2A gene polymorphism and trace elements in mother-newborn pairs in the croatian population. *J. Trace Elem. Med. Biol.* **45**, 163-70 (2018)
- 343 Dhanasekaran, R., Deutzmann, A., Mahauad-Fernandez, W. D., Hansen, A. S., Gouw, A. M. & Felsher, D. W. The MYC oncogene - the grand orchestrator of cancer growth and immune evasion. *Nat. Rev. Clin. Oncol.* **19**, 23-36 (2022)
- 344 Timm, D. E., Bowman, V., Madsen, R. & Rauch, C. Cryo-electron microscopy structure of a human PRMT5:MEP50 complex. *PLoS One* **13**, e0193205 (2018)
- 345 Van Vranken, J. G., Li, J., Mitchell, D. C., Navarrete-Perea, J. & Gygi, S. P. Assessing target engagement using proteome-wide solvent shift assays. *Elife* **10** (2021)
- 346 Duenas, M. E., Peltier-Heap, R. E., Leveridge, M., Annan, R. S., Buttner, F. H. & Trost, M. Advances in high-throughput mass spectrometry in drug discovery. *EMBO Mol. Med.* **15**, e14850 (2023)
- 347 Hammam, K., Saez-Ayala, M., Rebuffet, E., Gros, L., Lopez, S., Hajem, B., Humbert, M., Baudelet, E., Audebert, S., Betzi, S., Lugari, A., Combes, S., Letard, S., Casteran, N., Mansfield, C., Moussy, A., De Sepulveda, P., Morelli, X. & Dubreuil, P. Dual protein kinase and nucleoside kinase modulators for rationally designed polypharmacology. *Nat. Comm.* **8**, 1420 (2017)

- 348 Cho, J. H. & Han, J. S. Phospholipase D and its essential role in cancer. *Mol. Cells* **40**, 805-13 (2017)
- 349 Gavin, A. L., Huang, D., Huber, C., Martensson, A., Tardif, V., Skog, P. D., Blane, T. R., Thinner, T. C., Osborn, K., Chong, H. S., Kargaran, F., Kimm, P., Zeitjian, A., Sielski, R. L., Briggs, M., Schulz, S. R., Zarpellon, A., Cravatt, B., Pang, E. S., Teijaro, J., De La Torre, J. C., O'keeffe, M., Hochrein, H., Damme, M., Teyton, L., Lawson, B. R. & Nemazee, D. PLD3 and PLD4 are single-stranded acid exonucleases that regulate endosomal nucleic-acid sensing. *Nat. Immunol.* **19**, 942-53 (2018)
- 350 Landsverk, H. B., Mora-Bermudez, F., Landsverk, O. J., Hasvold, G., Naderi, S., Bakke, O., Ellenberg, J., Collas, P., Syljuasen, R. G. & Kuntziger, T. The protein phosphatase 1 regulator PNUTS is a new component of the DNA damage response. *EMBO Rep* **11**, 868-75 (2010)
- 351 Ohtani, K., Suzuki, Y., Eda, S., Kawai, T., Kase, T., Keshi, H., Sakai, Y., Fukuoh, A., Sakamoto, T., Itabe, H., Suzutani, T., Ogasawara, M., Yoshida, I. & Wakamiya, N. The membrane-type collectin CL-P1 is a scavenger receptor on vascular endothelial cells. *J. Biol. Chem.* **276**, 44222-8 (2001)
- 352 Wang, Q., Liu, H., Wang, Q., Zhou, F., Liu, Y., Zhang, Y., Ding, H., Yuan, M., Li, F. & Chen, Y. Involvement of c-fos in cell proliferation, migration, and invasion in osteosarcoma cells accompanied by altered expression of WNT2 and FZD9. *PLoS One* **12**, e0180558 (2017)
- 353 Mohammadi, A., Sorensen, G. L. & Pilecki, B. MFAP4-mediated effects in elastic fiber homeostasis, integrin signaling and cancer, and its role in teleost fish. *Cells* **11** (2022)
- 354 Epstein Shochet, G., Brook, E., Bardenstein-Wald, B. & Shitrit, D. TGF-beta pathway activation by idiopathic pulmonary fibrosis (IPF) fibroblast derived soluble factors is mediated by IL-6 trans-signaling. *Respir. Res.* **21**, 56 (2020)
- 355 Konigshoff, M., Balsara, N., Pfaff, E. M., Kramer, M., Chrobak, I., Seeger, W. & Eickelberg, O. Functional Wnt signaling is increased in idiopathic pulmonary fibrosis. *PLoS One* **3**, e2142 (2008)
- 356 Grimminger, F., Gunther, A. & Vancheri, C. The role of tyrosine kinases in the pathogenesis of idiopathic pulmonary fibrosis. *Eur. Respir. J.* **45**, 1426-33 (2015)
- 357 Wang, Y. C., Chen, Q., Luo, J. M., Nie, J., Meng, Q. H., Shuai, W., Xie, H., Xia, J. M. & Wang, H. Notch1 promotes the pericyte-myofibroblast transition in idiopathic pulmonary fibrosis through the PDGFR/ROCK1 signal pathway. *Exp. Mol. Med.* **51**, 1-11 (2019)
- 358 Lamb, J., Crawford, E. D., Peck, D., Modell, J. W., Blat, I. C., Wrobel, M. J., Lerner, J., Brunet, J. P., Subramanian, A., Ross, K. N., Reich, M., Hieronymus, H., Wei, G., Armstrong, S. A., Haggarty, S. J., Clemons, P. A., Wei, R., Carr, S. A., Lander, E. S.

- & Golub, T. R. The connectivity map: Using gene-expression signatures to connect small molecules, genes, and disease. *Science* **313**, 1929-35 (2006)
- 359 Li, A., Lu, X., Natoli, T., Bittker, J., Sipes, N. S., Subramanian, A., Auerbach, S., Sherr, D. H. & Monti, S. The carcinogenome project: In vitro gene expression profiling of chemical perturbations to predict long-term carcinogenicity. *Environ. Health Perspect.* **127**, 47002 (2019)
- 360 Carlo, M. I., Molina, A. M., Lakhman, Y., Patil, S., Woo, K., Deluca, J., Lee, C. H., Hsieh, J. J., Feldman, D. R., Motzer, R. J. & Voss, M. H. A phase IB study of BEZ235, a dual inhibitor of phosphatidylinositol 3-kinase (PI3K) and mammalian target of rapamycin (MTOR), in patients with advanced renal cell carcinoma. *Oncologist* **21**, 787-8 (2016)
- 361 Horvat Nk Fau - Lesinski, G. B. & Lesinski, G. B. Bring on the brequinar: An approach to enforce the differentiation of myeloid-derived suppressor cells. *J. Clin. Invest.* **23**, e165506 (2022)
- 362 Cuthbertson, C. R., Guo, H., Kyani, A., Madak, J. T., Arabzada, Z. & Neamati, N. The dihydroorotate dehydrogenase inhibitor brequinar is synergistic with ent1/2 inhibitors. *ACS Pharmacol. Transl. Sci.* **6**, 1242-52 (2020)
- 363 Yang, C., Zhao, Y., Wang, L., Guo, Z., Ma, L., Yang, R., Wu, Y., Li, X., Niu, J., Chu, Q., Fu, Y. & Li, B. De novo pyrimidine biosynthetic complexes support cancer cell proliferation and ferroptosis defence. *Nat. Cell Biol.* **25**, 836-47 (2023)
- 364 Balmanno, K. & Cook, S. J. Tumour cell survival signalling by the ERK1/2 pathway. *Cell Death Differ.* **16**, 368-77 (2009)
- 365 Hong, S. K., Yoon S Fau - Moelling, C., Moelling C Fau - Arthan, D., Arthan D Fau - Park, J.-I. & Park, J. I. Noncatalytic function of ERK1/2 can promote RAF/MEK/ERK-mediated growth arrest signaling. *J Biol. Chem.* **284**, 33006-18 (2009)
- 366 Macleod, G., Bozek, D. A., Rajakulendran, N., Monteiro, V., Ahmadi, M., Steinhart, Z., Kushida, M. M., Yu, H., Coutinho, F. J., Cavalli, F. M. G., Restall, I., Hao, X., Hart, T., Luchman, H. A., Weiss, S., Dirks, P. B. & Angers, S. Genome-wide CRISPR-Cas9 screens expose genetic vulnerabilities and mechanisms of temozolomide sensitivity in glioblastoma stem cells. *Cell Rep.* **27**, 971-86 (2019)
- 367 Rosas-Cruz, A., Salinas-Jazmin, N. & Velazquez, M. a. V. Dopamine receptors in cancer: Are they valid therapeutic targets? *Technol. Cancer Res. Treat.* **20**, 15330338211027913 (2021)
- 368 Bohnsack, K. E., Kleiber, N., Lemus-Diaz, N. & Bohnsack, M. T. Roles and dynamics of 3-methylcytidine in cellular RNAs. *Trends Biochem. Sci.* **47**, 596-608 (2022)

- 369 Mao, X. L., Li, Z. H., Huang, M. H., Wang, J. T., Zhou, J. B., Li, Q. R., Xu, H., Wang, X. J. & Zhou, X. L. Mutually exclusive substrate selection strategy by human M3C RNA transferases METTL2A and METTL6. *Nucleic Acids Res.* **49**, 8309-23 (2021)
- 370 Shi, T., Hu, Z., Tian, L. & Yang, Y. Advances in lung adenocarcinoma: A novel perspective on prognoses and immune responses of cenpo as an oncogenic superenhancer. *Transl. Oncol.* **34**, 101691 (2023)
- 371 Cao, Y., Xiong, J., Li, Z., Zhang, G., Tu, Y., Wang, L. & Jie, Z. CENPO expression regulates gastric cancer cell proliferation and is associated with poor patient prognosis. *Mol. Med. Rep.* **20**, 3661-70 (2019)
- 372 Liu, Z., Chen, C., Yan, M., Zeng, X., Zhang, Y. & Lai, D. CENPO regulated proliferation and apoptosis of colorectal cancer in a p53-dependent manner. *Discov. Oncol.* **13**, 8 (2022)
- 373 Prabhu, V. V., Allen, J. E., Dicker, D. T. & El-Deiry, W. S. Small-molecule ONC201/TIC10 targets chemotherapy-resistant colorectal cancer stem-like cells in an AKT/FOXO3A/TRAIL-dependent manner. *Cancer Res.* **75**, 1423-32 (2015)
- 374 Ralff, M. D., Kline, C. L. B., Kucukkase, O. C., Wagner, J., Lim, B., Dicker, D. T., Prabhu, V. V., Oster, W. & El-Deiry, W. S. ONC201 demonstrates antitumor effects in both triple-negative and non-triple-negative breast cancers through TRAIL-dependent and TRAIL-independent mechanisms. *Mol. Cancer Ther.* **16**, 1290-8 (2017)
- 375 He, L., Bhat, K., Ioannidis, A., Zhang, L., Nguyen, N. T., Allen, J. E., Nghiemphu, P. L., Cloughesy, T. F., Liau, L. M., Kornblum, H. I. & Pajonk, F. Effects of the DRD2/3 antagonist ONC201 and radiation in glioblastoma. *Radiother. Oncol.* **161**, 140-7 (2021)
- 376 Wang, W., Kim, S. H. & El-Deiry, W. S. Small-molecule modulators of p53 family signaling and antitumor effects in p53-deficient human colon tumor xenografts. *Proc. Natl. Acad. Sci. U. S. A.* **103**, 11003-8 (2006)
- 377 Zhang, W. & Liu, H. T. MAPK signal pathways in the regulation of cell proliferation in mammalian cells. *Cell Res.* **12**, 9-18 (2002)
- 378 Yue, J. & Lopez, J. M. Understanding MAPK signaling pathways in apoptosis. *Int. J. Mol. Sci.* **21** (2020)
- 379 Johnson, L. N., Noble, M. E. & Owen, D. J. Active and inactive protein kinases: Structural basis for regulation. *Cell* **85**, 149-58 (1996)
- 380 Gong, G. Q., Bilanges, B., Allsop, B., Masson, G. R., Robertson, V., Askwith, T., Oxenford, S., Madsen, R. R., Conduit, S. E., Bellini, D., Fitzek, M., Collier, M., Najam, O., He, Z., Wahab, B., Mclaughlin, S. H., Chan, A. W. E., Feierberg, I., Madin, A., Morelli, D., Bhamra, A., Vinciauskaite, V., Anderson, K. E., Surinova, S., Pinotsis, N., Lopez-Guadamillas, E., Wilcox, M., Hooper, A., Patel, C., Whitehead, M. A., Bunney,

- T. D., Stephens, L. R., Hawkins, P. T., Katan, M., Yellon, D. M., Davidson, S. M., Smith, D. M., Phillips, J. B., Angell, R., Williams, R. L. & Vanhaesebroeck, B. A small-molecule PI3K α activator for cardioprotection and neuroregeneration. *Nature* **618**, 159-68 (2023)
- 381 Von Kriegsheim, A., Pitt, A., Grindlay, G. J., Kolch, W. & Dhillon, A. S. Regulation of the RAF-MEK-ERK pathway by protein phosphatase 5. *Nat. Cell Biol.* **8**, 1011-6 (2006)
- 382 Liu, F., Iqbal, K., Grundke-Iqbal, I., Rossie, S. & Gong, C. X. Dephosphorylation of tau by protein phosphatase 5: Impairment in alzheimer's disease. *J. Biol. Chem.* **280**, 1790-6 (2005)
- 383 Sager, R. A., Dushukyan, N., Woodford, M. & Mollapour, M. Structure and function of the co-chaperone protein phosphatase 5 in cancer. *Cell Stress Chaperones* **25**, 383-94 (2020)
- 384 Oberoi, J., Dunn, D. M., Woodford, M. R., Mariotti, L., Schulman, J., Bourboulia, D., Mollapour, M. & Vaughan, C. K. Structural and functional basis of protein phosphatase 5 substrate specificity. *Proc. Natl. Acad. Sci. U. S. A.* **113**, 9009-14 (2016)
- 385 Zhi, X., Zhang, H., He, C., Wei, Y., Bian, L. & Li, G. Serine/threonine protein phosphatase-5 accelerates cell growth and migration in human glioma. *Cell Mol. Neurobiol.* **35**, 669-77 (2015)
- 386 Zuo, Z., Dean, N. M. & Honkanen, R. E. Serine/threonine protein phosphatase type 5 acts upstream of p53 to regulate the induction of p21(WAF1/CIP1) and mediate growth arrest. *J. Biol. Chem.* **273**, 12250-8 (1998)
- 387 Hong, T. J., Park, K., Choi, E. W. & Hahn, J. S. Ro 90-7501 inhibits PP5 through a novel, TPR-dependent mechanism. *Biochem Biophys. Res. Comm.* **482**, 215-20 (2017)
- 388 Stanford, S. M. & Bottini, N. Targeting protein phosphatases in cancer immunotherapy and autoimmune disorders. *Nat. Rev. Drug Discov.* **22**, 273-94 (2023)
- 389 Ahanin, E. F., Sager, R. A., Backe, S. J., Dunn, D. M., Dushukyan, N., Blanden, A. R., Mate, N. A., Suzuki, T., Anderson, T., Roy, M., Oberoi, J., Prodromou, C., Nsouli, I., Daneshvar, M., Bratslavsky, G., Woodford, M. R., Bourboulia, D., Chisholm, J. D. & Mollapour, M. Catalytic inhibitor of protein phosphatase 5 activates the extrinsic apoptotic pathway by disrupting complex II in kidney cancer. *Cell Chem. Biol.* **30**, 1223-34 (2023)
- 390 Das, N. D., Niwa, H. & Umehara, T. Chemical inhibitors targeting the histone lysine demethylase families with potential for drug discovery. *Epigenomes* **7** (2023)
- 391 Del Moral-Morales, A., Salgado-Albarrán, M., Ortiz-Gutiérrez, E., Pérez-Hernández, G. & Soto-Reyes, E. Transcriptomic and drug discovery analyses reveal natural

- compounds targeting the KDM4 subfamily as promising adjuvant treatments in cancer. *Front. Genet.* **13**, 860924 (2022)
- 392 Wu, Q., Young, B., Wang, Y., Davidoff, A. M., Rankovic, Z. & Yang, J. Recent advances with KDM4 inhibitors and potential applications. *J. Med. Chem.* **65**, 9564-79 (2022)
- 393 Antolin, A. A., Sanfelice, D., Crisp, A., Villasclaras Fernandez, E., Mica, I. L., Chen, Y., Collins, I., Edwards, A., Muller, S., Al-Lazikani, B. & Workman, P. The chemical probes portal: An expert review-based public resource to empower chemical probe assessment, selection and use. *Nucleic Acids Res.* **51**, D1492-D502 (2023)
- 394 Kornblau, S. M., Xu, H. J., Del Giglio, A., Hu, S. X., Zhang, W., Calvert, L., Beran, M., Estey, E., Andreeff, M., Trujillo, J. & Et Al. Clinical implications of decreased retinoblastoma protein expression in acute myelogenous leukemia. *Cancer Res.* **52**, 4587-90 (1992)
- 395 Lin, A., Giuliano, C. J., Sayles, N. M. & Sheltzer, J. M. CRISPR/Cas9 mutagenesis invalidates a putative cancer dependency targeted in on-going clinical trials. *Elife* **6** (2017)
- 396 Frye, S. V. The art of the chemical probe. *Nat. Chem. Biol.* **6**, 159-61 (2010)
- 397 Ioannidis, J. P. Why most published research findings are false. *PLoS Med.* **2**, e124 (2005)
- 398 Errington, T. M., Mathur, M., Soderberg, C. K., Denis, A., Perfito, N., Iorns, E. & Nosek, B. A. Investigating the replicability of preclinical cancer biology. *eLife* **10**, e71601 (2021)
- 399 Errington, T. M., Denis, A., Perfito, N., Iorns, E. & Nosek, B. A. Challenges for assessing replicability in preclinical cancer biology. *eLife* **10**, e67995 (2021)
- 400 Fernández Pinto, M. Methodological and cognitive biases in science: Issues for current research and ways to counteract them. *Perspect. Sci.* **31**, 535-54 (2023)
- 401 Baker, M. 1,500 scientists lift the lid on reproducibility. *Nature* **533**, 452-4 (2016)
- 402 Protzko, J., Krosnick, J., Nelson, L., Nosek, B. A., Axt, J., Berent, M., Buttrick, N., Debell, M., Ebersole, C. R., Lundmark, S., Macinnis, B., O'donnell, M., Perfecto, H., Pustejovsky, J. E., Roeder, S. S., Walleczek, J. & Schooler, J. W. High replicability of newly discovered social-behavioural findings is achievable. *Nat. Hum. Behav.* **8**, 311-319. (2023)

- 403 Ransohoff, D. F. Rules of evidence for cancer molecular-marker discovery and validation. *Nat. Rev. Cancer* **4**, 309-14 (2004)
- 404 Samsa, G. & Samsa, L. A guide to reproducibility in preclinical research. *Acad. Med.* **94**, 47-52 (2019)
- 405 Cruz, J. V. R., Batista, C., Afonso, B. H., Alexandre-Moreira, M. S., Dubois, L. G., Pontes, B., Moura Neto, V. & Mendes, F. A. Obstacles to glioblastoma treatment two decades after temozolomide. *Cancers (Basel)* **14**, 3203 (2022)
- 406 Neumeier, J. & Meister, G. Sirna specificity: RNAi mechanisms and strategies to reduce off-target effects. *Front. Plant Sci.* **11**, 526455 (2021)
- 407 Zhang, H., Zhang, Q., Tu, J., You, Q. & Wang, L. Dual function of protein phosphatase 5 (PPP5C): An emerging therapeutic target for drug discovery. *Eur. J. Med. Chem.* **254**, 115350 (2023)
- 408 Swingle, M., Ni, L. & Honkanen, R. E. Small-molecule inhibitors of ser/thr protein phosphatases: Specificity, use and common forms of abuse. *Methods Mol. Biol.* **365**, 23-38 (2007)
- 409 Pichavaram, P., Jablonowski, C. M., Fang, J., Fleming, A. M., Gil, H. J., Boghossian, A. S., Rees, M. G., Ronan, M. M., Roth, J. A., Morton, C. L., Zambetti, G. P., Davidoff, A. M., Yang, J. & Murphy, A. J. Oncogenic cells of renal embryonic lineage sensitive to the small-molecule inhibitor QC6352 display depletion of KDM4 levels and disruption of ribosome biogenesis. *Mol. Cancer Ther.*, OF1-OF14 (2024)
- 410 Brown, C. M. & Bidle, K. D. Attenuation of virus production at high multiplicities of infection in *aureococcus anophagefferens*. *Virology* **466-467**, 71-81 (2014)
- 411 Giuliano, C. J., Lin, A., Smith, J. C., Palladino, A. C. & Sheltzer, J. M. MELK expression correlates with tumor mitotic activity but is not required for cancer growth. *Elife* **7** (2018)
- 412 Lin, A., Giuliano, C. J., Palladino, A., John, K. M., Abramowicz, C., Yuan, M. L., Sausville, E. L., Lukow, D. A., Liu, L., Chait, A. R., Galluzzo, Z. C., Tucker, C. & Sheltzer, J. M. Off-target toxicity is a common mechanism of action of cancer drugs undergoing clinical trials. *Sci. Transl. Med.* **11** (2019)
- 413 Sun, D., Gao, W., Hu, H. & Zhou, S. Why 90% of clinical drug development fails and how to improve it? *Acta. Pharm. Sin. B.* **12**, 3049-62 (2022)